

Society of Automotive Engineers
of China (SAE-China)

Editor

Proceedings of SAE-China Congress 2014: Selected Papers



Lecture Notes in Electrical Engineering

Volume 328

Board of Series editors

Leopoldo Angrisani, Napoli, Italy
Marco Arteaga, Coyoacán, México
Samarjit Chakraborty, München, Germany
Jiming Chen, Hangzhou, P.R. China
Tan Kay Chen, Singapore, Singapore
Rüdiger Dillmann, Karlsruhe, Germany
Haibin Duan, Beijing, China
Gianluigi Ferrari, Parma, Italy
Manuel Ferre, Madrid, Spain
Sandra Hirche, München, Germany
Faryar Jabbari, Irvine, USA
Janusz Kacprzyk, Warsaw, Poland
Alaa Khamis, New Cairo City, Egypt
Torsten Kroeger, Stanford, USA
Tan Cher Ming, Singapore, Singapore
Wolfgang Minker, Ulm, Germany
Pradeep Misra, Dayton, USA
Sebastian Möller, Berlin, Germany
Subhas Mukhopadhyay, Palmerston, New Zealand
Cun-Zheng Ning, Tempe, USA
Toyoaki Nishida, Sakyo-ku, Japan
Federica Pascucci, Roma, Italy
Tariq Samad, Minneapolis, USA
Gan Woon Seng, Nanyang Avenue, Singapore
Germano Veiga, Porto, Portugal
Haitao Wu, Beijing, China
Junjie James Zhang, Charlotte, USA

About this Series

“Lecture Notes in Electrical Engineering (LNEE)” is a book series which reports the latest research and developments in Electrical Engineering, namely:

- Communication, Networks, and Information Theory
- Computer Engineering
- Signal, Image, Speech and Information Processing
- Circuits and Systems
- Bioengineering

LNEE publishes authored monographs and contributed volumes which present cutting edge research information as well as new perspectives on classical fields, while maintaining Springer’s high standards of academic excellence. Also considered for publication are lecture materials, proceedings, and other related materials of exceptionally high quality and interest. The subject matter should be original and timely, reporting the latest research and developments in all areas of electrical engineering.

The audience for the books in LNEE consists of advanced level students, researchers, and industry professionals working at the forefront of their fields. Much like Springer’s other Lecture Notes series, LNEE will be distributed through Springer’s print and electronic publishing channels.

More information about this series at <http://www.springer.com/series/7818>

Society of Automotive Engineers of China
(SAE-China)

Editor

Proceedings of SAE-China Congress 2014: Selected Papers



Editor
Society of Automotive Engineers of China
(SAE-China)
Beijing
China

ISSN 1876-1100 ISSN 1876-1119 (electronic)
ISBN 978-3-662-45042-0 ISBN 978-3-662-45043-7 (eBook)
DOI 10.1007/978-3-662-45043-7

Library of Congress Control Number: 2014951721

Springer Heidelberg New York Dordrecht London

© Springer-Verlag Berlin Heidelberg 2015

This work is subject to copyright. All rights are reserved by the Publisher, whether the whole or part of the material is concerned, specifically the rights of translation, reprinting, reuse of illustrations, recitation, broadcasting, reproduction on microfilms or in any other physical way, and transmission or information storage and retrieval, electronic adaptation, computer software, or by similar or dissimilar methodology now known or hereafter developed. Exempted from this legal reservation are brief excerpts in connection with reviews or scholarly analysis or material supplied specifically for the purpose of being entered and executed on a computer system, for exclusive use by the purchaser of the work. Duplication of this publication or parts thereof is permitted only under the provisions of the Copyright Law of the Publisher's location, in its current version, and permission for use must always be obtained from Springer. Permissions for use may be obtained through RightsLink at the Copyright Clearance Center. Violations are liable to prosecution under the respective Copyright Law.

The use of general descriptive names, registered names, trademarks, service marks, etc. in this publication does not imply, even in the absence of a specific statement, that such names are exempt from the relevant protective laws and regulations and therefore free for general use.

While the advice and information in this book are believed to be true and accurate at the date of publication, neither the authors nor the editors nor the publisher can accept any legal responsibility for any errors or omissions that may be made. The publisher makes no warranty, express or implied, with respect to the material contained herein.

Printed on acid-free paper

Springer is part of Springer Science+Business Media (www.springer.com)

Contents

1 The Axis Design and Layout of Automotive Door Hinges	1
Bingyu Zhang, Wei Yu and Yuanhong Wang	
2 Numerical Simulation of the Influence of Additional Aerodynamic Devices on the Aerodynamic Drag of Van-Body Truck	15
Dong Wang, Yansong Wang, Yu Han, Yan Dang, Dengyun Fan and Liguang Li	
3 Study on Matching Performance of the Load-Sensing Valve System with Independent Suspension Vehicles	27
Xiaoyun Si, Wenlun Ma, Yuchao Chen, Hongyu Zheng, Ying He and Zhanfeng Zhang	
4 Optimal Design and Test Research of Rubber Auxiliary Spring for Medium-Sized Truck	39
Fanlong Bu, Yuewei Li, Xiaotao Wu and Zhaoying Liu	
5 Application of Virtual ECU and Large Coverage Testing in the Development of Control Software for a Dual-Clutch Transmission	49
Lionel Belmon, GuangHui Zhang and Ronghui Zhang	
6 Modeling and Analysis of Torsional Vibration on Engine-generator System of Hybrid Electric Vehicle	59
Xiaofeng Ma, Ke Luo, Lijun Zhang, Hongzheng Cheng and Dejian Meng	
7 Pore-forming Technology Development of Polymer Separators for Power Lithium-ion Battery	71
Lina Yu, Dan Wang, Zhongling Zhao, Jian Han, Kejin Zhang, Xinran Cui and Zhou Xu	

8	Studies on the Working Mode of Hyperbranched New Materials STOBA in Lithium-ion Battery Cathode Materials	81
	Xinran Cui, Xinyan Mi, Tingting Cao, Tao Jiang, Huiming Chen, Zhongling Zhao and Kejin Zhang	
9	Preparation and Property of High Heat-Resistant Ceramic Composited PET Separator.	89
	Zhongling Zhao, Dan Wang, Lina Yu, Jian Han, Kejin Zhang, Xinran Cui, Tingting Cao and Shuli Chen	
10	Analysis of Shifting Quality Based on AMT of the Electric Vehicle.	97
	Bing-li Zhang, Xin-ping Wu, Zhong-wen Hu and De-ming Zhou	
11	Electric Vehicle Fault Diagnosis System Based on CAN-Bus	105
	Bingli Zhang, Wenjie Shi and Andong Ge	
12	Study on the Bending Fatigue of a Diesel Engine Crankshaft	111
	Shuai Teng, Shufen Wang, Zhangtao Yao, Zhongtai Li, Lei Guo, Hao Li and Jie Liu	
13	Simulation and Structural Design of AMT Switch Valve's Coil. . .	119
	Ling-ya Lu, Ji-hua Wang, Rong Fan, Yu-sheng Ju and Yong-ming Zhang	
14	Effect of Compression Ratio on Internal Combustion Rankine Cycle Based on Simulations.	129
	Yang Gao, Liguang Li, Xiao Yu, Jun Deng and Zhijun Wu	
15	The Organic Rankine Cycle System Development for Heavy-Duty Diesel Engine	139
	Junqi Dong, Jianzhang Wang, Rongyou Zhang and Bin Wang	
16	Study of Gasoline Engine Sticking.	149
	Yong He, Haizhu He, Qin Wang, Haihong Lin, Yunping Pu, Yang Qiu, Zhangsong Zhan, Long Min, Wei Deng, Qian Xu and Honggang Gou	
17	High Temperature Dependence of a Pulse Tube Engine	157
	Shaowei Zhu	
18	Technology Trends in Commercial Vehicle Base Engine Development.	165
	M. Neitz, A. Wiartalla, S. Lauer and P. Methfessel	

19	Line Filter-Based Parking Slot Detection for Intelligent Parking Assistance System	175
	Mengyang Fan, Zhencheng Hu, Kazukuni Hamada and Hui Chen	
20	A Hierarchical Road Identification Method for ABS Control	183
	Yue Shi, Hui Lu and Fan Yu	
21	NH3 Generator for Enhanced Low-Temperature SCR Performance; An Option also for Retrofit	191
	Winfried Steve Doelling, Yuhu Zhang, Sanxia Wang, Jun Li, Jan Margraf, Marco Mrosek, Thorsten Haake, Christof Luecking and Wolfgang Frank	
22	Material Data Management During Product Development for Environment Protection.	205
	Cheng Gao, Conghong Tu, Zhaojun He and Changxia Ma	
23	Profit Path Selection for Passenger Vehicle Enterprises Under Energy-Saving Target Constraints—Based on Cost Benefit Analysis	211
	Renzhi Lv, Jihu Zheng and Peng Zhang	
24	Improvement of Formability of Y-Shaped Tubular Part of 6016 Aluminium Alloy by Pulsating Hydroforming	221
	Zhimin Liu, Xialing Wu, Dongsheng Zhang, Yi Ding, Liyan Gao and Xiang Yan	
25	The New Technique of Servo-Flexible Stamping Applied in the Al Sheet Forming	227
	Zhimin Liu, Yi Ding, Xialing Wu, Dongsheng Zhang, Wenming Chen and Bo Gao	
26	Analysis of the Assembly Dimensional Chain About Automotive Exterior Parts and Optimization of Tolerance Allocation	235
	Changming Liang	
27	The Research of Dimensional Design “2MM Project” System and the Key Role in the Self-owned Vehicle Platform.	247
	Zhihan Zhou, Peng Tan, Changming Liang and Xiangfei Wang	
28	Optimization Design Method of School Bus Structure Lightweight on the Rollover Safety	261
	Ye Yu, Liang Ying, Ping Hu, Yang Yu, Xianda Li and Rong Fan	

29	Parameters Design of Dynamic Vibration Absorbers for Vehicle Half-shafts	269
	Yang Wang, Hui Wang, Liang Dong, Bowen Dong and Hongwei Wang	
30	Simulation and Validation of Engine Valvetrains System Dynamics	277
	Wenbo Niu, Lechao Tang, Wenhui Jiang and Tiancheng Li	
31	The Vehicle NVH Development and Engineering Application of the Lightweight Sound Package.	291
	Jun Zhang, Guanni Zhu, Xiaoxuan Zhang, Hongyu Liu and Congguang Liu	
32	Exhaust Hook Model Prediction of Vehicle Condition Based on Frequency Response Method	301
	Zhangming Su, Chao Ren, Zhongbiao Gou and Yanghui Xu	
33	An Investigation on Turbocharger Whine Noise.	313
	Zhang Song Zhan, Jin Yang, Jin Cai Yang, Jun Lan, Gang Liu, Yong Jiang Xu, Jin Cai and Liang Zhang	
34	Phenomenon and Analysis of Low-Frequency Standing Wave Inside Exhaust System.	325
	Shuo Zhang, Jian Pang, Haiyan Zhang, Liang Yang and Wei Qing	
35	Crack Identification of Vehicle Drive Axle Half Shaft Rotor System	335
	Daogao Wei, Bo Wang and Meiling Hu	
36	Study on Second-Order Vibration Caused by Secondary Couple of Cardan Joint for a 4WD Driveline.	345
	Yuanfeng Xia, Jian Pang, Chengtai Hu, Cui Zhou and Zhijun Zhang	
37	Optimization of Front Windshield Lower Beam Welding Assembly Based on NVH Performance.	355
	Cheng Yanan, Deng Feng, Ping Zhang and Haoliu	
38	Optimization Design Method of 4 × 4 Bus Power Train Layout	365
	Qing Chen, Ying Fu and Yongkun Hou	

39 A Study on the Noise Capability of Center Air Vents System 379
 Liqiong Mo, Liangda Li and Zhong Yang

40 Design and Development of Pop-up Engine Hood System with Dual Elastic Buffer and Evaluation of Performance of Pedestrian Protection 389
 Xinxian Li, Jiqing Chen and Fengchong Lan

41 Estimation of Vehicle Sideslip Angle with Adaptation to Road Bank Angle and Roll Angle 403
 Jie Ling, Hui Chen and Fan Xu

42 Vehicle Guiding System Through Image Processing in Crash and Misuse Tests 411
 Eloi Boix, Adrià Ferrer, Sandra Fernandez and Xavier Sellart

43 Vibration Isolation Performance Research of Commercial Truck’s Cab Suspension System Based on Road Load Data 425
 Xin Yan, Di Jiang, Zhongxiao Wang and Maolin Guo

44 A Normalized Approach for Evaluating Driving Styles Based on Personalized Driver Modeling. 433
 Bin Shi, Wuqiang Meng, Hui Liu, Jie Hu and Li Xu

45 Research on Performance Test Method of Lane Departure Warning System with PreScan 445
 Qiang Zhang, Daxing Chen, Yusheng Li and Keqiang Li

46 Research of Distributed Vehicle Electronic and Electrical Architecture 455
 Libo Zhang, Dongfeng Zhao and Junting He

47 The Gasoline Engine Starting Strategy Based on Air–Fuel Ratio Control 463
 Zhongtian Chen, Kai Wang, Chen Shen, Feng Xu, Long Qin, Jianbo Zheng, Xue Lei and Fanwu Zhang

48 Research on Diagnostic Strategy of Planar-type Oxygen Sensor Deactivation on Gasoline Engine EMS 471
 Long Qin, Feng Xu, Jianbo Zheng, Fanwu Zhang, Yongyi Huang, Zhongtian Chen, Xue Lei and Liuchun Yang

49 Airflow Estimation Control Strategy Based on Speed Density Method 483
Xue Lei, Chen Shen, Jianbo Zheng, Yao Zhou, Zhongtian Chen, Chunjiao Zhang, Min Chen, Long Qin and Fanwu Zhang

50 A Development Report of an Accurate Method of Detecting Systematic Refrigerant Leak Rate for Automotive HVAC Systems. 489
Kelvin Zhai, Zongshan Chen and Zhiping Ning

51 Compact Oxygen Sensor for Motorcycles: Concept of Simple Heaterless Sensors 497
Kinji Hodaira, Takehiro Watarai and Zhenzhou Su

52 HMAC-SHA1 Applied in the Diagnosis Service for Security Access 507
Yangchun Li, Dehua Zhao, Honglei Li and Zutao Kou

Chapter 1

The Axis Design and Layout of Automotive Door Hinges

Bingyu Zhang, Wei Yu and Yuanhong Wang

Abstract The method for automotive door hinge axis design and layout is introduced. An example of a front door hinge assembly is presented to show the detailed strategy and influence factors in door hinge axis design and layout, and then, their influence on other accessories of the door is illustrated.

Keywords Door hinge · Axis design · Layout

1.1 Introduction

The automotive door hinge assembly, which is used to connect the door with body and make the door rotate on a predefined axis, is an essential component for successfully opening and closing the doors.

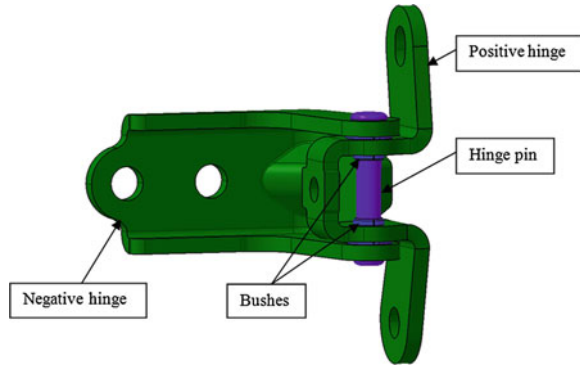
1.1.1 Basic Construction of Door Hinge

A commonly used hinge assembly is discussed in this paper. It contains 4 parts as shown in Fig. 1.1: negative hinge, positive hinge, hinge pin, and bushes.

The negative and positive hinges are fixed on the side panel of body and the door by welding or with bolts, respectively. The hinge pin, acting as the rotating axis of the hinge or even the door, is used to connect the above both parts. Therefore, the hinge pin will be subject to frictional load when the door is rotating, and the self-lubricating bushes are used to decrease the wear of hinge pin.

B. Zhang (✉) · W. Yu · Y. Wang
Changan Auto R&D Center, Beijing, China
e-mail: zby9021107@sina.com

Fig. 1.1 Construction of the commonly used door hinge assembly



1.1.2 Basic Functions of Door Hinge

1. Connect the door to the body so as to ensure their relative position.
2. Ensure the successful opening and closing of the doors.

1.1.3 Basic Requirements of Design and Layout of Hinge Axis

The following basic requirements should be met in design and layout of hinge axis.

1.1.3.1 Matching Surfaces

The matching surfaces between the hinge and door (or car body) should be smooth to ensure normal performances.

1.1.3.2 Coaxiality

When two or more hinge assemblies are working together, the coaxiality of all the hinge axes becomes the most important precondition for hinge layout.

1.1.3.3 Angle of Door Opening

The maximum opening angle of the hinge is directly determined by the opening degree of the door, which is usually defined by the packaging engineers. The door opening degree is relative to the space requirement for passenger getting on and off,

the structure features of A-pillar and B-pillar, etc. In general, the maximum opening degree of the hinge is 5–8° more than that of the door.

1.1.3.4 Performance

The automotive door is hanged on the side panel of the vehicle by using the upper and lower hinge assemblies. When the door is closed, it is supported by the hinges, the door lock, and the lock catch fixed on the B-pillar. When the door is opened, it is supported only by the hinges. So we should design a reasonable structure and choose suitable materials to enhance the stiffness and strength of the hinges, which helps to decrease the sagging of the doors.

1.2 Methods of Hinge Axis Design and Layout

There are several layout and design methods for hinges of various structures. In this paper, an example of a kind of commonly used hinge is presented to introduce the highlights in the axis design and layout. The most important tasks are to design the rotating axis and define the position of the hinge, which determine the kinematic property and force distribution of the door.

1.2.1 Hinge Axis Design

Several influence factors should be taken into account when designing the axis of a hinges.

1.2.1.1 Input Conditions

The following information should be definitely determined as input conditions for axis design.

Exterior CAS

Concept A Surface (CAS) is a rough external surface of car body, which is designed by the styling engineers and provides a precondition for automobile layout.

Maximum Opening Degree of the Door

As mentioned above, the maximum opening degree of the hinge is generally 5–8° more than that of the door.

At the early stage of the styling feasibility analysis, several questions should be focused on whether there is enough space for the passengers to get on and off easily; whether the instrument panel can get into the cabin successfully; and whether the structures of A-pillar and B-pillar are appropriate.

After all the above questions have been considered, the maximum opening degree of door will be finally determined.

Weight of the Door

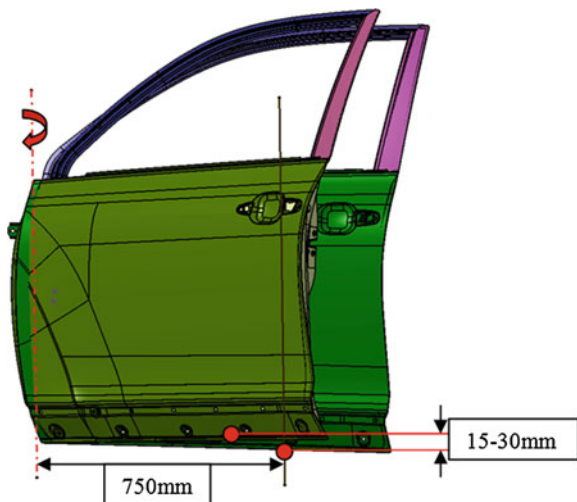
Although the accurate weight of the door cannot be given during door designing, the size of the door can be predicted according to the CAS, and then, the weight can be estimated by comparing its size, material, and structure with those of the reference vehicle door.

Door Lifting Height

The door lifting height is defined as the maximum lifting distance of the door measured while opening the door. The measurement point, as shown in Fig. 1.2, is located at the bottom edge of the car door and 750 mm away from the hinge axis.

This lifting height produces a self-closing tendency of the door, which helps to reduce the operating force while closing the door. But if the lifting height is too large, it will create a large force while opening the door. Therefore, a reasonable lifting height should be defined in order to provide convenience during opening and closing of the door.

Fig. 1.2 The measurement point for door lifting height



According to Chinese standard CJ137-1990, the transverse slope of the pavement is 2 %, and the maximum margin height is 200 mm [1]. In general, the recommended range of lifting height is from 15 to 30 mm.

Gap Value and Cut Line

Considering the appearance quality and the manufacturing precision, the styling engineers, dimension engineers, and structure engineers cooperate to determine the trend of cut line and the gap value. Then, optimization and adjustment are carried out according to the latest state of part layout. Finally, the cut line should not only meet the appearance quality requirements, but also have high manufacturing accuracy.

Steps to estimate the position of cut line (prepared for next stage):

1. Gap value: Ensure suitable gap values between fender and front door or front door and rear door when the doors are closed. The styling engineers preferably select the smallest possible gap value. However, the dimension engineers need a larger one. Therefore, a reasonable value must be determined to balance both aspects.
2. The cut line sketch (in CATIA V5): As basic principles of cut line, the fluency and smoothness are especially important. Make sure that the trend of cut line must be consistent with the vehicle style, and greater curvature must be avoided. Considering the matching relationship between the cut line and the fender, A-pillar, or rearview mirror, it is required that the x -direction distance between the cut line and the edge of front wheel eyebrow shall be no less than 80 mm. Furthermore, the transition from the upper parts of cut line to the A-pillar or rearview mirror must be smooth and natural.
3. Constraint point adjustment: Control the trend of cut line by adjusting the horizontal and vertical coordinates at 6–7 constraint points.

1.2.1.2 Preliminary Design of Hinge Axis

In this section, we mainly discuss the influence factors during preliminary designing of the door hinge axis, which is related to CAS, hinge axis angle, and the x -direction and y -direction distances between hinge axis and the outer door panel.

Requirements of CAS

The hinge layout and the CAS can be simultaneously designed by the commodity departments. The hinge layout is based on the body side arc and characteristics line provided by the CAS. Above the belting line, the thickness of the door decreases radically in the y -direction, and thus, there is not enough space to arrange these hinges. Therefore, the upper hinge assembly is usually arranged under the belting line.

Preliminary Determination of Hinge Axis Angles

Hinge axis angles should be considered in two directions. The longitudinal angle is defined as the angle between the projection of the hinge axis onto the $y = 0$ plane and the z -axis. And the lateral angle is defined as the angle between the projection of the hinge axis onto the $x = 0$ plane and the z -axis.

The door hinge axis angles are directly related to the door lifting height. In order to produce a self-closing tendency, the hinge axis should have a certain inward angle. Usually, the recommended value of this angle is $0\text{--}3^\circ$ on the basis of embedded analyzing and iterative practicing.

Considering the requirements of styling, the cut line position, and the safety gap between the door and the surrounding parts when opening and closing the door, a front or back rake angle seems to be necessary. It is suggested that this angle is $0\text{--}2^\circ$ after repeated practicing and verification.

Distances Between Hinge Axis and Outer Door Panel

Distance in y -direction should be no less than 20 mm based on the theory of dimension chain, as shown in Fig. 1.3. Dimension A (the distance between the hinge axis and the outer surface of the hinge) is about 10 mm. Dimension B (the distance between the outer surface of the hinge and the internal surface of the inner door panel) is about 4 mm. Dimension C (the thickness of the inner door panel) is always ranged from 1.2 to 1.6 mm. Dimension D (the distance between the outer surface of the inner door panel and the internal surface of the outer door panel) is at least 3 mm. Dimension E (the thickness of the outer door panel) is always ranged from 0.6 to 0.8 mm.

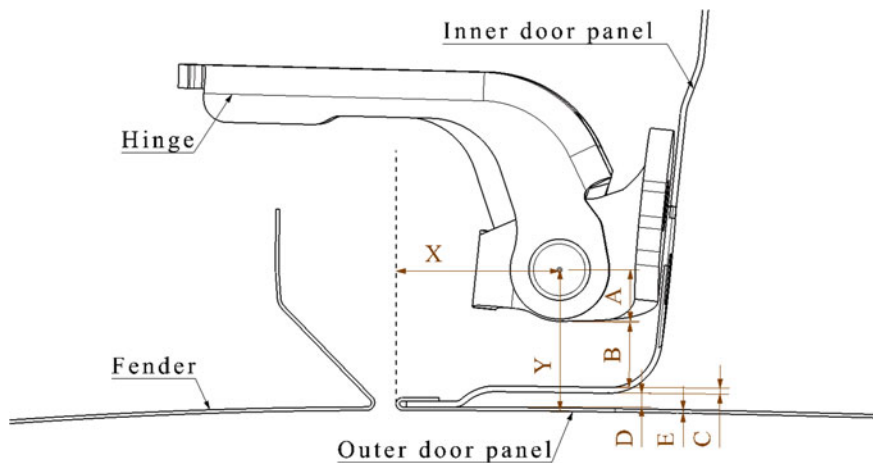


Fig. 1.3 Minimum distance between the hinge axis and the external surface of the door in y -direction

It is recommended that the distance in the x -direction is larger than that in the y -direction. In addition, smaller distance between the hinge axis and the front part of the vehicle will create less risk of the door interfering with the side body. Therefore, the x -direction distance is limited to a maximum of 50 mm, and 40 mm is usually the best choice.

Based on the principle of two points determining a line, two space points a and b are designed in the software CATIA V5, and the coordinates of the two points can be adjusted. If the line determined by a and b meets the requirements in Sect. 1.2.1.2, the preliminary hinge axis, which still needs to be optimized, is obtained.

1.2.1.3 Fine Adjustment

Now, the preliminary hinge axis has been obtained, and then, the next step is to adjust it accurately.

As an example, a front door and a fender are shown in Fig. 1.4. Firstly, the geometric data of the door and the fender are created in CATIA V5 according to the cut line and the gap value from the CAS. In order to ensure accuracy of the motion analysis, flanges and hems should be created in the CATIA data.

Finally, the reasonable cut line and hinge axis are obtained by adjusting the coordinates of the two points a and b repeatedly. In this process, the following influence factors shall be considered:

Minimum Motion Clearance

When the door is moving, it is expected that the minimum clearance between the outer door panel and the fender exceeds 2.5 mm.

The method of digital mock-up (DMU) motion analysis is usually applied to verify whether the minimum clearance is proper or not.

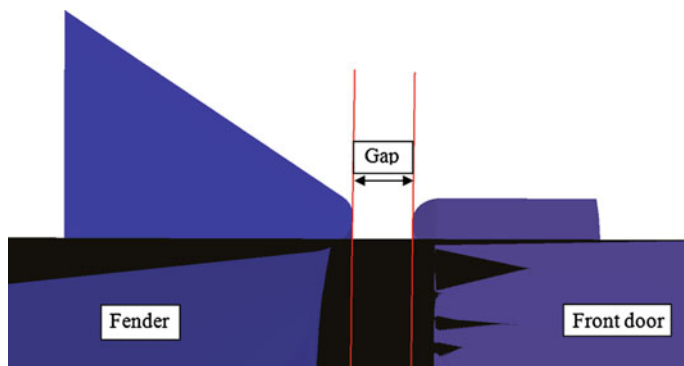


Fig. 1.4 Door and fender data created in CATIA V5 based on the CAS

Taking into full account the possible errors occurred in manufacturing and assembling, the motion of hinge axis is defined in a $4\text{ mm} \times 4\text{ mm}$ square area. When the hinge axis is moving forward and inward, the minimum clearance gets smaller, and in opposite, it gets larger.

This section discusses the worst state, which means the following conditions happen at the same time:

1. The gap value between the front door and the fender is 1 mm smaller than the actual value.
2. The hinge axis moves 2 mm toward the front of the vehicle.
3. The hinge axis moves 2 mm toward the inside of the vehicle.

If the hinge axis is in the worst state, as the point A shown in Fig. 1.5, the door must avoid interfering with the fender while opening or closing the door.

Door Lifting Height

It is evident that a significant relationship exists between the hinge axis angle and the door lifting height. A front or back rake angle decreases the lifting height. On the contrary, an inward or outward rake angle increases the lifting height.

Supposing that the inward rake angle has a fixed value and a front or back rake angle exists, the lifting height will considerably change with the door opening angle.

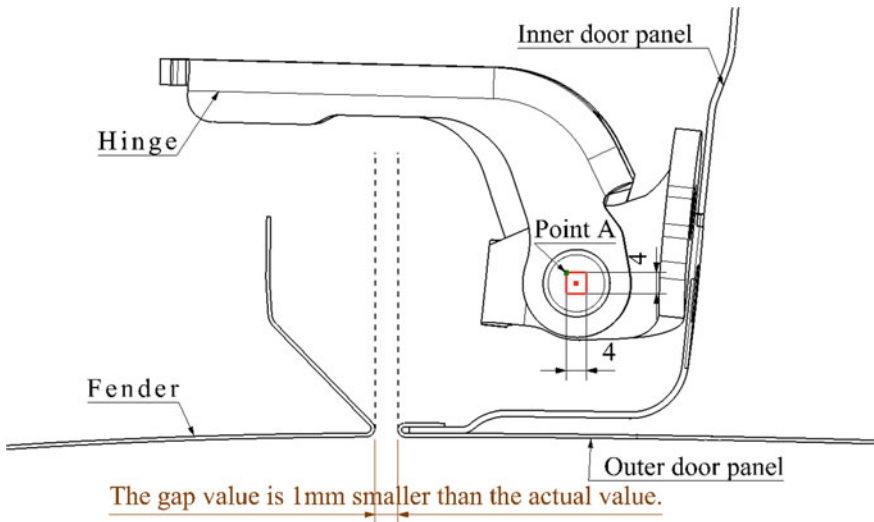


Fig. 1.5 The hinge axis in its worst condition

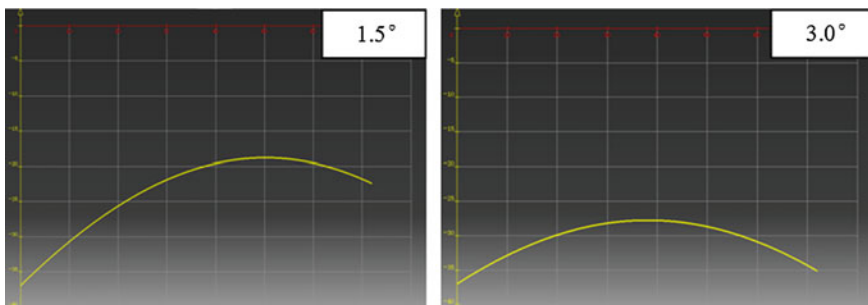


Fig. 1.6 The changing *curve* of door lifting height

1. Set the inward rake angle to 2° and the front rake angle to 1.5° and 3°, respectively

For these two states, the changing curves of lifting height are shown in Fig. 1.6. The horizontal axis shows the door opening angle, and the vertical axis shows the door lifting height. At the first stage of opening the door, the value of lifting height increases until it strikes a peak value, and then, the value decreases.

Comparing the two curves in Fig. 1.6, it is found that the peak value appears around the half opening angle of the limiter when the front rake angle is 3°. But the peak value occurs around the full opening angle of the limiter when the front rake angle is 1.5°.

2. Set the inward rake angle to 2°, the front rake angle to 0°, and the back rake angle to 1.5°

For these two states, the changing curves of lifting height are shown in Fig. 1.7. The lifting height apparently increases as the increase of the door opening angle.

For the front door, the curve shown in Fig. 1.6 (1.5°) is recommended. In this state, the operating force for opening and closing the door is appropriate.

For the rear door, the curve shown in Fig. 1.7 is recommended.

Actually, which of those curves is suitable depends on the structure, the styling, and the performance demands.

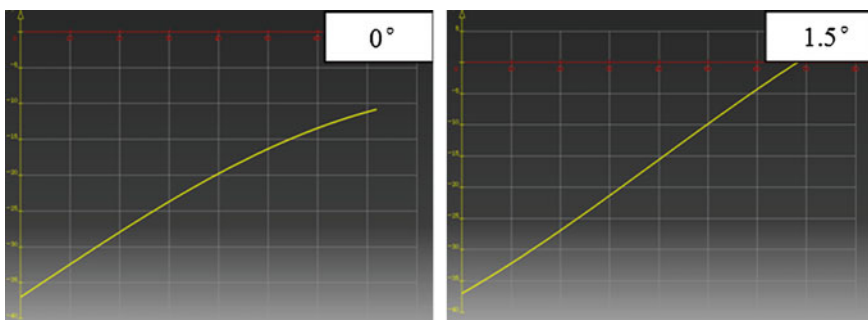


Fig. 1.7 The changing *curve* of door lifting height

1.2.2 Layout of Hinges

This section discusses how to arrange these hinges. Since the hinge axis has been already obtained, in order to determine the position of the hinge, the following factors should be highlighted: the structure of the hinge, position of hinge in the z -direction, distance between the upper and lower hinges, and minimum distance between the door and the hinge including bolts. All these factors constrain and affect each other.

1.2.2.1 Hinge Selection

For engineers, if the functions and performances of the hinge meet the related requirements, the best way to select the right hinge is to use as much more existing products as possible so as to enhance the generalization rate and cut the development cost.

However, in some specific cases, existing products cannot meet all the function and performance requirements, and thus, the material or structure of these hinges must be redesigned.

1.2.2.2 Position in the z -Direction

The position of the lower hinge is determined first. Considering the requirements of the installation space, the structure of the door, and the punching technique of the door panels, the distance between the lowest side of the hinge and the lower edge of the door should be generally more than 130 mm.

The position of the upper hinge in the z -direction is determined according to the design principle of the distances between the upper and lower hinges.

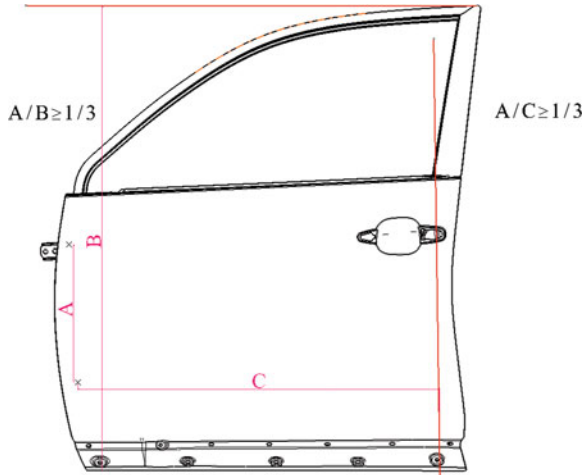
The design principle requires as larger distance as possible if the structure allows. The reason is that the larger the distance, the smaller the stress on the hinges in the x -direction, and it can effectively prevent the sagging of the assembled door.

As shown in Fig. 1.8, the value of A , which is the distance between the upper and lower hinges in the z -direction, is required no less than $1/3$ of the height of the door. The value of A/C , where C is the distance between the door hinge axis and the meshing point of the lock in the x -direction, is required no less than $1/3$.

1.2.2.3 Minimum Distance Between the Door and the Hinges

Based on repeated practice, the distance between the outer door panel and hinges including bolts is required at least 5 mm. If the maximum opening angle of the door is increased by 5° , the distance is required at least 3 mm.

Fig. 1.8 Distance requirements for the upper and lower hinges



1.3 Relationship with Other Accessories [2]

The design and layout of hinge axis provide the input conditions for the design of several accessories of the door. Meanwhile, the layout and design of the accessories constrain hinge layout in turn when the door hinge fails to meet any requirements of structures and arrangement of the accessories, and the readjustment of hinge layout seems to be essential.

1.3.1 Limiter of the Door

This section discusses the relationship between the hinge axis and the limiter layout. The hinge axis is one of the two rotating axes of the limiter, and the other is the axis of the limiter itself. These two axes must be mutually paralleled. The distance between the two axes is usually ranged from 60 to 80 mm.

The limiter should be arranged between the upper and lower hinges in the z -direction, the position of which can be determined by the actual situation. While opening the door, the motion clearance between the limiter and all the surrounding parts must be larger than 10 mm.

1.3.2 Door Lock

The lock should be arranged between the upper and lower hinges in z -direction and no lower than the center of gravity of the door. It is better to arrange the lock nearby the upper hinge.

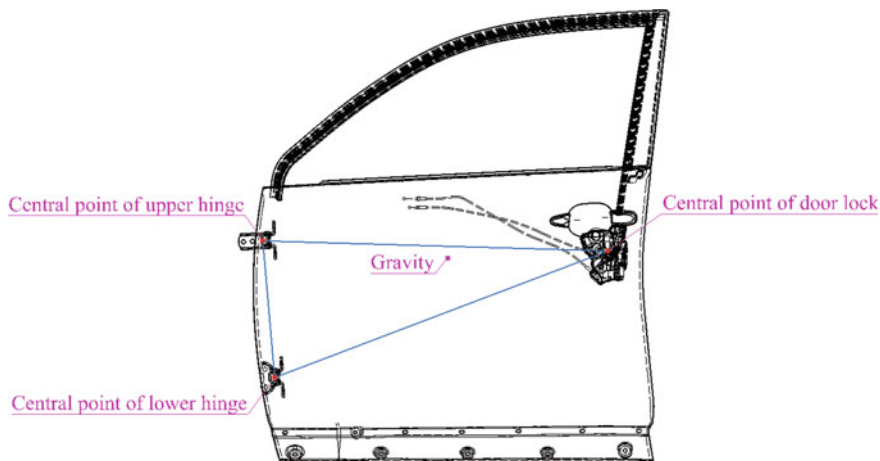


Fig. 1.9 Arrangement of the door locks

To ensure the reliability and stability of the door, its center of gravity must be located in the triangular region determined by central points of the upper and lower hinge and the door lock, as shown in Fig. 1.9.

The meshing plane of the lock and the lock pin must be perpendicular to the axis of hinge.

1.3.3 Front Edge of the Door

The hinge axis may affect the position of the door front edge and thus the sealing system and convenience of final assembly parts passing in or out. Therefore, while designing the front edge, the influence from the hinge axis should be considered. It is necessary to adjust the hinge axis in order to meet the requirements of the front edge design.

1.4 DMU Motion Analysis

DMU motion analysis is a general method which is used to check the assembling relationship, gaps, and motion tracks of various parts in the vehicle.

After both the axis and position of a hinge are determined, a DMU analysis should be done to check whether the gaps are reasonable during motion of the door.

All the front door, fender, rear door, rearview mirror, and side body are combined into one digital file, and a DMU kinematic simulation is created to analyze the process of opening and closing the door.

1.5 Conclusions

A front door is taken as example to introduce the methods of designing the hinge axis and determining the position of hinges, which can regulate the hinge layout in vehicle development.

Actually, the layout should be flexible according to specific situation, and repeated operations are implemented in each step. Various factors shall be considered while designing to get a reasonable layout, satisfy the passenger's demands, and obtain a vehicle most close to the ideal.

References

1. CJI37-1990 Code for transport planning on urban road
2. GB 15086-2013 Motor vehicles' door locks and door retention components performance requirements and test methods

Chapter 2

Numerical Simulation of the Influence of Additional Aerodynamic Devices on the Aerodynamic Drag of Van-Body Truck

Dong Wang, Yansong Wang, Yu Han, Yan Dang, Dengyun Fan and Liguang Li

Abstract With CFD software, the 3D flow field of a van-body truck and its aerodynamic drag coefficient are obtained based on numerical simulation. The Cd optimization of the truck is carried out by installing additional aerodynamic devices on the research above. Simulation results show that taper part installed on the tail of van postpones the flow separation, weakens tail vortex, and reduces the Cd. The wind deflector installed on the driver's cab minimizes the incoming flow that impacts the top of the van, especially the part higher than the driver's cab, and the airflow into the gap between driver's cab and van decreases, with lower pressure. As a result, the pressure drag of the driver's cab increases, while that of the van it decreases. And pressure drag of the whole vehicle is reduced with the Cd.

Keywords Van-body truck · CFD · Aerodynamic drag · Additional devices

2.1 Introduction

With the development of highway, and the growing transport demand, the van-body truck has become an important pillar of road transportation. Although the cost of a van-body truck is high, the ownership and operation speed continues to escalate because of its high transport efficiency and convenient handling; at the same time, the fuel economy of van-body truck has received more attention. Under the background of high efficiency and environmental protection in the world, energy conservation and emission reduction for truck have become over increasing stronger [1].

Conventional energy saving and emission reduction techniques include gains in fuel efficiency, optimization of exhaust system, lightweight technique, and so on [2].

D. Wang (✉) · Y. Wang · Y. Han · Y. Dang · D. Fan · L. Li
School of Automotive Studies, Tongji University, 4800 Cao'an Road,
Shanghai 201804, China
e-mail: wangdong@tongji.edu.cn

As for private cars, hybrid and new energy technologies are extensively used, and alternative fuel cars have widely deployed. The demand for transporting goods determines the truck with very good power performance, and thus, it starts from optimizing shape and using new materials and continues to reduce the truck's emissions. One important aspect of energy saving and emission reduction is vehicle aerodynamics, and it is one of development directions of truck to save fuel with lowering air drag. The influence from additional aerodynamic devices on van-body truck's aerodynamic drag and the reason for the influence are investigated with numerical simulation in this paper.

2.2 Numerical Simulation

2.2.1 Geometric Model

The object for the study is one domestic van-body truck; the overall dimensions are 7,260 mm \times 2,600 mm \times 4,000 mm, as shown in Fig. 2.1. The model consists of engine compartment, radiator, gearbox, cab, container and chassis, as well as the features of rearview mirror, air filter, suspension, fuel tank, battery, wheels and wheel cover, and so on, and thus, the model is close to real structure.

2.2.2 Computation Domain and Mesh Generation

To simulate the flow field around the truck, a rectangular boundary model is built. It is twice vehicle length in front of the truck and 7 times vehicle length behind the truck along length in order to make the trailing vortex fully developed, while it is twice vehicle width in both sides and 4 times vehicle height. The blockage ratio of the numerical model is 4 %.

In order to achieve high quality of shell element, the triangular element is used to mesh the complicated parts, and cracks and bolt holes are ignored because of their

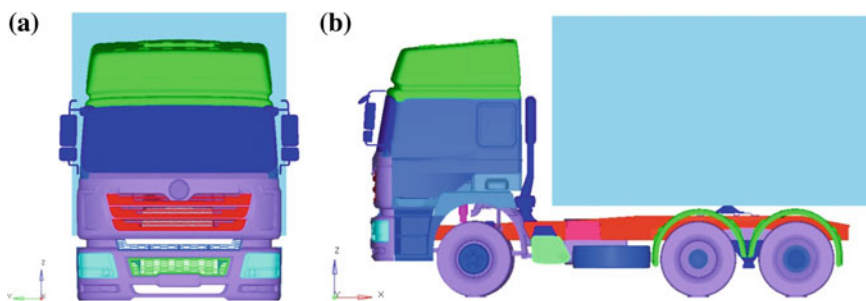


Fig. 2.1 Geometric model. **a** Front view. **b** Side view

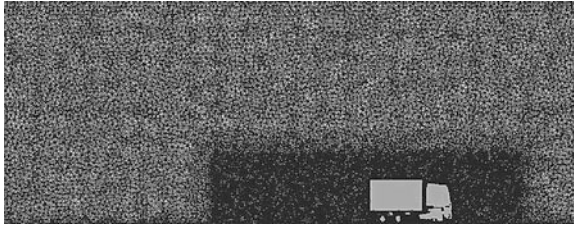


Fig. 2.2 Grid on the section $y = 0$

very weak effect to the truck's aerodynamic characteristics. Tetrahedral meshes are used to simulate the flow field, and the overall elements are 12 million. The flow field around the moving truck which is similar to blunt body with high Reynolds number is high turbulent. In order to get more accurate flow field, the density of the computing domain around the truck is increased as shown in Fig. 2.2.

2.2.3 Boundary Conditions

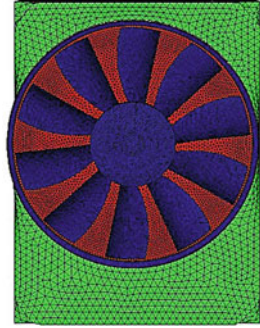
There are three kinds of flow boundary conditions used in the simulation: external boundary condition, porous media approach, and MRF fan. The moving velocity of the truck is 25 m/s, and a standard atmospheric pressure and normal atmospheric temperature are assumed. The boundary conditions of a numerical wind tunnel are given in Table 2.1.

The condenser, intercooler, and radiator located in the engine compartment cannot be fully penetrated. And it is assumed that their cores are simulated with porous media approach, which the condenser intercooler and radiator are treated as ventilation boundary with resistance coefficient. The pressure drop is simulated in the thickness direction with the porous media model and replaces the complicate structure with stable pressure change. For saving time and resource of the calculation, it is highly recommended to use the MRF method in front-end flow

Table 2.1 External boundary conditions

Surface	Boundary condition
Inlet	Velocity inlet, $u = 25$ m/s, $v = w = 0$
Outlet	Pressure outlet, standard atmospheric pressure
Ground	No slip ground ($u = v = w = 0$)
Slide and top	Stationary wall
Body surface	Stationary wall
Condenser, intercooler, and radiator	Porous media approach
Fan	MRF

Fig. 2.3 Grid around the fan



simulation [3]. When the MRF model is built, it is divided into motive region and static region as shown in Fig. 2.3. The fan rotation area is the uniform motion region, and the computation domain outside the fan rotation area is the static region.

2.2.4 Solution Parameters

The study object is a van-body truck with complicated shape. Air flows in and on the truck on which there are many components whose curvature changes sharply can cause flow separation. As a result, the turbulence model is employed with RNG k- ϵ model and non-equilibrium wall function for better adaptability. The convection term of the control equation iterates with second-order upwind scheme after a certain number of iterations of the first-order upwind scheme. The velocity–pressure couple method is the SIMPLE algorithm [4].

2.3 Results and Analysis

2.3.1 Resistance Characteristics Analysis

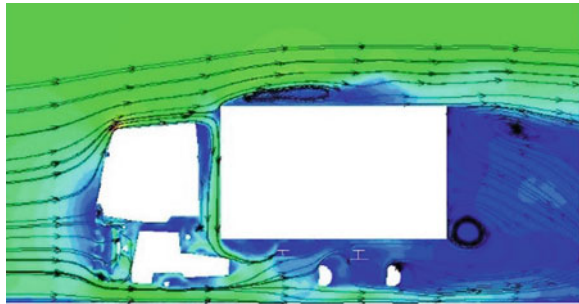
The coefficient of drag for the truck is 0.5629 where the aerodynamic drag of the container contributes the most and then the cab, the wheel, and other components, as shown in Table 2.2.

2.3.2 Analysis of External Flow Field

Figure 2.4 shows the streamline around the truck on the section $y = 0$, in which the incoming flow arrives at the cab and then is separated into 3 parts. Part one of the flow slips the windshield and flows over the cabin toward the rear part of the vehicle; part two of the flow goes through the grill toward the engine compartment

Table 2.2 Aerodynamics drag of heavy truck

Component	Drag coefficient	Proportion
Cab	0.1522	27.04 %
Container	0.2722	48.36 %
Rearview mirror	0.0177	3.15 %
Engine	0.0126	2.23 %
Driving system	0.0941	16.72 %
Underbody and other attachments	0.0141	2.5 %
Total	0.5629	/

Fig. 2.4 Streamlines in section $y = 0$ 

which provides the cooling airflow for parts in the engine compartment; part three of the flow goes from the lower of the cab to the rear of the vehicle.

The airflow separates above the leading upper corner of the container since there is a sharp turning. Some of the airstream separates, and vortices occur in the front of the container and above the container. The airflow above the vortex passes by the vortex toward the end of the container, and airstream twists down on the cross section of the container so that a downwash vortex is generated. Some airstream flows down to the gap and is separated at the corner of the tail edge of the cab, some of which forms vortex, and the rest bypasses the vortex and flows down through the chassis and finally goes out of the vehicle. On the cross section of the tail of the container, the airstream flows up and then forms an upwash vortex. At the bottom of the truck with complicated structure, many small vortices form which are dragged to the rear of the truck when advancing. Those vortices merge into large-scaled tailing vortices x with the downwash vortex and the upwash vortex.

The pressure distribution of the flow field around the truck depends on the airstream's movement when it flows around the vehicle body. When the truck is moving, the incoming airflow impacts the front fascia to form a stagnation point as shown in Fig. 2.5. Therefore, the highest positive pressure is located at the front fascia of the vehicle. On the front side of the container, especially in the region higher than the cab, the airstream is hampered with higher pressure. The airstream flows along the front cab, and the pressure decreases gradually. The region near the grill in the front of the fascia is of the positive pressure. Around the corners of the



Fig. 2.5 The pressure contour of section $y = 0$

windshield and the cab, the velocity of the airstream is higher compared with the narrow region of negative pressure. At the front of the cab’s upper wall, the airstream separation causes a negative pressure region.

2.3.3 Analysis of Internal Flow Field of Engine Compartment

As shown in Fig. 2.6, the incoming flow flows into the engine compartment through its bottom and the grill. Most of the airstream goes backward to provide the cooling air for heat-dissipating parts. The airstream partially flows over the cooling module since the air is blocked and directly goes toward the rear of the engine compartment and then flows into the chassis. There are also some airstreams that are directly pumped by the cooling fan into its rotating region from the bottom of the engine compartment, without going through the radiator, which does not give full cooling effect to lower the efficiency of the cooling module and to increase the driving resistance of the truck.

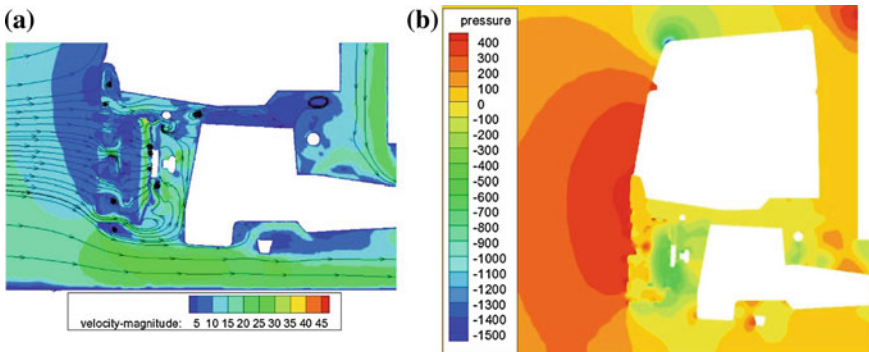


Fig. 2.6 Internal flow field of engine compartment. **a** Stream line on section $y = 0$ in engine compartment. **b** The pressure contour of section $y = 0$ near the cab

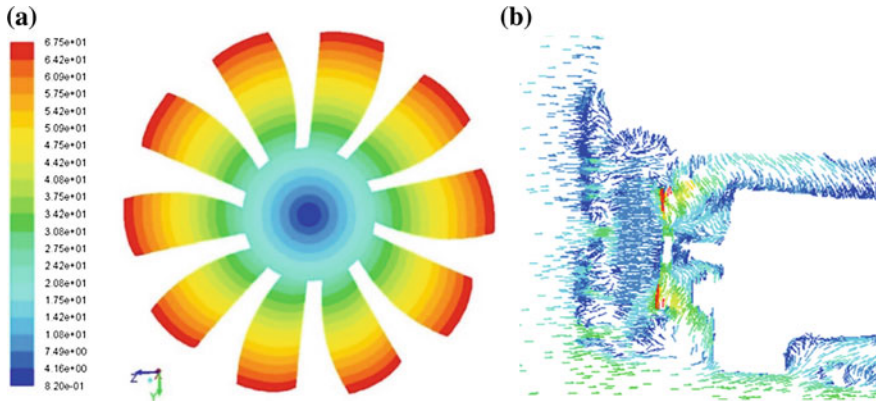


Fig. 2.7 Internal flow field of engine compartment. **a** Velocity contour of fan surface. **b** Velocity vector on section $y = 0$ of the front end of engine

The air flows out of the condenser and goes through the intercooler and radiator in turn. Since the resistance caused by the porous media exists, the velocity of the airstream drops, and then, the airflow through the cooling fan results in the increase in the pressure and velocity. Then, the airstream flows toward the engine and separates over the surface of the engine, and a part of which flows up over the top of the engine to cool the upper surface. However, there are also some dead zones over the engine where vortices are generated to block the flow of hot air. It does not only have an effect on the cooling efficiency of the radiator, but also increases the aerodynamic drag of the engine. The velocity of airstream is high in the rotation region of the fan, especially on blade edges, as shown in Fig. 2.7. The fan rotates to drive the air to rotate around it. Because of the pumping action of the fan, the kinetic energy of airstream increases, which improves the cooling of the heat exchangers.

The arrangement of components in the engine compartment is compact along with the rotation and pumping action of the fan; the flow field nearby is very complicated, and there are a lot of separation vortices. Finally, these airstreams flow from engine to the rear of the truck where they meet the flow field near the chassis.

2.4 Optimizing Analysis of Additional Devices

2.4.1 Geometry Model

The objects in this study are as follows: ① base model (Fig. 2.1); ② the base model with tail cone, whose side faces have an angle of 10° , while the top and bottom faces have an angle of 15° (Fig. 2.8a); ③ the base model equipped with fairing (Fig. 2.8b); and ④ the base model with both tail cone and fairing (Fig. 2.8c).

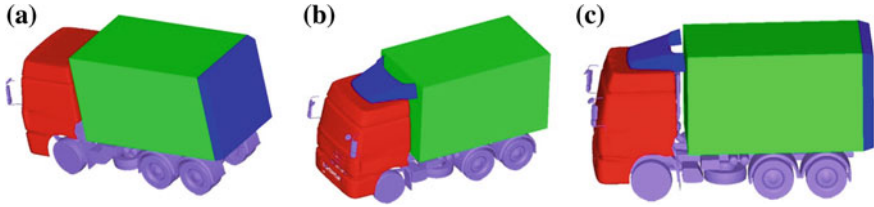


Fig. 2.8 Geometric model. **a** Truck with tail cone. **b** Truck with fairing. **c** Truck with both tail cone and fairing

Table 2.3 The aerodynamic drag coefficient of the truck with different additional devices

Model No.	Additional devices	Drag coefficient	Drop rate
①	None	0.5629	/
②	Tail cone	0.5365	4.69 %
③	Fairing	0.4940	12.24 %
④	Tail cone and fairing	0.4736	15.86 %

These numerical models are accomplished with the same method as the above, and the simulations are carried out with the same parameters, and the results are shown in Table 2.3.

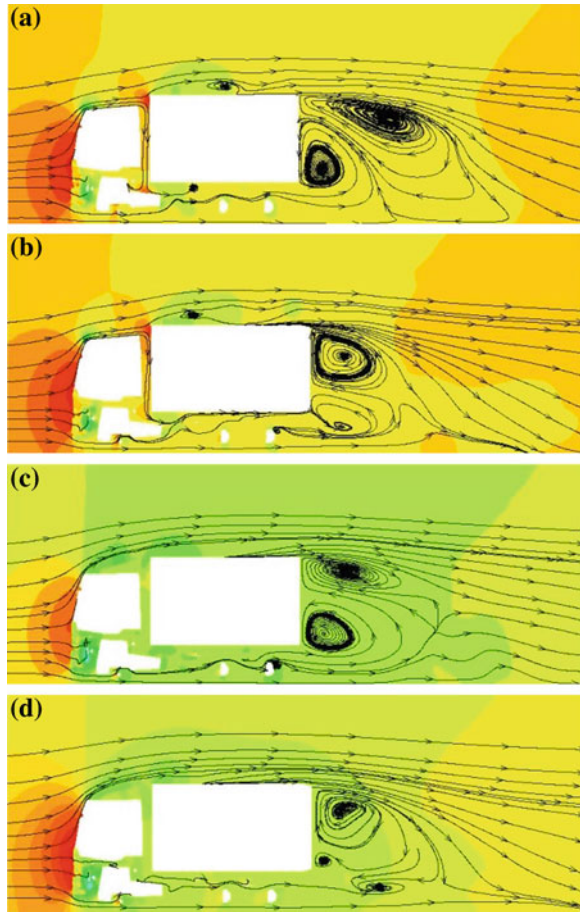
Table 2.3 shows that the installation of a tail cone lowers the aerodynamic drag coefficient by 4.69 %, while that decreases 12.24 % when installing a deflector. Compared with the tail cone, the deflector's drag reduction effect is better. When the truck is equipped with both tail cone and deflector, the drag coefficient would reduce considerably for better fuel economy.

2.4.2 Comparison of Velocity Distributions

The streamlines in section $y = 0$ of truck with different additional devices are shown in Fig. 2.9. The distribution of streamlines around the truck changes significantly.

Comparing Fig. 2.9a with b, it is found that the airstream distributes similarly in front of the truck no matter whether a tail cone is installed or not, but the model with a tail cone results in a smaller trailing vortex, because of the tail cone's guiding performance so that the airstream flows smoothly through the rear of the truck, and then, the airstream breaks away from the tail cone and generates flow separation. The tail cone efficiently puts off the flow separation, and it makes the separation vortex smaller and more far away from the truck. According to hydrodynamics, the pressure drag is intimately linked with the trailing vortex. The smaller the trailing vortex, the less the energy loss by the turbulence, which shows up as bigger static pressure of the tail and smaller differential pressure value between the front and back of the truck.

Fig. 2.9 Streamlines on section $y = 0$. **a** Truck without any additional devices. **b** Truck with tail cone. **c** Truck with fairing. **d** Truck with both tail cone and fairing



Comparing Fig. 2.9a with c, it is found that the installation of a deflector on the top of the cab makes airstream flow smoothly through the cab to the container, which considerably decreases the pressure between the cab and the container, so that the positive pressure generated in the front of the container is reduced, and then, the differential pressure between the front and rear of container decreases, and the container's aerodynamic drag coefficient reduces. At the same time, the differential pressure between the front and back of the cab increases as the pressure behind the cab reduced, but its effect is much smaller than that of the container, so the overall pressure drag of cab and container drops considerably to lower the aerodynamic drag coefficient of the truck.

Compared with other models, the streamline distribution in Fig. 2.9d is the best because of smoother streamlines in front of the truck and the smaller pressure difference in the gap between cab and container. At the same time, because of the

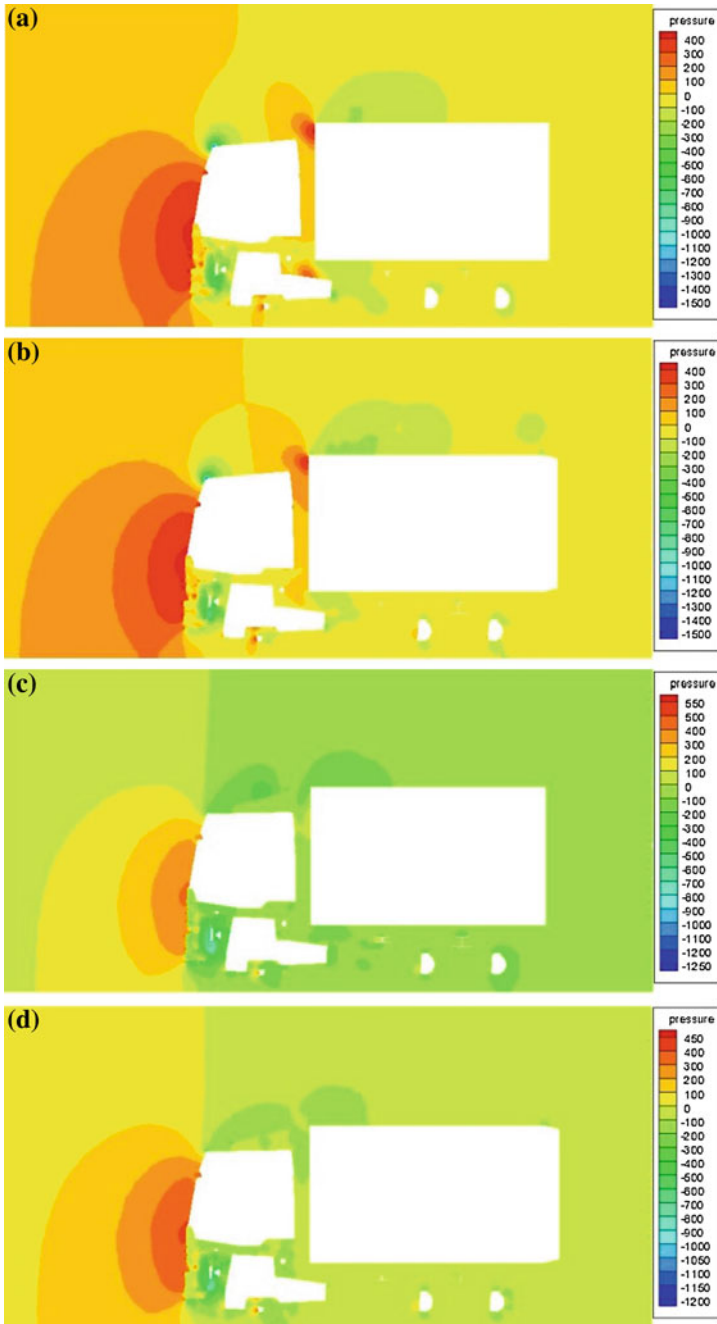


Fig. 2.10 Pressure contour of models with different additional devices on section $y = 0$. **a** Base model. **b** Base model with tail cone. **c** Base model with fairing. **d** Base model with both tail cone and fairing

guiding action of the fairing, airstream separation is put off and tailing vortex region becomes smaller. The energy loss decreases. Therefore, the aerodynamic coefficient of this model is the smallest.

2.4.3 Comparison of Pressure Distribution

Figure 2.10 shows the pressure contour of the model with different additional devices in section $y = 0$. As seen from Fig. 2.10b, d, there is a small negative pressure region on the top against the tail cone of the model equipped with one because of the airstream separation at the corner of the tail cone. From Fig. 2.10c, d, the fairing equipped on the top of the cab efficiently improves the pressure distribution in the front of the truck. Thanks to the guiding action of fairing, airstreams do not positively impact the part of container taller than the cab and the positive pressure of this part considerably reduces. Besides, since the fairing plays a sealing role in the gap between cab and container, the airstream going into the gap reduces sharply. All factors efficiently reduce the pressure resistance generated on the container.

Since the fairing is hollow, the airstreams behind the fairing flow backward because of the adverse pressure gradient to form vortex in the fairing. It results in loss of energy. As shown in Fig. 2.10c, d, the pressure of the flow field in the fairing is low, and lower than the positive pressure in the front end of the fairing. As a result, there is a pressure resistance applied on the fairing, and it would dissipate some energy. However, this can be ignored compared with the improvement of flow field caused by the fairing. In general, the fairing makes important positive influence on reduction of aerodynamic resistance of the truck.

2.5 Conclusions

With investigation of the aerodynamic additional devices which affect the aerodynamic characteristic of the truck, the aerodynamic coefficients under different circumstances are analyzed, for example, how the aerodynamic coefficient reduces by comparing with base model. And the conclusions come as follows:

1. If a tail cone is equipped in the rear of the truck, the flow separation can be put off and make the tailing vortex smaller for less energy loss. Besides, the pressure resistance applied on the container greatly drops and the aerodynamic coefficient also reduces.
2. Because of the fairing installed on the top of the truck, the airstreams do not impact the part of container taller than the cab positively. Besides, the air which goes into the gap decreases and the pressure lowers. The pressure resistance applied on the cab reduces to a certain extent, while the positive pressure in the

front end of the container becomes much lower. So the overall pressure resistance of the truck reduces as well as the aerodynamic coefficient.

3. If the truck is equipped with both tail cone and fairing, the flow field distribution would be the best. Under this circumstance, the truck's aerodynamic coefficient reduces significantly.

References

1. Zhang H, Zhong S (2009) Energy saving and emission reduction technology of vehicle and its development tendency. Forum on energy-saving emission reduction and new energy technology, China
2. Ni Y (2010) Lighten the burden on European and American type semi-trailer. Special Purpose Vehicle 10(8), China
3. He W, Ma J, Wang D, Yang Z (2007) Comparing MRF method with sliding mesh method for automotive front end airflow simulation. Comput Aided Eng 16(3), China
4. Patankar SV (1984) Numerical heat transfer and fluid flow. Science Press, Beijing

Chapter 3

Study on Matching Performance of the Load-Sensing Valve System with Independent Suspension Vehicles

Xiaoyun Si, Wenlun Ma, Yuchao Chen, Hongyu Zheng, Ying He and Zhanfeng Zhang

Abstract The load-sensing valve system can improve braking performance and stability of vehicles. The load-sensing valve system matching performance of the independent suspension is studied, and the kinematic model and mathematical model is established. By calculating and analyzing the model, a new method to match the load-sensing valve system for independent suspension vehicles, which helps us to solve the mismatch problem of the load-sensing valve system with the independent suspension vehicles, is obtained. This new matching method can improve brake performance, which has been proved by new vehicles.

Keywords Load-sensing valve · Independent suspension · Matching performance · Brake performance

3.1 Introduction

Brake performance directly impacts on people's safety. In order to maintain the brake performance and stability, the input braking pressure of the truck rear axle can be adjusted, that is, it is to dynamically adjust the braking force distribution ratio through rationally matching the rear axle's load-sensing valve system (braking force distribution adjusting device) when designing the truck air braking system. Distributing rationally the front and rear axle's braking force can make optimal use of the tire to road adhesion coefficient, enhance the braking performance and get the ideal adhesion coefficient utilization. During the braking process, rear wheels and

X. Si (✉) · W. Ma · Y. Chen · Y. He · Z. Zhang
R&D Center, China FAW Co. Ltd., Changchun, China
e-mail: sixiaoyun@rdc.faw.com.cn

H. Zheng
College of Automotive Engineering, Jilin University, Changchun, China

© Springer-Verlag Berlin Heidelberg 2015
Society of Automotive Engineers of China (SAE-China) (ed.),
Proceedings of SAE-China Congress 2014: Selected Papers,
Lecture Notes in Electrical Engineering 328, DOI 10.1007/978-3-662-45043-7_3

front wheels lock up at the same time, or the front wheels lock up in ahead, so as to prevent the truck from side-slip and swing, maintain better direction stability [1]. Moreover through matching the load-sensing valve performance, the amount of compressed air that needed during braking process decreases, which thus reduces the load ratio of the air compressor, saves energy, and reduces tire wear [2].

Getting accurate vehicle load information is core when matching the load-sensing valve performance, and for the load-sensing valve, the rear axle braking pressure is calculated according to the vehicle load information. For the truck equipped with tandem suspension (dependent suspension), the vehicle load information can be identified with the vertical distance between axle housing and frame feedback. The leaf suspension deformation is different under different load conditions, and the distance between the axle housing and frame also varies. As for the truck equipped with independent suspension, there's no relative motion between the axle housing and frame, and it is impossible to get vehicle load information through measuring the vertical distance between the axle housing and the frame. Researches show that the vehicle load information can be identified by measuring the relative rotation angle between the rod type roll stabilizer and vehicle frame, and then the system can calculate the rear axle input braking pressure. This paper focuses on matching the load-sensing valve of the independent suspension system, and proposes a new approach to match the load-sensing valve performance of the independent suspension, which gives a foundation for designing the braking system.

3.2 Working Principle of the Independent Suspension Load-Sensing Valve System and Modelling

3.2.1 Working Principle of the Load-Sensing Valve System

It is the most difficult to accurately get the truck's load condition information when matching the performance of the truck's independent suspension load-sensing valve system. Compared with the truck equipped with a dependent suspension system, there is no relative motion between the frame and the axle housing of the truck with an independent suspension. The axle and the components of the independent suspension system can't be used to identify the truck load condition information. Researches show that the stabilizer roll-over bar in the independent suspension system can be used to identify the truck load information accurately. Figure 3.1 shows the common layout of the stabilizer roll-over bar. Under ideal condition, when the truck changes from the no load to the full load, the frame moves in the vertical dimension and the deformation of the suspension is the same at both sides. The stabilizer roll-over rod rotates freely with respect to the frame in the sleeve, the angle is affected by the truck load condition and the suspension stiffness. The angle can be the input signal of the load-sensing valve. In practical, the road condition is

Fig. 3.1 Layout of the stabilizer roll-over rod



complicated, the suspension vibrates irregularly, tires receive shocks from the road, and the deformations of the suspension on each side are not the same. The above situations lead to the lateral inclination of the frame with respect to the road, then one side of the frame moves closely towards the spring support and accordingly the end of the stabilizer roll-over rod on this side moves up with respect to the frame, the other side moves away from the spring support and accordingly the other end of the stabilizer roll-over rod on the other side moves down with respect to the frame. The both ends of the stabilizer roll-over rod move in different directions, while the middle part of the rod doesn't move with respect to the frame [3]. Considering the feature of the stabilizer roll-over rod, and the work principle of the load-sensing valve, the turn-angle of stabilizer roll-over rod at its middle segment with respect to the frame can be the input signal to identify the truck load condition.

3.2.2 Load-Sensing Valve Motion Model

For the independent suspension vehicle, 3-D layout of the load-sensing valve system is shown in Fig. 3.2. The load-sensing valve is fixed on the cylindrical beam of the frame, the linkage used to fix the load-sensing valve is consist of rigid bars, and the bottom of the linkage is connected to the middle part of the stabilizer roll-over bar, and rotates with the stabilizer roll-over bar; the upper of the stabilizer roll-over bar is hinged with the load-sensing valve. When the truck load condition changes, the linkage can transfer the relative turn angle between the stabilizer roll-over bar and the frame to the load-sensing valve, and then the load-sensing valve will adjust the rear axle input braking pressure according to the input signal.

Figure 3.3 shows the plane kinematic of the load-sensing valve system. The degree of freedom of the system can be calculated as follow [4]:

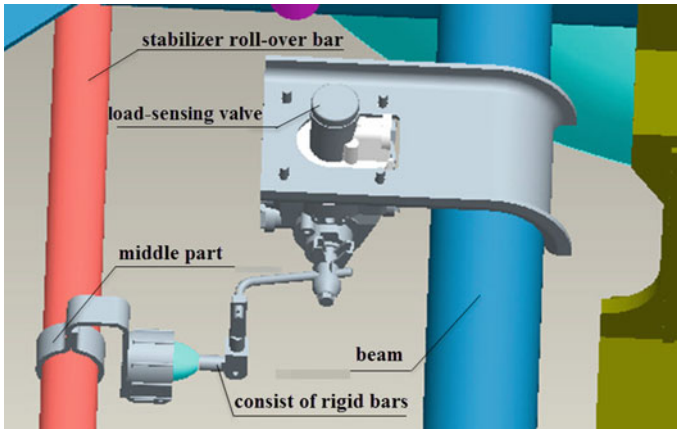
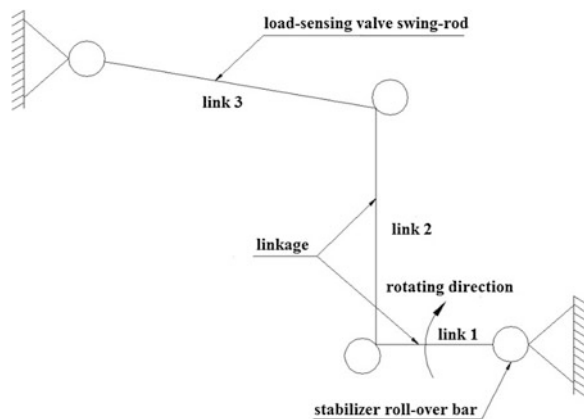


Fig. 3.2 3D layout of the load-sensing valve system

$$F = 3n - 2P_L - P_H \tag{2.1}$$

F —the degree of freedom of the linkage; n —the number of the moving link; P_L —the number of the lower pair in the linkage; P_H —the number of the higher pair in the linkage. After analysis, $n = 3$, $P_L = 4$, $P_H = 1$, according to the formula (2.1), $F = 3n - 2P_L - P_H = 3 \times 3 - 2 \times 4 - 1 \times 1 = 0$. The result indicates that the linkage can only move in a dimension. Therefore, when the given moving link of the three links in the load-sensing valve system regularly rotates, then other two links have only one certain position, that is, the linkage moves in a certain rule. When the link 1 turns an angle ϵ , the links 2 and 3 move to a certain position, and the size and the turn angle can be determined, as shown in the Fig. 3.3.

Fig. 3.3 Kinematical schematic diagram of the load-sensing valve system



3.3 Parameters Calculation for the Load-Sensing Valve System of Independent Suspension Vehicles

3.3.1 The Mathematical Model of the Load-Sensing Valve System

Figure 3.4 is derived from Fig. 3.3 and identifies the geometries, which is useful for the kinematic analysis of the load-sensing valve system. In Fig. 3.4, the solid lines represent the positions of the swing-rod of load-sensing valve and the connecting bar assembly under un-load condition and the dashed lines represent those under full-load condition. The physical significance of the parameters indicated in Fig. 3.4 are as followed: a —the length of the swing-rod of load-sensing valve; b , c —the lengths of the connecting bars; l_1 , l_2 —the layout sizes of the load-sensing valve and the transverse stabilizer; β —the effective angel range of the swing-rod of load-sensing valve between un-load and full-load conditions (it is generally set as 30°); η —the angel of load-sensing valve swing-rod under un-load condition; ε —the relative angel of the transverse stabilizer and the vehicle frame when the state of vehicle changes from un-load to full-load. Of these, l_1 , l_2 are defined during the arrangement process of the load-sensing valve system, the effective angel range of the load-sensing valve swing-rod is $\beta = 30^\circ$ and is symmetrically distributed in the horizontal direction, ε is defined in the arrangement and design calculation process. The unknown parameters, which should be calculated, are: a , b , c , η .

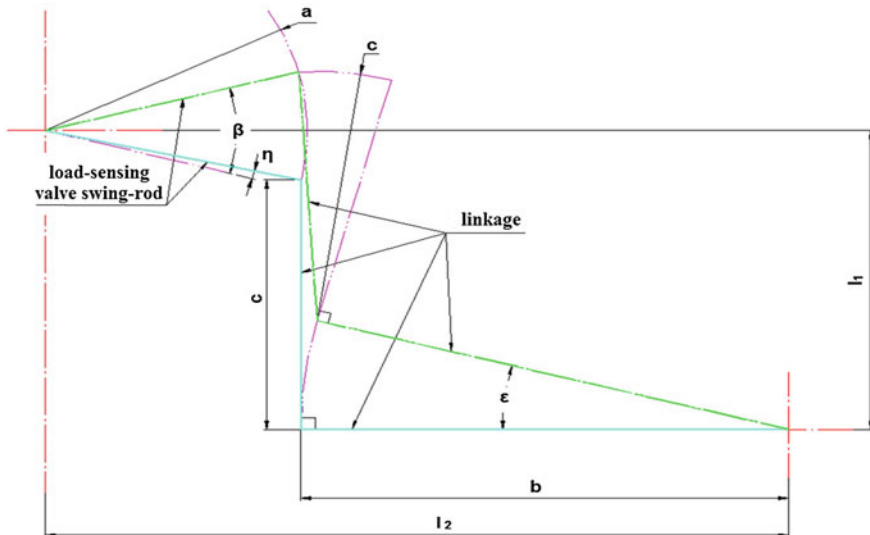


Fig. 3.4 Mathematical model of load-sensing valve system

3.3.2 Parameters Calculation for the Load-Sensing Valve

A specific 6×6 independent suspension vehicle is selected as an example for calculation. Table 3.1 shows the technical parameters of the vehicle.

The braking torques listed in Table 3.1 are determined based on the vehicle brakes. The synchronization friction coefficient is selected as 0.5 in the beginning of the braking system design process, and the tightening torques of the front and the rear axles are evaluated based on the friction coefficient of 0.5 [5]. The calculation process of the load-sensing valve system is as showed below.

3.3.2.1 Calculation of the Load-Sensing Valve's Output Pressure (P_2) Under Un-Load Condition

The characteristics of load-sensing valve system are the same as that of the load-sensing valve production used in the specific vehicle. Figure 3.5 shows the characteristic curve of the load-sensing valve, which describes the linear relationship between the control pressure P_4 and the output pressure P_2 when the swing-rod stays in a specific position.

Based on the parameters given in Table 3.1, and given the friction coefficient of 0.5 and un-load vehicle state, the wheel lock pressure of the front axle and the rear axle are 350 and 110 kPa, respectively. By matching load-sensing valve in rear axle, the rear axle input pressure can be set as 110 kPa when the front axle control pressure and the load-sensing valve control pressure are equal to 350 kPa.

The air supply pressure of the front and the rear axle brake circuit is set as: $P_1 = 750$ kPa. The installation angel of the load-sensing valve swing-rod is η in un-load vehicle state. According to the characteristic curve of the load-sensing

Table 3.1 The technical parameters of the vehicle

6×6		Un-load	Full-load
Parameters	W (Kg)	9,860	15,860
	Wf (Kg)	4,800	6,000
	Wr (Kg)	5,060	9,860
	L (m)	4.4	4.4
	Rk (m)	0.573	0.573
	Hg (m)	1.075	1.27
	a (m)	2.258	2.735
	b (m)	2.142	1.665
Working pressure (kPa)		750	750
Front axle tightening torque (Nm)		16,859	23,272
Front axle braking torque (Nm)		36,000	36,000
Rear axle tightening torque (Nm)		10,825	21,257
Rear axle braking torque (Nm)		48,000	48,000

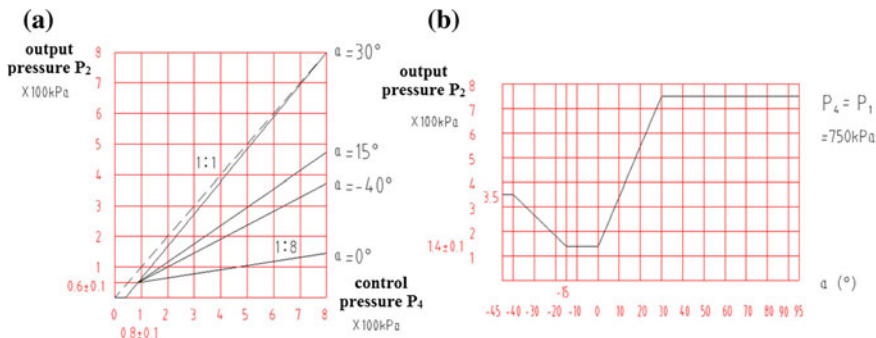


Fig. 3.5 Characteristic curve of the load-sensing valve system

valve in Fig. 3.5(a), when the load-sensing valve swing-rod stays at any particular position, the control pressure P_4 and the output pressure P_2 of the load-sensing valve show linear relationship. When the angel of load-sensing valve swing-rod is η , the P_4 - P_2 curve contains the following three points: (0.8, 0.6), (3.5, 1.1), (7.5, P_2). The point (0.8, 0.6) is the starting point of the curves (Fig.3. 5(a)). The coordinates of the point (3.5, 1.1) represent the wheel lock pressure of the front axle brake and the rear axle brake respectively under the condition of un-load vehicle state and the friction coefficient of 0.5. The point (7.5, P_2) represents that when the control pressure of the load-sensing valve $P_4 = 750 \text{ kPa}$, the output pressure is P_2 . Through the above three coordinates, the corresponding linear equation of the characteristic curve is as follows:

$$\frac{(1.1-0.6)}{(P_2-0.6)} = \frac{(3.5-0.8)}{(7.5-0.8)} \tag{3.1}$$

It can be calculated from Eq. (3.1) that when $P_4 = P_1 = 750 \text{ kPa}$ and the installation angel of the load-sensing valve swing-rod is η , the output pressure of the rear axle load-sensing valve is $P_2 = 190 \text{ kPa}$.

3.3.2.2 Calculation of the Load-Sensing Valve’s Pendulum Angel (η) under Un-Load Condition

It can be seen from Fig. 3.5(b) that even the air supply pressure $P_1 = 750 \text{ kPa}$, the output pressure P_2 changes when the load-sensing valve swing-rod angel changes. When β is in the range of $0-30^\circ$, the output pressure P_2 and the swing-rod angel η show linear relationship. The corresponding characteristic curve contains the following three coordinates: (1.4, 0), (7.5, 30), (1.9, η). Of these, the coordinates (1.4, 0) and (7.5, 30) are the starting point and ending point of the curve, respectively (Fig. 3.5(b)). The point (1.9, η) represents that when the swing-rod angel is η , the output pressure of the load-sensing valve is P_2 , in the example of this paper that

is $P_2 = 190$ kPa. Through the above three coordinates, the corresponding linear equation of the characteristic curve is as follows:

$$\frac{(30-0)}{(30-\eta)} = \frac{(7.5-1.4)}{(7.5-1.9)} \quad (3.2)$$

It can be calculated from Eq. (3.2) that when $P_4 = P_1 = 750$ kPa, the initial installation angel of the load-sensing valve swing-rod is $\eta = 2.5^\circ$. In this condition, the relationship of the control pressure P_4 and the output pressure P_2 of the load-sensing valve is linear and the ratio is about 5:1.

3.3.2.3 Calculation of the Lengths (a, b, c) of the Load-Sensing Valve Swing-Rod and the Connecting Rods

According to the changes of the rods position under different load conditions (un-load and full-load) which are indicated in Fig. 3.4, the following three equations concerning the parameters can be derived:

$$l_1 = c + a \times \sin\left(\frac{\beta}{2} - \eta\right) \quad (3.3)$$

$$l_2 = b + a \times \cos\left(\frac{\beta}{2} - \eta\right) \quad (3.4)$$

$$c^2 = \left\{l_1 + a \times \sin\left(\frac{\beta}{2}\right) - b \times \sin \varepsilon\right\}^2 + \left\{l_2 - a \times \cos\left(\frac{\beta}{2}\right) - b \times \cos \varepsilon\right\}^2 \quad (3.5)$$

In this example, the length of these rods is: $l_1 = 102.5$, $l_2 = 221$, $\varepsilon = 14.9^\circ$. It is already obtained that $\eta = 2.5^\circ$. And, the angel range of the load-sensing valve swing-rod is $\beta = 30^\circ$ and it is horizontally distributed symmetrically. According to the specific values of the parameters and Eqs. (3.3), (3.4), and (3.5), a , b and c can be calculated as: $a = 78.11$, $b = 145.23$, $c = 85.59$. In the matching process of an actual vehicle's load-sensing valve system, the parameter set of $a = 78$, $b = 145$, $c = 85$ satisfies the functional requirements of the load-sensing valve system and is easy to produce.

3.3.3 Overload Protection of the Load-Sensing Valve System

The load-sensing valve has the function of overload protection, and thus the internal mechanism of the load-sensing valve can ensure that the swing-rod automatically returns back to the limit state once any abnormal condition happens and the

connecting rod system breaks, which is illustrated in Fig.3. 5(b), where the swing-rod angel is 95°. It is known from the Fig. 3.5 that when the swing-rod angel is within the range of 30°–95°, the control pressure P_4 and the output pressure P_2 of the load-sensing valve show linear relationship with the ratio 1:1 and the load-sensing valve fails to regulate the output pressure based on the load status. But this characteristic has no influence on the braking performance of the vehicle and does not affect the safety of vehicle.

3.4 Road Test Verification

The ‘0’ type test under un-load status is chosen for the verification of the parameters matching method. The test data of the pressure of front and rear axle pipes are shown in Table 3.2, and the pipe pressure curves of the front and the rear axles are compared in Fig. 3.6 and Fig. 3.7. The test data shows that the relationship of the control pressure P_4 and the output pressure P_2 matched is linear in this paper: when

Table 3.2 Pressure of front and rear brake chamber in the 0 type test at the unloaded state of a vehicle

Speed (km/h)	Pressure of front axle pipe (kPa)	Pressure of rear axle pipe (kPa)
30 (un-load)	110	66
	190	82
	300	105
	350	115
	400	124
60 (un-load)	130	69
	200	85
	297	103
	360	118
	405	127

Fig. 3.6 The pipes pressure comparison for the front and rear axles ($v = 30 \text{ km/h}$)

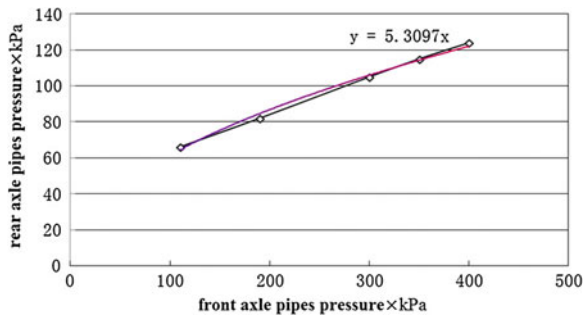
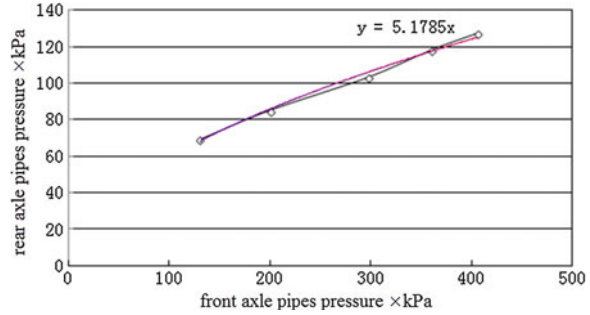


Fig. 3.7 The pipes pressure comparison of the front and the rear axles ($v = 60$ km/h)



the vehicle speed $v = 30$ km/h, $P_4/P_2 = 5.3097$, and when the vehicle speed $v = 60$ km/h, $P_4/P_2 = 5.1785$. The results are consistent with the previous theoretical results described in Sect. 3.2.2 and thus the correctness of the theoretical calculation and structural design aspects for the parameters matching of load-sensing valve system are verified.

3.5 Conclusions

The load-sensing valve system matching performance of independent suspension vehicles is studied and a new method for parameters matching problem of the load-sensing valve system with independent suspension is introduced. The load-sensing valve system has the following advantages: (1) Simple structure, easy to assemble and low cost. The connecting rod system of the load-sensing valve system is composed of several rigid rods and thus can be conveniently assembled. (2) The control information of the load-sensing valve is more accurate, which is helpful to accurately control the output pressure. The load-sensing valve is connected with the stabilizer roll-over rod through the connecting rod system. The relative motion of the two components is limited to relative rotation and there is no relative movement of the two components. It is known that the information comes from the suspension system cannot reflect the changes in vehicle loading state. The suspension system information is mainly generated by the suspension deformation of the vehicle rapidly changing road conditions and the horizontal and vertical relative displacement of the axles and the frame. With the structure mentioned-above, the information of the suspension motion and deformation will not transfer to the load-sensing valve and the accuracy of the input and output of the valve will be ensured. (3) The mathematical model and the parametric design method ensure the accuracy of the structural design and the motion control.

The method of matching load-sensing valve for independent suspension vehicles has been used in actual vehicles and the correctness of the method has been proved with the road braking and reliability test. The test results demonstrate that the matching results can improve the braking performance, reduce the amount of

compressed air in braking process and reduce tire wear. Therefore, the results of the matching performance study in this paper are correct and the new matching method developed here is indeed feasible and can be used as the post design basis of the braking system of independent suspension vehicles.

References

1. Yu Z, QunSheng X (2007) *Automotive theory*, 4th edn. Beijing, pp 102–118
2. Sun J (2007) Economical solution of the destruction of vehicle tires—WABCO sensor valves. *Special Purpose Vehicle* 26(10):25
3. Chen J (1994) *Automobile structure (II)*, 2nd edn. Beijing, pp 229–232
4. Cao S, Yang W (1994) *Mechanism and machine theory*, 1st edn. Wuhan, pp 7–18
5. Liu W (2001) *Automotive design*, 1st edn. Beijing, pp 685–690

Chapter 4

Optimal Design and Test Research of Rubber Auxiliary Spring for Medium-Sized Truck

Fanlong Bu, Yuewei Li, Xiaotao Wu and Zhaoying Liu

Abstract With CAE analysis software, combined with the characteristic of rubber auxiliary spring force, based on the elastic curve of design requirements as optimized objective, the optimal design of structure parameters for rubber auxiliary spring is realized. The optimized prototype for trial production makes the weight of suspension system successfully reduced by up to 20 %. It realizes the lightweight of vehicle. Test project design and verification on the rubber auxiliary spring body and suspension system are conducted, and the results show that rubber auxiliary spring is feasible in medium-sized truck applications and is worth to be popularized.

Keywords Medium-sized truck · Rubber auxiliary spring · Optimal design · Experimental study

4.1 Introduction

Since the axle weight of medium-sized truck rear suspension under full load is much bigger than under no load, in order to keep the vehicle with a relatively stable inherent frequency of the suspension and good ride comfort under different loads, it requires that the suspension system has good nonlinear characteristics [1]. At present, the rear suspension system of medium-sized truck in China generally adopts composite leaf spring suspension with two-grade stiffness, that its weight is big, and the change in suspension stiffness occurs at the moment of auxiliary leaf spring contact with main leaf spring, which results in poor ride comfort [2].

On the other hand, the energy shortage and environmental pollution problems have become prominent problems which restrict the sustainable development of Chinese automobile industry. Considering it from the social or economic benefits,

F. Bu (✉) · Y. Li · X. Wu · Z. Liu

Medium and Heavy Duty Vehicle Department, FAW R&D Center, Changchun 130011, China

e-mail: bfl171@163.com

© Springer-Verlag Berlin Heidelberg 2015

Society of Automotive Engineers of China (SAE-China) (ed.),

Proceedings of SAE-China Congress 2014: Selected Papers,

Lecture Notes in Electrical Engineering 328, DOI 10.1007/978-3-662-45043-7_4

the low fuel consumption and low-emission cars are the demand of the development of economical society. Automotive's lightweight technology is an important means to get the automobile fuel economy, and the relevant research data show that the increase of weight of automobile by 10 % makes the fuel efficiency increase by 6–8 % [3]. The application of rubber spring is also an effective means for lightweight of automobile.

In this paper, the rear suspension system of medium-sized truck adopts rubber auxiliary spring instead of auxiliary leaf spring of composite leaf spring suspension. With the nonlinear characteristics of auxiliary rubber spring, it combines with main leaf spring in order to bear axle load. CAE optimization analysis and experimental research for auxiliary rubber spring have been done. Results show that the rubber auxiliary spring features lightweight, simple structure, good elastic characteristics, and fatigue performance, which is worth being further popularized.

4.2 Rubber Auxiliary Spring's CAE Optimization Model

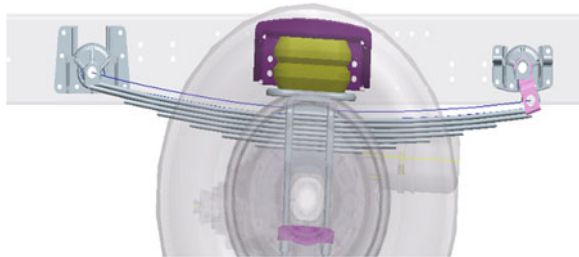
4.2.1 Rubber Auxiliary Spring's Simplified Force Model

Rubber auxiliary spring is installed in the rear suspension of a truck as shown in Fig. 4.1. Combined with the structure and force characteristics of rubber auxiliary spring, a simplified rubber auxiliary spring force model is established as shown in Fig. 4.2. Rubber auxiliary spring and the bottom plate are assembled together with bolts, and the bottom plate is fixed. The top plate is assumed to be rigid and applied with the concentrated or uniformly distributed load.

4.2.2 Optimization Results for Rubber Auxiliary Spring

Firstly, different-sized CAD models are plotted by using 3D drawing software PRO/E. According to the optimization process of 3D model, it is divided into three stages. At the first stage, the initial model of rubber auxiliary spring, as shown in Fig. 4.3, is gotten, its size (length \times width \times height) is 230 \times 130 \times 142 mm, and its

Fig. 4.1 Rubber auxiliary spring assembly model



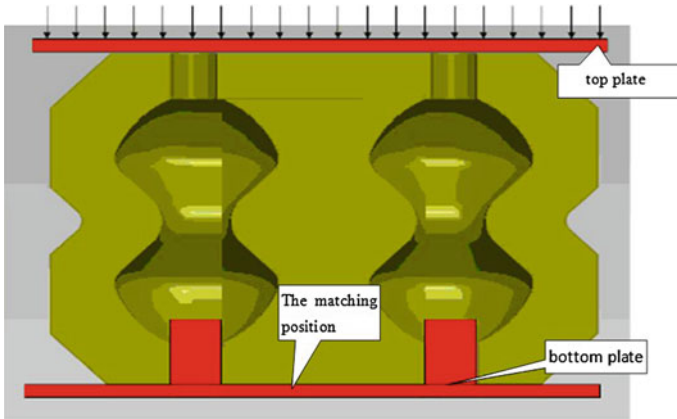
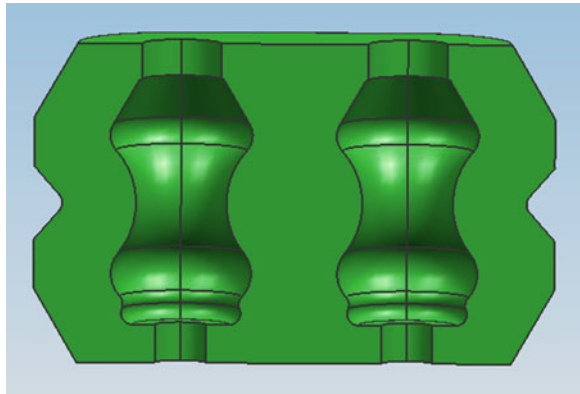


Fig. 4.2 Rubber auxiliary spring simplified force model

Fig. 4.3 Rubber auxiliary spring's initial CAD model



internal cavity structure is as shown in Fig. 4.3. At the second stage, four plans are designed, and in plan A, its size (length \times width \times height) is $230 \times 112 \times 142$ mm, and the inner cavity curve changes, but in other plans, we will change the height and internal cavity curve according to plan A. At the third stage, it is the final plan, the size (length \times width \times height) is $230 \times 112 \times 176$ mm, and the inner cavity curve is the same as that of the initial model. Then, the finite element analysis software HyperMesh is used to carry out the pretreatment of grid division. Finally, the stiffness analysis [4] is simulated with Abaqus, as shown in Fig. 4.4.

Figures 4.5, 4.6, and 4.7 are the simulation results for stiffness curve analysis of different hardness models at different stages. Results show that at the first stage, the curve fluctuations do not comply with the design requirements. At the second stage, the analysis results of different plan models of the same hardness N70 are obtained, and plans A or B and C within 0–30 mm conform to the design requirements, but if

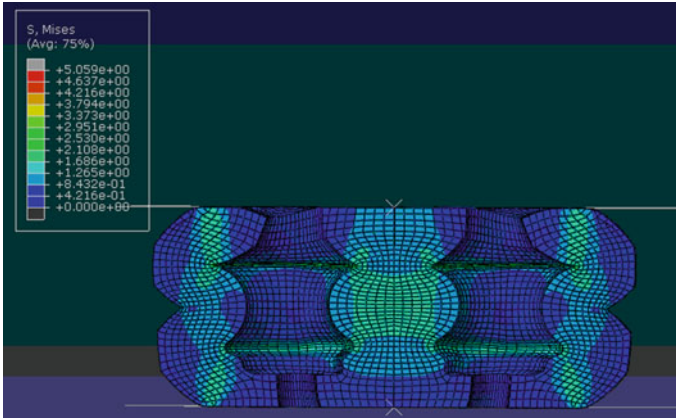


Fig. 4.4 Rubber auxiliary spring’s finite element analysis model

Fig. 4.5 The stiffness simulation curve at the first stage

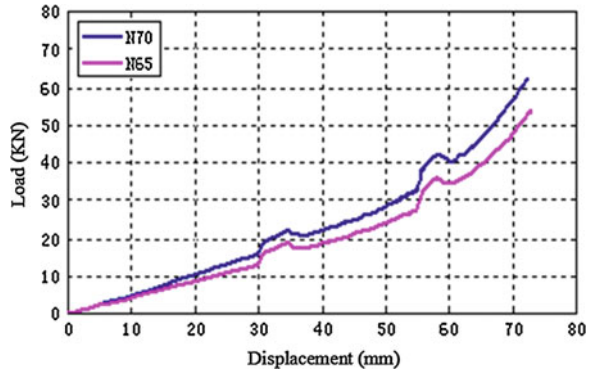
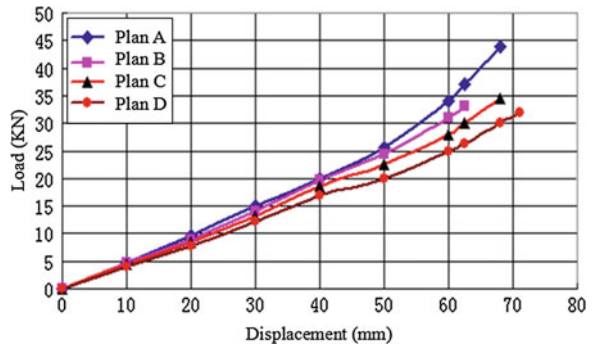


Fig. 4.6 The stiffness simulation curve at the second stage



the deviation of 30 mm is too large to meet the requirements, the plan D’s stiffness curve closes to the design requirements, but the value of stiffness is slightly large and thus the hardness adjustment is required. Considering that the bigger ultimate

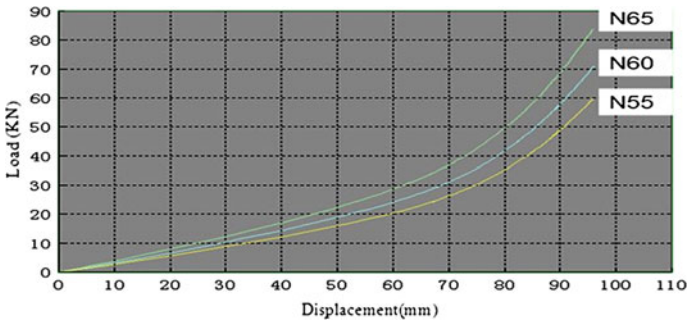


Fig. 4.7 The stiffness simulation curve at the third stage

deformation of truck rubber auxiliary spring is required, the hardness N60 plan at the third stage can finally satisfy the design requirements.

4.3 Rubber Auxiliary Spring Test Research

4.3.1 Rubber Auxiliary Spring Bench Test

According to the results of the optimization of rubber auxiliary spring, the hardness N60 plan of the rubber auxiliary spring is trial-manufactured for sampling (see Fig. 4.8). Results show that the weight is 5 kg, and the weight of suspension system reduces by up to 20 %. Further test research on the sample is done, and the bench test of rubber auxiliary spring body is conducted first (see Fig. 4.9), the contents of which include the static stiffness test, low-temperature test, and fatigue life test. The results show that the static stiffness curve of the sample is consistent with the simulated stiffness curve of a model (see Fig. 4.10). After frozen 2 hours in minus

Fig. 4.8 A sample of rubber auxiliary spring sample



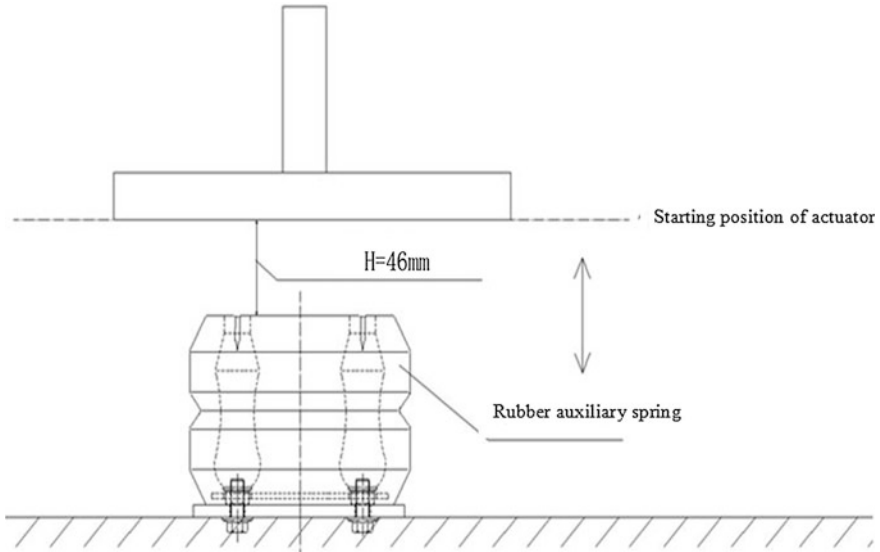
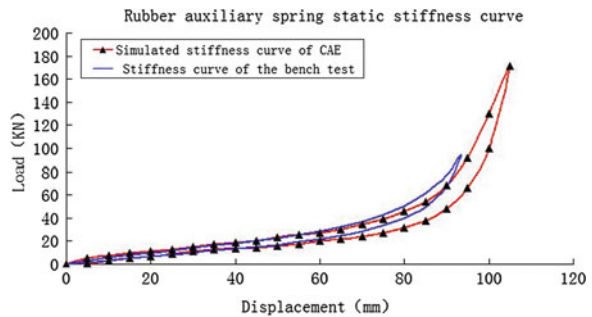


Fig. 4.9 Schematic diagram of bench test device for rubber auxiliary spring

Fig. 4.10 Stiffness curve of rubber auxiliary spring



40 temperature (see Fig. 4.11), the fatigue test is carried out for 500 times, and then, the rubber auxiliary spring is without any damage. The fatigue test of rubber auxiliary spring is done for 400,000 times, and the rate of change of its height and stiffness is less than 10 % (see Table 4.1).

After the completion of the bench test of rubber auxiliary spring, the bench test of rear suspension system is further done (see Fig. 4.12). The contents of the test include the static stiffness test, dynamic stiffness test, and fatigue test. The results of static stiffness test show that compared with the stiffness curve of leaf spring suspension (see Fig. 4.13), when the rubber auxiliary spring contacts with the main leaf spring, its stiffness curve is more softer, the stiffness of rear suspension is smaller, and its ride comfort is good, and when the jump magnitude reaches a

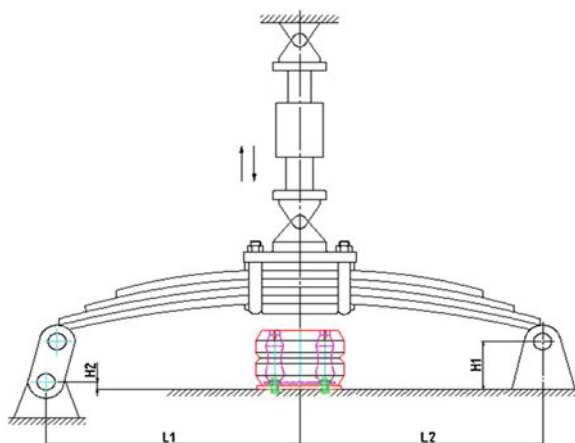
Fig. 4.11 Low-temperature test of rubber auxiliary spring



Table 4.1 Rubber auxiliary spring's fatigue test results

	Height	Stiffness
The initial state	176 mm	465.5 N/mm
After 400,000 times of fatigue test	165 mm	459.8 N/mm
Rate of change	-6.25 %	-1.22 %

Fig. 4.12 Schematic diagram of rear suspension system bench test



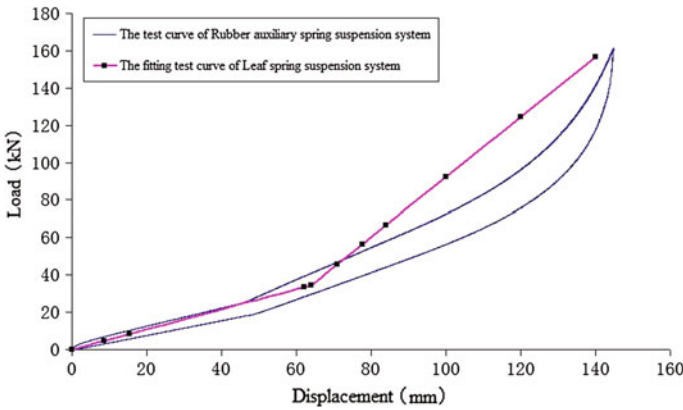


Fig. 4.13 Static stiffness curve of rear suspension system

certain value, the stiffness increases dramatically, and the rubber auxiliary spring is acted as a buffer.

The results of dynamic stiffness test show that at the same frequency, with the increase of the amplitude, the dynamic stiffness of rubber auxiliary spring suspension systems decreases (see Fig. 4.14). At the same amplitude, the dynamic stiffness has no significant change as the variation of frequency (1–2 Hz) (see Fig. 4.15). For the friction value of suspension system under the condition of truck’s normal amplitude of 5 mm, the friction of rubber auxiliary spring suspension system decreases by 33.3 % compared with the leaf spring suspension system (see Table 4.2).

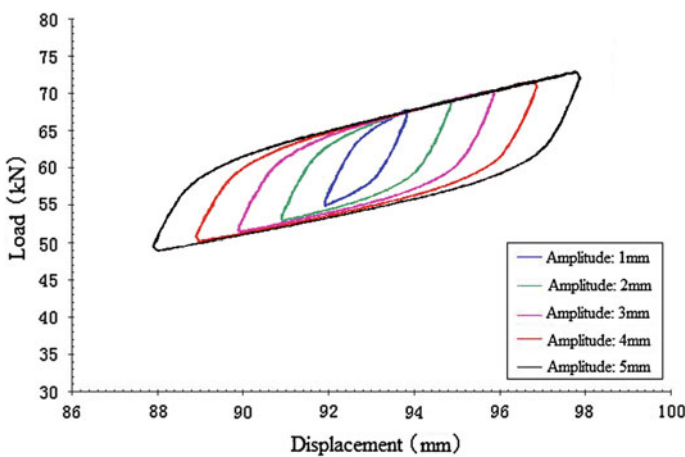


Fig. 4.14 Dynamic stiffness at the same frequency and different amplitude

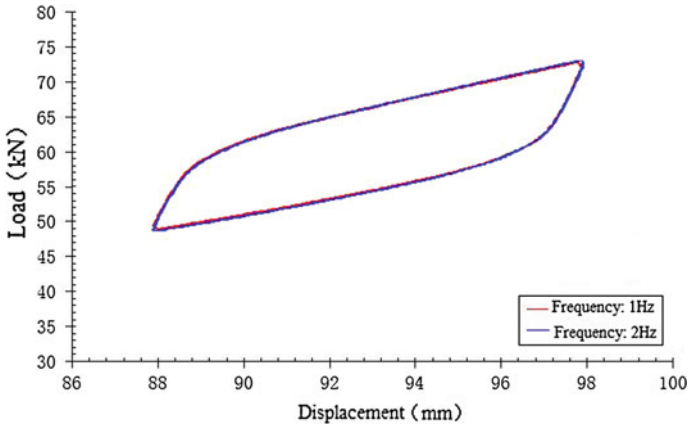


Fig. 4.15 Dynamic stiffness at the same amplitude and different frequency

Table 4.2 Comparison of friction values for suspension system

	Test conditions	Friction value (kN)
Leaf spring suspension system	Amplitude: 5 mm	7.5
Rubber auxiliary spring suspension system		5

The results of fatigue test are given in Table 4.3: The test results of rubber auxiliary spring suspension system achieve the objectives and requirements.

4.3.2 Actual Road Test of Rubber Auxiliary Spring

Reliability test and subjective evaluation test are carried on the 2# pavement of NongAn Test Field (12,000 km) (see Fig. 4.16). The results show that rubber auxiliary spring has high reliability and no fault which may affect its normal use, such as crack, deformation, and aging. When the braking causes any deformation of rear suspension, no transmission shaft interference phenomenon appears. The ride

Table 4.3 The test results of fatigue life

Name of assembly	The fatigue life (times)	Rate of change of peak load (%)
1# rubber auxiliary spring suspension system	200,700	3.3
2# rubber auxiliary spring suspension system	186,000	3.2
3# rubber auxiliary spring suspension system	182,600	3.4
The target value	≥100,000	≤10



Fig. 4.16 Actual road test vehicle with rubber auxiliary spring

comfort of the vehicle with rubber auxiliary spring suspension is better than that of the leaf spring suspension vehicle. And it further verifies the rationality and correctness of rubber auxiliary spring model optimization and bench test methods.

4.4 Conclusions

According to the characteristics of rubber auxiliary spring force, and the elastic curve design requirements as the optimization objective, the optimization design of structure parameters of the rubber auxiliary spring is obtained. The optimized prototype for trial production makes the weight of suspension system successfully decreased by up to 20 %. It realizes the lightweight of vehicle. Researches on the bench test of rubber auxiliary spring body and suspension system verify that the CAE optimization design is feasible and also provides the test basis for the development of similar products. Actual road test of rubber auxiliary spring further proves that the optimization design and test research method for rubber auxiliary spring are proper, and the rubber auxiliary spring is feasible in medium-sized truck applications and is worth to be popularized.

References

1. Sun B, Sun Q, Xu Z (2006) Nonlinear variable stiffness of rubber suspension structures sensitivity analysis and parameter optimization. *Manufact Autom* 28(02):1-4+9
2. Chen J (2008) *Construction of automobile*, 2nd edn. Machinery Industry Press, China, p 220
3. Jiang Y (2013) Present situation and development of auto lightweight technology in China. *China Packag Indus* (02):49-50
4. Zhou W, Huang Y, Ge Q (2011) Single bridge composite suspension rubber air spring stiffness analysis and parameter optimization. *Automobile Technol* (10):53-56

Chapter 5

Application of Virtual ECU and Large Coverage Testing in the Development of Control Software for a Dual-Clutch Transmission

Lionel Belmon, GuangHui Zhang and Ronghui Zhang

Abstract Automatic transmissions control systems have a key influence on the overall power train performance. These systems are complex to test and validate due to the interaction of mechanics, hydraulics, electronics, vehicle dynamics, driver inputs and transmission control software. How ECU virtualization and automated large coverage testing have been applied to test a transmission control software developed by FAW is introduced.

Keywords Automatic transmission · Simulation · Embedded software · Testing

5.1 Introduction and Objectives

Automatic transmissions control systems have a key influence on the overall power train performance. These systems are complex to test and validate due to the interaction of mechanics, hydraulics, electronics, engine control, vehicle dynamics, driver inputs and transmission control software. The objective of the presented work is to:

- (a) establish a virtual integration that can be used by software development engineers;

L. Belmon
Global Crown Technology, Beijing, China
e-mail: lionel.belmon@sae-china.org

G. Zhang · R. Zhang (✉)
FAW Group R&D Center, Changchun, China
e-mail: zhangguanghui@rdc.faw.com.cn

G. Zhang
e-mail: zhangguanghui1@rdc.faw.com.cn

- (b) implement a method that automatically generate a large test coverage for the system.

The transmission control unit (TCU) software testing must be conducted in a closed-loop simulation which integrates a vehicle plant model and the controller. There are several ways to achieve such a *closed-loop simulation* where the TCU interacts with a simulated vehicle. One possibility is to use hardware-in-the-loop (HiL) simulation, in which the real TCU controller is connected to a real-time vehicle emulator. Another possibility is to simulate the embedded software and the plant on a PC platform, without any hardware required. This methodology is based on ‘ECU virtualization’, and this is the method that we applied for this work. The virtual ECU running on PC is a very suitable *software* test object which can be fully inspected and debugged without limitations of embedded controllers on HiL.

In the current work, a method for performing large coverage testing has been implemented. To perform such large coverage testing, we first established a *System Under Test* with the following properties:

- High fidelity compared to execution of the embedded software in the vehicle
- Closed-loop simulation with the vehicle model
- Fast execution times and easily parallelizable
- Reproducible and deterministic

Using this *System Under Test*, we implemented a driving scenarios generator (QTronic Testweaver) which can generate, execute and evaluate the suitability of 1,000’s of drive scenarios. More information on the tools and process described above can be found in [1–5].

The results of this work enable very large test coverage to be generated within one night of execution, with reports automatically generated for possible system level issues.

5.2 Overview of the DCT350 Gearbox

We briefly introduce the transmission system which is considered in this paper. The DCT350 is a dual-clutch gearbox designed and produced by FAW. The TCU hardware is provided by continental, and the TCU application software is developed in-house by FAW.

The DCT350 has the following characteristics:

- 7 gears + Rear
- 350 Nm torque, for longitudinal application
- 2 wet dual clutches
- Hydraulic module for clutch and shift actuators control, engine-driven pump (Fig. 5.1)

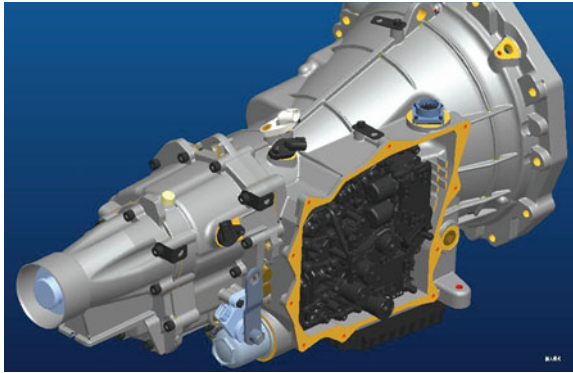


Fig. 5.1 Cutaway diagram of DCT350's hydraulic module

5.3 Control Software Development

The application software consists of numerous modules, and the core modules are the shift strategy and transmission coordinator. Figure 5.2 shows an overview of the modules.

A model-based design development method is implemented by FAW. The application software is generated from a Simulink model using the dSPACE TargetLink code generator. The generated tasks are then linked and integrated with the basic software (BS) of the TCU.

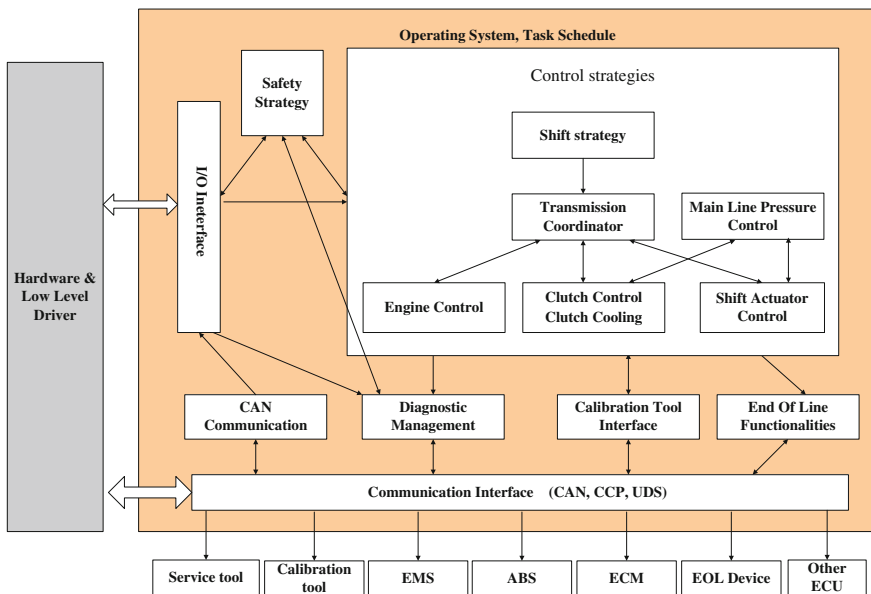


Fig. 5.2 Overview of TCU application software modules

5.4 Implementation of the System Under Test

The System Under Test is made of two parts: (a) a virtual ECU for DCT350 and (b) plant model simulation of the vehicle and gearbox.

The virtual ECU is built from the same embedded C-code which is used in the real TCU, but instead of running on the TCU hardware, the virtual ECU runs on normal Windows PC. Tasks and scheduling is simulated, interaction with the basic software is also emulated. Calibration parameters, fixed-point/floating-point conversions are also supported automatically. The above features are achieved by using the virtual integration tool QTronic Silver [2, 3]. Finally, the virtual ECU reproduces with high fidelity the actual behaviour and execution of the real TCU in the car, but can be made available on any engineer’s PC. Since the virtual ECU has the same code, same parameters and overall same behaviour as the real TCU, it is an excellent subject for performing tests.

The plant model of the vehicle and gearbox is required because the TCU manages dynamic processes (gear shifting) with closed-loop controls. Feedback from the vehicle sensors must thus be simulated. This is done with a plant model. FAW use such plant models on its hardware-in-the-loop test systems. For the current project, we reused the existing plant model and compiled it for our PC application QTronic Silver.

Figure 5.3 shows an overview of the virtual integration platform QTronic Silver, with the used modules for this project in bold red font (Virtual ECU/SBS, VS debugger, Simulink, CANAPE, Silver GUI, python module...)

A convenient dashboard and control panel were also built for easily interacting with the SUT (Figs. 5.4 and 5.5).

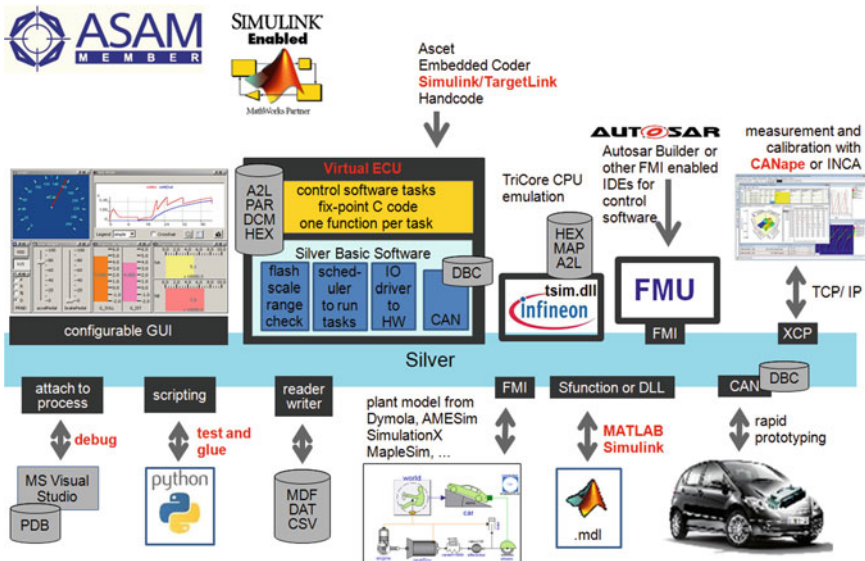


Fig. 5.3 Overview of the virtual integration platform QTronic Silver

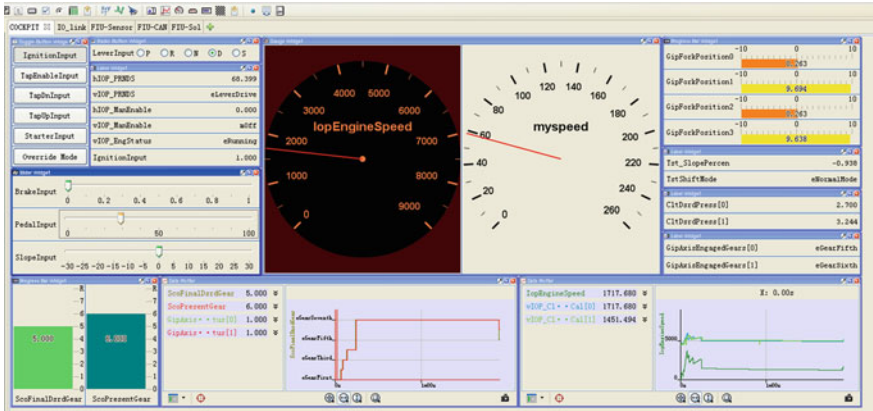
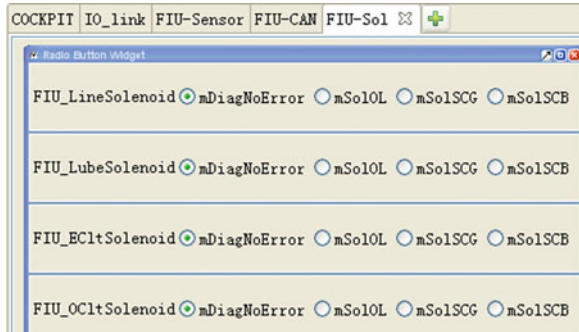


Fig. 5.4 Extract from the Silver dashboard for DCT350

Fig. 5.5 Extract from the fault insertion control panel for DCT350



The System Under Test can achieve all required test functions, in a similar manner as what is done on the HiL or in the real vehicle. Moreover, test requirements such as fault insertion can be implemented in a straightforward way since it is possible to control and modify any signal flowing between the plant and the virtual ECU.

5.5 Large Coverage Testing with QTronic TestWeaver

The driving concept for large coverage testing with TestWeaver is to automate the generation and the analysis of test scenarios. The System Under Test provided to TestWeaver is a black box which only exposes predefined interfaces, the so called instruments. TestWeaver can be connected to Silver via the Silver python module.

Implementing a TestWeaver set-up can be generally divided into 3 stages:

1. Definition and implementation of the system inputs/outputs to/from TestWeaver
2. Definition and implementation of system requirements and invariants
3. Creation and configuration of report generators

The definition of input/outputs is done in a python script, which can be automatically generated from the Silver GUI and then further edited and refined.

The system requirements and invariants are rules that the system must respect. For instance, simple system invariants are min/max checks on some variables, such as maximum engine speed or maximum clutch temperatures. More complex invariants are logical rules. These can be tested, using dedicated state machines implemented with TestWeaver python's library. When a system requirement is violated during a test case, TestWeaver can report it and the problematic scenario can be replayed and debugged in Silver.

Finally, the automatic report generators are configured in order to display and catch properties of interest such as

- System states test coverage
- Code coverage
- A2L discrete variables coverage
- Gear shift time, gear shift properties, gear shift oscillations
- Alarms and errors

More details about QTronic TestWeaver can be found in [6].

Figure 5.6 shows an overview of a TestWeaver project.

The implementation of TestWeaver for the DCT350 TCU testing used around 40 instruments (inputs, outputs, parameters) for cases without faults and a supplement or around 40 instruments related to fault insertion and fault reaction monitoring. Typical instruments are for vehicle speed, engine speed, engine torque, actuator positions, TCU states, etc.

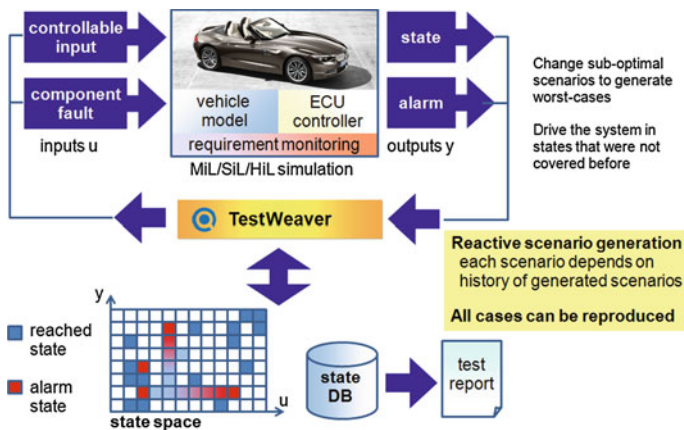


Fig. 5.6 Overview of a TestWeaver project

5.6 Results

Reports for analysing various properties of the system were established, including

- Coverage of reached gear shifts under various conditions
- Gear shift time analysis, under load and without load
- Clutch temperatures
- A2L variables range monitoring (detects signals that exceed prescribed min/max)
- A2L coverage for discrete variables
- Gear shift analysis during ‘change mind’ manoeuvre (pedal position changed during gear shift)

We give some examples below of typical reports obtained after a test run of around 500 scenarios.

The coverage of reached gear shifts can be displayed as a 2D chart where the x-axis represents the current gear and the y-axis the target gear. The chart allows a quick identification of gear shift sequences covered, as shown in Fig. 5.7.

The gear shift coverage can also be displayed as a table with links to corresponding scenarios. The table can also provide additional information, such as the slope or the gear lever position for the corresponding gear shift sequences. For instance, Fig. 5.8 shows that gear shift 2 → 1 has been tested for both ‘flat’ slope and ‘15 %’ slopes.

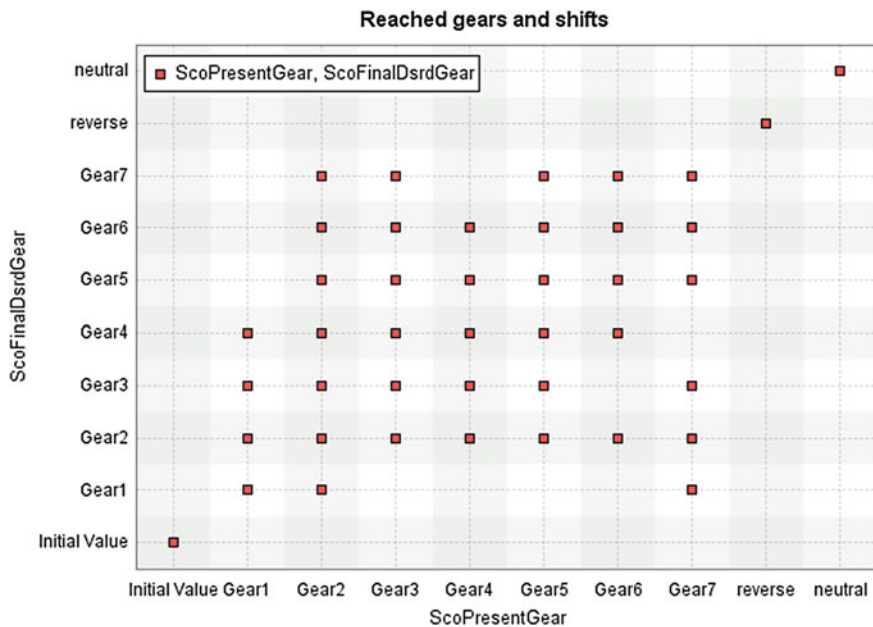


Fig. 5.7 Example of reached gear shift coverage—chart view

Coverage report

ScoPresentGear	ScoFinalDsrdGear	SlopeInput	GearLever	scenarios
Initial Value	Initial Value	-15%	P	[s203.0]
		Flat	P	[s0.0, s205.0]
		15%	P	[s204.0]
Gear1	Gear1	-15%	D	[s203.4, s203.5]
		Flat	R	[s135.0, s619.0]
			D	[s0.25, s0.26]
			S	[s66.6, s66.7]
		15%	D	[s204.4, s204.5]
	Gear2	-15%	D	[s203.16, s203.17]
		Flat	D	[s0.65, s0.66]
			S	[s66.16, s66.17]
	15%	D	[s204.15]	
	Gear3	Flat	D	[s16.22, s16.23]
Flat		D	[s141.17, s141.18]	
Gear2	Gear1	Flat	D	[s26.17, s27.17]
		15%	D	[s204.45]
	Gear2	-15%	D	[s203.18, s203.19]
		Flat	D	[s0.70, s0.71]
			S	[s66.18, s66.19]
	15%	D	[s204.16, s204.17]	
	Gear3	-15%	D	[s203.21]
		Flat	D	[s0.87, s0.88]
				S

Fig. 5.8 Example of reached gear shift coverage—table display

Apart from gear shift coverage, TestWeaver also reports the A2L coverage for discrete variables. Figure 5.9 shows an example of A2L discrete variable coverage.

For error and debugging, several analysis reports were set up. Of these, gear shift oscillation detection was implemented. Gear shifts’ oscillation for target gear is

Value coverage per signal - lowest coverage first

variable	coverage	comment	total values	reached	unreached
TstPreSelScheduleGear	77.8	the shedule desired preselect gear	9	7	2
ScoTstMinGear	77.8	the min gear come from TST and add some condition	9	7	2
TstMinGear	77.8	The final Minimum gear which is allowed to execute during shifting	9	7	2
ScoTstMaxGear	77.8	the max gear come from TST and add some condition	9	7	2
TstSchdMinGear	77.8	The Minimum gear before override mode	9	7	2
vIOP_ClutchSpdStates[...]	80.0	Clutch speed diagnostic from IOP.	5	4	1
vIOP_ClutchHardStates[...]	80.0	Clutch speed sensors diagnostic from IOP. It is a internal value in the IOP process.	5	4	1
vIOP_OutputSpdHardState	80.0	Output speed sensors diagnostic from IOP. It is a internal value in the IOP process	5	4	1
vIOP_OutputSpdState	80.0	Output speed diagnostic from IOP	5	4	1
ScoEngCntrlRqst	83.3	the request to engine system	6	5	1
GacAxisPressState	85.7	reset the solenoids when starting a new gear actuation	7	6	1
ScoLaunchStageOld	87.5	describe the car launch stage	8	7	1
ScoLaunchStage	87.5	describe the car launch stage	8	7	1
TstReviewedGearOld	88.9	The desired gear after optimization	9	8	1
TstScheduleGear	88.9	The desired gear before optimization	9	8	1
TstReviewedGear	88.9	The desired gear after optimization	9	8	1
GacTroubleGearOld	88.9	the Gear which was busy gear before.but work with error	9	8	1
GacTroubleGear	88.9	the Gear which was busy gear before.but work with error	9	8	1
TstReviewedGearOld_Va	88.9	The desired gear after optimization	9	8	1
TstScheduleGearOld	88.9	The desired gear before optimization	9	8	1
FitOilTempStates	100.0	sump oil temperature state	3	3	0
TstTireStatus	100.0		2	2	0
vIOP_EngStatus	100.0	Engine status(Ignition, idling, or running) from IOP.	3	3	0
GacMltpxCmndStatesOld[...]	100.0	the request to multiplex valves	2	2	0
GacControlMode	100.0	the gear actuation mode	7	7	0
ScoAxisStatus[...]	100.0	reflect axis fill status	7	7	0
ClcClutchFillStatusOld[...]	100.0	the clutch filling state	6	6	0

Fig. 5.9 Example of A2L discrete variable coverage

time	Changed Inputs	Target Gear oscill	Current Gear oscill	Target gear	Current gear	Clutch_heat A	Clutch_heat B	duration	Changed States
6.74		ok	ok	Gear2	Gear2	Ok	Ok	0.01	Sco_ShiftKind=Garage
6.75		ok	ok	Gear3	Gear2	Ok	Ok	0.29	ScoFinalDsrDGear=Gear3 Sco_ShiftClass=eShiftPos23 Sco
7.04		Oscill DsrD	ok	Gear2	Gear2	Ok	Ok	0.09	GipAxisVslsStatus0=eAxisNeutralize ScoFinalDsrDGear=G NoShift Sco_ShiftKind=Garage
7.13		Oscill DsrD	ok	Gear2	Gear2	Ok	Ok	0.36	lopEngineSpeed=High
7.49		Oscill DsrD	ok	Gear4	Gear2	Ok	Ok	0.31	ScoFinalDsrDGear=Gear4 Sco_ShiftClass=eShiftPos24 Sco
7.8	PedalInput=0%	ok	ok	Gear4	Gear2	Ok	Ok	0.03	
7.83		ok	ok	Gear2	Gear4	Ok	Ok	0.01	ScoFinalDsrDGear=Gear2 ScoPresentGear=Gear4 Sco_Sha
7.84		Oscill DsrD	Oscill Present	Gear4	Gear2	Ok	Ok	0.01	ScoFinalDsrDGear=Gear2 ScoPresentGear=Gear2 Sco_Sha
7.85		Oscill DsrD	Oscill Present	Gear2	Gear4	Ok	Ok	0.01	ScoFinalDsrDGear=Gear2 ScoPresentGear=Gear4 Sco_Sha
7.86		Oscill DsrD	Oscill Present	Gear4	Gear2	Ok	Ok	0.01	ScoFinalDsrDGear=Gear4 ScoPresentGear=Gear2 Sco_Sha
7.87		Oscill DsrD	Oscill Present	Gear2	Gear4	Ok	Ok	0.01	ScoFinalDsrDGear=Gear2 ScoPresentGear=Gear4 Sco_Sha
7.88		Oscill DsrD	Oscill Present	Gear4	Gear2	Ok	Ok	0.01	ScoFinalDsrDGear=Gear4 ScoPresentGear=Gear2 Sco_Sha
7.89		Oscill DsrD	Oscill Present	Gear2	Gear4	Ok	Ok	0.01	ScoFinalDsrDGear=Gear2 ScoPresentGear=Gear4 Sco_Sha
7.9		Oscill DsrD	Oscill Present	Gear4	Gear2	Ok	Ok	0.01	ScoFinalDsrDGear=Gear4 ScoPresentGear=Gear2 Sco_Sha

Issue in the gearshift control

Fig. 5.10 Example of issue identified by TestWeaver during testing—scenario report

usually a good indicator for gear shifting issues. We set up the detection mechanism so that repeated up changes/down changes of target gear were reported and put in 2 classes: oscillations faster than 10 ms and oscillations faster than 50 ms.

This ‘filter’ for target gear oscillations shows that the vehicle could be driven in a state where the gear shifting would fail. This state seems to appear after a change of accelerator pedal input position during a gear shift from 2nd to 4th gear. The TCU goes then in a mode where the target gear and current gear kept changing every 10 ms and the gearbox failed to achieve a proper shift. This process is illustrated in the ‘scenario’ report, as shown in Fig. 5.10.

The scenario can be replayed, and the root cause of the issue is analysed. Once the root cause is found, a modification can be implemented and tested again. In the above example, modelling errors in the plant model was found to be the cause of the abnormal gear shifting. This was fixed, and the abnormal gear shift case was solved. However, TestWeaver showed that under certain particular conditions, the tested TCU software version could enter a 10 ms upshift/downshift cycle.

5.7 Conclusions

The virtual integration established in this project provides FAW with an increased confidence in the quality and maturity of the TCU control software. The large coverage provided by TestWeaver allows finding issues and bugs that would potentially be missed out by HiL and drive tests.

References

1. Papkonstantinou N, Klinger S, Tatar M (2009) Test-driven development of DCT control software. In: 8th international CTI symposium innovative automotive transmissions, Berlin
2. Schaich R, Tatar M (2010) Automated test of the AMG speedshift DCT control software. In: 9th international CTI symposium innovative automotive transmissions, Berlin
3. Bruckmann H, Strenkert J, Wiesner B, Junghanns A (2009) Model-based development of dual-clutch transmission using rapid prototyping and SiL. *Getriebe in Fahrzeugen*, Friedrichshafen
4. Junghanns A, Mauss J, Tatar M (2008) Test automation based on computer chess principles. In: 7th international CTI symposium innovative automotive transmissions, Berlin
5. Belmon L, Xu Y (2012) Intelligent test-case generation for automated validation of TCUs. In: International CTI symposium innovative automotive transmissions, Berlin
6. Tatar M, Mauss J (2014) Systematic test and validation of complex embedded systems. *Embedded Real Time Software and Systems*, Toulouse

Chapter 6

Modeling and Analysis of Torsional Vibration on Engine-generator System of Hybrid Electric Vehicle

Xiaofeng Ma, Ke Luo, Lijun Zhang, Hongzheng Cheng and Dejian Meng

Abstract To analyze torsional vibration of the powertrain system for series hybrid vehicle, which consisted of dynamic vibration absorber (DVA), V12 diesel engine, speed increaser, and a generator, a lumped parameter model of torsional vibration and its vibration equation is established. Based on this model, the inherent vibration characteristic is calculated by using *Matlab*. And forced vibration analysis including order and resonance amplitude analysis is carried out considering no-load and full-load conditions. The results indicate that the working speed chosen is appropriate.

Keywords Engine-generator system · Torsional vibration · Inherent characteristics · Forced vibration · Order analysis

6.1 Introduction

Energy saving and environmental protection requirements make all kinds of electric vehicles at home and abroad an important technology and competition focus in recent years. Engine-generator system is the core of key parts in the powertrain of series hybrid vehicles, plug-in hybrid cars, and extended-range electric vehicles, playing an important role on working with high efficiency and low emissions. However, it may reduce the ride comfort and lead to structural fatigue damage and deterioration in vehicle acoustic quality if the engine-generator system is unreasonably designed [1, 2].

The key problem of engine-generator system is torsional vibration and control. It is usually studied using lumped parameter model, distribution model, and

X. Ma
China North Vehicle Research Institute, Beijing, China

K. Luo (✉)
School of Automotive Studies, Tongji University, Shanghai, China
e-mail: Luoke062731@163.com

K. Luo · L. Zhang · H. Cheng · D. Meng
New Clean Energy Vehicle Engineering Center, Tongji University, Shanghai, China

multi-body dynamics model and has obtained many results in analyzing engine crankshaft system, the transmission system, and the drive motor [3–7]. However, for the electric automobile engine-generator system, there are very few torsional vibration studies and proven modeling and simulation analysis method. Thus, establishing the system of the dynamic matching design method for the engine-generator system to analyze torsional vibration has important engineering value, guiding the determination of the ideal static working point, as well as the integration control in dynamic process.

This study began with torsional vibration modeling of V12 engine-generator in series hybrid vehicle using lumped parameter method. The second step of this study involved in calculating and analyzing inherent vibration characteristic and transient forced vibration, putting forward a method of selecting ideal working point. Then, this study verified the reasonability of selecting the working point by analyzing vibration characteristic in no-load and actual full-load condition. The results provide the hybrid electric vehicle with an important reference in engine-generator matching design and the selection of ideal working point.

6.2 Theoretical Modeling

6.2.1 Simplify and Modeling

The engine-generator system, as shown in Fig. 6.1, consists of a V12 engine, a speed increaser and a generator. The V12 engine is a supercharged diesel engine used in special vehicles, and the speeder uses straight tooth meshing transmission, while the generator is permanent magnet synchronous motor. The basic parameters are listed in Table 6.1.

Supposing that the each shaft section in the system can be divided into a disk that has concentrated moment of inertia and an elastic axis with no quality, this study established lumped parameter model of the engine-generator system with eleven degrees of freedom, considering external damping and shaft section damping, as is shown in Fig. 6.2, according to principles of equivalent on the natural frequencies

Fig. 6.1 Engine-generator structure diagram

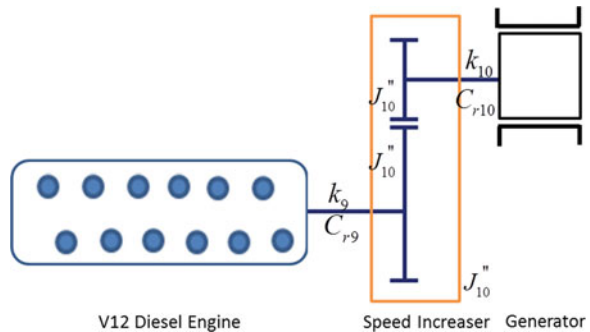


Table 6.1 Engine-generator system parameters

V12 engine	Ignition order	L1 → R6 → L5 → R2 → L3 → R4 → L6 → R1 → L2 → R5 → L4 → R3, Free end:1		
	Mass of piston and connecting rod assembly	3 kg		
	V-type angle	90°	Number of crank	6
	Rod length	283 mm	Rod radius	55 mm
Increaser	Gear ratio	33/64		
Generator	Rated speed	4,200 rpm	Rotor inertia	2.94 kgm ²
	Rated power	800 kw	Rated torque	1,819 Nm

and principles of equivalent on vibration modes of the torsional vibration system and the actual system.

The vibration differential equations can be expressed as:

$$\begin{cases}
 J_1 \ddot{\theta}_1 + k_1(\theta_1 - \theta_2) + c_{r1}(\dot{\theta}_1 - \dot{\theta}_2) = T_1 \\
 J_2 \ddot{\theta}_2 - k_1(\theta_1 - \theta_2) + k_2(\theta_2 - \theta_3) - c_{r2}(\dot{\theta}_1 - \dot{\theta}_2) + c_{r2}(\dot{\theta}_2 - \dot{\theta}_3) = T_2 \\
 J_i \ddot{\theta}_i - k_{i-1}(\theta_{i-1} - \theta_i) + k_i(\theta_i - \theta_{i+1}) - c_{ri-1}(\dot{\theta}_{i-1} - \dot{\theta}_i) + c_{ri}(\dot{\theta}_i - \dot{\theta}_{i+1}) \\
 \quad + c_{0i} \dot{\theta}_i = T_i (i = 3, 4, \dots, 8) \\
 J_9 \ddot{\theta}_9 - k_8(\theta_8 - \theta_9) + k_9(\theta_9 - \theta_{10}) - c_{r8}(\dot{\theta}_8 - \dot{\theta}_9) + c_{r9}(\dot{\theta}_9 - \dot{\theta}_{10}) = T_9 \\
 J_{10} \ddot{\theta}_{10} - k_9(\theta_9 - \theta_{10}) + k_{10}(\theta_{10} - \theta_{11}) - c_{r9}(\dot{\theta}_9 - \dot{\theta}_{10}) + c_{r10}(\dot{\theta}_{10} - \dot{\theta}_{11}) = T_{10} \\
 J_{11} \ddot{\theta}_{11}/r^2 - k_{10}(\theta_{10} - \theta_{11}) - c_{r10}(\dot{\theta}_{10} - \dot{\theta}_{11}) + k_{11}\theta_{11} + c_{011}\dot{\theta}_{11} = T_{11}
 \end{cases}
 \tag{6.1}$$

It can be rewritten in matrix form as:

$$[J]\{\ddot{\theta}\} + [C]\{\dot{\theta}\} + [K]\{\theta\} = [T]
 \tag{6.2}$$

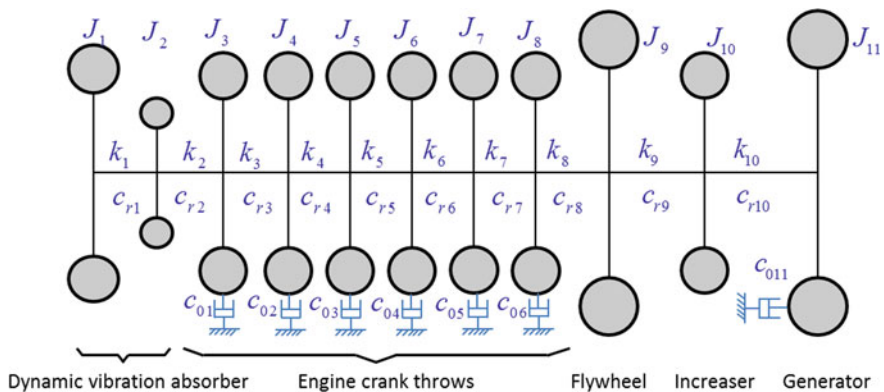


Fig. 6.2 Lumped parameter model of engine-generator system

where $\{\theta\} = \text{diag}(\theta_1, \theta_2, \dots, \theta_{11})$ is the angle vector of each degree of freedom in torsional vibration in lumped parameter model, $[J] = \text{diag}(J_1, J_2, \dots, J_{11})$ is the rotational inertia matrix, $[C] = [C_r] + [C_0]$ is the damping matrix, $[K]$ is stiffness matrix, and $[T] = [T_1, T_2, \dots, T_{11}]^T$ is the excitation torque vector.

6.2.2 Determination of Model Parameters

6.2.2.1 Rotational Inertia

Rotational inertia of each assembly unit J_i equals to the sum of its moment of inertia J_{i0} and half of the inertia of the connecting shaft. For example, J_3 equals to the inertia of the third crank J_{30} plus two half inertia of the connecting shaft named by k_2 and k_3 . More details are given in references [2–5].

The rotational inertia of speed increaser and generator is obtained according to what is said in above paragraph and the law of conservation of energy. Taking the speed increaser as an example, its rotational inertia can be obtained as:

$$J_{10} = J'_{10} + J''_{10}/r^2 + (J_{k9} + J_{k10})/2 \quad (6.3)$$

The symbols in the Eq. (6.3) are the same as that are shown in Fig. 6.1.

6.2.2.2 Torsional Stiffness

After simplifying, the system consists of 11 lumped rotatory inertias including dynamic vibration absorber (DVA), six cranks, a flywheel, a speed increaser and a generator rotor, and ten connecting shafts with no inertia. The stiffness of connecting shafts is obtained by using finite elements method.

6.2.2.3 System Damping

Shaft section damping and external damping are determined by empirical formula which refers to references [1, 5].

$$c_m = c_r k_n / \omega \quad (6.4)$$

$$c_{on} = c_e J_n \omega \quad (6.5)$$

where c_e and c_r are the damping coefficient of the unit, J_n and k_n are inertia and stiffness of certain degree of freedom, and ω is the angle velocity.

The parameters of the system are presented in Table 6.2.

Table 6.2 Parameters of lumped parameter model of engine-generator system

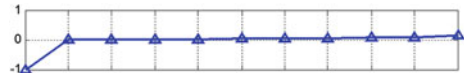
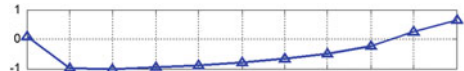
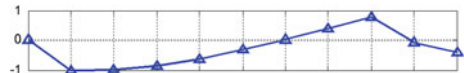
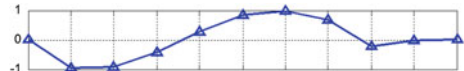

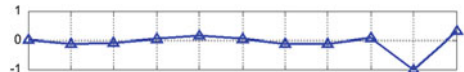
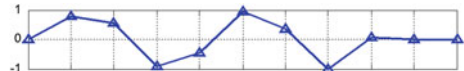
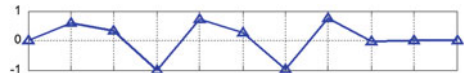

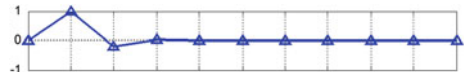
Parameters	Data
Torsional stiffness (MNm/rad)	$k_1 = 0.04, k_2 = 5.525, k_8 = 3.199, k_9 = 2.236, k_{10} = 6.65$ $k_3 = k_4 = k_5 = k_6 = k_7 = 4.398$
Rotational inertia (kgm ²)	$J_1 = 0.79, J_2 = 0.061, J_3 = 0.343, J_4 = 0.343, J_5 = 0.343,$ $J_6 = 0.343, J_7 = 0.343, J_8 = 0.343, J_9 = 2.603, J_{10} = 1.042, J_{11} = 2.94$
Damping	$c_r = 0.02, c_e = 0.04, c_{o11} = 0.025$ Nm rad/s

6.3 Engine-generator System Inherent Characteristic

Setting damping matrix $[C]$ and $[T]$ in Eq. (6.2) to be zero, the modal frequency and mode shape of each order can be obtained by using *Matlab*.

Table 6.3 illustrates torsional vibration inherent characteristic of engine-generator system, and it shows that:

Table 6.3 Engine-generator system inherent characteristic

Orders	Inherent frequencies/Hz	Mode shapes
1	35.9	
2	112.5	
3	198.6	
4	392.5	
5	620.3	
6	645.0	
7	828.1	
8	993.9	
9	1,101.9	
10	1,667.3	

1. There are ten inherent frequencies besides rigid body mode. The lowest one is 35.9 Hz, while the highest is 1667.3 Hz; and the first four-order inherent frequencies are less than 400 Hz, which are more likely to resonant in the range of system speed.
2. The first-order mode shape shows that it is mainly the vibration of the inertial mass of DVA which indicates its effectiveness in absorbing vibration. But in other orders, the inertial mass is always in the vicinity of a node, thus the amplitude is very small, indicating that the DVA does not match actual requirements.
3. In the second three modes, all degrees of freedom besides inertial mass of the DVA are in a state of strong vibration. The sixth-order mode is mainly the vibration of the speed increaser. The fourth-, fifth-, seventh-, eighth-, and ninth-order modes show that vibration of all the degrees of freedom besides crank throws is small. The tenth order is mainly the vibration of the shell of absorber.

6.4 Engine-generator System Forced Vibration

6.4.1 Excitation Torque [1]

6.4.1.1 Engine Excitation Torque

The torque, which actuates the crank throws, includes two parts. One is gas load while the other is the oscillating inertial force. They can be expressed as the equation:

$$M_g = \frac{\pi D^2}{4} P_g \frac{\sin(\alpha + \beta)}{\cos \beta} R \quad (6.6)$$

$$M_j = -m_j R \omega^2 \left(\sin \alpha + \frac{\lambda}{2} \sin 2\alpha \right) \frac{\sin(\alpha + \beta)}{\cos \beta} \quad (6.7)$$

where D is cylinder diameter, α is crankshaft angle, β is the angle between connecting rod and the center line of the cylinder, R is the crank shaft radius, m_j is the reciprocating inertial mass, and P_g is the gas pressure obtained by experiment, as shown in Fig. 6.3.

6.4.1.2 Generator Torque

In the actual working process and simulation, the generator torque is controlled by certain strategy. Figure 6.4 illustrates the relationship between generator speed and torque after control.

Fig. 6.3 Gas pressure at different crank shaft angle

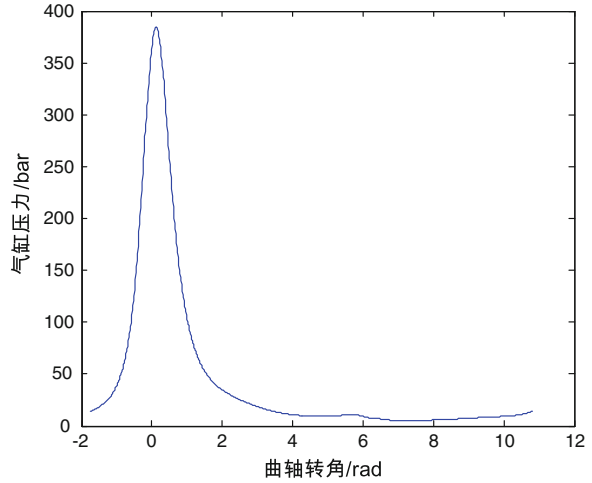
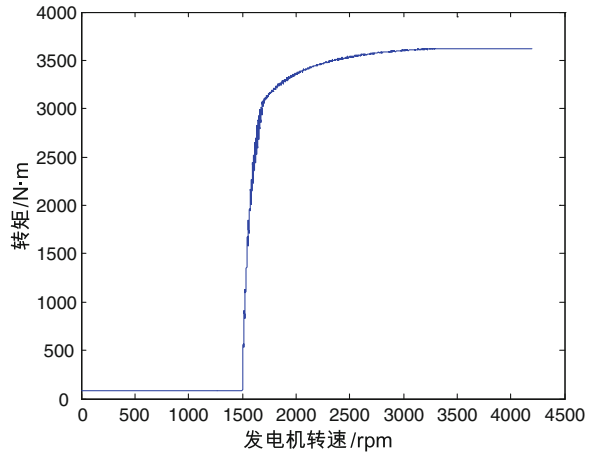


Fig. 6.4 Generator torque at different speed



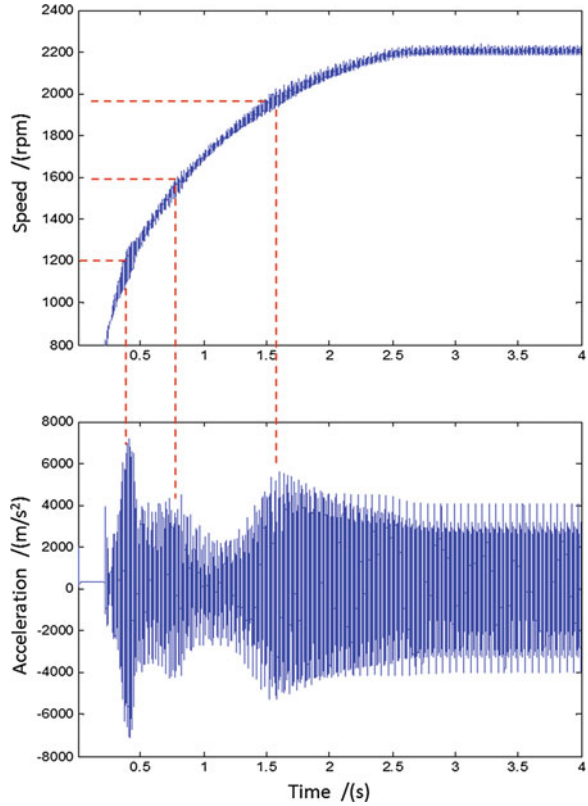
6.4.2 Forced Vibration Analysis in No-load Condition

No-load condition refers to a condition when generator does not generate current during the engine-generator system works and has important guiding significance in selecting the working point.

To determine the stable working speed range, time history of acceleration and velocity of each degree of freedom is presented in this section, analyzing vibration distribution of the system by using *Matlab* based on vibration equation.

Considering the similarity of the response of each part in the system, the engine speed and angular acceleration of the second crank throw are shown in Fig. 6.5. The result indicates that the engine-generator system resonate in speed range of

Fig. 6.5 Angular acceleration of the second crank throw and engine speed curve in no-load condition



1,000–1,500 rpm, near 2,750 rpm, 3,500 rpm, and 4,200 rpm as well as higher speed, at which the system should avoid working from the view point of vibration. Hence, speed range of 1,500–2,500 rpm, 3,000–3,300 rpm, and 3,600–4,000 rpm is preliminary selected as ideal working speed.

6.4.3 Forced Vibration Analysis in Full-load Condition

Knowing that the higher speed the system works at, the more resonance points it goes through, it is reasonable to select a low speed on basis of both performance and fuel economy. In this study, in meeting the requirements of this special vehicle, 2,200 rpm is selected as the working speed at which full-load forced vibration simulation is carried out below.

6.4.3.1 Full-load Forced Vibration Time-domain Analysis

Figure 6.6 shows the result of engine speed and angular acceleration of the second crank throw curve which indicates that the second crank throw has strong vibration in speed range of 1,100–1,300 rpm, 1,450–1,650 rpm, and 1,800–2,100 rpm. Other degree of freedom has similar conclusion.

6.4.3.2 Order Contribution Analysis

Since there are many orders in the vibration of engine crankshaft, order analysis of engine-generator system is carried out, providing a basis for vibration control. Figures 6.7 and 6.8 are three-dimensional waterfall and main order contrast figure of angular acceleration of the second crank throw obtained from full-load simulation. The diameter of circles indicated in Fig. 6.8 illustrates vibration amplitude.

Figures 6.7 and 6.8 show that there are 3.5th order, 4.5th order, 5.5th order, 6th order, and 7.5th order in angular acceleration signal of the second crank throw, and size of amplitude comparison is: $A_6 > A_{4.5} > A_{3.5} > A_{7.5} > A_{5.5}$.

Fig. 6.6 Angular acceleration of the second crank throw and engine speed curve in full-load condition

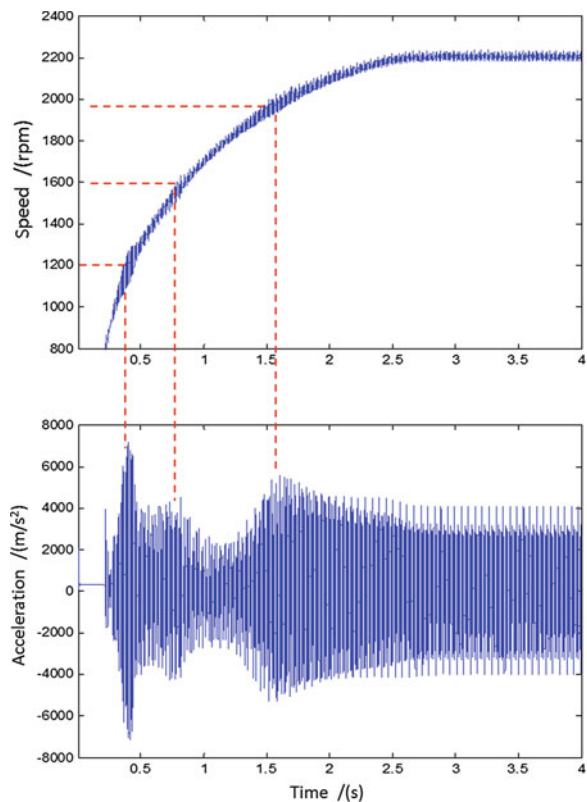


Fig. 6.7 Angular acceleration waterfalls of the second crank throw

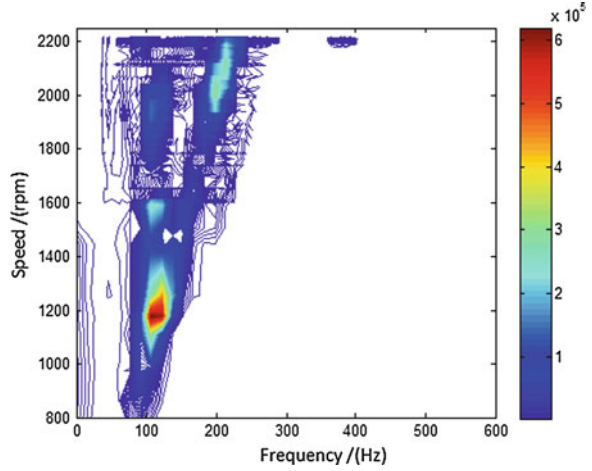
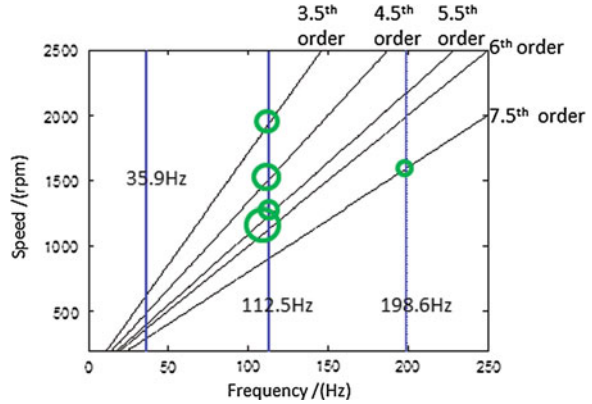


Fig. 6.8 Main order contrast of the second crank throw



Analogously, Fig. 6.9 presents angular acceleration orders of other degrees of freedom and the amplitude comparisons are re-expressed in Table 6.4.

The results presented in Table 6.4 indicate that:

- (1) Orders: Sensitive order sequence is different between each degree of freedom, but the main orders are several half orders on the basis of sixth order. A possible reason for these half orders is deformation of crankshaft.
- (2) Resonant frequency and speed range: 35.9, 112, and 198 Hz are the main resonant frequencies, but different moving parts vary in resonant frequency. What is more, vibration has high amplitude at some certain speed range due to different order. 5.5th order and 6th order result in high vibration amplitude at 1,100–1,300 rpm, 1.5th order and 4.5th order result in 1,450–1,650, while first order, 3.5th order, and 6th order result in 1,800–2,160 rpm.

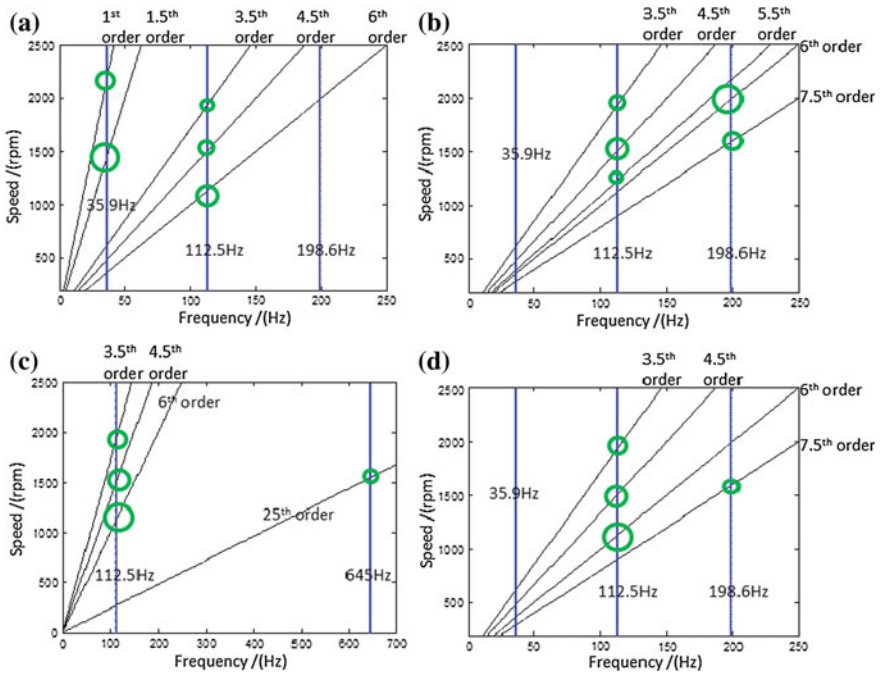


Fig. 6.9 Amplitude comparison of main orders of other degrees of freedom. **a** Main orders of inertial mass of DVA. **b** Main orders of flywheel. **c** Main orders of speed increaser. **d** Main orders of generator

Table 6.4 Amplitude comparison of main orders of other degrees of freedom

Degree of freedom	Amplitude comparison
Inertial mass of DVA	$A_{1.5} > A_6 > A_1 > A_{4.5} > A_{3.5}$
Shell of DVA	$A_6 > A_{4.5} > A_{3.5} > A_{5.5} > A_{7.5}$
Flywheel	$A_6 > A_{4.5} > A_{7.5} > A_{3.5} > A_{5.5}$
Speed increaser	$A_6 > A_{4.5} > A_{3.5} > A_{25}$
Generator	$A_6 > A_{4.5} > A_{3.5} > A_{7.5}$

- (3) The working point 2,200 rpm which is away from main resonance speed, at which each degree of freedom has relatively small amplitude of vibration, has a good performance in avoiding strong torsional vibration.

6.5 Conclusions

In this paper, a lumped parameter model of an engine-generator system used in hybrid electric vehicle is established and its inherent characteristics and forced vibration characteristics is calculated. By analyzing vibration mode distribution

under each mode frequency and orders of forced vibration signals as well as amplitude distribution of each order, a stable working speed that meets vibration requirements is reasonably selected.

The effectiveness of this dynamic model and reasonability of the working speed will be studied further combining with prototype test.

References

1. Zhang B (2009) Internal combustion engine dynamics. National Defence Industry Press, Beijing, pp 85–115
2. Zhou B, Jiang ZF, Zeng R (2010). The torsional vibration signal processing and analysis of automobile transmission shaft. In: 2010 2nd international conference on multimedia and computational intelligence, 978-1-4244-8462-1/10
3. Mendes A, Meirelles PS, Zampieri DE (2008) Analysis of torsional vibration in internal combustion engines: modeling and experimental validation. *Proc Inst Mech Eng Part K* 222:157–160
4. Huang YM, Horng CD (1999) Analysis of torsional vibration systems by the extended transfer matrix method. *ASME J Vibr Acoust* 121(2):250–252
5. Shangguan W, Chen C, Duan X et al (2012) Modeling and experimental validation of engine crankshaft torsional vibration. *J Vibr Measur Diagn* 32(4)
6. Jiaming C (1997) Design of responses to torsional vibration in engine shafting. *J Shanghai Univ Eng Sci* 11(3):32–36
7. Yue D, Zhang J (2010) Theory study of electro-mechanical coupling vibration on hybrid system shafts. *Tractor & Farm Transporter* 37(3):3–5

Chapter 7

Pore-forming Technology Development of Polymer Separators for Power Lithium-ion Battery

Lina Yu, Dan Wang, Zhongling Zhao, Jian Han, Kejin Zhang, Xinran Cui and Zhou Xu

Abstract To investigate the impact of the pore-forming agent on the performance of polymer membranes, four $\text{Al}_2\text{O}_3/\text{PVDF-HFP}$ separators with different pore-forming agents, n-butanol, deionized water, ethanol, and isopropanol are prepared by adding Al_2O_3 as the filler. The wettability, morphology, mechanism strength, and electrochemical properties of above membranes are characterized. Results show that the membrane prepared with n-butanol as the pore-forming agent has the best property, with electrolyte uptake rate of 420 %, ion transference number of 0.90, tensile strength of 14.93 MPa, conductivity of 0.50 ms/cm^{-1} , electrochemical stability of 5.2 V, and discharging specific capacity of 108 mAh/g at 4C with a LiFePO_4 half-cell.

Keywords Lithium-ion power battery · Pore-forming technology · Separators

7.1 Introduction

Porous separator is a critical component of power lithium-ion battery that is used to separate the positive and the negative electrode, which is one of the highest high-added value materials, accounted about 15 % of the batteries' cost. For preparing a qualified separator, the pore-forming technology is of most difficulty [1, 2], as micropore size and distribution will directly affect the separators porosity, permeability, uptaking, etc. To enhance the specific energy and high power discharging of lithium-ion batteries, it needs to further improve the porosity and reduce the thickness so as to obtain the separators with smaller ionic resistance. However,

L. Yu (✉) · D. Wang · Z. Zhao · J. Han · K. Zhang · X. Cui · Z. Xu
R&D Center, China FAW Co. Ltd., Changchun, China
e-mail: yulina@rdc.faw.com.cn

reducing the thickness will reduce its strength and thus affect the safety of power lithium battery [3].

In this paper, on the base of $\text{Al}_2\text{O}_3/\text{PVDF-HFP}$ separator by using the phase inversion [4], n-butanol, deionized water, ethanol, and isopropanol were selected to prepare four $\text{Al}_2\text{O}_3/\text{PVDF-HFP}$ separators, respectively. Then, the influence on the comprehensive performance of separator was investigated. Results show that n-butanol is optimized as the best pore-forming agent, on the one hand ensures the necessary mechanical strength, and on the other hand enhances the uptake of $\text{Al}_2\text{O}_3/\text{PVDF-HFP}$ separator, which significantly improves the discharging capacity at large current. In addition, the $\text{Al}_2\text{O}_3/\text{PVDF-HFP}$ polymer separator by n-butanol as pore-forming agent has such advantages as simple preparation process, low cost of the preparation, and easy to realize batch production. Predictably, inorganic nanoparticle/PVDF-HFP is a suitable separator for power lithium-ion battery.

7.2 Experimental

7.2.1 Preparation of Polymer Separators

An appropriate amount of PVDF-HFP was dissolved in acetone with refluxing at 60 °C and vigorous stirring for 2 h, then the suitable amounts of nano- Al_2O_3 were added into the solution, so mother liquor was obtained by continuously heating and stirring for 2 h. Then, the mother liquor was divided into four parts, followed by adding a certain amount of butanol, water, ethanol, and isopropanol by continuously heating and stirring for 2 h. The separator was obtained by casting method, then dried under vacuum at 65 °C for 5 h, and marked as A, B, C and D, respectively.

7.2.2 Polymer Separators Characterization

The FT-IR spectra (4,000–400 cm^{-1} , acquisition 32 times, resolution 2 cm^{-1}) were recorded with a Nicolet 6700 spectrometer.

The surface morphology of the separators was investigated by FE-SEM.

The wettability was tested by dropping a liquid electrolyte (1 M LiPF_6 in EC/DEC, v/v = 1:1) to the sample that was cut to 20 mm diameter.

The tensile properties of the separators were tested using tester (XLW, Lab-Think, China) according to test procedures provided in ASTM D882-09. The size was 20 mm × 60 mm (w × l).

The electrochemical stability window was examined in the cell of SS/electrolyte-soaked separators/Li by linear sweep age (LSV), at a scan rate of 1 mV/s over the range of 3–7 V, using 1 M LiPF_6 in EC/DMC/EMC (v/v/v = 1:1:1), the same below.

Ionic conductivity was examined by AC impedance with the cell of SS/electrolyte-soaked separators/SS, the frequency was 0.01–10⁶ Hz, and the age amplitude is 5 mV.

The lithium-ion transference number was measured by multi-potential steps with the cell of Li/electrolyte-soaked separators/Li, and the polarization age was 5 mV.

C-rate and cycle performance were characterized with half-cells of LiFePO₄ (LFP)/electrolyte-soaked separators/Li at the charging rate of 0.1C.

7.3 Results and Discussion

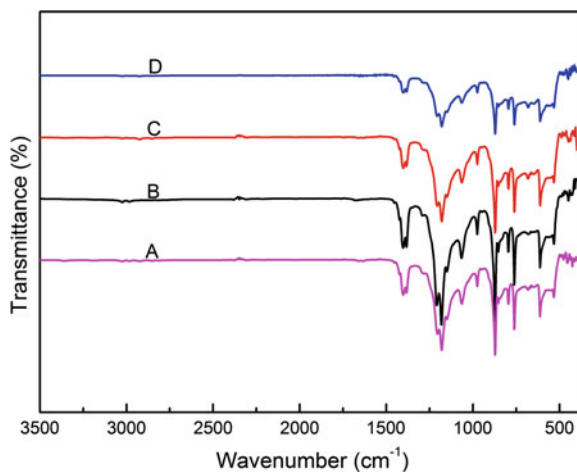
7.3.1 Preparation

To verify whether there are any residual solvents and pore-forming agents in the separator, four separators were analyzed by IR testing, and the results are as shown in Fig. 7.1. It can be found that the typical peaks of PVDF-HFP are 1,399, 1,178, 1,066, and 873 cm⁻¹. No carbonyl (C=O) stretching vibration peak shows that acetone solvent had been completely evaporated. In addition, 3,200–3,400 cm⁻¹, no O–H stretching vibration, shows that pore-forming agent in the process of vacuum drying had been completely volatilized.

7.3.2 Morphology

SEM morphologies for A, B, C, and D are as shown in Fig. 7.2. The pores in both A and B separators are extremely abundant, which distributed evenly and staggered with each layer, pore sizes are about 1 μm for A and 2 μm for B. In addition, there is

Fig. 7.1 The FT-IR spectra of A, B, C, and D separator



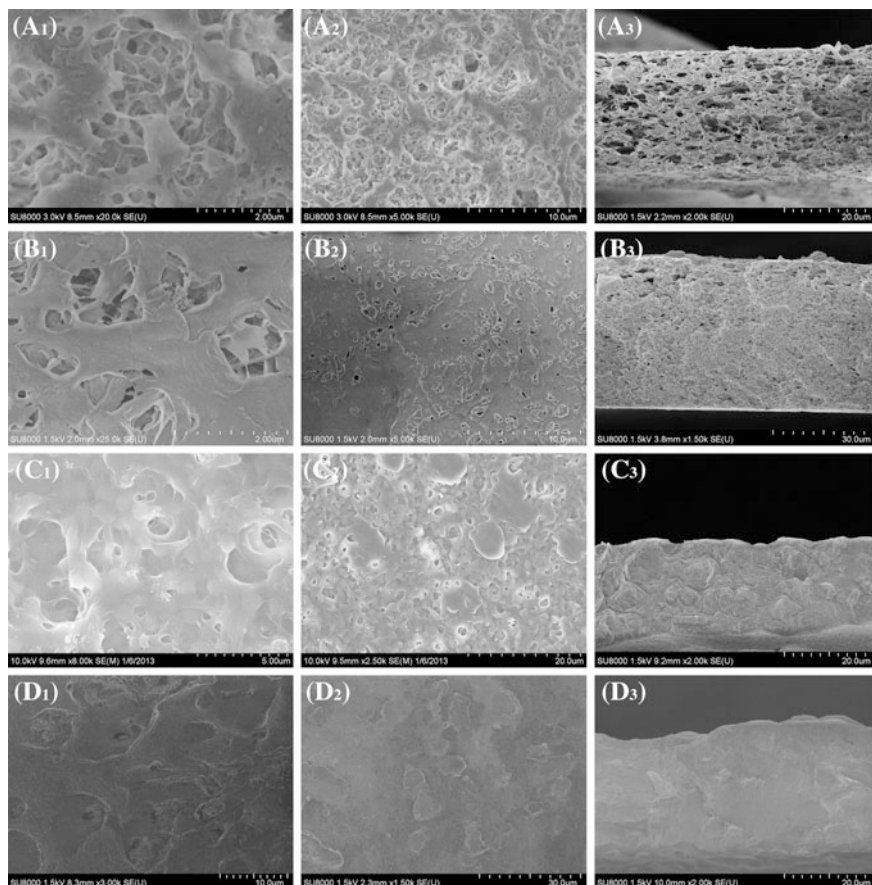










Fig. 7.2 FE-SEM photographs of: A_1 , A_2 —A separator surface; B_1 , B_2 —B separator surface; C_1 , C_2 —C separator surface; D_1 , D_2 —D separator surface; A_3 —A separator cross section; B_3 —B separator cross section; C_3 —C separator cross section; D_3 —D separator cross section

no three-dimensional hole on the cross section. Figure 7.2 (C_1) and (C_2) exhibit many three-dimensional pores with uniform distribution too, but the porosity is less than A and B on the cross section. As shown in Fig. 7.2 (D_1), (D_2), and (D_3), there is no pore distributed both on surface and cross section.

7.3.3 Wettability

In order to study the electrolyte-soaked behavior of $Al_2O_3/PVDF-HFP$ with different pore-forming agents, we cut the separator to 20 mm diameter, and then a drop of electrolyte was added on the sample, respectively. Pictures of dropping liquid

Table 7.1 Picture of wettability test

State	Picture			
	A	B	C	D
dropping before				
2 s after dropping				

before and after are as shown in Table 7.1. As shown in Table 7.1, A and B were quickly wetted and D the slowest. In general, the good or bad wettability is closely related to the pore structure, combined with Sect. 7.3.2, it may be due to the three-dimensional interconnected pore in A, B, and C, while there was no pore in D.

To further verify the influence of the pore-forming agent on uptaking of the separator, the uptake tests have been carried out [5], and its result is as shown in Fig. 7.3. As shown in Fig. 7.3, the uptake of A and B was the highest and D the worst, followed by C. It well agrees with the above description. In general, the more abundant the separator pores, the better uptake/keeping ability, which would promote the ionic conductivity, further provided enough channels for transmission of Li^+ .

7.3.4 Mechanical Properties

When the separator contacted with hard positive/negative surface, especially with the burr, big particulates with sharp corners, even with the dendrite within battery, and thus, the separator was worn out. Consequently, it may cause micro-short circuit or short circuit. Therefore, the separator should have proper mechanical strength. The four separators were cut to adequate size for the tensile strength and deformation test, and the test curves are as shown in Fig. 7.4. It is shown in Fig. 7.4 that the tensile strength of A was 14.93 MPa, and the deformation rate was

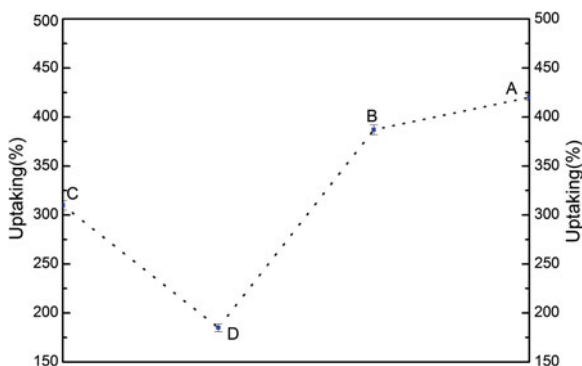
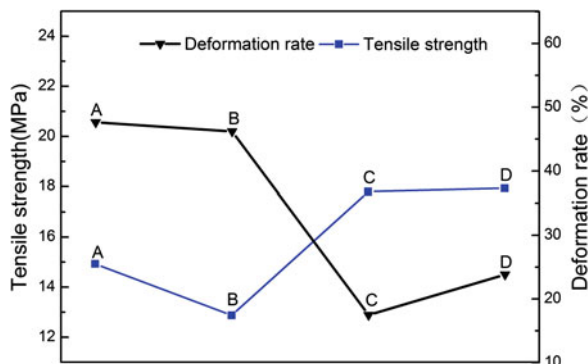
Fig. 7.3 Electrolyte uptaking of A, B, C, and D

Fig. 7.4 Tensile-deformation curves of A, B, C, and D



47.62 %; the tensile strength of C was 17.80 MPa, and the deformation rate was 17.46 %; and the tensile strength of D was 17.92 MPa, the deformation rate was 23.80 %. It suggests that there is no necessary link between the tensile strength and deformation. We must take account of both tensile strength and toughness; otherwise, the separator has high tensile strength but is brittle, which cannot meet the requirements of the use of lithium-ion battery.

7.3.5 Electrochemical Properties

7.3.5.1 Electrochemical Stability Window

In order to evaluate the impact of pore-forming agent on the stability of the separator in the electrolyte, electrochemical window was analyzed using a linear sweep voltage (LSV), as shown in Fig. 7.5. It shows that, the four separators has almost the same change trend in the electrode potential below 5.2 V, but when the electrode potential is greater than 5.2 V, the current of D changes abruptly, which means that the electrolyte starts to break down. The results show that there is less effect on the electrochemical stability of the same composition separator when different pore-forming agents are added.

7.3.5.2 Ionic Conductivity

To verify the effect of different pore-forming agents on the conductivity of polymer separators in the electrolyte, the AC impedance of the four separators was analyzed, as shown in Fig. 7.6. As shown in Fig. 7.6a, the body resistance of the electrolyte-soaked separator could be obtained by intersection of the curves with the horizontal axis of the coordinate, and therefore, the ionic conductivity could be calculated by the thickness, area and body resistance of the separator [6]. In this way, as shown in Fig. 7.6b, the ionic conductivity of A, B, C, and D are 0.47, 0.43, 0.34, and

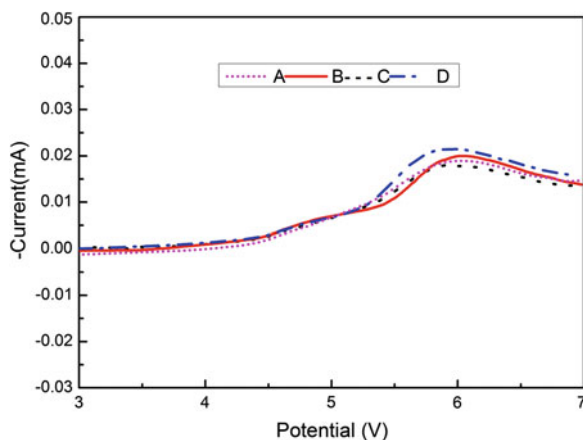


Fig. 7.5 Electrochemical stability window of SS/electrolyte-soaked separator/Li cells

0.12 ms/cm^{-1} , respectively. Generally, the level of conductivity is the integrated effects of both uptake and microstructure. Separator A has the highest conductivity, and D has the lowest conductivity because of different internal structures combined with Sect. 7.3.2 and Sect. 7.3.3.

7.3.6 Battery Performance

7.3.6.1 C-rate/Cycle Performance

In order to evaluate the effect of different pore-forming agents on the battery performance, the four separators were assembled cells for cycle performance test, and the curve was as shown in Fig. 7.7. It summarizes the discharge capacities of

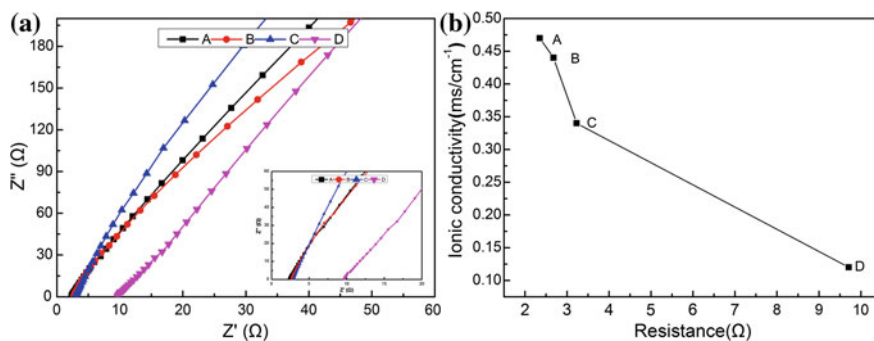
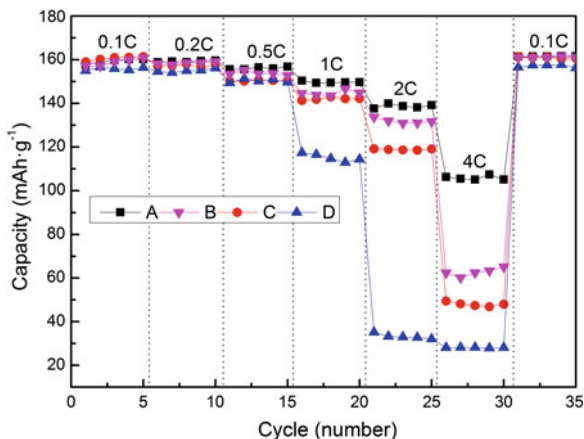


Fig. 7.6 Ionic conductivity for polymer electrolytes: **a** AC impedance of A, B, C, and D; **b** the calculated ionic conductivity data of A, B, C, and D

Fig. 7.7 Comparison of discharge C-rate capability between A, B, C, and D



the four separators as a function of cycles. Figure 7.7 shows that the four cells have similar capacity at low discharge rates, i.e., $C/10$, $C/5$, and $C/2$ C-rates, but A discharge capacity is slightly higher than that of B, C, and D. However, the discharge capacity of B, C, and D cells declines sharply at high discharge rates, i.e., 1C, 2C, and 4C rates. D discharge capacity is only 30 mAh/g, while A discharge capacity is still as high as 109 mAh/g at 4C. It suggests that the lower uptake and conductivity will reduce the Li^+ transmission rate of D and even further reduces the battery capacity.

7.3.6.2 Electrochemical Impedance

To learn more about the battery impedance changes in circular process, A and D were selected as the objects, the impedance after different cycles was tested after 0, 1st, 5th, 10th, 20th, and 35th cycles, and the results were shown in Fig. 7.8. In general, the semicircle of impedance spectra at the high frequency range represents the resistance of surface films on electrode materials and diagonal lines of impedance spectra at the medium-to-low frequency range can be ascribed to diffusion resistance of the electrolyte on the electrode materials [7]. Figure 7.8a shows that with the increasing of cycles, the resistance of electrochemical reaction reduces drastically, especially after the first cycle, from 1,000–300 Ω , while impedance is nearly the same after 20 cycles and 35 cycles, about 100 Ω . As shown in Fig. 7.8b, with the increasing of cycles, the resistance of electrochemical reaction decreases obviously, from 1,300–900 Ω at the first cycle, and the resistance is around 150 Ω after both 20 cycles and 35 cycles. Compared with A and D changes after each cycle of the electrochemical reaction resistance, A has a good interfacial compatibility stability [8, 9], and it can improve the uptake/keeping ability of liquid electrolyte. Combined with Sect. 7.3.3, it also suggests that the wettability of A is best. In addition, the change of impedance is closely related to the C-rate, it well agrees with Sect. 7.3.6.1.

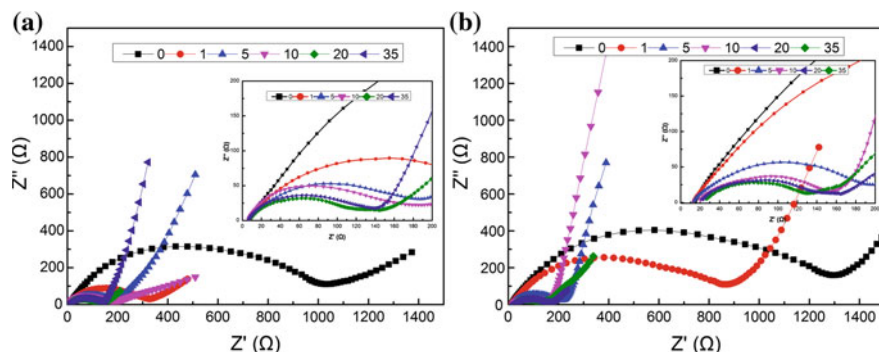


Fig. 7.8 Electrochemical impedance spectra of cells after 0, 1st, 5th, 10th, 20th, and 35th cycle: **a** A separator; **b** D separator

7.4 Conclusions

Comparing the effects of pore-forming agents, n-butanol, deionized water, ethanol, and isopropanol on properties of $\text{Al}_2\text{O}_3/\text{PVDF-HFP}$ separator, it is demonstrated that using n-butanol as pore-forming-agent, uptake, ion transference number, tensile strength, ionic conductivity, electrochemical stability window, and C-rate/cycle is more excellent than the other three. In addition, $\text{Al}_2\text{O}_3/\text{PVDF-HFP}$ polymer separator with n-butanol as pore-forming agent has simple preparation process, low cost, and easy to realize batch production; it is a highly promising separator for power lithium-ion battery.

References

- Ren X, Wu F (2002) Preparation of membrane for polymer lithium ion batteries by adding PAN. *Battery Bimonthly* 32(S1):36–37
- Zhao Y, Wang T, Xu F et al (2004) Preparation of P(VDF-HFP)/PMMA blend polymer electrolyte membrane with water as material for phase separation and pore producer. *Chem J Chin Univ* 25(5):922–925
- Orendorff CJ (2012) The role of separators in lithium-ion cell safety. *Interface-Electrochem Soc* 21(2):61–65
- Yu L, Wang D, Zhang K et al (2013) Preparation and properties of $\text{Al}_2\text{O}_3/\text{PVDF-HFP}$ separators for power lithium-ion batteries. *Automot Eng* 35(11):972–977
- Fu D, Luana B, Argue S et al (2012) Nano SiO_2 particle formation and deposition on polypropylene separators for lithium-ion batteries. *J Power Sources* 206:25–333
- Fu Z, Hong F, Sun C et al (2013) Influence of solvent type on porosity structure and properties of polymer separator for the Li-ion batteries. *J Solid State Electrochem* 17:2167–2172
- Lee JR, Won JH, Kim JH et al (2012) Evaporation-induced self-assembled silica colloidal particle-assisted nanoporous structural evolution of poly (ethylene terephthalate) nonwoven composite separators. *J Power Sources* 216:42–47

8. Zhang J, Yue L, Kong Q et al (2013) A heat-resistant silica nanoparticle enhanced polysulfonamide nonwoven separator for high-performance lithium ion battery. *J Electrochem Soc* 160(6):A769–A774
9. Zhou X, Yue L, Zhang J et al (2013) A core-shell structured polysulfonamide-based composite nonwoven towards high power lithium ion battery separator. *J Electrochem Soc* 160(9): A1341–A1347

Chapter 8

Studies on the Working Mode of Hyperbranched New Materials STOBA in Lithium-ion Battery Cathode Materials

Xinran Cui, Xinyan Mi, Tingting Cao, Tao Jiang, Huiming Chen, Zhongling Zhao and Kejin Zhang

Abstract Self-terminated oligomers with hyperbranched architecture, also known as STOBA, are combined with lithium-ion battery cathode materials by two different ways: mechanical blending and surface coating. The comparative electrochemical analyses of the assembled coin cells demonstrate that for the materials gained through mechanical blending, no blocking effects are observed at high-temperature condition. For the surface coating ones, STOBA has slight impact on the cell performance at room temperature, but when the ambient temperature exceeds the cross-linking temperature, large area of cross-linking will occur on the surface of the electrode materials, which prevents the lithium ion from extracting and inserting. As a result, the battery totally loses charge–discharge capacity in the high rate discharge condition to ensure the safety when operating at high temperatures.

Keywords Lithium-ion battery · High temperature safety · Hyperbranch · Mechanical blending · Surface coating

8.1 Introduction

In the last twenty years, demands for energy were growing rapidly. Lithium-ion secondary batteries are widely used as energy storage devices in many fields such as mobile devices, electric vehicles, and large machinery [1, 2], because of their high energy density, long cycle life, high reliability, etc. [3].

These international uses of lithium-ion batteries are, however, accompanied with increasing safety concerns. Several fire accidents, such as fire and explosion of personal computer or electric vehicle caused by overheating of the battery, have been reported [4]. Besides, the abused use of batteries, such as overcharging and

X. Cui (✉) · X. Mi · T. Cao · T. Jiang · H. Chen · Z. Zhao · K. Zhang
R&D Center, China FAW Co. Ltd., Changchun, China
e-mail: cuixinran@rdc.faw.com.cn

short circuit, also restricts its applications [5, 6]. Therefore, some necessary measures including improving the thermal stability of battery materials, using safer electrolyte system and adding safety materials upon high temperature, have to be taken in order to avoid the cells from burning and exploding [7, 8].

Recently, a polymeric material consisting of self-terminated oligomers with hyperbranched architecture, also known as STOBA, is reported to possess many superior properties, such as good heat and flame resistance, heat cross-linking, low smoke and low toxicity, etc. [9]. In this paper, the working modes of this material in the cathode active material were explored. The materials and lithium-ion battery cathode material were mechanically blended and surface coated, respectively. Then, best working mode and working effect were proved through comparing the results of the electrochemical performance of the assembled button cells.

8.2 Experiments

8.2.1 *Synthesis of Hyperbranched New Material STOBA*

Firstly, the monomers of *N,N'*-(4,4'-diphenylmethane) bismaleimide were synthesized through a dehydration reaction in an organic solvent reflux system, with nickel acetate as catalysts [10]. Then, the monomers of *N,N'*-(4,4'-diphenylmethane) bismaleimide were mixed with barbituric acid according to a proper proportion to carry out polymerization reactions. Finally, the oligomers of *N,N'*-(4,4'-diphenylmethane) bismaleimide were got after a series process of washing, filtering, and drying [11].

8.2.2 *Mechanical Blending with Cathode Materials*

The cathode materials LiFePO_4 (BASF) were mechanically blended with hyperbranched new material STOBA according to a mass ratio of 100:2, using NMP as solvent. LiFePO_4 , VGCF (as conductive additives), and PVDF (as binders) were mixed uniformly with a mass ratio of 8:1:1 to get slurry. After coating and drying under vacuum, cathode plates were obtained.

8.2.3 *Surface Coating on Cathode Materials*

Using N-methyl-2-pyrrolidone (NMP) as solvent, the cathode materials LiFePO_4 , conductive additives VGCF, and binders (polyvinylidene fluoride; PVDF) were mixed uniformly with a mass ratio of 8:1:1 to get slurry. The materials were dried under vacuum after coating. Then, the synthesized hyperbranched new materials STOBA were dissolved in NMP according to a 2 % weight fraction. The solution

was coated uniformly on the cathode plates. And then, the materials were dried under vacuum after coating once again to obtain cathode plates.

8.2.4 High-Temperature Processing of Cathode Electrodes

The electrodes obtained through Sects. 2.2 and 2.3 were heated two hours under vacuum at 180, 220 and 250 °C, respectively. The button-type battery assembly was carried out after the electrodes were cooled to room temperature.

8.2.5 The Assembly of 2032 Button Cells

The 2032 button cells were assembled in a glove box filled with high-purity argon using the electrodes obtained from the un-heated plates from 2.2 to 2.3 and heated plates from 2.4 as positive electrodes, commercial lithium tablets as negative electrodes, the EC + DMC + EMC (volume ratio of 1:1:1) solution with 1 mol/L LiPF₆ as electrolyte, and celgard 2,400 membrane as diaphragm.

8.2.6 Electrochemical Measurement

The electrochemical measurements were carried out using LAND cell testing system at room temperature. Charge–discharge cycles were tested in a potential range of 2.5–3.8 V. Cyclic voltammograms (CVs) and electrochemical impedance spectroscopy (EIS) were carried out using electrochemical workstation. And the CVs were scanned at a rate of 0.1 mV/s.

8.3 The Comparison of Electrochemical Properties

8.3.1 Electrochemical Properties After Mechanical Blending

Figure 8.1a and b show the curves of the discharge capacity versus cycle number for the mechanical blend electrodes (M-LFP) made from different heating temperature at 0.1 and 1 °C rate, respectively. The initial charge–discharge profiles at the rate of 0.1 °C are shown in Fig. 8.2.

As shown in Fig. 8.1a and b, the charge–discharge profiles of 30 (0.1 °C) and 50 (1 °C) cycles are presented for all the samples, and the cells generally have almost the same starting voltage during the first cycles. Therefore, it is reasonable to predict that the performances of the cathode plates are not affected by heated treatment, resulting

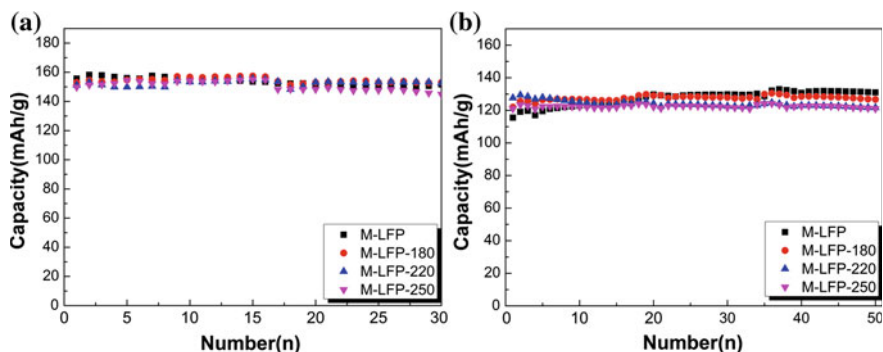
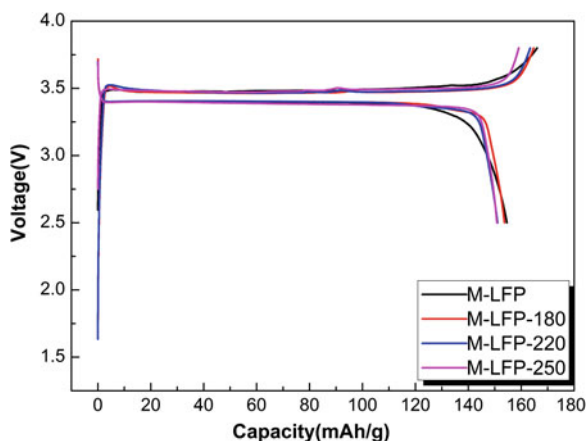


Fig. 8.1 Cycling performance of mechanically blended electrodes (J-LFP) at different temperature (room temperature, 180, 220, 250 °C) at the rate of 0.1 °C (a) and 1 °C (b)

Fig. 8.2 First charge–discharge potential profiles of the mechanically blended electrodes (J-LFP) at different temperature (room temperature, 180, 220, 250 °C) at the rate of 0.1 °C



in no apparent differences in capacity and cycling stability. From Fig. 8.2, it is clear that first charge discharge plateaus are observed for all the samples within the charge discharge voltage range of 2–3.8 V, indicating that no structural damage is caused because of high temperature. Thereby, we believe that temperature has little impact on the electrodes, and the STObA materials do not achieve the blocking effects at the same time when incorporated through mechanical blending.

8.3.2 Electrochemical Properties After Surface Coating

Figures 8.3a and b present the comparison of the initial charge and discharge curves and CVs curves of the electrodes obtained through surface coating. The charge and discharge profiles at the rate of 0.1 and 1 °C are shown in Figs. 8.4a and b, respectively. Figure 8.5 shows the impedance spectra before and after cycling.

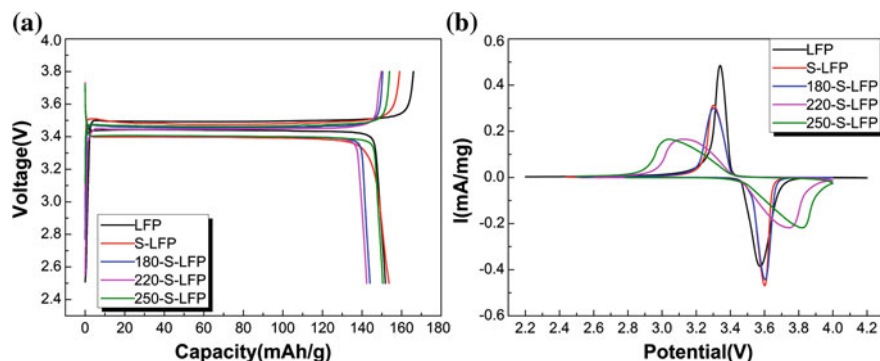


Fig. 8.3 First charge–discharge potential profiles at the rate of $0.1\text{ }^{\circ}\text{C}$ (a) and CVs curves scanning rate of 0.1 mV/s (b) of the un-coated electrodes (LFP) and surface coated electrodes (S-LFP) at different temperature (room temperature, 180, 220, 250 $^{\circ}\text{C}$)

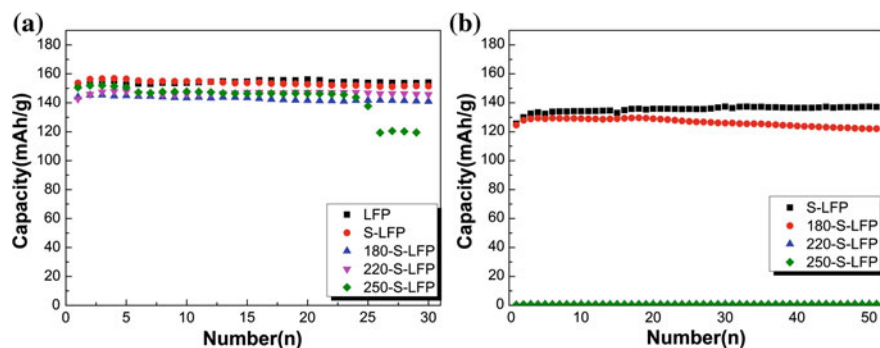


Fig. 8.4 Cycling performance of the un-coated electrodes (LFP) and surface coated electrodes (S-LFP) at different temperature (room temperature, 180, 220, 250 $^{\circ}\text{C}$) at the rate of $0.1\text{ }^{\circ}\text{C}$ (a) and $1\text{ }^{\circ}\text{C}$ (b)

As shown in Fig. 8.3a, all materials show one voltage plateau at the range of 3.4–3.5 V on charge and discharge, indicating that the incorporation of STOBA has little effects on the initial charge–discharge performance. The initial CVs curves for all the electrodes at a scanning rate of 0.1 mV/s are shown in Fig. 8.3b. All the curves of the electrodes show a similar profile, which indicates that the reaction mechanism does not change during the lithium extraction/insertion process for the coated electrode, while all redox peaks, corresponding to the charging and discharging plateau of the batteries, are shifted after the surface coating and heating treatment. As shown in Fig. 8.3b, one oxidation peak of the native electrode is observed at around 3.34 V, coupled with one reduction peaks at 3.57 V. In the case of surface coated electrode at 220 $^{\circ}\text{C}$, the oxidation peaks shift down to 3.14 V, while the reduced peaks shift up to at 3.74 V. As a result, bigger potential

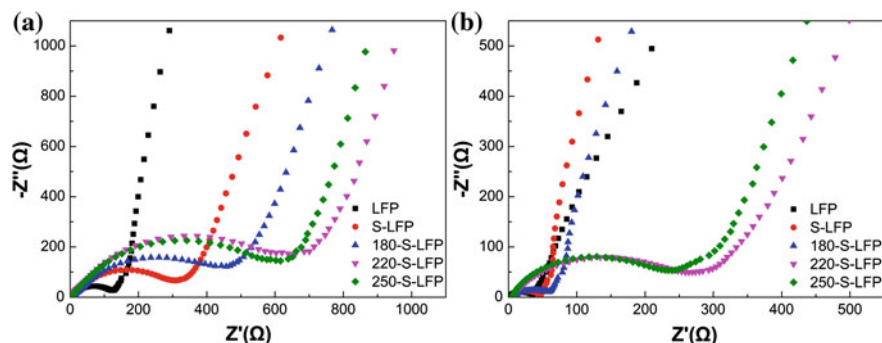


Fig. 8.5 Nyquist plots for the initial EIS (a) and EIS after 50 cycles (b) of the un-coated electrodes (LFP) and surface coated electrodes (S-LFP) at different temperature (room temperature, 180, 220, 250 °C)

differences between oxidation and reduction peaks are observed, indicating a more obvious polarization of the electrode material, especially for the coated samples at higher temperature. At the same time, the weakened sharpness is also observed for the samples, indicating in a less stable charge and discharge plateau [12]. Due to the weak conductivity of hyperbranched STOBA materials, a slightly coating on the surface of the electrode will result in an increase of the polarization of the materials in a certain extent. And after high-temperature treatment, the coating materials will cross-link, resulting in more obvious polarization phenomenon, which makes the cell performance at high magnification decrease dramatically, which achieves the goal of safe use of the battery at high temperature.

As shown in Fig. 8.4a, the samples show similar discharge capacity (140–160 mAh/g) at the rate of 0.1 °C. While for the coated sample at 250 °C, the capacity decreases significantly after 25 cycles compared with that of the un-coated materials. The electrochemical cycling performance was also tested at the elevated rate (1 °C). As seen in Fig. 8.4b, all the samples show the decreased discharge capacity compared with those tested at the rate of 0.1 °C. For the coated samples at room temperature, the capacity stays stable at 135 mAh/g even after 50 cycles. While for the coated sample at 180 °C, capacity decreases gradually. After 50 cycles, the discharge capacity of the sample decreases down to 120 mAh/g from 135 mAh/g. Obviously, no capacity is observed for the coated electrodes (220 and 250 °C) after heated at above cross-linking temperature under vacuum condition. It demonstrates that the surface coating materials will create cross-linking rapidly in high-temperature environments (220 and 250 °C) caused by the short circuit or other reasons, which would help to stop the electrochemical reaction from happening, cut off energy conversion, and prevent further deterioration of danger.

In order to understand the differences in the electrochemical properties caused by surface coating and different temperatures, the kinetics parameters were measured in the EIS experiments. The initial EIS spectra of the materials are shown in Fig. 8.5a. The semicircle in the middle frequency range reflects the charge transfer

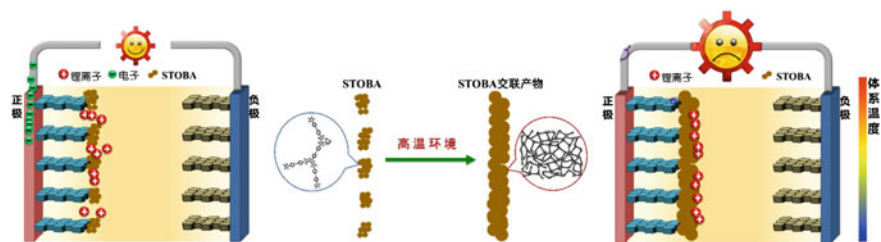


Fig. 8.6 Proposed schematic representation of working processes of the hyperbranched new materials STOBA

resistance on the interface of cathode/electrolyte (Rct) [13]. Obviously, The Rct of the materials increases dramatically after surface coating, and it grows gradually with the increasing of temperature. The EIS curves after 50 cycles at 1 °C rate were also tested, as shown in Fig. 8.5b. The charge transfer resistance of both S-LFP and 180-S-LFP is very close to that of the un-coated sample. Large increases of Rct may be caused by surface coating at the temperature over cross-linking temperature, indicating that the repeated extracting and inserting will penetrate the non-cross-linked bismaleimide oligomer coating, resulting in a not lasting effect on the electrochemical properties of the materials. However, lasting blocking cell reactions will occur once cross-linking is formed to form a protection upon high temperature.

Based on the results above, a possible working process for the coated electrodes was proposed. As shown in Fig. 8.6, lithium ion will extract and insert through the STOBA material normally at room temperature. When the temperature of the battery increases due to some abnormal factors, such as short circuit, large area of cross-linking will occur after a series of reaction: free radicals will transfer to form oligomers, and then polymerize with monomers. As a result, this will protect the lithium ion from extracting and inserting, until the battery disconnects.

8.4 Conclusions

In conclusion, the hyperbranched new materials STOBA have little effects on the batteries performance in the normal working state of the batteries. However, under certain conditions, such as diaphragm failure because of a sudden heating caused by the electrical short circuit or electrical fault, the surface coating of the lithium-ion battery cathode materials would cause large area of cross-linking, which prevents the lithium ion from extracting and inserting and effectively blocks the cell reaction. As a result, the safety of the batteries operated at high temperatures is substantially improved, especially when operated during large charge–discharge rate processes.

References

1. Armand M, Tarason JM (2008) Building better batteries. *Nature* 451(7179):652–657
2. Vincent CA (2000) Lithium batteries: a 50-year perspective, 1959–2009. *Solid State Ionics* 134(1/2):159–167
3. Tarascon JM, Armand M (2001) Issues and challenges facing rechargeable lithium batteries. *Nature* 414(6861):359–367
4. Chen YH, Tang ZY, Lu XH, Tan CY (2006) Research of explosion mechanism of lithium-ion battery. *Prog Chem* 18(06):823–831
5. Maleki H, Deng G, Anani A, Howard J (1999) Thermal stability studies of Li-ion cells and components articles. *J Electrochem Soc* 146(9):3224–3229
6. Spotnitz R, Franklin J (2003) Abuse behavior of high-power, lithium-ion cells. *J Power Sour* 113(01):81–100
7. Wang XM, Yasukawa E, Kasuya S (2001) Nonflammable trimethyl phosphate solvent containing electrolyte for lithium-ion batteries. *J Electrochem Soc* 148(10):A1058–A1071
8. Mandal BK, Padhi AK, Shi Z et al (2006) Thermal runaway inhibitors for lithium battery electrolytes. *J Power Sour* 161(2):1341–1345
9. Lin C, Wu HC, Pan JP, Su CY, Wang TH, Sheu HS, Wu N (2013) Investigation on suppressed thermal runaway of Li-ion battery by hyper-branched polymer coated on cathode. *Electrochimica Acta* 101(1):11–17
10. Cao N, Yuan HT, Fu YH, He JH (2007) Catalytic synthesis of N,N'-(4,4'-diphenylmethane) bismaleimide. *J Beijing Univ Chem Technol* 34(6), 594–603
11. He YR, Dai PB, Xu JW, Lu YQ, Wang H (2013) Synthesis and resistive switching characteristics of Ethyl Methacrylate/*N, N'*-4, 4'-Diphenylmethane—Bismaleimide copolymer. *Adv Mater Res* 788(2):159–163
12. Gabaly FE, McCarty KF, Bluhm H, McDaniel AH (2013) Oxidation stages of Ni electrodes in solid oxide fuel cell environments. *Phys Chem Chem Phys* 15:8334–8341 doi: [10.1039/C3CP50366F](https://doi.org/10.1039/C3CP50366F)
13. Abe T, Ohtsuka M, Sagane F, Iriyama Y, Ogumi Z (2004) Lithium ion transfer at the interface between lithium-ion-conductive solid crystalline electrolyte and polymer electrolyte. *J Electrochem Soc* 151(11):A1950–A1953

Chapter 9

Preparation and Property of High Heat-Resistant Ceramic Compositated PET Separator

Zhongling Zhao, Dan Wang, Lina Yu, Jian Han, Kejin Zhang, Xinran Cui, Tingting Cao and Shuli Chen

Abstract Polyethylene terephthalate (PET)–Al₂O₃ ceramic compositated separator is prepared with organic adhesives PDA, inorganic adhesives, silane-coupling agent, and colloidal silica. The obtained separator is characterized in different ways. Morphology characterization by SEM shows that porous separator is obtained, and Al₂O₃ is evenly distributed on it. The Gurley number of the separator is 8 s/100 cc. Thermal behavior investigation and linear sweep voltammetry test show that the prepared separator has an outstanding thermal performance and electrochemical stability. Half-cell assembled with the compositated separator reveals an outstanding cycle performance and a good rate performance. Therefore, the separator may be a suitable and excellent candidate for application in power battery, especially the one with higher safety.

Keywords Lithium-ion battery · Separator · PET · Al₂O₃

9.1 Introduction

As the most appropriate candidate for EV/HEV batteries, the further application of lithium-ion batteries (LIBs) had been limited due to their potential safety problems for a long time. For practice, many studies have focused on improving the separators' performance, such as modification of polyolefin porous membrane [1, 2], namely PP or PE, and application of other materials, namely PET, PI, and PSA [3–5]. Among these materials, novo ceramic compositated materials, especially ceramic compositated PET material, have been mostly noted because these ceramic composites can bring wonderful cycle/rate performance to LIBs. The binders of the most ceramic compositated PET separators as reports were organic binders, such as

Z. Zhao (✉) · D. Wang · L. Yu · J. Han · K. Zhang · X. Cui · T. Cao · S. Chen
R&D Center, China FAW Co. Ltd, Changchun, China
e-mail: zhaozhongling@rdc.faw.com.cn

SBR [6] and PVDF-HFP [7], which would melt as temperature elevated because they often had lower melting point. In serious condition, the battery could not hold on, even short circuit or explosion.

In this paper, ceramic composited PET separator with inorganic binder was prepared and characterized, and the results showed that the obtained separator has wonderful thermal performance and wide electrochemical stable window. Compared with half-cell with polyolefin separator, the one with the composited separator exhibited higher cycle/rate performance. So, it may be a suitable candidate for EV/HEV cells, especially the one with outstanding safety.

9.2 Experiments

9.2.1 Preparation

Polydopamine-modified PET nonwoven was achieved by a self-polymerization of dopamine in 10 mmol L⁻¹ PET-immersed dopamine solution [2]. After washing several times with deionized water and drying in vacuum oven, the modified PET was dipped into a composite solution prepared by mixing moderate colloidal silica and Al₂O₃ and silane-coupling agent KH560. Then, the well-wetted PET was dried at 105 °C for 1 h first and then solidified at 210 °C for 1 h. After compressed with 30 MPa a few seconds, ceramic composited PET separator was obtained.

9.2.2 Morphology

The surface morphology of PET-based composite nonwoven was investigated with a field-emission scanning electron microscopy (FE-SEM, Hitachi SU-8000).

9.2.3 Thermal Performance

The thermal shrinkage behavior of the separator and polyolefin separator was determined by placing in an oven and heated at 200 °C for 1 h.

9.2.4 Electrochemical Performance

Electrochemical stability was evaluated by linear sweep voltammetry of Li/electrolyte-soaked separator/SS cell at a scan rate of 1 mV/s over the range of 3–7 V by

an electrochemical working station (CHI760D, Chenhua, Shanghai), where the Li was served as a reference and counter electrode and the SS as the working electrode.

C-rate and cycle performance were characterized by a LiFePO₄ (LFP, theoretical specific capacity 170 mAh/g) 2025 half-cell by a charge and discharge tester (CT2001A, LAND, Wuhan). C-rate test was carried out by discharging at different discharging rates, such as 0.1, 0.2, 0.5, 1, and 2 °C, with a charging rate of 0.1 °C. Cycle test was carried out by discharging at 0.5 °C, with a charging rate of 0.2 °C. The cutting voltage was set at 2.2 and 3.8 V. The electrolyte used for the former test was 1 M LiPF₆ in a mixing solvent (EC/DMC, v/v = 1:1).

9.3 Results and Discussion

9.3.1 Preparation

The structure of polydopamine is as shown in Fig. 9.1. As described in the reference [8], the surface layers of polydopamine will be closely cohered with the PET substrate, on which many hydroxyl groups spread, which could improve the surface energy sharply and could improve the cohesive force of PET substrate and ceramic slurry. Furthermore, hydroxyl groups could react with the ceramic as the elevation of temperature and –O–Si–O–bond generated, so the cohesive force of PET and ceramic would be dramatically increased.

9.3.2 Morphology

Figure 9.2 shows the SEM image of the obtained composited separator. The larger particles in Fig. 9.2 are Al₂O₃ (0.4 μm), and the smaller ones spreading on Al₂O₃ are SiO₂ which were dispersed in Si-sol and served as binder after solidification at 210 °C.

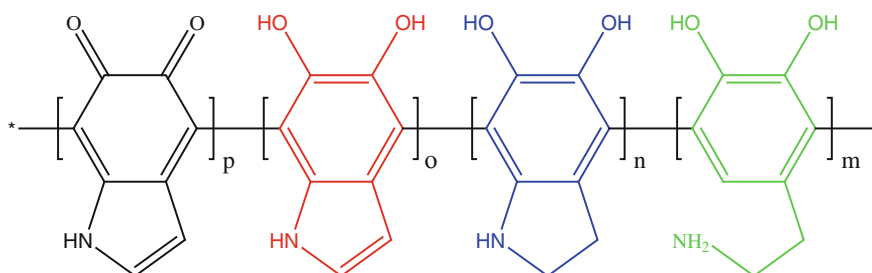


Fig. 9.1 The structure of polydopamine. Reprinted with the permission from Ref. [9]. Copyright 2013 by American Chemical Society

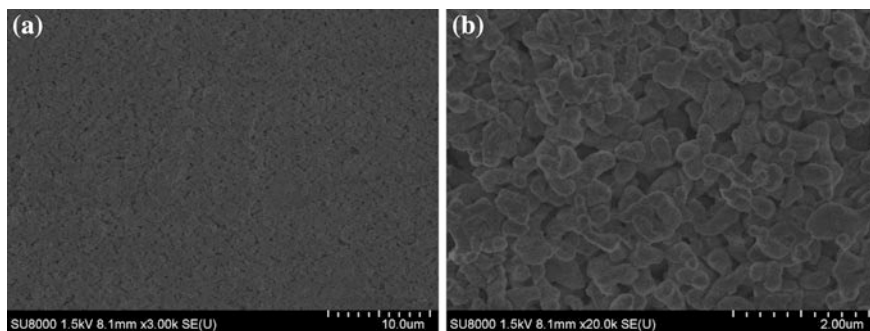


Fig. 9.2 The SEM of composited separator (**a** $\times 3,000$, **b** $\times 20,000$)

Besides, a smooth and uniform surface is shown in Fig. 9.2, in which Al_2O_3 and pore scatter uniformly. Further test shows that its Gurley number was 8 s/100 cc, lower than many commercial polyolefin separators. The result means that the separator had better permeability and would lower the resistance of Li ion which swung between anode and cathode, and improve the rate performance of LIBs.

9.3.3 Thermal Shrinkage

The result of thermal shrinkage test is shown in Fig. 9.3. A folded vegetable paper was used to support the testing sample for avoiding the influence of the sample holder. It can be found that PE and PP lost its original dimension completely because they were melt at 135 and 165 $^\circ\text{C}$, respectively [10]. On the other hand, the ceramic composited PET separator kept its original dimension. The result is very interesting and significant, because the dramatic antithermal shrinkage performance enables the cell to hold intercircuit broken even temperature elevated to 200 $^\circ\text{C}$ or higher, where the safety of LIBs would be ensured to a higher level. So, it may be a suitable candidate for EV/HEV cells, especially the one with outstanding safety.

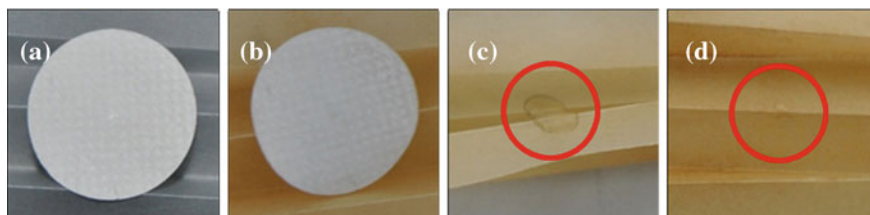
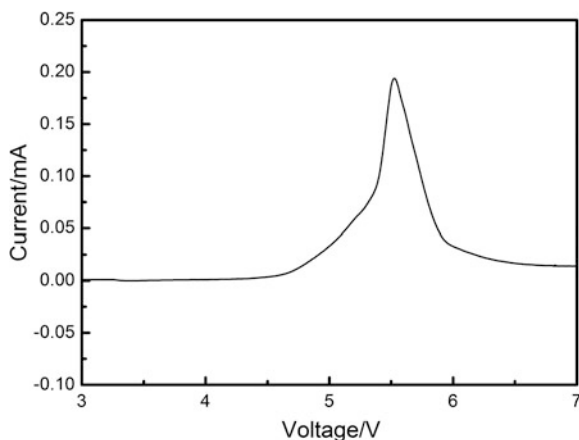


Fig. 9.3 Photograph of thermal shrinkage of testing samples. **a** PET- Al_2O_3 - (ambient); **b** PET- Al_2O_3 (200 $^\circ\text{C}$, 1 h); **c** PE (200 $^\circ\text{C}$, 1 h); and **d** PP (200 $^\circ\text{C}$, 1 h)

Fig. 9.4 The curve of LSV of Li/separator/SS



9.3.4 Electrochemical Performance

9.3.4.1 Electrochemical Stability

Figure 9.4 shows the curve of LSV of the cell Li/electrolyte-soaked ceramic composited PET separator/SS. Generally, the current would stay at around 0 mA just as the voltage was scanning from lower to higher. When the voltage is lifted up to a certain value, the current changes suddenly, the alteration of the trend of current means that some electrochemical reaction occurs, and thus, the value is the electrochemical stability window [11], which means that when voltage is below the value, the electrolyte (including the liquid electrolyte and the separator) is stable. Usually, the liquid electrolyte for LSV test is simple, commercial, and stable one, so the value could represent the stability of the separator. From Fig. 9.4, it can be found that the window is 4.5 V, lower than the cutting voltage of many cathode materials. It could be applied in many cells.

9.3.4.2 Rate/Cycle Performance

The cycle and rate performance of the tested half-cell is shown in Fig. 9.5a and b. As shown in Fig. 9.5a, it can be found that the specific capacity of the cell is 153.3 mAh/g after 35 cycles, and from Fig. 9.5b, it can be found that the discharging capacity is 130.6 mAh/g at 1.0 °C and 56.3 mAh/g at 2.0 °C, higher than the corresponding half-cell with commercial PP separator (Celgard 2500) reported previously [12]. Besides, it can also be found that the discharging plateau is kept as a line from Fig. 9.5b, which means that the composited separator has good stability.

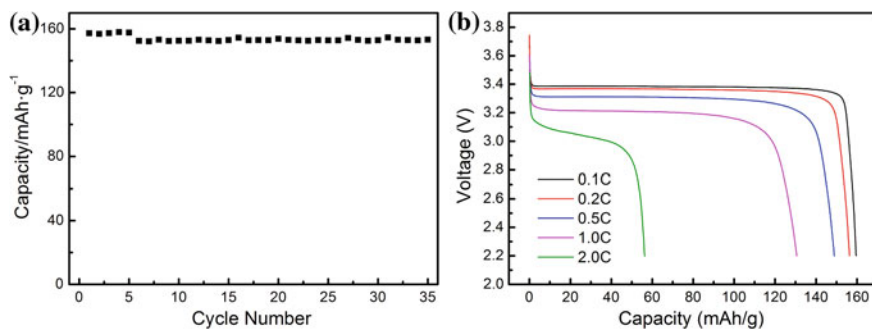


Fig. 9.5 The cycle (a) and rate (b) performance of LFP half-cell (a, the charging and discharging rate of cycle 1–5 was 0.1 C)

9.4 Conclusions

Al_2O_3 ceramic composites separator was prepared with organic adhesives PDA, inorganic adhesives, solidified silane-coupling agent, and solidified colloidal silica. Then, the morphology, thermal shrinkage, and electrochemical performance were characterized. Morphology characterization shows that porous separator is obtained and has a Gurley number of 8 s/100 cc. The Al_2O_3 particles are distributed evenly on the separator. Also, the prepared separator exhibits outstanding thermal stable performance and electrochemical stability. Compared with the half-cell assembled with commercial PP separator, the one with the composites separator reveals an outstanding cycle performance and a good rate performance. Therefore, the separator may be a suitable and excellent candidate for application in power battery, especially the one with higher safety. Next, the batch preparation and its engineering technology will be carried out.

References

1. Fang J, Kellarakis A, Lin Y-W et al (2011) Nanoparticle-coated separators for lithium-ion batteries with advanced electrochemical performance. *Phys Chem Chem Phys* 13:14457–14461
2. Ryou M-H, Lee YM, Park J-K et al (2011) Mussel-inspired polydopamine-treated polyethylene separator for high-power Li-ion batteries. *Adv Mater* 23:3066–3070
3. Hao J, Lei G, Li Z et al (2013) A novel polyethylene terephthalate nonwoven separator based on electrospinning technique for lithium ion battery. *J Membr Sci* 428:11–16
4. Zhou X, Yue L, Zhang J et al (2013) A core-shell structured polysulfonamide-based composite nonwoven towards high power lithium ion battery separator. *J Electrochem Soc* 160(9): A1341–A1347
5. Jiang W, Liu Z, Kong Q et al (2013) A high temperature operating nanofibrous polyimide separator in Li-ion battery. *Solid State Ionics* 232:44–48

6. Lee J-R, Won J-H, Kim JH et al (2012) Evaporation-induced self-assembled silica colloidal particle-assisted nanoporous structural evolution of poly(ethylene terephthalate) nonwoven composite separators for high-safety/high-rate lithium-ion batteries. *J Power Source* 216:42–47
7. Jeong H-S, Choi E-S, Lee S-Y (2012) Composition ratio-dependent structural evolution of SiO₂/poly(vinylidene fluoride-hexafluoropropylene)-coated poly(ethylene terephthalate) nonwoven composite separators for lithium-ion batteries. *Electrochim Acta* 86:317–322
8. Lee H, Dellatore SM, Miller WM et al (2007) Mussel-inspired surface chemistry for multifunctional coatings. *Science* 318(5849):426–430
9. Liebscher J, Mrówczyński R, Scheidt HA et al (2013) Structure of polydopamine: a never-ending story? *Langmuir* 29(33):10539–10548
10. Wang D, Zhang K, Xu D et al (2011) An experiment study on the characteristics of separator film in lithium ion battery for vehicles. *Automot Eng* 33(10):94–897
11. Lina Y, Wang D, Zhang K et al (2013) Preparation and properties of Al₂O₃/PVDF-HFP separators for power Lithium-ion batteries. *Automot Eng* 35(11):972–977
12. Wang D, Zhao Z, Yu L et al (2014) Polydopamine hydrophilic modification of Polypropylene separator for lithium ion battery. *J Appl Polym Sci* 131(15):40543–40549

Chapter 10

Analysis of Shifting Quality Based on AMT of the Electric Vehicle

Bing-li Zhang, Xin-ping Wu, Zhong-wen Hu and De-ming Zhou

Abstract After analyzing the shifting process and the shifting shock of automated transmission, the shifting process is divided as following five phases: unload, back gear, synchronization, in-gear, and load. The shifting quality is optimized by controlling the electric motor and gearbox in a coordinated way. In addition, the models of automated shift, coordination controller (including logical control model of the above phases), electric motor, vehicle dynamic, and shock extent are established based on MATLAB/Simulink. The simulation results show that taking coordination control can decrease shifting shock extent and optimize shifting quality.

Keywords AMT · Electric vehicle · Shifting shock · Shifting quality · Coordinated control

10.1 Introduction

With the problems of environmental pollution, energy shortage are increasingly serious, developing zero emission, low noise, and high-efficiency electric vehicle has become an inevitable trend. To improve the electric vehicle power and economy, meanwhile reduce the battery and drive motor requirements, 2–3 gear automatic mechanical transmission is selected.

At present, there are some researches about electric vehicles' AMT, but that of shifting performance is fewer. Reference [1] matched the transmission parameters of two-speed electric vehicles and developed a dynamic shifting strategy, but without studying the shifting process and shock; Ref. [2] introduced the shifting shock generation mechanism of clutch-less AMT, but did not discuss the coordinated control methods in depth.

This paper analyzed the AMT shifting process and shifting shock generation mechanism, developed a coordinated control approach to optimize shifting quality,

B.-l. Zhang · X.-p. Wu (✉) · Z.-w. Hu · D.-m. Zhou
School of Machinery and Automobile Engineering, Hefei University of Technology,
Hefei 230009, China
e-mail: 1015291056@qq.com

and simultaneously verified the effectiveness of coordinated control method depend on the MATLAB/Simulink simulation.

10.2 Research on Shifting Process and Shifting Quality

10.2.1 Shifting Process Analysis

The drive motor needs to undertake the following functions for the clutch omitted in the integrated automatic transmission:

1. In order to interrupt the drive line, the output torque of drive motor should be reduced to zero before shifting to neutral position.
2. Before in gear, the speed of drive motor should be controlled initiatively to reduce slipping-friction work loss.
3. After in gear, the drive motor torque need change according to the loading curve to meet the shifting quality standard.

These functions above require the drive motor controller can control the motor torque and speed accurately. The functions (1) and (3) belong to torque adjustment, and the function (2) belongs to speed regulation. The motor should switch operational mode among torque, speed, and free mode during shifting. Therefore, according to the motor operating mode and shift actuator movement, the shifting process can be divided into five phases: motor torque unload, back gear to neutral position, motor speed synchronization, in gear, and motor torque load.

Combining the drive line with the above analysis, it is easy to know that the differences of dynamic model exist only in the transmission structure. So this paper can model based on the power transmission mode among the synchronizer, transmission input, and output shaft, and the schematic diagram is shown in Fig. 10.1.

The dynamic mathematical model can be built based on the schematic diagram of driveline as follows:

$$\begin{cases} I_{i^*}d\omega_m/dt = M_m - M_a/i_g \\ I_{o^*}d\omega_o/dt = M_o - M_d/i_o \end{cases} \quad (10.1)$$

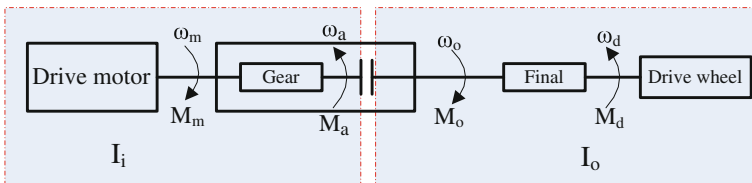


Fig. 10.1 The schematic diagram of driveline

I_i, I_o represent the inertia of the input and output part of synchronizer separately, i_g, i_o represent the transmission ratio and the final ratio, respectively, M_m, ω_m, M_d represent the torque, speed of drive motor, and vehicle resistance torque.

In both unload and load phase, the gear transmission exists in sliding sleeve. The speed and torque of drive and driven transmission gear is equal, respectively: $M_a = -M_o, \omega_a = \omega_o$, the dynamic mathematical model of driveline is definite; but during in-gear phase, the slipping-friction work replaces gear transmission in sliding sleeve. The friction torque of the active and driven synchronizer is $M_a = -M_o$, and the speed of the drive and driven ring is $\omega_a \neq \omega_o$.

10.2.2 Studies of the Influence Factors of Shifting Quality

There are three shifting quality evaluation indexes: the shifting shock, the shifting time, and the slipping-friction work [3]. This paper mainly studies the first one.

10.2.2.1 Effects on the Shifting Shock During Torque Unload and Load

The shift shock can be expressed as the gradient of vehicle longitudinal acceleration, known from the analysis of transmission dynamic system [4], in unload and load phases, the driveline has a definite dynamic relation. Assuming J as the vehicle equivalent rotational inertia (converted from the translational mass and the rotational part), the shifting shock can be expressed as:

$$j = \frac{da(t)}{dt} = \frac{ri_g i_o}{J} \left(\frac{dM_m}{dt} - \frac{1}{i_g i_o} \frac{dM_d}{dt} \right) \quad (10.2)$$

where r is the drive wheel radius, and $a(t)$ is the vehicle longitudinal acceleration.

According to the equation formula (10.2), in unload and load phases, the shifting shock is proportional to the gradient of drive torque, and if the gradient of drive torque is too large, it will create a big shifting shock which affects the vehicle ride comfort. Therefore, it is necessary to develop a detailed control strategy to control the gradient of drive torque in unload and load phases.

10.2.2.2 Effects on the Shifting Shock During In-gear and Synchronization Phases

During the in-gear phase, the transmitted torque of synchronizer M_t is equal to the motor drive torque M_m in Eq. (10.2). Therefore, Eq. (10.2) can be rewritten as:

$$j = \frac{da(t)}{dt} = \frac{ri_g i_o}{J} \left(\frac{dM_t}{dt} - \frac{1}{i_g i_o} \frac{dM_d}{dt} \right) \quad (10.3)$$

Due to the requirements of vehicle acceleration performance, shifting time is very short, the vehicle drag torque can be considered as a constant, therefore Eq. (10.3) can be simplified as:

$$j = \frac{da(t)}{dt} = \frac{r_i i_0}{J} \frac{dM_t}{dt} \quad (10.4)$$

Since M_t is proportional to gear force F , so if you want to control the extent of shifting shock within limits, the gradient of axial force on shift fork should be controlled.

Assuming the synchronous time as ΔT , the angular velocity difference of the driving gear and the driven gear as $\Delta\omega$ before in-gear phase, therefore, average torque \overline{M}_t delivered by the synchronizer during synchronization phase is:

$$\overline{M}_t = I_i \frac{\Delta\omega}{\Delta T}. \quad (10.5)$$

If the synchronization time is consistent, \overline{M}_t is proportional to $\Delta\omega$, the gradient of M_t which increased from 0 increases with $\Delta\omega$ within ΔT , therefore, in order to reduce the shifting shock, rotational speed difference between the driving and driven part of the synchronizer must be adjusted by the drive motor.

10.3 Development of AMT Control Strategies

Based on the above analysis, the coordinate control unit (CCU) controls the drive motor and the shift actuator to work together to make up for omitting of clutch in the integrated structure. CCU gets into the shift process based on the shift control signal, while collects drive motor speed, torque, shift actuator position signals to switch different modes in the process, the shift flowchart throughout the shifting process is shown in Fig. 10.2.

In load or unload phases, the drive motor output torque curve is determined by the standards of shift shock, as shown in Fig. 10.3, according to the national standard, $j \leq 17.64 \text{ ms}^{-3}$ and the Eq. (10.2), the maximum gradient of driving torque is obtained:

$$\frac{dM_m}{dt} = \frac{J * j}{r_i i_0} \quad (10.6)$$

The CCU outputs the torque control signal which meets the requirements of change rate to the motor controller through CAN bus, controls the motor to gradually reach the target status, and then determines whether the current phase is accomplished or not by difference of electromagnetic torque and the target torque.

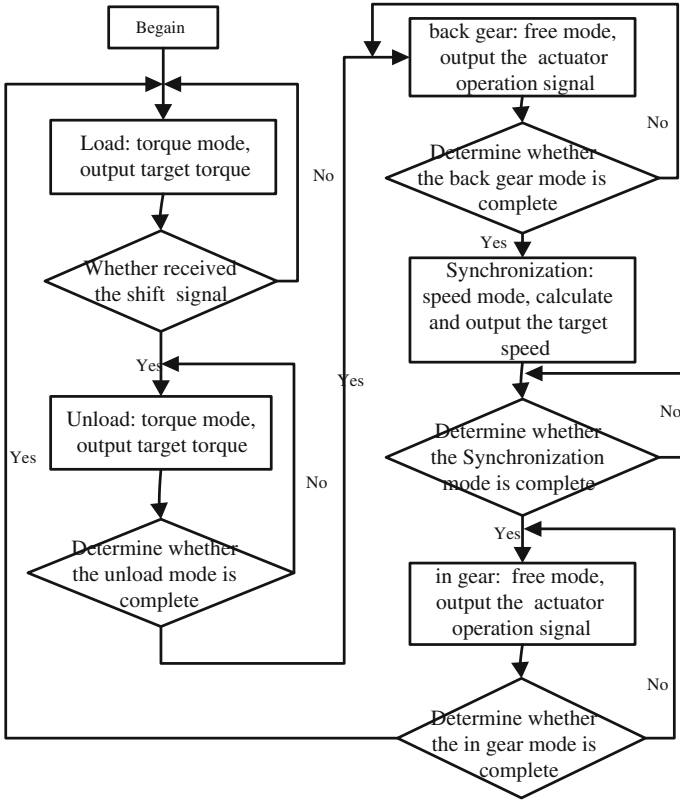
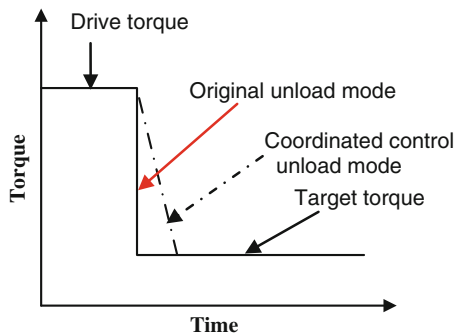


Fig. 10.2 Shift flowchart

Fig. 10.3 Coordinated unload mode



In speed control stage, CCU determines the target speed according to the transmission output shaft speed and target gear ratio, as shown in formula: $n_{mb} = i_g n_1$, the end of synchronization is judged by whether the speed difference is in a certain range or not.

As the shift shock in back gear phase is little, the back gear speed can be picked appropriately, but by the foregoing analysis, in-gear phase, the CCU determines the in-gear force change ratio by the standards of shift shock: $j = \frac{da(t)}{dt} = \frac{r_{ig}i_0}{J} \frac{dM_t}{dt} \propto \frac{r_{ig}i_0}{J} \frac{dF}{dt}$, then, outputs the actuator drive signals, finally, judge whether this phase is completed or not according to the position signals.

10.4 Simulation and Analysis

In this paper, the automatic shift model, coordination controller model (including unloading, loading curves, and logic control model of five automatic shifting stages), drive motor and its control model, vehicle dynamics model, and the shift shock models were established based on Simulink/Stateflow. The overall simulation model is shown in Fig. 10.4.

The main parameters of the model are given in Table 10.1.

The simulation results are as shown in Fig. 10.5, which a and b correspondingly represent gear and vehicle speed, respectively, the transmission shift in 2/4.8 s, combined with b and c we can conclude that motor speed decline in upshift and rise

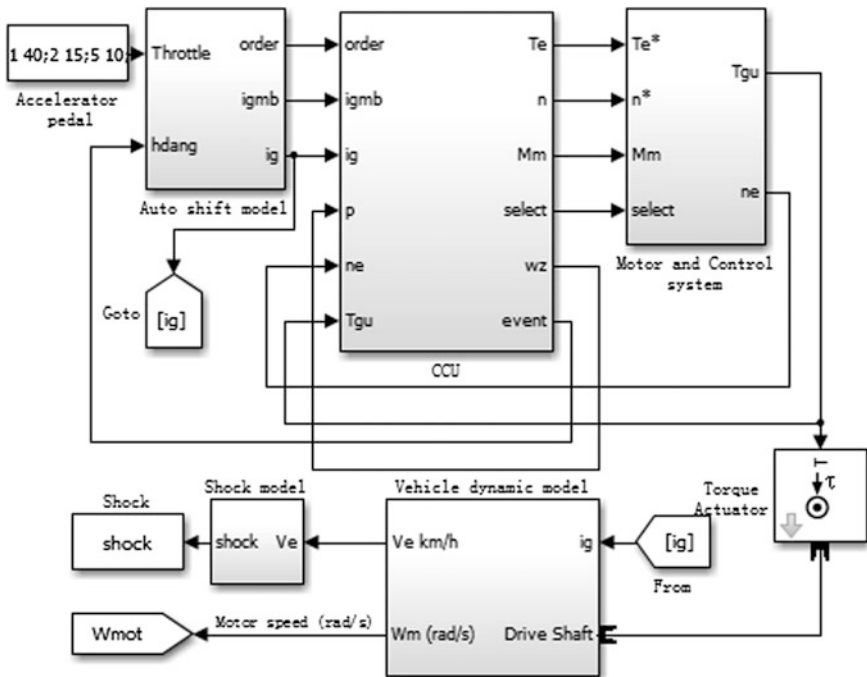


Fig. 10.4 Control system model

Table 10.1 Vehicle parameters

Parameter name	Value	Parameter name	Value
Curb weight	1,325 kg	i_{g2}	1.21
Air drag coefficient	0.315	i_0	4.3
Auto frontal area	2.87 m ²	rated voltage	312 V
Wheel radius	0.291 m	rated power	18 KW
i_{g1}	1.92	rated speed	3,000 rpm

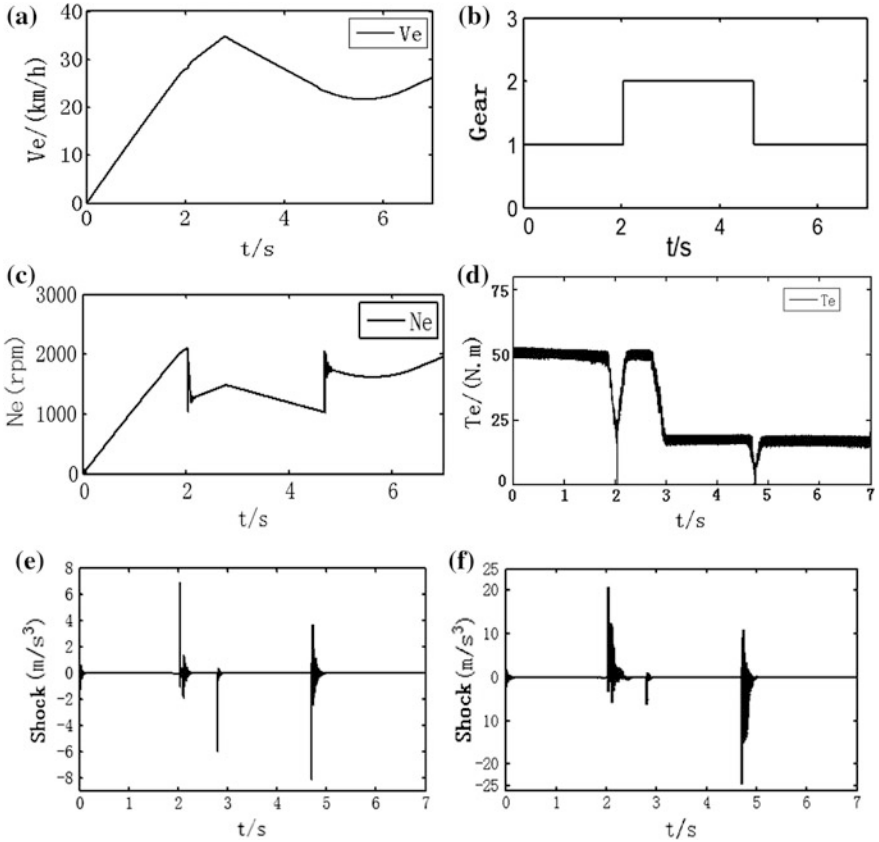


Fig. 10.5 The simulation results: **a** Vehicle speed, **b** Gear, **c** Motor speed, **d** Motor torque, **e** With coordinated control, and **f** Without coordinated control

in downshift, moreover decline and rise ratio is equal to the ratio of target gear ratio and current gear ratio, in line with the principle of active synchronize.

The curve shown in Figures e and f can be obtained from the vehicle speed simulation. It is easily known that the shift shock has large fluctuations at shift points

2, 4.7 s, and there are also obvious shock at starting and climbing. These obvious shocks are in accordance with the shock generation mechanism. Comparing the Figures e and f, under the effect of coordinated control unit, the shock remains unchanged when car starts at 0 s or and climbs at 2.8 s, but decreases from $-25\text{ms}^{(-3)}$ to $-8\text{ms}^{(-3)}$ at 2 and 4.7 s, shift quality has been significantly improved.

10.5 Conclusions

By analyzing the transmission shift process and the shift shock generation mechanism, this paper proposed the coordinated control method to develop torque curve which meet the requirements of shift shock, and coordinate the work of the drive motor and shift actuator. By modeling and simulation in MATLAB/Simulink, the results show that the transmission can shift according to the developed shift process, while CCU can reduce the transmission shift shock and compensate for the effects of a clutch omission in shifting process and to improve shift quality.

References

1. Qing-hua J (2011) Parameters matching and optimization for powertrain and research on automatic shift schedule of electric vehicle. Master thesis, Hunan University, Changsha
2. Yang W, Jun-qiang X (2009) A study on the mechanism and counter measures for shift-impact in AMT. *Automot Eng* 31(3):253–257
3. Ming Y, Datong Q (2009) Shift performance control for mild hybrid electric vehicle equipped with automatic manual transmission. *J Mech Eng* 45(5):108–114
4. Jian-jun H (2012) Coordination matching control method of amt gear shifting for pure electric car. *China J Highw and Transp* 25(1):152–158

Chapter 11

Electric Vehicle Fault Diagnosis System Based on CAN-Bus

Bingli Zhang, Wenjie Shi and Andong Ge

Abstract With the advantages of non-pollution, low noise, and high energy efficiency, electric cars have become an important trend. The vehicle fault diagnostic protocol ISO15765 is introduced, and a CAN-based (Controller Area Network) fault diagnosis system and diagnostic trouble codes (DTCs) for electric cars are designed. The CAN communication networks are tested by CANoe software, and the results show that the networks meet the requirements.

Keywords EV · CAN-bus · Fault diagnosis system

11.1 Introduction

The CAN-bus (Controller Area Network) is currently one of the world's most widely used automotive buses. Germany's Bosch designed the CAN-bus to solve problems found in modern vehicles' electronic control systems, including reducing the number of wire harnesses, enhancing the ability to process large amounts of communications data at high speeds and other demands required to accommodate contemporary information exchange needs [1]. After several decades of development, the CAN-bus has not only become the standard protocol for automotive networks in Europe, but is also widely used as a standard by motorcar firms in other countries throughout the world due to its small data structure, its flexible communication capabilities, and its nondestructive arbitration field features. The CAN-bus standard has become one of the underlying standards for contemporary buses.

The purpose of this paper is to tackle the key problems of the pure electric car by studying and analyzing the automotive CAN-bus protocol and then designing a

B. Zhang · W. Shi (✉) · A. Ge
College of Machinery and Automobile Engineering, Hefei University of Technology,
Hefei, China
e-mail: yy1016xs@qq.com

diagnostic system and diagnostic trouble codes (DTCs) for electronic control units based on this protocol. The system produced by this research and development conforms to the ISO15765 fault diagnosis standard.

11.2 ISO15765 Protocol

The ISO15765 standard satisfies the UDS diagnostic service requirements and is used for the CAN-bus. Its architecture is as shown in Fig. 11.1.

The application layer is based on the content of the diagnostic services defined in the ISO14229 and the ISO15765-3 standards. This layer enables the unified diagnostic services of ISO15765, including the diagnostic and communication management functions, the data transmission function, the stored data transmission function, the input/output control function, the remote activation of routine functions, and the upload/download function [2], and etc.

The network layer is defined in the ISO15765-2 standard. Its main effect is to provide interfaces for the application layer and to establish data communication between different nodes in the network layer. The network layer also provides grouping, flow control, reconstruction, and other functions particularly for long messages (i.e., more than 8 bytes). The data link layer and the physical layer are defined in the ISO11898 standard. Its data unit protocol uses a CAN-frame and has a nondestructive arbitration-domain mechanism. The physical media of the physical layer uses the CAN-bus with its high communication rate, long transmission distance, and strong anti-jamming capability, as well as other features.

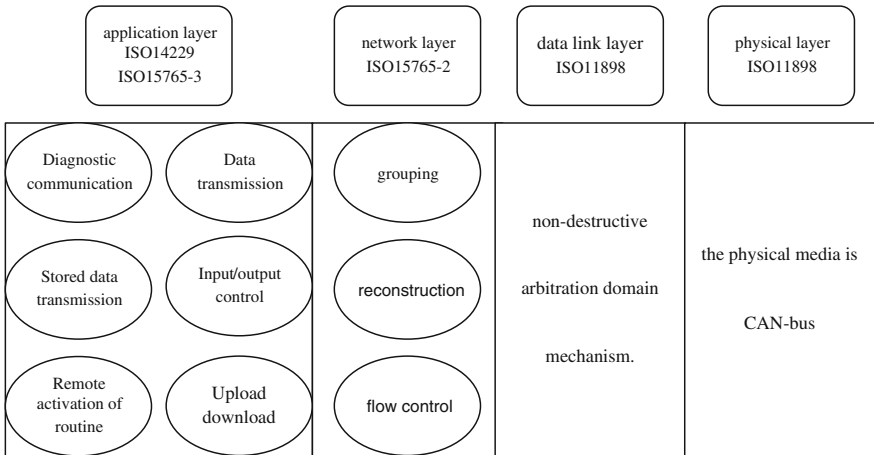


Fig. 11.1 The architecture of ISO15765

11.3 Diagnostic System

At present, the diagnostic techniques for a linear system are relatively mature and can provide theoretical support for the fault diagnosis of nonlinear systems. The diagnostic technology for electric cars can use traditional internal combustion engine cars' mature fault diagnosis methods as a reference point. Currently, there are three advanced basic methods for fault diagnosis: modeling analysis, signal model analysis, and knowledge reasoning. The modeling analysis method is primarily used on a linear system, which can be described accurately using a mathematical model. The signal model analysis method uses a signal model directly, instead of a mathematical model, and thus, the applicable scope is wider. Knowledge reasoning fault diagnosis is a hot research field with great application prospects, which includes expert system methods, fuzzy reasoning methods, pattern recognition methods, and bus network methods and so on.

11.3.1 CAN-Bus network

This paper designs a fault diagnosis system for electric car based on CAN-bus. The CAN-bus's network topology structure is as shown in Fig. 11.2.

This paper designs two-way CAN-bus for the CAN-bus network, namely high-speed CAN and low-speed CAN [3]. Since the power train system of electric car, such as motor controller, ABS controller, and battery management system, requires higher real-time performance and reliability, the high-speed CAN-bus communication is adopted. Nevertheless, other nodes' real-time requirements are relatively low; the low-speed CAN-bus communication is adopted.

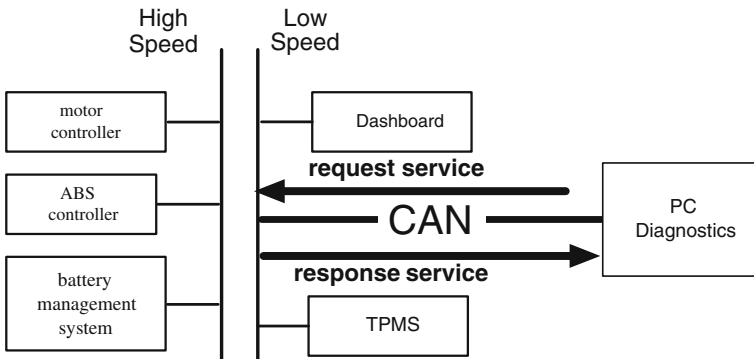


Fig. 11.2 Topology structure

Table 11.1 Diagnostic trouble code

High byte				Low byte											
1	0	0	1	0	0	1	0	0	0	1	1	0	1	0	0
B		2		3				4				5			

11.3.2 Diagnostic Trouble Code

The DTC is an important part of the fault diagnosis system. For the pure electric car used for this project, this paper designs standard DTCs that are 2 bytes and 5 bits [4]; the first bit is the alphabet, followed by four-digit bits, as shown in Table 11.1.

The first letter indicates the system to which a fault belongs. For example, B (1 0) indicates the vehicle body, P (0 0) indicates the power system, C (0 1) indicates the chassis, and U (1 1) indicates the network system.

The second digit indicates the type of fault. For example, 0 represents the general fault codes as defined in the relevant ISO standards, 1 represents the extended fault codes as defined by the manufacturers, 2 or 3 (which includes letters of different systems) represents different meanings, and 4 is reserved for future use.

The third digit indicates the faulty subsystem. For example, P10xx represents motor controller faults, P11xx represents battery management system faults, and P12xx represents charger controller faults.

The fourth and fifth digits indicate more specific faults and types of faults for a particular subsystem. The fourth digit may represent different sensors or actuators within a subsystem, the fifth digit indicates specific electronic information, such as high or low voltage, fast or slow response, or signal exceeds a limit value.

For example, P1100 indicates that the battery management system module voltage is low, P1101 indicates that the battery management system module voltage is too high, P1001 indicates motor controller temperature is too high, P1010 indicates that the motor voltage is too low, and P1021 indicates that the motor temperature is overhigh.

11.4 Communication Verification

In order to verify the validity of the design, simulation tests are conducted using CANoe software. CANoe software is a development environment for the CAN-bus developed by Vector of Germany. CANoe is used to complete the modeling, simulation, and testing of CAN communication networks, due to its strong functionality and its simple operations. Through the CANoe software, the nodes on the CAN-bus can be fully virtualized, and then, a simulation can be conducted.

To build a simulation model, first, use the CANdb++ Editor to create the database files, including bus nodes, each node’s message, the environment variables, and the signal parameters of the messages. Second, use the panel editor to create a graphical

status display and control panel, enabling developers to easily change the variables. Third, use the simulation setup window to import the nodes created in the database one by one, and then, set the baud rate. Finally, use the CAPL programming language to design the sending and receiving of messages, edit the environment variables, and establish the control and communication functions between nodes. The system simulation model is now set up as shown in Fig. 11.3.

After the simulation model is established, we can simulate and debug the network by changing the information fed into the simulation model. The functionality of several aspects was tested for this paper, including the following: whether or not each node can complete the required requirements; whether or not the work process of each node is perfect; whether the bus peak load rate and average load rate meet the requirements; and whether the message sending cycle on the bus and the delay rate meet the requirements.

The comprehensive test is as shown in Fig. 11.4. By trace window, the messages on the network can be traced in real time. The bus load rate and the bus peak load rate can be shown on the Bus Statistics window. The transmitting frequency and the error frames can be shown on the Frame Histogram window. The results show that the CAN communication networks created for this paper meet all the requirements above.

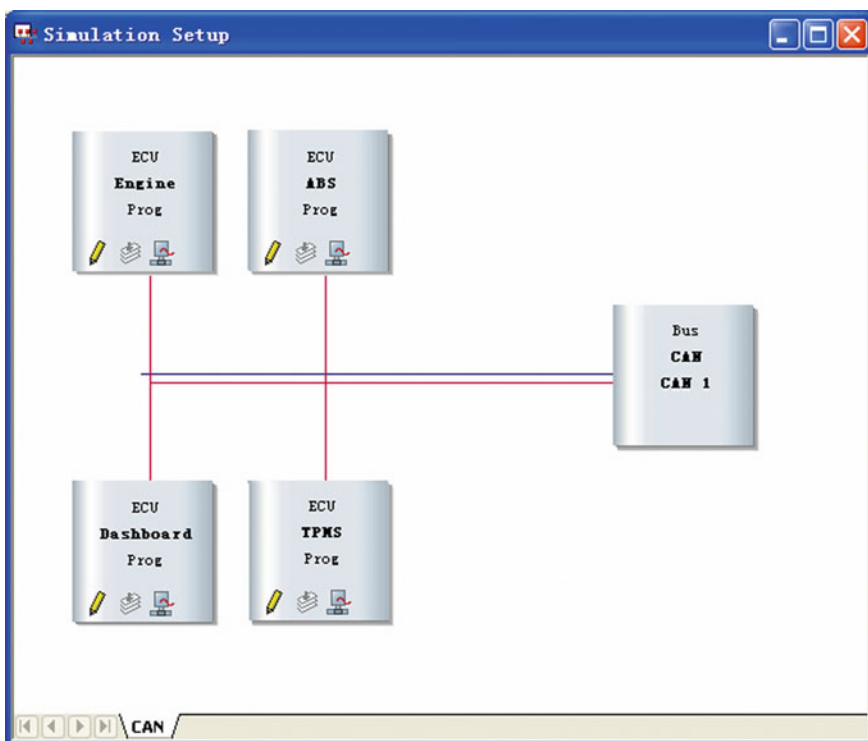


Fig. 11.3 Simulation model

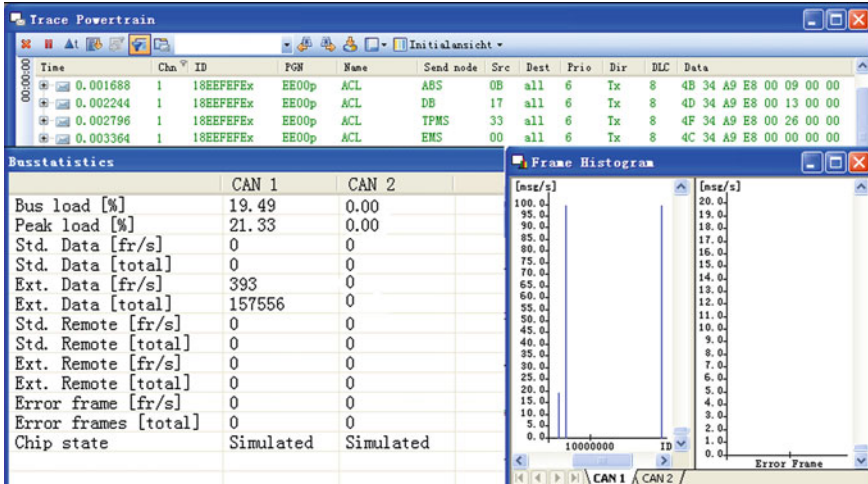


Fig. 11.4 Comprehensive test

11.5 Conclusions

ISO15765 establishes a unified diagnostic service based on the CAN-bus protocol standard, which is the development trend of future vehicle onboard diagnostic protocols. This paper develops CAN-bus network for pure electric car and uses the CANoe software to complete the development of virtual ECU nodes. These tests demonstrate that the communication functions of CAN networks can be achieved.

References

1. Hou Q (2011) Research on vehicle control unit for electric vehicles with battery ultra capacitor dual energy sources. Master thesis, Hefei University of Technology
2. Liu L, Xu A, Song Y (2012) Research and development of vehicle unified fault diagnostic protocol. *Comput Eng* 38:9–13
3. Zhang H, Zhan D, Lin C (2008) Design of vehicle fault diagnosis system based on CAN bus. *Automot Eng* 30:934–937
4. ISO15031-6 (2006) Road vehicles: diagnostic trouble code definitions

Chapter 12

Study on the Bending Fatigue of a Diesel Engine Crankshaft

Shuai Teng, Shufen Wang, Zhangtao Yao, Zhongtai Li, Lei Guo, Hao Li and Jie Liu

Abstract A finite element model of a diesel engine crankshaft is established with ANSYS and FE-SAFE softwares. Then, the bending moment and fatigue life of crankshaft bending are calculated. Finally, the crankshaft bending fatigue test is carried out on test bench, both the simulation results of the finite element software and experimental results are consistent, and the results show that the combination method of simulation software and bench test proves the journal fillet of crankshaft connecting rod is the weakest part of crankshaft bending fatigue, and it provides an important significance for the design and production of crankshaft.

Keywords Crankshaft · Bending fatigue · ANSYS/FE-SAFE · Fatigue test

12.1 Introduction

Crankshaft is one of the most important parts of an internal combustion engine, its main function is to transfer and output power, under the gas pressure inside the cylinder, reciprocating and rotating inertia force, torque, etc., and it is of great significance for the reliability and performance of the diesel engine [1]. The actual analysis of crankshaft fracture has proved that the failure modes of the crankshaft are mainly bending fatigue damage. In this paper, a diesel engine crankshaft is studied by using ANSYS/FE-SAFE software, the crankshaft stress and fatigue is simulated, and then, the crankshaft bending fatigue test is used for verification,

S. Teng (✉) · S. Wang · Z. Yao · Z. Li · L. Guo · H. Li
Research and Development Center, China National Heavy Duty Truck Group Co. LTD.,
Jinan 250002, China
e-mail: tengshuai2001@sohu.com

J. Liu
College of Mechanical and Electronic Engineering, Shandong University of Science
and Technology, Qingdao 266510, China

© Springer-Verlag Berlin Heidelberg 2015
Society of Automotive Engineers of China (SAE-China) (ed.),
Proceedings of SAE-China Congress 2014: Selected Papers,
Lecture Notes in Electrical Engineering 328, DOI 10.1007/978-3-662-45043-7_12

in order to improve the crankshaft fatigue performance and provide important and significant guide.

12.2 Finite Element Stress Analysis

In this study, 3D entity design of crankshaft is firstly built by using Pro/E software; one crank unit of the crankshaft is taken as the analysis object; then, through the interface between ANSYS and Pro/E, the solid model is imported into ANSYS software; and finally, the material parameters of crankshaft listed in Table 12.1 are input simulation software.

12.2.1 Meshing

The finite element model is meshed in the ANSYS software. During the meshing process, select the solid 186 to provide 20-node hexahedron unit. Crankshaft fillet and oil hole, oil position is sensitive to local stress concentration; in these local grid the refinement need to be done [2], as shown in Figs. 12.1 and 12.2, the local grid refinement of crank fillet, the whole finite element model is composed of a total of 473,839 nodes, and 298,686 units.

12.2.2 Applied Load

Under the gas pressure and the inertial force of piston and connecting rod reciprocating motion, the actual operation of crankshaft is extremely complex. In order to analyze the crankshaft bending moment on the crank shaft force, combined with the name of the crankshaft bending moment calculation results of the work, to transform applied load at the other end of the main journal, the given bending moment is 6 kN m. The freedom constraints in different directions are applied on the main journal and at the end of the journal of the connecting rod.

Table 12.1 Material properties

Material	42CrMo
Young's mod (N/mm ²)	210,000
Poisson's ratio	0.3
Tensile strength/MPa	1,050
Density kg/m ³	7,800

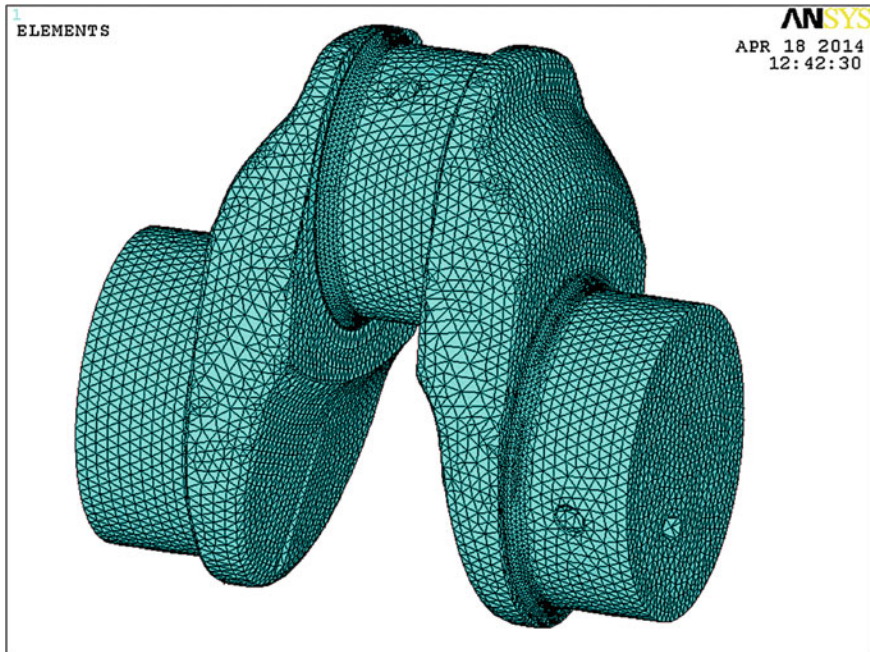


Fig. 12.1 Finite element grid of a crank unit

12.2.3 Stress Analysis

As shown in Figs. 12.3 and 12.4, the maximum strain value of static analysis of crankshaft is 0.707 mm; the maximum Von Mises stress distribution on the journal fillet of the connecting rod is 605 MPa, which is significantly higher than the other positions.

12.3 The Calculation of Fatigue Life by ANSYS/FE-SAFE

ANSYS analysis results are imported into the FE-SAFE fatigue life calculation software [3]. This paper uses the ANSYS/FE-SAFE Seeger material data estimation method [4].

In the setting of fatigue calculation, according to the manufacturing process, the crankshaft surface roughness is: $0.6 \mu\text{m} < Ra < 1.6 \mu\text{m}$. In FE-SAFE data file window, import load time history curve, select analyses uniaxial stress–life curve von Miss–Goodman algorithm, the application of Miner linear cumulative damage rule, after the input intensity limit and modulus of elasticity, the S–N fatigue life curve of 42CrMo is displayed (as shown in Fig. 12.5).

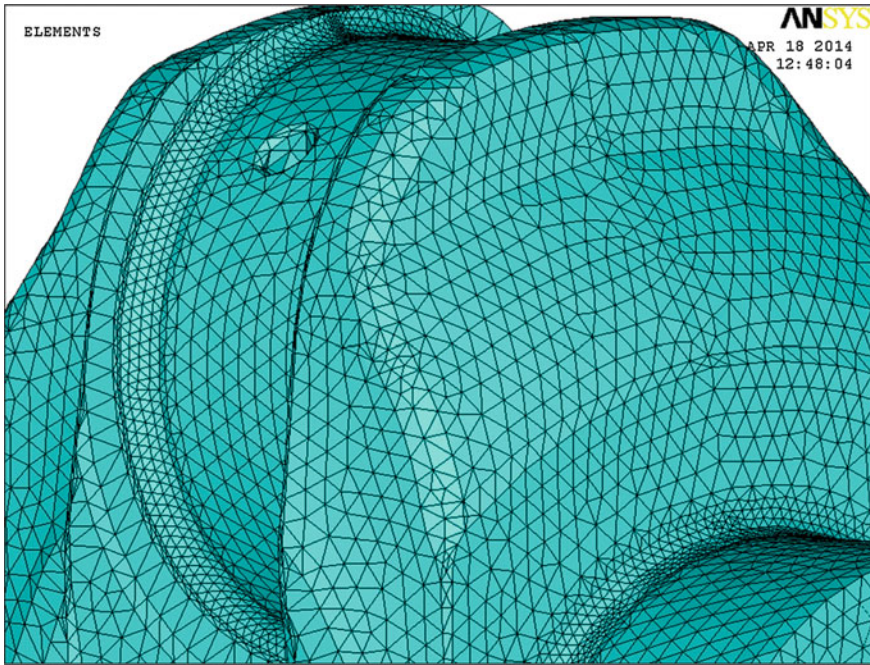


Fig. 12.2 Local grid refinement of a crank fillet

As shown in Fig. 12.6, through ANSYS post-processing, the crankshaft fatigue life is shown in the form of cloud pictures. The weakest failure position in crankshaft bending fatigue is connecting rod's journal fillet area, and the shortest fatigue life is $N = 10^{4.937} = 86,497$ times.

12.4 The Crankshaft Bending Fatigue Test

In the crankshaft fatigue strength of the study, calculation and experiment are two main methods; fatigue test is an effective method for evaluation of the crankshaft structural strength [5]. In this paper, fatigue test was done on the crankshaft bending fatigue test bench (as shown in Fig. 12.7) and the design of bend fatigue test is the main location of evaluation on crankshaft main bear bending load effect. The test bench is magnetic resonance vibration table, with dynamic test frequency up to 35–300 Hz, and it features good reliability, high precision, and strong anti-interference ability.

In this paper, the single crank is used, and thus, you must cut the crankshaft into a crank unit, including a connecting rod journal and two main journals. Crankshaft

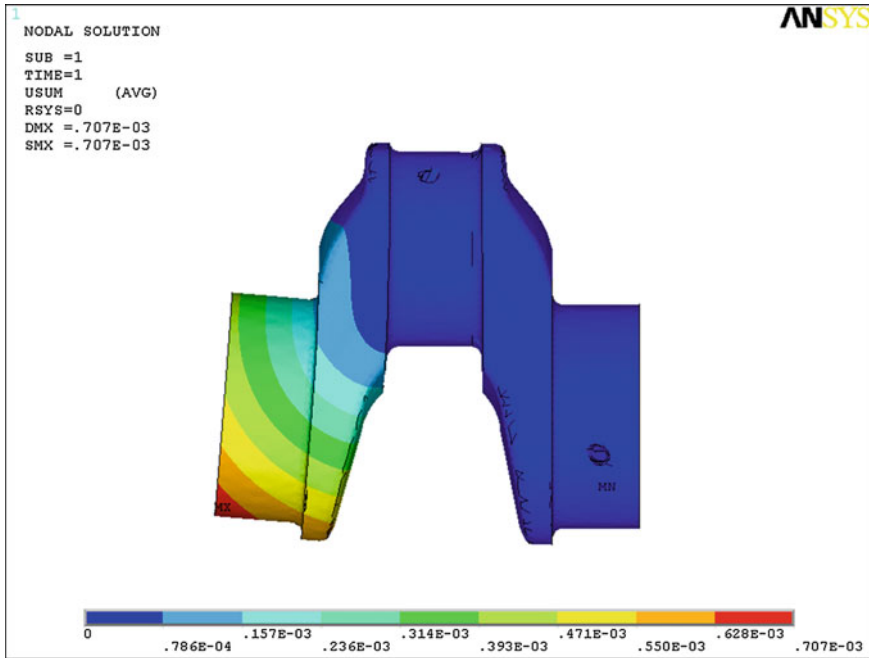


Fig. 12.3 The strain distribution of crank

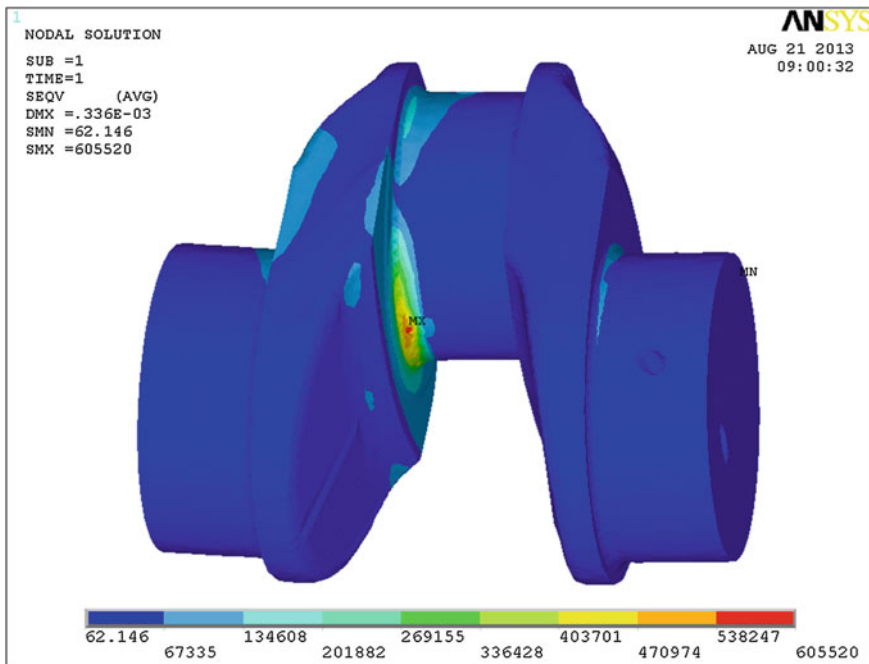


Fig. 12.4 The stress distribution of crank

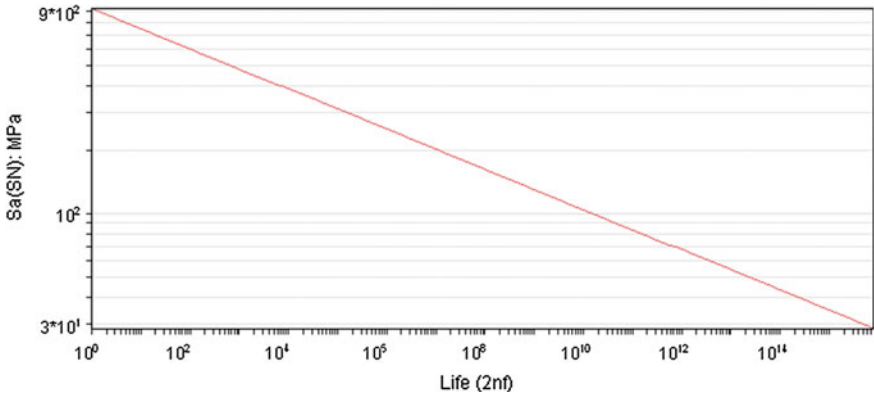


Fig. 12.5 The S-N curve of 42CrMo

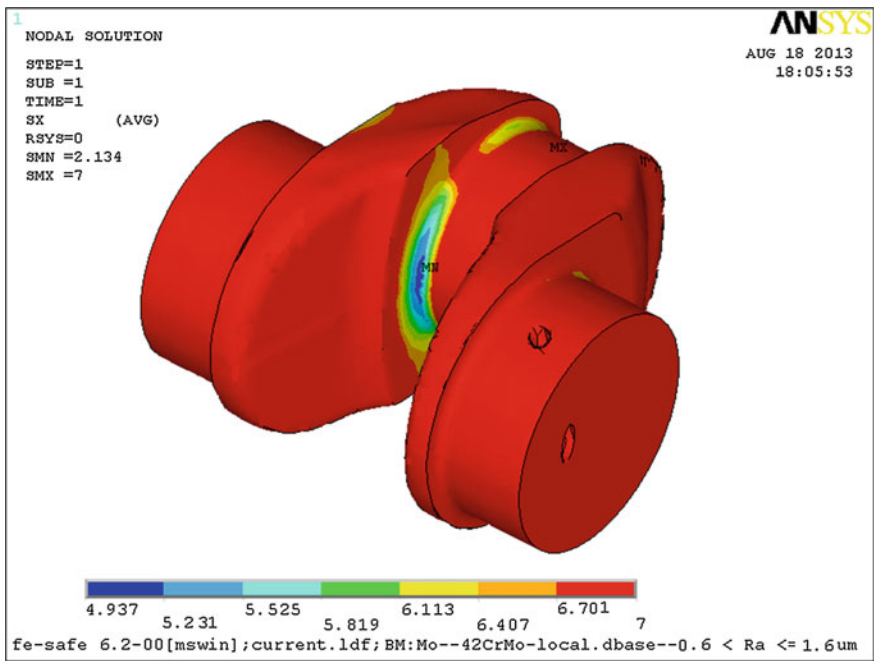


Fig. 12.6 The distribution of crankshaft bending fatigue life

sample is applied in 6 kN m dynamic load, stress ratio $R = -0.2$, and under the action of sinusoidal cyclic loading experiment.

As shown in Fig. 12.8, after 149,000 times of the cyclic test, some cracks appears on the crankshaft bending test sample and are just located at the journal fillet of the connecting rod, and the actual fractures are highly consistent with those

Fig. 12.7 Test bench of crankshaft fatigue



Fig. 12.8 Fatigue failure location of crankshaft



ones computed by FE-SAFE. All the actual processing of the crankshaft, main journal and connecting rod journal are made by induction hardening processing, tensile strength and fatigue limit equivalent also get bigger, and thus, the actual service life of the crankshaft will be greater than the compute life.

12.5 Conclusions

In this paper, finite element analysis of crankshaft bending stress and fatigue are made through joint application of software PROE, ANSYS, and FE-SAFE; the test bench for crankshaft bending fatigue test is carried out; the following are the conclusions:

Finite element calculation of the fatigue model established by 3D software is feasible, reasonable, and proper.

The simulation result is consistent with the actual test result; those prove the journal fillet of the crankshaft connecting rod is the weakest part of the crankshaft bending fatigue damage.

The combining methods of numerical simulation and bench fatigue test, especially in the design stage of the crankshaft, can avoid the consumption of the time and material in the experimental study, also improve the crankshaft design accuracy, and provide the reliable basis for strengthening the crankshaft fatigue life.

References

1. Yang LS (1984) The internal combustion engine design. China Agricultural Machinery Press, Beijing
2. Guo L (2009) Investigation on powertrain structure's vibration and noise performance based on virtual forecast technology. Zhejiang University, Hangzhou
3. Jiang NC (2006) ANSYS and ANSYS/FE-SAFE software engineering application and example. Hehai University Press, Nanjing
4. Peter A (2009) A critical review of the Baumel-Seeger method for estimating the strain-life fatigue properties of metallic materials. Eng Integrity 10(27):6–11
5. Zhou X (2003) The crankshaft bending fatigue test system research and development. Zhejiang University, Hangzhou

Chapter 13

Simulation and Structural Design of AMT Switch Valve's Coil

Ling-ya Lu, Ji-hua Wang, Rong Fan, Yu-sheng Ju
and Yong-ming Zhang

Abstract The effects of the position relationship between work air gap and coil, the coil wire diameter, and the coil turns on the electromagnetic characteristics are analyzed by using the software Ansoft Maxwell. The coil parameters are determined by optimizing the coil design.

Keywords Coil of AMT switch valve · Maxwell · Structural design

13.1 Introduction

In the operation of the automatic transmission of the solenoid valve, the solenoid valve is driven by the electromagnetic force. Since the excitation current flows into the coil to create a magnetic potential and generating a suction magnetic flux, the design of solenoid coil is very important.

In this paper, Ansoft Maxwell is used to simulate electromagnetic properties of the solenoid valve coil, and the influence of the position relationship between work air gap and coil, wire diameter and number of turns, and other parameters on the electromagnetic properties is analyzed so as to guide and validate the structural design of the solenoid coil.

13.2 Introduction to Solenoid Coil

Solenoid coil is generally divided into framework, no-framework, circles, squares, and other types of coil structures, and the pattern will largely affects the performance of the solenoid valve. No-framework coil means no support wires of the coil

L.-y. Lu (✉) · J.-h. Wang · R. Fan · Y.-s. Ju · Y.-m. Zhang
Wuxi Fuel Injection Equipment Research Institute, Wuxi 214063, China
e-mail: lly@wferi.com

frame. The coil and core is combined closely with the band, so the part heat of the coil can be transmitted to the core. The framework coil's wire is wound on bobbins, as framework plays a supportive role in the wire.

To ensure that the designed coil has a sufficient electromagnetic force, the rational design of coil turns, winding thickness, and wire thickness are determined according to valve structure, so as to fix the dimensions of the coil.

13.3 Simulation of Solenoid Coil

To determine the selected coil's geometry and parameters are reasonable, it is necessary to simulate the solenoid valve and its coil. It was calculated by using Ansoft Maxwell herein.

Since the automatic transmission solenoid valve has axis symmetrical structure (see Fig. 13.1), the two-dimensional form can reflect the three-dimensional one of the situation, so we use an idealized treatment [1]:

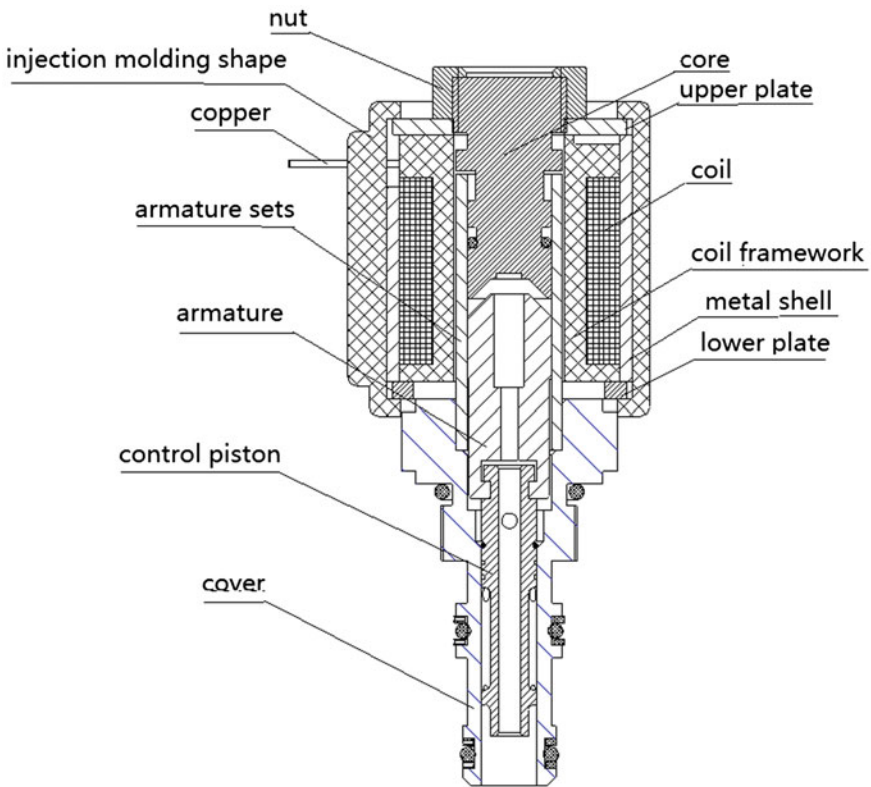


Fig. 13.1 Schematic diagram of a solenoid valve

1. To ignore the axial hole in control piston and the groove in core.
2. As the permeability of weak magnetic materials (seals, nylon gaskets, springs, coil framework, injection molding shape, etc.) is very small, close to the permeability of air, they are ignored when making the model.
3. Solenoid valve cover, armature sets, core, and other stationary items with Boolean operations can be regarded as a whole.
4. Smooth processing is done on some of the details in the geometry.

Based on the above assumptions, a static two-dimensional electromagnetic field was analyzed. Figure 13.2 shows a two-dimensional model, main parts of the material are shown in Table 13.1, the mesh is shown in Fig. 13.3, and the flux is shown in Fig. 13.4. When the coil is energized, the magnetic field is generated around it, so the magnetic field lines can vividly describe the distribution. Figure 13.4 shows the magnetic lines of force through the electromagnetic valve member (nut, core, armature, and cover) and the coil member (metal shell, upper

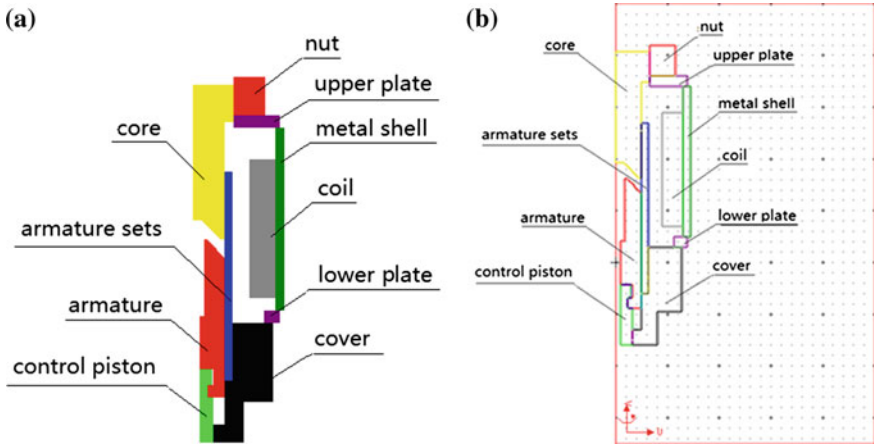
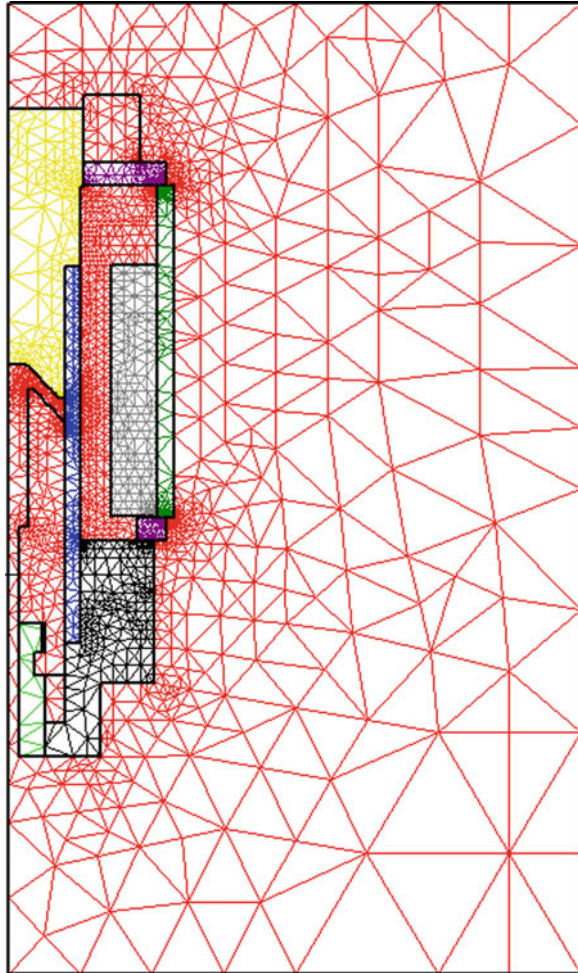


Fig. 13.2 2D model

Table 13.1 Main component materials

Component	Materials
Cover	Y15Pb
Armature	Y15
Armature sets	Stainless steel
Core	Y15
Control piston	Steel_1010
Coil	Copper
Metal shell	Steel_1010
Upper plate and lower plate	Y15
Nut	Steel_1010

Fig. 13.3 Simulation grid map

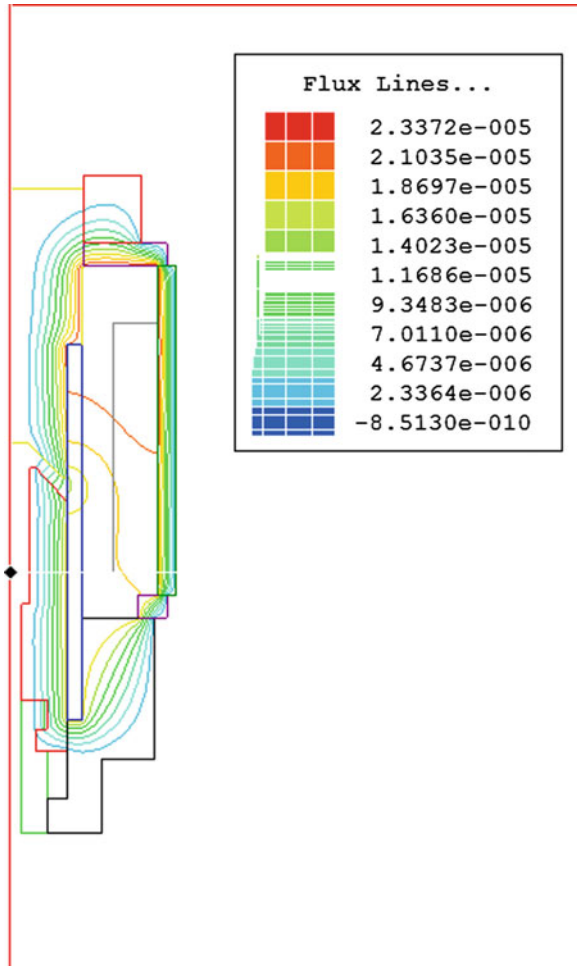


plate, and lower plate), to form a complete loop, which constitute the main magnetic flux path; a small part of the flux is in the air in the model does not affect the magnetic properties.

13.3.1 Influence of the Relative Position of the Coil and the Air Gap

Because of the loss of the air gap flux diffusion, the total loss of the coil and the loss distribution is largely influenced by the position of the coil and the gap's size. According to statistics, the coil is placed within a certain distance from air gap or

Fig. 13.4 Distribution of magnetic field lines



the coil is placed on a certain area with an accurate calculation, the gap diffusion flux loss can be reduced [2].

Since the other parameters remain constant in the model, coil is moved toward axial direction, changing the relative position of the coil and the air gap. Electromagnetic force is shown in Fig. 13.5. In Fig. 13.5, using the underside of the coil as zero benchmark coordinates, while the relative position of the coil is 2 mm, and at this time, the relative position of the air gap is 7.8 mm, coil is moved toward axial direction 3 mm, to change the relative position of the coil and the air gap. Figure 13.5 shows that with the changing of the relative position of the coil from 2 to 5 mm, electromagnetic force gets bigger before they are smaller, i.e., the position of the coil relative to the air gap has an optimum position where the electromagnetic force is maximal. Therefore, considering the limits of the coil housing structure, the coil arranged in mid-position with respect to the air gap is appropriate.

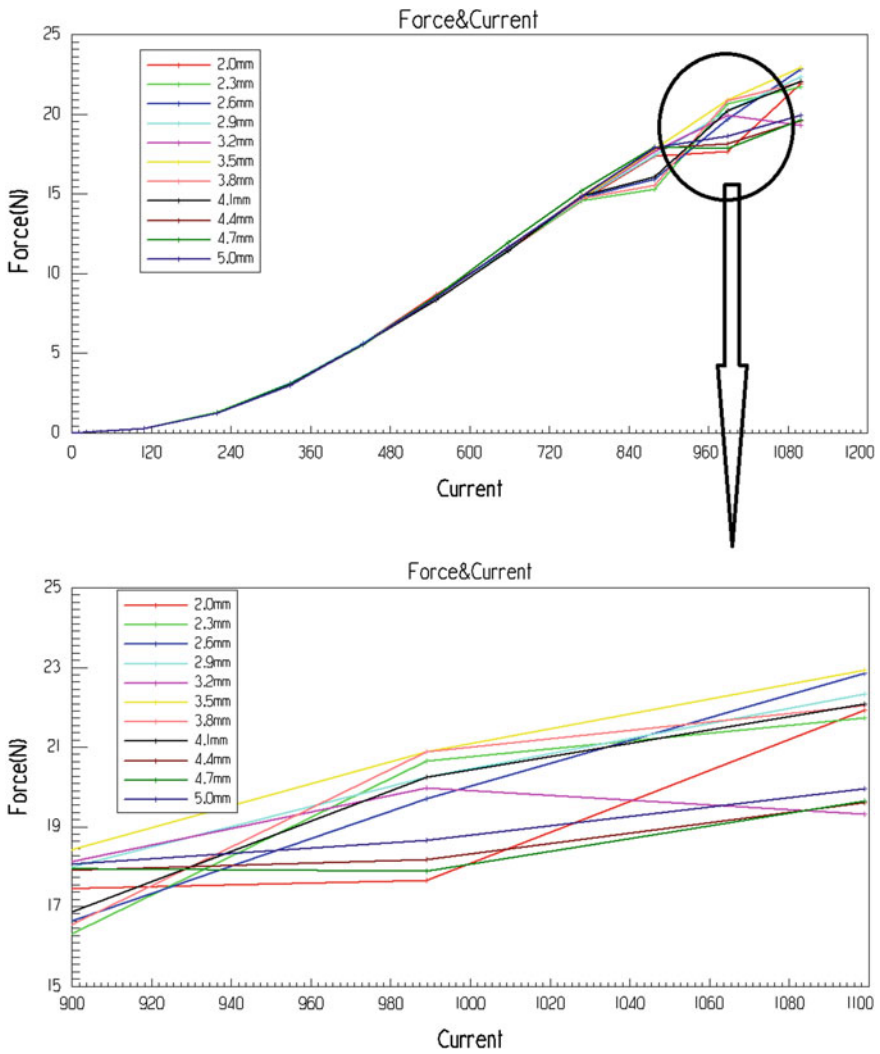


Fig. 13.5 Electromagnetic force changes with the air gap's relative position

13.3.2 Influence of the Wire Diameter

The formula is as follows:

$$b \cdot h = K \cdot A \cdot N \times 10^{-6} \tag{13.1}$$

Table 13.2 Calculated results in different coil diameters

Diameter (mm)	Axial length of the coil (mm)	Ampere-turns (A N)	Electromagnetic force (N)
0.18	17.82	890.19	17.10
0.19	19.85	991.85	19.27
0.20	22	1,099	19.09
0.21	24.25	1,211.65	23.06
0.22	26.62	1,329.79	25.17

$$R = \rho \cdot L \cdot N/A \quad (13.2)$$

where b is the width of the coil (m), h is the height of the coil (m), K is a rolling coefficient of the wire (and generally 1.1–1.2), A is a coil conductor cross section (mm^2), N is the number of turns, R is coil resistance Ω , ρ is the resistivity of the wire $\Omega \text{ mm}^2/\text{m}$, and L is the average length of one turn of the coil wire (m).

According to Eqs. (13.1) and (13.2), remaining parameters are constant, change the diameter of the wire coil only, as the coil in a fixed width, height and ampere-turns are proportional to the square of the diameter.

Changing the wire diameter reflects the change of the coil height in the model. The simulation result of electromagnetic force is shown in Table 13.2.

According to the results, the electromagnetic force becomes larger as the diameter becomes thicker. During the design process, it is necessary to choose an appropriate diameter with considering of electromagnetic force and geometry.

13.3.3 Influence of Coil Turns

The influence of the solenoid valve coil turns on electromagnetic properties is the one of the inductance, essentially. When the other parameters remain the same, to increase the coil turns can enhance the magnetic potential energy and promote the conversion of electricity and magnetism, which enhances the electromagnetic force, thus the armature can obtain bigger acceleration.

Keep the other parameters in the model of constant, only change the coil turns means change the turns of ampere. The simulation results of the electromagnetic force are shown in Table 13.3. As shown in Table 13.3, with the increase in the number of turns of the coil, the electromagnetic force is increased significantly. However, because of the coil bobbin and the size of the structure, the number of turns cannot be increased too much; on the other hand, too many turns means a corresponding increase in the inductance and the resistance, the response time is lengthened, the solenoid valve is not conducive control.

Table 13.3 Results of different turns

Turns	Electromagnetic force (N)
1,700	17.83
1,750	18.32
1,800	18.62
1,850	19.09
1,900	19.52
1,950	19.98
2,000	20.39

13.4 Design of Solenoid Coil

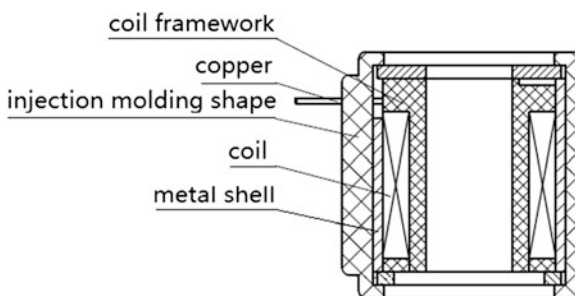
This type of solenoid coil is used to control the work of automatic transmission solenoid valve, and it is suitable for coil that has a framework. Compared with no-framework coil, it has no outer insulation, but the cooling becomes worse. A schematic cross-sectional structure of a solenoid coil is shown in Fig. 13.6.

According to the design principle of the automatic transmission solenoid valve, the solenoid coil is installed in the outer of the armature, so the inner diameter slightly larger than the outer diameter of armature sets. The inner surface of the top cover in framework has a leakproof ring with a raised edge and positioning convex platform matching with the winding spool. There are two grooves for fitting copper in framework. Framework's materials commonly used in ceramic, plastic, bakelite, and vulcanized fiber for electrical purposes; selection of materials has a certain impact on the quality and stability of the coil. In this paper, framework choose nylon with glass fiber which with excellent wear resistance and self-lubricating, high mechanical strength.

In order to reduce the impact on interference of the external electromagnetic and coil itself on the external electric circuit, use metal shell in the structure to close the coil, and it must be grounded firmly to isolate with the external electric circuits, as well as metal shell enhances magnetic.

Copper is used as the power terminal. As copper is often exposed, if it contacts with corrosive solvent, even if copper has no active chemical properties, fracture will be caused by corrosion, so it requires cladding and good solderability on

Fig. 13.6 Structural diagram of the structure of an electromagnetic coil



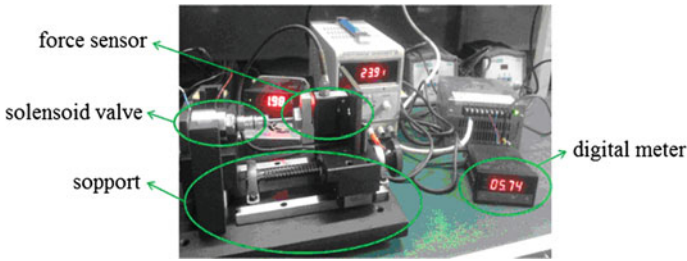


Fig. 13.7 Electromagnetic force test equipment

copper's surface. When coated copper contacts with corrosive solvents, coating acts as the anode and copper acts as cathode, which protects the copper. It can prolong the life of copper and save the cost. In this paper, the copper outer has tin plating, as tin is chemically active than copper, and it has relatively low melting point, and tinning process is easy to operate.

The coil wrapped by injection in order to seal as well as to ensure the insulation and heat dissipation.

In this paper, the framework using nylon supports wire wound, metal shell and upper plate and lower plate use magnetic material, copper outer has tin plating.

13.5 Electromagnetic Force Test

Electromagnetic force testing device is shown in Fig. 13.7. The solenoid valve is placed on the support, and an electromagnetic force is designed herein after the solenoid is energized. Since the control piston is in a stationary state, it is subject to an electromagnetic force acting on the force sensor which displays on the digital meter. By controlling the voltage or current of the coil, the change of electromagnetic force was observed.

Combining with simulation and practical test, 0.2-mm enameled round copper wire is used and turns from 1,800 to 1,900 is appropriate.

13.6 Conclusions

1. According to Maxwell simulation results, the magnetic of solenoid valve and coil is complete and effective, which indicates a reasonable structure design of solenoid coils;
2. Simulation calculations show that the coil assembly position, structure, number of turns, and wire diameter have an impact on the electromagnetic force;

3. By the electromagnetic force test, the simulation results validate the reliability and effectiveness. Combining with automatic transmission solenoid coil, the wire diameter and number of turns are preferably selected in order to improve the electromagnetic properties of valve.

References

1. Sun C, Ren H (2009) Design and performance simulation on the electro-magnet of normally open typed high speed switch valve. *J Mach Des* 6:10–12
2. Song R, Li L, Xia S (2012) Coil design and electromagnetic characteristics simulation of solenoid valve for high-pressure pump of Gasoline direct injection system. *Mod Veh Power* 4:10–13

Chapter 14

Effect of Compression Ratio on Internal Combustion Rankine Cycle Based on Simulations

Yang Gao, Liguang Li, Xiao Yu, Jun Deng and Zhijun Wu

Abstract A thermodynamic model of an ideal internal combustion Rankine cycle (ICRC) is established based on the first law of thermodynamics, and the effect of compression ratio on the performance of ICRC is studied by simulation. The injected water absorbs the combustion heat and evaporates into vapor after being injected at the top dead center. Water vapor becomes part of the working gas, and calculation results show that the in-cylinder pressure increases. Increasing compression ratio of ICRC can improve cycle performance more than traditional cycle. When compression ratio increases from 9.2 to 14 and injection temperature is 120 °C, the thermal efficiency increases from 4.9 % (no water injection) to 22.4 % (injected water mass = 140 mg).

Keywords Compression ratio · ICRC · Ideal cycle · Thermodynamic model

14.1 Introduction

The rapid development of automobile industry has brought great challenges to global energy and environment problem. Researchers are exploring new technologies with lower energy cost and emissions. Oxy–fuel combustion technology uses oxygen instead of air. Exhaust gas is recycled back into the cylinder to control combustion temperature as well as to make up the volume of missing N₂ to ensure there is sufficient gas to maintain the temperature and heat flux profiles [1]. The advantage of this technology is the accommodation for the capture and sequestration of carbon dioxide. It can also reduce NO_x emissions. Clean Energy System Inc. combined oxy–fuel combustion technology with Rankine cycle by injecting water into the gas generator to produce a steam-rich mixture as part of the working gas. High efficiency was achieved with low cost in power plants [2].

Y. Gao · L. Li · X. Yu · J. Deng · Z. Wu (✉)
School of Automotive Studies, Tongji University, Shanghai 200092, China
e-mail: zjwu@tongji.edu.cn

© Springer-Verlag Berlin Heidelberg 2015
Society of Automotive Engineers of China (SAE-China) (ed.),
Proceedings of SAE-China Congress 2014: Selected Papers,
Lecture Notes in Electrical Engineering 328, DOI 10.1007/978-3-662-45043-7_14

The internal combustion Rankine cycle (ICRC) [3] engine transplants CES technology into reciprocating engine with water injection during the combustion process. The injected water evaporates into vapor after heat absorption. It improves the expansion work and controls the in-cylinder temperature. The CO_2 is separated from the exhaust gas by condensation to realize ultra-low emission. The simulation study of the effect of EGR rate on oxy-fuel internal combustion engine was carried out with a three-dimensional model [4]. In addition, an ICRC engine test bench was built up [5], and the influence of injection water, injection temperature, and injection timing on the performance of ICRC engine was studied [6, 7].

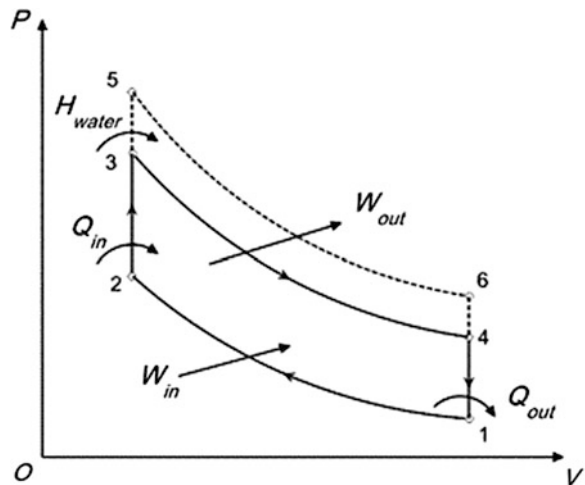
In this paper, a thermodynamic model is established to describe the ideal ICRC process based on the experimental results, and the performance of ICRC under different compression ratios is calculated and discussed.

14.2 The Ideal ICRC Thermodynamic Model

14.2.1 Ideal Cycle of ICRC

ICRC can be abstracted to an Otto cycle combined with water injection process, as shown in Fig. 14.1. Experimental results show that the combustion process, water injection, and water evaporation are relatively fast. Therefore, these processes are assumed to be instantaneous. The cycle 1–2–3–4 is an Otto cycle. Process 3–5 represents the water injection, and a new cycle with water injection 1–2–5–6 is obtained. Processes 1–2, 3–4, and 5–6 are adiabatic. W_{in} is the compression work, W_{out} is the expansion work, Q_{in} is the combustion heat, and H_{water} is the enthalpy of the injection water.

Fig. 14.1 Ideal ICRC process



14.2.2 Model Establishment

A thermodynamic model is established based on the ideal process of ICRC. The STANJAN software of Reynolds is used to calculate the thermodynamic process. The thermodynamic state of each point is recorded. The software of MATLAB is also used in solving the energy equation during the water injection process.

The main equation applied in this model is as follows:

The adiabatic processes 1–2, 3–4, and 5–6 could be calculated as follows:

$$p_1 v_1^k = p_2 v_2^k \quad (14.1)$$

The energy conversation with water injection process can be expressed as follows:

$$m_{\text{water}} h_{\text{water}} = m_5 u_5 - m_3 u_3 \quad (14.2)$$

$$m_5 = m_3 + m_{\text{water}} \quad (14.3)$$

$$u_5 = C_{v5} T_5, u_3 = C_{v3} T_3 \quad (14.4)$$

The pump work of injection water is as follows:

$$W_{\text{pump}} = m_{\text{water}} (P_{\text{inj}} v_{\text{inj}} - P_0 v_0) \eta_{\text{pump}} \quad (14.5)$$

where C_v is the specific heat capacity. In order to eliminate huge error, C_v is calculated as the equation followed instead of constant value:

$$C_v = a_0 + a_1 T + a_2 T^2 + \dots + a_n T^n \quad (14.6)$$

The suitable temperature range for the coefficient a_0 – a_n given by Ref. [8] is no higher than 1,500 °C. Therefore, extrapolation method [9] is employed, and here, n is set to 4.

The indicated work W_i , thermal efficiency η_i , and indicated mean effective pressure IMEP can be obtained as:

$$W_i = W_{5-6} - W_{1-2} - W_{\text{pump}} \quad (14.7)$$

$$\eta_i = W_i / Q_{\text{in}} = W_i / (m_{\text{fuel}} H_u) \quad (14.8)$$

$$\text{IMEP} = W_i / V_{\text{disp}} \quad (14.9)$$

Table 14.1 Engine parameters and boundary conditions

Cylinder configuration	Single cylinder
Fuel	C ₃ H ₈
Bore × Stroke (mm)	56.5 × 49.5
Displacement (ml)	124
Compression ratio	9.2
Intake composition	45 % O ₂ + 55 % CO ₂
Oxy/fuel ratio	20
Injected water temperature (°C)	120
Injected water pressure (MPa)	20
Injected water mass	20 mg maximum

14.2.3 Boundary Conditions

The parameters of the test bench engine and the boundary conditions for the calculation in this model are listed in Table 14.1.

The initial pressure and temperature are 0.05 MPa and 27 °C, respectively. The intake composition is set as the mixture of O₂ and CO₂ to simulate EGR. The concept of “oxy/fuel ratio” is used here because the intake composition is changed. It refers to the mass ratio of the intake gas and fuel. Compression ratio increases from 9.2 to 14, and injected water mass increases from 20 mg to maximum for each cycle. The limitation of injected water mass aims to ensure that the exhaust temperature is higher than the threshold. Hence, the water remains in gas phase at the bottom dead center. The threshold changes in different conditions. When injection temperature is 120 °C and compression ratio is 9.2, the threshold is 140 mg; and when compression ratio is 14, the threshold is 180 mg. The limit of injected water mass is 60 mg in experiment, because more injected water will lead to poor cycle performance.

14.2.4 Model Verification

Figures 14.2 and 14.3 show the comparison of the in-cylinder pressure between water injection cycle and no water injection cycle in ICRC engine, respectively. Water injection process can improve the in-cylinder pressure, and the combustion phasing is retarded. The calculated peak in-cylinder pressure is higher than the experimental result. This is due to the hypothesis that the cycle is adiabatic and the chemical reaction is instantaneous. Meanwhile, the evaporation of water is also assumed to be instantaneous; thus, the influence of water vapor on in-cylinder pressure is all reflected at the top dead center. Therefore, the calculated in-cylinder pressure increment brought by the water injection is also greater than the experimental result. Despite the difference in value, the tendency of the effect of water injection in calculated result and that in the experimental result match well.

Fig. 14.2 Experimental results of the effect of water injection on in-cylinder pressure

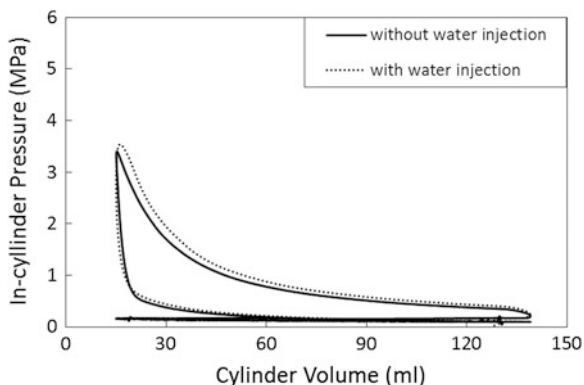
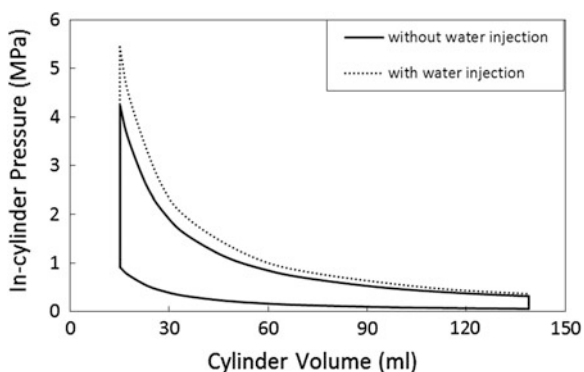


Fig. 14.3 Calculation results of the effect of water injection on in-cylinder pressure



14.3 Calculation Results Analysis

14.3.1 Effect of Water Injection on Cycle Performance

The effect of water injection process on peak in-cylinder temperature and pressure is shown in Fig. 14.4. On the one hand, the injected water absorbs the heat from the gas in cylinder, which decreases the in-cylinder temperature and pressure; on the other hand, the injected water evaporates into gas phase, which increases the amount of working gas and the in-cylinder pressure. Calculation results indicate that the latter affects more significant than the former. Therefore, the in-cylinder pressure increases.

Water vapor begins to act as the major working gas with the increase of injected water mass. Figure 14.5 shows the work composition for each cycle, and the injected water mass is 60 mg and theoretical maximum of 140 mg, respectively. The work generated by the water vapor increases from 49.2 to 68.3 %. Because the working gas increases, the work output, thermal efficiency, and the IMEP improve.

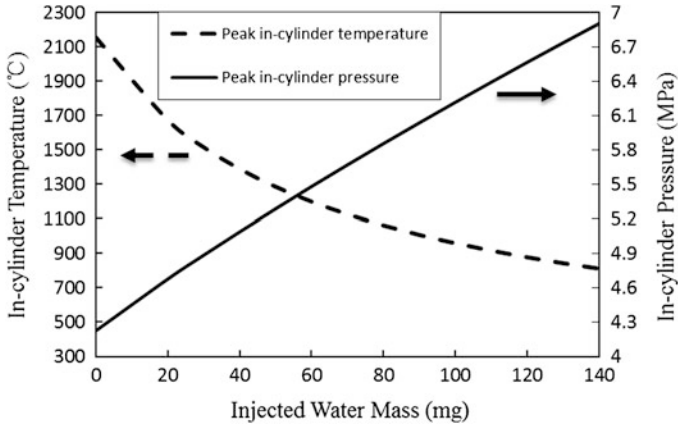


Fig. 14.4 Effect of water injection on peak in-cylinder temperature and pressure

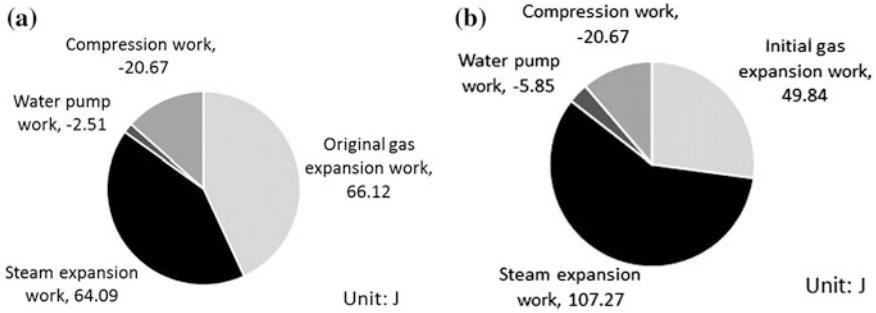


Fig. 14.5 Composition of the cycle work, **a** injected water mass = 60 mg, **b** injected water mass = 140 mg

It is observed from Fig. 14.6 that when injected water mass is 60 mg, thermal efficiency increases from 34.8 to 43.6 %, and IMEP increases from 0.68 to 0.88 MPa; when injected water mass reaches 140 mg, the thermal efficiency and IMEP increase to 54 % and 1.1 MPa, respectively.

14.3.2 Effect of Compression Ratio on Cycle Performance

The effect of compression ratio on in-cylinder pressure and temperature under maximum injected water mass is reported in Figs. 14.7 and 14.8. It is obvious that the peak in-cylinder pressure increases with larger compression ratio. The in-cylinder pressure decreases rapidly in the expansion stroke and almost remains the same value at bottom dead center under different compression ratios.

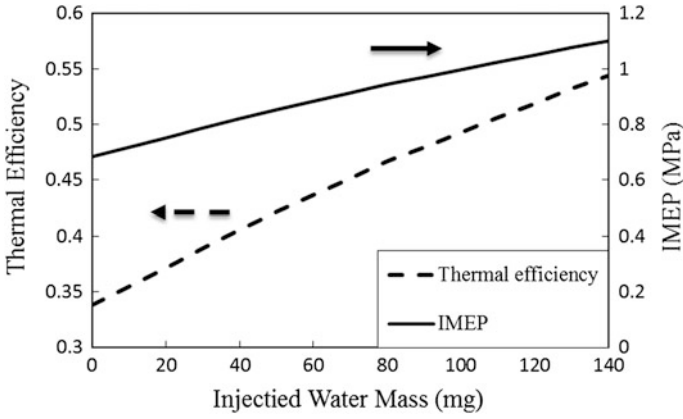


Fig. 14.6 Effect of water injection on thermal efficiency and IMEP

Fig. 14.7 Effect of compression ratio on in-cylinder pressure

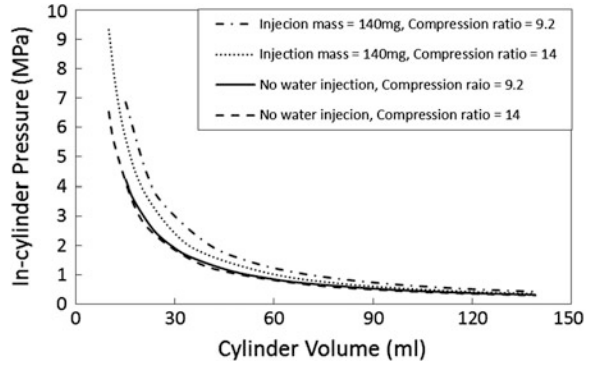
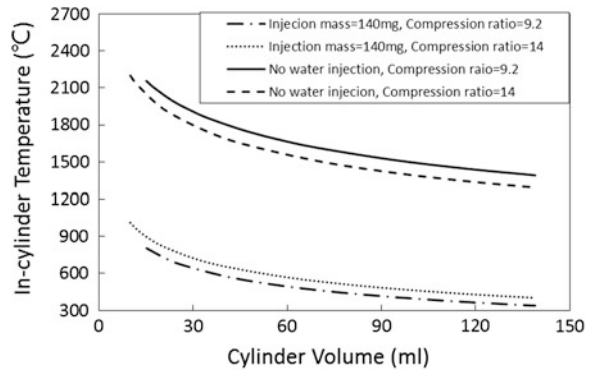


Fig. 14.8 Effect of compression ratio on in-cylinder temperature



It is observed from Fig. 14.8 that the in-cylinder temperature declines sharply with water injection. The compression ratio has little influence on peak in-cylinder temperature, when there is no water injection. The in-cylinder temperature decreases fast during the expansion stroke, and the exhaust temperature under the compression ratio of 14 is lower than that of 9.2. However, when injected water mass is 140 mg, both peak in-cylinder temperature and exhaust temperature increase with the increase of compression ratio.

It is mainly because the heat capacity of gas increases with temperature. When there is no injection water, the in-cylinder temperature and the gas heat capacity are relatively high. Therefore, the change in energy reflects more on in-cylinder pressure rather than on in-cylinder temperature. The in-cylinder temperature decreases obviously under water injection conditions. Therefore, the gas heat capacity decreases rapidly. Therefore, the change in energy reflects more on in-cylinder temperature, and the peak in-cylinder temperature increases obviously with the increase of compression ratio.

Figure 14.9 shows the effect of compression ratio on IMEP, and the injected water mass is 0, 60, and 140 mg, respectively. When the compression ratio is 9.2, IMEP increases from 0.68 to 0.88 MPa and 1.09 MPa with the increased injected water mass. The increment is 0.41 MPa. When the compression ratio is 14, the IMEP increases from 0.78 to 1.19 MPa and 1.55 MPa. The increment is 0.77 MPa.

With more expansion work output, the thermal efficiency improves with the increased compression ratio, as shown in Fig. 14.10. It is commonly known that larger compression ratio brings higher thermal efficiency. The increment of thermal efficiency brought by the corresponding increase of compression ratio is even greater in water injection cycles. When there is no water injection, compression ratio increases from 9.2 to 14 that can improve the thermal efficiency from 33.8 to 38.7 %. When injected water mass is 60 mg, the same increment of compression ratio can improve the thermal efficiency from 43.4 to 59 %. When the injected water mass reaches 140 mg, the thermal efficiency improves from 54 to 76.4 %. The improvement in thermal

Fig. 14.9 Effect of compression ratio on IMEP

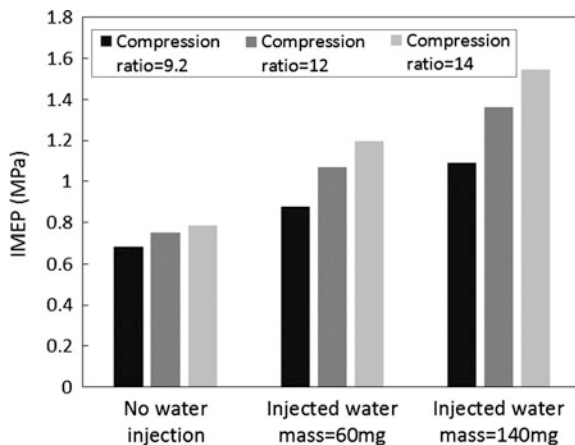
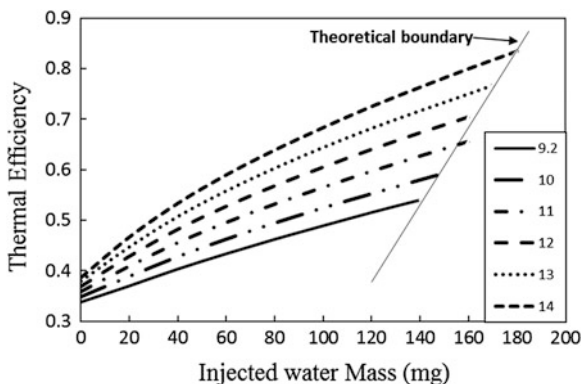


Fig. 14.10 Effect of compression ratio on thermal efficiency



efficiency increases from 4.9 to 22.4 %. In addition, higher compression ratio can also increase the theoretical maximum injected water mass. The theoretical boundary of the injected water mass under different compression ratios is shown in Fig. 14.10.

The combination of higher compression ratio with ICRC achieves higher thermal efficiency than with no water injection cycle. The injected water increases the amount of working gas, leading to the increase of in-cylinder pressure and expansion work output. The expansion work of water vapor increases even larger as the compression ratio increases, which just reflects the advantage of ICRC.

Moreover, water is injected directly into the cylinder at the top dead center rather than being mixed with the fuel and oxygen and then sucked into the cylinder during intake stroke. Vapor, as part of the working gas, does not consume compression work. The pump work of liquid water is far less than that of pressure equivalent gas. Therefore, direct water injection improves the thermal efficiency further.

Increasing compression ratio in conventional spark ignition engines is limited by the knock. ICRC engine introduces water injection process to achieve higher working output and thermal efficiency. The water injection process will decrease the in-cylinder temperature. The injected water also results in some inhibition of combustion and flame propagation. Therefore, the tendency of knock can be reduced through reasonable water injection strategy, and higher compression ratio can be employed.

14.4 Conclusions

1. Injected water increases the amount of working gas, and the expansion work output and thermal efficiency are improved. When injected water temperature is 120 °C, 140 mg injected water increases the thermal efficiency from 33.8 to 54 %.
2. Increasing compression ratio of ICRC improves the expansion work of water vapor and achieves much higher thermal efficiency than traditional cycle. When compression ratio increases from 9.2 to 14, 140 mg injected water mass can increase the thermal efficiency from 4.9 to 22.4 %.

Acknowledgments This study is supported by National Science Foundation of China (51076118, 51006075), Program for New Century Excellent Talents in University (NCET-10-0605), and Shanghai Rising-Star Program (11QH1402500).

References

1. Buhre BJP, Elliott LK, Sheng CD et al (2005) Oxy-fuel combustion technology for coal-fired power generation. *Prog Energy Combust Sci* 31(4):283–307
2. Pronske K, Trowsdale L, Macadam S et al (2006) An overview of turbine and combustor development for coal-based oxy-syngas systems. In: *ASME Turbo Expo 2005: power for land, sea and air*
3. Bilger RW (1999) Zero release combustion technologies and the oxygen economy. In: *5th international conference on technologies and combustion for a clean environment, Lisbon, Portugal*, pp 1039–1046
4. Yu X, Wu Z (2001) Simulation on effect of EGR on oxy-fuel IC engine. *Appl Mech Mater* 790:130–134
5. Fu L, Yu X, Deng J, Wu Z (2013) Development of internal combustion Rankine cycle engine test system. *Chin Intern Combust Engine Eng* 06:87–92
6. Wu Z, Yu X, Fu L et al (2014) Experimental study of the effect of water injection on the cycle performance of an internal combustion Rankine cycle engine. *Proc IMechE Part D: J Automobile Eng* 228(5):580–588
7. Yu X, Wu Z, Fu L et al (2013) Study of combustion characteristics of a quasi internal combustion Rankine cycle engine. *SAE technical paper*, 2013-01-2698
8. Bejan A (1988) *Advanced engineering thermodynamics*. Wiley, NY
9. Rao X (1997) Calculation of C_p , m of gases at high temperature by using extrapolation method. *J Southwest Pet Inst* 03:93–95+98

Chapter 15

The Organic Rankine Cycle System Development for Heavy-Duty Diesel Engine

Junqi Dong, Jianzhang Wang, Rongyou Zhang and Bin Wang

Abstract Based on the waste heat characteristic of the coolant and exhaust gas in heavy-duty diesel engine, the organic Rankine cycle (ORC) commercial product system is developed. The waste heat source is the engine jacket water and exhaust gas, and the jacket water is used as the heat source media which is used to heat the evaporator of the ORC system. The working fluid is the R245fa, and the plate-type condenser and evaporators are used. In the ORC system and 200-kW engine, the expander and generator can bring 14.5 kW electric energy in the normal working condition. The efficiency based on the first law of thermodynamics is 7.2 %; the completely generating efficiency is 6.25 %.

Keywords Diesel engine · Organic rankine cycle · Waste heat · Electricity generation

15.1 Introduction

In the internal combustion (IC) engine, there is about approximately 40 % efficiency to convert the fuel energy to mechanical work. The remaining energy is lost through waste heat that is predominantly rejected from the engine through the cooling and exhaust system [1]. To improve the fuel economy in automobiles with IC engine, various techniques to recover this waste heat energy are being investigated. One of these technical routes, the organic Rankine cycle (ORC) technology has become more and more attractive in the heavy-duty IC engine. The most important characteristic of the ORC system is the ability to absorb the low-grade heat source [2–5].

Now, the waste heat recovery technology based on the ORC has been becoming the standard technology in the next-generation IC [6]. The famous IC company has

J. Dong (✉)
Yinlun Company, Industry Zone, Tiantai, Zhejiang, China
e-mail: dongjunqi2008@163.com

J. Wang · R. Zhang · B. Wang
Zhejiang Yinlun Machinery Co., Ltd., Tiantai, Zhejiang, China

been researching and studying the waste heat recovery in 10 years ago, such as the Cummins and Caterpillar. At the same time, the vehicle manufacturers and IC companies had set up the associated R&D project under the government support, for example the Navistar company and Volvo truck company. However, there is very little work which had been done about the ORC technology research or product development in the domestic IC or vehicle company from the public report. There is only some groundwork that had been done about the ORC in the IC field in the testing laboratory of the university from the public paper [7].

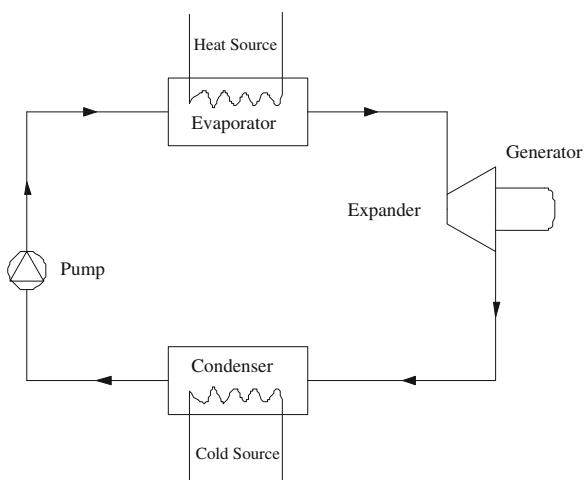
The authors developed the 15 kW power range ORC commercialization of prototype based on the ICE waste heat in this paper. The main work is commercial ORC plant development in the project. The waste heat is from the exhaust gas and coolant in the ICE engine. The engine's rated power is 200 kW, with 6 cylinders.

15.2 Organic Rankine Cycle (ORC)

15.2.1 Introduction to ORC Principle

The ORC system is similar to the classic Rankine cycle, including 4 main processes and 4 main components. They are the pump, evaporator, expander, and condenser, respectively. Figure 15.1 shows the principle diagram for the ORC system. First, the pressure of working fluid will be raised by the pump, and then, the organic working fluid evaporates and overheats in the evaporator by absorbing the heat from the high-temperature heat source. After the evaporator, the organic working fluid becomes the high-temperature and high-pressure gaseous fluid. Then, the working fluid expands and works in the expander. After the expander, the working fluid enters the condenser, in which the working fluid condenses and becomes the

Fig. 15.1 The schematic diagram of an ORC system



liquid by releasing heat to the cold source. In the next step, the working fluid is pumped into the evaporator and the whole cycle is realized.

15.2.2 Thermophysical Property of the Working Fluid

The size of the system components, the design of expansion machine, the system stability and safety and environmental concerns, and the selection of working fluids are very important for the ORC system's performance and economy because they may affect the efficiency of the system. Table 15.1 gives the thermal physical properties of some types of working fluids.

Except for the structural point of view and type of atoms in the fluid molecule, the working fluid can be categorized according to its saturation vapor curve. This saturation vapor curve is one of the most crucial characteristics of the working fluid in an ORC system. This feature affects the fluid applicability, cycle efficiency, and arrangement of associated equipment in a power generation system. As shown in Fig. 15.2, there are three types of vapor saturation curves in the temperature–entropy

Table 15.1 The thermophysical properties of some working fluids

Working fluid	Molecular weight g/mol	Critical pressure KPa	Critical temperature °C	Global warming potentia (GWP)	Ozone-depleting potential (ODP)
R245fa	134	3,640	154.1	950	0
R123	153	3,670	183.8	120	0.012
R134a	102	4,066	101.1	290	0

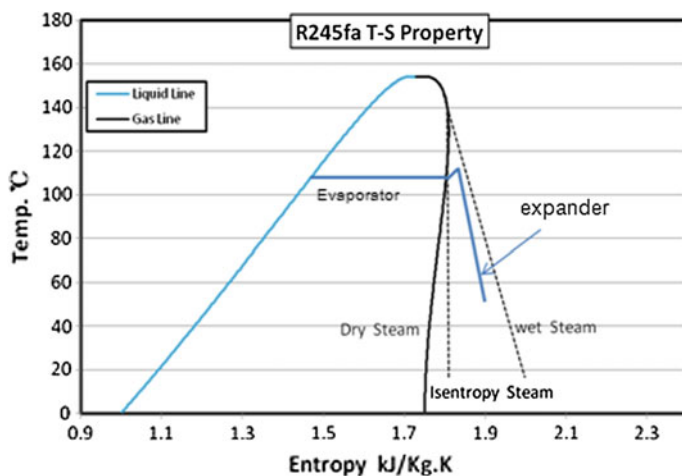


Fig. 15.2 The working fluid's T–S curve

(T–S) diagram: a dry fluid with positive slope, a wet fluid with negative slope, and an isentropic fluid with nearly infinitely large slope [2]. If the working fluid is the dry fluid, then the working fluid could not enter into the two-phase zone after the expander. This is very useful for the life of the expander in ORC systems. If the working fluid becomes the liquid or condenses at the end of the expander, this is an unfavorable and unacceptable phenomenon for the expander during the working process of ORC.

As for the working fluid R245fa, it has the good thermophysical property and the dry fluid characteristic, and thus, it has been accepted widely as one of the working fluids in the ORC system. In our ORC plant, the R245fa has been selected in the ORC system as the working fluid.

15.3 ORC System Development for Engine Waste Heat

15.3.1 *The ORC Systems for Engine Waste Heat*

In the engine, the fuel is the total heat source, one part is used to do work as the useful part, which is about only 40 % of total heat source from fuel, and the other part was exhausted to the atmosphere in variety forms of waste heat, such as exhaust gas, radiation, and coolant heat. To protect the engine, the coolant or water was used as the cooling media to cool down the engine cylinders during the ordinary working process. Figure 15.3 shows the ORC system based on the engine waste heat, which is the high-temperature exhaust gas and coolant heat. For the engine with 200 kW rated power, there is much waste heat exhausted to the atmosphere. This part heat can be used as ORC heat source and to generate electricity by ORC system's generator. First, the coolant which is used to cool the engine cylinder is pumped to the exhaust gas heat exchanger and then be cooled in evaporator and then return to the engine. During recovering, the coolant is heated by the high-temperature exhaust gas and absorbs the heat energy from the exhaust gas and then the coolant enters the evaporator and engine in turn. In the ORC system, the coolant is used as the media of heat source, which absorbs the heat energy from the engine cylinder and exhaust gas.

15.3.2 *Data Reduction and Analysis*

The whole ORC system was regarded reaching the steady condition when all the sensors do not change. The test data are recorded by the data acquisition system, in which the sampling rate is 0.2 Hz. To clearly analyze the thermodynamic process, the data reduction is expressed according to the following equations:

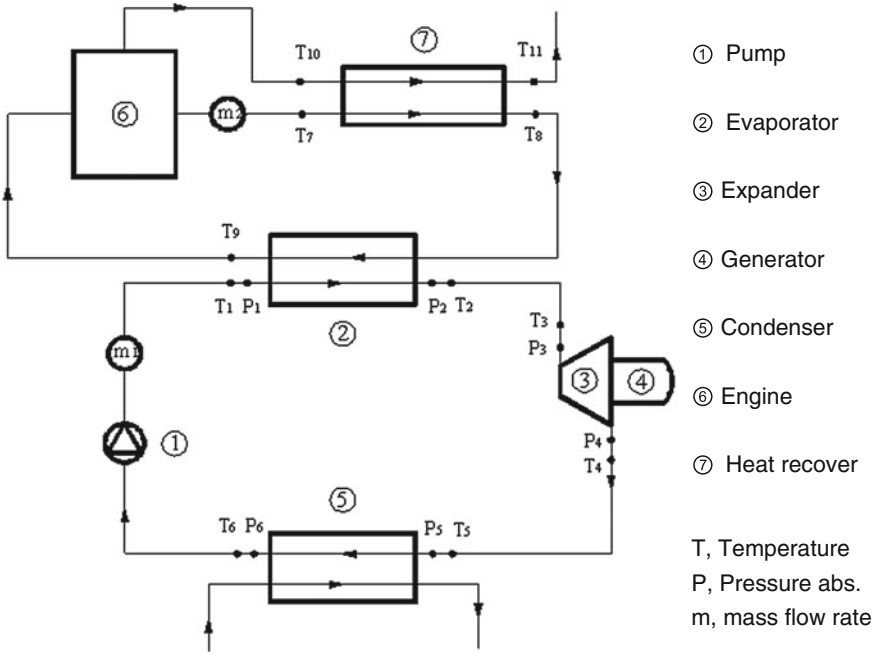


Fig. 15.3 Test diagram for ORC systems and engine waste heat.

1. The total quantity of engine's waste heat

$$Q:Q = Q_w + Q_e \tag{15.3.1}$$

2. The heat quantity absorbed by the working fluid

$$Q:Q = m \times (h_1 - h_4) \tag{15.3.2}$$

3. The work of expander

$$W:W = m \times (h_1 - h_2) \tag{15.3.3}$$

4. Isentropic efficiency of expander:

$$\eta_s = \frac{h_1 - h_2}{h_1 - h_{2s}} \tag{15.3.4}$$

5. Heat rejection for the condenser

$$Q_c: Q_c = m \times h_3 - h_4 \quad (15.3.5)$$

6. Generating efficiency of the ORC system:

$$\eta = \frac{E}{Q} \quad (15.3.6)$$

7. Net generating efficiency of the ORC system:

$$\eta_e = \frac{E - E_1}{Q} \quad (15.3.7)$$

In the above equations, the Q_w and Q_e are the heat quantity of coolant and exhaust gas, respectively; $h_1, h_2, h_3, h_4,$ and h_s are the enthalpy of the corresponding location. As shown in Fig. 15.3, m is the mass flow rate of the working fluid. E and E_1 are the electricity generation and consumption of the ORC system, such as the pump and control system.

15.4 Engine Parameters

In the test bench, there is a volume meter to get the real water flow rate. And to keep the ORC system and engine system heat-balanced and to reduce the temperature variation and frequency control of the ORC pump, the engine water flow should be no less than 12.5 m³/h. To get more evaporator temperature, the outlet temperature of water from engine should be close to the warning temperature, the temperature of which is mostly 85–90 °C. Table 15.2 gives the parameters of the engine.

Table 15.2 Engine parameters and running parameters

Description	Value
Cylinders	6
Cylinder diameter/stroke	120/145 mm
Rate power	200 kW
Rate speed	1,500 rpm
Compression ratio	17.5: 1
Warning temperature	95 °C
Exhaust gas max. temperature	650 °C
Real exhaust gas temperature	570 °C
Water flow rate testing	3.33 L/s

15.5 Test Results and Discussion

To clearly describe the test process and working conditions of the ORC system and engine, Fig. 15.4 shows the real-time working condition of the ORC system and engine. From the ORC system starting to generate electricity to its steady condition, the test data recording time is about 2.5 h. From Fig. 15.4, we can see that the generated electricity power, consumption power, and pump frequency are in a very stable condition after about 20 min. The steady quantity of electricity generation is about 14 kW, and the consumption power is about 1.9 kW. In the system, there is a frequency pump to control the flow rate of the working fluid according to the overheat degree at the outlet temperature of evaporator. And during 2 h, the pumping frequency of the working fluid almost remains unchanged, and this shows that the ORC system based on the engine waste heat using the coolant as the media heat transfer is very appropriate and effective. From Fig. 15.4, it can also be shown that the engine coolant temperature in the inlet and exit positions is very stable, and it can be effectively obtained a very suitable temperature according to the ORC system, without any frequently control requirement from the control system of the ORC unit.

Figure 15.5 shows the curves for the generated electricity power and net power of the ORC system under the different water outlet temperature from the engine cylinders. According to Fig. 15.5, we can see that the generator power reduces with the increase of coolant outlet temperature of an engine. However, the net power has no obvious reduction with the increase of the coolant outlet temperature. The generated electricity efficiency and net power efficiency are, respectively, 7.4 and 6.4 % under the coolant temperature of 94.4 °C, and both these efficiencies are 6.7 and 6.2 % under the coolant temperature of 100.9 °C.

As shown in Fig. 15.6, there is the variation characteristic between the pressure ratio of expander and the outside cold water temperature. The cold water

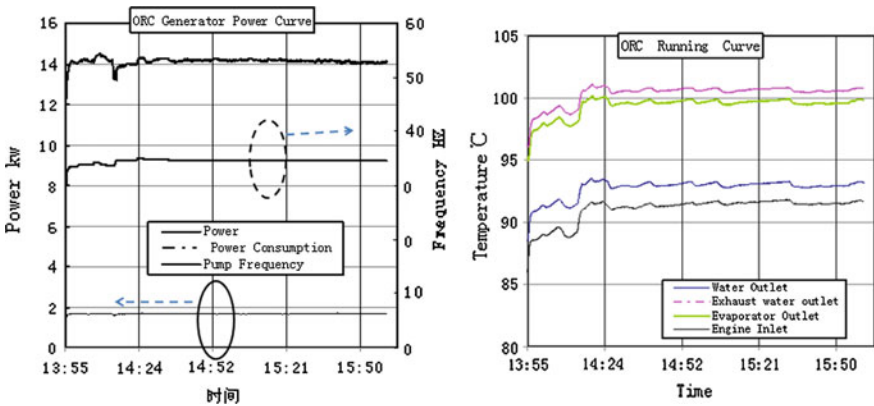


Fig. 15.4 Generator power running curve

Fig. 15.5 Generated energy and efficiency

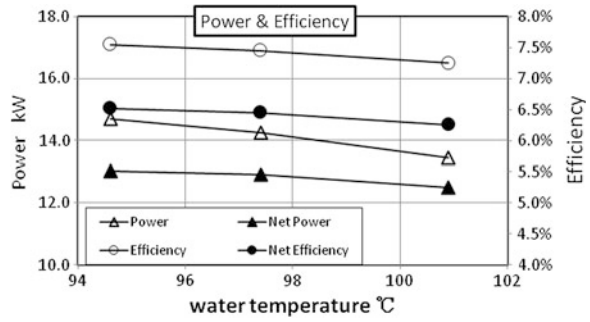
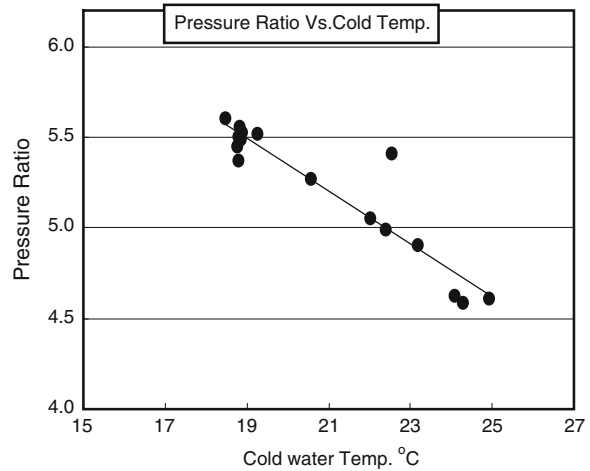


Fig. 15.6 Pressure ratio versus cold temperature



temperature is the inlet temperature of the condenser cool water. From Fig. 15.6, there is an obvious linear relationship between the expander pressure ratio and the cold water temperature. The pressure ratio will increase with the decrease of cold water temperature under the working condition.

15.6 Conclusions

The ORC technology is a very attractive scheme in improving the engine efficiency and reducing fuel consumption ratio as for the much waste heat in the engine. In the study, the ORC commercial plant of 15 kW level had been developed.

1. Using the engine cylinder water as the ORC heat source media is a very proper selection viewing from the technology and economy aspects, which leaves out other hot media and reduces the power consumption.

2. The big stable generator power is 15.4 kW, and the net power is 13.6 kW based on 200 kW engine waste heat. The efficiency of the ORC system is 7.7 %.
3. The overheat degree has no direct effect on the generator power under the same heat quality
4. The pressure ratio will increase with the decrease of the cold water temperature.

References

1. Armstead JR (2014) Review of waste heat recovery mechanisms for internal combustion engines. *J Therm Sci Eng Appl* 6:014001-9
2. Declaye S, Quoilin S (2013) Experimental study on an open-drive scroll expander integrated into an ORC (organic Rankine cycle) system with R245fa as working fluid. *Energy* 55:173–183
3. Bao J, Zhao L (2013) A review of working fluid and expander selections for organic Rankine cycle. *Renew Sustain Energy Rev* 24:325–342
4. Kang SH (2012) Design and experimental study of ORC (organic Rankine cycle) and radial turbine using R245fa working fluid. *Energy* 41:514–524
5. Bombarda P, Invernizzi CM, Pietra C (2010) Heat recovery from diesel engines: a thermodynamic comparison between Kalina and ORC cycles. *Appl Therm Eng* 30:212–219
6. Howel T (2011) Development of an ORC system to improve HD truck fuel efficiency. In: DEER 2011 conference
7. Xie H, Yang C (2013) Dynamic behavior of Rankine cycle system for waste heat recovery of heavy duty diesel engines under driving cycle. *Appl Energy* 112:130–141

Chapter 16

Study of Gasoline Engine Sticking

Yong He, Haizhu He, Qin Wang, Haihong Lin, Yunping Pu,
Yang Qiu, Zhangsong Zhan, Long Min, Wei Deng, Qian Xu
and Honggang Gou

Abstract In optimization example of the throttle body sticking and crankcase ventilation pipes sticking of a gasoline engine, the causes of sticking are analyzed, and combining with experimental verification, the solutions for sticking removal are presented.

Keywords Sticking · Throttle body · Crankcase ventilation · EFI enrichment

16.1 Introduction

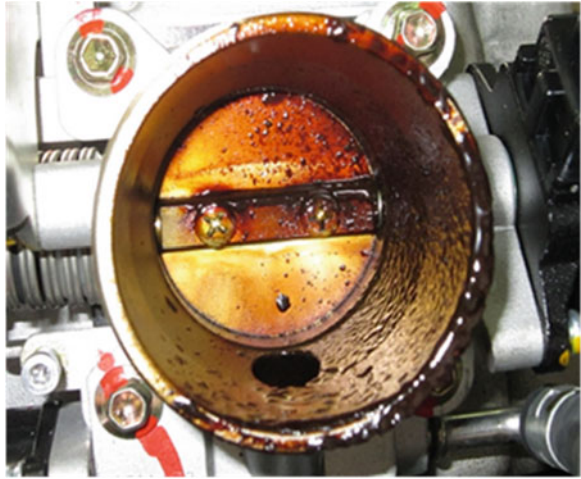
Sticking in the throttle body affects the opening and closing of the throttle body. In severe cases, the sticking makes it difficult or even impossible to open the valve of the throttle body, especially for electronic throttle body. Sticking in the crankcase ventilation pipes may affect the flow area of blowby gas and even block the crankcase ventilation pipes, leading to positive pressure in the crankcase and oil leaks. Sticking in the throttle body and crankcase ventilation pipes may seriously affect the engine performance (e.g., [1]). This paper focuses on and illustrates the situation of throttle body sticking and crankcase ventilation pipes sticking as well as the solutions.

16.2 Phenomenon of Sticking

In this section, we have showed the images about the throttle body and crankcase ventilation pipes through reliability experiments.

Y. He (✉) · H. He · Q. Wang · H. Lin · Y. Pu · Y. Qiu · Z. Zhan · L. Min · W. Deng · Q. Xu
H. Gou
Chongqing Changan Automobile Co. Ltd., Chongqing, China
e-mail: 407056385@qq.com

Fig. 16.1 Sticking in the throttle body



16.2.1 Sticking in the Throttle Body

As shown in Fig. 16.1, the sticking mainly adheres to the inner wall and valve of the throttle body.

16.2.2 Sticking in the Crankcase Ventilation Pipes

As shown in Fig. 16.2, the sticking in the crankcase ventilation pipes mainly adheres to the inner wall of the metal pipeline.

Fig. 16.2 Sticking in the crankcase ventilation pipes



16.3 Analysis of the Causes of Sticking

In this section, we investigate sticking and related experimental symptoms, and reasonably explain the causes of sticking.

16.3.1 Analysis of Sticking

According to the spectral analysis, the elements of sticking all come from inside the engine. The elements are the cooling deposition of the combination of gases in engine crankcase which includes gasoline vapor, oil vapor, the waste gas after burning, and the reaction product of the three gas mixture. In addition, the colloid in the gasoline will produce sticking after burning, and heavy distillates such as cyclanes and olefins also make great influence on the formation of sticking. Despite the high olefin content of octane in gasoline, sticking and carbon deposition are easily formed.

16.3.2 Experimental Situation and Analyses of Sticking Generation

Table 16.1 shows the experimental situation of a gasoline engine after reliability experiment. The oil temperature is detected in the oil pan.

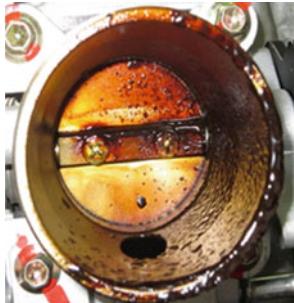
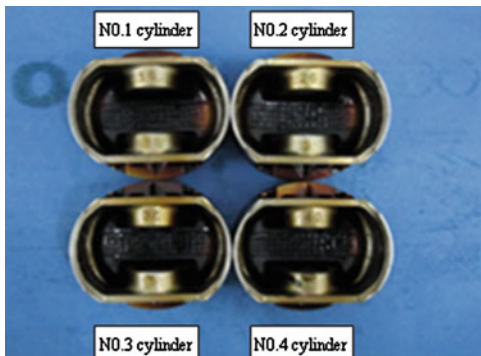
According to experimental situation, the bottom surface of the pistons is *black*, which indicates the high temperature of the piston surface, and the high heat load of engine. Meanwhile, the high oil temperature in the crankcase in the experiment indicates that the engine crankcase temperature is high, too.

According to the analyses above, the high speed and high load of the engine lead to high temperature in the piston and crankcase. In this case, the gasoline vapors, oil vapors, and the waste gas after burning form a kind of sticking in the crankcase at high temperature.

16.3.3 Formation Mechanism of Sticking in the Throttle Body and Crankcase Ventilation Pipes

As shown in Fig. 16.3, according to the crankcase's ventilation structure (e.g., [2]), the sticking in the crankcase flows through the engine system along with blowby gas. When it flows through the crankcase ventilation pipe and throttle body, the sticking is easily condensed on the metal surface of the pipeline and stick to it, along with the decrease of temperature of the blowby gas.

Table 16.1 The sticking situation after reliability experiment

Oil temperature	≤139 °C
Sticking in the throttle body	
Blacking at the bottom surface of piston	

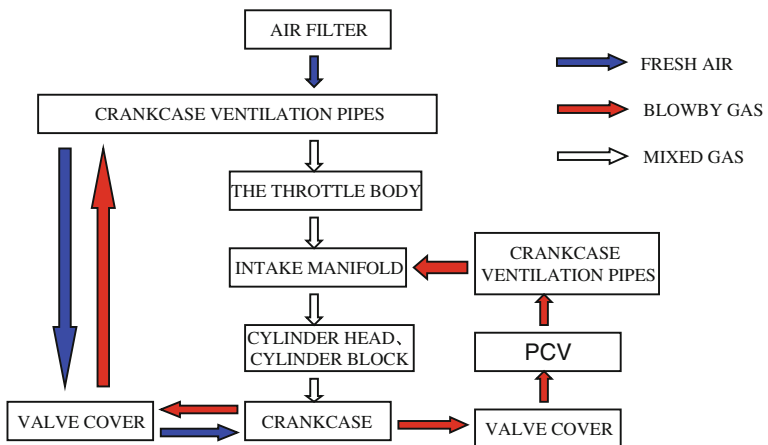


Fig. 16.3 The crankcase ventilation structure

16.4 Optimization Measures on Engine Sticking

In the verification of optimization measures on gasoline engine sticking, the EFI enrichment program implemented in high-load and high-speed region of an engine is used to reduce the temperature of the piston surface, and thus to lower the ambient temperature of the crankcase, and finally to prevent engine sticking at high temperature.

16.4.1 Cooling Effect Verification of EFI Enrichment Program

As shown in Table 16.2, the temperature changes are detected when the air-fuel ratio lambda is adjusted and other parameters remain unchanged. It is seen from the experimental data the 0.1 reduction in lambda is associated with around 50 degrees decrease in engine exhaust temperature. The cooling effect and rules are obvious.



16.4.2 Reliability Experimental Verification of EFI Enrichment Program

EFI enrichment program is implemented in high-load and high-speed region of an engine and decreases lambda value by 0.1, and the reliability experimental verification results are given in Table 16.3. The test results show that the crankcase oil

Table 16.2 Effect of lambda adjustment on engine exhaust temperature

Engine speed	Lambda	Engine exhaust temperature (°C)
6,000	0.8	783
	0.75	768
	0.7	742
	0.65	723
5,200	0.86	807
	0.85	811
	0.8	778
	0.75	754
	0.7	730
4,400	0.87	764
	0.85	758
	0.8	739
	0.75	716
	0.7	690

Table 16.3 Reliability experimental results of EFI enrichment program

Oil temperature	≤129 °C
No sticking in the throttle body	
No blacking at the bottom surface of pistons	

temperature is lowered, no blacking at the bottom surface of pistons, no sticking at the surface of engine throttle body, and no sticking at the inner wall of crankcase ventilation metal pipes.

16.4.3 Effects of EFI Enrichment Program on Engine Performance

When lambda is excessively enriched, in order to lower the temperature, the ignition angles cannot be adjusted. Therefore, the burning rate goes down, the maximum combustion temperature drops, the cycle thermal efficiency decreases, and the high-speed power is lost. In addition, if the lambda is excessively enriched, it can also cause the carbon deposition more on the top of the piston and piston rings side, which easily produces local hot spots. The piston ring being locked and scuffing of cylinder bore is also possible because of excessive carbon deposition.

Therefore, the lambda must be properly enriched. And as the experiment shows, it has little effect on the engine performance and carbon deposition on piston. And for the vehicle fuel consumption, since the lambda enriched is in high-speed and high-load region, BSFC has slightly increased, which does not affect the vehicle NEDC cycle fuel consumption (the increase of fuel consumption is basically equal to the enriched proportions of lambda. For example, if the lambda is enriched from 0.8 to 0.7, BSFC increase is about $(0.8/0.7 - 1) \times 100\% = 14.3\%$. Because lambda enriched is in high-speed and high-load region, it does not affect the vehicle consumption in the actual driving process. NEDC driving cycle is less than 4,400 rpm, so lambda enriched does not affect fuel consumption of NEDC driving cycle in high-speed and high-load region).

16.5 Conclusions

High temperature of piston and crankcase is caused by engine's high heat load designed in high-speed and high-load region, which makes the gasoline vapors, oil vapors, and the waste gas after burning possible to form a kind of sticking in the crankcase.

Sticking can condense and adhere to the metal surface in the throttle body and crankcase ventilation pipes.

With regard to engine sticking because of high heat load, the EFI appropriate enrichment can effectively reduce the surface temperature of piston and the ambient temperature of crankcase, and thus effectively solve the engine throttle body sticking and crankcase ventilation pipes sticking problems.

References

1. Tiankai (2000) The impact and control of gasoline deposits of vehicle exhaust, environmental sciences, Guangzhou pp 13–16
2. Zhou S (2004) The crankcase ventilation and pollution control, commercial vehicles in 2004, 9:81–84

Chapter 17

High Temperature Dependence of a Pulse Tube Engine

Shaowei Zhu

Abstract A pulse tube engine, which has no any moving part at high temperature, is a new type heat engine to generate power by using heat. It is a reverse of pulse tube refrigerator that already uses in space as a high-reliable sensor cooler. It is a potential new method to generate power or cooling power by using car waste heat. Its temperature dependence is investigated by a numerical simulation, which shows that its swept volume ratio of displacer over expand, and the phase angle difference between displacer and expander is almost no change with temperature change, which is very convenient for controlling the engine when high temperature is changed, which is common in the car.

Keywords Pulse tube · Regenerator · Engine · Refrigerator · Waste heat · Linear motor

17.1 Introduction

The car waste heat recover is an old topic. To use the Stirling engine [1] to change the waste heat as work is one of the old ideas of waste heat recover. Stirling engine has high efficiency but high cost. Thermal acoustic engine [2, 3] is a heat engine, which has no any moving part. It is a new concept for car waste heat recovering. It is simple but low power density. With a long time development, both are still in laboratory, and it is very difficult to imagine the application in the near future. A pulse tube engine [4] is a reverse of a pulse tube refrigerator, which already use in spacer as a high-reliable sensor cooler. There is no any moving part at high temperature in the pulse tube engine. Therefore, it is a potential new method for car waste heat recovering. The temperature of the waste gas of the car depends on load.

S. Zhu (✉)

School of Mechanical Engineering, Tongji University, 4800 Cao'an Road,
Shanghai 201804, China
e-mail: swzhu2008@yahoo.com

So, the temperature dependence of the pulse tube engine should be investigated. The temperature dependence of a pulse tube engine is simulated by a numerical simulation method, which is developed for the pulse tube refrigerator.

17.2 Structure

Figure 17.1 shows the schematic of a pulse tube engine. An after cooler, a regenerator, a heater, and a pulse tube are connected one by one. Heat is inputted from the heater. An expansion piston gets work. A displacer, which is in room temperature, is the phase shift for the pulse tube.

The reliable and simple method to transfer out the power is to use a linear generator to generate electricity power. Using crankshaft to drive the piston and displacer is a difficult method because of oil lubrication. Oil should not flow into the regenerator and on any hot part. A crankcase and working space should be separated. This will increase the cost and decrease the life time. To use the linear generator is simple. The linear generator generates electricity power. The displacer is driven by gas pressure.

17.3 Advantages

In the Stirling engine, the displacer must be at high temperature. In the pulse tube engine, the displacer is at room temperature. So, it can be made by plastic. Plastic is cheaper comparison with stainless steel or high-temperature alloy. And room temperature part is more reliable than high temperature parts.

Fig. 17.1 Schematic of a pulse tube engine. 1 After cooler, 2 regenerator, 3 heater, 4 pulse tube, 5 gas distributor, 6 displacer, 7 and expander

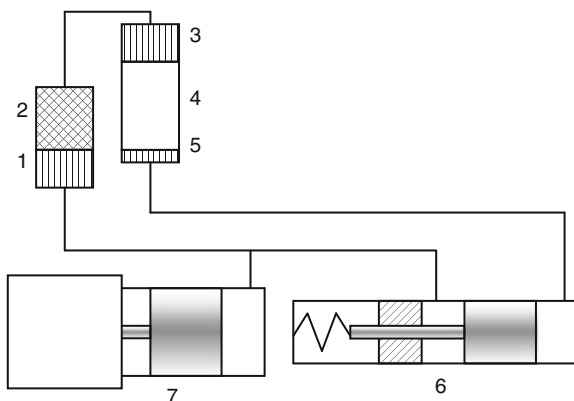
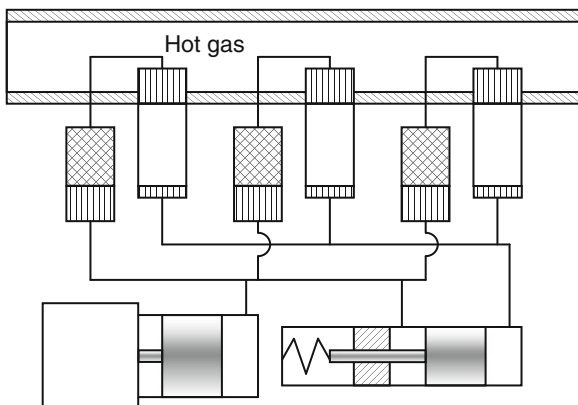


Fig. 17.2 Schematic of multi-pulse tube engine



One head is not effective to recover the waste heat because the waste gas temperature decreases gradually when the gas is cooled. Multi-heads are needed for higher efficiency, as shown in Fig. 17.2, which is much simpler than a multi-head Stirling engine. In the multi-head Stirling engine, there are several cylinders and pistons that work at high temperature. In the multi-head pulse tube engine, just pipes work at high temperature. There is a clear difference of reliability and cost.

17.4 Numerical Simulation

As a first step, the motion of the piston and displacer is assumed as sine wave. The numerical method is same as that in reference [4].

The volume of the expansion space

$$V_c = V_{cd} + 0.5V_{c0}(1 - \cos(2\pi ft - \varphi_0)) \quad (17.1)$$

The volume of the displacer space

$$V_D = V_{Dd} + 0.5V_{D0}(1 - \cos(2\pi ft)) \quad (17.2)$$

The swept volume ratio

$$a = \frac{V_{c0}}{V_{d0}} \quad (17.3)$$

where V_{cd} is the dead volume of the expansion space, V_{c0} is the swept volume of the expansion space, φ_0 is the phase angle difference between the expansion space and

the displacer space. V_{Dd} is the dead volume of the displacer space, and V_{D0} is the swept volume of the displacer space.

The swept volume ratio and phase angle are two important parameters and should be optimized to get high efficiency. If the optimum point does not change with temperature or slightly change with temperature, it is very convenient for the control of the engine.

17.5 Temperature Dependence

Table 17.1 lists the basic data of the engine. A total of 2 MPa helium gas is charged to the engine. The high temperature is 900 K, and the room temperature is 300 K. Working frequency is 100 Hz.

Figure 17.3 shows the output power, input heat, and percentage of Carnot versus swept volume ratio of the displacer over the expander and phase angle difference between displacer and expander at 900 K. There is an optimum swept volume ratio and phase angle difference with which the percentage of Carnot gets highest. In the calculation range, the heat and power increase with the increase of swept volume ratio and phase angle difference.

Figure 17.4a shows the equivalent PV diagrams in the pulse tube. Equivalent PV diagrams in the pulse tube is from the imagine gas piston in the pulse tube. It indicates that there is sufficient distance between the hot gas and room temperature gas in the pulse tube. Figure 17.4b shows the PV diagrams the displacer and expander. It is similar to that in Stirling engine. The gas in the pulse tube can be considered as part of the displacer.

Figure 17.5 shows the percentage of Carnot at high temperature of 750, 600, and 450 K. It is shown that the peak point of percentage of Carnot is almost unchanged when high temperature decreases. This means that it is not needed to change the phase angle difference or swept volume ratio when high temperature is changed.

Table 17.1 Main parameters of the refrigerator

After cooler	Gap width 0.785 mm, height 0.33 mm, length 40 mm
Regenerator	$\Phi 50$ mm \times 60 mm, mesh wire diameter 0.1 mm, porosity 0.7
Heater	Gap width 0.785 mm, height 0.33 mm, length 40 mm
Pulse tube	$\Phi 50$ mm \times 200 mm
Expander swept volume	200 cm ³
Room temperature	300 K
High temperature (Th)	900 K
Charge pressure	2 MPa
Frequency	100 Hz
Working medium	Helium

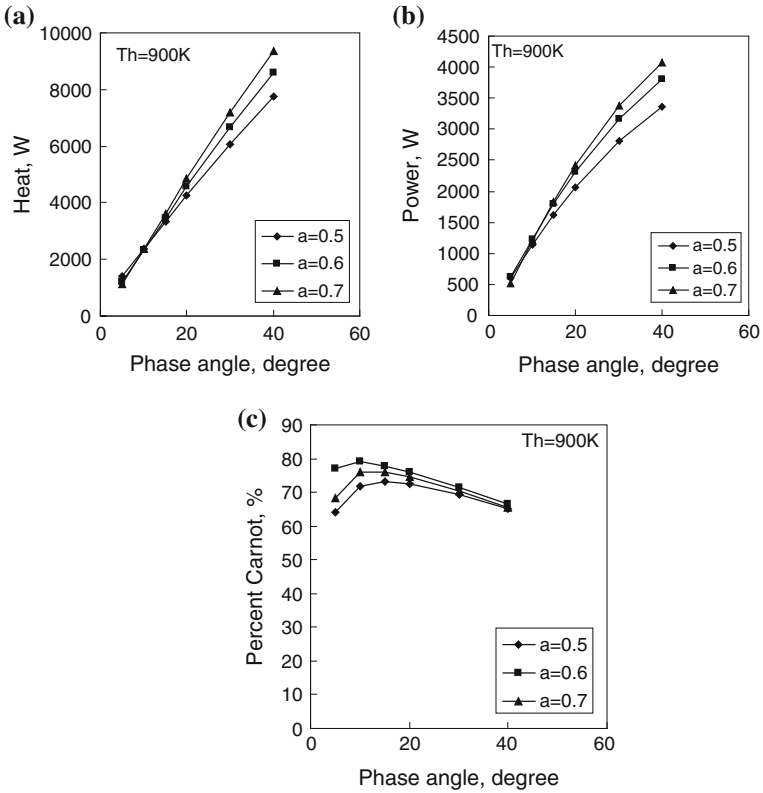


Fig. 17.3 a Input heat at 900 K, b output power at 900 K, and c percentage of Carnot at 900 K

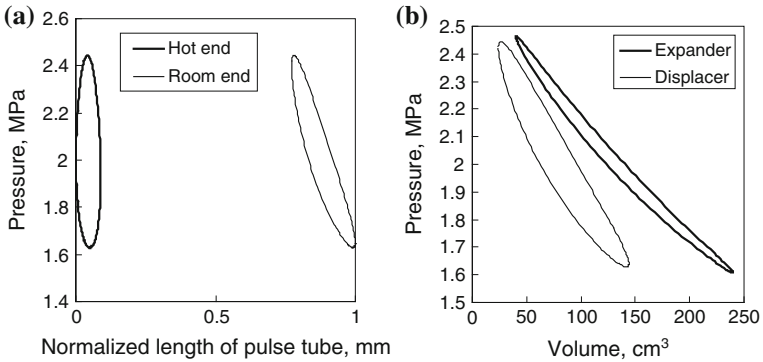


Fig. 17.4 a Equivalent PV diagrams, and b PV diagrams

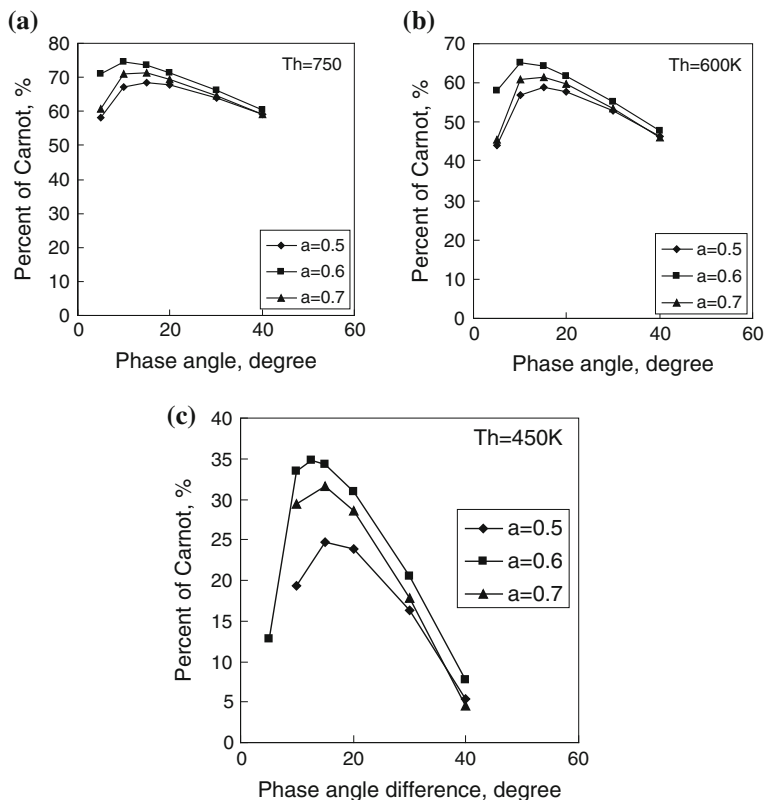


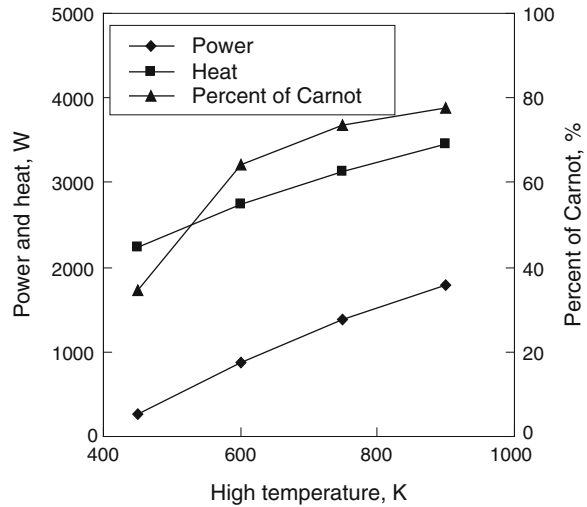
Fig. 17.5 **a** Percentage of Carnot at 750 K, **b** percentage of Carnot at 600 K, and **c** percentage of Carnot at 600 K

This is very convenient for controlling of the engine when the high temperature is changed, which is common in the car.

Figure 17.6 shows the heat, power, and percentage of Carnot versus high temperature at swept volume ratio 0.6 and phase angle difference of 15° . The heat, power, and percentage of Carnot decreases with the decrease of the high temperature.

At 450 K, the power is very small and percentage of Carnot is also very low. It does not mean that this type of engine is not good at low-temperature range. A balance design may be needed.

Fig. 17.6 High temperature effect



17.6 Conclusions

In the pulse tube engine, the optimum value of the swept volume ratio of the displacer space over the expansion space and the phase angle difference between the displacer space and the expansion space are almost unchanged with the change in temperature.

References

1. Katayama M, Sawada D (2013) Development of exhaust heat recovery Stirling engine for small car. In: Proceedings of the 16th symposium on Stirling cycle, pp 1–4
2. Backhaus S, Swift GW (1999) A thermoacoustic Stirling heat engine. *Nature* 399:335–338
3. Hasegawa S, Yamaguchi T, Oshino Y (2013) A thermoacoustic refrigerator driven by a low temperature-differential, high-efficiency multistage thermoacoustic engine. *Appl Therm Eng* 58 (1–2):394–399
4. Zhu SW, Nogawa M (2010) Pulse tube stirling machine with warm gas-driven displacer. *Cryogenics* 50:320–330

Chapter 18

Technology Trends in Commercial Vehicle Base Engine Development

M. Neitz, A. Wiartalla, S. Lauer and P. Methfessel

Abstract Commercial vehicles will have to meet increasing requirements in the future with regard to further reductions in emissions and fuel consumption. A holistic view of the subjects, thermodynamics/after treatment of exhaust gases and base engine design/mechanics, is essentially necessary in order to achieve an optimum condition with regard to product and operating costs. In the following report, FEV presents some examples that show, which potentials can still be exploited in the further development of the basic engines of commercial vehicles, one of the more progressive examples being the reduction of the number of cylinders for heavy-duty truck engines from 6 to 4.

Keywords Heavy-duty · Downsizing · Number of cylinders · Cylinder liner · High-pressure injection · Cylinder head · Peak firing pressure

18.1 Introduction

The limit values for pollutant emissions of commercial vehicle diesel engines have drastically been reduced during the last two decades. Up to now, this has been an essential driving force for the development of engine technologies. In the future, CO₂ limit values are sustaining the pressure for further development.

The after treatment of exhaust gases, which to an increasing degree is required for the achievement of legally defined goals, makes a holistic view of the subjects, thermodynamics/after treatment of exhaust gases and base engine design/mechanics essentially necessary, in order to achieve an optimum condition with regard to product and operating costs. One of the objectives is, for example, to meet the most

M. Neitz (✉) · A. Wiartalla · S. Lauer
FEV GmbH, Aachen, Germany
e-mail: neitz@fev.com

P. Methfessel
RWTH Aachen University, Aachen, Germany

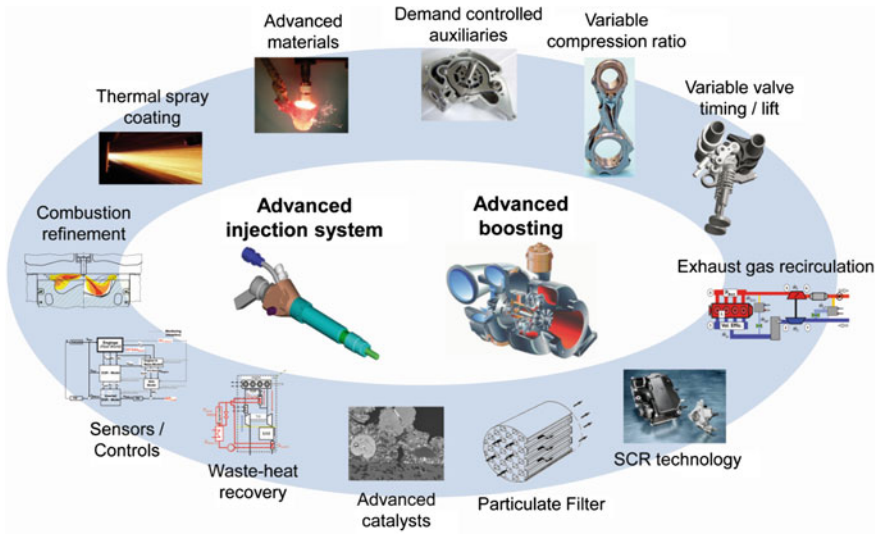


Fig. 18.1 Potential technologies for the reduction of emissions and CO₂

favorable point in the trade-off between the complexity of the base engine—among others caused by high peak pressure capability, high injection pressure, elaborate EGR, and charge air cooling—and the complexity of the after treatment of exhaust gases. The systems required today and in future for after treatment of exhaust gases may cause costs on a scale approximate to that of the base engine and thus increase the cost pressure on the engine.

Figure 18.1 shows an impression of the range of measures and technologies, which—with an individually different degree of maturity each—are available for handling future requirements. In this paper, exemplary issues are examined and possible trends for future base engine development are discussed, which helps to achieve the above described optimization.

18.2 Consideration of Selected Topics of Base Engine Development

18.2.1 Displacement/Downsizing/Number of Cylinders

For the reduction of the NO_x raw emissions, high EGR rates are used today, often up to full load engine operation. The reduced oxygen content in the charge air has to be compensated by a higher degree of supercharging. Under these circumstances dual-stage turbo-charging is required to provide increased boost pressures for achieving a top specific power output of more than 30 kW/l, which leads to higher peak pressure requirements on the engine. For an existing engine, this way might be

the most favorable one. For a complete new development, however, the question arises, if the cost increase due to expensive turbo-charging technology and high peak pressure capability, should not be countered with a limitation of power density, i.e., a correspondingly larger displacement. Moreover, downsizing in connection with an increased peak pressure does not necessarily promise significant friction reduction. Figure 18.2 shows the comparison of two design variants for a medium-duty truck engine. In this example, the displacement is reduced through a proportional reduction of stroke and bore by maintaining the stroke/bore ratio. This downsizing requires dual-stage turbo-charging leading to a peak pressure increase by approximately 30 bar. Despite of a smaller bore diameter, the gas force remains more or less constant. Therefore, a reduction of the bearing diameters and with that of the bearing friction and the oil flow through the bearings is impossible. Only the lower piston speed caused by the slightly smaller stroke at unchanged engine speed has a friction-decreasing effect. This positive effect is partially compensated by the additional oil flow through the second turbocharger, which results in a higher oil pump driving power. The friction contributions of crank shaft, valve train, water pump, and alternator remain the same. Therefore, the friction estimate shows only a small difference in the frictional torque, only the thermodynamic fuel consumption advantages via a shift in the operating point, can be realized. Only a reduction of the number of cylinders would offer a significant potential for decreasing the engine friction.

Medium-Duty Truck Engine, 206 kW, 1100 Nm			
		Base Engine	„Downsized“ Engine
Turbocharging		1-stage	2-stage
Bore	[mm]	110	104
Stroke	[mm]	123	116
Displacement	[l]	7,01	5,91
Stroke/Bore Ratio		1,12	1,12
Mean Piston Speed	[m/s]	9,0	8,5
Gas Force at 220 bar Cyl. Pressure	[kN]	209	
Gas Force at 250 bar Cyl. Pressure	[kN]		212

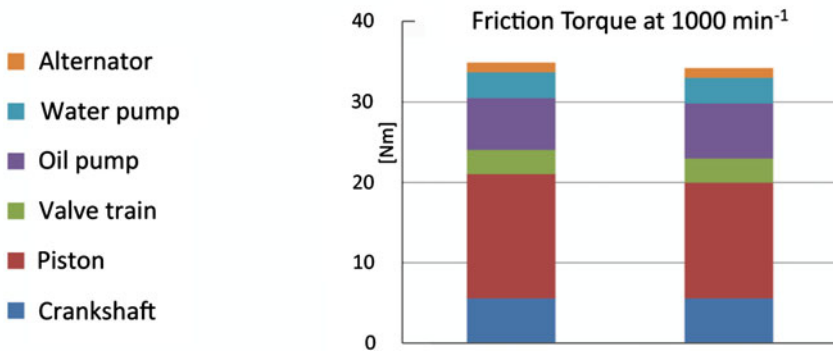


Fig. 18.2 Effect of downsizing on the engine friction

Due to dual-stage turbo-charging and the measures necessary to cope with high peak pressure and increased thermal load, the cost of the engine will increase significantly.

The cost comparison in Fig. 18.3 clearly shows that downsizing is financially only attractive, if the number of cylinders is reduced as well. Even the use of mass balancing shafts for the elimination of the free inertia forces of second order, in order to optimize the NVH behavior of the 4 cylinder, is more than covered by the cost advantage compared with a 6 cylinder.

Under the above-mentioned points of view, the introduction of large 4-cylinder engines instead of the normal 6-cylinder engines would be beneficial. A 4-cylinder with a cylinder displacement of approximately 2l, common for HD engines, could successfully enter the performance class of 300 kW, which represents the main quantity in drive systems for 40 t long-haul trucks and consequently provide a considerable saving potential. The significantly shorter length of the 4-cylinder would provide free space in the engine compartment, which could be used for the increased space requirement regarding exhaust gas after treatment and cooling. In addition, a weight advantage of approximately 150 kg is to be expected even under consideration of mass balancing shafts, which can be directly used to increase the payload of the vehicle. The higher torque fluctuation due to the smaller cylinder number would probably be in the focus of development, in order to meet customers' NVH requirements. Basically, there is the question of customer acceptance of such engines in a rather conservative market. In passenger cars, the trend for a lower number of cylinders is in full swing. Here, a large number of 6-cylinder engines

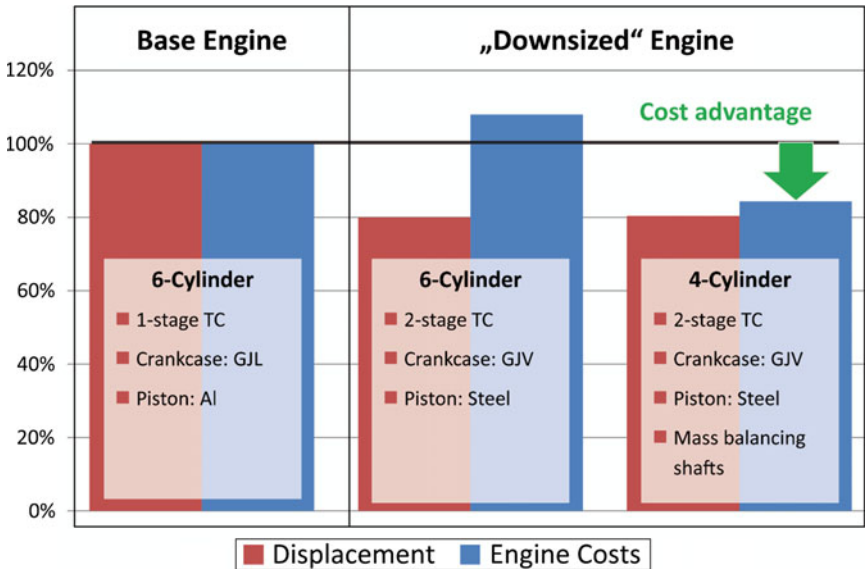


Fig. 18.3 Effect of downsizing and reduction of the number of cylinders on engine costs

have been replaced by 4-cylinder engines with higher power density. The substitution of 4-cylinder by 3-cylinder engines in the middle-class segment is imminent.

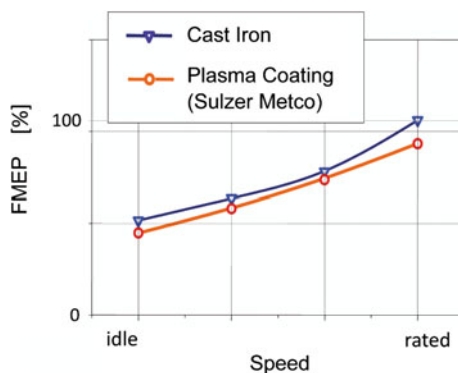
18.2.2 Thermal Spray Coatings for Cylinder Liner

The methods for application of thermal spray coatings to the cylinder running surface [1], which are meanwhile available for series application, offer a potential for reducing the friction, as shown in Fig. 18.4. This technology—originating from passenger car engines—has also already been used for commercial vehicles. Furthermore, it allows the free choice of the running surface material independent of the basic material of the cylinder liner. Therefore, an argument for the use of separate cylinder liners becomes invalid. If—as it is common practice at medium-duty engines already today—crankcases with integrated cylinder liners (“parent bore”) were used instead of wet cylinder liners, significant potentials regarding production costs of the crankcase and cylinder spacing could be opened up, as shown in Fig. 18.5 [2]. In case of an engine overhaul, the worn cylinders would have to be bored out and a new spray coating be applied, instead of exchanging the separate cylinder liners. Special overhaul pistons with slightly increased diameter would not be required for it. However, corresponding production facilities are needed for carrying out such overhaul work. But at least in technically highly developed markets with good infrastructure, it should be possible to implement this technology.

18.2.3 High-Pressure Injection

Over the years, the injection pressure of commercial vehicle engines has continuously been increasing [3]. An increased injection pressure leads to a shorter injection duration and offers the potential for smaller injection holes at the nozzle. Through this, a better atomization of the injection is achieved, which results in a quicker

Fig. 18.4 Potential of liner coating for friction reduction



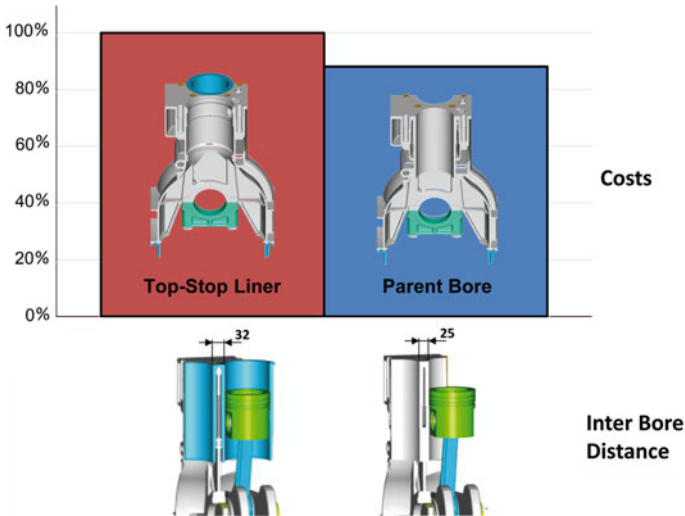


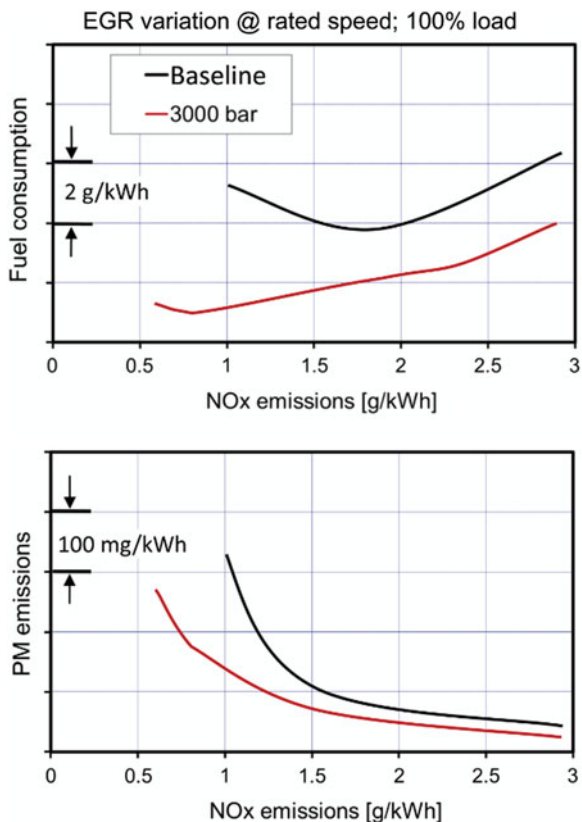
Fig. 18.5 Advantages of parent bore compared to wet cylinder liners

combustion. This generally leads to reduce the fuel consumption and particle values at, however, increased NO_x emissions, requiring a retarded begin of injection, which can partially compensate the fuel consumption and particle emission advantage. At the same time, it has to be considered that an increase in the injection pressure by means of increased driving power of the high-pressure pump as well as possible leakages in the injector may have a negative effect on fuel consumption.

Despite of these previously mentioned trade-offs, increased injection pressures up to 3,000 bar can achieve both improved emissions and improved fuel consumption. The basis for this are modern injection systems, as described in [3] and [4], which are statically mostly leakage free and also dynamically achieve significantly reduced leakages. The change from a conventional to a mostly leakage-free injection system already results in a reduction of emission-neutral fuel consumption within the range of 1 % at part load as well as at rated power. An additional increase of the injection pressure to 3,000 bar then offers further potential for an improvement in the NO_x particle trade-off as well as in fuel consumption in a wide range of the engine map and in particular also at full load (Fig. 18.6). If the engine design has the potential for increasing the cylinder peak pressure, the resulting emission advantage can be turned into a further significant reduction of fuel consumption by an adaptation of the injection strategy.

The above shows that, on the one hand, there are still considerable potentials for the improvement of emissions as well as fuel consumption to be realized in the future regarding combustion development and engine calibration, and on the other hand, these improvements lead to new requirements on the engine design (e.g., regarding the peak pressure resistance).

Fig. 18.6 Potential of efficient injection systems



18.2.4 Cylinder Head Design (Material and Design Features)

Constantly increasing cylinder peak pressures combined with a high power density create great challenges in particular to the cylinder head. The selection of materials and the design principle or component geometry are the key issues for the layout.

Increasing the strength of the material is a suitable means to improve the HCF behavior. Consequently, some manufacturers switch from normal gray cast iron to cast iron with vermicular graphite. With GJV450, a material is available, which very well tolerates the high-frequency load from the combustion pressure in the cylinder and allows peak pressures far beyond 200 bar without the need for detailed optimization of the geometry in the highly loaded areas as required for normal gray cast iron (GJL250). The heat conductivity, which is significantly reduced compared with GJL, causes an essential aggravation regarding thermo-mechanical fatigue (LCF) in the thermally highly loaded areas, in particular in the valve bridges in the flame deck. Cracks in the valve bridges can be successfully avoided only by intensive cooling and drastic reduction of the wall thicknesses in these areas. At the early design stage of a cylinder head, more attention must be paid to provide a

sufficient width for the valve bridges when determining the valve positions and sizes, in order to meet the requirements on cooling. This may indicate that compromises regarding the valve diameters and consequently the cross sections available for the gas exchange shall be made in order to achieve an adequately acceptable number of thermal load cycles corresponding to the targeted engine lifetime.

The cylinder head height is an essential boundary condition for the achievable global stiffness of the cylinder head and with that an indicator for the admissible peak pressure. In Fig. 18.7, a benchmark of the relative height of cylinder heads is shown for engines with a bore diameter between 90 and 140 mm. The specific value of the relative height is defined as the ratio of the height of the valve spring support to the cylinder bore diameter. The relation between durably acceptable peak pressure and relative cylinder head height is shown on the right side of the diagram. Under favorable conditions, a peak pressure of well over 200 bar can also be realized with GJL. The plotted examples for GJV prove that this is much easier with a material of higher strength.

A further design feature, which positively influences the stiffness of the cylinder head, is the cast injector dome. In comparison, a separate, inserted injector sleeve offers more favorable conditions for cooling in the thermally highly loaded area around the injector and between the valves. Furthermore, it is beneficial for casting the cylinder head, as the water jacket core is connected to the outside via the central nozzle area. Therefore, an intermediate deck that can be advantageously used to guide the coolant to the crucial areas can be easily realized with regard to casting. An injector sleeve, however, cannot take on a supporting function in the cylinder head structure. This can, for example, be compensated by a material of higher strength.

The above influences suggest the conclusion that for engines with rather moderate values of power density and consequently also cylinder peak pressure, but

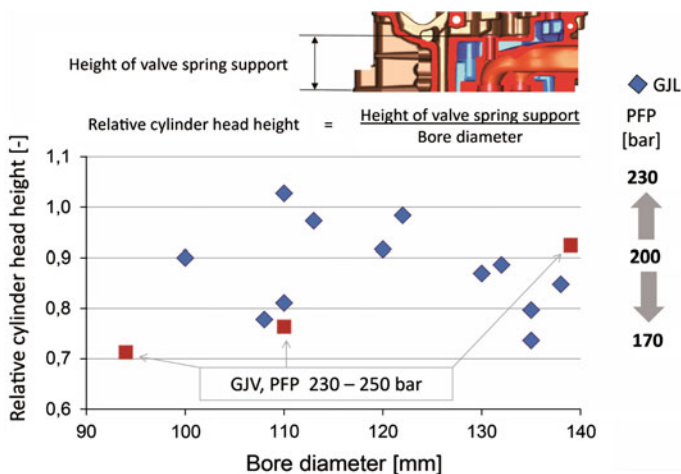


Fig. 18.7 Relation of cylinder head height—peak pressure potential

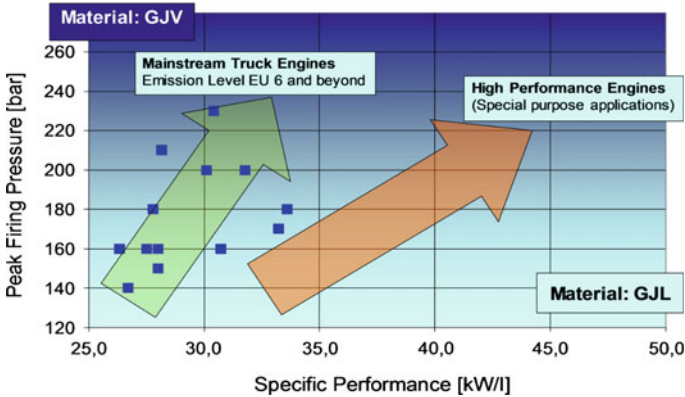


Fig. 18.8 Relation of cylinder head material to requirements regarding peak pressure and power density

high lifetime requirements, the material GJV—possibly in a variant with higher strength compared with the standard material GJL250—in connection with the cast injector dome is the most efficient alternative, last but not least also from a cost point of view. For engines with higher power density and consequently higher thermal load on the cylinder head, the requirement of creating optimal boundary conditions for the cooling is gaining in importance. This is a strong indication for using an injector sleeve. Extreme peak pressure requirements might require the use of GJV to achieve HCF durability, and the LCF problem increases with increasing power density at the same time. Figure 18.8 illustrates these dependencies.

18.3 Prospects

Besides many new technology fields, e.g., exhaust gas after treatment and hybrid drive systems, the base engine also offers substantial development potential in the future. Here, injection and turbo-charging technologies represent key areas. New technologies—if not compulsory required by legislation of emissions or fuel consumption—must offer a cost advantage for the ultimate customer, i.e., in the sum of purchase and operating costs.

Detailed optimizations will be employed in many areas. A more fundamental issue is the possible adaptation of the base engine concept to modified boundary conditions, which are supported by the availability of new technologies. Condensed down to one question, one could ask: Will in future 40 t long-haul trucks be driven by 4-cylinder engines with a displacement of approximately 8–9l, dual-stage turbo-charging, a common rail system with 3,000 bar injection pressure, and a crank case with parent bore?

References

1. Blume W, Verpoort C, Bobzin K, Ernst F, Richardt K, Schlaefer T, Schwenk A, Cook D, Flores G (2008) Thermal spraying of nano-crystalline coatings for al-cylinder bores. SAE international, SAE 08M-271
2. Neitz M, Quadflieg FJ, Ruhkamp L, Wartmann P (2005) Trend setting engine architecture for HD truck engines driven by future development targets. In: AC-Kolloquium "Fahrzeug- und Motorentechnik", Aachen, 14
3. Ruhkamp L, Kind M, Laumen HJ, Maassen F, Mashida M, Takeuchi K, Shinohara Y, Herrmann OE, Kudo T, Nakagawa M, Rajamani V (2011) Further options for diesel engine improvements by increased injection pressure up to 3000 bar. In: AC-Kolloquium "Fahrzeug und Motorentechnik", Aachen, 20
4. Herrmann OE, Joyce M, Nakagawa M, Suzuki K, Uchiyama K, Takeuchi K, Körfer Th, Ruhkamp L, Laumen HJ, Rajamani V, Schönfeld S (2010) Ultra high pressure fuel injection for minimized engine-out emissions of HD diesel engines. In: Tagung "Diesel- und Benzindirekteinspritzung", Haus der Technik, Berlin

Chapter 19

Line Filter-Based Parking Slot Detection for Intelligent Parking Assistance System

Mengyang Fan, Zhencheng Hu, Kazukuni Hamada and Hui Chen

Abstract A computer vision-based system is proposed to detect four types of commonly used parking slots for intelligent parking assistance system (IPAS). It consists of two submodules, i.e., around view construction and parking slot detection. A line filter is designed to abstract central points of parking lines. The designed line filter makes full use of the feature of parking lines that are brighter than its neighborhood. Geometry constraints of parking slots are used to localize parking slots. The proposed system has been validated on a model car equipped with SH7766 embedded platform and a Nissan vehicle. The accurate detection rate is 87.5 %, and the average position error of four corners of the parking slot is 10 cm. It is robust to light variation, strong shadow, and partial occlusion of parking lines.

Keywords Intelligent parking assistance system · Parking slot detection · Computer vision · Line filter · Around view

19.1 Introduction

Intelligent parking assistance system (IPAS) consists of four components, i.e., parking space detection, path planning, path tracking, and human-machine interface (HMI) [1]. The detected parking space is the input of other components, and its accuracy and precision drastically affect the performance of the whole system, and thus, reliable parking space detection is crucial.

M. Fan · H. Chen (✉)

School of Automotive Studies and Clean Energy Automotive Engineering Center,
Tongji University, Shanghai 201804, China
e-mail: hui-chen@tongji.edu.cn

Z. Hu · K. Hamada

Graduate School of Science and Technology, Kumamoto University, Kumamoto, Japan

© Springer-Verlag Berlin Heidelberg 2015

Society of Automotive Engineers of China (SAE-China) (ed.),

Proceedings of SAE-China Congress 2014: Selected Papers,

Lecture Notes in Electrical Engineering 328, DOI 10.1007/978-3-662-45043-7_19



Fig. 19.1 Four types of parking slot

Many different approaches of parking space detection have been proposed. These methods can be divided into three categories: (1) laser scanner-based method; (2) ultrasonic or short-range radar-based method; and (3) computer vision-based method [2].

Although the accuracy and recognition rate of laser scanner-based method is high, the price of scan-type laser is too high to be used in mass production case [3]. Since the cost of sensors is low, the ultrasonic radar and short-range radar are widely used, but they have drawback against slanted surface and often fail to find slanted free space [4]. Camera has merits of low cost, and images provide abundant information of the environment. Motion stereo-based, monocular vision-based, and optical flow-based parking space detection methods have been proposed [5–7]. Light variation, strong shadow, and road texture are challenges for computer vision-based method.

In this paper, we propose a line filter-based approach to detect four types of commonly used parking slot, as shown in Fig. 19.1. It is robust to light variation, strong shadow, and occlusion of parking lines.

The proposed system consists of two submodules, i.e., the around view construction and the parking slot detection. The main novelty of the proposed system is the line filter-based parking line extraction method. The designed line filter could exclude the edges which do not correspond to parking lines, and it is robust to lighting variation and shadow. In addition, geometry constraints are used to localize parking slots.

19.2 Around View Construction

Around view is a kind of virtual image taken from the sky showing the circumstance around the vehicle within a certain distance. Proposed system compensates the fisheye distortion of input images captured by four cameras, transforms the undistorted images into bird's-eye view images, and then constructs the around view of the ego vehicle by matching four bird's-eye view images [2].

Around view image eliminates the perspective distortion of objects attached onto the ground surface, so the geometry features of parking slot could be used, which contributes to the recognition of parking slots painted on the ground surface [2]. In addition, the surrounding of ego vehicle is provided by around view, which enables driver to easily monitor the ongoing parking process.

19.3 Parking Slot Detection

19.3.1 Line Filter Convolution

A line filter is convolved with the gray scale of around view image in horizontal and vertical directions to abstract central points of parking lines. The designed line filter makes full use of the feature of parking lines that are brighter than its neighborhood. Compared with other common used edge detectors, such as Sobel edge detector and Canny edge detector, the line filter could exclude the edges which do not correspond to parking lines and it is robust to lighting variation and shadow.

Figure 19.2 shows the structure of designed filter. Horizontal and vertical convolution results can be calculated according to Eqs. (19.1) and (19.2).

$$H(x, y) = \frac{1}{n} \sum_{i=1}^n (L(x + i, y) - L(x - i, y)) \tag{19.1}$$

$$V(x, y) = \frac{1}{n} \sum_{j=1}^n (L(x, y + j) - L(x, y - j)) \tag{19.2}$$

where $H(x, y)$ and $V(x, y)$ are, respectively, horizontal convolution result and vertical convolution result of the pixel whose coordinate is (x, y) . $L(x, y)$ is the intensity value of the pixel (x, y) .

Figure 19.3 shows the profile of horizontal and vertical convolution results of the around view image along scan lines. $H(x_{\text{left}}, y_{\text{left}})$ (horizontal convolution result of the left edge point of a parking line) is supposed to be a peak, and $H(x_{\text{right}}, y_{\text{right}})$ (the result of the right edge point) is supposed to be a valley. The center point of a parking line corresponds to the center of a peak–valley pair.

19.3.2 Line Extraction and Clustering

After center points of parking lines being recognized, lines are abstracted using Hough transform, which is a popular tool for line detection due to its robustness to noise and missing data. Thereafter, these lines would be clustered to same group if they meet the following three conditions.

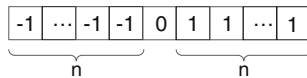


Fig. 19.2 The structure of line filter

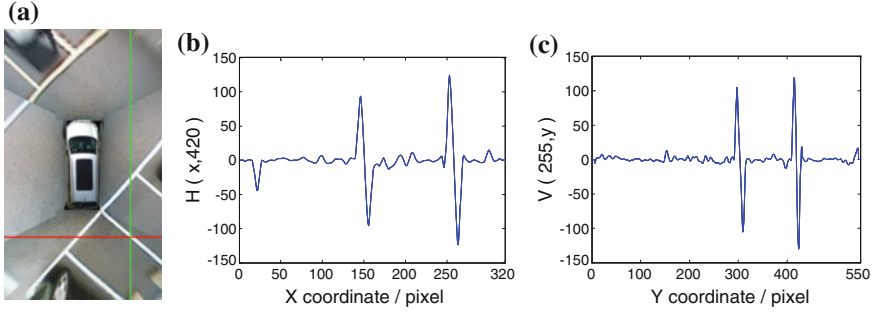


Fig. 19.3 **a** A 320×550 pixel image, with red scan line $y = 420$ and green scan line $x = 255$; **b** horizontal convolution results along scan line $y = 420$; and **c** vertical convolution results along scan line $x = 255$

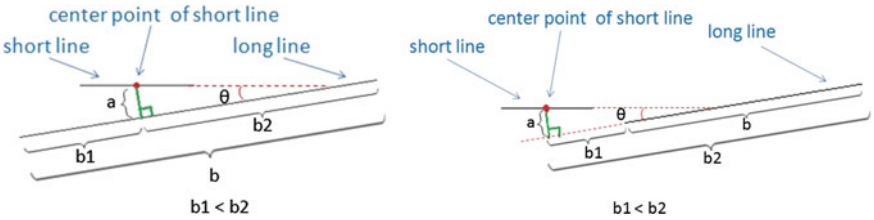


Fig. 19.4 Line clustering parameters

1. $\theta < 6^\circ$
2. $a < 6$ cm
3. $b_1 < (b/2 + 100)$ cm

where θ , a , b_1 , b_2 , and b are illustrated in Fig. 19.4.

19.3.3 Parking Slot Localization

Various kinds of constraints have been used to enhance the efficiency of parking slot recognition [8]. In this paper, we make use of geometry constraints of a parking slot that consists of pairs of parallel lines within a certain distance and pairs of lines perpendicular to each other. Figure 19.5 shows the flowchart of localization algorithm.

Two lines whose distance is between 2.0 and 2.5 m and orientation difference is less than 8° are denoted as Pattern A, and two lines whose distance is between 4.8 and 5.5 m and orientation difference is less than 8° are denoted as Pattern B. Since

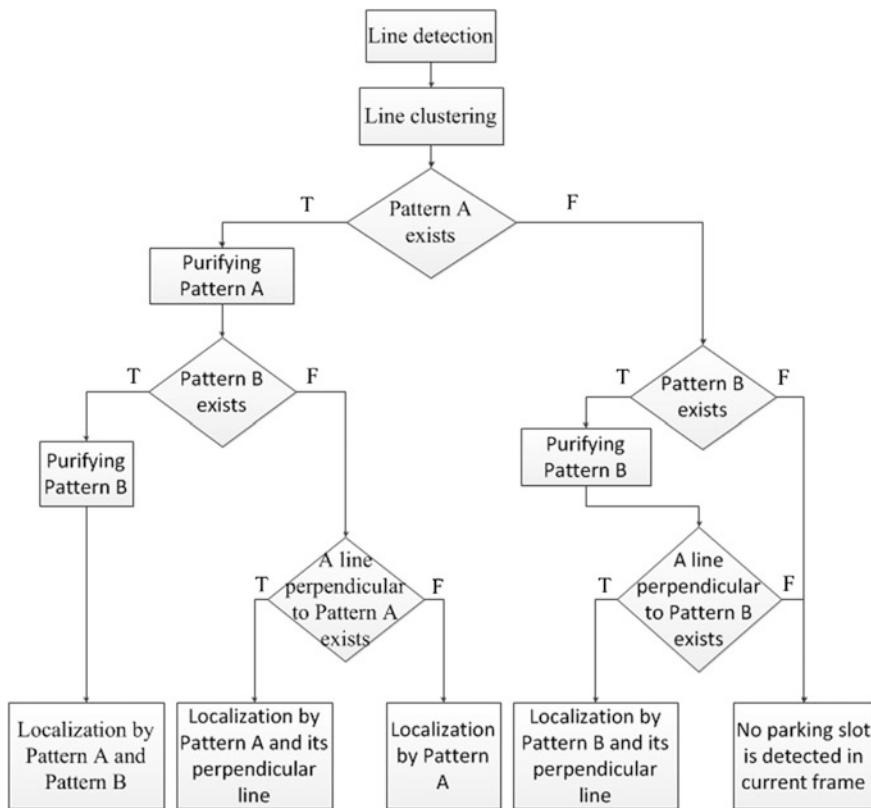


Fig. 19.5 Flow chart of parking slot localization algorithm

spurious Pattern A or Pattern B is inevitably included during the searching process, it is necessary to purify them by excluding spurious Pattern A and Pattern B. A parking slot could be localized by seeking for Pattern A and Pattern B, purifying Pattern A and Pattern B, and subsequently searching their potential perpendicular lines.

19.4 Experiment Results

The proposed system has been validated on a model car equipped with the SH7766 embedded platform developed by Renesas Company, as shown in Fig. 19.6. Black papers with white parking lines have been printed to simulate different parking scenarios, and experiment results for different types of parking slots are shown in Fig. 19.6.

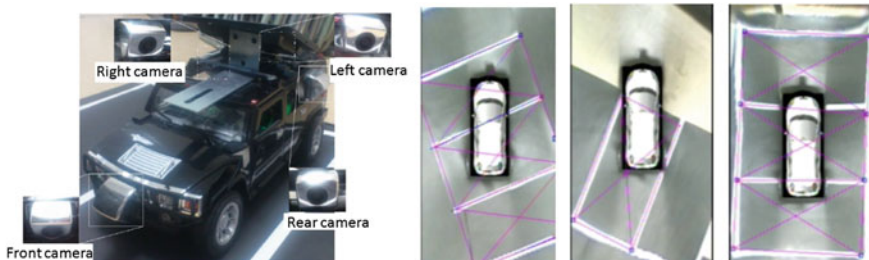


Fig. 19.6 Model car equipped with SH7766 platform and the experiment results



Fig. 19.7 Results of detected parking slot

Thereafter, the field experiments have been implemented on a Nissan vehicle equipped with an industrial personal computer and four cameras. Detection performance was evaluated by applying the proposed system to 40 cases corresponding to the four types of parking space. The accurate detection rate is 87.5 %, and the average position error of four corners of the parking slot is 10 cm. Some experiment results are as shown in Fig. 19.7, from which we can know that the proposed system works well even in the condition that lighting condition greatly varies, strong shadow and obstacles exist, and parking lines are partially occluded.

Fig. 19.8 Invalid parking slot



19.5 Conclusion and Future Work

In this paper, a line filter-based parking slot detection system for IPAS has been presented. It is valid for four types of parking slots and robust to light variation, strong shadow, and occlusion of parking lines. The average position error of four corners of the parking slot is 10 cm.

Future work will focus on excluding parking slots which are occupied by other vehicles or obstacles. And we intend to optimize the present system to make it valid for some rare parking slots as shown in Fig. 19.8.

References

1. Cheng K, Chen H (2013) Path following of a fully-automatic parking assist system. *Automobile Technol* 10:26–29
2. Jung HG, Kim DS, Yoon PJ, Kim J (2006) Structure analysis based parking slot marking recognition for semi-automatic parking system. In: *Structural, syntactic, and statistical pattern recognition*, pp 384–393
3. Jung HG, Cho YH, Yoon PJ, Kim J (2008) Scanning laser radar-based target position designation for parking aid system. *IEEE Trans Intell Transp Syst* 9(3):406–423
4. Jung HG, Kim DS, Yoon PJ, Kim J (2007) Light stripe projection based parking space detection for intelligent parking assist system. In: *IEEE intelligent vehicle symposium*, pp 962–968
5. Suhr JK, Jung HG, Bae K, Kim J (2010) Automatic free parking space detection by using motion stereo-based 3D reconstruction. *Mach Vision Appl* 21:163–176
6. Jung HG, Kim DS, Yoon PJ, Kim J (2006) Parking slot markings recognition for automatic parking assist system. In: *IEEE intelligent vehicle symposium*, pp 106–113
7. Schuele K, Raaijmakers M, Neumaier S, Hofmann U (2013) Detecting parallel moving vehicles with monocular omnidirectional side cameras. In: *IEEE intelligent vehicle symposium*, pp 567–572
8. Jung HG, Lee YH, Kim J (2010) Uniform user interface for semiautomatic parking slot marking recognition. *IEEE Trans Veh Technol* 59(2):616–626

Chapter 20

A Hierarchical Road Identification Method for ABS Control

Yue Shi, Hui Lu and Fan Yu

Abstract A hierarchical road identification method is proposed for an anti-lock braking system (ABS) to enhance the braking performance under complicated conditions. The identification is firstly achieved on the wheel layer by fusing the information of wheel slip, wheel acceleration, vehicle acceleration, and pressure increment error between two consecutive control cycles. Then, the identification on the full-vehicle layer is implemented, starting with analyzing the wheels' status acquired from the wheel layer and ending with a further confirmation via comparing the modified wheel slip integral and the braking pressure information between the bilateral wheels. The proposed method is realized in the form of statecharts. A series of simulation experiments are conducted and the results verify the effectiveness of the designed method.

Keywords Road identification · ABS · Statecharts · Hierarchical control · Simulation

20.1 Introduction

Among the mainstream of the active electronic safety systems for vehicles nowadays, ABS is the most widely equipped one and makes great contribution to maintain the braking efficiency as well as the drivers' handling capability during an emergency brake [1, 2]. A good ABS performance relies greatly on an efficient and accurate identification of the road condition. For this, many efforts have been poured into this research field. Fang et al. [3] suggested a method to identify the split- μ road by comparing the difference of the front wheels' slip integrals to a threshold. Hebden et al. [4] used a sliding mode controller to assist a conventional

Y. Shi · H. Lu · F. Yu (✉)
School of Mechanical Engineering, Shanghai Jiao Tong University, Shanghai,
People's Republic of China
e-mail: fanyu@sjtu.edu.cn

ABS to improve the vehicle stability when the vehicle is braking on a split- μ surface. Aly [5] identified the road condition and the optimal wheel slip for split- μ road via a fuzzy controller. Wang and Sun [6] introduced a concept of *Road Condition Characterized Factor* to identify the μ -jump during the braking process.

A comprehensive road identification method with a hierarchical structure was presented in this paper. First, a detection of the road condition under a single wheel was proposed. Then, the identification on the full-vehicle layer was accomplished via fusing some essential information, such as the road identification result of the wheel layer, the wheel slip integral, and the increment and decrement of the braking pressures in each wheel cylinder. Final, a series of simulation tests were carried out to validate the effectiveness of the proposed method.

20.2 Road Identification on Wheel Layer

A typical ABS control cycle (control cycle for short) of an individual wheel is shown in Fig. 20.1 and can be divided into the following four stages via correspondingly defining the value of the *Wheel Slip Status*, S_{ij} (Note that an offset value 40 is added to S_{ij} for better demonstration):

1. Stable:	$T_0(n) - T_1(n)$,	$S_{ij} = 1$;
2. Slip excessively:	$T_1(n) - T_2(n)$,	$S_{ij} = 2$;
3. Recovering:	$T_2(n) - T_3(n)$,	$S_{ij} = 3$;
4. Recovery assured:	$T_3(n) - T_0(n + 1)$,	$S_{ij} = 4$;

where n represents the n th control cycle. During the given procedure, the characteristics of some vehicle state variables can provide crucial information to reflect the real-time road conditions, as they possess significantly different characteristics when the vehicle is braking on different roads. Therefore, it is more than possible to identify the road condition in real time during the braking process by deliberately choosing the state variables for observation. In this work, the selected variables include the wheel acceleration a_{ij} , the wheel slip λ_{ij} , the vehicle acceleration a_{veh} , and the wheel cylinder pressure increment $P_{inc,ij}$ and decrement $P_{dec,ij}$ within a control cycle.

The real-time surface status under a single wheel, $Surf_{ij}$, can be classified into the three following categories according to the change of the tire–road friction coefficient (Table 20.1).where $F_{lh,ij}$ and $F_{hl,ij}$ are the flags representing the changes of the surface condition, from low to high and from high to low, respectively. When the vehicle starts braking with ABS activated, $Surf_{ij}$ is initially set to ‘constant’ as default, and both of the flags are set to 0. Provided that the vehicle is initially braking on a low- μ road, then under either of the following conditions, we may confirm that the wheel is undergoing a surface change from low- μ road to high- μ road, as shown in Fig. 20.2a.

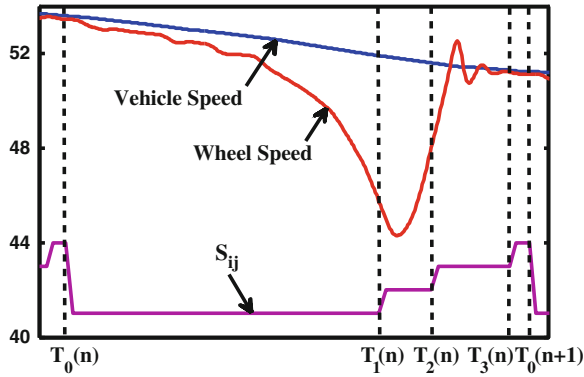


Fig. 20.1 Wheel Slip Status

Table 20.1 Definition of $Surf_{ij}$ and F_{ij}

$Surf_{ij}$		F_{ij}			
		$F_{lh,ij}$		$F_{hl,ij}$	
1	Constant	0	Low to high negative	0	High to low negative
2	Low to high	1	Low to high positive	1	High to low positive
3	High to low				

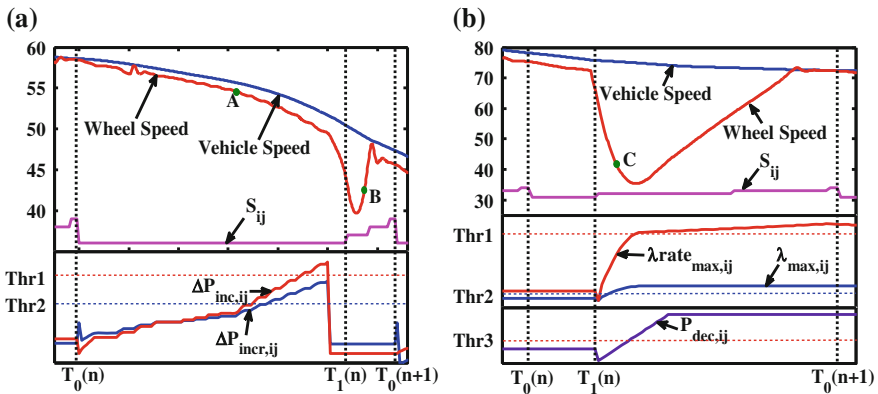


Fig. 20.2 Surface change under a single wheel. a Low to high. b High to low

Condition a: Both $\Delta P^n_{inc,ij}$ and $\Delta P^n_{incr,ij}$ exceed certain boundaries, respectively, if the wheel is at the stable stage of the n th control cycle (Point A, $S_{ij} = 1$), where

$$\Delta P^n_{inc,ij} = P^n_{inc,ij} - P^n_{incref,ij}, \quad \Delta P^n_{incr,ij} = \frac{\Delta P^n_{inc,ij}}{P^n_{incref,ij}} \quad (20.1)$$

Condition b: If the wheel is in the middle of a control cycle (Point B, $S_{ij} \neq 1$), then the excess of a_{whl} over a certain threshold, which suggests that the wheel is recovering as fast as it does on a high- μ road, is required.

On the contrary, if the vehicle is initially braking on a high- μ surface, it requires not only a consideration of the *Wheel Slip Status* (Point C in Fig. 20.2b, $S_{ij} = 2$), but also the information of the wheel slip and the pressure reduction to identify whether the wheel is entering a slippery region during the brake. Define

$$\lambda_{\text{max},ij}^t = \max_{\tau \in [T_0^t, t]} \left(\lambda_{ij}^\tau \right), \quad \lambda_{\text{rate}^t_{\text{max},ij}} = \frac{\lambda_{\text{max},ij}^t}{v_{\text{Ref}}} \times 100 \% \quad (20.2)$$

where v_{ref} represents the reference speed of the vehicle. If both λ_{ij} and $\lambda_{r,ij}$ exceed their previous maximum values, respectively, with a companion of a large $P_{\text{dec},ij}$ in this control cycle, the slump of the tire–road friction coefficient is then detected.

20.3 Road Identification on Full-Vehicle Layer

To establish the structure of the road identifier on the full-vehicle layer, the definitions of Surf_v and its transition state variable F_v are given in Table 20.2.

By synthesizing the identification results from the wheel layer, a general picture of the road condition can be revealed. If $F_{\text{lh},lf}$ ($F_{\text{hl},lf}$) and $F_{\text{lh},rf}$ ($F_{\text{hl},rf}$) are raised simultaneously, then the road condition is recognized as low to high (high to low) on the full-vehicle layer. However, in order to avoid false identification, the split- μ and high-to-split road cannot be simply recognized only based on the identification results from the wheel layer, and a further confirmation is consequently required.

For the split- μ situation, the wheel on the low- μ road is firstly assumed to be the wheel which is excessively slipping in the first control cycle. Define the pressure decrement deviation between the front wheels to be (because of the symmetry

Table 20.2 Definition of Surf_v and F_v

Surf_v		F_v			
0	Untested	0	No change	5	Left low confirmed
1	Homogeneous	1	Homogeneous confirmed	6	High to right low
2	Right low possible	2	Right low possible	7	High to left low
3	Left low possible	3	Left low possible	8	Low to high
4	Right low confirmed	4	Right low confirmed	9	High to low
5	Left low confirmed				

of the vehicle, the left wheels are assumed to be on the slippery road here as an example, likewise in the later context)

$$\Delta P_{\text{dec},f}^1 = P_{\text{dec},lf}^1 - P_{\text{dec},rf}^1 \quad (20.3)$$

where the superscript 1 represents the 1st control cycle. And define the modified wheel slip integral [3, 6]:

$$\Delta \lambda_{\text{int},f} = \lambda_{\text{int},lf} - \lambda_{\text{int},rf} \quad \lambda_{\text{int},ij}^t = \int_{T_0^n}^t (\lambda_{ij}^\tau - \lambda_{\text{thr},ij}^\tau) d\tau \quad (20.4)$$

Provided that $\Delta P_{\text{dec},f}^1$ and $\Delta \lambda_{\text{int},f}$ exceed certain thresholds, respectively, soon after the establishment of the assumption (generally a delay of couple of milliseconds), the identification of the split-mu road can be confirmed within the first control cycle.

For the high-to-split situation, which is far more dangerous, a direct and timely confirmation is desirable. $Surf_{ij}$ and S_{ij} of the bilateral front wheels are examined; meanwhile, a cluster of selected variables, as listed below, are observed:

1. $a_{\text{max},lf}^t = \max_{\tau \in [0,t]} (a_{lf}^\tau)$;
2. $P_{\text{dec},rf}$;
3. $\lambda_{\text{int},rf}$;

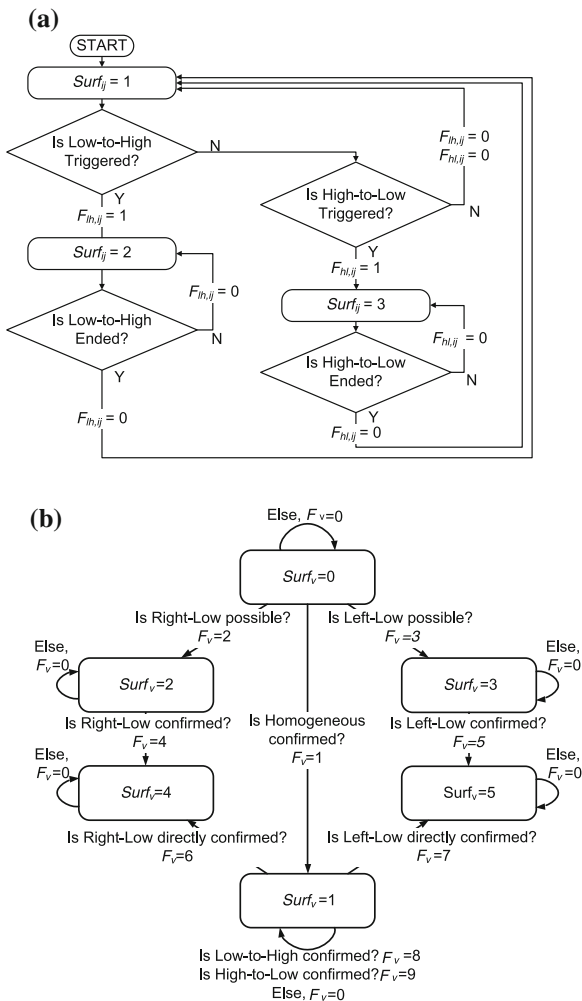
where $a_{\text{max},lf}^t$ represents the maximum deceleration of the left front wheel. Provided that these variables exceed or within certain preset corresponding ranges, respectively, the identification of the road condition is then confirmed without delay. The overall scheme of the road identification method on wheel layer and full-vehicle layer is presented in Fig. 20.3a, b, respectively. The method with such structure can be implemented in the form of state machine by defining $Surf_{ij}$ and $Surf_v$ as the outputs of a Moore machine and $F_{lh,ij}$, $F_{hl,ij}$, and F_v as the outputs of a Mealy machine [7, 8].

20.4 Simulation Results

The proposed method was separately verified through simulation experiments on the four aforementioned roads, where the tire-road friction coefficient was set to 0.2 and 0.9 for the low-mu part and high-mu part of the road, respectively. As shown in Fig. 20.4, the proposed method was capable of identify the road conditions timely and accurately; thus, the ABS controller adjusted the braking pressure according to

Fig. 20.3 Scheme of the road identification method.

a Wheel layer. **b** Full-vehicle layer



the road condition. Good ABS performances were consequently achieved in all simulated cases. Specifically, in the cases of split-mu and high-to-split, the lateral acceleration and the yaw rate were both restricted within admissible ranges, respectively, since the right front wheel, which is on the high-mu surface, immediately copies the pressure reduction operation from the left one as soon as the road identification was completed.

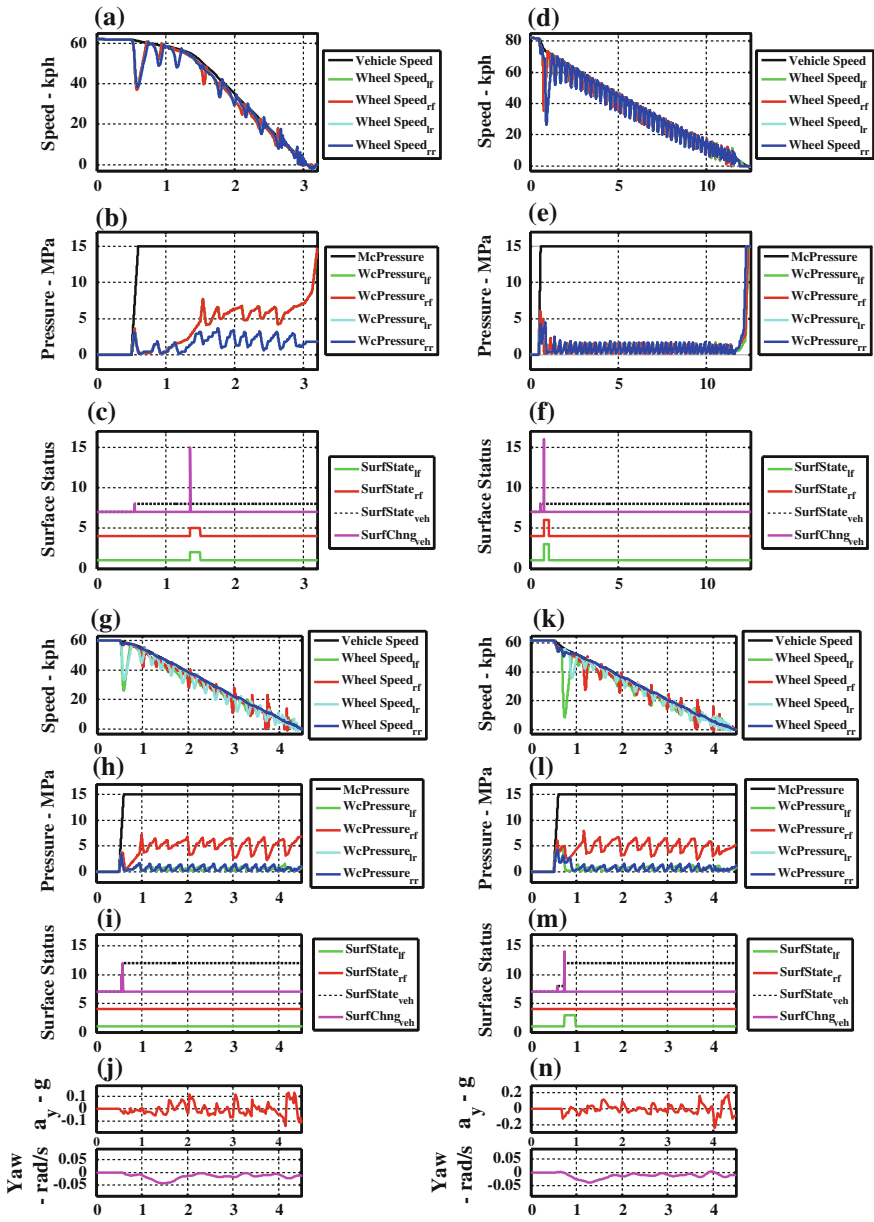


Fig. 20.4 Simulation results on different roads. a-c Low-to-high. d-f High-to-low. g-j Split-mu. k-n High-to-split

20.5 Conclusions

A hierarchical road identification method which is capable of recognizing multiple kinds of road conditions was designed to enhance the ABS performance. The method was fulfilled in the form of statecharts with the observation and analysis of a cluster of crucial variables. A series of simulation experiments were carried out in the conditions of low-to-high, high-to-low, split- μ , and high-to-split, respectively, and the results verified the effectiveness of the proposed method.

Acknowledgments This work has been supported by the National Natural Science Foundation of China (Grant No. 51375299) and the Ministry of Transport Project (Grant No. 2013319817190, Key Laboratory of Vehicles Detection, Diagnosis and Maintenance Technology).

References

1. Fan Y, Yi L (2005) Vehicle system dynamics. Mechanical Industrial Press, Beijing
2. Oniz Y, Kayacan E, Kaynak O (2009) A dynamic method to forecast the wheel slip for antilock braking system and its experimental evaluation. *IEEE Trans Syst Man Cybern* 39(2):551–560
3. Fang Y, Chu L, Sun W et al (2010) Identification and control of split- μ road for antilock braking system. In: 2nd international conference on advanced computer control (ICACC), Shenyang, China, pp 298–301
4. Hebden RG, Edward C, Spurgeon SK (2003) An application of sliding mode control to vehicle steering in a split- μ manoeuvre. In: Proceedings of American control conference, Denver, USA, pp 4359–4364, 4–6 June
5. Aly AA (2010) Intelligent fuzzy control for antilock brake system with road-surfaces identifier. In: Proceedings of IEEE international conference on mechatronics and automation, Xi'an, China, pp 699–705, 4–7 Aug
6. Wang B, Sun R (2012) A research on road condition identification based on characterization factors. *Automot Eng* 34(6):506–510, 522
7. Harel D (1987) Statecharts: a visual formalism for complex systems. *Sci Comput Program* 8(3):231–274
8. Drusinsky D, Harel D (1989) Using statecharts for hardware description and synthesis. *IEEE Trans Comput Aided Des* 8(7):798–807

Chapter 21

NH₃ Generator for Enhanced Low-Temperature SCR Performance; An Option also for Retrofit

Winfried Steve Doelling, Yuhu Zhang, Sanxia Wang, Jun Li, Jan Margraf, Marco Mrosek, Thorsten Haake, Christof Luecking and Wolfgang Frank

Abstract Combustion engine emissions of vehicles under real drive condition require special attention. Since the implementation of Euro 4 technology for commercial vehicles in 2005, the SCR technology has been established for NO_x reduction worldwide. Traditionally, the reduction agent NH₃ is generated from aqueous urea solution (AdBlue/DEF) in the exhaust line upstream of the SCR catalyst. In contrast to the technology described in this paper, this generation happens within a separate reactor, which is decoupled from the exhaust line. Here, the thermal energy required is induced via partial exhaust flow and an electrically heated hydrolysis catalyst. Therefore, the NH₃ can be generated widely independent from the exhaust temperature and mixed in the main exhaust line with the exhaust gases short way upstream of the SCR catalyst. As a result, when using low-temperature active catalysts, this technology yields particularly high NO_x conversion rates for new engine developments as well as for retrofit applications and convinces with an outstanding real drive emission level. Some aspects of the development of components and systems are described. Furthermore, the verification is shown with engine test bench WHTC using a retrofitted four-cylinder diesel engine.

W.S. Doelling (✉)

Alantum Europe GmbH, Raiffeisenallee 6, 82041 Oberhaching, Germany
e-mail: wdoelling@alantum.com

Y. Zhang · S. Wang · J. Li

Alantum Advanced Material and Technology (Shanghai) Co., Ltd, No. 366 Sunshine Road, Forward Hi-tech Zone, Jiading, Shanghai 201822, China

J. Margraf · T. Haake · C. Luecking · W. Frank

TWINTEC Technologie GmbH, Stockumer Str. 28, 58453 Witten, Germany

M. Mrosek

TWINTEC Technologie GmbH, Eduard-Rhein-Strasse 21-23, 53639 Königswinter, Germany

© Springer-Verlag Berlin Heidelberg 2015

Society of Automotive Engineers of China (SAE-China) (ed.),

Proceedings of SAE-China Congress 2014: Selected Papers,

Lecture Notes in Electrical Engineering 328, DOI 10.1007/978-3-662-45043-7_21

Keywords SCR · Urea solution · Low temperature · Ammonia generator · Partial flow hydrolysis

21.1 Introduction and Background

The SCR technology has been applied in automotive mass production from 2005 [1] and is because of the established diesel NO_x reduction technology, for automotive and off-road applications.

New regulations put a strong focus on real-use situations, which as a consequence take the lower exhaust temperature level into account. This becomes part of the certification procedures with lower temperature emission cycles.

21.2 Technical Challenges

The SCR technology in use today offers its best performance at certain temperature levels.

Firstly, the energy is needed to release the reduction agent ammonia (NH₃) from the aqueous urea solution (AdBlue/DEF), and secondly, the catalytic process on the SCR catalyst requires a certain temperature level for operation. For various reasons, this temperature level in the exhaust gases may not always be available in today's daily use of vehicles and NRMM. As a result, the NO_x reduction performance may not always be as it is designed to be.

Technical solutions to improve this situation need to be developed in the following domains:

- Low-temperature active SCR catalysts with high conversion performance,
- Generation of the reduction agent ammonia/NH₃ with less dependency of the exhaust gas temperature level,
- Effective gas–gas mixing of exhaust gas with NH₃ short way upstream of the SCR catalyst.

21.3 The Solution: The On-vehicle Urea to Ammonia Converter

The technology is based on a NH₃ generation in a separate device, the ammonia generator, which is located in a partial exhaust stream [2]. The basic principle is described as follows:

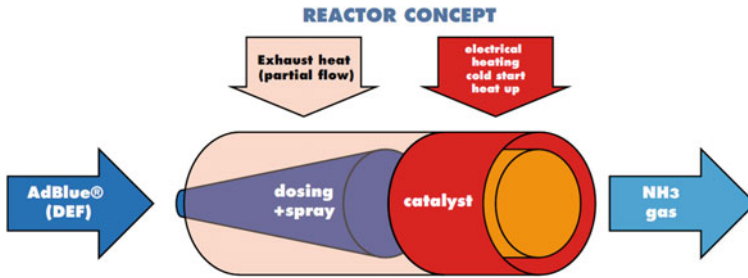


Fig. 21.1 Concept of an ammonia (NH₃) reactor

- Incoming: Aqueous urea solution, partial exhaust flow, electric energy,
- Outgoing: Ammonia NH₃, partial exhaust stream.

Figure 21.1 illustrates the NH₃ reactor setup.

21.3.1 Working Principle of the NH₃ Generator

The aqueous urea solution (AdBlue/DEF) is metered by the “standard” urea dosing system and injected by its “standard injector” into the generator. The generator is designed to use two heat sources, one by one or both together. Heat source #1 is a partial exhaust gas flow, which is taken off the exhaust line at preturbo position. The mass flow rate is up to 5 % of the exhaust mass flow. Heat source #2 is an electrically heated catalyst (metal substrate). The heating power of the catalyst is controlled by PWM using a temperature sensor. Downstream of this catalyst, a second catalyst (not heated) may be placed in order to extend the capacity of the NH₃ formation in the generator. Figures 21.2 and 21.3 show the full SCR exhaust after-treatment setup using the ammonia generator.

21.3.2 Advantages and Trade-offs

The system is to a great extent independent of load level of the engine with respect to mass flow, exhaust temperature, and exhaust pressure. It takes comparatively little time to heat up the system until dosing readiness for AdBlue/DEF is achieved. Therefore, it enables an early NO_x reduction operation and contributes to lower NO_x emissions. It enables an optimized packaging of the exhaust line and requires no hydrolysis and evaporation path. It requires short mixing lengths from ammonia gas inlet to the SCR catalyst, and it is as well suitable for close-coupled catalyst and very compact exhaust after-treatment designs. The gas–gas mixture enables an intense mixing of the gases and a uniform flow on the catalysts. This system is used

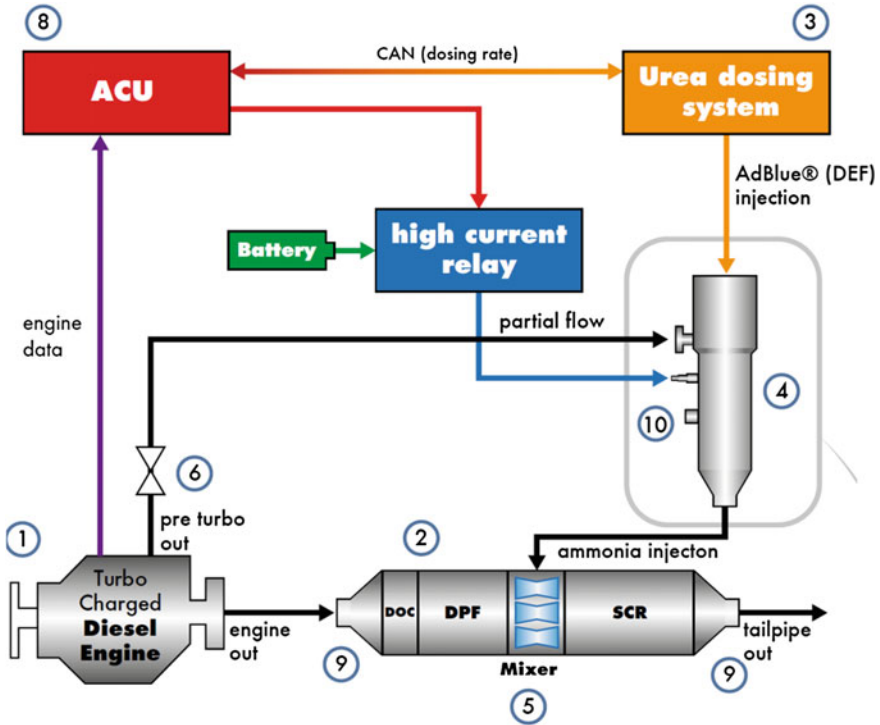


Fig. 21.2 SCR exhaust after-treatment setup with ammonia generator

Turbo Diesel engine (1), Exhaust System with PM- and NOx reduction (2), Ammonia (NH₃) Generator (4) and Mixing Unit (5).

Urea Solution (DEF) is injected via Urea Dosing System (3) into Ammonia Generator (4). NH₃ is generated inside and injected into Exhaust Mixing Unit (5).

The generator uses the heat sources from pre turbo exhaust gas (6) and electrically heated catalyst (7)

Partial flow is defined by orifice (6).

Injection control by ACU (8), Urea Dosing System (3), Temperature- (10) and NOx Sensor (9).

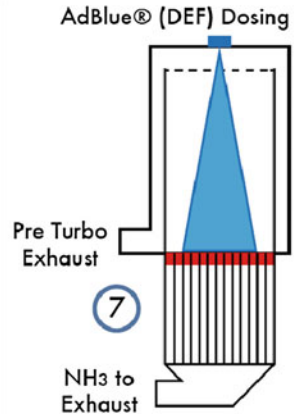


Fig. 21.3 Function and details of a SCR exhaust after-treatment setup with ammonia generator

to prevent the deposits on the catalysts in the main exhaust line and thus reduces failures of SCR on DPF systems due to the deposit formation.

The superb performance with the ammonia generator is achievable by accepting the following trade-offs. The ammonia generator is a separate device, which requires packing space, mounting parts, pipes and connectors, cable, heat shield for thermal protection, and electric energy.

However, the overall target of reducing NO_x emission under operation condition with lower temperature level can be fully achieved.

21.4 Development and Realization

During the development process, the following aspects require special attention:

- Partial exhaust mass flow preturbo takeoff,
- Spray evaporation chamber,
- Hydrolysis catalysts,
- Temperature-controlled NH₃ generation,
- Avoidance of deposits,
- Merging and mixing NH₃ within exhaust line,
- Layout design of SCR catalysts in exhaust line.

Some of these major aspects will be explained in detail.

21.4.1 *Partial Exhaust Mass Flow Preturbo Takeoff*

The partial exhaust mass flow preturbo takeoff is necessary for the reasons to provide pressure gradient over the generator and to provide thermal energy for the NH₃ generation. The design of the partial flow rate is adjusted in such a way that there is no remarkable effect on the maximum engine power.

Figure 21.4 shows its mounting on the engine, upstream of the turbocharger.

21.4.2 *Layout of Hydrolysis Catalysts*

The design of the hydrolysis catalyst is necessary to come to an optimum performance of NH₃ conversion with respect to packaging.

A base matrix-type metal substrate catalyst is used. The hydrolysis catalyst contains two consecutive catalysts, the first of which is equipped with electrically heating function and the second of which is an unheated type. The heated catalyst had a cell density of 160 cpsi at the heated slice. This catalyst remained unchanged throughout the variation tests as well as the hydrolysis coating. The target of the

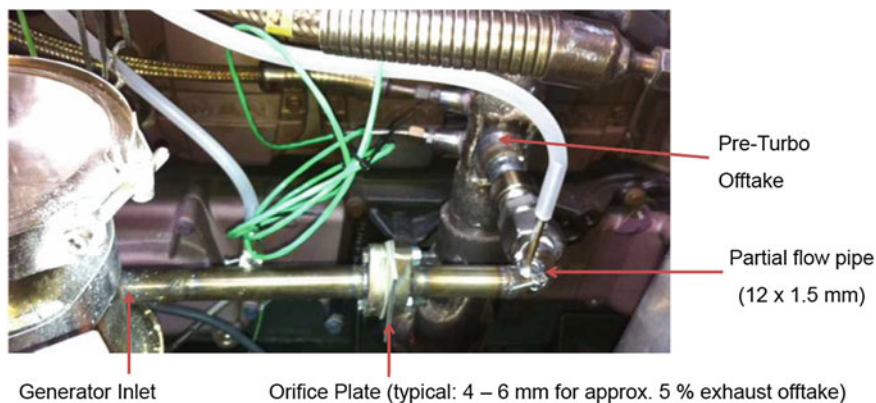


Fig. 21.4 Partial exhaust mass flow takeoff unit and mounting position

second hydrolysis catalyst in the consecutive setup is to optimize the impact of the NH_3 performance of the generator.

The conversion tests were carried out on an engine test bench using a diesel engine with 180 kW rated power. The operation conditions conform to ISO 8178 Type C1. The evaluation demonstrates the impact of the design of the substrate on the NH_3 conversion efficiency, which is set to have an overall value within the range of 94–98 %.

21.4.3 Avoidance of Deposits

Under normal operating conditions, this is not an issue. However, the formation of deposits can be intentionally activated for certain operation conditions such as extreme overdosing for longer period with low exhaust temperatures and mass flows. However, with a dedicated heating strategy of the hydrolysis catalyst, it is possible to remove those deposits. Therefore, this technology offers beneficial technical possibilities opposite to the traditional AdBlue/DEF direct dosing technology into the exhaust line.

21.4.4 Layout Design of SCR Catalysts in Exhaust Line

In the previous chapters, it is shown that technical aspects have to be considered to achieve a good NH_3 formation performance in the generator even at low exhaust temperatures. Today's SCR catalysts do not provide a significant NO_x conversion at low exhaust temperature. They are designed for temperature in the range of 250–550 °C to provide good performance. An adequate low-temperature active

SCR coating is required to take full use of the availability of ammonia gas (NH₃). As a consequence, a low-temperature active SCR coating is preferably applied. In addition, a state-of-the-art vanadia-based SCR catalyst is used as a slip catalyst.

21.4.5 Performance Verification of the System

For verification of the previously demonstrated development work for individual components or aspects, several tests with “full systems,” which comprise urea dosing unit, NH₃ generator, and exhaust system, were done on engine test bench, on chassis dynamometer, and on buses.

21.4.6 Chassis Dynamometer Millbrook Test Procedure

The Millbrook London Transport Bus (MLTB) drive cycle is generated using real-time data collection from a London bus working on route 159 [3]. The vehicle speed over time is within the range of 20–45 km/h, includes the idling phases, and does not exceed 50 km/h. A bus (5.8-L engine, 179 kW, Euro III) is equipped with an exhaust after-treatment system, as shown in Fig. 21.2, containing DOC, DPF, and SCR catalyst of which one part had a low-temperature active SCR coating and the other had a vanadia-type standard coating with a slip catalyst coating at the outlet of the catalyst unit. A series of urea dosing units feature the setup. The emissions were measured using Millbrook test procedure. Figure 21.5 illustrates the chassis dynamometer setup.



Fig. 21.5 Chassis dynamometer setup at Millbrook

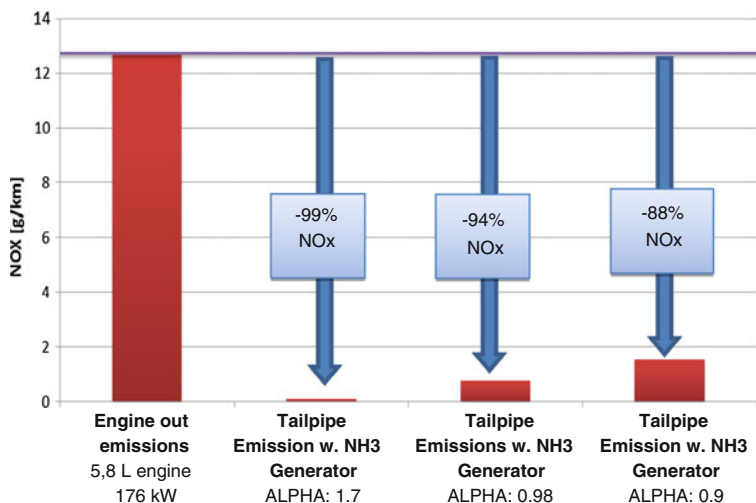


Fig. 21.6 NOx reduction with the NH3 generator with different NH3/NOx ratios

The tests were performed with the NH3 generator system at different NH3/NOx (ALPHA) ratios. ALPHA = 1 means that stoichiometrically, the exact amount of ammonia is generated for the respective NOx amount. ALPHA > 1 means more NH3 than stoichiometrically necessary, and ALPHA < 1 means less NH3 generation.

The emission reduction that has been achieved with the NH3 generator is shown in Fig. 21.6. With ALPHA 0.98, a NOx reduction of 94 % is achieved, and with ALPHA 1.7, even 99 % is achieved. Even with ALPHA 0.9, a NOx reduction of 88 % is obtained.

The transient behavior is easy to handle. State-of-the-art urea injection control strategies have been used with individual modifications for the NH3 generator control by flow rates, exhaust temperatures, urea demand, etc. The result was a well-balanced system with high NOx reduction performance, neglecting the available ammonia slip and very good transient behavior.

21.4.7 Real Drive School Bus Data

This bus was then observed under real operating conditions of the daily school bus service in a British city for several months. Figure 21.7 shows the data collected over the full drive cycle with and without NH3 generator. The readiness of NOx sensor is set at 130 °C. The data show a NOx conversion with NH3 generator from 150 °C exhaust temperatures with the respective setup of the SCR catalyst including a low-temperature active SCR catalyst, and the NOx tailpipe outlet data are recorded to have a reduction rate of approx. 80 % just from the starting and

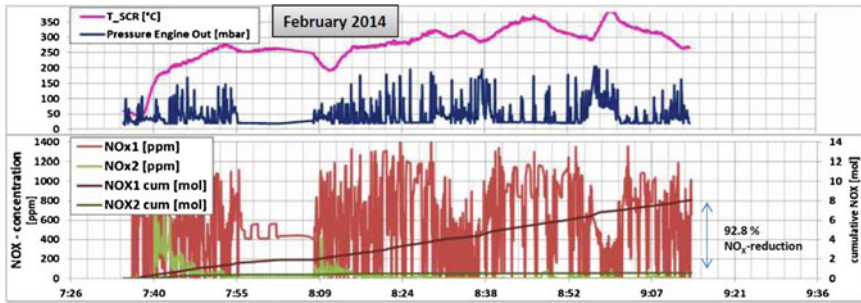


Fig. 21.7 Temperature and NOx emissions' course of the full drive cycle

gradually increasing up to 90 %. The cumulated NOx values are reduced by 92.8 % over the full morning school service.

21.5 Technical Feasibility Test

The tests are carried out on Yuchai 4D140-30 engine, displacement is 4.2 L, and rated power is 103 kW/2,800 rpm. The engine was calibrated to CHINA III. The engine calibration was not changed during the tests. The engine dynamo in the Alantum test laboratory in Shanghai was an AVL DYNOROAD SL 330 kW/ 1,400 Nm. PM measurement system was an AVL 472 smart sampler, Sartorius MSA2.7S-0CE-DF. FTIR was an AVL SESAM i60 FT. Soot concentration was measured by AVL 483. China IV-certified fuel with 50 ppm S was used.

A NH3 generator was installed on the Yuchai 4D engine taking an approx. 3 % exhaust bypass flow from the exhaust manifold before the TC without influencing the maximum power of the engine.

The exhaust after-treatment system uses a standard D 9.5" × 6" DOC, followed by either the NH3 injection from the ammonia generator with a simple mixer or a standard urea injection pipe for an airless Bosch urea injector with a mixer at the outlet (Fig. 21.8). The mixing length for the NH3 injection is 18 cm including the cone to the SCR catalyst, and the mixing length for the urea injection system setup is 60 cm. The main investigations have been performed with a standard vanadia–tungsten oxide–titanium oxide-based SCR catalyst (VWT) with two bricks of D 9.5" × 6". The outlet section of the SCR catalyst includes an ammonia slip catalyst. A low-temperature active SCR catalyst is investigated alternatively. A Bosch DEXTRONIC 2.2 dosing system is injected into either the NH3 generator or the insulated exhaust pipe directly. Urea liquid conforming to SAE-China J2901-2013 was used.

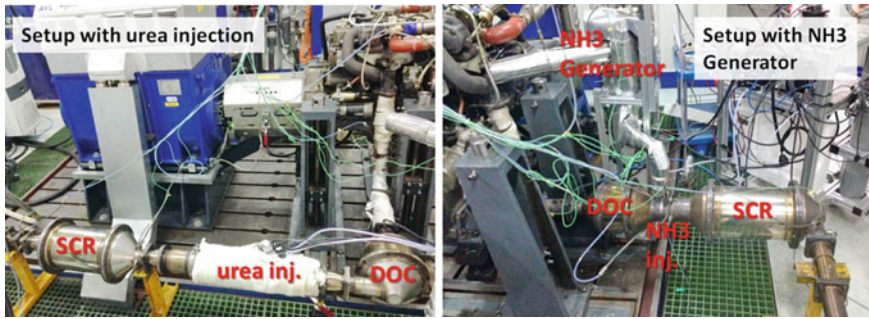


Fig. 21.8 Installation of urea-based system versus system with the ammonia generator

21.5.1 Test Matrix and Scope

Scope of the test is to compare the NOx reduction potential in the WHTC and ETC cycles comparing a system setup with the Ammonia generator versus a standard setup with direct urea injection into the exhaust pipe.

The criteria for proper system operation were defined to achieve a maximum NOx reduction while having $a < 10$ ppm NH3 slip (cycle average), and for the urea injection system, no remarkable urea deposits in the exhaust pipe or on the mixer.

The exhaust system back pressure was set for all configurations and the baseline measurements to 22 kPa at the TC outlet using an exhaust valve.

The following test matrix was performed (Table 21.1).

21.5.2 Test Results

After taking the baseline raw emission measurements in the ETC and WHTC cycles, the standard SCR system is installed. The urea injection is adjusted for a transient operation based on the NOx inlet mass flow considering a minimum urea injection release temperature of 210 °C. Even with a standardized airless urea injection pipe with double-wall insulation and mixer, the challenge is the control of the allowable urea flow at exhaust temperatures below 250 °C upstream of the SCR catalyst. The urea injection is tuned in a way to target maximum NOx reduction, on

Table 21.1 Test matrix for investigation on Yuchai 4D engine

System	DOC	Reducing agent	SCR	Test cycle
Baseline	No	No	No	WHTC + ETC
Standard	Pt based	Urea	VWT	WHTC + ETC
NH3 generator	Pt based	Ammonia	VWT	WHTC + ETC
NH3 generator	Pt based	Ammonia	Low-temp. cat	WHTC

the one hand, and to avoid heavy urea deposits and keep the ammonia slip below 10 ppm average, on the other hand. In Fig. 21.9 and Fig. 21.10, the results from the tests are summarized.

NOx reductions of 86 % in the ETC and 25 % in the WHTC have been measured using the vanadia-based SCR catalyst.

With the ammonia generator installed, the urea is injected into the ammonia generator. Therefore, the NH3 injection release into the exhaust is only limited by the performance of the SCR catalyst. Deposits in the exhaust system could not occur any more.

NOx reductions of 91 % in the ETC and 54 % in the WHTC have been measured using the vanadia-based (VWT) SCR catalyst. The effect of using NH3 instead of urea became very obvious for the cold WHTC test.

Low-temperature (LT) optimized SCR catalysts are sensitive to sulfur and has been tested to date with <10 ppm sulfur content, and a suitable engine lubrication oil is used. With such a LT catalyst—without ammonia slip catalyst—a NOx reduction of 84 % is achieved in the WHTC test while using the NH3 generator technology (Figs. 21.9).

Fig. 21.9 NOx reduction comparison of urea- versus ammonia generator-based system in the combined WHTC test cycle

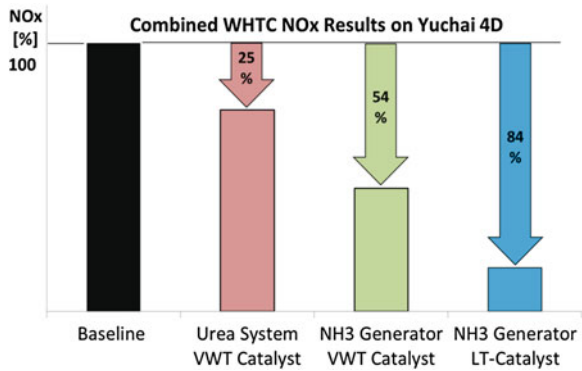


Fig. 21.10 NOx reduction comparison of urea- versus ammonia generator-based system in ETC

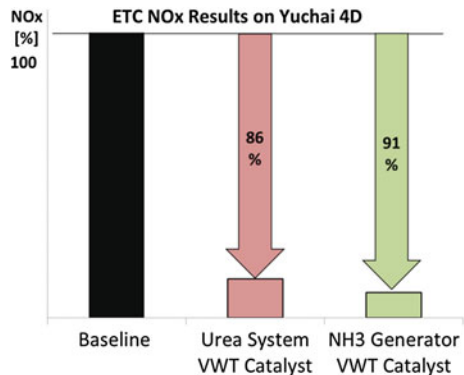


Fig. 21.11 Temperature comparison of urea- versus NH₃ generator-based system in the hot WHTC test cycle

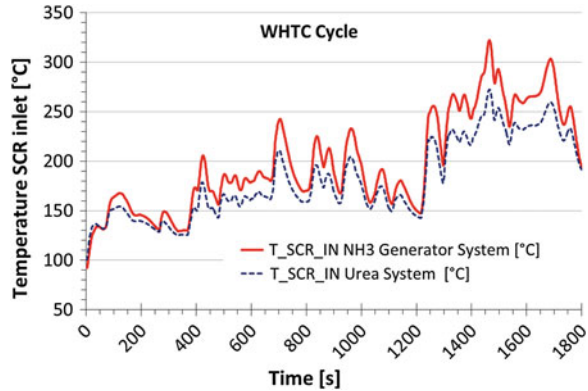
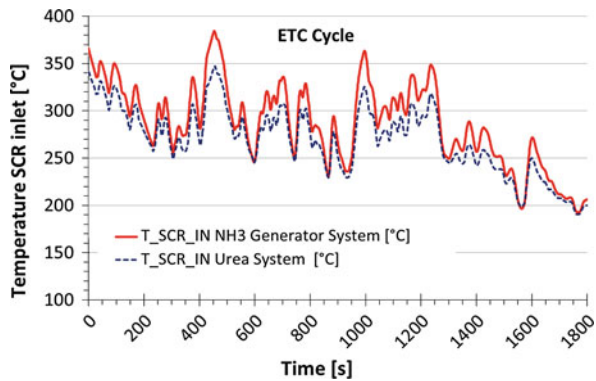


Fig. 21.12 Temperature comparison of urea- versus NH₃ generator-based system in the ETC test cycle



Besides the effects of injecting ammonia versus urea, there are changes in the system setup required to comply with the needs of urea injection. For the system with urea injection, the exhaust pipe length before the urea injection nozzle, the length to the mixer, and the mixing length are important parameters for a proper system operation. The guidelines from the urea nozzle manufacturers have been used for the setup, resulting in the lower SCR inlet temperatures (see Figs. 21.11, 21.12).

21.6 Summary and Conclusions

New engine developments are driven by emission regulations and fuel efficiency improvements. The emission regulations worldwide reflect more and more the real driving conditions with test cycles, such as the low-load WHTC and MLTB. The engine out exhaust temperatures during such test cycles are very low and thus not in favor for a good functionality of advanced catalytic exhaust after-treatment systems.

An ammonia generator system located in a partial flow is used for the tests which decouples the processing of the reduction agent urea from the exhaust line into a separate reactor.

It is shown that SCR systems can achieve high NO_x conversion performance under low-temperature operation. Bus retrofit projects with the ammonia generator and a SCR system with a low-temperature active catalyst have shown NO_x reductions >90 % using the MLTB as well as under real driving conditions of a school bus service.

A SCR system is applied on a standard CHINA III Yuchai 4D engine to investigate the potential of the ammonia generator technology under Chinese conditions. The engine calibration is not changed, which means that it is not optimized for the WHTC. The vanadia-based SCR system with direct urea injection into the exhaust line shows a NO_x conversion of 25 % in the WHTC. With the ammonia generator, a NO_x conversion of 54 % is achieved using the same vanadia-based SCR catalyst, and with a low-temperature active SCR catalyst, the NO_x conversion increases up to 84 %.

The ammonia generator offers the potential to increase the low-temperature performance of SCR systems dramatically due to the availability of NH₃ in a wide range of engine operation points while avoiding issues with urea deposits in the exhaust line. Due to the ease of NH₃ injection into the exhaust line and its mixing, the SCR and exhaust routing design are rather flexible and compact. Extensive development of specifically designed urea injection and mixing sections can be avoided.

The ammonia generator can be applied to new engine developments as well as for retrofits.

The widely used SCR systems need to be developed toward higher performance at low exhaust temperatures. The ammonia generator offers the potential to increase the low-temperature performance of SCR systems significantly and thus may contribute as enabler for future NO_x emission targets.

References

1. Selective Catalytic Reduction (SCR) as original equipment in Commercial Vehicles: A Milestone in Exhaust Aftertreatment Technology. Dr.-Ing. Wolfgang Frank, Dr.-Ing. Georg Huethwohl, Dr. rer. nat. Bernd Maurer. Aachen: Aachener Kolloquium Fahrzeug- und Motorentechnik GbR, 2005. Kolloquium Fahrzeug- und Motorentechnik, Aachener, 14, pp 1297–1309
2. Gerhart C, Sattelmayer T, Toshev P (2013) Ammonia gas generator. WO 201304634 World
3. Partnership, Low Carbon Vehicle. www.lowcvp.org.uk. [Online] <http://www.lowcvp.org.uk/initiatives/lceb/lceb-testing/lceb-test.ht>

Chapter 22

Material Data Management During Product Development for Environment Protection

Cheng Gao, Conghong Tu, Zhaojun He and Changxia Ma

Abstract In order to meet China's 'Requirements for Prohibited Substances on Automobiles' and EU ELV 2000/53/EC, OEMs request the suppliers to comply with the relevant regulation requirements. Considering the regulation, customer, and self-requirements, the United Automotive Electronic Systems Co., Ltd. develops the material data management system (MDS). With the system implementation, the prohibited substance management is fully integrated into the production development process. In order to attach the goal of high efficiency, accuracy, convenience, and real time for material management during product development, the system includes several functions, such as prohibition substance analysis, material report submission, flexible configuration due to regulations, traceability of material usage, historical material data storage, and real-time data exchange with International Material Data System (IMDS) or China Automotive Material Data System (CAMDS). The working efficiency and data safety are improved with this system.

Keywords ELV regulation · Forbidden substance · Material data management system · IMDS/CAMDS report

22.1 Introduction

With the development of vehicle industry, air condition inside vehicle and restricted substances are paid more and more attention all over the world. Europe issued ELV (End-of-Life Vehicle) in 2000, which restricts the use of lead, cadmium, mercury, and hexavalent chromium. China issued the regulation 'Requirements for prohibited substances on automobiles' on February 19, 2014. It will be implemented on June 1, 2014.

C. Gao (✉) · C. Tu · Z. He · C. Ma
United Automotive Electronic Systems Co., Ltd., Shanghai 201206, China
e-mail: cheng.gao@uaes.com

In order to comply with the regulations, the vehicle companies use International Material Data System (IMDS) or China Automotive Material Data System (CAMDS) to collect material data from their supply chains. Suppliers also use IMDS/CAMDS directly to submit material data, in which way brings several drawbacks as below shown:

1. IMDS/CAMDS is based on Internet. The low rate makes poor efficiency;
2. The difference of IMDS/CAMDS causes double work to make material reports;
3. It is inconvenient to share material reports;
4. It is difficult to fully track the usage of limited substances;
5. It is hard to guarantee the accuracy of material data;
6. There is no 100 % guarantee of safety of data or authority control.

UAES developed a new material data management system (MDS), which is embedded in current PDM system to avoid these defects.

22.2 Material Data Management System (MDS)

22.2.1 General Train of Thought

The MDS is developed to fulfill the goal of high efficiency, accuracy, convenience, and real time for material management during product development (Fig. 22.1). The system includes the prohibition substance analysis and material reports submission, which also allows flexible configuration due to regulations, traceability of material usage, historical material data storage, and real-time data exchange with IMDS/CAMDS.

22.2.2 Technical Solution

MDS is embedded into current Siemens PDM, and thus it does not need additional devices or networks. The system is also designed as similar Human–Machine Interface (HMI) as IMDS/CAMDS, and thus it is easy for users to be familiar with it. Figure 22.2 shows MDS structure and function.

Main functions of MDS:

1. Flexible configuration for regulations and customer requirement. The system allows customizing the prohibited substances according to regulations and customer requirements.
2. Reference for environmentally friendly materials. It is possible for users to search and choose friendly materials in MDS, which helps users to prevent prohibition substances or high-risk materials during product development.

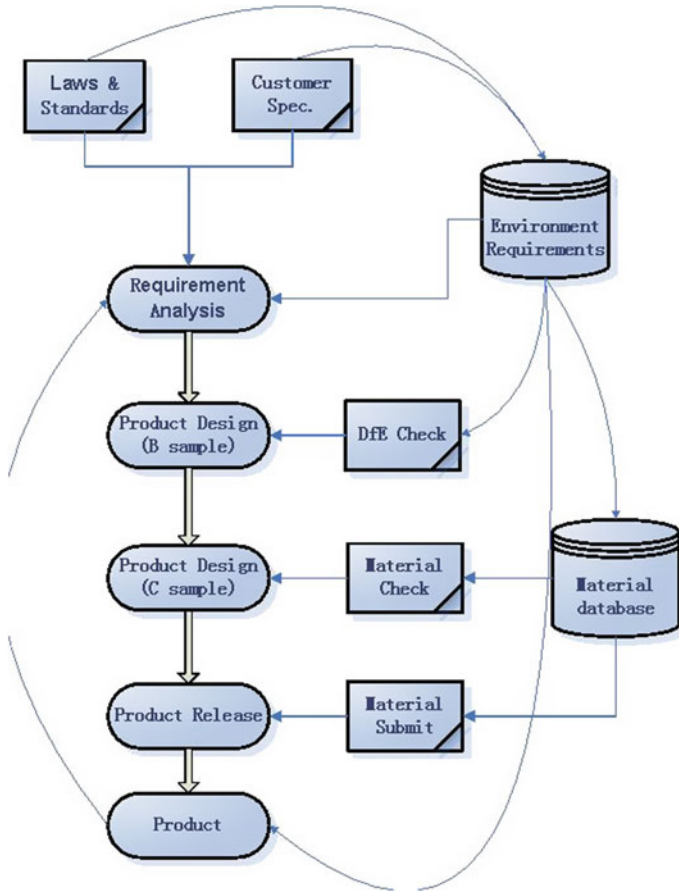


Fig. 22.1 Material data management during product development

3. Bidirectional interface. The MDS transfers real-time data with IMDS/CAMDS and downloads enterprise data automatically, which makes local management possible. High efficiency and data safety are improved in this way.
4. Search and share of material data. Material data from suppliers is transferred to MDS. Users can directly find the corresponding material data with the developing part. That makes share of data possible.
5. Material data approval. MDS provides a graphical interface and allows customizing data approval procedure according to company's procedure.
6. Material data report submission. Material data report can be created and submitted automatically according to the current bill of material (BOM) in PDM, which is totally manual work before.

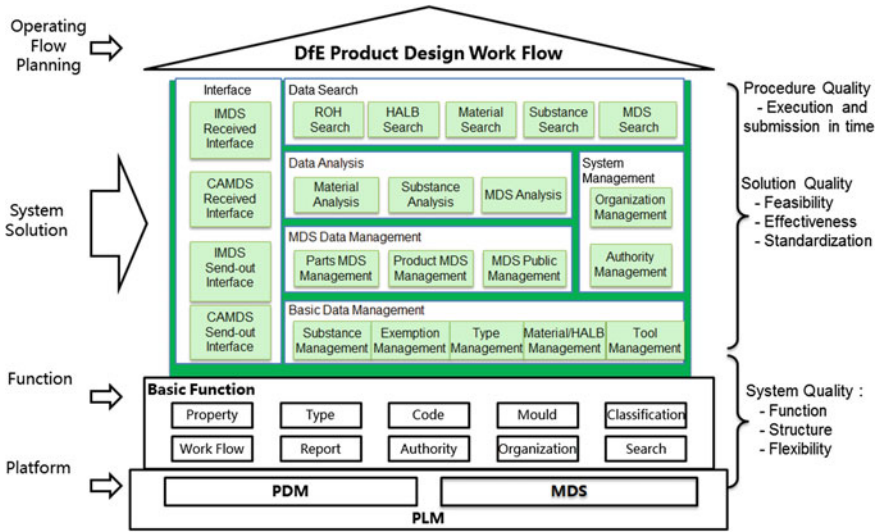


Fig. 22.2 MDS structure and function

7. Prohibition substances monitoring. If some user wants to find out which products use a prohibition substance, he can filter a related list out. This function let users easier to make analysis.
8. Authority management: The MDS administrator can define different roles and control the authority.

22.3 Main Innovations

In order to protect the system, UAES applies the software copyright successfully. The main innovations are as follows:

1. The new material data system is based on the current PDM. Normally, it is necessary to purchase extra devices for an independent MDS and users will take a lot of time to learn the new system. The new material data system is based on the current PDM, and thus additional hardware such as devices is not necessary. Another advantage is that the interface is similar as IMDS interface, and thus it helps users familiar with this system quickly. The MDS saves both time and money.

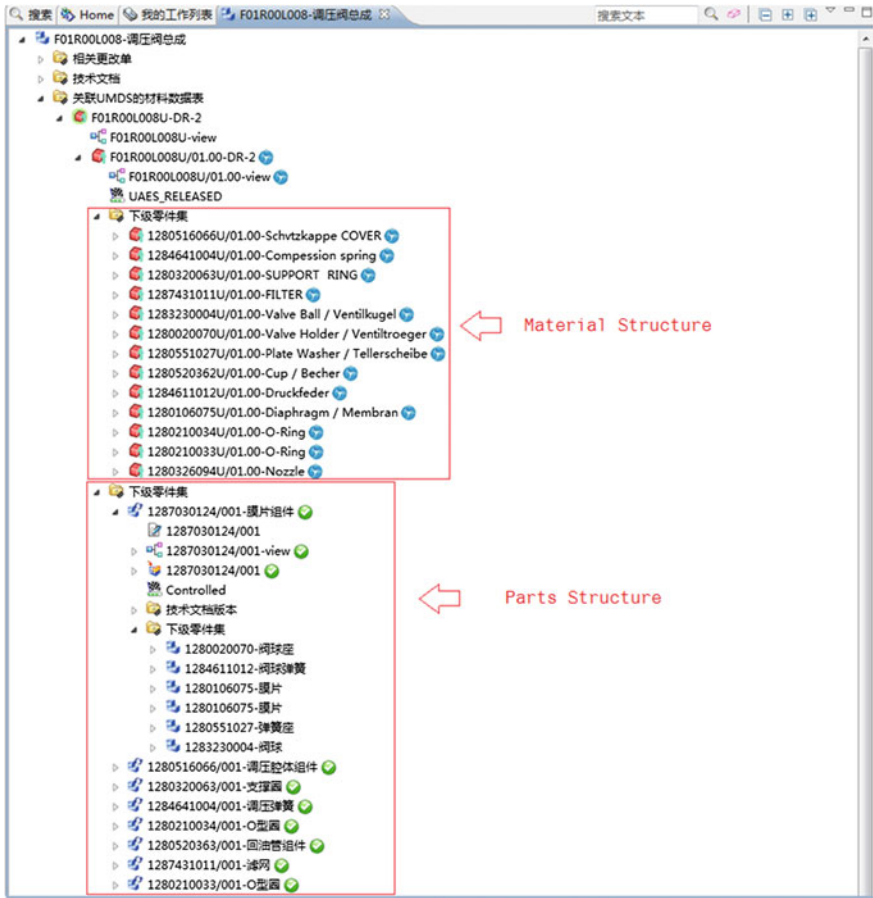


Fig. 22.3 Material data and technical documents are in the same page in PDM

2. Realization of bidirectional interface with IMDS/CAMDS. When some material report is needed to submit to customer through IMDS/CAMDS, it is totally manual work before. Since MDS realizes bidirectional interface with IMDS/CAMDS, it makes the process automatically, and it makes sure that there is no difference of reports between IMDS and CAMDS.
3. Intelligent design for the environment. With the search function in MDS, it is easier for users to check related product regulatory when a new regulation coming. Users can quickly respond to take necessary measures.
4. Visual material data. Both material data and BOM structure are in the same item in PDM, so it is convenient for users to view the data and relationship (Fig. 22.3).

22.4 Achievement of Implementation

After MDS is implemented, several benefits are achieved as follows:

1. Prohibited substance regulations and customer requirements can be implemented inside company effectively. The material data management is fully integrated in the product development process with technical tools.
2. The work efficiency is improved. Because material data reports are generated automatically, a lot of time is saved.
3. Data quality is improved. With this technical tool, approval procedure and report versions controlling are strengthened.
4. Data security and sharing are enhanced. Material data is established as the in-housing system. Reasonable authority controlling is implemented.

22.5 Summary

MDS is based on years of experience of material data management and focused on the user's actual needs, so it makes material data management modern, intelligent, and humanized. It creates social benefits and reminds more and more people to pay attention to environment protection.

Chapter 23

Profit Path Selection for Passenger Vehicle Enterprises Under Energy-Saving Target Constraints—Based on Cost Benefit Analysis

Renzhi Lv, Jihu Zheng and Peng Zhang

Abstract This paper aims to solve the problem that under the economic situation, how to deal with the energy-saving objection and profit for enterprises dealing with passenger vehicle. The research in this paper mainly includes three aspects: firstly, to elaborate the theoretical basis of cost-benefit analysis and the feasibility of applying the analysis on this issue; secondly, to sort out the optional ways of pursuing the maximum self-interest for enterprises dealing with passenger vehicles under the restriction on energy-saving objection; and thirdly, to make a cost-benefit analysis on each way and come to a reference conclusion to the business decision. In this paper, the path choice model under the cost-benefit analysis method is built, which can assist enterprises in making a scientific choice aiming at their own fund structures, in order to seek for the highest level of profit. The core conclusion papers can help enterprises to build routing paradigm and can guide enterprises to make scientific decision.

Keywords Cost-benefit · Maximize profits · Energy-saving objection

23.1 Research Background and Value

Currently, Chinese economic and social development has been in the complex situation of “three-periods superposition,” namely the shifting period of economic growth, the agonizing period of structural readjustment, and the digestion period of initial stimulating policy, so the economic growth is bound to pay certain costs of slowdown. Meanwhile, governments at all levels have intensified the enterprise

R. Lv (✉) · J. Zheng · P. Zhang

Automotive Data Center, China Automotive Technology and Research Center,
68 East Xianfeng Road, Dongli District, Tianjin 300300, China
e-mail: lvrenzhi@catarc.ac.cn

© Springer-Verlag Berlin Heidelberg 2015

Society of Automotive Engineers of China (SAE-China) (ed.),

Proceedings of SAE-China Congress 2014: Selected Papers,

Lecture Notes in Electrical Engineering 328, DOI 10.1007/978-3-662-45043-7_23

integration, elimination of backward capacity, and governance of environmental pollution, and the structural readjustment has been endowed with new connotation. Along with the tide of economic structural readjustment and industrial upgrading at the present stage, automobile industry has also entered the crucial stage of transformation and readjustment.

The adjustment of automobile industry involves not only initiative adjustment of the market, but also national policy control. As the main benefited and performing party in the industrial adjustment, enterprises play an important role in this round of readjustment. At present, the restriction on energy-saving objective aims at enterprises dealing with passenger vehicles, namely the reflection of national policy control, while enterprises dealing with passenger vehicles positively push out energy-saving products and new energy products, namely the expression of responding to national policies and pursuing the maximum self-interest.

Focusing on the topic of this paper, enterprise production is a profit-seeking behavior in nature, and then under the current background of economic and social development, how to maximize the self-interest for enterprises dealing with passenger vehicles becomes a practical issue drawing urgent concern from the industry and enterprises. The research in this paper mainly includes three aspects: firstly, to elaborate the theoretical basis of cost-benefit analysis and the feasibility of applying to the analysis on this issue; secondly, to sort out the optional ways of pursuing the maximum self-interest for enterprises dealing with passenger vehicles under the restriction on energy-saving objection; and thirdly, to make a cost-benefit analysis on each way and come to a reference conclusion to the business decision.

23.2 Theoretical Basis and Innovative Points

In terms of the nature of enterprises, they are organizations seeking for profits. The profit requires comprehensively considering the cost and benefit as well as input and output. Microeconomics points out that enterprises need to meet the principle that the marginal income of output is equal to the marginal cost while taking the maximum profit; in other words, the benefit obtained from outputting per unit of product is equal to the cost of outputting per unit of product. When enterprises are confronted with several paths of operation; that is, the combination of different production factors leads to the output of different commodities, the cost-benefit analysis method seems especially critical.

The cost-benefit analysis is a method of evaluating the project value by comparing the cost and benefit of the project. As an economic decision-making method, the cost-benefit analysis method aims to obtain the maximum benefit by right of the minimum cost based on investment decision, or obtain the maximum benefit by right of fixed cost.

Thus, it can be seen that it is practical to study how to maximize the profit of enterprises based on cost-benefit analysis method. In view of the research subject in this paper, enterprises dealing with passenger vehicles are faced with multiple paths

under the restriction on national energy-saving objective and driven by their own profit-seeking behaviors. The issue highlighted in this research to evaluate the cost and benefit brought by different paths, so as to assist enterprises in conducting scientific decision-making. It is just the innovative point and value of this research.

23.3 The Path Choice Under the Cost-Benefit Analysis

The Development Planning of Energy-saving and New Energy Automobile Industry (2012–2020) published by the State Council in 2012 clearly proposed to establish an improved management system of automobile energy saving and published the regulation on the fuel consumption of automobile [1]. Ministry of Industry and Information, together with National Development and Reform Commission, Ministry of Commerce, General Administration of Customs, State Administration of Quality Inspection, and Ministry of Finance and State Administration of Taxation, organizes the automobile industry to launch the research and formulation on the Accounting Method of Average Fuel Consumption for Enterprises Dealing With Passenger Vehicles, and the reporting and accounting management of average fuel consumption for passenger vehicle enterprises. It is reported that the punishment regulation on passenger vehicle enterprises failing to meet the average fuel consumption has been positively promoted as well.

The energy-saving management of passenger vehicles considers the reality of tense energy structure in China practically; moreover, it belongs to national guidance on the transformation of Chinese passenger vehicle industry from the perspective of top-level design in nature [2]. The past 10 years is a period experiencing various types of technical progress for Chinese passenger vehicle products. There is still space of growth for the passenger vehicle market in the future. However, the growth interval is relatively stable, while the competition becomes more and more fierce. In the future, passenger vehicle market should adapt to the upgrade of consumption structure to greater extent and stretch the product quality vertically, which has posed a greater challenge on enterprises [3].

According to measurement and calculation, domestic enterprises of passenger vehicles failing to meet the requirements of energy-saving objective accounted for about one-third of the total accounting volume in 2012 and 2013. As the market supply party, enterprises dealing with passenger vehicles have an urgent need to solve the contradiction between the restriction of national energy-saving objective and their own output of market-oriented products. Given that enterprises intend to seek profits, the solution to this contradiction should aim at the maximum profit.

In order to make the research practicable, it requires proposing the following hypotheses:

Hypothesis 1 Enterprises dealing with passenger vehicles pursue the maximum profit [4].

Enterprise production function:

$$y = f(x_1, x_2, \dots, x_n) \quad (23.3.1)$$

where the production function can be interpreted through inputting n factors, x_1, x_n and combining them, to reach the state of maximum output.

Profit function:

$$\pi = p * f(x_1, x_2, \dots, x_n) - w_1 * x_1 - w_2 * x_2 - \dots - w_n * x_n \quad (23.3.2)$$

where π refers to profit and the model aims to solve the rationing levels of x_1, x_2, \dots, x_n when is n maximized; among them, p refers to the average price of output products, w_1, \dots, w_n are corresponding prices to n factors, x_1, \dots, x_n . Here, p and $w_1 \dots w_n$ are external decisive values; that is, they are not affected or partially affected by the interference from behaviors of enterprises; in order to make the research framework practicable, suppose they are fixed values.

Hypothesis 2 The capitals for operation of enterprises dealing with passenger vehicles are fixed.

Suppose that the enterprise invests one fixed amount of capitals to improve its own operation status or seek for self-development. This amount of capitals can be recorded as \bar{M} .

In view of the research contents of this paper, (\bar{M}) is enough to support the enterprise to meet the requirements of energy-saving objective.

Hypothesis 3 Enterprises dealing with passenger vehicles are faced with the fine due to substandard situation.

Enterprises dealing with passenger vehicles should pay the bill for their own behaviors in the form of the fine because they fail to meet the standard. Since the fine modes and categories are beyond the keynotes discussed in this paper, which supposes that the enterprises dealing with passenger vehicles should pay the fee N for their substandard situations according to measurement and calculation, here, the fine \bar{N} guided by the government is fixed.

Based on the above hypotheses, enterprises dealing with passenger vehicles pursue the maximum profit and their operating funds are fixed. Enterprises can adopt three modes at least when coping with the substandard situation: firstly, to accept the fine and \bar{M} requiring to be paid by \bar{N} without any other use; secondly, using \bar{M} to improve the product structure. \bar{M} is based on the existing product structure in the enterprise, to optimize the structure, introduce new product lines, and make them meet the requirements of energy-saving objective; however, the enterprise should bear the risk of market return decline brought by the structural readjustment of products while meeting the standard; thirdly, using \bar{M} to improve the energy-saving technical storage, introduce new technologies, and upgrade existing products to energy-saving products, so as to meet the requirement of

energy-saving objective; however, the enterprise should bear the risk of market return decline under the premium effect brought by the input of new product technologies while meeting the standard. It is worth mentioning that there is also a transboundary circumstance besides the above three contextual models. Taking the introduction of new energy product for example, the introduction of new energy product will have an influence on both product structure and energy-saving technology [5]. Objectively speaking, analyzing the behaviors such as the introduction of new energy products is more meaningful to enterprises, and two-way influence accords with the actual situation to greater extent.

For the sake of research, this paper will discuss the optional behaviors for passenger vehicle enterprises to pursue the maximum profit in the mode of fixed fund investment from four aspects, and the cost-benefit analysis method is adopted. Four optional behaviors are as follows:

1. \bar{M} requiring to be paid by \bar{N} without any other use.
2. To improve the product structure without changing technical storage.
3. To improve the technical storage without changing product structure.
4. Taking the introduction of new energy product for example, both product structure and technical storage change.

23.3.1 The Cost-Benefit Analysis Under Payment Behavior

Taking \bar{M} requiring to be paid by \bar{N} alone into account without any other use, the cost-benefit analysis of the enterprises is as shown in Table 23.1.

At this time, the profit function of the enterprise is:

$$\pi^1 = -p \times f(x_1, x_2, \dots, x_n) - w_1 \times x_1 - w_2 \times x_2 - \dots - w_n \times x_n \bar{N} \varphi \quad (23.3.3)$$

That is,

$$\pi^1 = \pi - \bar{N} - \varphi \quad (23.3.4)$$

Table 23.1 Circumstance 1 cost-benefit analysis

<i>Cost</i>
1. To pay the fine \bar{N}
2. The potential risks of existing competitive position, enterprise image, and reputation, etc. resulted from that, the product technologies fall behind like products are recorded as φ
<i>Benefit</i>
1. To keep the current benefit

The original π unit profit which has been carved up $\bar{N} + \varphi$ due to energy-saving objective should be made up with \bar{M} .

23.3.2 Using \bar{M} to Improve Product Structure and Remain Technique Reserve

Using \bar{M} to improve own product structure, optimize the curb weight and vehicle fuel consumption, and introduce new energy-saving products so as to meet the requirement of energy-saving objective, under this circumstance, the cost-benefit analysis of the enterprises is as shown in Table 23.2: \bar{M} .

At this time, the profit function of the enterprise is

$$\pi^2 = p' \times f(x_1, x_2, \dots, x_n)' - w_1 \times x'_1 - w_2 \times x'_2 - \dots - w_n \times x'_n - A - B - \varphi \tag{23.3.5}$$

$$\pi^2 - \pi = p' \times f(x_1, x_2, \dots, x_n)' - p \times f(x_1, x_2, \dots, x_n) - \sum_{i=1}^n w_i(x'_i - x_i) - A - B - \varphi \tag{23.3.6}$$

That is,

$$\pi^2 = \pi + p' \times f(x_1, x_2, \dots, x_n)' - p \times f(x_1, x_2, \dots, x_n) - \sum_{i=1}^n w_i(x'_i - x_i) - A - B - \varphi \tag{23.3.7}$$

The original profit structure is broken, and $A + B + \varphi$ requires to be paid by \bar{M} .

Table 23.2 Circumstance 2 cost-benefit analysis

<i>Cost</i>
1. The production cost A from newly added equipment like product line and labor input
2. The sales cost B from the introduction of new products
3. The loss of potential market interest brought by the change of product structure is recorded as φ
<i>Benefit</i>
1. The change of output structure and income restructuring (p' as the average price of new product structure).

23.3.3 Using \bar{M} to Improve Technique Reserve, and Remain Product Structure

Using \bar{M} to improve own energy-saving technical storage, introduce new technology, and upgrade the existing products to energy-saving products, so as to meet the requirement of energy-saving objective, under this circumstance, the cost-benefit analysis of the enterprises is shown in Table 23.3.

At this time, the profit function of the enterprise is

$$\pi^3 = p'' \times f(x_1, x_2, \dots, x_n) - w_1 \times x_1 - w_2 \times x_2 - \dots - w_n \times x_n - C - D - E - \varphi \tag{23.3.8}$$

$$\pi^3 - \pi = (p'' - p) \times f(x_1, x_2, \dots, x_n) - C - D - E - \varphi \tag{23.3.9}$$

That is,

$$\pi^3 = \pi + (p'' - p) \times f(x_1, x_2, \dots, x_n) - C - D - E - \varphi \tag{23.3.10}$$

$C + D + E + \varphi$ requires to be paid by \bar{M} .

23.3.4 Taking the Introduction of New Energy Products for Example, Both Product Structure and Technical Storage Change

The introduction of new energy product will have an influence on both product structure and energy-saving technology. The cost-benefit analysis of the enterprises is as shown in Table 23.4.

Table 23.3 Circumstance 3 cost-benefit analysis

<i>Cost</i>
1. The technology R&D and input cost C
2. In the new technology application, the production cost D for newly added equipment and labor input
3. In the new technology application, the sales cost E for updated products
4. Due to technology introduction, the potential risk resulted from that traditional products is not accepted by consumers is recorded as φ
<i>Benefit</i>
1. The change of technical composition makes the product price increase. (p'' as the average price of new technology product)

Table 23.4 Circumstance 4 cost-benefit analysis

<i>Cost</i>
1. The technology R&D and input cost α
2. The production cost from newly added equipment like new energy product and labor input β
3. The sales cost from new energy products γ
4. The potential risk resulted from the change of product structure and unfavorable market promotion of new energy products is recorded as φ
<i>Benefit</i>
1. The income restructuring and $p^{\text{new energy}}$ as the price of new energy product. Suppose the prices of other products remain unchanged

At this time, the profit function of the enterprise is

$$\pi^4 = p \times f(x_1, x_2, \dots, x_n) + p^{\text{new energy}} \times f(x_1, x_2, \dots, x_n)^{\text{new energy}} - w_1 \times x_1 - w_2 \times x_2 - \dots - w_n \times x_n - \alpha - \beta - \gamma - \varphi \tag{23.3.11}$$

$$\pi^4 - \pi = p^{\text{new energy}} \times f(x_1, x_2, \dots, x_n)^{\text{new energy}} - \alpha - \beta - \gamma - \varphi \tag{23.3.12}$$

That is,

$$\pi^4 = \pi + p^{\text{new energy}} \times f(x_1, x_2, \dots, x_n)^{\text{new energy}} - \alpha - \beta - \gamma - \varphi \tag{23.3.13}$$

\overline{M} used for payment $\alpha + \beta + \gamma + \varphi$.

23.4 Conclusions

To sum up, this paper makes a cost-benefit analysis on four optional plans for substandard enterprises dealing with passenger vehicles when coping with the dual issue, namely the requirements of energy-saving objective and the behavior of pursuing the maximum profit, and concludes 4 modes of enterprise profit ($\pi^1; \pi^2; \pi^3; \pi^4$) which may change based on the original profit level (π) of the enterprise.

Compared with theoretical analysis, although the cost-benefit analysis of the first three models becomes complex gradually, they can bring more market opportunities for the enterprise. The fourth model (taking the introduction of new energy products for example) approaches the actual operation of enterprise to the most; besides, under the background that new energy products can enjoy favorable policies, such as government subsidy and number-shaking convenience in cities with purchase limitation, enterprises contending for layout should focus on long-term planning and current expected revenue.

This paper builds the path choice model under the cost-benefit analysis method, which can assist enterprises in making a scientific choice aiming at their own fund structures, in order to seek for the highest level of profit.

References

1. The State Council (2012) The development planning of energy-saving and new energy automobile industry (2012–2020)
2. Ouyang M (2006) The development strategy and countermeasures for domestic energy-saving and new energy automobile. *China Energ Sci Technol* 28(4):318–321
3. Research Department of Industrial Economy of the Development Research Centre of the State Council (2012) Report on China Automobile Industry Development, 1st edn. Social Sciences Academic Press, Beijing, pp 1–10
4. Nicholson W (2005) *Microeconomic theory: basic principles and extension*, 9th edn. Thomson/South-Western, Mason, p 258
5. Wang C (2010) The analysis on current situation of new energy automobile development in china and research on strategic planning. Master's Dissertation of Tianjin University

Chapter 24

Improvement of Formability of Y-Shaped Tubular Part of 6016 Aluminium Alloy by Pulsating Hydroforming

Zhimin Liu, Xialing Wu, Dongsheng Zhang, Yi Ding, Liyan Gao and Xiang Yan

Abstract The improvement of formability by pulsating hydroforming process of 6016 aluminum alloy tubular part of one car is examined using finite element simulation. The effects of the amplitude and cycle number of pressure in the pulsating hydroforming are investigated. It is found that the observation of deformation behaviors, using different oscillation way of internal pressure, the formability is improved by preventing local defects. The simulation results reveal that the height of ramose tube of 6016 aluminum alloy tubular part is improved from 7.10 to 14.31 mm, by optimizing the pulsating load curves of amplitude and cycle number on the process of hydroforming.

Keywords Aluminum alloy tubular part · Pulsating hydroforming · Formability · Pressure oscillation · Load curves of internal pressure

24.1 Introduction

Compared with traditional structure components, the hydroforming technology has many advantages over conventional stamping processes call save material, decrease mass, saving of joining, reduction of secondary operations, and increase rigidity as an advanced plastic forming technology [1]. Recently, it has developed rapidly and become a hot research subject in plastic processing. A lot of vehicle components were made of complex hollow tubes with various sections and axial shape; therefore, the research of hydroforming technology has great meaning for engineering

Z. Liu (✉) · X. Wu · D. Zhang · Y. Ding · L. Gao · X. Yan
Beijing Automotive Technology Center, BAIC MOTOR Co., Ltd, Beijing 101300, China
e-mail: 0071iuzhimin@163.com; shumingxing1962@126.com

theory and practice. As one of lightest structural material, aluminum alloys have high potential application in automobile manufacture. However, poor formability at the room temperature prevented its wide application, so the improvement of the formability was highly demanded.

Recently, a new hydroforming technology called pulsating hydroforming was proposed by Mori et al. [2–4]. Through loading the oscillation of internal pressure in the forming process, the deformation behavior was greatly improved by the pulsating hydroforming. In this paper, the formability of a 6016 aluminum tubular part of one car was examined, and several loading curves of internal pressure were discussed in the pulsating hydroforming process by finite element simulation. Finally, the mechanism of improvement of formability by the oscillation of internal pressure was also analyzed.

24.2 The Finite Element Model

Numerical simulation not only acts as a design verification tool, but also becomes an important method to explore novel processes. In this research, using finite element simulation, a Y-shaped tubular part of one car was assessed to determine the formability of 6016/T4 aluminum alloy. In this model, the wall thickness of tube is 1 mm, the outer diameter of ramose tube is 34.8 mm, and the outer diameter of left tube is 35 mm, and the outer diameter of the right tube is the same as left tube.

The finite element model of Y-shaped tubular part was established, as shown in Fig. 24.1. The tube is assumed as a deformed body. The left and right punch, balance punch, and die are assumed as rigid bodies. The material constitutive relation curves obtained from the tensile tests are used in this simulation, and the true stress–strain curve of 6016 aluminum alloy was as shown in Fig. 24.2.

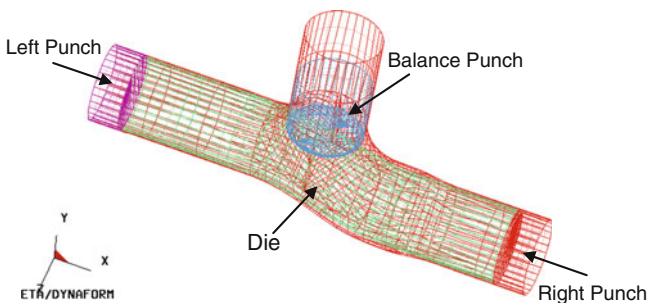
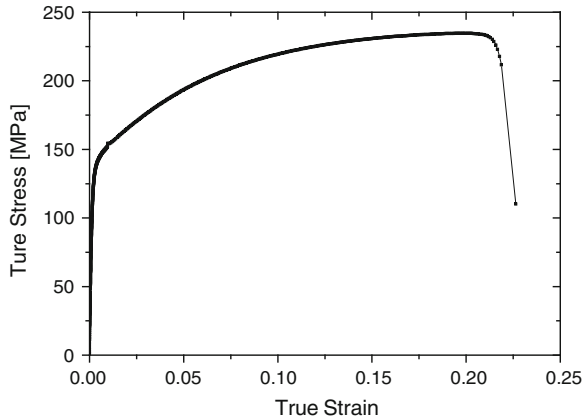


Fig. 24.1 Y-shaped tubular part finite element model

Fig. 24.2 True stress–strain curves of 6016 aluminum alloy



24.3 Load Curves of Internal Pressure

The path of internal pressure for the pulsating hydroforming can be expressed by Zhang et al. [1],

$$P = P_t - P \sin 2\pi\omega t \tag{1}$$

where P is the amplitude of the cycle of the pressure, ω is the number of cycles per unit punch stroke, t is time, and $P(t)$ is a function of load curves of the pressure.

As shown in the Fig. 24.3, four types of load curves of internal pressure are set to examine the effect of oscillation of pressure during the hydroforming. And the first type curve that was proposed by Mori is shown in Fig. 24.3a.

24.4 Results and Mechanism Analysis

The effect of four types of load curves of internal pressure was given in Fig. 24.4. It was found that the height of ramose tube of 6016 aluminum alloy tubular part was 7.10, 9.01, 7.25, and 14.31 mm, respectively. From the Fig. 24.4d, it can be seen that the formability of aluminum tube is improved obviously by the fourth load curve of internal pressure. As shown in the Fig. 24.4b, the formability of aluminum tube is also improved by the second load curve of internal pressure. Moreover, as seen in the Fig. 24.4a, c, the formability of aluminum using the first load curve is nearly equal to that using the third load curve.

Some investigators considered that the formability improved by pulsating hydroforming in which the effect on formability should be understood from two different aspects of process parameters and material properties [1–4]. The tube is uniformly expanded by repeating the appearance and disappearance of small wrinkling, and the contact friction force between the tube and die is reduced under

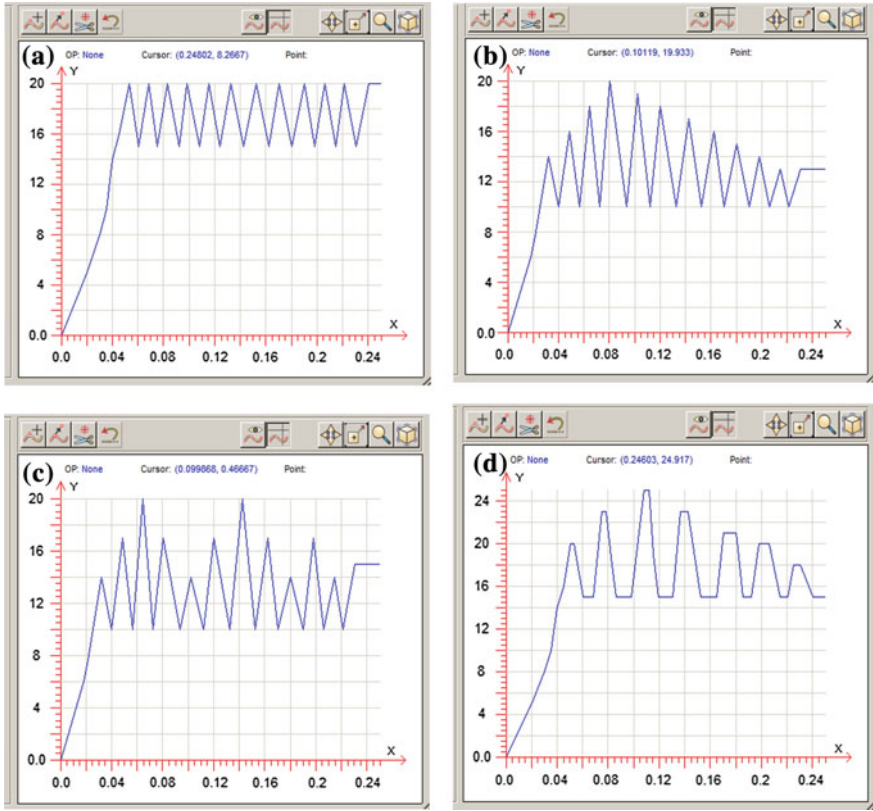


Fig. 24.3 Four types of load curve of pressure used in hydroforming

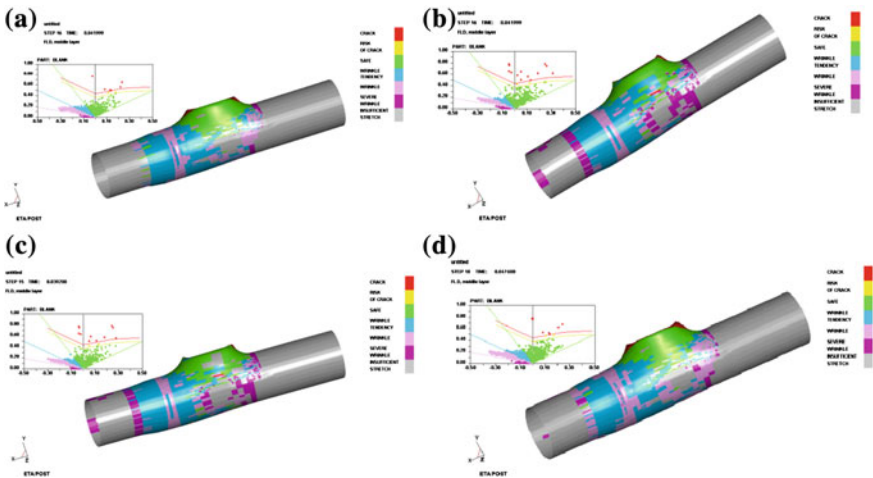


Fig. 24.4 Forming limit diagram of four types load curves of internal pressure

the pulsating load path condition. Furthermore, in this research, both the second and fourth load curves of internal pressure exhibit a monotonic increase in the initial stage, and then arrive at the maximum value. Subsequently, the internal pressure decreases and drives to a steady value. This type of load curve is similar to the curve of minimum wrinkles in the stamping process [5]. Therefore, in the pulsating hydroforming, internal pressure should monotonically increase firstly in order to avoid the appearance of large wrinkling, and then, the internal pressure arrives at the peak. Subsequently, the pressure decreases and drives to a steady value, for the sake of avoiding the brittle fracture occurring near the flat portion of ramose tube shoulder.

24.5 Conclusions

The pulsating hydroforming is attractive for the improvement of the formability of tubes. The effects of the amplitude and cycle number of pressure in the pulsating hydroforming were investigated. It was found from the observation of deformation behaviors that, using different oscillation way of internal pressure, the formability was improved by preventing local defects. In the four types of pulsating hydroforming, the formability of 6016 aluminum alloy tubular part is largely improved by one type of load curve of internal pressure, which is similar to the curve of minimum wrinkles in the stamping process. And the simulation results revealed that the height of ramose tube of 6016 aluminum alloy tubular part was improved from 7.10 to 14.31 mm, by optimizing the pulsating load curves of amplitude and cycle number on the process of hydroforming.

References

1. Zhang S, Xu Y, Cheng M et al (2013) Technology and equipment of the pulsating hydroforming technology. *J Mech Eng* 49(24):1–6
2. Mori K, Maeno T, Maki S (2007) Mechanism of improvement of formability in pulsating hydroforming of tubes. *Int J Mach Tools Manuf* 47:978–984
3. Mori K, Patwari AU, Maki S (2004) Improvement of formability by oscillation of internal pressure in pulsating hydroforming of tube. *CIRP Ann Manuf Technol* 53(1):215–218
4. Loh-Mousavi M, Mori K, Hayashi K et al (2007) 3-D finite element simulation of pulsating T-shape hydroforming of tubes. *Key Eng Mater* 340:353–358
5. Liu Z, Xing S, Bao P et al (2013) A new equation of load curve of critical wrinkles variable blank holder force in the warm deep-drawing of twin-roll cast mg sheets. *Proc FISITA 2012 World Automot Congr* 199:11–22

Chapter 25

The New Technique of Servo-Flexible Stamping Applied in the Al Sheet Forming

Zhimin Liu, Yi Ding, Xialing Wu, Dongsheng Zhang, Wenming Chen and Bo Gao

Abstract The variable blank holder force (VBHF) deep-drawing process of Al sheet is studied by the finite element method, and based on the VBHF, a new technique of variable punch velocity (VPV) is proposed. The simulation indicates that this new servo-flexible stamping can improve the deep drawability of Al sheet obviously. The limited drawing ratio (LDR) of Al circular cup is improved from 1.48 to 1.60, and the height Al square cup is improved from 19.8 to 39.8 mm. Finally, the Al hood of one car of drawing process is simulated by the new technique, and results show that the deepness of Al hood is improved by about 30 %.

Keywords Al sheet · Variable blank holder force · Servo-flexible stamping · Variable punch velocity · The limited drawing ratio

25.1 Introduction

As one of lightest structural material, aluminum alloys have high potential application in automobile body manufacture [1]. However, poor formability at the room temperature prevented its wide application, so the improvement of the formability was highly demanded [2, 3]. The stamping technique of variable blank holder force (VBHF) was the effective way to improve the formability of sheet, forming precision and surface quality [4, 5]. Therefore, how to implement the VBHF technology has become one of the research emphases in the field of sheet metal forming [6]. Recently, several press builders developed metal forming presses that utilize the mechanical servo-drive technology. The mechanical servo-drive press offers the

Z. Liu (✉) · Y. Ding · X. Wu · D. Zhang · W. Chen · B. Gao
Beijing Automotive Technology Center, BAIC MOTOR Co., Ltd, Beijing 101300, China
e-mail: 007liuzhimin@163.com; shumingxing1962@126.com

flexibility of a hydraulic press (infinite slide speed and position control, availability of press force at any slide position) with the speed accuracy and reliability of a mechanical press [7]. The new servo-drive presses can satisfy the requirement of implement VBHF simultaneously with variable punch velocity (VPV) and stepwise motion of the servo-flexible stamping. And using NURBS curve to control the servo press slide motion curve makes it possible to optimize the stamping process characteristic curves.

In this paper, a new technique of VPV based on the VBHF was proposed, and the deep drawability of the aluminum alloy sheet was discussed using NURBS curve to optimize the stamping process characteristic curves.

25.2 Cup Finite Element Model

Circular cup and square cup drawing tests were performed to determine the LDR and formability of 6016/T4 aluminum alloy. In this model, a sheet with a circular geometry, 96 mm in diameter, and 1 mm in initial thickness, was used in the simulation. Moreover, a sheet with a square geometry, 332 mm in length and 328 mm in width, and the same initial thickness as above circular geometry, was also used in the simulation.

In this research, numerical simulation is performed using the commercial explicit finite element software Dynaform. The finite element model is established, as shown in Fig. 25.1, according to the dimensions used in the deep drawing (Table 25.1). The blank is assumed as a deformed body. The punch, die, and blank holder are assumed as rigid bodies. The material constitutive relation curves obtained from the above tensile tests are used in this simulation.

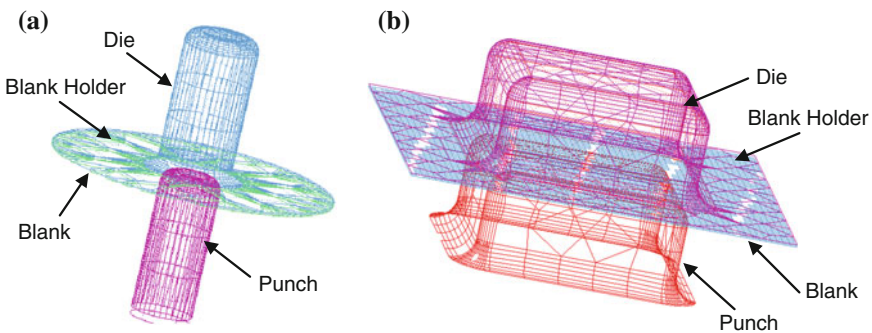


Fig. 25.1 Cup finite element model. **a** Circular cup. **b** Square cup

25.3 Results of Deep Drawing

It was found that 6016 aluminum alloy sheets had poor deep-drawing formability at room temperature, as shown in Fig. 25.2. From Fig. 25.2a, brittle fracture occurred near the flat portion of punch shoulder of circular cup when the punch stroke is 13 mm, and the calculated LDR value is 1.48. For the square cup, the punch stroke is only 19.8 mm.

Table 25.1 Processing parameters of deep drawing

	Punch width	Punch length	Punch diameter (mm)	Tools clearance (mm)	Round radius of punch (mm)	Round radius of die (mm)
Circular cup	–	–	42.5	1.1	9	47
Square cup	197	200	–	1.2	10	15

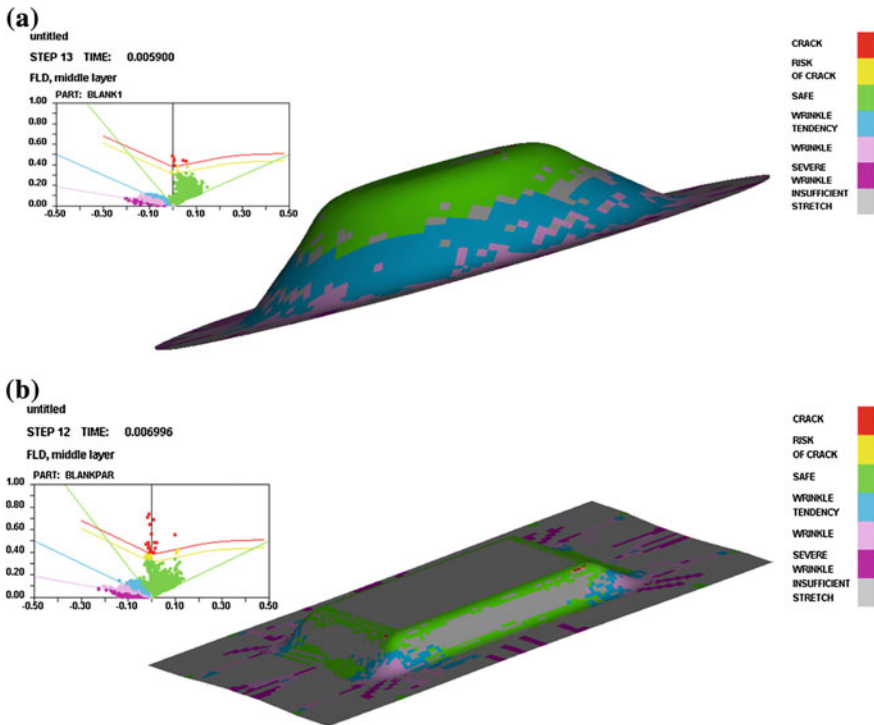


Fig. 25.2 Forming limit diagram. **a** Circular cup. **b** Square cup

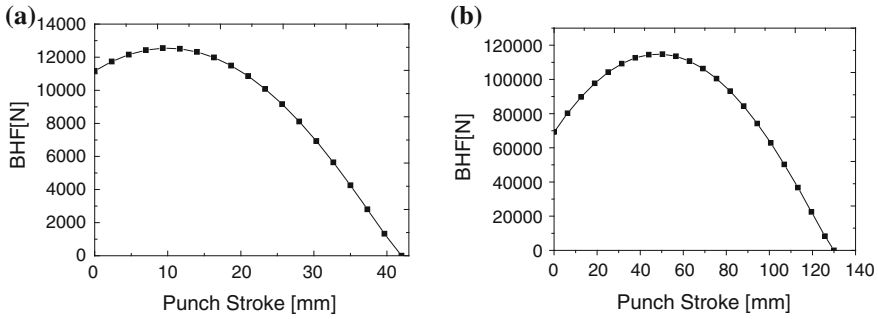


Fig. 25.3 Curve of the VBHF in deep drawing. a Circular cup. b Square cup

25.4 Numerical Studies of the VBHF

A lot of experiments proved that the VBHF technique can improve the drawability of metal sheet. For the VBHF technique, the VBHF engineering equation of the curve of minimum wrinkles is the most important. Based on the plastic theory and energy method, the theoretical mathematic models of BHF can be given as [5]:

$$Q = 1.5K \frac{y_0}{t} \times \frac{\pi r^2}{4} \times \frac{1}{n^3} (1 - \rho)^{1+n} \times \frac{\frac{\rho}{m} \left\{ \frac{1}{n} \left[\left(\frac{\rho}{m} \right)^n - 1 \right] - \ln \frac{\rho}{m} \right\}^2}{\left(\frac{\rho}{m} - 1 \right) \left\{ \frac{1}{n} \left[\left(\frac{\rho}{m} \right)^n - 1 \right] - \frac{1}{1+n} \left[\left(\frac{\rho}{m} \right)^n - \frac{m}{\rho} \right] \right\}} \tag{25.1}$$

where K is the strength-hardening coefficient, n is the strain-hardening exponent, t is the sheet thickness, $\rho = R_r/R_0$ denotes the deep-drawing phase, and $m = r/R_0$ expresses the deep-drawing ratio.

According to the variation rules of BHF in deep drawing, as shown in Fig. 25.3, a curve of the VBHF is designed for numerical simulation.

According to the variation rules of BHF, the calculated FLD of the VBHF is as shown in Fig. 25.4. It can be seen that the LDR of circular cup can reach 1.54, and the height of square cup improved from 19.8 to 28.5 mm.

25.5 Numerical Studies of the VPV Based on VBHF

Many research reports on the approach of VPV indicated that the VPV technology can improve the drwability of metal sheet [7]. The stamping process characteristic of curves can be optimized by using NURBS curve in the simulation, as shown in Fig. 25.5.

The new servo-flexible stamping technique of VBHF combined with VPV was proposed in our posted research of magnesium sheet stamping [6], which utilized to

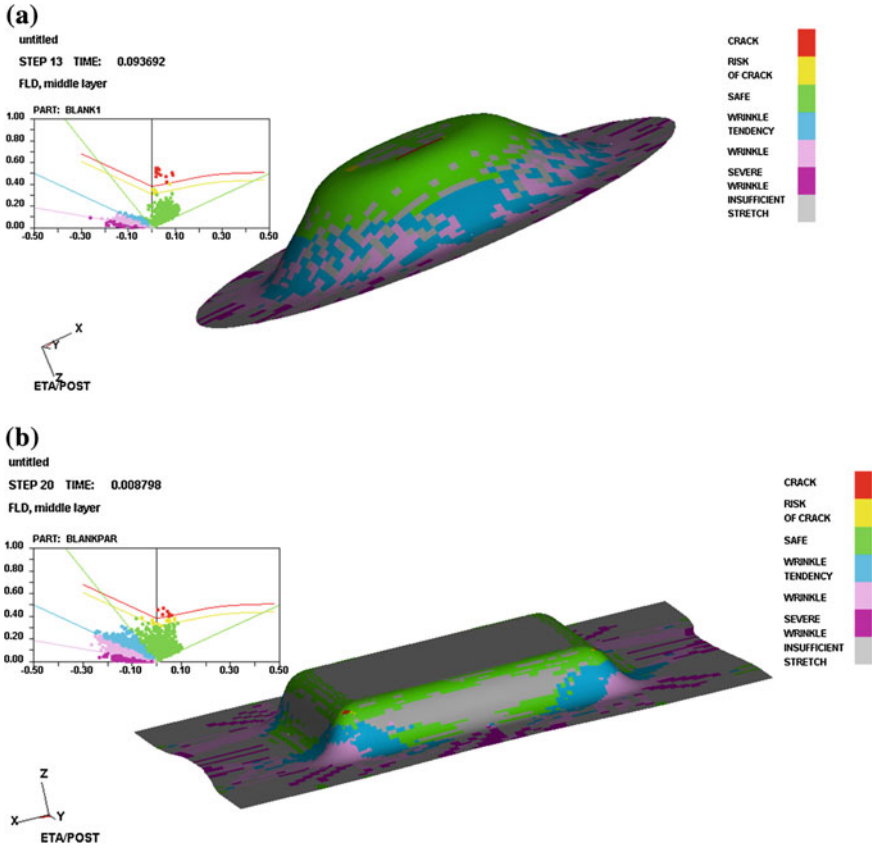


Fig. 25.4 Forming limit diagram. a Circular cup. b Square cup

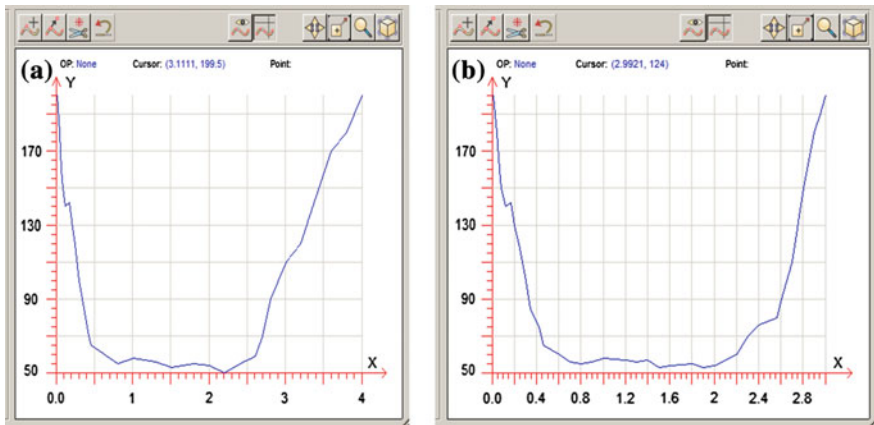


Fig. 25.5 The stamping process characteristic of VPV curves. a Circular cup. b Square cup

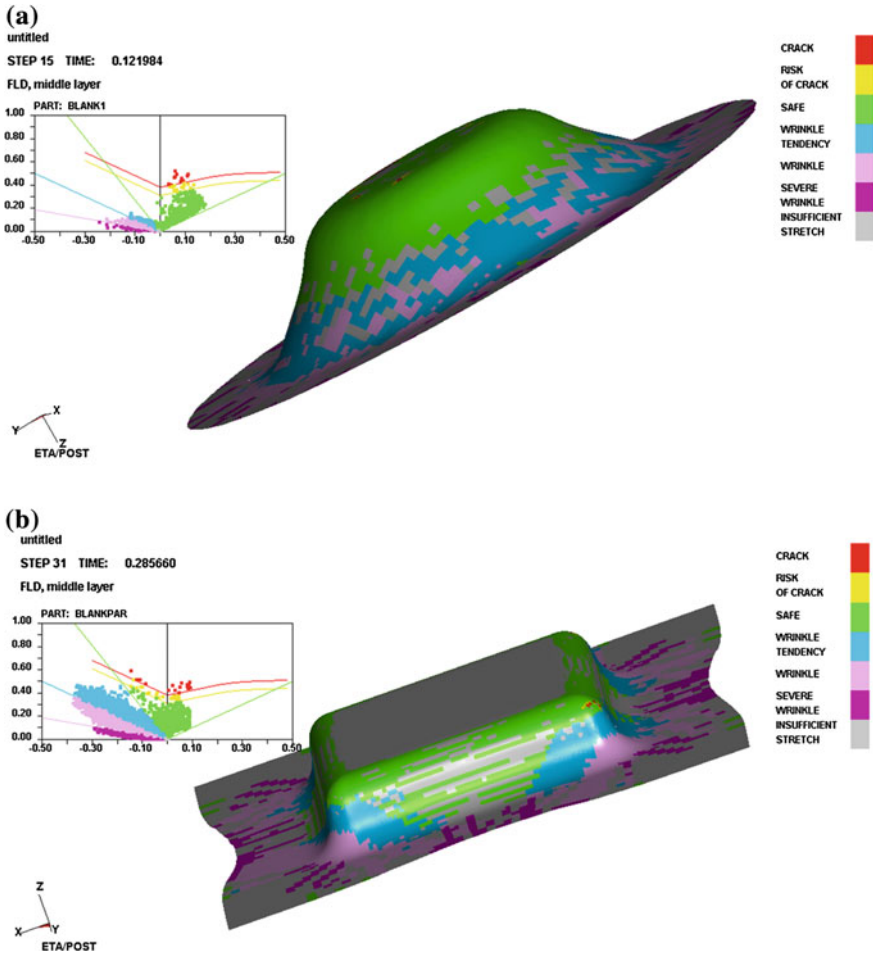


Fig. 25.6 Forming limit diagram. a Circular cup. b Square cup

implement the VBHF simultaneously with VPV and stepwise motion, and the LDR of magnesium sheet was improved observably. The FLD of aluminum sheet using the new stamping technique of VBHF combined with VPV, as shown in Fig. 25.6. It is revealed in Fig. 25.6 that the LDR of circular cup can reach 1.60, and the height of square cup improved from 19.8 to 39.8 mm.

Furthermore, the Al hood of one car of drawing process was simulated with the new technique. The FLD of Al hood was as shown in Fig. 25.7. It is revealed that the deepness of Al hood can be improved by about 30 %, using the new technology. Therefore, it can be predicted that the new servo-flexible stamping will become a new potential stamping process in the future.

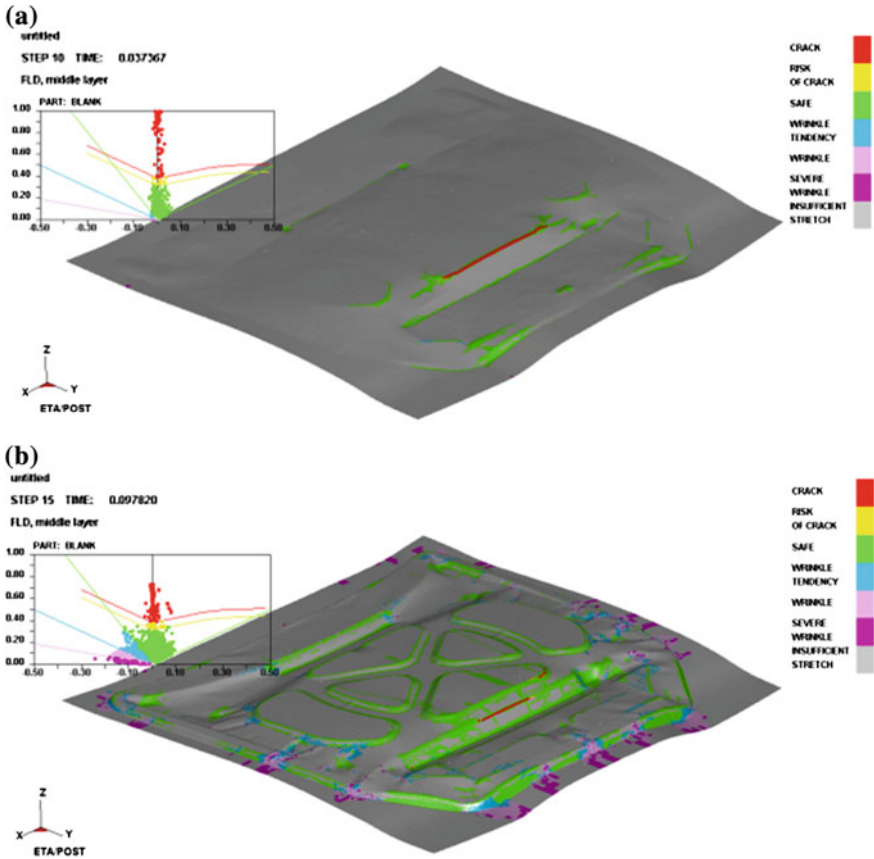


Fig. 25.7 Forming limit diagram. a Normal stamping. b The new technology

25.6 Conclusions

Based on the VBHF, a new technique of VPV was proposed. The simulation indicated that the new servo-flexible stamping can improve the deep drawability of Al sheet obviously. It is revealed that the limited drawing ratio (LDR) of Al circular cup was improved from 1.48 to 1.60, and the height Al square cup was improved from 19.8 to 39.8 mm, using the new technique of VBHF combined with VPV.

Finally, the Al hood of one car of drawing process was simulated by the new technique, and the results revealed that the deepness of Al hood can be improved by about 30 %.

References

1. Miler S, Zhuang L, Bottoema J, Wittebrood AJ (2000) Recent development in aluminium alloys for the automotive industry. *Mater Sci Eng A* 280:37–49
2. Semiatin SL, Frey N, Walker ND et al (1986) Effect of deformation heating and strain rate sensitivity on flow localization during the torsion testing of 6061 aluminum. *Acta Metall* 34 (1):167–176
3. Zhou JM, Qi LH, Chen GD (2006) New inverse method for identification of constitutive parameters. *Trans Nonferrous Met Soc China* 16(1):148–152
4. Yoshihara S, Manabe K, Nishimura H (2005) Effect of blank holder force control in deep-drawing process of magnesium alloy sheet. *J Mater Process Technol* 170(3):579–585
5. Chang QF, Li DY, Peng YH (2007) Experimental and numerical study of warm deep drawing of AZ31 magnesium alloy sheet. *Int J Mach Tools Manuf* 47:436–443
6. Liu Z, Xing S, Bao P, et al (2013) A new equation of load curve of critical wrinkles variable blank holder force in the warm deep-drawing of twin-roll cast mg sheets. In: *Proceedings of the FISITA 2012 world automotive congress* 199:11–22
7. Osakada K, Mori K, Altan T (2011) Mechanical servo press technology for metal forming. *CIRP Ann Manuf Technol* 60:651–672

Chapter 26

Analysis of the Assembly Dimensional Chain About Automotive Exterior Parts and Optimization of Tolerance Allocation

Changming Liang

Abstract The assembly effect of automotive exterior parts directly affects the automobile modeling design, and the gap and flush of automotive exterior parts are essential to evaluate assembly effect of automotive exterior parts. In the assembly relation of the machine, the assembly dimensional chain consists of relevant parts size or mutual position relation. The gap and flush of automotive exterior parts can be considered as a closing link of assembly dimensional chain, while the size and position relation of parts do influence the gap and flush, that should be understood as component link of assembly link. According to the basic principle of the mathematical statistics, the assembly dimensional chain should be calculated by statistical tolerance formula. In the four parameters, there are four different optimizing methods of tolerance allocation when three of them are stable. The analysis of assembly dimensional chain of automotive exterior parts should not be adopted into earlier designing stage, but also into later producing stage.

Keywords Automotive exterior parts · Gap and flush · Assembly dimensional chain · Tolerance allocation

26.1 Meaning to Study Automotive Exterior Parts Assembly Dimensional Chain

The assembly effect of automotive exterior parts directly affects the automobile modeling design. And the gap and flush of automotive exterior parts are essential to evaluate assembly effect of automotive exterior parts. Also, it becomes one important evaluating indicator for automotive quality. Generally, foreign mature auto-company owns a team responsible for preliminary design and production

C. Liang (✉)

Changan Auto Global R&D Centre, Changan Automobile Co. Ltd., Chongqing, China
e-mail: 332640385@qq.com

process control of exterior parts. In this paper, in view of assembly dimensional chain, the gap and flush of exterior parts were analyzed; and according to tolerance allocation, various solutions to reach the target were proposed.

26.2 Distribution Regularity of Automotive Exterior Parts Quality and Definition of Assembly Dimensional Chain

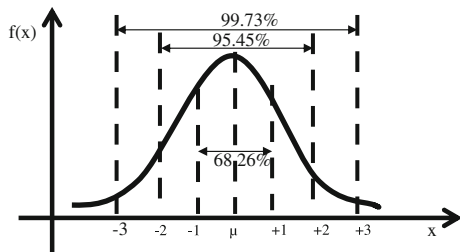
26.2.1 Normal Distribution Regularity of Auto Parts Quality

The distribution regularity of parts quality should be understood before researching the assembly dimensional chain of automotive exterior parts. Five elements should be considered in the producing process of auto parts; they are individual, machine, material, regulation, and circumstance. Every factor will affect the quality fluctuation of parts at last, but if it is under the normal fluctuation, as tiny waste, normal quality fluctuation of original material would not lead the fluctuation of final larger parts. This is so-called normal fluctuation. The distribution of statistic data approximately accords with normal distribution, when under the influence of normal fluctuation. As shown in Fig. 26.1, it features the peak in the middle and valley at both sides, and the left and the right are balanced and never meet the requirements. The parameters of normal distribution can be described by average value (mean value) and range (standard deviation). According to normal distribution, approximate 0.27 % of the area lies outside $\mu \pm 3\sigma$, so it can be deemed as a small probability event. There may be some unusual fluctuations that lead to fluctuation of quality date, if the area lies within $\pm 3\sigma$.

The parts in statistical process control can be described by a function, as follows [1]:

$$f(x) = \frac{1}{\sigma\sqrt{2\pi}} e^{-\frac{(x-\mu)^2}{2\sigma^2}}$$

Fig. 26.1 Normal distribution



$$\mu = \frac{\sum_{i=1}^N x_i}{N} = \frac{x_1 + x_2 + x_3 + \cdots + x_N}{N} \quad \sigma = \sqrt{\frac{\sum_{i=1}^N (x_i - \mu)^2}{N}}$$

Explanation should be taken here, the μ and σ cannot be got at actual measure, and they are mean to be in its totality. So, the σ used in actual working effectively is the s of small sample, and the N is the n of small sample. The function aforementioned can be expressed as below.

$$\bar{X} = \frac{\sum_{i=1}^n x_i}{n} = \frac{x_1 + x_2 + x_3 + \cdots + x_n}{n} \quad s = \sqrt{\frac{\sum_{i=1}^n (x_i - \bar{x})^2}{(n-1)}}$$

26.2.2 Evaluating Standard of Assembly Dimensional Chain Based on Automotive Exterior Parts Gap and Flush

The dimensional chain is close-sized group that consisting of interconnected dimensions during the machine assembling or parts machining [1]. Every size of dimensional chain is called link, including closing link and component link [1]. Closing link is the last link during machining or assembly; meanwhile, all the other links that affect closing links are named component link [1]. Component link includes increasing link and decreasing link [1]. When the other condition keeps invariable, increasing link is one component link that will increase the closing link when its size increase. Decreasing link is one component link that makes the size of closing link small when its size increases. In the assembly relation of the machine, the assembly dimensional chain consisted of relevant parts size or mutual position relation [1]. The closing link of assembly dimensional chain is the requirement of assembly precision or technical; in other words, it can be depicted with size or mutual position relation of finally formed parts. The gap and flush of automotive exterior parts can be considered as a closing link of assembly dimensional chain, while the size and position relation of parts do influence the gap and flush that should be understood as component link of assembly link.

26.3 Analysis and Calculation of Automotive Exterior Parts Assembly Dimensional Chain

The analysis and calculation methods of assembly dimensional chain about automotive exterior parts should be divided into positive calculation and inverse calculation [1]. Supposing the basic sizes and deviation of parts which have connections with gap and flush are known, the calculation process, making out the basic size and deviation of assembly precision, is positive calculation [1].

Supposing the basic size and deviation of assembly precision (closing link) are known, the calculation process, making out the basic size and deviation of parts, is inverse calculation [1]. It is used in the product design process, in order to confirm the size and the processing precision of parts. The basic size of closing link is the value of appearance gap and flush. The analysis process in this paper should be used at the design stage and in the practical production. To analyze and calculate assembly dimensional chain, there are two methods: One is extremum method and the other one is probabilistic method [2].

26.3.1 Extremum Method

Component link for assembly dimensional chain can achieve the assembly accuracy; this assembly method can be called swap method. The assembly dimension should be calculated by extremum method. The tolerance of all component links, which belong to dimensional chain, is equal to or less than the tolerance of closing link called assembly accuracy [1].

$$T_0 \geq \sum_{i=1}^n |\xi_i| T_i$$

where

- T_0 the tolerance range of closing link
- T_i the tolerance range of component link
- ξ_i the scaling factor of component link
- n the number of component links

According to liner dimensional chain: $|\xi_i| = 1$, the follow increasing link's coefficient is positive; decreasing link's coefficient is negative.

26.3.2 Probabilistic Method

Probabilistic method: The method permits that most of products will reach the requirement when assembled, and which save the process of selecting or changing the size or position during the assembly, is called interchange method. The process of completely interchangeable method is easy; but it is not easy to build the relation of closing link and component link, when the relation should be based on both maximum and minimum. It makes the parts assembling tough when the value of closing link is given, and each tolerant of component link is too strict. According to the basic principle of the mathematical statistics, firstly, the chance of extreme value in machining error is tiny; secondly, the situation that part deviation reaches the limit at the same time could be less likely to happen. So, the assembly dimensional chain should be calculated by statistical tolerance formula.

26.3.2.1 Standard Deviation of Closing Link

The following function will express the dimensional chain, when based on the truth that the most quality of dimensional chain’s component link conforms to the normal distribution. Supposing there is a functional relation between closing link A_0 and component link A_i , and A_0 is a function of A_i . Referring to the theory of probability method, the relation of individual random variable (component link) root mean square deviation σ_i and the sum of random variable (closing link) σ_0 ’s root mean square should be expressed as below [2]:

$$\sigma_0 = \sqrt{\left(\frac{\partial A_0}{\partial A_1}\right)^2 \sigma_1^2 + \left(\frac{\partial A_0}{\partial A_2}\right)^2 \sigma_2^2 + \dots + \left(\frac{\partial A_0}{\partial A_{n-1}}\right)^2 \sigma_{n-1}^2}$$

where

- σ_0 standard deviation of closing link
- $\sigma_1 - \sigma_{n-1}$ standard deviation of component link
- n number of dimensional chain
- $\frac{\partial A_0}{\partial A_1}, \dots, \frac{\partial A_0}{\partial A_{n-1}}$ each one is the scaling factor of ξ_1, \dots, ξ_{n-1}

This function should be expressed as [2]:

$$\sigma_0 = \sqrt{\sum_{i=1}^{n-1} \xi_i^2 \sigma_i^2}$$

If both component link’s deviation and closing link’s deviation follow normal distribution, while the distribution is equal to the tolerance range, $T_i = 6\sigma_i$, there is a relationship between closing link tolerance and component link tolerance. There is a need to explain here, the tolerance range is the range of finished parts tolerance, instead of design tolerance [2].

$$T_0 = \sqrt{\sum_{i=1}^{n-1} \xi_i^2 T_i^2}$$

26.3.2.2 The Average Deviation of Closing Link

When the deviation of component link is in a situation of symmetrical distribution, the average Δ_0 of closing link is as below [2]:

$$\Delta_0 = \frac{EI_0 + ES_0}{2} \quad \Delta_0 = \sum_{i=1}^{n-1} \xi_i \Delta_i$$

where

- Δ_i is the average of component link
- EI_i is the lower deviation of component link
- ES_i is the upper deviation of component link
- EI_0 is the lower deviation of closing link
- ES_0 is the upper deviation of closing link

26.3.2.3 The Extreme Deviation of Closing Link

The extreme deviation of component link [2]:

$$ES_i = \Delta_i + \frac{T_i}{2} \quad EI_i = \Delta_i - \frac{T_i}{2}$$

The extreme deviation of closing link [1]:

$$ES_0 = \Delta_0 + \frac{T_0}{2} \quad EI_0 = \Delta_0 - \frac{T_0}{2}$$

26.4 The Optimized Tolerance Allocation of Automotive Exterior Parts

The analysis of assembly dimensional chain of automotive exterior parts should not be adopted into earlier designing stage, but also into later producing stage. In order to optimize the design, which contains the basic size and deviation of relevant dimensional chain parts, assembly dimensional chain should be calculated repeatedly. Those assembly dimensional chains, which cannot meet the designing demands, should be taken into analysis during the following producing. To reach the designing requirements, these steps should be considered: counting quality date, optimizing the tolerance range, and average of each assembly parts. Redesigning the assembly dimensional chain should be taken, even there are a few parts that cannot be adjusted. In conclusion, parameters, which affect the gap and flush (closing link) of automotive exterior parts, include “ n ” (the number of assembly dimensional chains), “ T_i ” (the range of each component links’ tolerance range), “ Δ_i ” the average of each component links, and “ ξ_i ” the scaling factor of each component links. These parameters together have an effect on “ T_0 ” (the tolerance range of closing link) and “ Δ_0 ” (the average of closing link). In the four parameters, there are four different optimizing methods of tolerance allocation when three of them are stable. The four methods are collectively called optimization of tolerance, because they are referring to the point of average and tolerance range.

26.4.1 The Change of Dimensional Chain Number—Reduce Component Link and Cut Down the Dimensional Chain

The tolerance range should be decreased, when some component links have been reduced or current numerous component links have been taken placed by minority component links. This kind of optimization scheme for dimensional chain has been mainly adopted into earlier design stage and should be taken as priority, when it finds out that fewer links meet the requirement after the analysis of assembly dimensional chain.

For example, as well known, the tailgate of a two box car has been assembled on the back of the car, and it comes out that there are two designing schemes for tailgate locating—one is to make the corresponding installing hole of tailgate hinge as the locating hole; the other is to locate the gap of tailgate and head cover directly, according to the tooling plan. There are two scheme tables, as shown in Tables 26.1 and 26.2, and the tolerance of tooling precision could be ignored because it shows a little high by here. It comes out a result clearly that the scheme has been adopted below is better, by the reason of the less “*n*” (the tooling scheme numbers of dimensional chain links).

Table 26.1 The change of dimensional chain number

Num	Dimensional chain component link	T_i		$6\sigma_i$	Δ_i	ξ_i
		ES ₀	EI ₀			
1	The tailgate hinge locating hole on body-in-white	+1.5	-1.5	3.0	0	1
2	The tailgate hinge fix nut hole	+0.5	-0.5	1	0	1
3	The nut position on hinge	+0.5	-0.5	1	0	0.7

Table 26.2 Scheme tables

Num	Dimensional chain component link	T_i		$6\sigma_i$	Δ_i	ξ_i
		ES ₀	EI ₀			
1	Body-in-white that matching the tailgate	+1.5	-1.5	3.0	0	1
2	The tailgate that matching the body-in-white	+0.5	-0.5	1	0	1

26.4.2 T_i (The Tolerance Range of Component Link)—Reduce the Range of Tolerance Range of Component Link

In order to reduce the fluctuating range of final exterior parts’ gap and flush, when the number of component link is not allowed to reduce, to diminish the tolerance range of parts, which changes 6σ (the tolerance range of individual component

link), could reach the goal. This method is often used for meeting the higher requirement of parts' precision. As example mentioned above (Table 26.2), calculated T_0 (final tolerance range of closing link) is 3.16, and Δ_0 (average of closing link) is 0. As ± 1.58 (the range of tolerance range) is still too large, the only way to meet the designing requirement is to cut down the range of component link's tolerance range. If the tolerance of component link 1 has been changed into ± 0.8 , the tolerance range of closing link then has been increased to ± 0.94 , and the designing requirement could be reached at last, as shown in Table 26.3. There are many situations suit for this kind of scheme, as the situation that when in the earlier designing stage, as the situation that the tolerance range of produced parts should be improved. This kind of scheme, as an optimizing measure, asks for higher precision, strict controlling process and more cost.

Table 26.3 Scheme tables

Num	Dimensional chain component link	T_i		$6\sigma_i$	Δ_i	ξ_i
		ES ₀	EI ₀			
1	Body-in-white that matching the tailgate	+0.8	-0.8	1.6	0	1
2	The tailgate that matching the body-in-white	+0.5	-0.5	1	0	1

26.4.3 Δ_i (Average of Component)—Tolerance Range's Range Matching of Component Link

When T_i (the tolerance range of component link) is unchangeable, and the numbers of links are unable to reduce, there is a third optimizing scheme. For producing qualified parts as more as possible, and for making Δ_0 (average of closing link) close to the theoretical value, Δ_i (average of component link) should be deviated. During this kind of scheme, every distribution of component links should be analyzed. This optimizing measure is mainly concentrated on actual producing process. For example, during assembling, deviation of the cumulative, which explained as unqualified problem, shows up when qualified parts have been assembled, should be fixed by optimization of tolerance allocation method. The specific practice is to calculate the dimensional chain repeatedly by counting up the quality of every parts of component links. In view of cost, time and process, it suggests that only one part, which one is easy to modify, should be modified, after assuring which parts could be revised. For example, Δ_n is a revisable part, then the value, average of the part needs to deviate, should be calculated by Δ_0 (average of closing link) subtracting other parts' deviation of the cumulative value. This scheme is useful in producing process.

Table 26.4 The analysis on the dimensional chain

Num	Dimensional chain component link	T_i		$6\sigma_i$	Δ_i	ζ_i
		ES ₀	EI ₀			
1	Tolerance distribution of spoiler	+1.0	0	1.0	0.5	1
2	Tolerance distribution of tailgate’s spoiler base	+1.0	0	1.0	0.5	1
3	Tolerance distribution of hinge base	+0.3	0	0.3	0.15	0.7
4	Tolerance distribution of tailgate’s spoiler base (tailgate’s standard, no effect)	0	0	0	0	0
5	Tolerance distribution of white body’s hinge base	+1.0	0	1.0	0.5	1
6	Tolerance distribution of white body and spoiler	0.6	0.2	0.4	0.4	1

$$\Delta_n = \Delta_0 - (\Delta_1 + \Delta_2 + \dots + \Delta_{n-1})$$

As shown in Table 26.4, the analysis on the dimensional chain of hatchback car spoiler and side gap explains the distribution by practicality.

The formula, average of closing link, is like this: $\Delta_0 = 0.5 + 0.5 + 0.15 + 0 + 0.5 + 0.4 = 2.05$. When the average deviation of the gap is 2.05, which cannot meet the designing requirement ± 1.5 , some parts should be revised. As the spoiler is easy to modify, it becomes to an adjustment item at last. The average deviation of revised spoiler could be worked out 1.55, and scaling factor is -1 , by using formula “ $\Delta_n = \Delta_0 - (\Delta_1 + \Delta_2 + \dots + \Delta_{n-1})$,” when Δ_n is known as the average of revised spoiler. It comes out that the spoiler is a decrease link.

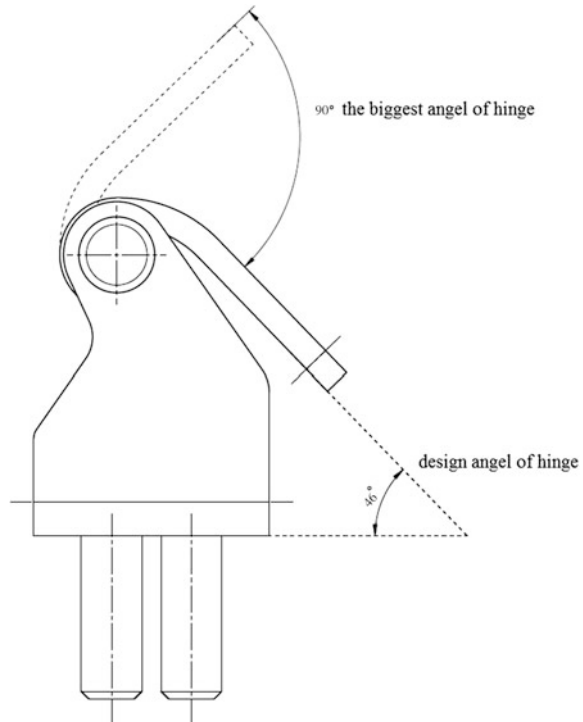
26.4.4 ζ_i (Scaling Factor of Component Link)—Optimization of Component Link Scaling Factor

In the stage of designing, ζ , the scaling factor of component link should be revised in most cases. The optimization of ζ involves the revising assembly structure usually. Take an instance, as shown in Table 26.5.

Table 26.5 Scaling Factor of Component Link

Num	Dimensional chain component link	T_i		$6\sigma_i$	Δ_i	ζ_i
		ES ₀	EI ₀			
1	The tailgate hinge locating hole on body-in-white	+1.5	-1.5	3.0	0	1
2	The tailgate hinge fix nut hole	+0.5	-0.5	1	0	1
3	The nut position on hinge	+0.5	-0.5	1	0	0.7

Fig. 26.2 The angle of tailgate hinge



The scaling factor of dimensional chain 3 is 0.7, which is calculated by the angle 46° of tailgate hinge, Fig. 26.2. To optimize the scaling factor ζ , increasing the angle should be done, and then, the tolerance range of closing link gets influenced.

26.5 Conclusions

The gap and flush of automotive exterior parts are essential to measure the quality of automotive exterior parts. The analysis and calculating of automotive exterior parts gap and flush should become a piece of systematic work. During the analysis of assembly dimensional chain, when designing, it has to do well with the tolerance distribution, as well as to optimize the affected parameters as possible. In practice, the assembly dimensional chains, which fail to meet the designing requirement, should be analyzed and calculated. The tolerance optimization is significant and specific, as parts producing always cannot meet the designing demand. All these should be done by referring to the factors: time, cost, and so on.

References

1. Wang X (2007) Technology of mechanical manufacture. China Machine Press, Beijing
2. Xu X (2005) Interchangeability and technological measurement. Hunan University Press, Hunan

Chapter 27

The Research of Dimensional Design “2MM Project” System and the Key Role in the Self-owned Vehicle Platform

Zhihan Zhou, Peng Tan, Changming Liang and Xiangfei Wang

Abstract The related concepts of dimensional design “2MM” engineering of the automotive products are introduced. The dimensional design “2MM” engineering is the foundation of vehicle dimensional manufacturing “2MM” project. This paper introduces the route and method of vehicle dimensional manufacturing “2MM” project in the auto product design process under the current developmental model of Chang An company and the functional attributes of vehicle dimension; it also emphasizes the key role that played by vehicle dimensional design “2MM” engineering in the own brand car company for building the car platform, finally through a series of problems, cause the related thinking, for example system construction, personnel training, in the field of vehicle dimensional development in the own brand car company.

Keywords 2MM · Vehicle · Car dimension · Dimensional engineering · Platform

27.1 Introduction

27.1.1 Introduce Automobile Products About 2MM Project

The automobile product’s 2MM project is used for automobile product’s continuous improvement indicator (CII), also six times variance “6 σ ” to control body-manufacturing quality, to use the most economic cost of manufacture, improving the overall quality of automobile products. We should pay attention to CII as this is not the measurement data actual deviation of body-manufacturing quality but the comprehensive evaluation about the body-manufacturing size stability index. The automobile industry 2MM project must take the enterprise other aspects of

Z. Zhou (✉) · P. Tan · C. Liang · X. Wang
Changan Auto Global R&D Centre, Changan Automobile Co. Ltd.,
Chongqing 401120, China
e-mail: zhouzh@changan.com.cn

management under advisement systemically, From product development design to manufacturing and from the enterprise internal management to enterprise external environment Must form a kind to 2MM project as the main body size products quality management system. At present, foreign automobile industry is involved not only in the application of vehicle manufacturing about 2MM project, but also in parts manufacturing application of 2MM project. To sum up, The automobile products 2MM project is an important content of the quality management system, So how to form complete accurate evaluation index about finish car and body and parts take the enterprise other aspects of management under advisement systemically used to effectively guide the auto product size manufacturing 2MM project development and this is what 2MM project to solve the problems also is the key introduced in this paper.

27.1.2 The Importance of Dimensional Design 2MM Project

Long-term since, the product design process to the dimension of the relevant design is based on the experience to develop. In order to validate the rationality of the design, we must put in more time, energy and money at the trial production process. Because the rationality of the design of dimensional tolerance design in the design stage is without effective guarantee of verification, the trial production process will expose a lot of manufacturing size deviation problem and die; fixture and check fixture were repeated. It is difficult to meet the delicate process level about the joint venture. In order to obtain better dimension quality, we introduce the various improvement measures during the put into production stage such as parts coordinate fixture (PCF) and unit checking fixture (UCF), but price expensive fixture can barely find problems and not prevent problems. This is the importance of the scientific and rationality about dimensional design. For this, today in domestic projects, dimensional engineering being recognized as the development of the majestic, we put forward the concept of dimensional engineering to reduce and avoid design flaws and is used to effectively support the development of 2MM project.

27.1.3 The Development of Dimensional Design 2MM Project to Promote Established the Automobile Platform

At present, domestic self-owned vehicle is in the stage of establishing a platform of the automobile companies that want to establish core competitiveness; the one important part is to establish automobile platform. About automobile platform, the domestic automobile enterprise pay more attention to the finish car performance or function, less consider manufacturing process. This is due to the objective environment and traditional knowledge. For example as long as the investment fund,

who can be made little imagine, foreign car companies who have hundred years of experience in making cars now have lean accumulation process. Especially domestic machinery-manufacturing industry level was nowhere foreign counterparts, how can we catch up? So in the objective environment, the better dimension of a car is only accidental, because we cannot copy and be in accordance with the same standard globalization put into production. Based on the delicate process, this paper will expound evaluation automobile of good platform, and how to establish good automobile platform. We must abandon the old ideas about technology that can solve all dimensional quality problems, from the design phase to dimensional engineering design company, to establish good automobile platform.

27.2 The Understanding of the System Car Dimensional Attributes

If we stand in the user’s angle, he can perceive about gap, leaking, technics rough, buckling of ring or perceived quality and so on; If we stand in professional designer’s angle, he is concerned about whether we can reach the system performance indicators and functions; if we stand in the finish car angle, the object will develop to a finish car dimensional integration design and control of the category. Though we will do the finish car dimensional integration design and control well, we need to understand that the finish car dimensional integration design and control attribute first. At present, dimensional engineering team about CA has obtained a better effect in the dimension of the finish car and research aspects of knowledge attribute.

According to the function of finish car, dimension can be divided into the appearance dimensional attributes, the function dimensional attributes and the assembling dimension; according to the object category, it can be divided into the finish car dimensional attributes, the body in white attributes, the systematic of dimensional attributes and the parts of dimensional attributes. According to the manufacturing process, this can be divided into the finish car-link dimensional attributes of OEM (for example welding assembly and general assembly) and supplier-link dimensional attributes. The purport of research for the finish car attributes is that we will do the size of the finish car attribute classification analysis and Select the key dimension, the important dimension, the usual dimension and find out the most basic way to deal with to differentiated designs and controls.

This is a continuous process about researching and meeting the finish car dimensional attributes; at the same time, this is a cross subject similar quality perception. The work’s development can help us establish manufacture dimensional goal about each finish car platform. The goals of finish car dimensional engineering are used in the process of research and manufacturing. The goals of finish car dimensional engineering are constant as a whole and balance of the process; we need to consider about modelling, construction, costing, function, assign, process

and so on. The development of the dimensional design 2MM project is to complete target about decomposition finish car dimension at model design process. It can be output dimensional engineering design material and target file of systematic, complete and scientific at the phase of put into production start-up. It can promote the development of dimension manufacturing 2MM project.

27.3 The Development of Dimensional Design 2MM

27.3.1 The Dimensional Engineering in Styling and Programme Phase

When it comes to the factors that influence automobile styling, mechanical engineering, aerodynamics, ergonomics and fashion aesthetics are usually considered to be the primary research object all the time. But with the increasingly high demand for automotive products and increasing attention to the appearance details, the delicate process is gradually becoming an important factor of the vehicle shape. Owing to the growing contradictions between styling, manufacturing processes, cost and structural design, the styling work faces a serious challenge. How to get a higher appearance quality with lowest cost, the simplest process and general structural design becomes a new subject of automobile styling design. The achievement of delicate process is a prerequisite to raise appearance aesthetic quality, while the development of systematized dimensional engineering ensures the delicate process.

We can move the dimensional engineering feasibility analysis and dimensional tolerance analysis forward to the modelling phase and pre-assess the deviation of manufacturing segment in modelling conceptual, rendering and phase main sectional plane phase. The main work of dimensional engineering in model stage is to evaluate the appearance of aesthetic quality and the susceptibility of internal-external gap and offset dimension. At the same time, with the platform design theory, the development of the familial and standardized design can promote the own brand automotive enterprises to gradually form the familial style. Compared to the mature companies in the automotive products, they all have adopted a familial model and series of gap and offset section to ensure the appearance of aesthetic quality, reduce the visual susceptibility and weaken the poor aesthetic quality caused by model and potential manufacture dimensional deviation. Especially to the middle- and low-grade car, it must proceed from the low-cost perspective, give consideration to aesthetics and manufacturability and get a good manufacturability in appearance in order to reduce the difficulty in moulding and assembly of the parts, reduce the difficulty and complexity of process control, reduce the accumulated error caused by the manufacturing segment and avoid the fizzle caused by mismanagement in the large-scale production stage.

27.3.2 The Development of Dimensional Engineering in Engineering Design Phase

The development of dimensional engineering in our country almost started with engineering design phase. Increasingly, enterprises begin to place a great deal of importance on dimensional engineering design in engineering design phase. Dimensional engineering in engineering design phase include three parts: set up an objective of vehicle dimensional engineering, dimensional tolerance design of each component and dimensional tolerance-integrated control of vehicle dimensional engineering. The accurate definition of the objective of vehicle dimensional engineering is a systematic project which also represents the level of awareness of OMEs and dimensional engineering developing personnel of vehicle dimensional property. The objective of vehicle dimensional engineering is the final objective of vehicle dimensional development, as mention above, which is composed of the target of vehicle appearance dimension, vehicle performance dimension, vehicle assemble dimension and vehicle evaluate dimension.

The definition of the objective of vehicle dimension, for own brand automotive enterprise, is a continuous process that needs refinement and improvement all the time. Vehicle dimensional development in engineering design stage is a process of effective decomposition to the objective of vehicle dimension. How to verify the accuracy of the objective formulated, and how to evaluate the rationality of product structure design, process plan, the parts datum and tolerance strategies, in addition to recurring to the existing mature design experience, dimension chain calculation verification is also adopted more often. Dimensional engineering design verification tools have been widely used in automobile design and development process. Tolerance analysis of one-dimensional chain has been widely used in mature auto companies in North America for a long time. As we all know, automobile manufacturing is a complex process, from single piece to unit assemblage, each manufacturing link is likely to lead to tolerance accumulation. Tolerance analysis of one-dimensional chain also has limitations, especially for the automobile body that has complex surface and sub-block. There are two reasons: the first reason is that this analysis can only decompose the dimensional chain in one direction; but automobile parts are almost irregular so that the discrepancy in one direction may be caused by several directions. The second reason is that tolerance analysis of one-dimensional chain requires engineers to master the mature experience and skills. With the application of computer, more and more enterprises begin to use the computer-aided method, apply Monto Kano algorithm and introduce three-dimensional tolerance analysis methods to verify the dimensional chain. This method is more intuitive, and make up for the disadvantages of one-dimensional tolerance analysis, such software, for example, 3DCS, VIS VSA, and CETOL, has been widely applied. With the development of technology, the solutions for flexible assembly deformation and welding assembly deformation are gradually formed, which also lay a good foundation for “2MM” project of dimensional design.

The complete vehicle dimensional evaluation system has not yet been established in the product design stage, so that the domestic own brand automotive enterprise does not have the vehicle dimension-integrated development capabilities, and the vehicle dimensional evaluation is usually put into the start-up phase and the mass production stage. With the mastery of one-dimensional chain analysis and three-dimensional tolerance simulation analysis capability, Chang An has basically established the vehicle dimensional evaluation system in product engineering stage, namely vehicle dimension-integrated control capability. In order to make vehicle dimensional development to be a closed loop in design phase, the evaluation of vehicle appearance dimension, vehicle performance dimension and vehicle assemble dimension must be finished before design data are congealed. The following files that form the database and deviation model of vehicle dimensional tolerance can be outputted through the systematized design and integrated development of dimensional project; these include the complete dimensional control strategy, product structure strategy and linchpin process strategy of each system, the tolerance objective of BIW dimensional control point, the datum, and dimensional and GD&T tolerance of parts. This series of documents direct the structure design and technology development of body, while they can also direct the frock development and dimensional development. If we bring the evaluation targets of vehicle dimensional manufacture “2MM” project into the design phase, such is vehicle dimensional design “2MM” project. The development of vehicle dimensional design can help us to realize the difficult and focal point in manufacture process more accurately; this also can make the manufacturing process more pointed and guiding and have a definite target. The concrete method is as follows.

27.3.3 The Development Measure of Automobile Dimensional Design “2MM” Project

The all-process dimensional engineering analysis relies on the dimensional deviation 3-D dimensional simulation analysis and dimensional SE means. In modelling stage, we can use dimensional chain method to promote the perception quality.

In engineering design phase, this can be used to direct the locating datum strategy design of the parts, raise the level of precision of dimensional and GD&T design; we can also evaluate and control vehicle and BIW dimensional deviation design. This can be used to raise the level of precision vehicle and white body dimension continually in start-up phase and the mass production stage (Fig. 27.1).

The internal and external offset size tolerance simulation analysis, base on the externality style, the dimension defect sensitivity and perceptive quality, combined with the industry delicate craft level, the internal and external offset size tolerance design and size deviation 3-D simulation work can verify the feasibility of body structure design, assembly benchmark of part, the rationality of tolerance and the

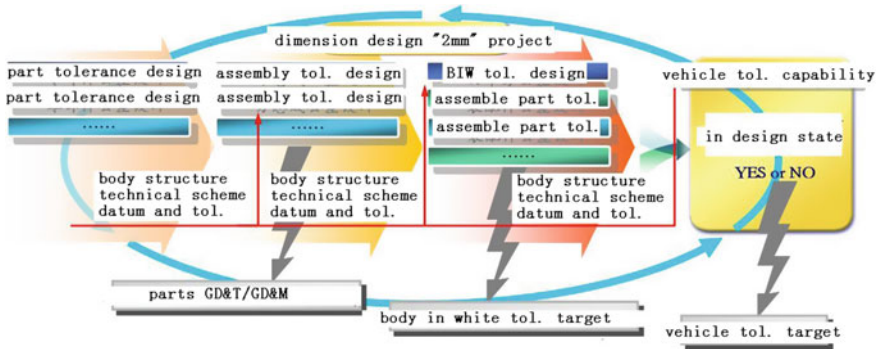


Fig. 27.1 The implementation street map of vehicle dimensional design “2MM” project

assembly process strategy, and identify the key structure. Key parts and the key feature sizes can influence the stability of internal and external broken size (Fig. 27.2).

The automobile assembly performance dimensional tolerance simulation analysis is based on the key assembly size, which can ensure the main vehicle performance, such as sealing size, engine assembly size, chassis control points size, four-wheel location parameters, important man-machine and regulations such as, dimensional deviation 3-D simulation technology can be used to develop the top-down assembly dimensional analysis of vehicle, BIW and parts, verify the feasibility of body structure design, assembly benchmark of part, the rationality of tolerance and the assembly process strategy, develop the fine design work of size tolerance of BIW and parts and identify the key structure, the key parts and the key feature sizes which can influence the stability of the automobile assembly performance dimensional tolerance (Fig. 27.3).

Simulation analysis of BIW dimensional tolerance, BIW is the carrier of vehicle assembling and the foundation of vehicle delicate technology and vehicle function; BIW multi-operation are composed by hundreds of impulse welding parts, which are assembled and welded by many processes. Simulation analysis of BIW dimensional

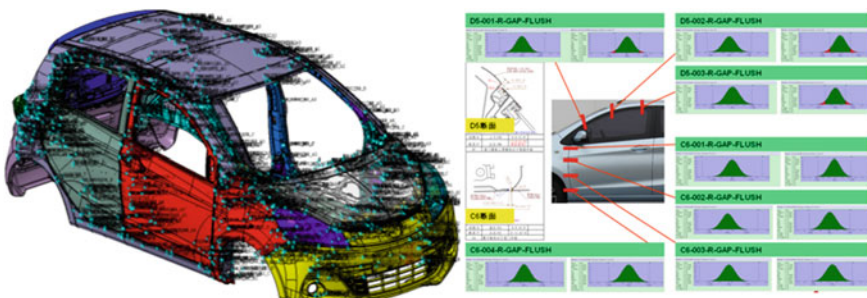


Fig. 27.2 The internal and external offset size tolerance simulation analysis

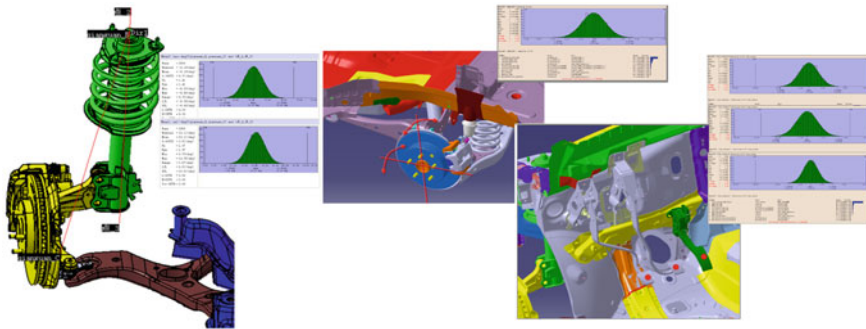


Fig. 27.3 Vehicle performance dimensional tolerance simulation analysis

tolerance can effectively direct the design of BIW dimensional tolerance and guarantee the realization of assembling function in design phase. Dimensional deviation 3-D simulation technology can be used to develop the top-down assembly dimensional analysis of vehicle, BIW and parts, verify the feasibility of body structure design, assembly benchmark of part, the rationality of tolerance and the assembly process strategy, develop the fine design work of size tolerance of BIW and parts, and identify the key structure. Key parts and the key feature sizes can influence the stability of internal and external broken size (Fig. 27.4).

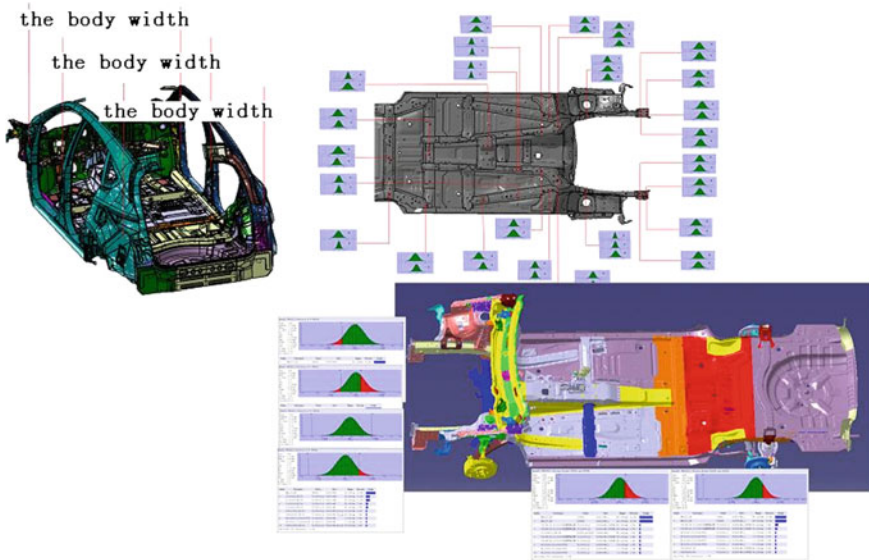


Fig. 27.4 Simulation analysis of BIW dimensional tolerance control points

Chang An has already basically established the deviation simulation analysis system of vehicle internal-external gap and offset dimension and vehicle main function dimension, mastered the deviation simulation analysis capability of BIW assemble dimension that has been already used in the projects and mastered the capability of vehicle dimensional design “2MM” project which can be used to direct the development of vehicle and parts dimension manufacture “2MM” project.

27.3.4 The 3-D Simulation of Dimensional Deviation Analysis Example

Chang An makes use of the 3-D simulation tolerance analysis software of USA DCS Inc, which is based on the CATIA software environment (hereinafter referred to as 3DCS). 3DCS can simulate the process of the spare part welding and assembling. By giving the spare part tolerance and the number of welding and assembling, we can get the tolerance of the measure point, distance, angle and so on.

Below, we use the 3DCS analysis of the engine parameter as an example, and introduce the process of the 3DCS analysis.

The input of the 3DCS analysis needed is as follows: (1) 3-D data, (2) the main location point of the spare part, (3) the particular tolerance of the spare part, (4) the process of the welding technological process and the gripping device information and (5) the measuring point of the BIW (Fig. 27.5).

The output of the 3DCS analysis included is as follows: (1) the measuring point tolerance distribution map, (2) the measuring point mid-value offset, (3) the measuring point tolerance impact factor and their percentage, (4) the geometrical factor of the tolerance and so on. According to the output, we can analyse the reason for the measuring point tolerance overproof, by means of optimizing the assemble sequence, technological process, product structure, the main location point of the spare part, tolerance grade, and so on, reduce the susceptibility and the geometrical

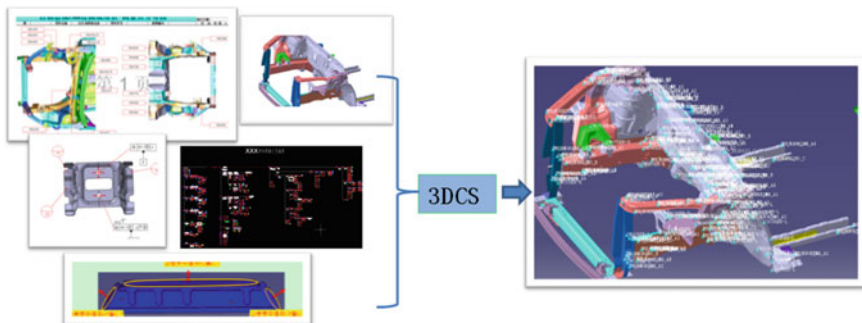


Fig. 27.5 Sketch map of the 3DCS modelling

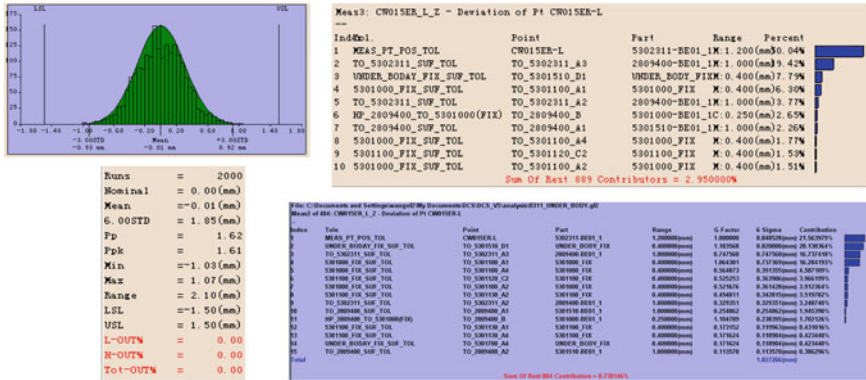


Fig. 27.6 Sketch map of the 3DCS output

factor of the tolerance source or decrease the number of the dimensional chain. To make the tolerance achieve the designing requirement simultaneously, request the product engineers and the process engineers to execute the optimized programmes (Fig. 27.6).

27.3.5 The Programme and Implementation of Dimensional Measurement System

In the process of dimensional design and production of vehicle and parts, the systematic dimensional measurement planning is a support of dimensional deviation evaluation of parts. The final and primary temporary lodging of vehicle dimensional measure system is the measuring points of vehicle, BIW and parts. The rich experience of measuring system programme is essential to the dimension measuring points design, and this can guarantee the dimension of vehicle, BIW and parts to be evaluated effectively and confirm the measuring point quantity and position rationally; at the same time, the cost also should be considered. The classification, progressive and step-by-step design philosophy of dimension measuring point corresponds to each dimension and development and management phase, such as full dimension measuring point in mould debugging phase, dimension measuring point in production phase and dimension evaluating measuring points of process control. And in the second, it is the application of dimension testing instrument, the checker is applied prominently to dimension measuring of body parts, while CMM is not commonly used at this stage, but with the innovation of detection technology, more and more advanced measuring equipments continue to be applied in the automotive industry, for example laser rang finder, white light scanner, open checker, synthetical matching sample holder and function primary model, etc.

27.3.6 Establish the Effective Feedback Mechanism of Manufacture Dimensional Deviation Data and Design Dimensional Tolerance Model

It is helpful to advance the systematized implementation of manufacturing “2MM” project by gradually establishing the database management system of dimensional discrepancy of OMEs and supplier and change the situation to make the paper as a carrier to manage the dimensional measurement date. The daily control and prewarning system of the dimensional discrepancy, which is concerned with dimensional tolerance database and tolerance capability model, can quickly and effectively solve the dimensional quality questions in the production process, get feedback of the design, promote the development of dimensional design “2MM” project and assure the first design is the right one (Figs. 27.7 and 27.8).

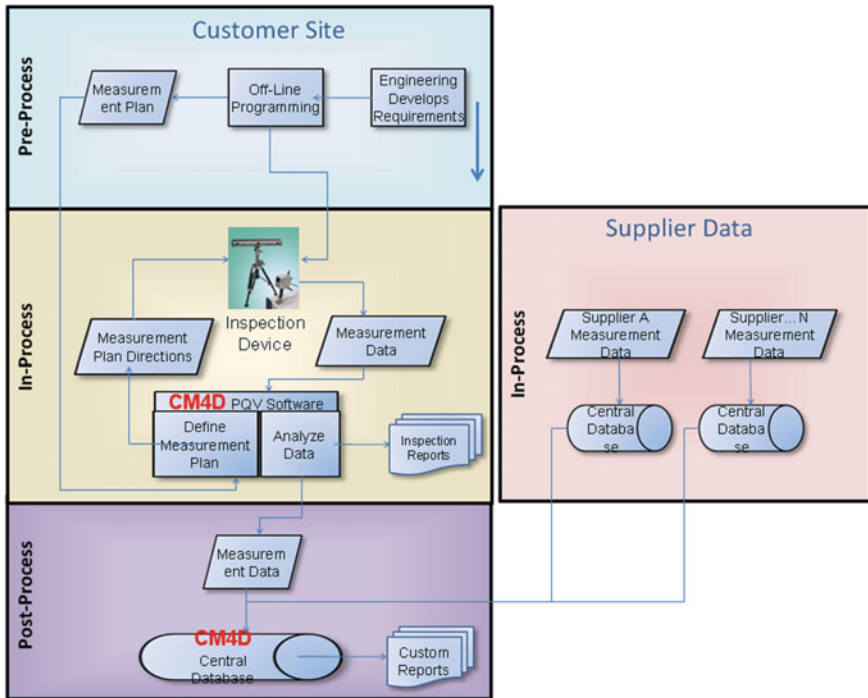


Fig. 27.7 CM4D dimensional management platform

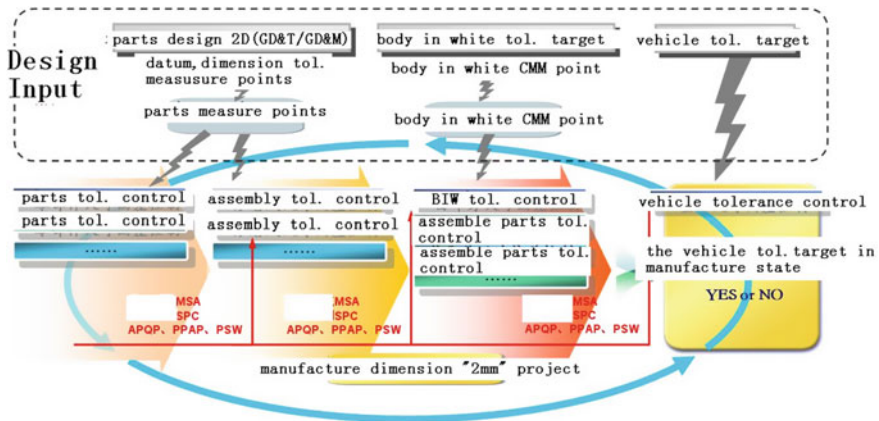


Fig. 27.8 The implementation map of vehicle dimensional manufacture “2MM” project

27.3.7 Chapter 3: The Key Role of Models Platform Building Process Dimensional Design “2MM”

In earlier years, some enterprise started car manufacturing industry, completely copy matured overseas models, but out of manufacture vehicle size quality is acceptable, the reasons for the size of the vehicle is not relevant design all-round development, from the deep analysis, reading for only good structure scheme (data), with no corresponding system of the technology strategy, spare parts benchmark and tolerance strategy, dimension check strategy, produce “don’t change the little wrong, change the big mistake” phenomenon, from which we can see that system to carry out the size of the importance of engineering design. At present, the domestic-independent brand automobile enterprise is mainly divided into three categories: the first kind is the former, the second is vehicle design and produce depend on overseas company, temporary does not have the size integrated design ability. Relegated to the various types of the manufacturers have relatively typical representative models, from the delicate process up evaluation, has its distinct characteristics. To be sure that the individual models of the car to world-class large force levels, this is just from the user angle to evaluate, but from automakers level, whether you can do it the global production, remote replication, this model can provide a full range of models for subsequent reference for design of, or can rise to the height of the platform vehicles, suspect.

At this stage of the new models manufacturing investment accounts for manufacturers of relatively high phenomenon in the independent auto enterprise are relatively stability, most of the manufacturing defects and size have cost the rectification of the no responsibility to design in the link with. Application size design “2MM” engineering scientific means the size, the performance level, the appearance of the size and the effective assembly size design verification and evaluation, and carry out the effective size deviation white body design verification and evaluation.

Good models platform, to the maximum extent is required to meet manufacturing requirements and reduce manufacturing cost, can more easily achieve exquisite craft, can realize structure strategy and technology strategy that embraces the more general standard module, such as deputy frame module, glass lift module and front-end appearance structure module.

The independent brand automobile enterprise in modelling platform building stage, need to carry out a large number of engineering precompetitive research work, will be package, engineering, performance, process development, development work moved forward, make modelling platform itself also enough to support platform of development system, modular design gradually realize. Establish modelling platform, the vehicle platform, the structure modular design system, and formed the platform development system, package, engineering development, performance, process development, development of all aspects of investment amount. Modelling of genes (platform), and the platform of the structure is modular development system, can significantly reduce the new car model development, engineering design, performance, process development, development effort and time period; all kinds of verifying test amount can effectively avoid the happening of the common problems. At the same time, the new models of project development cycle, project staff investment, project cost inputs are significantly reduced. The development mode of the platform fundamentally lifts up car by the overall efficiency of product research and development system, especially the efficiency of engineering development, research and development are shifted from the platform to make the change in advanced technology research, vehicle integration development, delicate process up development; making the independent brand automobile enterprises development system in a short time can catch up with the world first-class enterprise research and development system of the car.

In the process of platform building models, the level of integration design is one of the key size, one of the size of the integrated design process, is also gradually formed the size of platform, modular design process. Body structure in which the platform, modular design concept and the universal, in the process manufacture aspect also realization generalization and modular, in the aspect of design and controlling the gap and flush, advanced enterprises have been in appearance on dimensional chain form the generalization.

Last word: The independent brand automobile enterprises need to think problems or suggestions

1. Some size problem in the design state, not size closed-loop design, manufacturing stage in put forward the quality requirements of the very demanding is not reasonable, is also difficult to reach.
2. Why joint venture in vehicle size development (design) ability is very mature (foreign complete design) under the configuration have large-size quality control team, it is the domestic auto parts suppliers and the reality of working staff. Extensions thinking, the independent brand enterprise vehicle size design ability, there are insufficient, and put into production start-up phase of the

development and the size of the size administration shows do not improve, will lead to the vehicle craftsmanship difficult to ascend, for the cost of measurement size cannot improve.

3. Setting up internal dimensional expert team, through the dimensional expert team, to form the covers research and development, manufacturers process, quality, production control, purchasing every link the size of the complete development system.
4. Accurate positioning dimension engineers work functions. Dimension engineers, product engineers, process engineer, quality engineer, supplier technical support engineer, the core function of dimension engineer should be the integration design and controlling of vehicle.

Reference

1. The implementation map of vehicle dimension manufacture “2MM” project Vehicle manufacture of China 2007/New year Unknown

Chapter 28

Optimization Design Method of School Bus Structure Lightweight on the Rollover Safety

Ye Yu, Liang Ying, Ping Hu, Yang Yu, Xianda Li and Rong Fan

Abstract Based on the ECE R66 standard, a FEM model of a school bus was established and the rollover crash was simulated by LS-DYNA. According to the inbreak criterion of living space and the deformation level of side vertical beams, the side vertical beams and top arch beams were redesigned to make them light and safe. It was proved that the redesign can guarantee the safety of rollover crash and reduce the weight of whole bus simultaneously.

Keywords School bus · Rollover crash · Lightweight · Numerical optimization

28.1 Introduction

In recent years, the accidents of school bus have happened frequently, mostly in the form of rollover crash [1]. Thus, in regard to the rollover standard, on the basis of ECE R66, this paper established a CAE model of a school bus and examined its rollover crash safety by using LS-Dyna for numerical simulation. Besides, the lightweight structure design of school bus body and component were conducted and its liability was also studied which provided important design data and basis of school bus [2–4].

Y. Yu · L. Ying · Y. Yu · X. Li · R. Fan
School of Automobile Engineering,
Dalian University of Technology, Dalian, People's Republic of China
e-mail: yuye_eagle@foxmail.com

P. Hu (✉)
State Key Laboratory of Structural Analysis for Industrial Equipment,
Dalian University of Technology, Dalian, People's Republic of China
e-mail: pinghu@dlut.edu.cn

28.2 Rollover Test

Rollover experiment: At the beginning of experiment, school bus was held on a platform which could roll, as shown in Fig. 28.1. Then, the platform started to roll at the speed of 5°/s to the stage that school bus was instable. After that, gravity would drag school bus till it finally touched ground and stopped deforming process [5, 6]. In this paper, simulation was conducted when school bus first hit the ground and ended while the deformation was over. The angular velocity of school bus was obtained by law of conservation of energy presented as

$$\omega = \frac{v}{l} = \frac{\sqrt{2g \left[1 - \sin \left(\arctan \frac{B+t}{h_0} - \arcsin \frac{h}{H} \right) \right]}}{4\sqrt{(B+t)^2 + h_0^2}} \tag{28.1}$$

where v, ω are the linear and angular velocity of CG'' , respectively, m is the mass of school bus, and g is acceleration of gravity.

Relative parameters of school bus in this paper is show in Table 28.1, substituted into Eq. (28.1) get $\omega = 2.387$ rad/s.

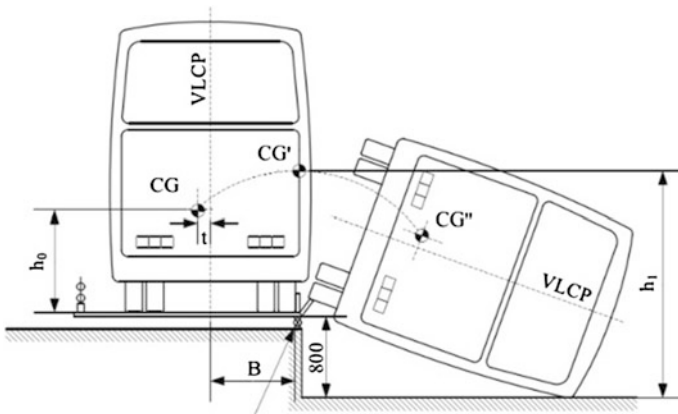


Fig. 28.1 Position change of bus's centroid

Table 28.1 Relative parameters of school bus (unit mm)

Name	Height (H)	Height of centroid (h ₀)	Centroid offset (t)	Half width (B)	Height of platform (h)	Length of bus (L)
Value	3,100	1,216	16	1,200	800	10,040

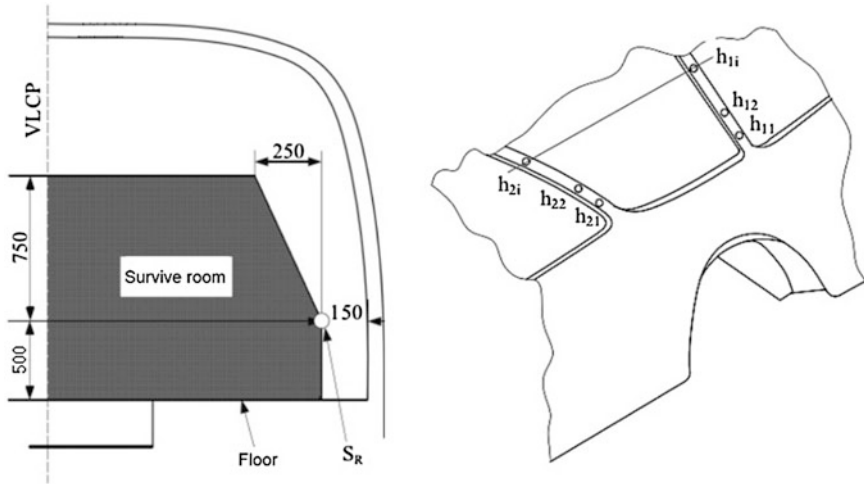


Fig. 28.2 Cross section of surviving room (*left*) and deflection of side vertical beams (*right*)

According to ECE R66, surviving room cannot be invaded during the rollover test and at the end of crash. Surviving room’s cross section is shown in Fig. 28.2 (left) [7]. The deflection of side vertical beams is another rollover crash safety index, which is smaller, the safer.

28.3 Finite Element Numerical Simulation of Rollover Crash

28.3.1 A Finite Element Mesh Model of School Bus Based on Rollover Crash Safety

A finite element mesh model of a school bus was built based on the CAD model in this paper, which accord with the real school bus, including the unitized frame, chassis, skin, and some other parts like electrical machine and battery built as rigid body with exact mass (as shown in Fig. 28.3). The center of mass of both element model and real bus is nearly same. There are almost 186,000 elements and 192,000 nodes in this finite element mesh model.

Most parts of the mesh model are modeled as deformable body, which are meshed with quadrilateral shell elements and a few of triangular shell elements. To make sure whether simulation is accurate enough, the length–width ratio of quadrilateral shell elements should be less than 3, warp degree should be less than 20° , Belytschko–Tsay shell element type should be used, and the one-dimensional rigid body should be used as the connection of parts. The material model should be Cowper–Symonds strain rate model which fits the mild steel materials, so $C = 30(1/s)$,

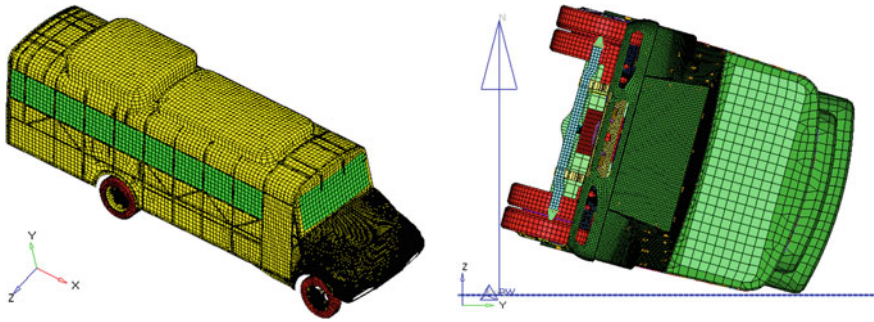


Fig. 28.3 Finite element mesh model of whole school bus (*left*) and the moment of the initial crash (*right*)

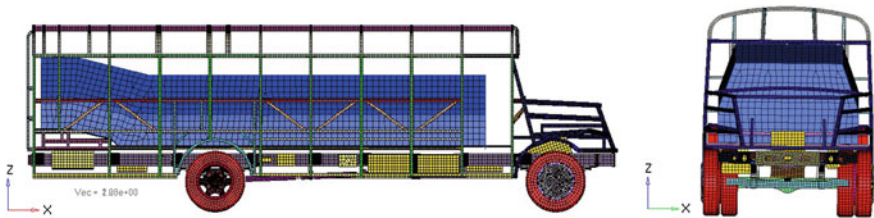


Fig. 28.4 Surviving room finite element model

$P = 5$. And surviving room is built as rigid body and fastened on floor, based on some related standards, and has no contact with other parts so the result could show whether survive room was invaded by other parts, as shown in Fig. 28.4.

28.3.2 Numerical Simulation of School Bus Rollover Crash

Numerical simulation of rollover crash is performed using LS-Dyna software. Figure 28.5 shows that the simulation result at time 0.12 s by using LS-Dyna and the relative position of survive room and side vertical beams at time 0.8 s.

28.3.3 Rollover Crash Numerical Simulation Results Analysis

As shown in Fig. 28.5, though the right-side beam is very close to surviving room, surviving room is not invaded by side vertical beams. As shown in Table 28.2, the front-side vertical beams' deflection is bigger than the rear ones, because at the

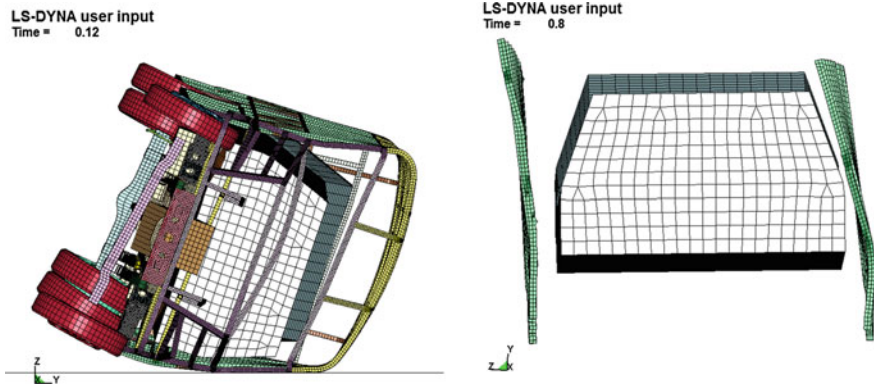


Fig. 28.5 Numerical simulation result at time 0.12 s in LS-Dyna and relative position of survive room and side vertical beams at time 0.8 s

Table 28.2 Deflection of origin school bus’s right-side vertical beams (numbered from school bus head to rear) (unit: mm)

1	2	3	4	5	6	7	8	9	AVG
943	933	913	894	878	864	841	823	781	874.9

initial crash time, the skin and frame of battery located on the rear hit the ground first and absorb some crash energy, most of which should have been absorbed by the rear-side vertical beams.

From the results of rollover crash numerical simulation, side vertical beams and top arch beams absorb the most crash energy and are most liable to get deflection. However, the maximum deflection of side vertical beams can directly decide whether side vertical beams invade surviving room and harm passengers or not. So side vertical beams and top arch beams are very worthy to optimal design.

28.4 Lightweight Structure Optimization Design Based on Rollover Crash Safety

28.4.1 New Structure Design

According to the analysis of origin school bus rollover crash numerical simulation results, side vertical beams and top arch beams mainly have bending deformation during the crash. Therefore, increase in the flexural rigidity of those beams which is determined by second moment of area could decrease bending deflection effectively

Fig. 28.6 Cross-sectional optimization of side vertical beams and top arch beams

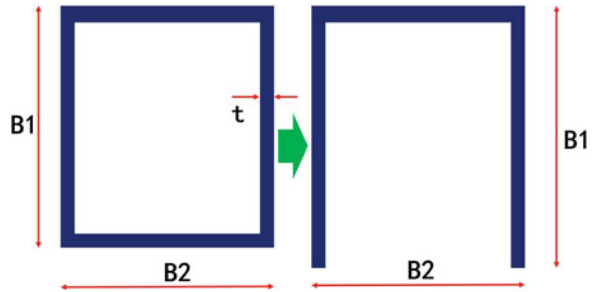


Table 28.3 Size of cross section of side vertical beams and top arch beams

	B1 (mm)	B2 (mm)	Thickness (mm)	Second moment of area (kg mm ²)	Mass (%)
Rectangle	50	40	2.0	86690.67	100
C type	58	40	1.6	87589.24	71.07

during rollover crash. In the meantime, to reduce the mass of school bus, a new high-strength and lightweight structure of side vertical beams and top arch beams is designed in this paper. As shown in Fig. 28.6 and Table 28.3, its cross-sectional shape has changed from rectangle to C type, and also its material use DP980; instead, the details of DP980 property are shown in Table 28.4.

28.4.2 Results Analysis

The rollover crash numerical simulation results of the new design school bus model are as shown in Fig. 28.7 and Table 28.5. Side vertical beams don't invade survive room and are further from the survive room than the origin, and also deflection of side beams are smaller than the original ones. At last, the new design school bus reduces 94.5 kg in total.

Table 28.4 Mechanical property of DP980

0.2 % Yield strength	Tensile strength	e _u (%)	e _t (%)	n	r
552 MPa	972 MPa	9.9	13.9	0.13	0.76

Fig. 28.7 Relative position of surviving room and side vertical beams at time 0.8 s

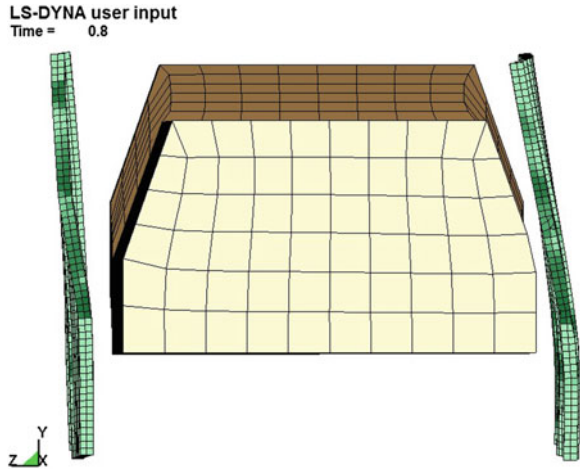


Table 28.5 Comparison between the side vertical beam deflection of the origin and the new design (unit: mm)

Numbers	1	2	3	4	5	6	7	8	9	AVG
Origin	943	933	913	894	878	864	841	823	781	874.9
New	911	899	879	862	849	840	824	820	796	853

28.5 Conclusions

Through the rollover crash numerical simulation of a school bus by using LS-Dyna software and its results, which shows that surviving room has not been invaded, the origin school bus researched in this paper is safe enough for rollover crash. A new high-strength lightweight structure is applied to side vertical beams and top arch beams, and it proves that this new structure can provide rollover crash safety effectively and reduce structure weight at the mean time by rollover crash numerical simulation. This structure can provide two advantages to electric school bus: One is rollover crash safety, and the other is to reduced energy consumption and improved range by reducing weight.

The new high-strength lightweight structure introduced in this paper has good effect in rollover crash safety; however, it does not prove to be good in other aspect of safety, which needs further research.

Acknowledgments This work was funded by the “973” National Basic Research Project of China (No. 2010CB832700), National Science and Technology Support Plan (No. 2013BAG05B01), and the Fundamental Research Funds for the Central Universities (DUT14RC(3)032). These supports are gratefully acknowledged. Many thanks are due to the referees for their valuable comments.

References

1. Huang D (2013) Rollover crash simulation analysis and optimization of a long head type school bus. *Mech Electr Technol* 3:105–107
2. Qi W (2010) Rollover crash simulation and optimization of bus based on ECE R66 standards. *Automot Eng* 12(32):1042–1046
3. LIANG CC, Le GE (2010) Analysis of bus rollover protection under legislated standards using LS-DYNA software simulation techniques. *Int J Automot Technol* 4(11):495–506
4. Yi-Ming S, Hong-Jian SI, Guan-Fei Z (2013) The study of bus safety based on the rollover test simulation. *J Chongqing Univ Technol (Nat Sci)* 2(27):2
5. Hu P (2012) The research of the coach rollover's simulation and the experimental verification. Chang'an University, Xi'an
6. Li Y (2012) Study on the key technology of design and optimization for coach rollover crashworthiness. S China Univ Technol, Guangzhou
7. Subic A, He J (2010) Improving bus rollover design through modal analysis. *Int J Crashworthiness* 2:139–152

Chapter 29

Parameters Design of Dynamic Vibration Absorbers for Vehicle Half-shafts

Yang Wang, Hui Wang, Liang Dong, Bowen Dong
and Hongwei Wang

Abstract It is effective method to reduce resonance of shaft to installs an absorber on it. And the performance of the absorber is due to its design parameters. The model parameters are identified by component analysis approach in this work. Based on the mechanics models to build mathematics modals, the computer program for calculating optimal parameters of absorber is written with MATLAB. The design of program is accuracy and credibility and verified by the vehicle test.

Keywords Dynamic vibration absorber (DVA) · Modal identification · Matlab

29.1 Introduction

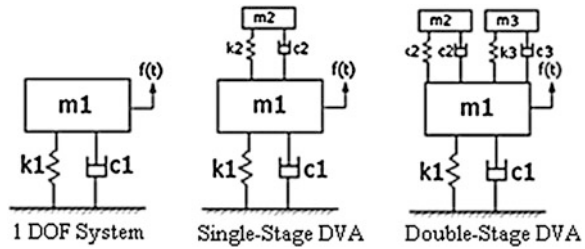
People's requirements of vehicle driving comfort keep increasing, which makes local brand companies attach great importance to vehicle NVH performance. As an important NVH optimum technique, dynamic vibration absorber is often applied on vehicle half-shafts to control the resonance problems of running vehicles. The validity and performance of DVA are determined by the calculation and design of its parameters. If the DVA is not well designed, vehicle NVH performance will be worsened. Based on dynamic vibration theories, this work developed an optimal parameter calculation procedure, which applies the amplitude amplification factor as the evaluation index, for the DVA design.

29.2 Basic Theories of DVA

The basic principle of DVA is that, an additional spring-mass system is added on the primary system, which will produce a vibration, the phase of which is 180° away from the primary system, thereby the vibration of the primary system under

Y. Wang (✉) · H. Wang · L. Dong · B. Dong · H. Wang
Brilliance Auto R&D Center, Shenyang, China
e-mail: wang.yang@brilliance-auto.com

Fig. 29.1 Multi-DOF mass-spring-damping system



certain frequency will be decreased [1]. When the exciting force is under single frequency or low frequency, the effect of DVA is very obvious [2]. To reduce the modal peak of SDOF system, the single-stage or multi-stage mass-spring-damper system is introduced into the multi-degree of freedom system, which is shown in Fig. 29.1. The modal peaks of primary system can be effectively decreased through reasonable allocation of the mass, stiffness, and damping of DVA.

29.2.1 Dynamic Model of Half-shaft DVA

The first bending mode of half-shaft will cause resonance problems. Due to the low modal density of half-shaft, it can be treated as a single-DOF system [3]. In addition, considering single-stage DVA is often applied for half-shaft resonance problems, the DVA of half-shaft is equivalent to a 2-DOF model, as shown in Fig. 29.2.

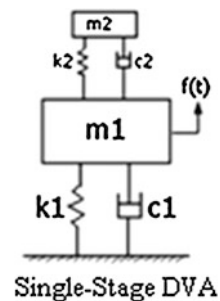
According to Newton’s Laws, the vibration equation of this system is as follows:

$$m_1\ddot{x}_1 + c_1\dot{x}_1 + c_2(\dot{x}_1 - \dot{x}_2) + k_1x_1 + k_2(x_1 - x_2) = f(t) \tag{29.1}$$

$$m_2\ddot{x}_2 + c_2(\dot{x}_2 - \dot{x}_1) + k_2(x_2 - x_1) = 0 \tag{29.2}$$

where m_1 is the mass of half-shaft, c_1 is the damping ratio of half-shaft, k_1 is the stiffness of half-shaft, x_1 is the displacement of half-shaft, m_2 is the mass of DVA,

Fig. 29.2 Single-stage DVA



c_2 is the damping ratio of DVA, k_2 is the stiffness of DVA, and x_2 is the displacement of DVA.

The equations above can be expressed in matrix as

$$\begin{pmatrix} m_1 & 0 \\ 0 & m_2 \end{pmatrix} \begin{pmatrix} \ddot{x}_1 \\ \ddot{x}_2 \end{pmatrix} + \begin{pmatrix} c_1 + c_2 & -c_2 \\ -c_2 & c_2 \end{pmatrix} \begin{pmatrix} \dot{x}_1 \\ \dot{x}_2 \end{pmatrix} + \begin{pmatrix} k_1 + k_2 & -k_2 \\ -k_2 & k_2 \end{pmatrix} \begin{pmatrix} x_1 \\ x_2 \end{pmatrix} = \begin{pmatrix} f(t) \\ 0 \end{pmatrix} \quad (29.3)$$

or

$$M\ddot{X} + C\dot{X} + KX = F \quad (29.4)$$

29.2.2 Evaluation Function

The amplitude amplification factor (AAF) is defined as the ratio of exciting force and the response displacement. So the AAF of single-DOF system is [4]

$$\beta_1 = \frac{X}{X_0} = \frac{1}{\sqrt{(1 - \lambda^2)^2 + (2\zeta\lambda)^2}} \quad (29.5)$$

where λ is the ratio between exciting frequency and nature frequency, and ζ is the damping ratio. This work takes AAF as the evaluation function, which means the smaller of AAF, the better the system is. Equation (29.4) can be converted into frequency domain, that is

$$\begin{aligned} X(w) &= (-w^2M + jwC + K)^{-1}F(w) \\ &= \{k_0 \times (-w^2M + jwC + K)^{-1}\} \frac{F(w)}{k_0} \end{aligned} \quad (29.6)$$

where $F(w)$ is the amplitude of exciting force, $X(w)$ is the amplitude of response displacement, $F(w)/k_0$ is the static vector of displacement, and k_0 is the equivalent stiffness of primary system.

According Eq. (29.5), one can get

$$\begin{pmatrix} X_1 \\ X_2 \end{pmatrix} = \{k_0 \times (-w^2M + jwC + K)^{-1}\} \begin{pmatrix} B_1 \\ 0 \end{pmatrix} \quad (29.7)$$

and

$$\begin{pmatrix} \beta_1 \\ \beta_2 \end{pmatrix} = \frac{k_1}{m_1} \left\{ \begin{array}{c} -w^2 \begin{bmatrix} 1 & 0 \\ 0 & u_1 \end{bmatrix} + \\ w_{n1}^2 \begin{bmatrix} 1 + u_1 \lambda_1^2 & -u_1 \lambda_1^2 \\ -u_1 \lambda_1^2 & u_1 \lambda_1^2 \end{bmatrix} + \\ jww_{n1} \begin{bmatrix} 2\xi_1 + 2\xi_2 u_1 \lambda_1 & -2\xi_2 u_1 \lambda_1 \\ -2\xi_2 u_1 \lambda_1 & 2\xi_2 u_1 \lambda_1 \end{bmatrix} \end{array} \right\}^{-1} \quad (29.8)$$

where X_1 is the displacement of primary system, X_2 is the DOF of DVA, B_1 is the static displacement, k_1 is the stiffness of primary system, m_1 is the mass of primary system, w is the exciting frequency, u_1 is the ratio of m_2/m_1 , λ_1 is the ratio of w_2/w_1 , ξ_1 is the damping ratio of primary system, ξ_2 is the damping ratio of DVA. The element in the first line of the first column is the AAF of the primary system.

29.3 Calculation of the Optimal Parameters

29.3.1 Modal Identification

According to Eq. (29.7), the optimal parameter can be obtained is the ratio of mass, damping, and frequency between the primary system and DVA are known. Therefore, the modal of primary system needs to be identified to obtain such parameters. Due to the low modal density of half-shaft, the component analysis method could be applied for modal identification as follows [3]

$$\xi_e = \frac{\Delta w}{w_0} \quad (29.9)$$

$$K_e = \frac{1}{2\xi_e H_m} \quad (29.10)$$

$$M_e = \frac{K_e}{w_0^2} \quad (29.11)$$

where ξ_e is the damping ratio, w_0 is the angular resonance frequency, Δw is the half power band, K_e is the equivalent modal frequency, H_m is the peak of mobility, M_e is the equivalent modal mass.

29.3.2 Calculation Results

After input the local mobility of half-shaft into the program, the least squares method [5] was used to fit the design in order to reduce errors caused by experimental error. The fitting results are shown in Fig. 29.3. Based on the fitting results, the component analysis method was used for parameter identification. The optimal parameter of AAF and its values were the output. Subject to space limitations, the maximum mass absorber can reach 0.5 kg, the natural frequency of which is 84 Hz, and the damping ratio is 0.05. Figure 29.4 shows the comparison results with and without DVA on half-shaft. From the result, we can find that the peak of primary system was effectively decreased.

Fig. 29.3 Fitting of local mobility

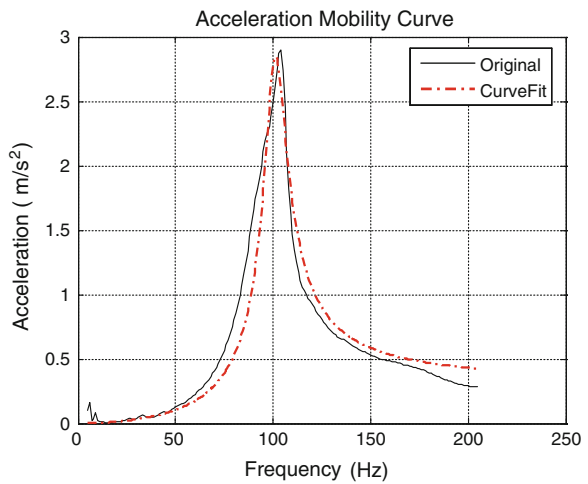
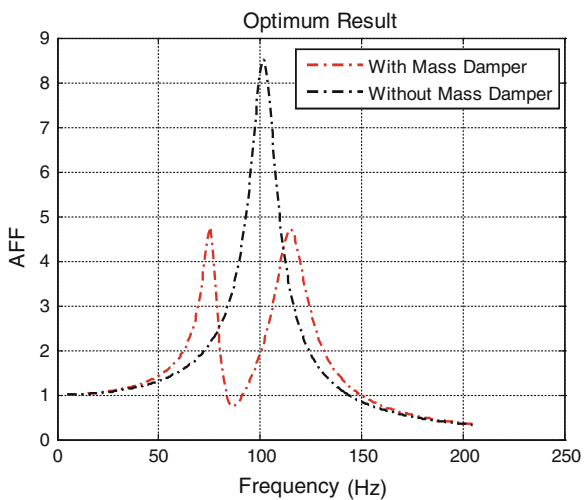


Fig. 29.4 Optimal calculation results



29.4 Experimental Verification

Following the calculated parameters of DVA, a prototype was made for the real test on vehicle. The prototype of DVA is shown in Fig. 29.5. The measured SPL of the noise at driver's inner ear under acceleration condition is shown in Fig. 29.6. From the figure, we can find that the peak at 3,000 rpm is completely eliminated.

The measured vibration of the acceleration pedal is shown in Fig. 29.7. The figure shows that the peak at 3,000 rpm is totally removed. Through the experimental verification, the validity of the designed DVA was proved.

Fig. 29.5 Prototype of designed DVA



Fig. 29.6 Measured SPL at driver inner ear

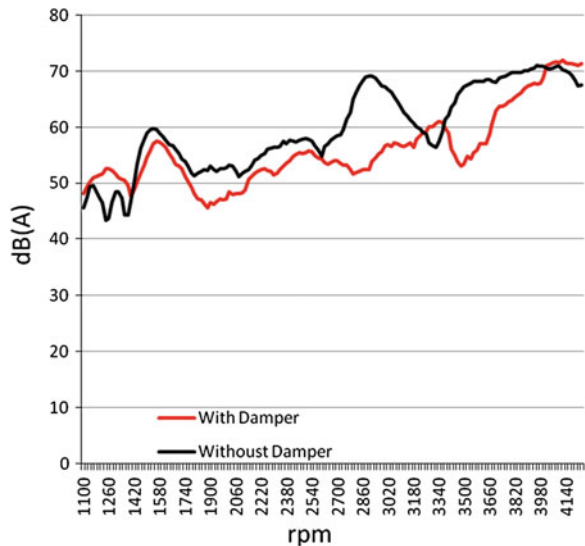
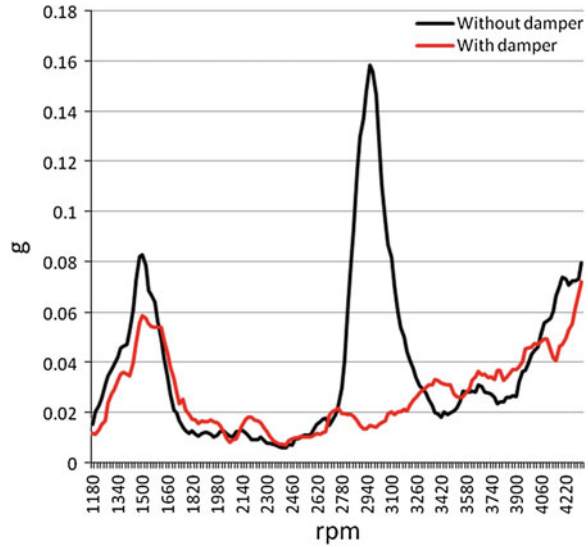


Fig. 29.7 Vibration of acceleration pedal



29.5 Conclusions

The component analysis method proposed in this work was proved effective for modal parameter identification. And the optimization process which takes AAF as the evaluation function was also feasible for the first-order bending mode of half-shaft control. The accuracy of the calculation process was confirmed by the test results.

References

1. Pang J, Zhan G, He H (2006) Vehicle noise and vibration-theory and application. Beijing Institute of Technology Press, Beijing
2. Li Y, Gu Y, Jin C (2011) Optimal design of automobile's vibration absorber, *Vib Noise Control* 31(6):123–126
3. Lin X (1994) *Vibration modal identification and its application*. Southeast University Press, Nanjing
4. Zhu Z, Gong X, Du G (2001) *Basic theory of acoustic*. Nanjing University Press, Nanjing
5. Sun X (2005) *Tutorial of matlab 7.0*. Tsinghua University Press, Beijing

Chapter 30

Simulation and Validation of Engine Valvetrains System Dynamics

Wenbo Niu, Lechao Tang, Wenhui Jiang and Tiancheng Li

Abstract The dynamic behavior of the valvetrains for a gasoline engine is simulated using a multi-valvetrain dynamic model, of which the stiff parameters are calculated by finite element method. Then, the simulation results of camshaft torques and valve forces are validated by experiments, and the calculated data are consistent with the test data. Based on the correct model, the sensitivities of dynamic loads influencing NVH of the engine directly are analyzed, and the primary influencing factors of the fluctuation of camshaft force, torque, and spring force have been found, and further, dynamic force optimization direction for NVH performance of valvetrain has been pointed out.

Keywords Valvetrains · Dynamic analysis · Dynamic force · NVH

30.1 Introduction

The noise and vibration performance is an important target in the engine development process. Along with the engine rotating, the noise and vibration could be generated by many excitations including cylinder pressures, inertia forces of crankshaft system, dynamic forces of belt-chain system, and the valvetrains. The dynamic forces of the valvetrains are critical for simulation of the engine radiated noise.

Valvetrains dynamics characteristics are considered to be a major area for valvetrains researching in many documents. In the experimental aspect [1–3], a method for measuring valve lift and velocity was introduced using a high-speed laser vibrometer, and the measurement results are highly accurate [1]. Sometimes,

W. Niu (✉) · L. Tang

State Key Laboratory of Comprehensive Technology on Automobile Vibration and Noise and Safety Control, China FAW R&D Center, Changchun 130011, China
e-mail: niuwenbo@rdc.faw.com.cn

W. Jiang · T. Li

China FAW R&D Center, Changchun 130011, China

© Springer-Verlag Berlin Heidelberg 2015

Society of Automotive Engineers of China (SAE-China) (ed.),

Proceedings of SAE-China Congress 2014: Selected Papers,

Lecture Notes in Electrical Engineering 328, DOI 10.1007/978-3-662-45043-7_30

the noise and vibration could be measured directly to analyze the noise source and critical factor [2]. But in the product development stage, effective simulation should be performed to analyze the valvetrains dynamic behaviors and optimize the designs. In the simulation aspect, valve motion and the components stress have been simulated widely [4–7]. But the valvetrain dynamic forces on the engine when valvetrains operating are more important to the noise and vibration performance of the engine.

In this paper, the results of camshaft torques, bearing forces, spring forces, and valve forces are discussed based on the valvetrains dynamics model of a 4-cylinder gasoline engine. The camshaft torque and valve forces were measured to validate the simulated data. Finally, the sensitivities of dynamic loads influencing NVH of the engine directly are analyzed to find the primary factors.

30.2 Valvetrains Dynamic Model

Valvetrain dynamic model is established according to a 4-cylinder gasoline engine valvetrains, and Fig. 30.1 shows the frame. Four valves in each cylinder are derived by two camshafts directly, and intake camshaft with VVT or exhaust camshaft is supported by five bearings, respectively.

The valvetrain is modeled by software EXCITE TD. Valves, springs, and tappets are modeled by mechanics elements, and the important parameters such as cam profile, valve timing, and oil prosperities are considered, Fig. 30.2 shows the single-valvetrain model. Based on the single-valvetrain model, a multi-valvetrains dynamic model is established to simulate the camshaft torque and bearing forces. In the multi-valvetrains model (Fig. 30.3), camshaft is modeled by elastic beams

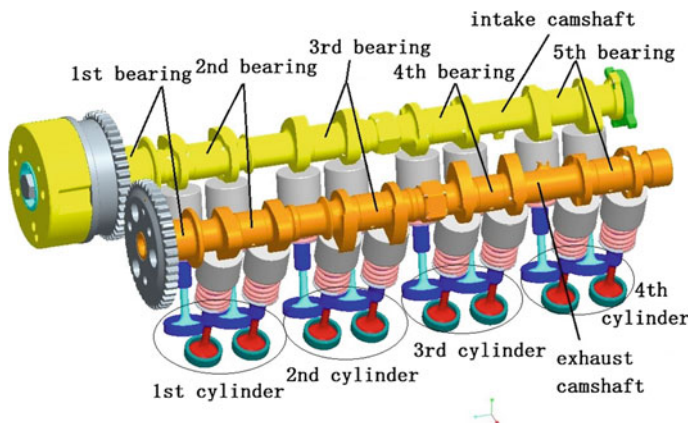
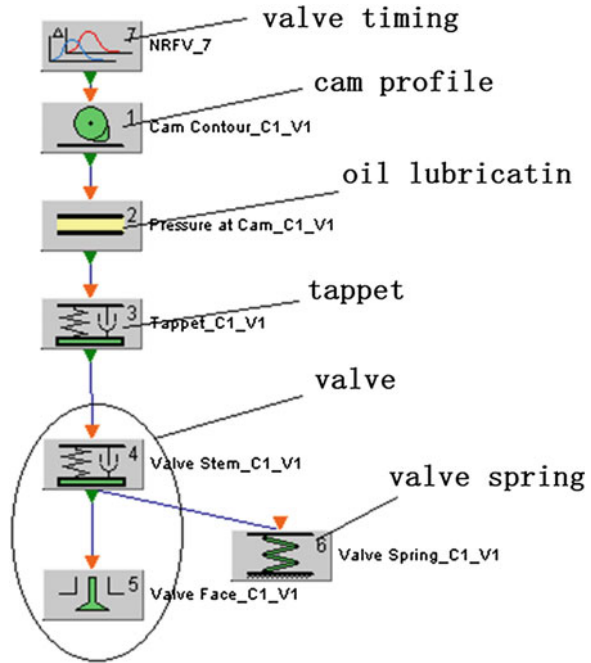


Fig. 30.1 Valvetrains of a gasoline engine

Fig. 30.2 Single-valvetrain model



assembly, and the stiffness parameters of valvetrains are calculated by finite element method, and the damping ratio of the components is estimated.

30.2.1 Flexical Camshaft Model

Camshaft is modeled by elastic beams assembly, and this method is verified by comparison of the shaft modes with the mode results calculated by FEM. Table 30.1 lists the results calculated by the two methods, and the differences of the same mode order in 3,000 Hz are lower than 1 %, so the elastic beam method is feasible.

30.2.2 Components Stiffness

The stiffness of components is critical to the valvetrains dynamics characteristics, and FEM is used to calculate the stiffness of components exactly. When the camshaft is assembled on the cylinder head, the stiffness of all bearings is differential, and Table 30.2 lists the equivalent stiffness values of components. Because the tappet stiffness is variable with the contacting position of the cam and tappet, the stiffness values of different positions are calculated (Fig. 30.3 and Table 30.3).

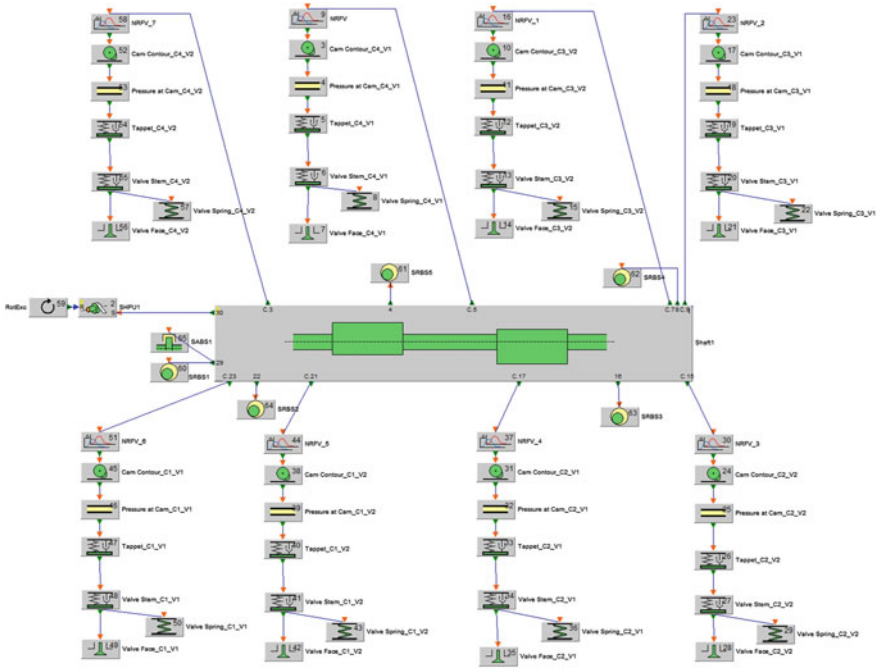


Fig. 30.3 Multi-valvetrains model

Table 30.1 Modes of camshaft models

Orders	Mode of intake camshaft (Hz)			Mode shape
	Elastic beam method	FEM	Ratio of differences (%)	
1	604.9	607.9	-0.49	Bending
2	605.5	609.1	-0.59	Bending
3	1,653	1,641	0.73	Bending
4	1,654	1,646	0.49	Bending
5	2,579	2,583	-0.15	Torsional

30.3 Simulation Analysis

30.3.1 Camshaft Torque Analysis

Figure 30.4 shows the intake camshaft torque curves in the engine speed 1,000 and 3,000 r/min. Camshaft torque fluctuates four times in a rotating period according to the fire order. In the high engine speed operation, high-frequency fluctuation of

Table 30.2 Stiffness of exhaust valvetrain

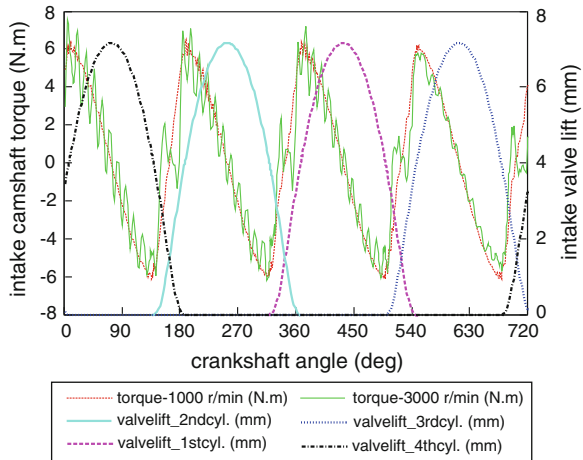
Bearings	Stiffness (N/mm)	
	Direction Y	Direction Z
1 st bearing	7.98e4	1.20e5
2 nd bearing	8.53e4	1.82e5
3 rd bearing	8.54e4	1.94e5
4 th bearing	8.56e4	1.95e5
5 th bearing	7.94e4	1.85e5
Valve bottom part	1.01e5	
Valve upper part	9.13e4	

**Direction Y* Perpendicular to center line of camshaft and center line of cylinder, *Direction Z* Center line of cylinder

Table 30.3 Stiffness of tappet

Contacting Position Eccentricity (mm)	Stiffness (N/mm)
0	5.22e4
4.67	3.75e4
9.33	1.55e4

Fig. 30.4 Intake camshaft torque in engine speed 1,000 and 3,000 r/min



camshaft torque exists. The curve of torque in engine speed 3,000 r/min is analyzed by FFT, and the frequency of fluctuation is about 1,440 Hz. The camshaft torsional mode is calculated using FEM in this assembly condition, and the torsional frequency is 1,442 Hz (Fig. 30.5), so the high-frequency fluctuation is correlated with the camshaft torsional mode.

Fig. 30.5 FFT of exhaust camshaft torque in engine speed 3,000 r/min

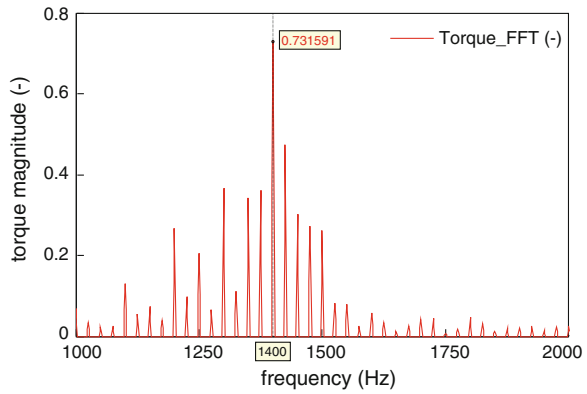
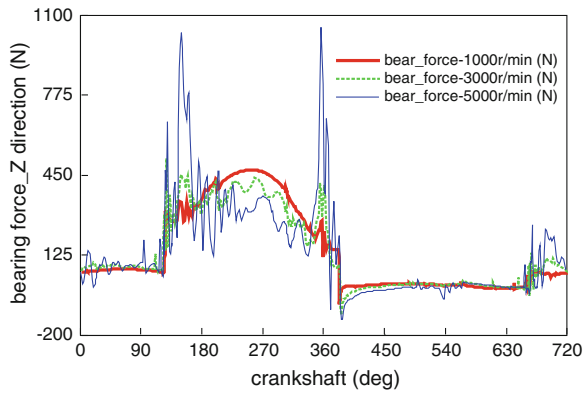


Fig. 30.6 The 2nd bearing force of exhaust camshaft



30.3.2 Bearing Force Analysis

Figure 30.6 shows the 2nd bearing vertical force of the exhaust camshaft. The curve is associated with the bearing layout, because the adjacent valvetrain forces mainly act on this bearing. In the engine speed 1,000 r/min, the maximum force is found in the maximum lift moment. As a contrast, the maximum force exists in the valve-opening or valve-closing phase in the engine speed 5,000 r/min, so the effect of the valvetrain inertia force increases along with the engine speed.

30.3.3 Spring and Valve Force Analysis

Figure 30.7 shows the exhaust valve spring force curve of the first cylinder, and the force is corresponding to the valve lift. In the high-speed operation, the fluctuation

Fig. 30.7 Exhaust spring force of the first cylinder

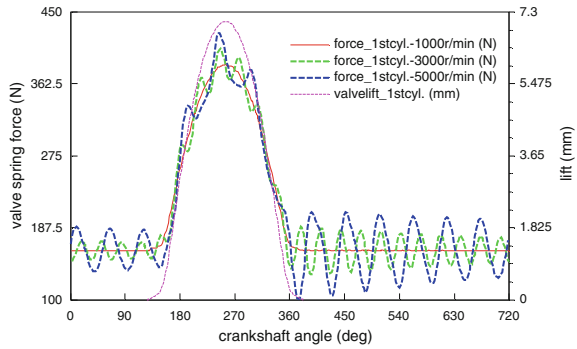
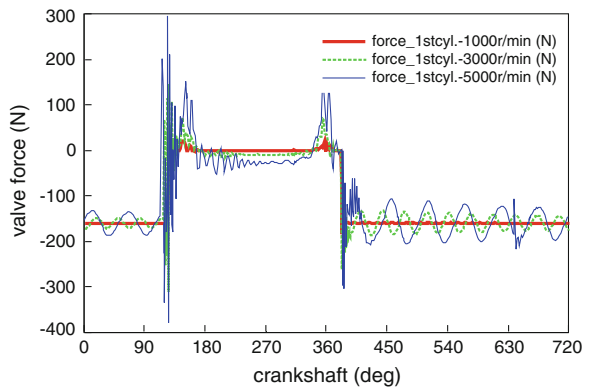


Fig. 30.8 Exhaust valve force of the first cylinder



magnitude of the force increases, and the fluctuation frequency is correlated with the spring natural frequency in the assembly condition.

In the valvetrain model, the valve is divided into two parts, and Fig. 30.8 shows the internal force of the exhaust valve in the first cylinder. As same as the spring force, the valve force fluctuates in high-speed operation, and it is related to valve inertia force in opening phase and spring force in closing phase.

30.4 Experimental Validations

For validating the simulation results, the camshaft torques and valve forces were measured. The test rig was builded based on engine cylinder head, and it was driven by a motor. The strains of camshaft and valve were measured in the all operations, and the camshaft torque from the chain pulley and the force in the middle of valve were calibrated according to the strain data.

30.4.1 Camshaft Torque Validation

Figures 30.9 and 30.10 show the contrast of simulation results and experimental results in engine speed 1,000 and 3,000 r/min, respectively. The simulation results are basically consistent with the experimental results. The average torque of test was 1.3 N m in engine speed 1,000 r/min and 3.3 N m in engine speed 3,000 r/min. The average torques represent the losses of power in the actual operation. Subsequently, the frictional parameters in the multi-valvetrains model were modified to make the simulated average torques consistent with the tests.

Fig. 30.9 Intake camshaft torque of simulation and test in engine speed 1,000 r/min

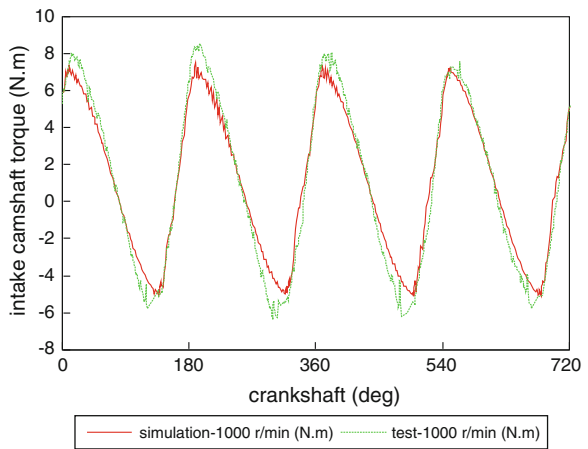


Fig. 30.10 Intake camshaft torque of simulation and test in engine speed 3,000 r/min

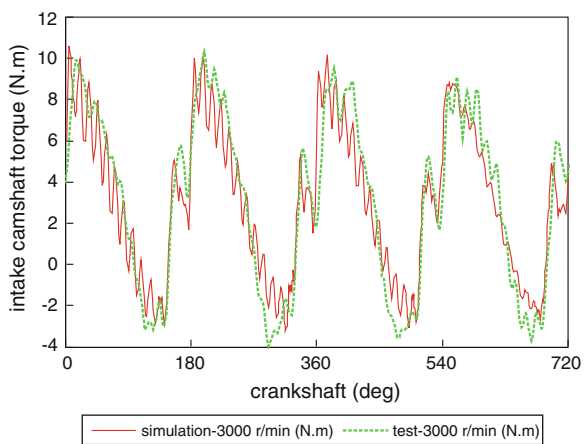
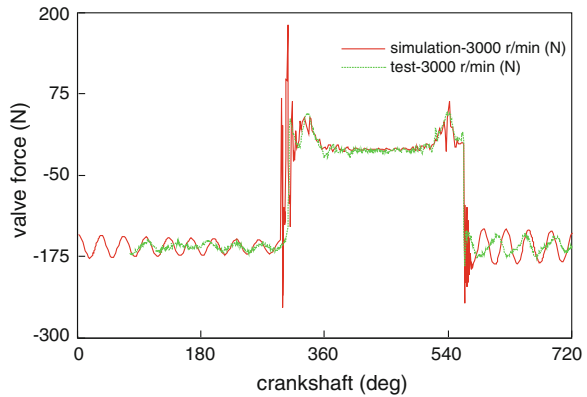


Fig. 30.11 Exhaust valve force of the third cylinder in engine speed 3,000 r/min



30.4.2 Valve Force Validation

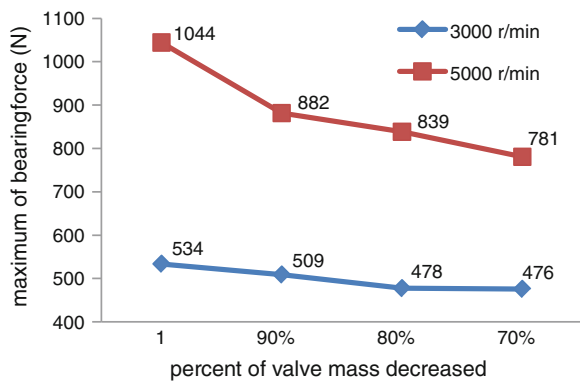
Figure 30.11 shows the exhaust valve forces of the third cylinder in the engine speed 3,000 r/min. The simulation results of valve forces are basically consistent with the experimental results.

30.5 Sensitivity Analysis of Dynamical Forces

30.5.1 Valvetrain Mass Influence Analysis

In the engine operation, valvetrains dynamical forces are influenced by themselves masses. Figure 30.12 shows when the mass of valvetrains is reduced by 30 %, the maximum of bearing forces is reduced by 10.9 or 25.2 % in the engine speed 3,000 or 5,000 r/min, respectively.

Fig. 30.12 Camshaft bearing forces influenced by valvetrains mass



The mass of valvetrains mainly influences the high-frequency characteristics of camshaft torques. For researching the influences, the curves of camshaft torques are high-pass filtered with the cutoff frequency 1,000 Hz (Fig. 30.13). Figure 30.14 shows when the mass of valvetrains is reduced by 30 %, the peak–peak value of high-frequency parts of camshaft torque is reduced by 36.4 or 49.1 % in the engine speed 3,000 or 5,000 r/min, respectively.

30.5.2 Spring Stiffness Influence Analysis

When the stiffness is reduced by 30 %, the camshaft torque is reduced by 29.8 or 27.7 % in the engine speed 1,000 or 3,000 r/min, respectively (Fig. 30.15). But in the engine speed 5,000 r/min, there are no obvious rules because of high-frequency component influenced by valvetrains dynamics.

Fig. 30.13 Filter analysis of camshaft torque curve

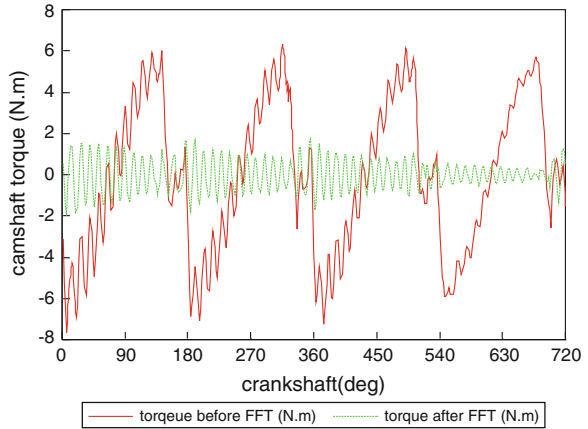


Fig. 30.14 High-frequency fluctuation of camshaft torque influenced by valvetrains mass

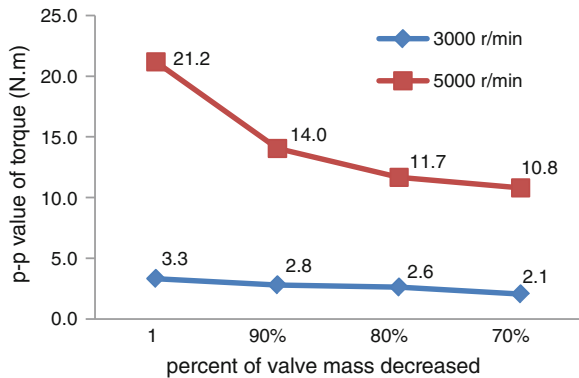
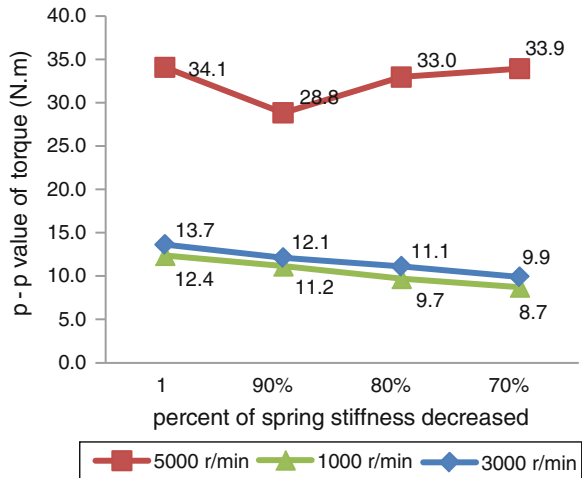


Fig. 30.15 Peak-peak valve of camshaft torque influenced by valve spring stiffness



30.5.3 Cam Profile Influence Analysis

In theory, the valvetrain moves according to the cam profile, but in the high engine speed condition, the valvetrain dynamic characteristics are critical. In the cam profile design processing, valvetrain dynamics should be considered as important as the volumetric efficiency [8, 9]. In the engine speed 3,000 r/min, the sharp fluctuation of camshaft torque is found in the valve-opening stage (Fig. 30.4), and it is corresponding with the cam profile. Profile 1 and profile 2 are designed in the base of the original profile (Fig. 30.16), and the acceleration amplitudes of profile 1 and profile 2 are all lower than original, so the volumetric efficiency is affected by the profiles. Figure 30.17 shows the camshaft torques using those three profiles in the

Fig. 30.16 Acceleration curve design of cam profile

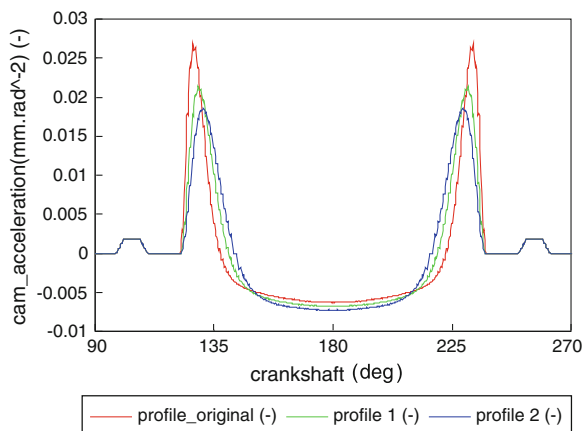
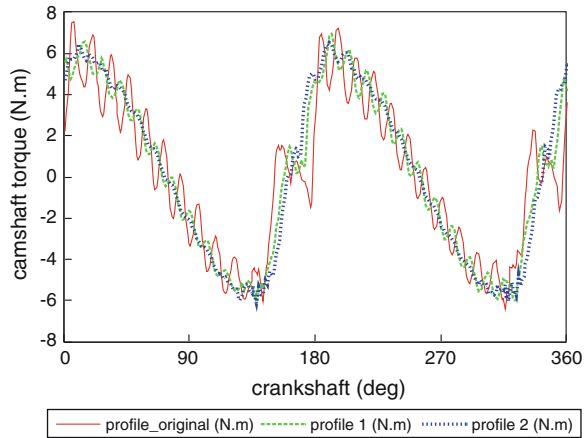


Fig. 30.17 Camshaft torques contrast of different cam profiles



engine speed 3,000 r/min, and the camshaft torque with profile 1 also has a slight sharp fluctuation, while there is no sharp fluctuation with profile 2.

30.6 Conclusions

In this paper, a simulation method of valvetrains dynamics was discussed, and the simulated results were validated by the experimental data. The following trends were observed from the valvetrains dynamic model:

1. The fluctuations of camshaft torques are related to valve motion periodically, and the period is correlated with the cylinder numbers. In the high engine speed, high-frequency fluctuations are obvious, and the frequency is correlated with the torsional mode of camshaft in assembly.
2. The bearing forces are influenced by the valve spring forces and the inertia forces of valvetrain, and in the high engine speed, the maximum of bearing force is determined by the mass and acceleration of valvetrains.
3. In the valve-closed stage, the valve and spring forces are influenced by the spring natural frequency.
4. The weight reduction of valvetrains is an important role to the camshaft torque and bearing forces. In the low engine speed, the camshaft torque is reduced proportionally to the valve spring stiffness. The reasonable cams profile will improve the fluctuation of camshaft torque.

References

1. Jeff GS (2004) New equipment and methodology to perform high speed valvetrain dynamics testing and analysis. SAE paper 2004-01-1720
2. Hwang S-Y, Kang K-T (2005) Noise reduction and sound quality improvement of valve train in V6 gasoline engine. SAE paper 2005-01-1834
3. Luo H, Xia T-Q (2007) Analysis on valve train noise of engine. *J Chongqing Univ (Nat Sci Ed)* 30(9):5–8
4. Frendo F, Vitale E (2004) Development of a lumped-parameter model for the dynamic analysis of valve train systems. SAE paper 2004-32-0051
5. Lin Y, Ramachandra P (2004) Valve train dynamic analysis and validation. SAE paper 2004-01-1457
6. Hao YG, Xiao Y (2006) The computation of valve train based on rigid-flexible coupled kinetics model. *Veh Eng* 165(5):31–35
7. Qin W, He J (2009) A study on the simulation of valve train assembly of a V-type engine based on multi-body system dynamics. *Trans Beijing Inst Technol* 29(10):869–872
8. Farzin HM (2010) Development of an automated cam profile designer and optimizer. SAE paper 2010-01-1108
9. Dumitru MB (2010) Modeling and analysis of valve train, part I—conventional systems. SAE paper 2010-01-1198

Chapter 31

The Vehicle NVH Development and Engineering Application of the Lightweight Sound Package

Jun Zhang, Guanni Zhu, Xiaoxuan Zhang, Hongyu Liu and Congguang Liu

Abstract Although automobile lightweight technology is the R&D focus of automotive engineering at current, it brings little attention in automotive industry for the lightweight technology of the interior trim and sound package material. Furthermore, there are less research and engineering application on it. This paper presents a control process and mechanism of sound package lightweight development, which is aimed at NVH performance and explains the specific methods in used. The paper illustrates a new feasible scheme of lightweight project, with a case of 2,500 g/mm² dash insulator. Considering the actual engineering factors of dash leakage effect, etc., the statistic energy analysis (SEA) simulation and experiment results show the improvement of the sound quality performance of interior automobile with approximately 55 % decrease of the weight. This paper contributes to improve the understanding level and engineering application for sound package lightweight development in automotive industry.

Keywords Sound package · Dash insulator · Lightweight · NVH · Sound quality

31.1 Introduction

The automotive industry is currently facing several major problems, such as energy crisis, environmental protection, and safety and comfort requirements. One effective solution is to design the lighter weight vehicle. For traditional ICE engine vehicle, the 60 % fuel is consumed to itself weight rolling and aerodynamic resistance. If the

J. Zhang (✉) · G. Zhu · X. Zhang · H. Liu · C. Liu
Changan Auto Global R&D Center NVH Department, Chongqing 401120, China
e-mail: zj_zmkm@126.com

G. Zhu
e-mail: zhugn@changan.com.cn

J. Zhang
State Key Laboratory of Vehicle NVH and Safety Technology, Chongqing 401120, China

vehicle weight is reduced by 10 %, it can save 10–15 % fuel. Especially for HEV and EV vehicles, the lightweight vehicle will improve driving mileage and dynamic performance. Therefore, the lightweight vehicle design has become an important trend in the current automotive industry. Usually, the main way of lightweight car is the use of alternative light metal and nonmetal materials. Another is the optimal design of vehicle structure. In general, the body is accounted for about 1/3 of the total car weight. Usually, lightweight measures for the body will weaken the whole body dynamic performance, such as stiffness, strength, crashworthiness, reliability, and NVH. Therefore, it is a tough challenge for metal part lightweight development to achieve both the desired body functional performances and weight targets. The skeleton body lightweight design is more complex and comprehensive process to find the best compromises between various disciplines.

But for the body interior sound package components, such as dash insulator, carpet, headliner, package tray, and other sound-absorbing trims, the developed functions of acoustic material are relatively independent, which is not too much trade-offs with various vehicle performances. Sound package is mainly used to block sound from entering the passenger compartment and to absorb the noise energy inside the cabin.

Usually, the lightweight design for acoustic packaging components is feasible in automobile development. If we only change the sound package product, there is relatively few engineering modification work involved to other body products. Therefore, the lightweight sound package research has become one of the focuses of automobile industry in recent years. Zhang et al. [1] presented a unique process to set an acoustical component target as a combined effect of sound transmission Loss (STL) and absorption. This process utilizes a statistical energy analysis (SEA) vehicle level model to create a spreadsheet based response surface model. Duval et al. [2] described an alternative treatment, which consists of a micro-perforated film top layer and fibrous decoupler layer. Prototype dash mats were constructed after performing SEA and FEA vehicle level assessments of constructions, using flat stock insertion loss and absorption data. Ernster et al. [3] presented the acoustical evaluation of a cotton fiber absorbing material, which was done using measurements of material properties along with sound pressure level from road testing of a fully assembled vehicle. The improvement was approximately 1.5 dB over the frequency range of 1,000–6,300 Hz. The acoustic material weight is reduced by 30 %, but there are still few systematic research and engineering application for acoustic lightweight sound package.

This paper presented a procedure of sound package lightweight development. A new feasible scheme of lightweight project is provided by the 2,500 g/mm² dash insulator case. Considering the dash leakage effect, the SEA simulation and experiment measurement results are proved to improve the sound quality performance of interior automobile with approximately 55 % decrease of the weight. This paper is benefited for improving the understanding level and engineering application for sound package lightweight development in automotive industry.

31.2 Lightweight Sound Package Engineering Development and Strategy

For the vehicle NVH control, there are three key elements of source, path, and response, respectively. Sound package is mainly used to control the noise propagation path and noise leakage, which can not only reduce the noise level, but also can improve the sound quality to meet the expectations of driver and passengers. Vehicle sound package designers have the goal to design vehicle parts that is to attenuate power train, wind and road/tire noise from entering the vehicle while complying with cost, weight, and packaging constraints. Figure 31.1 shows a typical arrangement of sound package.

The metal-based and plastic material application replaced for steel has been the focus of lightweight vehicle development. But for vehicle sound package lightweight technology, there are four main categories in general: (1) the application technology of lightweight materials, such as low density, high ratio foam, and porous fiber materials; (2) application of a new type of acoustic structure assemble, such as micro-perforated composite, multilayer wool felt or foam layer combination; (3) lightweight application technology based on multi-attribute optimization design, such as a test or simulation analysis method is used to identify the noise transfer characteristics and guide the design layout of acoustic material; (4) new vehicle manufacturing and installment technology can reduce the trim relevant components in used, such as trim adhesive process instead of welding studs.

Noise reduction (NR) of interior sound packages depends on two factors: one is STL of insulation material, which is a property of insulation materials itself, and the other is the absorption of the interior, which is a property of the interior environment. Thus, there are some new lightweight design concepts to use a low STL insulation material with a high absorption interior system to achieve equivalent NR. By the way, the lightweight development of sound package should be combined with a variety of means test and simulation analysis.

31.3 Lightweight Dash Insulator Development and Engineering Application

31.3.1 *The Lightweight Dash Insulator Concept*

The dash insulator is installed between engine and the driver side, which can effectively attenuate noise transmitted from the power train and the front tires to the inside of the vehicle. Always, the dash insulator is considered as the most important acoustic piece to control the noise level and sound quality in passenger compartment.

At present, the conventional construction of sound insulator is two-layer structure form, as shown in Fig. 31.2a. The commonly used “heavy layer” material is EVA, EPDM, or PVC. And the “soft layer” includes the cotton felt, PU foam, or

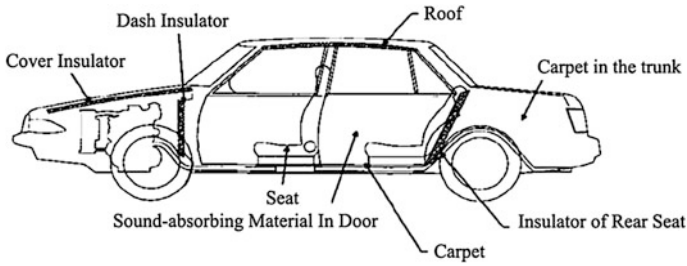


Fig. 31.1 Typical sound package arrangement

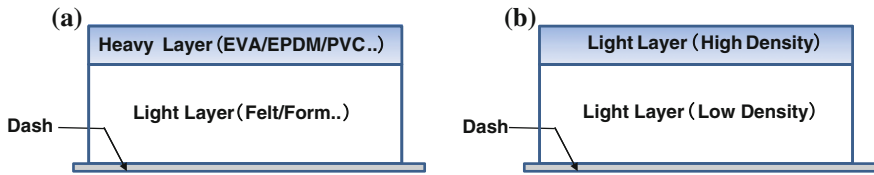


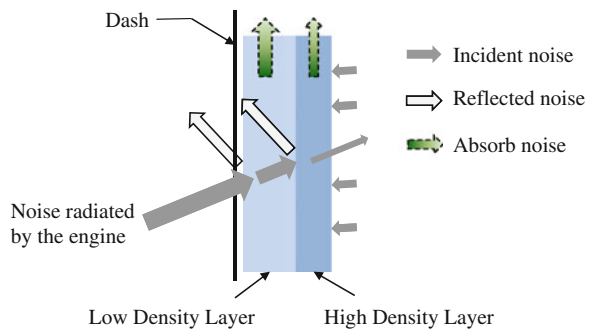
Fig. 31.2 The two-layer acoustic structure of dash insulator. **a** Traditional dash insulator. **b** Lightweight dash insulator

other thermoplastic fiber materials. The main effect of heavy layer is to insulate the noise transmission as the sound barrier. Otherwise, the soft layer is mainly to absorb the sound energy.

Because of the weight reduction need for the traditional heavy layers material, the paper illustrates a kind of new lightweight insulator design concept (see Fig. 31.2). High density of soft material is used to replace the traditional “heavy layer.”

In addition, the intermediate film such as PE materials is often inserted between the two soft layers. The three-layer dash insulator can improve the sound insulation performance at low-frequency range and reduce the sound absorption performance at high-frequency range. A dual density product can be considered a hybrid. It is absorptive, but also acts as a barrier. The basic acoustic mechanism is shown in Fig. 31.3. With respect to the traditional dash insulator, the lightweight scheme concept solves the problem of sound absorption performance at

Fig. 31.3 The acoustic mechanism of the two-layer acoustic dash insulator



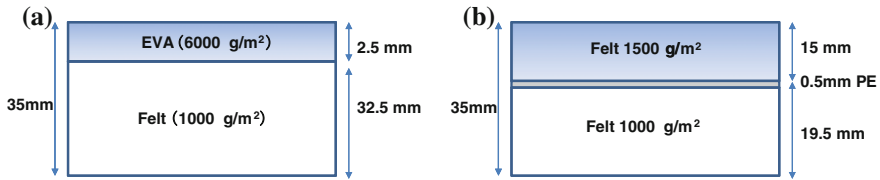


Fig. 31.4 The engineering application of the lightweight dash insulator design. **a** The dash insulator used before. **b** The design of lightweight dash insulator

high-frequency range and can reduce 30–60 % in weight, which can significantly enhance the sound quality in the passenger compartment.

In this paper, combined with a small passenger car project case, a new feasible scheme of lightweight concept is presented by the 2,500 g/mm² dash insulator (see Fig. 31.4). Compared with the used dash acoustic assembly, the sample piece is produced and the weight is reduced by 55 %. Barring the pass through and aperture, the total surface is 1.2 m².

31.3.2 SEA Simulation of the Lightweight Dash Insulator Design

SEA simulation tool is a well-established technique, commonly used in the car industry vehicle development process to provide design recommendations. SEA is most specifically implemented in early stages for weak path analysis, target setting, concept evaluation, or even design sensitivity analysis and can be easily combined with other measurement procedures.

The sound package lightweight technologies can be developed at first by SEA simulation taking into account both insulation and absorption properties of the dash mat. It is a feasible method to use the coupled reverberant room equation to evaluate the acoustic performance, instead of the reference SEA model (33.1). Noise attenuation level NR index is used to quantify its acoustic performance level.

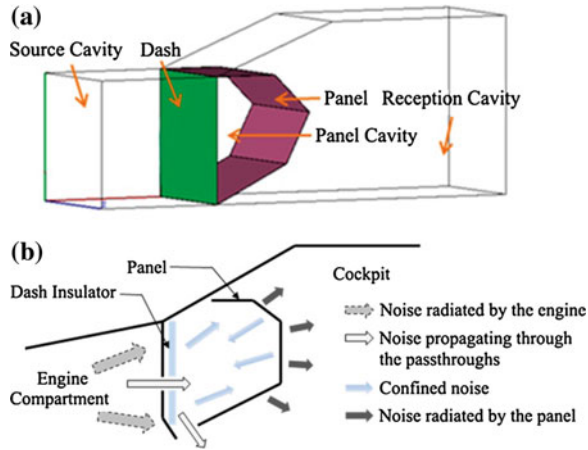
$$NR = SPL_1 - SPL_2 = TL - 10 \log(S/A); \quad \text{with } A = \sum_i \alpha_i \cdot S_i \quad (33.1)$$

where:

- NR noise reduction (dB), subtraction in dB of the SPL₁ in the emission cavity and of the SPL₂ in the reception cavity
- TL transmission loss (dB)
- S_i The component surface of the dash metal sheet coupling the cavities
- A equivalent absorption area of the reception cavity
- α_i the component absorption coefficient

For the simulation of dash insulator and dashboard leakage, the composite transmission loss between trimmed and bare steel metal is obtained by Eq. (33.2).

Fig. 31.5 The SEA model and mechanism for lightweight dash insulator. **a** Reference SEA model. **b** Sound transmission schematic diagram through dash



$$TL_{\text{comp}} = 10 \log \left(\frac{S_T}{S_W \tau_W + S_H \tau_H} \right) \tag{33.2}$$

where:

- τ_W transmission coefficient without leakage;
- τ_W transmission coefficient with leakage;
- TL_{comp} composite transmission loss (dB);
- S_T total surface of the trimmed metal sheet coupling the cavities;
- S_T the surface without leakage; and
- S_T the surface with leakage

In the dash insulator SEA simplified model (see Fig. 31.5), dash metal thickness is assumed to be 1 mm. The leakage area is defined according to the actual situation. Sound excitation source is defined as a white noise in the engine bay, and the sound absorption characteristics of instrument panel cavity is obtained by the material surface acoustic measurement data.

Through the multiple design optimizations, the acoustic behavior of the lightweight dash mat is achieved at a similar level, which can allow a weight reduction of 43 % compared to the traditional insulation reference (see Fig. 31.6a). But it is still important that the vehicle firewall must be designed to minimize holes and gaps, such as the steer lower shaft t, the HVAC pipe, the brake pump, and other wiring garments, which can degrade acoustic isolation.

The leakages of the pass-troughs are represented as equivalent trim uncovered areas. With 1 % of uncovered areas as shown in Fig. 31.6b, the noise attenuation performance for the leakage effect has low sensitivity compared with the traditional dash insulator. The surface absorption performance of lightweight dash insulator is better especially between the middle- and high-frequency ranges.

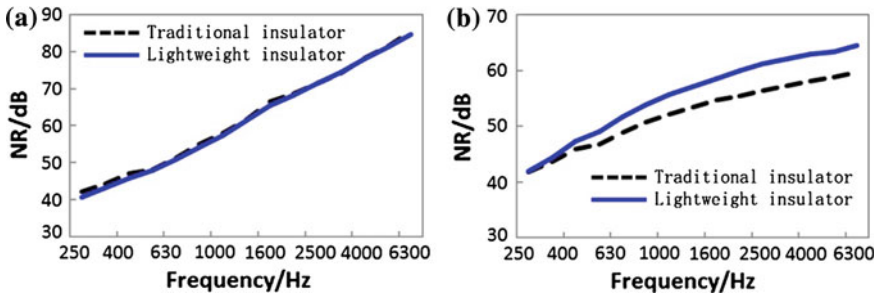


Fig. 31.6 The SEA results and comparison for dash insulator. **a** NR comparison (without leakage). **b** NR comparison (1 % uncovered area)

31.3.3 Test and Analysis for Lightweight Insulator

31.3.3.1 Acoustic Test and Analysis in Impedance Tubes

Acoustic characteristics of lightweight insulator material, such as absorption coefficient and transmission loss, can be tested and compared in impedance tubes. As shown in Fig. 31.7, the sound absorption performance of double felt is far superior to the traditional “Felt-EVA” dash insulator material with the same thickness. What’s more, in the frequency range of 1,000–2,500 Hz, the sound absorption coefficient of double felt increased more than 3 times, which will observably improve the interior sound quality. However, according to the principle of sound insulation by mass, double felt has a lower transmission loss performance level as its surface density is only 1/4 of the EVA material (5,900 g/cm²). The vehicle acoustic performance measurements are needed to validate the effect of the two acoustic parameters.

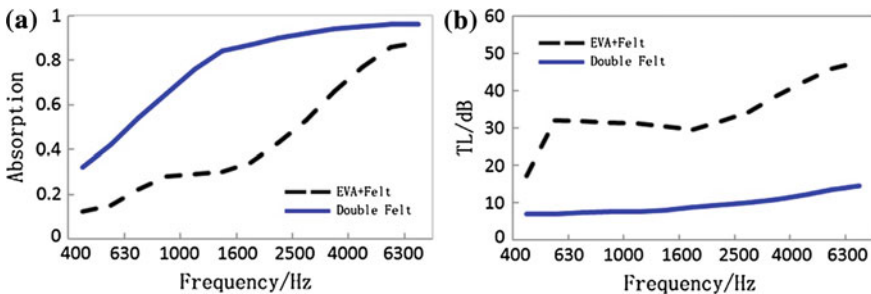
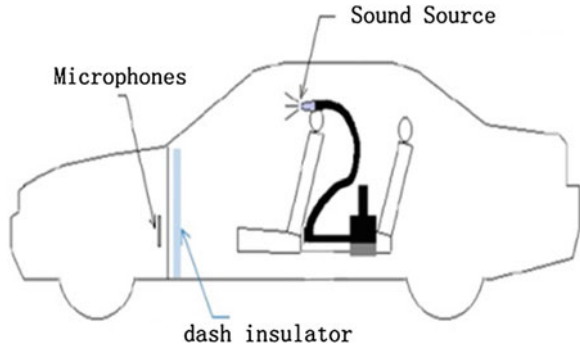


Fig. 31.7 Acoustic test result in impedance tubes. **a** Result comparison of the absorption coefficient. **b** Result comparison of the transmission loss

Fig. 31.8 Layout of acoustic transfer function test

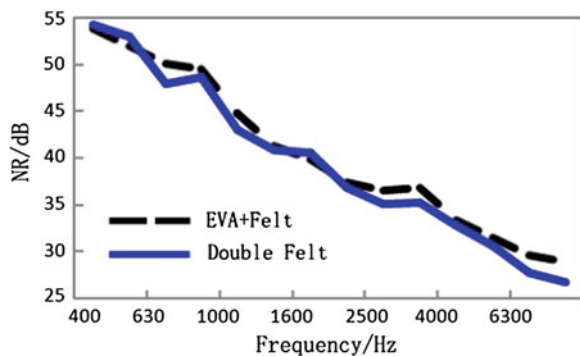


31.3.3.2 Test and Analysis of the Acoustic Transfer Function of a Vehicle

As an acoustic test in impedance tubes only simply reflect the performance of the material in itself, test and comparison of the NVH performance of a vehicle are required to weight the value of the lightweight double felt dash insulator through replacing the “Felt-EVA” insulator in a small passenger vehicles. The acoustic transfer function test of the engine compartment to the interior compartment is just such a way to evaluate the effect of absorption and insulation in a vehicle, as well as to be used for acoustic material design and optimization of different noise transfer paths. The test generated engine noise reduction (ENR) data using the reciprocal point source method (RPSM) in a semi-anechoic room, which is set up by placing a high-frequency sound source (HFSS) at the desired interior positions and placing microphones in the vehicle engine compartment (see Fig. 31.8). After average processed data, the overall effect of the dash insulator on the noise from the engine compartment to the interior compartment is attained.

As shown in Fig. 31.9, acoustic performance after 600 Hz frequency range has improved when the double felt insulator is fitted, especially in the range of 2,000–4,000 Hz acoustic transfer function is reduced by about 2.5 dB, which has a great impact on improving the interior sound quality in the passenger compartment.

Fig. 31.9 Result of acoustic transfer function test



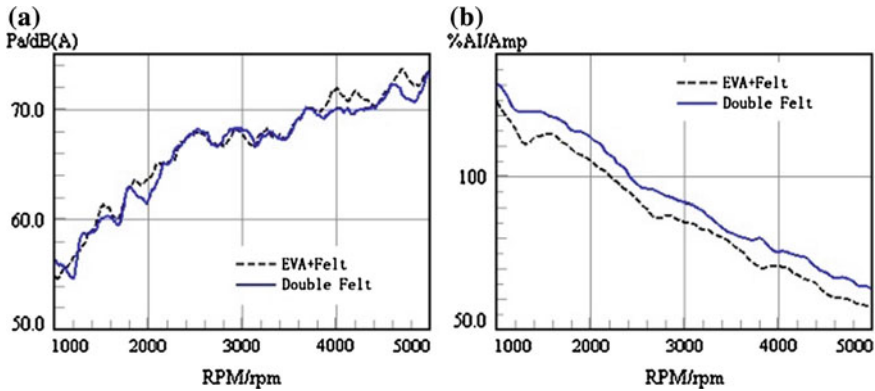


Fig. 31.10 Result of interior noise at full throttle acceleration in second gear. **a** Result of the sound pressure level. **b** Result of the open articulation index

31.3.4 Test and Analysis of the NVH Performance of a Vehicle on Road

Considering the attenuation of the noise from the power train and the chassis is the main impact on the NVH performance of a vehicle by the lightweight dash insulator, and test is taken under the driving conditions at full throttle acceleration in second gear and 60 km/h.

As shown in Fig. 31.10, driving in second gear, the car that was fitted with the double felt insulator did not lead to an increase in the sound pressure level of the car. What's more, it reduced about 2.3 dB(A) in the 3,800–5,000 rpm of engine speed, while the open articulation index increased by about 7 %, as well as the subjective evaluation can feel the proportion of high-frequency component in the interior noise reduced.

Similar result appeared when driving in 60 km/h, which also showed a decrease of the interior noise pressure level and an evident increase of the open articulation index to approximately 10 %. In addition, the sharpness index is reduced 10 % as well. All of these objective indexes reflect significant improvement in the sound quality when the lightweight double felt dash insulator is used (Fig. 31.11).

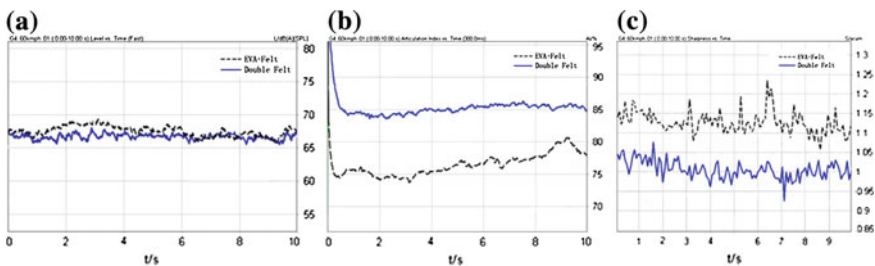


Fig. 31.11 Result of interior noise in 60 km/h uniform. **a** Result of the sound pressure level. **b** Result of the open articulation index. **c** Result of the sharpness index

31.4 Conclusions

This paper presented a procedure of sound package lightweight development. A new feasible scheme of lightweight project is provided by the 2,500 g/mm² dash insulator case. Considering the dash leakage effect, the SEA simulation and experiment measurement results are proved to improve the sound quality performance of interior automobile with approximately 55 % decrease of the weight. This paper is benefited for improving the understanding level and engineering application for sound package lightweight development in automotive industry.

References

1. Zhang Q, Parrett A, Zopp A (2013) Lightweight acoustic system performance target setting process. SAE technical paper 2013-01-1982
2. Duval A, Rondeau J, Bischoff L, Deshayes G (2009) Generalized light-weight concepts: improving the acoustic performance of less than 2500 g/m² insulators. SAE technical paper 2009-01-2136
3. Ernster S, Tudor J, Kathawate G (1999) Acoustical advantages of a new polypropylene absorbing material. SAE technical paper 1999-01-1669

Chapter 32

Exhaust Hook Model Prediction of Vehicle Condition Based on Frequency Response Method

Zhangming Su, Chao Ren, Zhongbiao Gou and Yanghui Xu

Abstract Exhaust model prediction based on local modeling method usually produces great error. To better predict hook model of vehicle condition, basic hook model of vehicle condition is established, and important corrections of hemming and baffle finite element (FE) models are carried out, as the real hook stiffness is the combination of hook body stiffness and its boundary stiffness. Model frequency response analysis is done on three hook examples which are directly connected to an exhaust muffler. Prediction results are in good agreement with the experiment results, and error is less than 0.6 %. The improved method is much more efficient in predicting the hook model of vehicle condition.

Keywords Frequency response method · Exhaust hook · Vehicle condition · NVH

32.1 Introduction

Hooks play an important role in the automobile exhaust system structure, which generally consists of five parts: flexi-pipe, silencers, pipes, hooks, and isolators. Usually, hooks are fastened on pipes or mufflers by soldering seam [1]. As the hot end of exhaust system is directly connected to an engine, structural loads in correspondence with ignition frequency are easily transmitted to the vehicle body through hooks. In extreme condition, the transmitted load may be greatly magnified when natural frequency of hook is consistent with that of excitation force. As a result, vehicle interior vibration and noise can be increased significantly [2, 3]. The prior way to avoid such situation is improving the first-order mode of exhaust hook. For a four-cylinder and four-stroke engine, the main ignition order is second order.

Z. Su (✉) · C. Ren · Z. Gou · Y. Xu
Automotive Engineering Institute, Guangzhou Automobile Group Co., Ltd., Guangzhou,
China
e-mail: suzhangming@gaei.cn

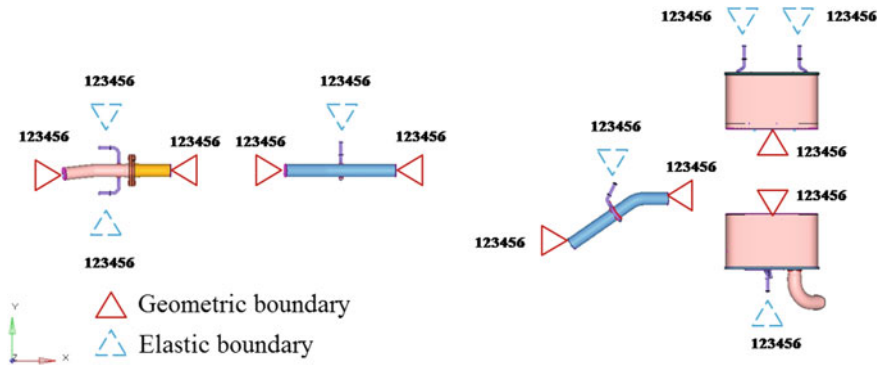


Fig. 32.1 FE model of hooks using local modeling method

Thus, the first-order hook mode of vehicle condition should be greater than 200 Hz as corresponds to 6,000 rpm.

Establishing accurate boundary conditions in finite element (FE) model is the major difficulty when predicting hook model of vehicle condition. The real hook stiffness characteristics are the combination of hook body stiffness and its boundary stiffness. The FE model of the pipes and mufflers which the hooks fastened to have a great effect on the prediction result. The traditional method, also called local modeling method, usually introduces a new boundary by cutting off the model 200 mm beyond the hooks. This method is considered to be simple and efficient, but the result is usually overestimated. In many cases, natural frequency of hooks predicted by local modeling method can be 10–50 Hz greater than that of experimental result of vehicle condition. The FE model of hooks using local modeling method is shown in Fig. 32.1.

The present method here gives better accuracy in predicting hook model of vehicle condition. Basic hook model of vehicle condition is firstly established in a FE code. Detail FE model corrections of hemming and baffler inside the muffler are carried out, as the real hook stiffness of vehicle condition is the combination of hook body stiffness and its boundary stiffness. Modal frequency response analysis is used to predict hook model.

32.2 Theory of Modal Frequency Response

Modal frequency response analysis is an alternate approach to computing the frequency response of a structure. This method uses the mode shapes of the structure to reduce the size, uncouple the equations of motion (when modal or no damping is used), and make the numerical solution more efficient. Since the mode shapes are typically computed as part of the characterization of the structure, modal frequency response is a natural extension of a normal mode analysis [4–7].

To proceed, temporarily ignore all damping, which results in the undamped equation for harmonic motion at forcing frequency.

$$-\omega^2[M]\{x\} + [K]\{x\} = \{P(\omega)\} \quad (32.1)$$

where $[M]$ is modal mass matrix, $[K]$ is modal stiffness matrix, and P modal force vector. In uncoupled form, the equations of motion are written as a set of uncoupled single degree-of-freedom systems as

$$-\omega^2 m_i \xi_i(\omega) + k_i \xi_i(\omega) = p_i(\omega) \quad (32.2)$$

where m_i is the i th modal mass, k_i is the i th modal stiffness, and p_i is the i th modal force.

Once the individual modal responses $\xi_i(\omega)$ are computed, physical responses are recovered as the summation of the modal responses using

$$\{x\} = [\phi]\{\xi(\omega)\}e^{i\omega t} \quad (32.3)$$

where the mode shapes $[\phi]$ are used to transform physical coordinates into modal coordinates.

32.3 Basic Model and Corrections

Basic hook model of vehicle condition is established in a FE code. Detail FE model corrections of hemming and baffle are carried out, as the real hook stiffness is the combination of hook body stiffness and its boundary stiffness.

32.3.1 Basic Hook Model of Vehicle Condition

The real boundary condition of hook of vehicle condition is complicated. The basic part of exhaust hook is usually fastened on muffler or pipe by soldering seam, while the head is connected to a rubber isolator. Both the soldering seam and rubber isolator have great effect on the hook model prediction, which the local modeling method mentioned previous is not taken into consideration. Soldering seam is modeled with three-dimensional (3D) solid element. Rubber isolator is modeled with 1D spring element (CBUSH) and defined with three-directional dynamic stiffness. All six degrees of freedom (DOF) of the isolator on the car body side are set zero, as is shown in Fig. 32.2. Exhaust hook FE model of vehicle condition is shown in Fig. 32.3.

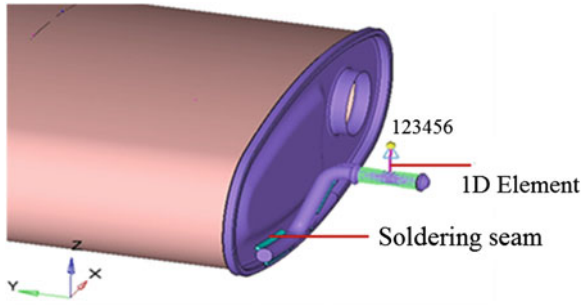


Fig. 32.2 Boundary conditions of hooks. Soldering seam is modeled with 3D solid element. Rubber isolator is modeled with 1D spring element (CBUSH)

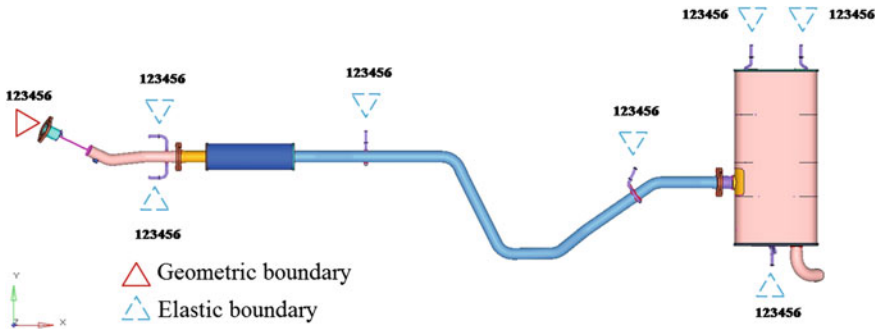


Fig. 32.3 Exhaust hook FE model of vehicle condition. All six degrees of freedom of the isolator on the car body side are set zero

32.3.2 Hemming Corrections

Hemming structure has significant effect on hook model prediction. Further corrections must be carried out to establish accurate hemming model, as additional stiffness caused by friction between two faces inside the hemming structure is not considered in a conventional FE code, as is shown in Fig. 32.4a. As a result, the local hemming stiffness in FE model is usually weaker than that of a trial sample. One simple way to strengthen the local hemming stiffness is adding some 1D rigid elements between hemming shells in circumferential direction of the muffler, as shown in Fig. 32.4b.

As is shown in Fig. 32.5a and b, frequency response curve of hook changes significantly after hemming corrections. The first-order frequency increases by 12 Hz after correction. More importantly, the interference peaks disappear after hemming corrections, and the hook modes become more obvious. Thus, hemming correction is very necessary when predicting hook model with FE method.

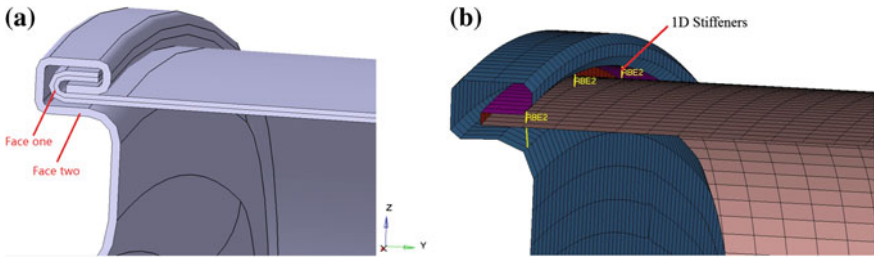


Fig. 32.4 Hemming structure of actual sample (a); strengthened FE model of hemming (b)

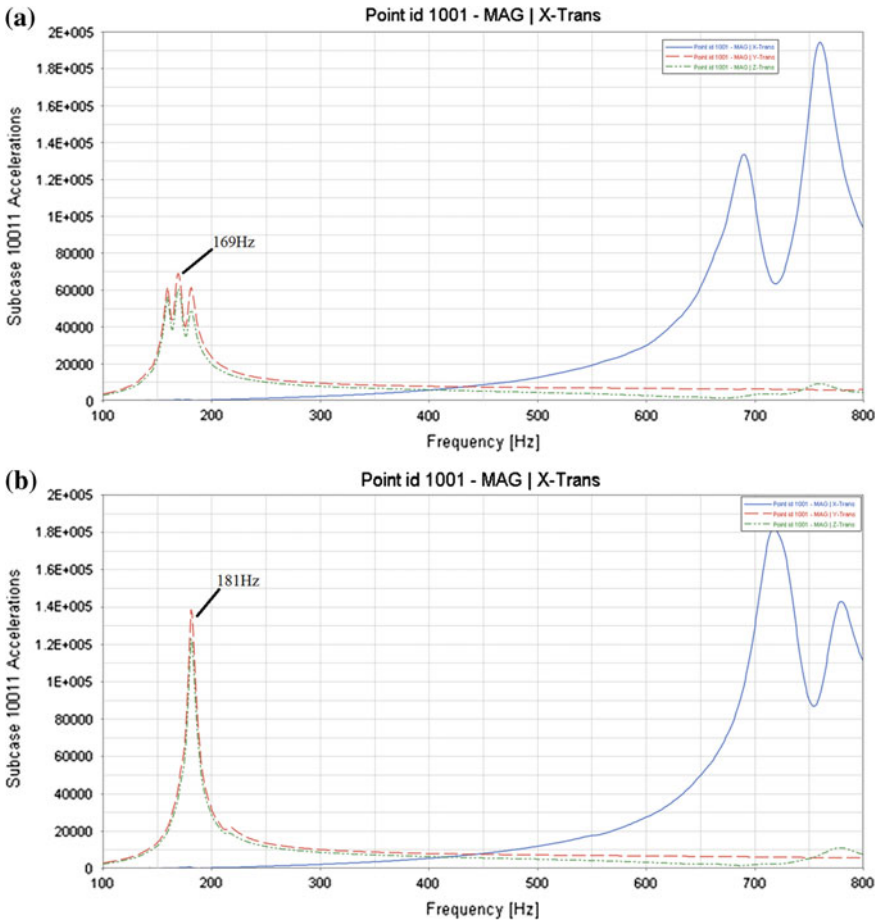


Fig. 32.5 Frequency response of hook before correction (a); frequency response of hook after correction (b)

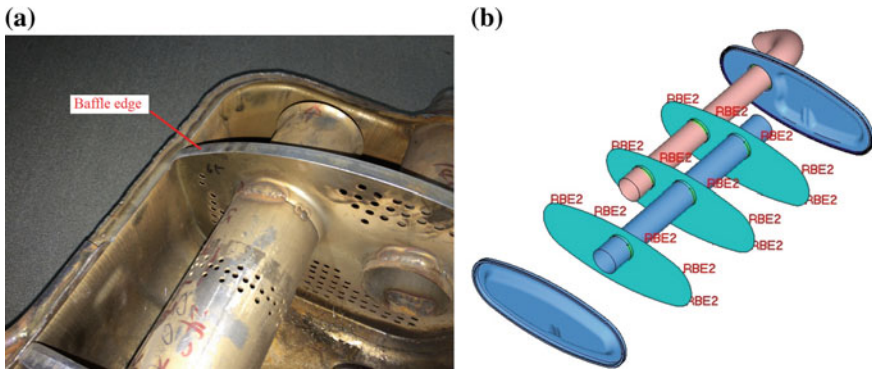


Fig. 32.6 Baffle edge of a trial sample (a); baffle FE model after correction (b)

32.3.3 Baffle Corrections

Baffle structure inside muffler also has significant effect on hook model prediction, as false modes of hook caused by abnormal vibration of baffle and pipe may appear. In a trial sample, friction between baffle edge and muffler shell usually produces additional frictional stiffness, which is not taken into consideration in FE models. Thus, baffle model correction is necessary to strengthen the local stiffness of baffles. One simple way to strengthen baffle structure is adding some 1D rigid element in circumferential direction of the baffle, as shown in Fig. 32.6b. Baffle structure of a trial sample is shown in Fig. 32.6a.

The effect of baffle stiffness on hook model is clearly explained by comparing Fig. 32.7a with b. Abnormal vibration of baffles and pipes disappears after correction, and hook modes become more obvious.

32.4 Result and Validation

Three hooks (5#, 6#, 7#) directly connected to a rear muffler are selected as examples, as is shown in Figs. 32.8 and 32.9. Important corrections of hemming and baffle are carried out after the basic hook model of vehicle condition is finished. Unit force is applied to the hooks, and modal frequency response analysis is done with a conventional FE code. Prediction results of the three hooks are shown in Figs. 32.10a, 32.11a, and 32.12a, respectively.

To verify the prediction results, experiment is carried out on the hook samples, which are also carried out on vehicle condition. Frequency response test is done with the help of a famous vibration test system. Experimental results of the three hooks are shown in Figs. 32.10b, 32.11b, and 32.12b, respectively. Difference between prediction results and experimental results is shown in Table 32.1.

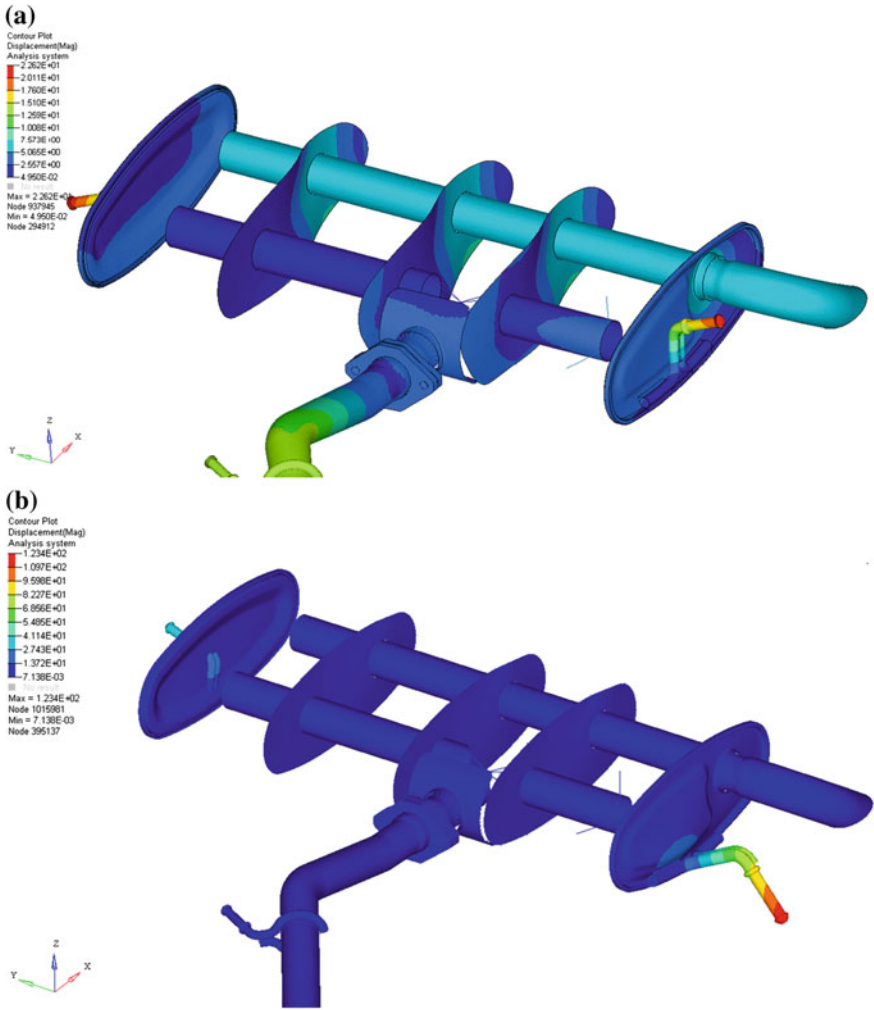


Fig. 32.7 Modal shape of hook before correction (a); modal shape of hook after correction (b)

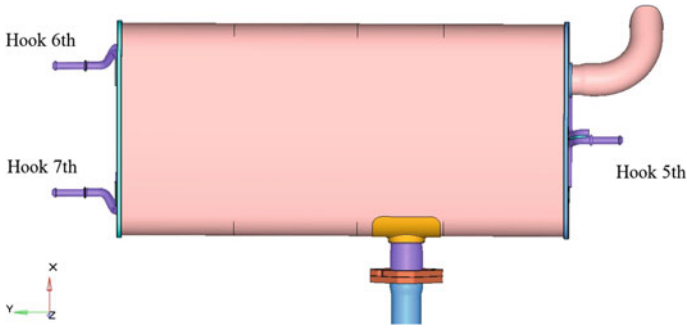


Fig. 32.8 FE model of three hook examples (5#, 6#, 7#) directly connected to a rear muffler

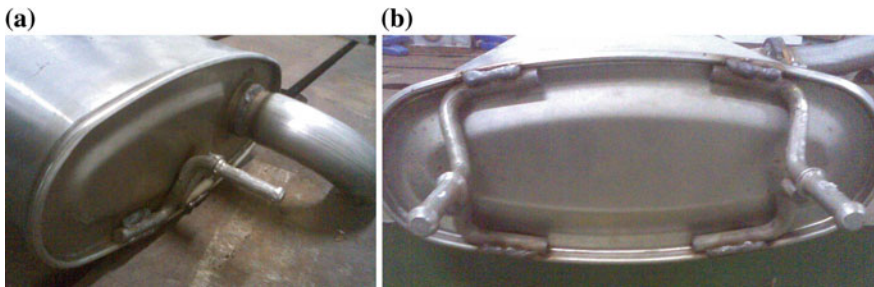


Fig. 32.9 The 5th hook trial sample (a); the 6th and 7th hook trial samples (b)

Prediction results are in good agreement with the experiment results, and the error is less than 0.6 %. More importantly, besides the first peak, the other peaks in the frequency response curves are also in good agreement with each other. The main reason is that almost all interference peaks are eliminated after hemming and baffler corrections as discussed in Sects. 32.3.2 and 32.3.3.

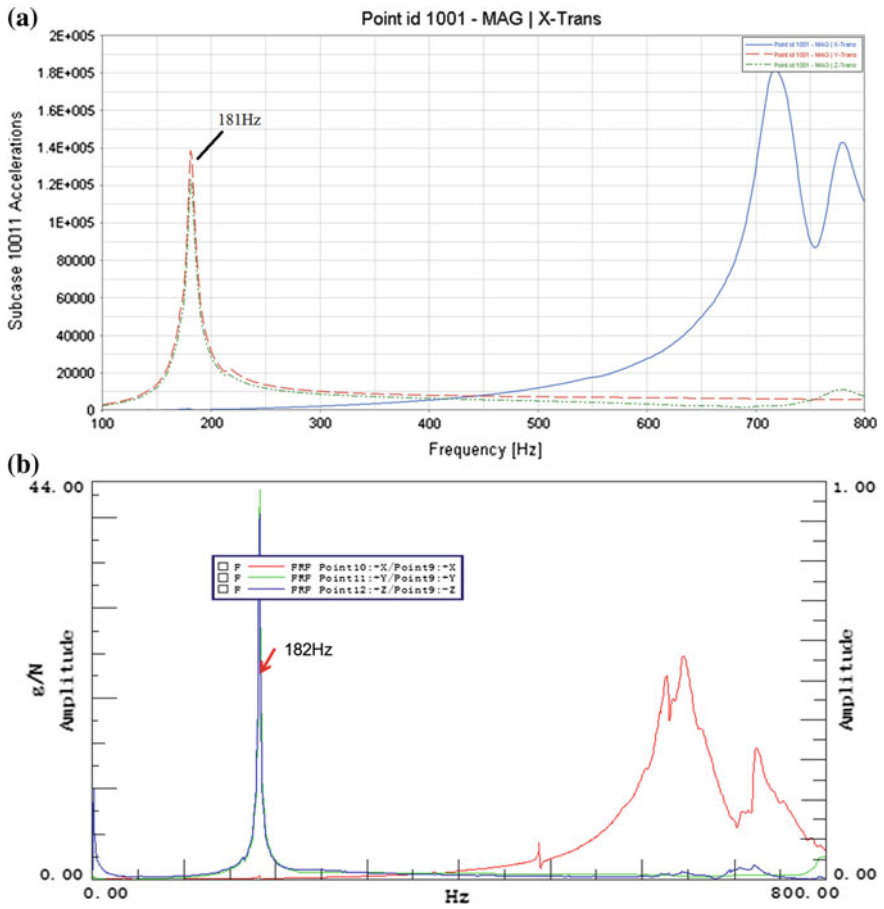


Fig. 32.10 Prediction result of the 5th hook (a); experimental result of the 5th hook (b)

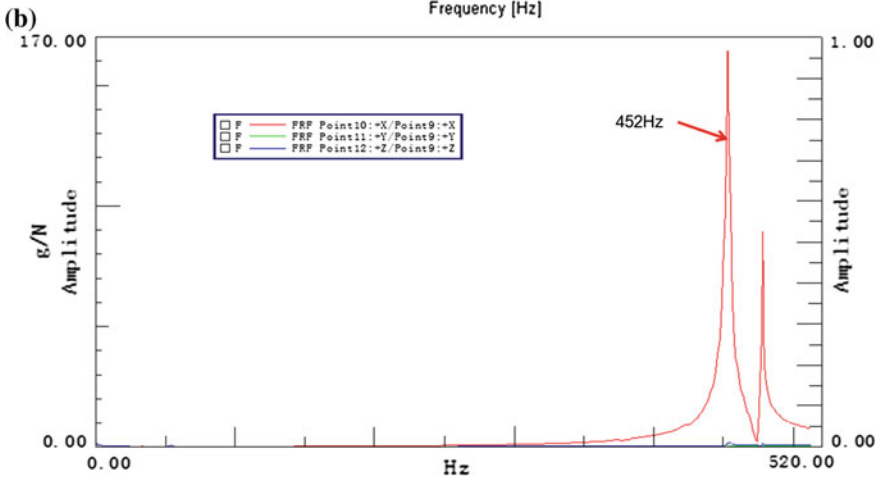
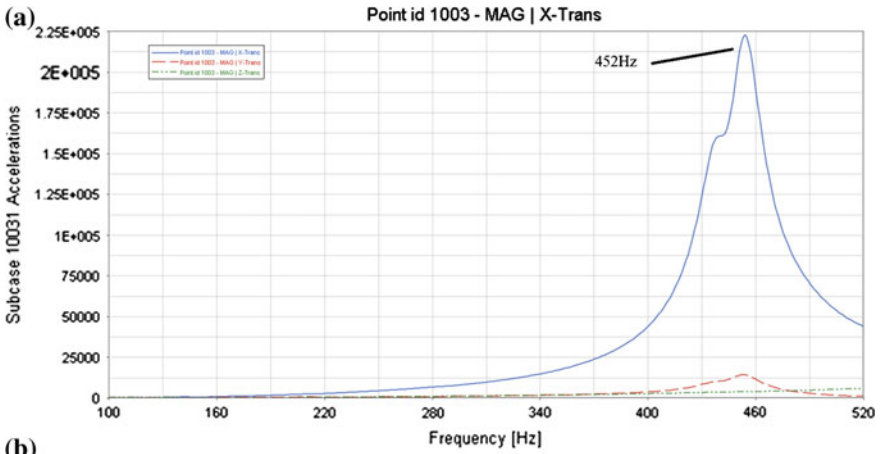


Fig. 32.11 Prediction result of the 6th hook (a); experimental result of the 6th hook (b)

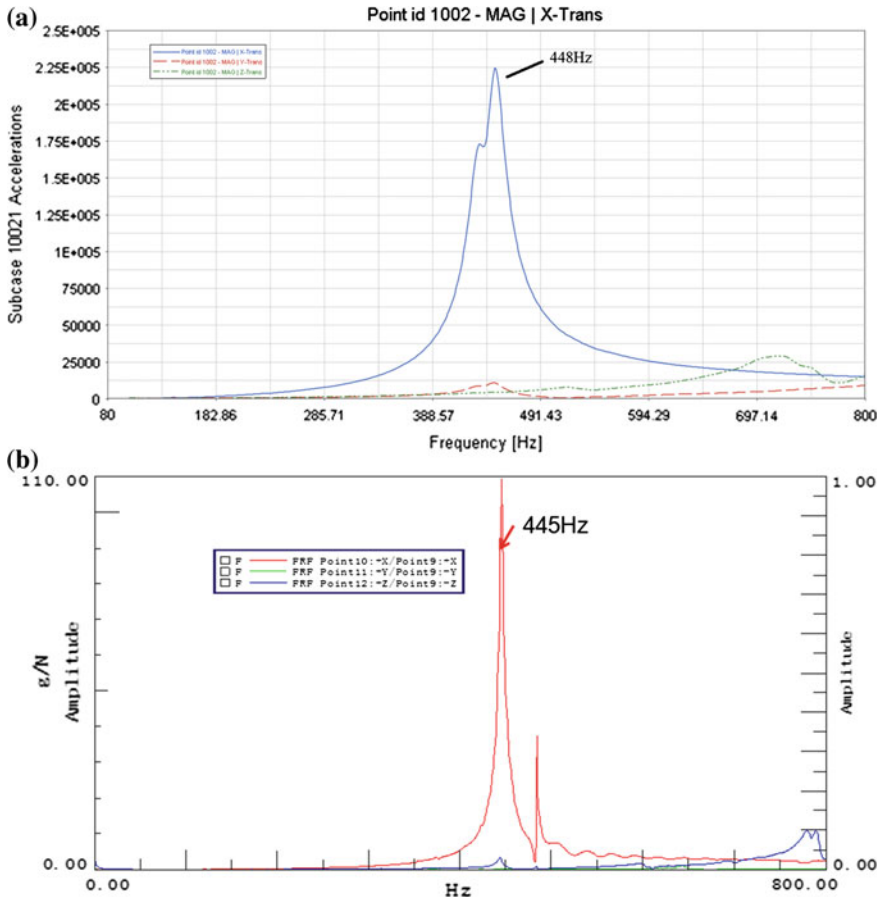


Fig. 32.12 Prediction result of the 7th hook (a); experimental result of the 7th hook (b)

Table 32.1 Comparison of prediction results and experimental results. The first-order mode of hook examples (5#, 6#, 7#)

Hooks	Prediction result (Hz)	Experimental result (Hz)	Error (%)
5th	181	182	0.5
6th	452	452	0
7th	448	445	0.6

32.5 Conclusions

This article mainly investigates the hook model prediction of vehicle condition. Basic hook model of vehicle condition is firstly established, and important corrections of hemming and baffle models are carried out, as the real hook stiffness is the combine of hook body stiffness and its boundary stiffness. Modal frequency response analysis is done on three hook examples (5#, 6#, 7#) directly connected to a rear muffler. Prediction results are in good agreement with the experiment results, and error is less than 0.6 %. More importantly, besides the first peak (the first-order mode of hook), the other peaks of the prediction curves are also in good agreement with those of experimental curves. The main reason is that almost all interference peaks are eliminated after hemming and baffle corrections. The presented method gives better result in predicting hook model of vehicle condition.

References

1. Chen LL, Li SC, Shi Y (2013) Optimization of isolator position of passenger car exhaust system. *J Mech Eng Autom* 180(5):56–60
2. Ni J, Shen ZH, Jin H (2011) A study on modal and vibration performance and components sensitivity of vehicle exhaust system. *J Autom Technol* 11:9–12
3. Yao YS, Ma FW, Feng ZX (2011) Influence of exhaust isolator locations on vehicle interior noise level. *J Eng Sci* 32(4):30–33
4. Pang J, Chen G, He H (2006) *Automotive noise and vibration: principle and application*. Beijing Institute of Technology Press, Beijing
5. Tian LS, Li XH, Ma YF (2012) *MSC/Nastran basic dynamic analysis guide*. China Waterpower Press, Beijing
6. Ni ZH (1989) *Mechanical vibrations*. Xi'an Jiaotong University Press, Beijing, pp 161–207
7. Tony L, Schmitz K, Scott S (2011) *Mechanical vibrations: modeling and measurement*. Springer, New York, pp 176–178

Chapter 33

An Investigation on Turbocharger Whine Noise

Zhang Song Zhan, Jin Yang, Jin Cai Yang, Jun Lan, Gang Liu,
Yong Jiang Xu, Jin Cai and Liang Zhang

Abstract There are two main reasons for turbocharger whine noise in vehicle, unbalance and pressure pulsation, and they have the same characteristic but different mechanism. The different methods are studied in this paper to improve the different whine noise. Nonlinear order pick-up method is applied in analysis of whine noise contribution and the objective evaluation standard about turbocharger whine noise is established.

Keywords Engine NVH · Turbo charger whine · Unbalance · Pressure pulsation · Nonlinear

33.1 Introduction

In general, the turbocharger for passenger car runs at the speed from 60,000 to 250,000 rpm (vs. rotor shaft). In run-up operating condition, there is whistle noise called turbocharger whine noise or TC whine noise that is caused by the vibration of rotor or pulsation of airflow. The whine noise is synchronous to turbocharger shaft speed, and its main center frequency is typical in the range of 1,200–4,000 Hz [1] for the passenger car. There are two kinds of whine noise, unbalance whine and pulsation whine. The unbalance whine is caused by rotor of unbalance, and the other one is caused by pressure pulsation from the compressor. The whine noise transfers to the cabin by the structure borne and airborne path. The whine is easy to be identified and it affects the acoustic quality in the cabin [5]. For investigation of

Z.S. Zhan · J. Yang (✉) · J.C. Yang (✉) · J. Lan · G. Liu · Y.J. Xu · J. Cai · L. Zhang
Powertrain Global R&D Center, Chang An Automobile Co. Ltd, Chong Qing, China
e-mail: yangjin@changan.com.cn

J.C. Yang
e-mail: yangjc@changan.com.cn

J. Yang · J.C. Yang · G. Liu · Y.J. Xu · J. Cai · L. Zhang
State Key Laboratory of Vehicle NVH and Safety Technology, Chong Qing, China

TC whine noise and the application of main transmissions analysis technique and improvement methods, signals of unbalance vibration and pressure pulsation noise are tested.

33.2 The Investigation on the TC Whine Noise

33.2.1 The Different Mechanisms of the TC Whine

33.2.1.1 The Mechanism of the Unbalance Whine

The turbocharger rotor generates centrifugal force that cannot keep the balance when the turbocharger unbalance mass exists. The centrifugal force is an additional force to the rotor that also is called unbalance force that shows as F , $F = m\omega^2e$, the force is linearly proportional to the frequency of the rotor speed [2].

In Fig. 33.1, the rotor shaft bends and vibrates because of the excitation that comes from the radial force. At the same time, the large unbalancing forces act on gas airflow and the bearings, and therefore it causes a whine noise called unbalance whine. Because the frequency of unbalance whine is equal to the rotor speed (rev/s), it is also called the first-order unbalance whine. Figure 33.2a shows the graduate level of first-order vibration rise with increasing unbalance value. The smaller unbalance value, the lower vibration level.

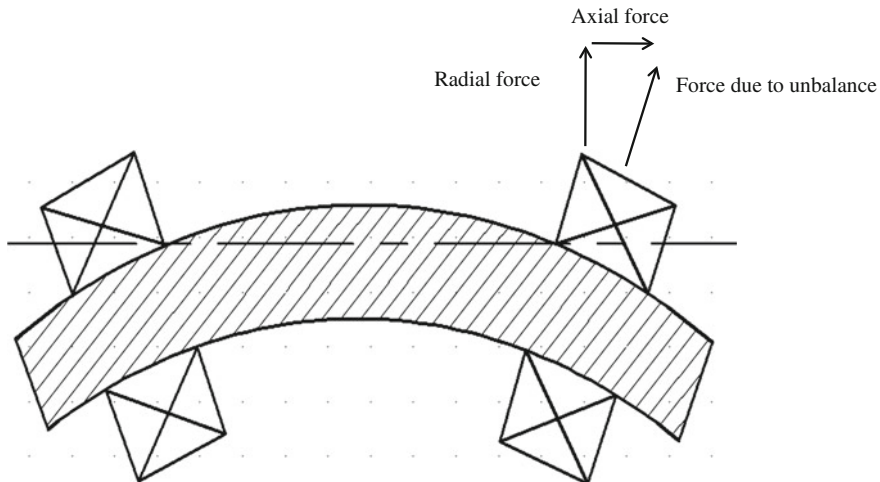


Fig. 33.1 The analysis of the centrifugal force on the rotor system

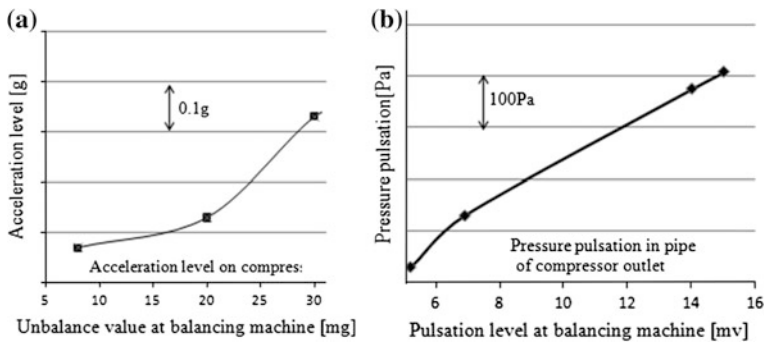


Fig. 33.2 The influence on vibration and pulsation of TC due to unbalance and pulsation level

33.2.1.2 The Mechanism of the Pulsation Whine

The compressor inner airflow is uneven airflow described by Lagrange equations as, $p = p(a, b, c, t)$, $\vec{v}(a, b, c, t) = \frac{\partial \vec{r}(a, b, c, t)}{\partial t}$. The pressure pulsation caused by unsteady airflow acts on medium in the compressor which changes over time [3]. The noise is called pulsation whine noise, and its frequency $f = i \cdot n / 60$, where i represents the order, $i = 1, 2, 3 \dots$, the n represents the rotor speed, rev/min. When $i = 1$, the first-order pulsation whine is strong enough to be heard. Figure 33.2b indicates that the graduate level of first-order pressure pulsation rises with increasing pulsation level.

33.2.2 The Characteristic of TC Whine Noise

The characteristic of the TC whine noise is nonlinear order that is different to engine's order noise because of turbocharger shaft speed is not synchronous to engine speed.

Figure 33.3 shows the curves of the first-order whine, the first pressure pulsation and the first-order unbalance vibration. These curves look identical. Their frequency is in the range of 1,250–2,000 Hz and is increasing with engine speed. This noise sounds like whistle and it is easy to be perceived by people.

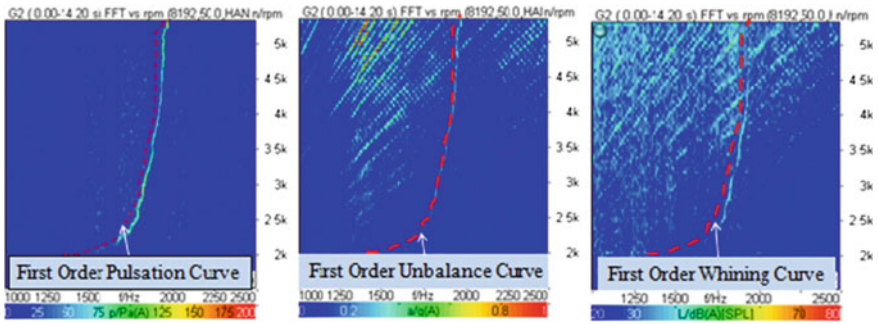


Fig. 33.3 The colormap about pulsation, unbalance, and whine noise

33.2.3 The Transmission Path Analysis (TPA) of TC Whine Noise

33.2.3.1 The TPA of Unbalance Whine Noise

The unbalance whine noise is classed as structure borne noise that transmits by structure mostly, as show in Fig. 33.4.

33.2.3.2 The TPA of Pulsation Whine Noise

The pressure pulsation of airflow occurs at the end of compressor blade, the wall of compressor, and the pipe of compressor’s outlet. The wrap method is applied for the identification of the main transmissions of pulsation whine. Figure 33.5b shows a slight decrease on the amplitude of pulsation whine by wrapping surface of compressor. Figure 33.5c shows a significant decrease on the amplitude of pulsation whine in range of 2,600–2,800 Hz by wrapping the pipe of compressor’s outlet.

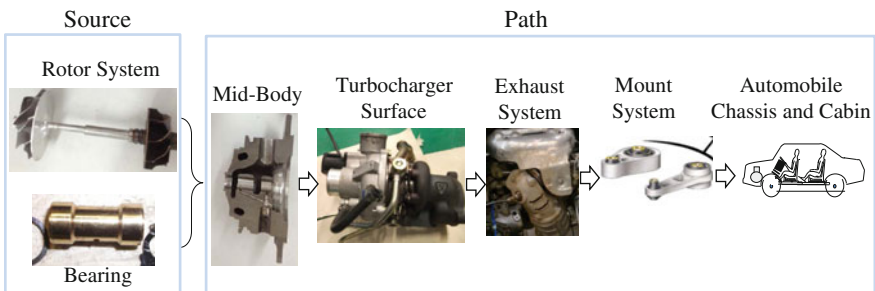


Fig. 33.4 The TPA of the unbalance noise

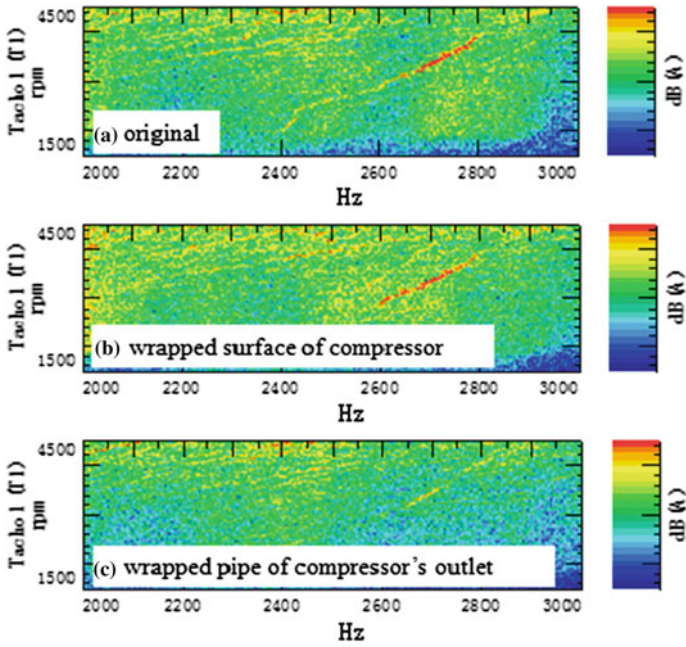
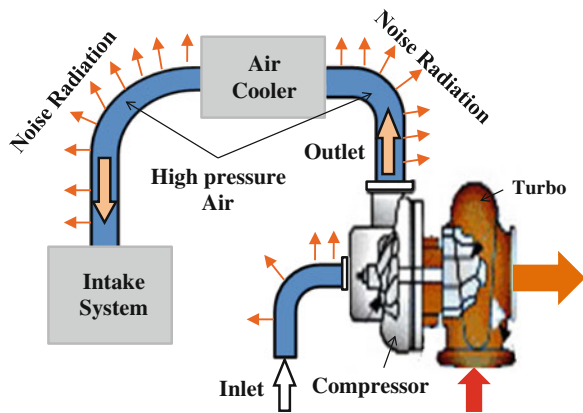


Fig. 33.5 The comparison of whine noise

Fig. 33.6 The TPA of pulsation whine



The result indicates that the most of pulsation whine noise goes with the high pressure airflow and radiates from the pipe of compressor's outlet. The main transmissions are as shown in Fig. 33.6.

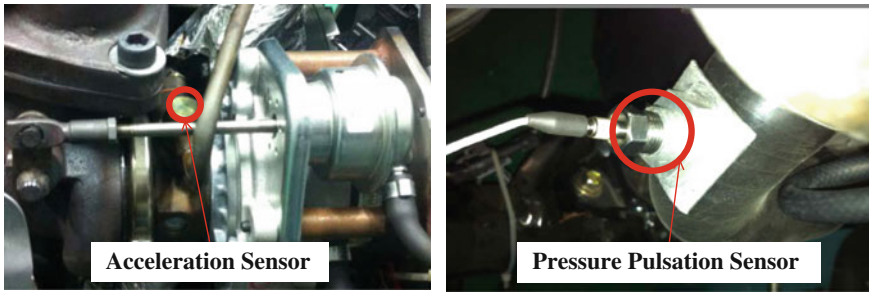


Fig. 33.7 The test location on turbocharger

33.2.4 The Analysis Methods of TC Whine Noise

In order to improve the acoustic quality and reduce the cost on the vehicle, it is needed to analyze the contribution of TC whine noise to the overall noise, to evaluate and reduce the possibility of TC whine in the phase of NVH development of powertrain. The analysis process includes signal testing, contribution analysis of TC whine noise to the overall noise, root cause analysis of first-order whine, and the optimization validation.

33.2.4.1 Signal Testing

For representing the level of unbalance vibration and the pressure pulsation exactly, the sensors are installed onto the especial location. In Fig. 33.7, an acceleration sensor is installed at the middle of the turbocharger, and a pressure pulsation sensor is installed at the pipe of compressor's outlet. In the measurement, two vibration signals and an acoustic signal are tested in run-up operating condition.

33.2.4.2 The Contribution Analysis of the First-order Whine Noise to the Overall Noise

The first-order whine curve is nonlinear, and it can be obtained by the nonlinear order pick-up method [4]. The frequency of the first-order whine is equal to the rotor speed (rev/s). The rotor speed m can be calculated by the formula, $m = fz \times 60$, where $z = 1$. Therefore, the nonlinear whine curve is changed to linear whine curve in the colormap [4].

Figure 33.8a shows the nonlinear characteristic of the first-order whine curve, x-axis is the frequency (Hz) and y-axis is the TC rotor speed (rpm). In the engine speed of 3,250–3,680 rpm, and the frequency of 2,600–2,700 Hz, the first-order whine becomes much larger, which can be perceived as the TC whine noise. Figure 33.8b shows the colormap changing from Fig. 33.8a after applying the

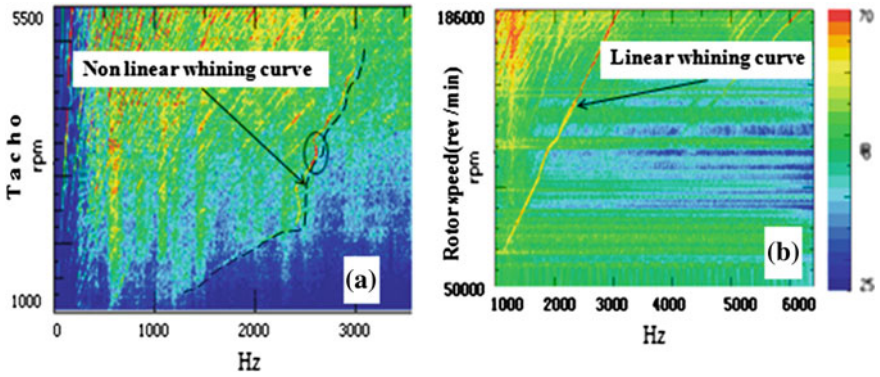


Fig. 33.8 The nonlinear curve turns to linear by transferring the reference speed from engine to TC rotor

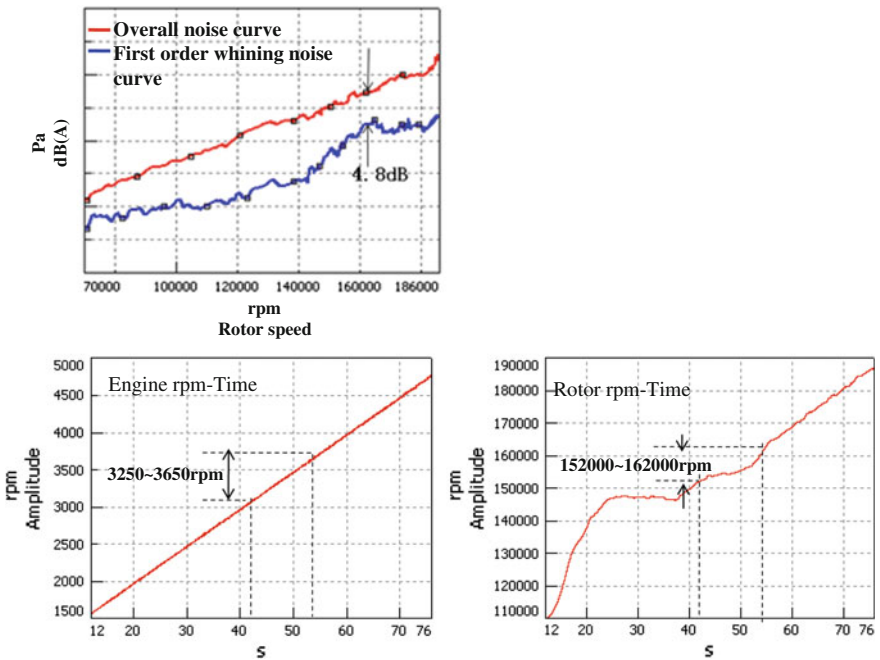


Fig. 33.9 Difference between first whine noise and overall noise

nonlinear order pick-up method, and then the first-order whine noise curve turned to straight from bent. As shown in Fig. 33.9, the overall noise level increases smoothly and linearly when the engine runs up, while in the range of 156,000–162,000 rpm, there is a clear peak on the first-order whine curve of the TC noise. In the whole run-up operating condition, the average difference between the overall level curve

and the first-order curve is 7.4 dB (A). But at the peak area, it is much small as 4.8 dB (A). Based on the objective evaluating standard of the order whine noise, it will cause TC first-order whine at the peak area. In the subjective evaluating result, people can clearly perceive the TC first-order whine in engine speed range of 3,250–3,680 rpm under the same load condition. Both the subjective and the objective evaluation method show good correlation. This result shows that we can correctly evaluate the whine noise by making use of the contribution analysis method and make it possible to evaluate the TC whine in an objective way.

33.2.4.3 The Root Cause Analysis of the TC First-order Whine

The recent research has indicated that the characteristic of two kinds of the TC first-order whine noise is the same, and we cannot directly recognize the kind of the whine from the colormap. In this paper, we analyze the first-order vibration and pulsation, and then figure out the reason of the whine noise by an actual case.

A subjective evaluation result shows the first-order whine noise is clearly perceived when the engine speed runs in the range of 2,300–2,600 rpm on vehicle. Figure 33.10 shows in engine speed range of 2,300–2,600 rpm, the whine characteristic, whose frequency is around 1,783–1,833 Hz, can be obviously observed in the cabin noise test data. We cannot identify the kind of the TC first-order whine,

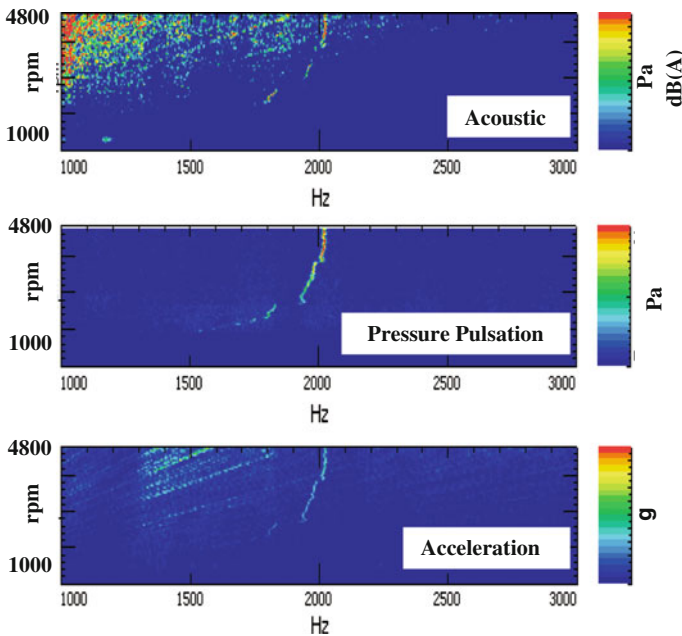
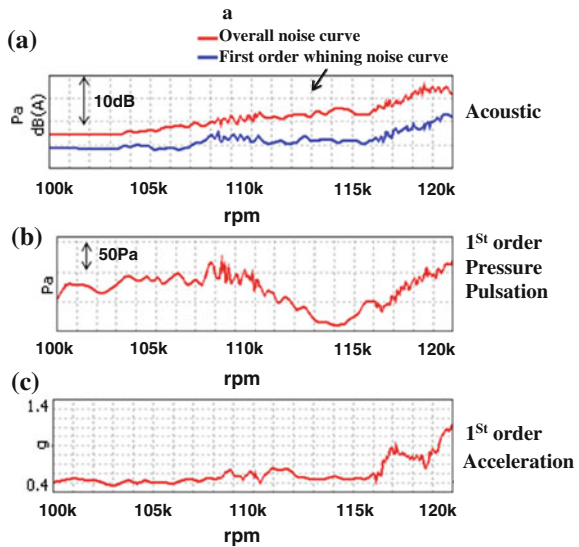


Fig. 33.10 Acoustic, pulsation, and acceleration

Fig. 33.11 Compare among the first curves



because both the first pressure pulsation and the unbalance vibration have a big value at this moment.

Applying the nonlinear order pick-up method, we obtain the first whine, first pressure pulsation, and the first vibration accelerate separately. Figure 33.11a shows in the rotor speed of 107,000–110,000 rpm, the overall curve characteristic and the first whine curve have the same, they all exist many peaks in the focus speed range. The smallest difference value between the overall curve and the first whine curve is only 3.3 dB (A). The Fig. 33.11a also indicates that the peaks of the overall noise curve are contributed by the first whine noise. Figure 33.11b shows in the pressure pulsation curve, there are many peaks in rotor speed range of 107,000–110,000 rpm that like the first whine noise curve and the biggest pressure pulsation reach at 200 Pa. Figure 33.11c shows in the same rotor speed range, the first vibration curve is smooth. Besides, with the same type turbocharger, there is no whine noise when the first pressure pulsation smaller than 150 Pa and the first vibration accelerate smaller than 1 g on the vehicle. According the above analysis results, the TC first-order whine is caused by the pressure pulsation.

33.2.5 The Optimizing for the First Whine Noise of TC

Generally, we will control the whine noise from both excitation source and the transfer path. And in this paper, mostly research the transfer path control strategy, we optimize the TC whine noise by reducing the power of noise that radial to the air. Figure 33.12a shows engine noise spectrum map, in engine speed range of 2,000–2,700 rpm, the TC first-order whine, whose centered frequency is 1,950 Hz

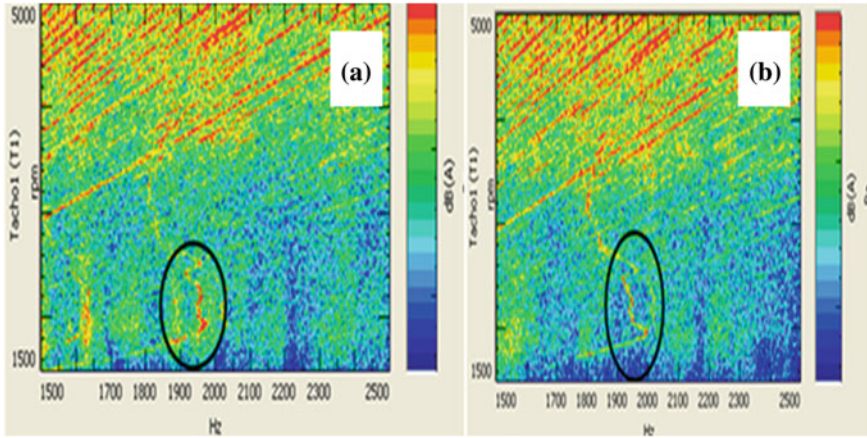
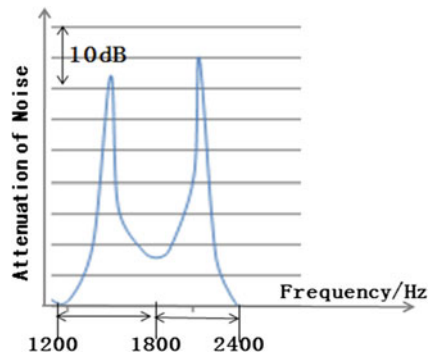


Fig. 33.12 Effect of the designed muffler

Table 33.1 The design parameter of noise muffler

The design parameter of noise muffler		
Parameter	Value	Source of value
Center frequency f (Hz)	1,950	Acoustic measure
Temperature of air T (k)	390	Temperature measure
Location acoustic velocity C (m/s)	410.9	$C = 340 + 0.60 * (T - 273)$
Length of muffler L (m)	0.053	$L = 1/4 * C/f$
Diameter of muffler d (m)	0.015	Experience
Modify length L_a (m)	0.046	$L_a = L - 4 * d/(3 * 3.14)$

Fig. 33.13 The transfer loss curve of muffler



and bandwidth is 100 Hz, can be obviously observed. Based on the centered frequency, we design a muffler to optimize the whine. The design detail sees in Table 33.1 [6]. Figure 33.13 shows in range of 1,800–2,400 Hz, the attenuation of

noise is 35 dB which meets the design requirement. Figure 33.12b depicts the first-order whine noise level decrease significantly in range of 1,900–2,000 Hz by applying the designed muffler and achieves the noise goal.

33.3 Conclusions

1. The first-order whine of turbocharger includes unbalance whine and pulsation whine. The unbalance whine is the structure born noise that transmits to the cabin via engine mount system. Whereas the pulsation whine is the airborne noise most of which transmits to the cabin by radiating from the pipe of compressor outlet and exhaust system. The level of first-order vibration rises with increasing unbalance value, and the level of first-order pressure pulsation enhances with increasing pulsation level.
2. The contribution of the first-order whine noise to overall noise can be calculated when using the nonlinear order pick-up method. In this way, we can correctly evaluate the whine noise and make it is possible to evaluate the TC whine in an objective data compared to the subjective way.
3. The research results show that the primary selection is to decrease the power of whine noise on the transmissions.

References

1. Stoffels H, Schroerer M (2003) NVH aspects of a downsized turbocharged gasoline powertrain with direct injection, paper no. SAE International, 1664. 2003.01
2. Li HB (2006) The institute about the TC rotor system vibration on IC engine. Vibration-Principle and Application, paper no. 2006.6
3. Yuan SQ, Xue F, Yuan JP, Tang Y (2009) The study on the reference between the flow noise and pressure pulsation in centrifugal pump. Hydromechanics and Mechanism, paper no. 2009.9
4. Yang JC, Yang J (2013) Study on separating technology of engine non-linear order noise. Automotive NVH Engineer, paper no. 2013.9
5. Rämme H, Åbom M (2007) Acoustics of turbochargers. SAE.2007.1
6. Pang J, Chen G, He H (2006) Automotive noise and vibration-principle and application. Beijing Institute of Technology Press, Beijing

Chapter 34

Phenomenon and Analysis of Low-Frequency Standing Wave Inside Exhaust System

Shuo Zhang, Jian Pang, Haiyan Zhang, Liang Yang and Wei Qing

Abstract Based on theoretical analysis and numerical simulation, the paper analyzes standing wave mechanism in exhaust system. The standing waves are founded in the exhaust orifice noise from a vehicle testing. An acoustic model for the exhaust system is established, and orders' acoustic characteristics for the tailpipe noise are analyzed where a resonant peak is caused by the standing wave. A method is proposed to eliminate the standing wave noise by inserting a perforated resonator on the tailpipe. Three resonators with different volumes are compared, and the best one is chosen to control the low-frequency standing wave noise.

Keywords Exhaust system · Standing wave · Acoustic analysis · Muffler

34.1 Introduction

NVH is a major index to decide a vehicle's comfort ability, while exhaust noise is one of the major vehicle noise sources. The exhaust low-frequency noise impacts the subjective auditory cognitive features, such as sound strength, booming, and annoyance. It is extremely important to control low-frequency noise in order to suppress the booming and annoying sound at exhaust orifice.

Domestic and foreign scholars carried out extensive research and experimental analysis on the exhaust low-frequency noise problems and provided control methods from two aspects. One method is to increase muffler volume and modify muffler internal structure. The other method is to adjust the tailpipe length. Selamet and Ji [1] analyzed sound characteristics of special mufflers with extended inlets and outlets or offset inlets and outlets using 2D and 3D analytical methods. Selamet

S. Zhang · J. Pang (✉) · H. Zhang · L. Yang · W. Qing
Changan Auto Global R&D Center, 401120 Chongqing, China
e-mail: pangjian@changan.com.cn

S. Zhang · J. Pang · H. Zhang · L. Yang · W. Qing
State Key Laboratory of Vehicle NVH and Safety Technology, 401120 Chongqing, China

and Ji [2] and Wu et al. [3] analyzed sound characteristics of a muffler with single inlet and dual outlets and a muffler with dual inlets and single outlet by modal grid method. Zhao [4] studied the influence of tailpipe length and diameter on engine performance and tailpipe orifice noise.

The paper analyzes low-frequency standing wave characteristics of an exhaust orifice noise and provides the control methods. The test results show that the methods can effectively solve the low-frequency standing wave problem.

34.2 Mechanism of Standing Wave in Exhaust System

34.2.1 Mechanism of Standing Wave in Pipe

Sound inside a pipe is assumed as plane-wave propagation. There exist incident wave and reflective wave when sound propagates inside the pipe, as shown in Fig. 34.1.

The sound pressure at any point inside the pipe is summation of incident sound pressure p_i and reflective sound pressure p_r , and expressed as follows

$$p(x, t) = P_i e^{j(\omega t - kx)} + P_r e^{j(\omega t + kx)} \tag{34.1}$$

Assume that the incident wave magnitude and reflective wave magnitude are equal, i.e., $p_i = p_r = p$; then,

$$p(x, t) = 2P \cos \omega t \cos \frac{2\pi f}{c} x \tag{34.2}$$

The summed pressure is a function of time and space, as shown in Fig. 34.2. Magnitude of the summed pressure varies with locations. Some location where the

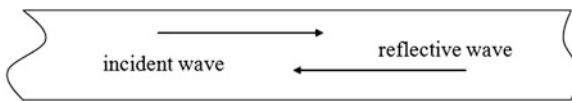
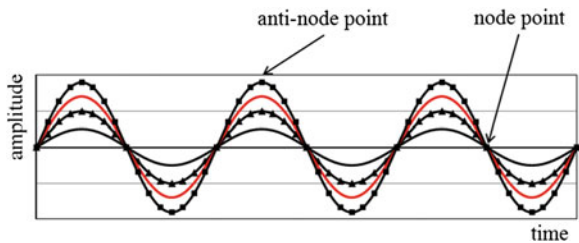


Fig. 34.1 Sound wave in a pipe

Fig. 34.2 Standing wave in a pipe



magnitude is zero is called node points. Some location where the magnitude reaches a maximum value is called antinode points.

34.2.2 Standing Wave in Exhaust System

Standing wave could appear in two sections inside an exhaust pipe. One section is the middle pipe, and the other one is the tailpipe, as shown in Fig. 34.3.

The standing wave inside the middle pipe: There exist incident wave and reflective wave at interactions between manifold and pipe, and between pipe and muffler due to difference in the section areas, which causes the standing wave. Assume the mufflers' volume is enough big; the two ends of the pipe can be regarded as "end open" boundary conditions [5].

The standing wave inside the tailpipe: There exist incident wave and reflective wave inside the tailpipe because the impedance between the tailpipe and the atmosphere does not match, which causes the standing wave. When the muffler has enough volume, the tailpipe can be regarded as "end open" boundary conditions.

The standing wave in the exhaust system can be calculated using the "end open" boundary conditions, and corresponding frequencies are expressed as follows:

$$f = \frac{(2n - 1)c}{2L} \tag{34.3}$$

where $n = 1, 2, 3, \dots$; c is sound speed; L is pipe length.

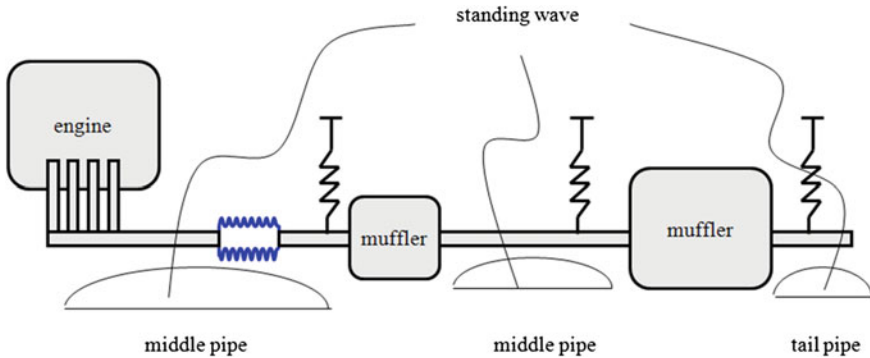


Fig. 34.3 Standing wave in an exhaust system

34.3 Phenomenon and Analysis of Low-Frequency Standing Wave in the Tailpipe

34.3.1 Description of Low-Frequency Standing Wave

During a vehicle development, a special sound phenomenon for the four-cylinder engine is found as follows: There exist three big peaks for tailpipe noise for WOT condition at 1,400; 2,100; and 4,000 rpm, respectively, as shown in Fig. 34.4. The contributions for the three peaks come from 6th order, 4th order, and 2nd order, respectively, but they correspond to one frequency at 130 Hz [5], as shown in Fig. 34.5.

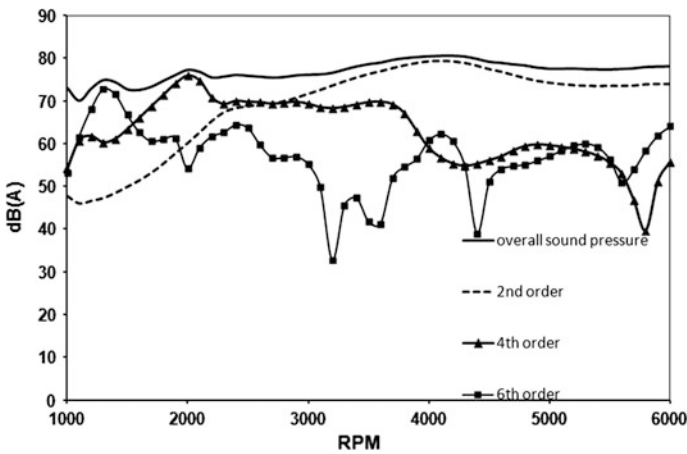


Fig. 34.4 Overall and order components of the exhaust orifice noise

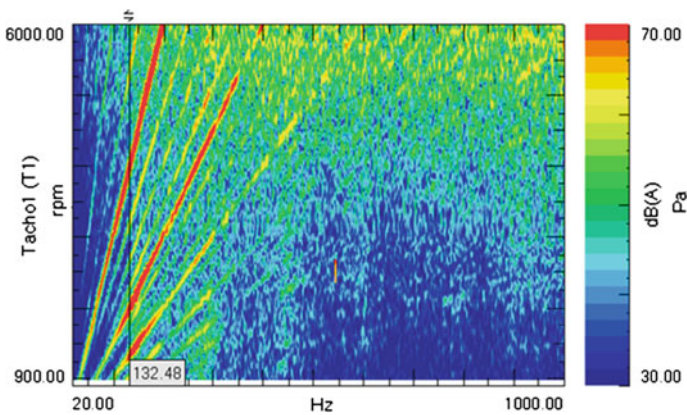


Fig. 34.5 Colormap for the orifice noise

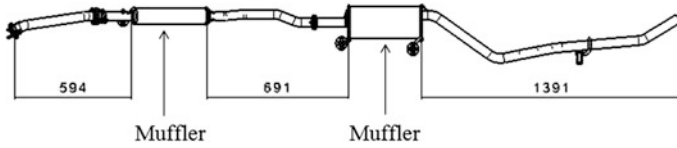


Fig. 34.6 The exhaust dimension layout

Figure 34.6 shows the exhaust dimension layout. The tailpipe length is 1,391 mm. Assume the tailpipe temperature is 230 °C; corresponding sound is 450 m/s. According to Eq. (34.3), the standing wave frequency inside the tailpipe is 130 Hz which is consistent with above test results.

In order to confirm that the standing wave is caused by the tailpipe, the tailpipe is extended to 2,500 mm. The test results show that the resonant frequency of the orifice noise reduces from 130 to 68 Hz as shown in Fig. 34.7. The 68-Hz standing wave corresponded with the 2,500-mm length pipe; thus, the 130 Hz noise can be confirmed from the original tailpipe.

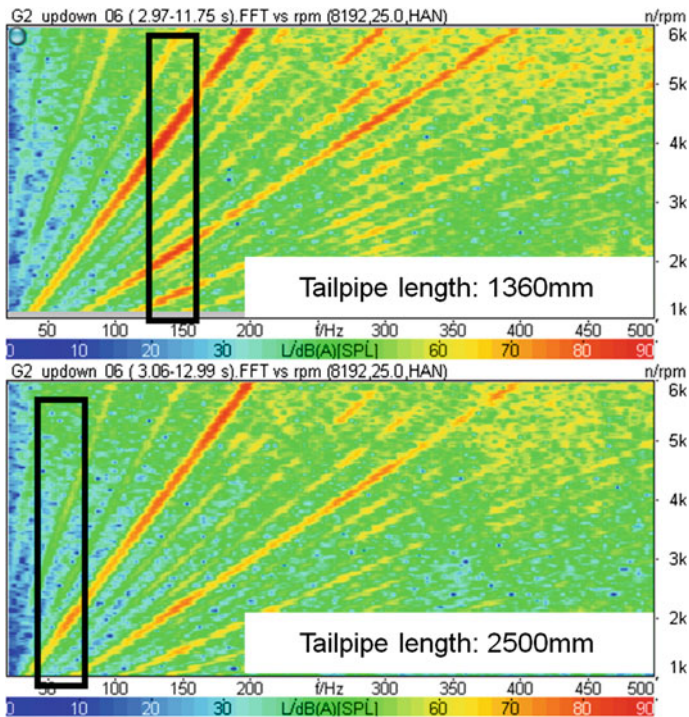


Fig. 34.7 Orifice noise for two tailpipes with different lengths

34.3.2 Simulation Analysis of the Exhaust System Standing Wave

There are three ways to solve the standing wave. The first method is to insert additional 130 Hz Helmholtz resonator. The second one is to adjust the tailpipe length in order to shift the standing wave frequency. The third method is to insert a muffler to break the standing wave. For the first method, in order to tune Helmholtz resonator to reach 130 Hz at 230 °C, according to the formula $f = \frac{c}{2\pi} \sqrt{\frac{S}{Vl}}$, resonator neck diameter and length are chosen as 35 and 30 mm, respectively, and the volume has to be 5 L [6]. Since the volume is too big to package in the vehicle, the method is gave up. For second method, the tailpipe length is limited by the vehicle's dimension and package, so the method is impossible for engineering practice. For the third method, an additional smaller resonator is inserted on the tailpipe, so the tailpipe is divided into two parts, which means the tailpipe length is shortened. The smaller resonator also reduces the resonant noise, as shown in Fig. 34.8.

A 1-D acoustic model for the engine and the exhaust system is built using GT-power. Three perforated mufflers with diameters 75 mm (option 1), 104 mm (option 2), and 120 mm (option 3), respectively, are designed within the possible package space. The exhaust orifice noise for the three cases is calculated and compared (Figs. 34.9 and 34.10; Table 34.1).

The noise peaks at low and middle rpm reduce with the increase in the pipe diameters. The option 3 has the best result, and the low-frequency standing wave is eliminated for the orifice noise. The peaks at 4,000 rpm for 2nd order, at 2,100 rpm for 4th order, and at 1,400 rpm for 6th order are significantly reduced compared with the original design, as shown in Figs. 34.11, 34.12, and 34.13.

Inserting the additional perforated resonator brings a lot of benefits, such as the standing wave is eliminated, the linearity for over sound pressure is improved, and the order noise peaks are significantly reduced (Fig. 34.14).

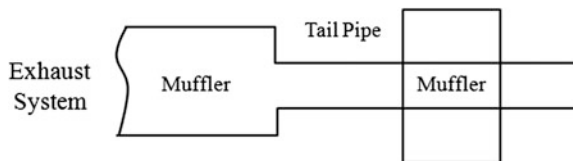


Fig. 34.8 An additional smaller resonator is inserted on the tailpipe

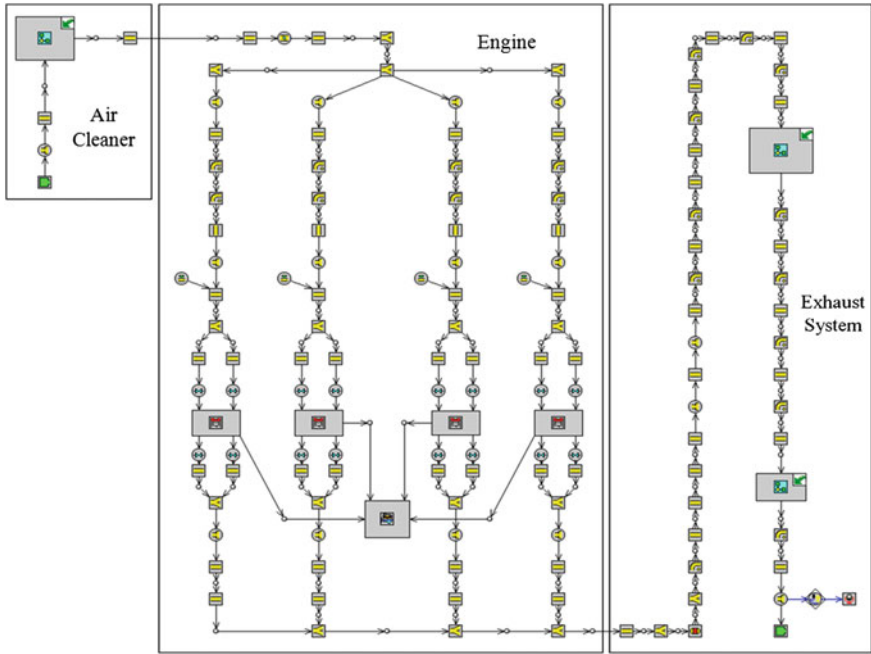
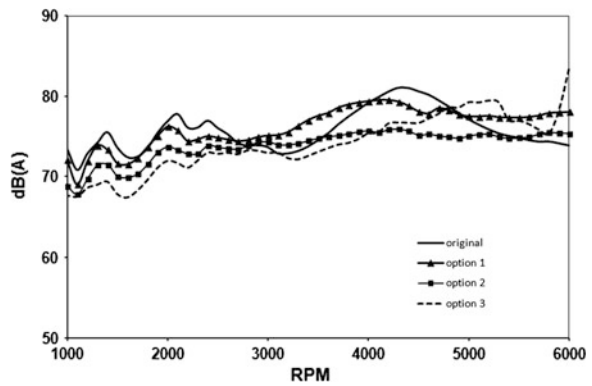


Fig. 34.9 1-D acoustic model for the engine and the exhaust system

Fig. 34.10 Comparison of orifice noise for different structures



34.3.3 Verification of the Improved Case

According to the simulation results for above cases, option case 3 has the best results. The hardware for option 3 is manufactured and installed on the exhaust system. The test results show that the optimized case reduces the peaks of the overall noise and the standing wave is eliminated.

Table 34.1 Options for three perforated resonators


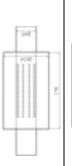

Project	Major diameter (mm)	Minor diameter (mm)	Volume (<i>L</i>)	Perforator diameter (mm)	Perforation rate (%)	Structure
Option 1	75	45	0.8	3	20	
Option 2	104	45	1.3	3	20	
Option 3	120	45	2.3	3	20	

Fig. 34.11 Comparison of second-order noise for different structures

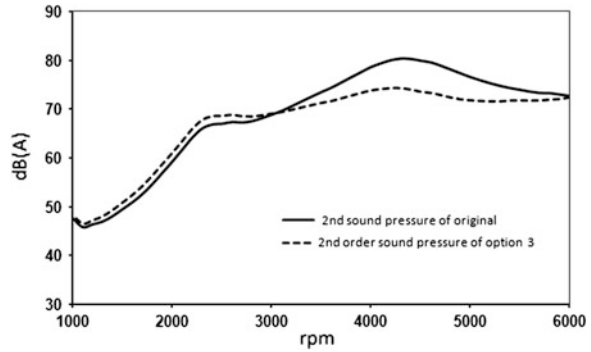


Fig. 34.12 Comparison of fourth-order noise for different structures

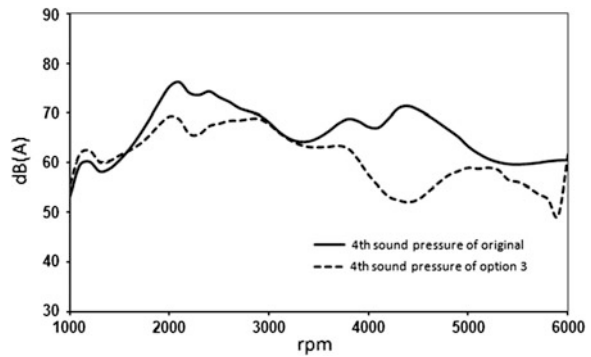


Fig. 34.13 Compare of sixth-order noise for different structures

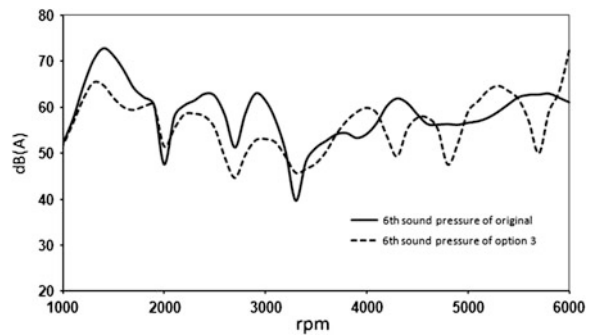
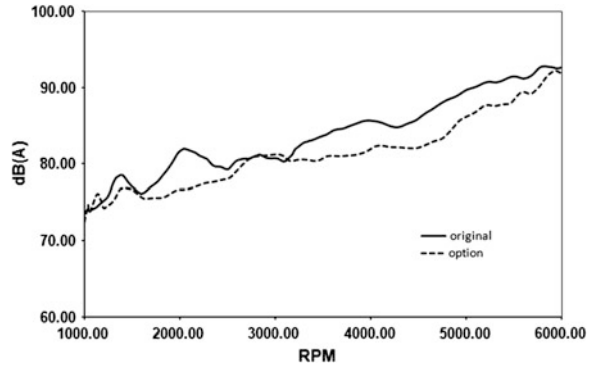


Fig. 34.14 Experimentation compares overall sound pressure in different structures



34.4 Conclusions

1. The long tailpipe easily causes low-frequency standing wave. If there exist several peaks in the overall tailpipe noise, the standing wave formula can be used to judge whether there exists standing wave.
2. There are three methods to control standing wave inside tailpipe: inserting an additional resonator, adjusting the tailpipe length, and breaking the standing wave. In this paper, the first method is used and good results are achieved.
3. The bigger the volume of the additional resonator, the better the results for eliminating the standing wave. The volume of a resonator can be chosen by a project requirement and possibility.

References

1. Selamet A, Ji ZL (1998) Acoustic attenuation performance of circular expansion chambers with offset inlet/outlet: I. Analytical approach. *J Sound Vib* 213:601–617
2. Selamet A, Ji ZL (2000) Acoustic attenuation performance of circular expansion chambers with single inlet and double outlet. *J Sound Vib* 229:3–19
3. Wu CJ, Wang XJ, Tang HB (2008) Transmission loss prediction on a single-inlet/double-outlet cylindrical expansion-chamber muffler by using the modal meshing approach. *Appl Acoust* 69:173–178
4. Zhao Q (2010) The effect of exhaust tailpipe on engine performance and tailpipe noise. *Int Combstion Engines* 06:003
5. Pang J (2006) *Automotive noise and vibration-principle and application*, vol 1. Beijing Institute of Technology Press, Beijing
6. Qiu Q-L, Min Y-F (2013) Two solutions to eliminate standing waves of exhaust systems noise and vibration control

Chapter 35

Crack Identification of Vehicle Drive Axle Half Shaft Rotor System

Daogao Wei, Bo Wang and Meiling Hu

Abstract Drive axle half shaft system is simplified to a single-span and double-cantilever rotor system, taking slant crack, bearing and tire sine excitation into consideration, 8-DOF dynamic equations are founded. Based on this model, the cracked half axle rotor system under high-speed drive condition is investigated by numerical simulation. The results indicate that: compared with uncracked half shaft system, cracked half shaft lateral vibration shows second harmonic generation, quadruplicated frequency and their combined frequencies with VC vibration frequency, and their corresponding amplitudes increase with the increase of crack depth. Therefore, slant crack information of axle shaft can be gained from the above three nonlinear factors.

Keywords Axle shaft · Slant crack · Rotor · Bearing · Harmonic frequency

35.1 Introduction

Vehicle axle shaft is a solid shaft to transmit power between differential and drive wheel. The half axle system that includes axle shaft and wheel is a functional part as well as safety part in high speed.

If crack occurs between half axle and hub, the cracked position may break under multiple forces. The break could lead to interruption of power or car slipping with handbrake on. In 2013, Beijing Hyundai recalled some SantaFe Automobiles because forging process quality problems in the drive axle joints might lead to crack occurring on the right of the drive axle. In 2014, GM recalled 170,000 CRUZE 2013–2014 models in the USA because the right front axle might crack and fall off, giving consumers and the company some economic losses.

D. Wei (✉) · B. Wang · M. Hu
School of Mechanical and Automotive Engineering, Hefei University of Technology,
Hefei, China
e-mail: weidaogao@huft.edu.cn

Crack, as one of the axle shaft major failures, is a very big danger. Therefore, it is necessary to find crack failure to prevent accidents and catastrophic economic losses.

Since the 1970s, there are extensive and in-depth studies on domestic and international recognition on the cracked rotor dynamics and cracks [1–8], but the research on crack identification of vehicle drive axle shaft rotor system are rarely reported. Most studied [9–11] on the axle materials, processing and fatigue failure, but ignoring the establishment of rotor dynamics model and studying the dynamic characteristics with numerical calculation method. This aspect of literature is also rarely reported.

Therefore, this paper established a multidimensional dynamic model of the cracked axle rotor system and analysed dynamic characteristics of the system influenced by three nonlinear factors including the crack, the bearing force and road excitation. Slant crack information is identified from three nonlinear factors and can also provide theoretical reference for crack dynamic monitoring of axle systems.

35.2 Dynamic Model of Vehicle Half Axle System

35.2.1 Mechanics Model of Cracked Half Axle

This paper taking a domestic commercial vehicle as a reference model, the simplified mechanics model of the vehicle half axle system is as shown in Fig. 35.1. The meanings of the symbols shown in Fig. 35.1 are as follows: xyz is the fixed coordinate system for the system, xoz is the tire rotation plane, x is the forward direction of the car in which the tire rotates clockwise, y is the axial direction of the axle, z is the direction perpendicular to the ground, m_1 is the quality of half axle gear, m_2, m_3 are the equivalent qualities of half shaft on the bearings, m_4 is the equivalent mass of the brake and wheel assembly (hereinafter referred to as wheel), l_i ($i = 1, 2, 3$) is equivalent distance between the discs, d is the diameter of the shaft, R is the rolling radius of the tire, Ω is the angular velocity of axle system, $F_{x2}, F_{z2},$

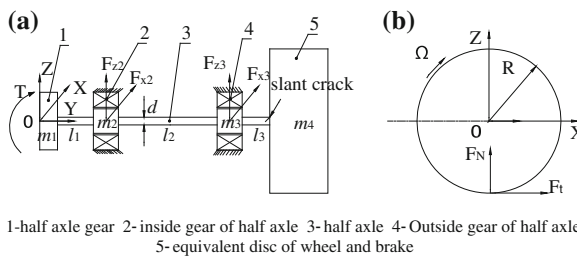


Fig. 35.1 Mechanics model of cracked axle system. **a** Main view of half shaft system. **b** Left view of differential equation of system

F_{x3} , F_{z3} are the supporting forces for the two rolling bearings and T is the drive torque. The following assumptions are made to build mechanical model: (1) assuming the car is travelling straight, the wheel does not bear lateral force; (2) assuming that the crack is 45° open slant crack on the axle, and the crack locates at the junction of axle hub and a half shaft; (3) assuming axle support bearings are the same rolling bearing at both ends.

35.2.2 Differential Equation of System

Based on the mechanics model of drive axle shaft system with cracked shaft as shown in Fig. 35.1, 8-DOF differential equation of the rotor system can be derived by using Lagrange's equation.

$$\begin{cases} m_1\ddot{x}_1 + c_{1x}\dot{x}_1 + k_{1x}(x_1 - x_2) = 0 \\ m_1\ddot{z}_1 + c_{1z}\dot{z}_1 + k_{1z}(z_1 - z_2) = 0 \\ m_2\ddot{x}_2 + c_{2x}\dot{x}_2 + k_{1x}(x_2 - x_1) + k_{2x}(x_2 - x_3) + k_b x_2 = F_{x2} \\ m_2\ddot{z}_2 + c_{2z}\dot{z}_2 + k_{1z}(z_2 - z_1) + k_{2z}(z_2 - z_3) + k_b z_2 = F_{z2} - m_2 g \\ m_3\ddot{x}_3 + c_{3x}\dot{x}_3 + k_{2x}(x_3 - x_2) + k_{3x}(x_3 - x_4) + k_b x_3 = F_{x3} \\ m_3\ddot{z}_3 + c_{3z}\dot{z}_3 + k_{2z}(z_3 - z_2) + k_{3z}(z_3 - z_4) + k_b z_3 = F_{z3} - m_3 g \\ m_4\ddot{x}_4 + c_{4x}\dot{x}_4 + k_{3x}(x_4 - x_3) + k_{xy}(z_4 - z_3) = m_4 e \Omega^2 \cos(\Omega t) + F_t \\ m_4\ddot{z}_4 + c_{4z}\dot{z}_4 + k_{3z}(z_4 - z_3) + k_{zx}(x_4 - x_3) = m_4 e \Omega^2 \sin(\Omega t) - m_4 g + F_N \end{cases} \quad (35.1)$$

where m_j is the mass of the j th disc, $j = 1, 2, 3, 4$; x_j, z_j are the horizontal and vertical displacements of the j th disc centroid; c_{jx}, c_{jz} are the horizontal and vertical damping; k_{ix}, k_{iz} are the horizontal and vertical stiffness of i th shaft, $i = 1, 2, 3$;

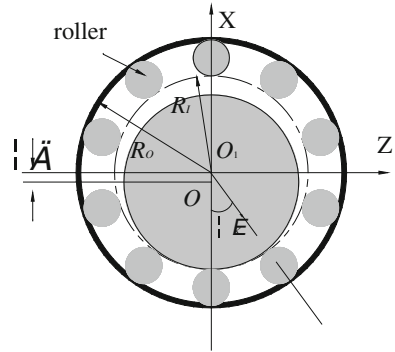
$[k]_g = \begin{bmatrix} k_x & k_{xz} \\ k_{zx} & k_z \end{bmatrix}$ is the 3rd shaft coupled stiffness matrix with slant crack, k_{xz}, k_{zx}

define coupled stiffness between horizontal and vertical, and the values are equal to 0 when no crack appears, F_t is the driving force, $F_t = T/R$; e is eccentricity of the 4th disc; g is the gravitational acceleration; F_N is the sinusoidal excitation force from ground, $F_N = G + m_4 A w^2 \sin(2\pi f t)$, where A is the amplitude of the sinusoidal excitation, G is the wheel load, $w = 2\pi f = \pi V/S$ (V is the speed of car, S is the half-wavelength of ground) and f is the frequency of road excitation force to tire.

35.2.3 Selection of Rolling Bearing Model

The model of rolling bearing, as shown in Fig. 35.1, is that of JIS6308, the bearing is simplified as two degrees-of-freedom system with radial clearance and Hertz contact between race and rolling elements [12, 13] and its mechanical model is

Fig. 35.2 Mechanics model of drive axle bearing



shown in Fig. 35.2. The outer race of the ball bearing is assumed to be fixed to the rigid support, and the inner race is assumed to be fixed to the shaft in this study. Rolling bearing subjects to forced vibrations generated from the rotor unbalance excitation, the vibration frequency is the rotation frequency of the rotor, while rolling bearings will also produce varying compliance (VC) vibration frequency ω_{VC} which is excited by the overall stiffness of the bearing continuously changing because of periodical variety of the bearing parameters [12, 14, 15]. Therefore, it is a parameter excited frequency.

Assuming the motion between the roller and the races is pure rolling, and then, the angular velocity of the rolling bearing cage is ω_{cage} , the varying compliance frequency is

$$\omega_{VC} = \omega_{cage}N_b = \Omega \left(\frac{R_i}{R_i + R_o} \right) N_b = \Omega B_N \tag{35.2}$$

where R_i and R_o are the inner and outer race radius, N_b is the number of rolling elements for the rolling bearing, and B_N is the ratio of the varying compliance vibration frequency and the rotational frequency. By considering that the angular spacing of the rolling elements is constant, the angular space between two balls is equal to $\Delta\theta = 2\pi/N_b$. Each angular position of the ball is θ_k , the deformation of the normal contact between the k th roller and race is

$$\begin{aligned} \Delta_k &= x \cos(\theta_k) + z \sin(\theta_k) - \delta \\ &= x \cos\left(\frac{2\pi}{N_b}(k-1) + \omega_{cage}t\right) + z \sin\left(\frac{2\pi}{N_b}(k-1) + \omega_{cage}t\right) - \delta \end{aligned} \tag{35.3}$$

where $k = 1, 2, 3, \dots, N_b$, x, z are the horizontal and vertical displacements of the centroid of inner race, and δ is the radial clearance between races and rolling element.

Considering the Hertzian contact theory, the restoring force between the k th roller and race can be estimated

$$F_k = \begin{cases} K_H(\Delta_k)^{3/2}, & \Delta_k \geq 0 \\ 0, & \Delta_k < 0 \end{cases} \quad (35.4)$$

where K_H is the stiffness of Hertzian contact. Then, the total restoring force components F_z and F_x in z - and x -directions are expressed as $F_z = \sum_{i=1}^{N_b} F_k \cos\theta_k$, $F_x = \sum_{i=1}^{N_b} F_k \sin\theta_k$, so the restoring force components of half shaft's two rolling bearing in the horizontal and vertical direction can be obtained by using the Eqs. (35.2)–(35.4)

$$\begin{cases} F_{x2} = F_x, F_{z2} = F_z, x = x_2, z = z_2 \\ F_{x3} = F_x, F_{z3} = F_z, x = x_3, z = z_3 \end{cases} \quad (35.5)$$

35.2.4 Selection of Crack Model

According to authors' knowledge, there are mainly two models calculating the stiffness of the cracked shaft: the open crack model and response-dependent breathing crack model. In this paper, the crack on shaft is assumed to be open crack, and there are basically three methods for this form of crack, which are equivalent method, numerical method, and Dimarogonas method [2, 3]. Compared to the other two methods, Dimarogonas method has many advantages such as high precision and convenience. The method can be used to derive the bending stiffness matrix of cracked-rotor vibration when coupling between z - and x - directions be considered. So it's helpful in discussing cracked-rotor coupled vibration problem.

Dimarogonas method uses stress intensity factor and energy release rate to calculate the stiffness. In order to find the additional flexibility of cracked half shaft, the relationships among the additional flexibility, energy release rate and stress intensity factor should be introduced. The relation between energy release rate and stress intensity factor is

$$W = \iint \left(\frac{1}{E'} K_I^2 \right) d\vartheta dY = \iint \left(\frac{1-\mu^2}{E} K_I^2 \right) d\vartheta dY \quad (35.6)$$

where ϑ is the depth of the crack section, Y is the width of the crack section, and K_I is the stress intensity factor of opening type.

Since the support stiffness of the rolling bearing is large enough, the additional local flexibility of uncracked shaft is [4]

$$[c_s] = \text{diag} \left[\frac{l_3^3}{3EI} \quad \frac{l_3^3}{3EI} \right] \quad (35.7)$$

where I is the inertia of shaft and l_3 is the length of shaft. The flexibility of cracked shaft is the sum of additional flexibility and the flexibility of the uncracked shaft

$$[c] = [G_1][\Delta c][G_2] + [c_s] \quad (35.8)$$

$$[\Delta c] = \frac{\partial^2 W}{\partial q_i \partial q_j} \quad (35.9)$$

where $[G_1]$, $[G_2]$ define the transfer matrix, $[\Delta c]$ is the additional local flexibility matrix and q_i , q_j define the corresponding load in each direction.

Under the rotating reference coordinates, the stiffness matrix of cracked shaft $[k]_l$ is the reciprocal of flexibility matrix $[c]$

$$[k]_l = [c]^{-1} \quad (35.10)$$

The stiffness matrix under fixed coordinate can be found by

$$[k]_g = [H]^{-1}[k]_l[H] \quad (35.11)$$

where $[H]$ is the coordinate conversion matrix.

35.3 Simulation and Analysis of System's Dynamic Characteristics

Taking a domestic light vehicle as sample, the differential equations of drive axle half shaft system are established based on the car. Combining the selected bearing and crack model, the dynamic characteristics of the system are calculated with fourth-order Runge–Kutta method. Then, the wheel vibration characteristics, which are obtained from uncracked and cracked under different depths in high speed, can provide crack recognition information of half shaft and provide theory reference for finding and diagnosing crack fault. The needed parameters for calculation are listed in Table 35.1, and the results are as shown in Figs. 35.3 and 35.4 and Table 35.2.

The specific value of the multi-frequency response diagram shown in Figs. 35.3 and 35.4 are summarized and listed in Table 35.2, where f is the frequency component of road excitation force to tire, $1x$, $2x$, $4x$ define the main frequency and harmonic generations, $f_{VC} = \frac{\omega_{VC}}{\Omega}$ is the ratio of VC vibration frequency and the angular velocity of tire, it can be seen that the vibration of wheel centroid in x -direction appear four frequency components, respectively, $1x$, $f_{VC} - 1x$, f_{VC} , $2f_{VC}$, and the vibration amplitude corresponding to $1x$, $f_{VC} - 1x$ is much less than the amplitude corresponding to the VC vibration frequency which are consistent with the results appear in the literature [12, 14, 15] when no crack appears. Compared to uncracked system, more frequency components appeared in the cracked system at the same direction that are, respectively, $2x$, $4x$, $2f_{VC}$, $f_{VC} + 2x$, $f_{VC} - 2x$, $2f_{VC} - 2x$, and all the amplitudes corresponding to $1x$, $2x$, $4x$, $f_{VC} + 2x$, $f_{VC} - 2x$, $2f_{VC} - 2x$ increase

Table 35.1 Calculating parameters

Parameter	Unit	Value
m_1	kg	3
m_2	kg	3.5
m_3	kg	3.5
m_4	kg	50
E	pa	2.1×10^{11}
l_1	m	0.12
l_2	m	0.58
l_3	m	0.057
d	m	0.04
e	m	0.03
T	N m	900
S	m	6
A	m	0.05
R_i	m	0.02
R_o	m	0.045
N_b		10
K_H	$N/m^{3/2}$	13.34×10^9
δ	μm	40
R	m	0.5
c_{1x}, c_{1z}	N s/m	3,000
c_{2x}, c_{2z}	N s/m	2,000
c_{3x}, c_{3z}	N s/m	5,000
k_b	N/m	1.4×10^6
G	N	50,000

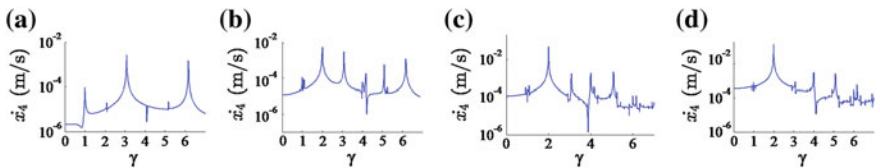


Fig. 35.3 Spectrum of wheel in x -direction with different crack depths when $V = 30$ m/s. **a** $S = 0d$, **b** $S = 0.1d$, **c** $S = 0.3d$ **d** $S = 0.4d$

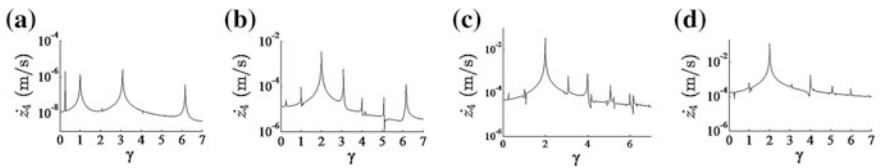


Fig. 35.4 Spectrum of wheel in z -direction with different crack depths when $V = 30$ m/s. **a** $S = 0d$ **b** $S = 0.1d$ **c** $S = 0.3d$ **d** $S = 0.4d$

Table 35.2 Amplitude–frequency distribution characteristics of x -direction vibration corresponding with the change of crack depth s when $V = 30$ m/s

Frequency ratio γ	Crack depth				
	$S = 0d$	$S = 0.1d$	$S = 0.3d$	$S = 0.4d$	
Amplitudes of x -direction	$1x$	9.37e-5	1.12e-4	2.51e-4	8.19e-4
	$f_{vc} - 1x$	1.97e-5	No prominent	No prominent	No prominent
	$2x$	No prominent	5.69e-3	4.81e-2	1.41e-1
	f_{vc}	2.68e-2	3.09e-3	1.82e-3	8.90e-4
	$f_{vc} + 1x$	No prominent	No prominent	No prominent	No prominent
	$4x$	No prominent	5.96e-5	1.89e-3	3.21e-3
	$2f_{vc} - 2x$	No prominent	1.88e-4	3.59e-4	No prominent
	$f_{vc} + 2x$	No prominent	5.81e-4	2.71e-3	2.71e-3
	$2f_{vc}$	1.47e-3	1.26e-3	1.22e-4	5.70e-4
	f	2.06e-6	2.55e-5	9.62e-5	No prominent
	$1x$	1.38e-6	9.23e-5	1.46e-4	5.99e-4
	$f_{vc} - 1x$	No prominent	No prominent	No prominent	No prominent
	$2x$	No prominent	3.42e-3	3.37e-2	1.21e-1
	f_{vc}	2.65e-6	5.83e-4	5.90e-4	5.37e-4
$4x$	No prominent	3.03e-5	7.71e-4	1.76e-3	
$2f_{vc} - 2x$	No prominent	No prominent	9.12e-5	No prominent	
$f_{vc} + 2x$	No prominent	3.19e-5	2.25e-4	4.07e-4	
$2f_{vc}$	3.65e-7	1.21e-4	7.60e-5	2.80e-5	

with the increasing of crack depth, instead the corresponding amplitude of f_{vc} , $2f_{vc}$ decrease with increasing depth of the crack.

The vibration of wheel centroid in z -direction appears four frequency components, respectively, f , $1x$, f_{vc} , $2f_{vc}$, and the corresponding amplitudes are small, when no crack appears. And compared to uncracked system, more frequency components appeared in the cracked system at the same direction which are, respectively, $2x$, $4x$, $f_{vc} + 2x$, $f_{vc} - 2x$, $2f_{vc} - 2x$, and the amplitudes corresponding to $1x$, $2x$, $4x$, $f_{vc} + 2x$ increase with the increasing of crack depth, instead the corresponding amplitude of $2f_{vc}$ decrease with increasing depth of the crack, f_{vc} corresponding amplitude shows the tendency of decrease at first and then increase with the increasing of the depth of crack.

In conclusion, the second and fourth harmonic frequency and the frequencies they combined with the VC vibration frequency formed by the sum and difference do not appear in uncracked system; the emergence of them and the corresponding amplitudes increase with the increasing of the depth of crack are important symbol of crack existence and extension.

35.4 Conclusions

Based on a certain type of vehicle drive axle shaft system with slant crack as the research content, established the mechanics model of the system, and taking slant crack, bearing and tire sine excitation into consideration, 8-DOF dynamic equations were founded. Considering the three nonlinear factors, the cracked half axle rotor system under high-speed drive condition was investigated by numerical simulation. Analysis of the vibration characteristics of the wheel is helpful to gain slant crack information of axle from the above three nonlinear factors.

Acknowledgments This research is supported by the National Science Foundation of China (Nos 51375130, 51050002).

References

1. Sundermeyer JN, Weaver RL (1995) On crack identification and characterization in a beam by non-linear vibration analysis. *J Sound Vib* 183(5):857–871
2. Dimarogonas AD (1996) Vibration of cracked structures: a state of the art review. *Eng Fract Mech* 55(5):831–857
3. Darpe AK (2007) Coupled vibrations of a rotor with slant crack. *J Sound Vib* 305(1):172–193
4. Lin YL, Chu FL, Hao RJ (2008) Dynamic analysis of a Jeffcott rotor system with an opening slant crack on its shaft. *J Vib Shock* 27(1):25–29
5. Wei DG, Hu ML, Ma Q et al (2013) Nonlinear dynamic characteristics of sugarcane cutter system with cracked shaft. *Trans Chin Soc Agric Mach* 44(s2):80–85
6. Wei DG, Hu ML, Ma Q et al (2014) Analysis on crack identification in shaft of sugarcane cutter system. *J South China Agri Univ* 3:105–110
7. Sinou J-J (2008) Detection of cracks in rotor based on the 2X and 3X super-harmonic frequency components and the crack-unbalance interactions. *Commun Non-linear Sci Numer Simul* 13:2024–2040
8. Sekhar AS, Balaji Prasad P (1997) Dynamic analysis of a rotor system considering a slant crack in the shaft. *J Sound Vib* 208(3):457–473
9. Zhao J, Wang HR, Zhou B et al (2011) The analysis on the driver shafts's early fracture causes of the 10 kilometers internal-geared axle. *China Society of Automotive Engineering Materials Branch of the Tenth physical and chemical testing, failure analysis Symposium*, 273-277
10. Zuo XR (2011) Analysis and improvement on early failure of Dongfeng axle shaft. *Automobile Technol Mater* 7:31–34
11. Wang JJ (2014) Vehicle driving axle half shaft fracture analysis. *Adv Mater Res* 912:658–661
12. Harsha SP (2006) Nonlinear dynamic response of a balanced rotor supported by rolling element bearings due to radial internal clearance effect. *Mech Mach Theory* 41(6):688–706
13. Jang G, Jeong SW (2004) Vibration analysis of a rotating system due to the effect of ball bearing waviness. *J Sound Vib* 269(3):709–726
14. Tiwari M, Gupta K, Prakash O (2000) Dynamic response of an unbalanced rotor supported on ball bearings. *J Sound Vib* 238(5):757–779
15. Cheng M, Meng G, Wu B (2011) Nonlinear dynamics of a rotor-ball bearing system with Alford force. *J Vib Control*, doi:1077546311405701

Chapter 36

Study on Second-Order Vibration Caused by Secondary Couple of Cardan Joint for a 4WD Driveline

Yuanfeng Xia, Jian Pang, Chengtai Hu, Cui Zhou and Zhijun Zhang

Abstract Based on the mechanism of secondary couple caused by cardan joint, this paper analyzes the reasons for the secondary couple and second-order vibration of a 4WD driveline resulting from cardan joint excitation. According to test results, the paper analyzes the influence parameters, including variation of propeller shafts' angle, selection of joint type, input torque of propeller shaft, and rigid body modes of rear axle, on the second-order vibration. Finally, the paper provides the control methods to reduce the second-order vibration caused by the cardan joints.

Keywords Cardan joint · Second-order vibration · 4WD · Rigid body mode of axle · ODS

36.1 Introduction

Currently, the four-wheel drive (4WD) system is widely used in sports utility vehicle (SUV) due to the increasing demand of fuel efficiency and dynamic performance by customers. Generally, there are two kinds of 4WD systems, one based on the front wheel drive (FWD) system and the other based on the rear wheel drive (RWD) system. The FWD system has been more and more popular. The customers and manufacturers have already paid more and more attention to the noise, vibration, and harshness (NVH) problems caused by the driveline of 4WD vehicle.

The universal joints, which are commonly used in the automotive driveline, are divided into two categories: One is the constant-velocity universal joint, and the other is the inconstant-velocity universal joint. The cardan joint, which belongs to inconstant-velocity universal joint, is widely applied in automotive driveline due to

Y. Xia (✉) · J. Pang · C. Hu · C. Zhou · Z. Zhang
Changan Auto Global R&D Centre, Changan Automobile Co Ltd, Chongqing, China
e-mail: xyuanfeng2007@163.com

Y. Xia · J. Pang · C. Hu · C. Zhou · Z. Zhang
State Key Laboratory of Vehicle NVH and Safety Technology, Chongqing, China

© Springer-Verlag Berlin Heidelberg 2015
Society of Automotive Engineers of China (SAE-China) (ed.),
Proceedings of SAE-China Congress 2014: Selected Papers,
Lecture Notes in Electrical Engineering 328, DOI 10.1007/978-3-662-45043-7_36

its simplicity and low cost. The cardan joint produces torque and velocity fluctuation during torque transmission [1]. Specifically, for a constant driveshaft speed, the driveshaft's speed fluctuates with a frequency corresponding to twice the rotational speed of the driveshafts. The propeller shafts with multi-cardan joints are commonly applied to commercial vehicles and trucks to transmit torque. The driveline torsional vibration correlates with the phase arrangement of multi-universal joints [2]. The shudder vibration of vehicle body [3] and cabin's low-frequency booming [4] are easily excited by cardan joint with a secondary couple for RWD and 4WD vehicles, especially the driveline running at the low-gear and high-torque conditions.

Based on the single cardan joint, this paper analyzes the theory and phenomenon of secondary couple and second-order vibration caused by the cardan joint. Some controlling methods for second-order vibration caused by the cardan joint are provided according to theoretical analysis and test results. Firstly, the test results validate the influence of propeller shaft's angle variation and arrangement on second-order vibration. Secondly, the flexible coupling, which presents an excellent NVH property in the solution of second-order vibration, is analyzed by NVH test. Thirdly, the influence of propeller shaft's input torque on second-order vibration is validated. Finally, the second-order vibration transfer path is found by static model analysis and operational deflection shape analysis of rear axle.

36.2 Mechanism of Second-Order Excitation Force

The 4WD driveline system based on FWD system consists of power plant, power takeoff unit (PTU), propeller shaft, independent axle, front half shaft, rear half shaft, and four wheels, as shown in Fig. 36.1. The cardan joint is the source of second-order vibration.

Figure 36.2 shows that the cardan joint is operated under a nonzero driveline angle. The relationship between the velocity of the driving yoke and driven yoke is presented as follows:

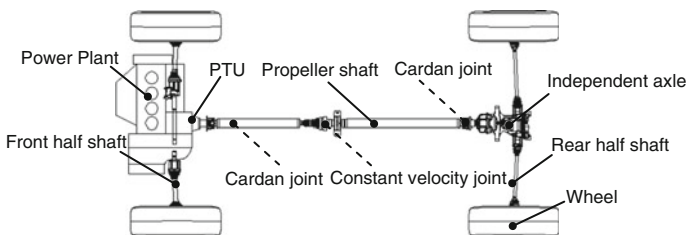


Fig. 36.1 The 4WD driveline layout

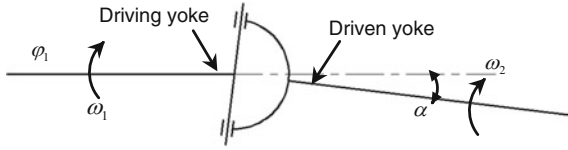
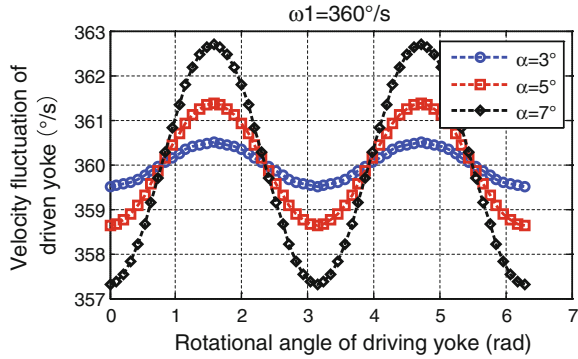


Fig. 36.2 Rotational movement of a cardan joint

Fig. 36.3 Velocity fluctuation of driven yoke with different angles



$$\frac{\omega_2}{\omega_1} = \frac{\cos\alpha}{1 - \sin^2\alpha \sin^2\varphi_1} \tag{36.1}$$

where ω_1 is the velocity of the driving yoke, ω_2 is the velocity of the driven yoke, φ_1 is the rotational angle of the driving yoke, and α is the angle between driving yoke and driven yoke. If the driving yoke rotates with a constant speed ($\omega_1 = 360^\circ/\text{s}$), the velocity of the driven yoke fluctuates twice per rotation, as shown in Fig. 36.3. The larger the cardan joint angle, the greater the velocity fluctuation.

When the angle α is not equal to zero, the cardan joint not only produces velocity fluctuation, but also produces an oscillating secondary couple which is a function of driveline angle and transmitted torque. Generally, the secondary couple produced by driving yoke is [5]

$$C_1 = T_1 \tan\alpha \cos^2\varphi_1 \sqrt{1 - \sin^2\alpha \sin^2\varphi_1} \tag{36.2}$$

and the secondary couple caused by driven yoke is [6]

$$C_2 = T_1 \sin\alpha \sin^2\varphi_1 \sqrt{1 + \tan^2\alpha \cos^2\varphi_1} \tag{36.3}$$

where T_1 is the input torque transmitted by driving yoke.

As shown in Eqs. (36.2) and (36.3), the secondary couple of driving yoke and driven yoke is a function of rotational angle (φ_1) of the driving yoke. The

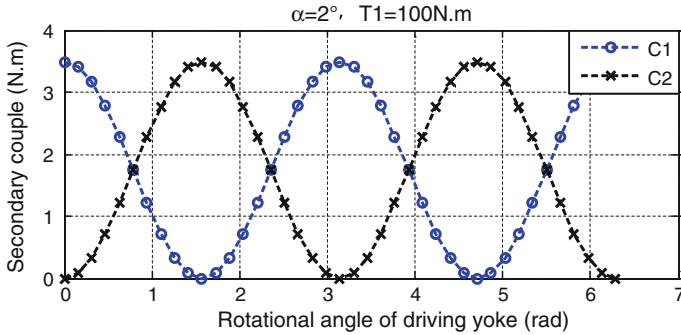


Fig. 36.4 The secondary couple of driving yoke and driven yoke

secondary couple C_1 and C_2 fluctuates with δ period when $\alpha = 2^\circ$ and $T_1 = 100 \text{ N m}$, as shown in Fig. 36.4. The secondary couple is supported by bearing and produces second-order force on bearing, which is the reason for second-order vibration driveline.

36.3 The Phenomenon of Second-Order Vibration Caused by Cardan Joint

The vibration and noise of driveline are measured by tracking propeller shaft’s rotational speed, arranging microphone at driver’s seat and passenger’s seat, and fixing acceleration sensors at PTU, central bearing support, rear axle, and floor of vehicle body. Figures 36.5 and 36.6 show the noise and vibration color maps of key points at inside and outside of the vehicle, and the overall value of second-order noise and vibration. The second-order vibration at axle caused by cardan joint presents two peaks around 760 rpm (25 Hz) and 1,200 rpm (40 Hz), respectively. The cabin noise and body floor vibration present similar feature that the vehicle body has a shudder vibration with great acceleration around 760 rpm, and the cabin has a low-frequency boom with great second-order noise around 1,200 rpm.

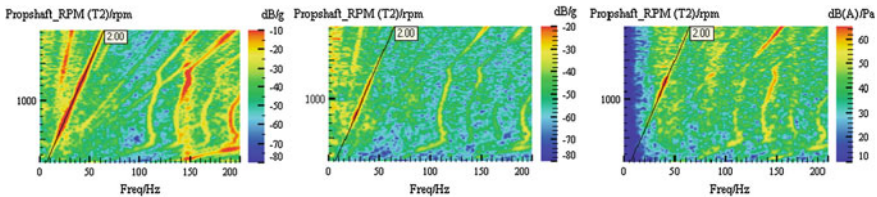


Fig. 36.5 The noise and vibration color maps of key points at inside and outside of the vehicle

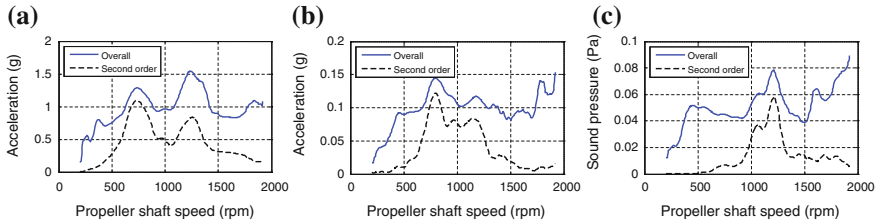


Fig. 36.6 The overall value of second-order vibration and noise. **a** Vibration of axle, **b** vibration of floor, and **c** acoustic of cabin

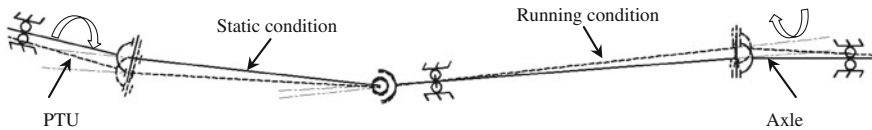


Fig. 36.7 The angle variation of driveline at low-gear and high-torque conditions

36.4 The Test Analysis and Control Methods for Second-Order Vibration

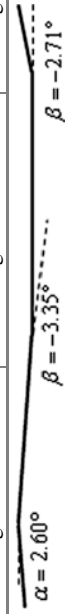
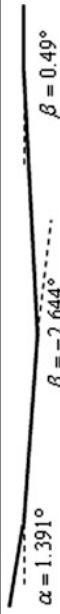
According to the theoretical analysis and test results, the driveline second-order vibration is produced by second-order force caused by the cardan joint and relates to propeller shaft's angle and input torque. The major control factors to reduce the second-order vibration include propeller shaft's angle, optimizing joint types, decreasing input torque, and increasing decouple of axle mode from excitation source and transfer path.

36.4.1 Propeller Shaft's Angle and Driveline Layout

As shown in Eqs. (36.2) and (36.3), the second couple is proportional to propeller shaft's angle. Therefore, it is effective to reduce second-order vibration by decreasing propeller shaft's angle. At the low-gear and high-torque conditions, rolling back the power plant induces PTU output shaft downward and increases the front cardan joint angle, while rolling back the axle makes the torque transfer device position up and increases the rear cardan joint angle, as shown in Fig. 36.7. Both cases worsen the secondary vibration.

The power plant's output torque and axle input torque determine the propeller shaft's angle in case of constant driveline layout. Therefore, it is very important to reasonably arrange the propeller shaft's angle, especially for the cardan joint angle. Table 36.1 shows the subjective evaluation results for two propeller shaft's layouts. The layout 1 increases the propeller shaft's angle, but the layout 2 decreases the

Table 36.1 The evaluation results for two propeller shaft's layouts

Number	Subjective	Front angle	Middle angle	Rear angle
1	Good	 $\alpha = 2.60^\circ$ $\beta = -3.35^\circ$ $\beta = -2.71^\circ$		
2	Bad	 $\alpha = 1.391^\circ$ $\beta = -2.644^\circ$ $\beta = 0.49^\circ$		

propeller shaft's angle, though the layout 2 has better driveline NVH properties than layout 1.

36.4.2 The Universal Joint Types

Generally, it is effective to cancel the second-order vibration caused by cardan joint by the application of constant-velocity joint instead of cardan joint [7]. Figure 36.8 shows the measured vibration on the axle for application of flexible coupling (near constant-velocity universal joint). Although flexible coupling with Y-type yoke cancels the second-order vibration caused by cardan joint, the third-order vibration is presented clearly under running condition. Since flexible coupling has a good damping performance, the third-order vibration is far less than second-order vibration.

36.4.3 Input Torque of Propeller Shaft

According to Eqs. (36.2) and (36.3), the secondary couple is proportional to input torque. Therefore, it is effective to decrease second-order vibration by reducing input torque. The torque transfer device (TTD) modulates axle input torque by controlling the pressing force of friction plates. The torque at AUTO mode is much smaller than LOCK mode. Figure 36.9 shows the measured vibration on the axle under AUTO mode.

36.4.4 Decouple of Axle Rigid Mode

The axle rigid modes are easily excited by second-order force caused by cardan joint and produce modal resonances which are transferred to vehicle body. Decoupling of axle rigid modes is very important to reduce noise and vibration caused by second-order force. The axle bounce modal frequency and lateral modal

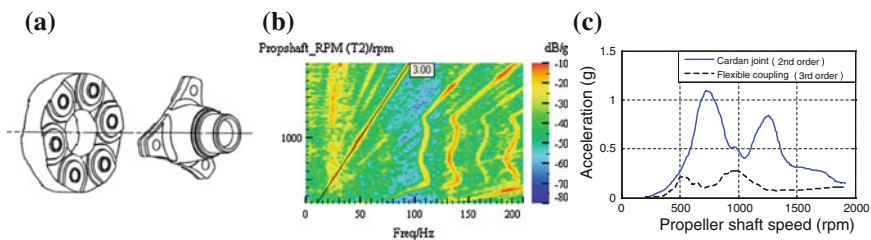


Fig. 36.8 The axle vibration with flexible coupling. **a** Flexible coupling, **b** vibration of axle, and **c** second-order vibration of axle

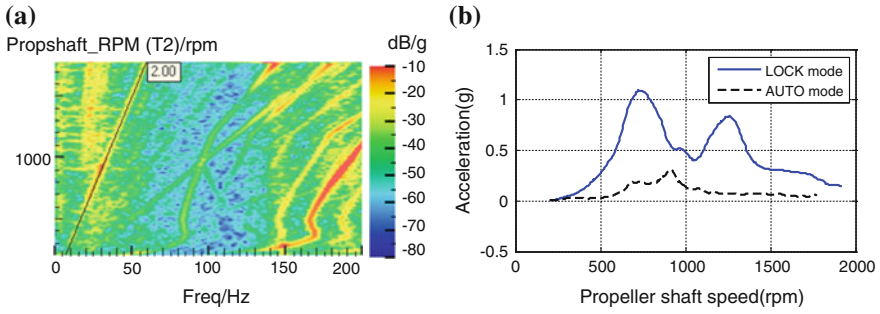


Fig. 36.9 The axle vibration with different running modes. **a** Vibration of axle and **b** second-order vibration with different modes

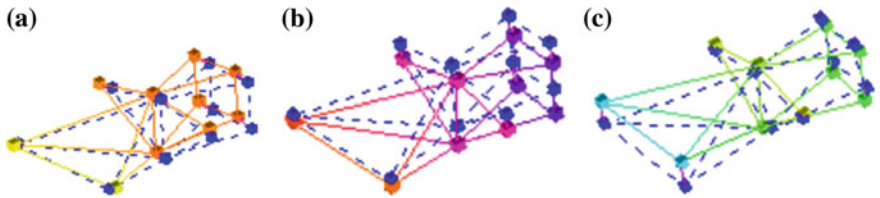


Fig. 36.10 The rigid mode of axle under static condition. **a** Bounce mode (22 Hz), **b** lateral mode (24 Hz), and **c** pitch mode (34 Hz)

frequency are 25 Hz, and pitch modal frequency is 40 Hz, as shown in Fig. 36.10, which are consistent with the frequencies for the vibration problem.

Generally, not all axle rigid modes can be excited under running conditions. The operational deflection shape (ODS) is used to analyze the key modes which amplify the second-order vibration at operating conditions. Figure 36.11 shows the axle ODS results at low-gear and high-torque conditions. The axle lateral mode couples with vertical mode around 25 Hz and produces a coupling resonance. Similarly, a pitch modal resonance is generated around 40 Hz, which coincides with problem frequency.

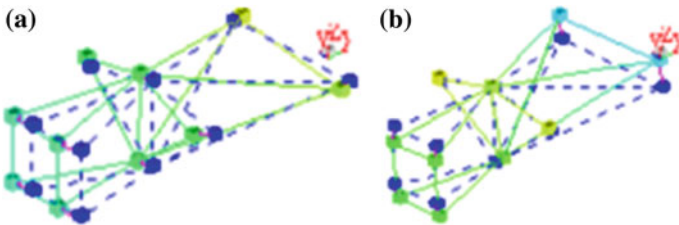


Fig. 36.11 The ODS results of axle. **a** Couple mode (25 Hz) and **b** pitch mode (40 Hz)

36.5 Conclusions

Based on the theory of secondary couple caused by cardan joint, this paper analyzes the reasons for the secondary couple and second-order vibration of a 4WD driveline resulted by cardan joint. According to the theoretical analysis, the test results validate the influence of parameters, including variation of propeller shafts' angle, selection of joint type, input torque of propeller shaft, and rigid body modes of rear axle, on the second-order vibration. The following conclusions can be drawn according to the theoretical analysis and test results.

- (1) The driveline second-order vibration results from the secondary couple and second-order force caused by cardan joint.
- (2) The value of second-order force is related to propeller shaft's angle and driveline layout, and the second-order vibration can be reduced by reasonable arrangement of driveline layout.
- (3) The flexible coupling can cancel the second-order vibration caused by cardan joint effectively. But the flexible coupling produces a third-order vibration under the large propeller shaft's angle.
- (4) The second-order vibration can be reduced effectively by decreasing input torque of propeller shaft.
- (5) The second-order force caused by cardan joint easily excites the axle lateral mode and vertical mode and produces a coupled resonance.

References

1. Wagner ER (1979) Universal joint and driveshaft design manual, SAE Advances in Engineering Series(AE) No.7, Second Printing
2. Wu G, Shi W, Chen Z (2013) The effect of multi-universal coupling phase on torsional vibration of drive shaft and vibration of vehicle, SAE Technical Paper 2013-01-1490
3. Wellmann T, Govindswamy K (2009) Development of a multi-body systems approach for analysis of launch shudder in rear wheel driven vehicles, SAE Technical Paper 2009-01-2073
4. Wellmann T, Govindswamy K(2007) Aspects of driveline integration for optimized vehicle NVH characteristics, SAE Technical Paper 2007-01-2246
5. Ota M, Kao M (1984) Lateral vibrations of a rotating shaft driven by a universal joint. Bulletin of JSME 27(231):2002–2007
6. Burkhalter R, Mazziotti PJ (1956) The low silhouette drive line, SAE Technical Paper
7. Rabeih EMA, Demerdash SMEI (2002) Investigation of the vehicle ride vibration effect on the driveline fluctuations, SAE Technical Paper 2002-01-3065

Chapter 37

Optimization of Front Windshield Lower Beam Welding Assembly Based on NVH Performance

Cheng Yanan, Deng Feng, Ping Zhang and Haoliu

Abstract To meet the need of pedestrian protection and ensure the vehicle has good energy absorption when the head hit the windshield, the front windshield lower beam welding assembly was required to be designed open section. As a result, the vibration of the front windshield and firewall became strong, and the interior booming noise problem could be caused. In order to solve this problem, the simulation method was carried out to optimize the booming noise in this paper, the vibration of the front windshield and firewall was reduced by enhancing the windshield support structure, and meanwhile, the noise transfer function was improved. The improved solution was validated in real vehicle. The test also shows that enhancing windshield support structure can effectively improve the high-speed booming noise.

Keywords Lower beam welding assembly · Booming noise · Stiffness · Transfer function

37.1 Introduction

When the car impacts the pedestrian unfortunately during the traffic accident, usually the front of the car hits the pedestrian, and in the process of crash, the legs and head of the pedestrian are the most frequent part of injury. The damage of head is more severe than the legs because it may lead to people's direct death when the head hits the engine hood or the windshield.

To meet the increasingly stringent requirements of regulatory for pedestrian protection, almost all of well-known car factories make corresponding car body changes at the early design stage. For example, engine hood being changed energy absorption, front windshield lower beam welding assembly being changed weak,

C. Yanan (✉) · D. Feng · P. Zhang · Haoliu
NVH Institute, Technology Center, Dongfeng Motor Corporation, Wuhan, China
e-mail: chengyn@dfmc.com.cn

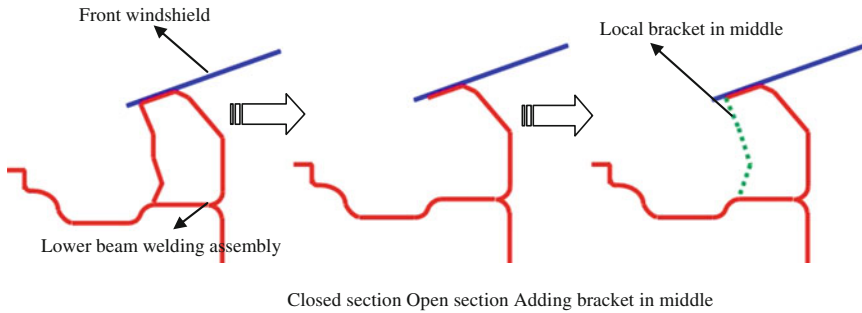


Fig. 37.1 Design evolution of front windshield lower beam section

and so on. In this paper, the NVH problems induced by soften windshield support structure and the improvement ideas were introduced.

The front windshield support structure consists of A-pillar, front roof beam, and lower beam welding assembly. In tradition, the windshield supporting structure was made closed section to provide strong support for windshield, but in order to meet the pedestrian protection requirement, the lower support stiffness cannot be designed too high, and the open-section front windshield lower beam welding assembly was widely used in car body design (as showed in Fig. 37.1), but the open section which has the character of lower stiffness often brings NVH problems. Adding local bracket in the middle of lower beam welding assembly to improve the low-speed booming problem was researched by Tonge [1].

The windshield with the open-section lower beam welding assembly has lower global and more local modes. If these vibration modes couple with that in cab cavity mode, it will bring about booming problem which has serious influence on vehicle NVH performance. On the premise of pedestrian protection, the high-speed booming noise was improved by optimizing the local mode of front windshield on the basis of the original middle support bracket in this paper, and the object of booming noise in whole speed range was finally achieved.

37.2 Mechanism of Booming Induced by Engine Vibration

The basic principle of vibration and noise can be summarized as source, transfer path, and response. The phenomenon of engine vibration-induced booming noise is described, as shown in Fig. 37.2: Due to the action of combustion pressure, the engine will vibrate, the vibration will transfer to body connecting point via engine mount and then transfer to body, which will lead to body panel vibration, and if the vibration mode coupled with the in cab cavity mode, high-pressure pulsation will occur, and this is the mechanism of booming.

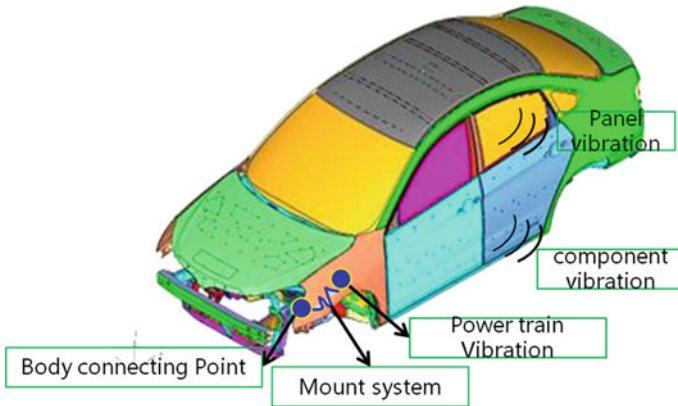


Fig. 37.2 Schematic of booming induced by engine vibration

In real automotive engineering, according to document [2], it is difficult to change engine-side vibration and stiffness of mount rubber, and optimization of noise transfer function of trimmed body is usually the most effective and efficient method. In car body structure design, front windshield, which is a large flat and smooth panel, is mostly the main contribution panel for booming noise.

37.3 Problem Description of Developed Vehicle

The engine-side vibration of a sport utility vehicle without balance shaft module is obviously larger than the benchmark vehicle with balance shaft module [3], but the target of interior booming noise cannot be worse than the benchmark vehicle in performance definition. So it is a challenge for design engineers. After the NVH tuning in mule (self-owned chassis and power train with benchmark vehicle's body) phase, the target of interior booming noise was achieved. But when the real physical prototype came out, the booming noise at a specific high speed was also felt by subjective evaluation engineer. According to objective test for vehicle three-gear wide-open throttle, the 2nd booming noise at the specific high speed was 4 dB exceeding the target, as the dotted line shown in Figs. 37.3 and 37.4.

37.4 Root Cause Analysis

The targets of intake and exhaust system were achieved in the mule car phase, and the only difference between mule car and real physical prototype is the trimmed body, and thus, the question focuses on the trimmed body. According to transfer

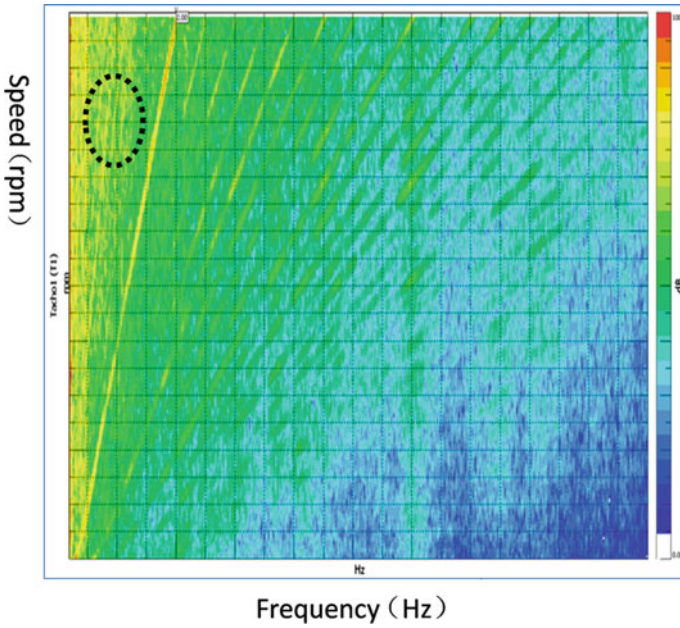
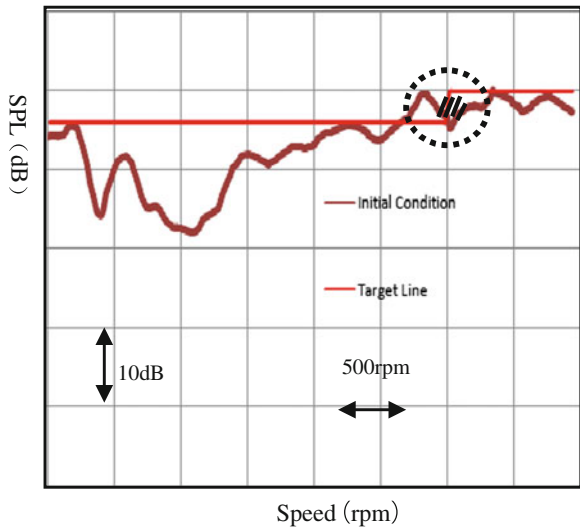


Fig. 37.3 3D Map of interior noise

Fig. 37.4 Booming noise



path analysis in test, there is an obvious peak value in the noise transfer function of front shock absorber Y direction at the frequency of booming noise, as the dotted lines shown in Fig. 37.5.

Fig. 37.5 Test result of absorber Y direction NTF

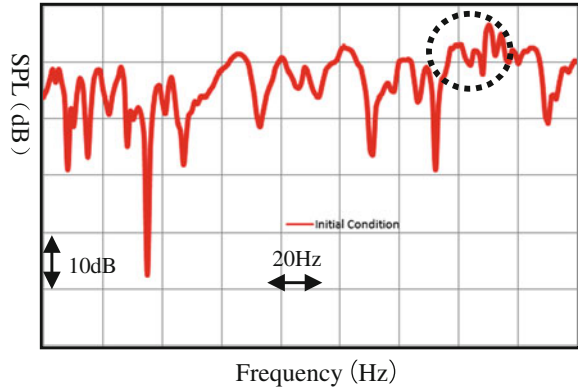
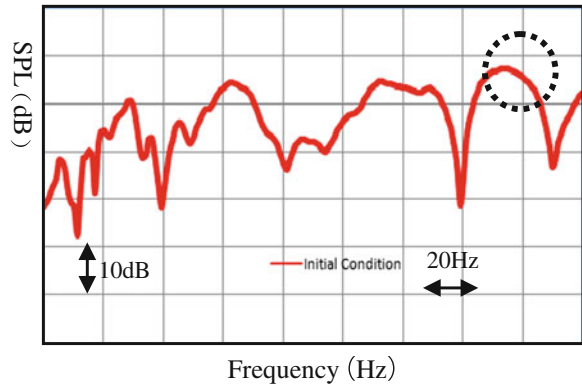


Fig. 37.6 Simulation result of absorber Y direction NTF



The simulation results show the same with the results of test problems, as shown in Fig. 37.6. As the advantage of high efficiency, low cost, and the operating deformation shape (ODS) and panel contribution could be rapidly and vividly shown in computer, the ODS and panel contribution analysis was carried out (as shown in Fig. 37.7). In order to see the contribution of local area panel, the windshield was divided into 9 areas (panel divided as shown in Fig. 37.8), the results show that the front windshield area 6, front windshield area 3, and the firewall were the main contribution panel to the NTF peak value.

As the last response system, it is difficult to modify the front windshield, so the optimization focuses on the boundary component of windshield. We checked the design of local structure (Fig. 37.9) and found that there are one bracket in the middle of lower beam assembly and one small bracket in the right (dotted line), but no support in the left as the restriction of wiper motor's mounting and DMU. It is also shown that the left lower area was the most contribution panel in simulation above. As shown in the section (Fig. 37.10), the vibration in direction of firewall

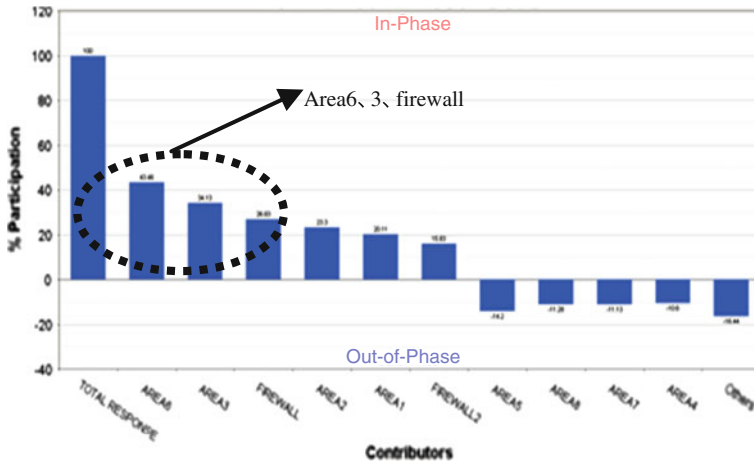


Fig. 37.7 Panel contribution analysis

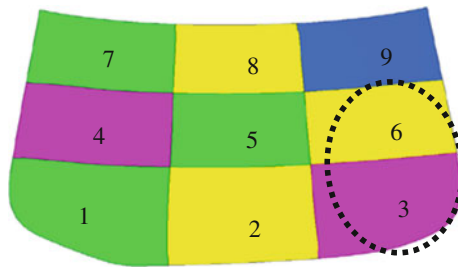


Fig. 37.8 Divisions of front windshield

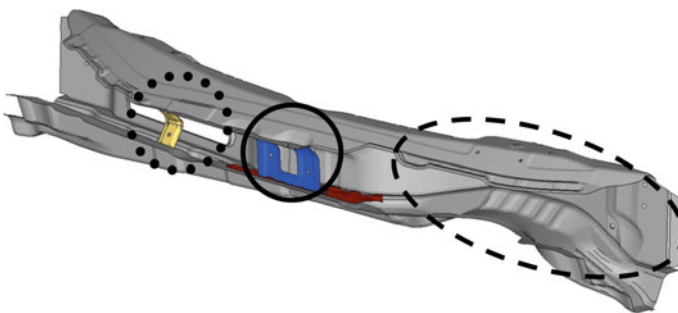


Fig. 37.9 Sketch of front windshield lower beam

fore-and-aft and windshield up-down can be easily excited, which leads to the final booming noise. Therefore, we decide to optimize the local structure of lower beam welding assembly and shift the natural frequency away from the exciting frequency.

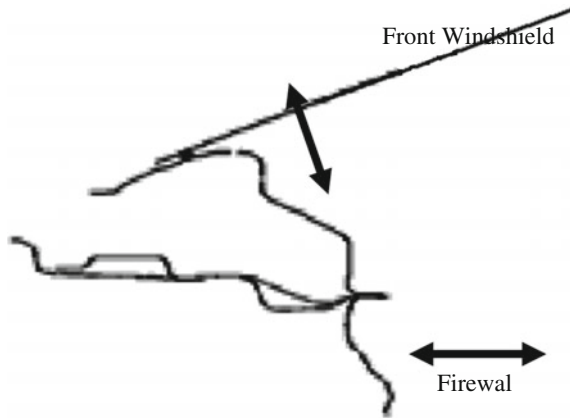


Fig. 37.10 Section sketch of front windshield lower beam

37.5 Optimization Solution and Verification

It is the most valid method to add supporting bracket in the left lower of front windshield (verified by simulation), but there is no space. Thinking the principle of seesaw, adding support in the right may also have effects. After communication with the body design engineer, the final solution was shown in Fig. 37.11: The right bracket was new added, and the middle bracket was optimized by topography optimization method. The effect verified by NTF simulation was as shown in Fig. 37.12. It is obviously shown that 3 dB was reduced in peak value. In the same time, the contribution of windshield area 3 was also reduced, as shown in Fig. 37.13.

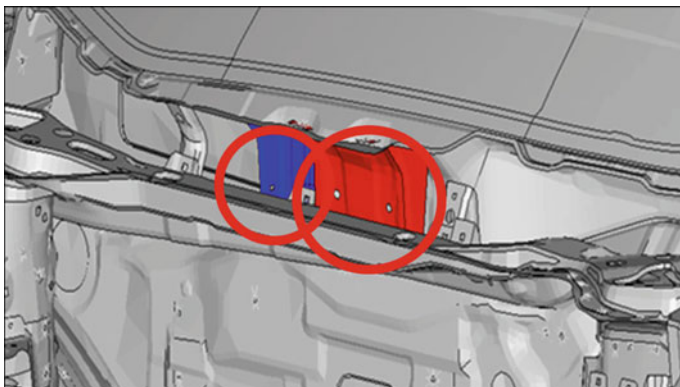


Fig. 37.11 Sketch of enhancing lower beam

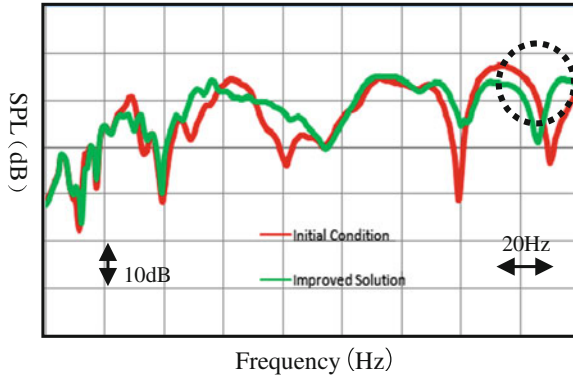


Fig. 37.12 NTF simulation contrast of enhancing

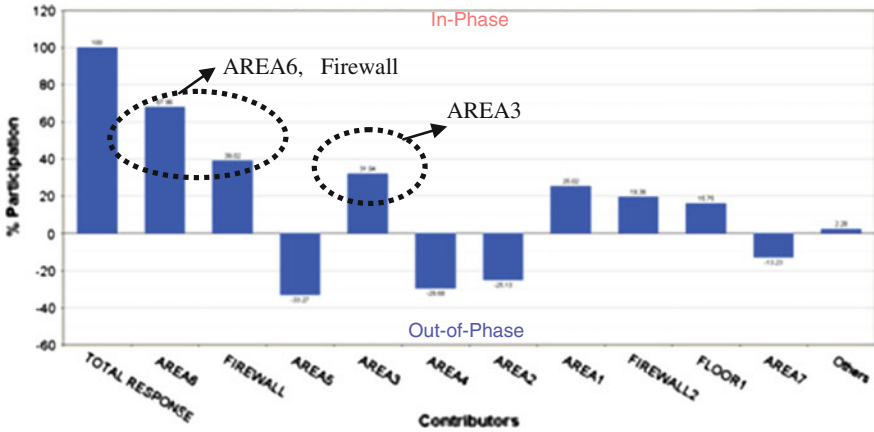


Fig. 37.13 Panel contribution after front beam enhanced

The improved vehicle with newly welding bracket (Fig. 37.14) was verified: Fig. 37.15 was the NTF's test contrast, and Fig. 37.16 shows the comparison of interior booming.

It is shown that about 10 dB can be reduced in NTF, 3 dB was reduced in booming noise, and the object target was achieved.

By virtue of local modification of front windshield lower welding beam assembly, there is no dramatic effect for pedestrian protection. Due to the paper's length limit, the result of pedestrian protection simulation in detail was not shown here.

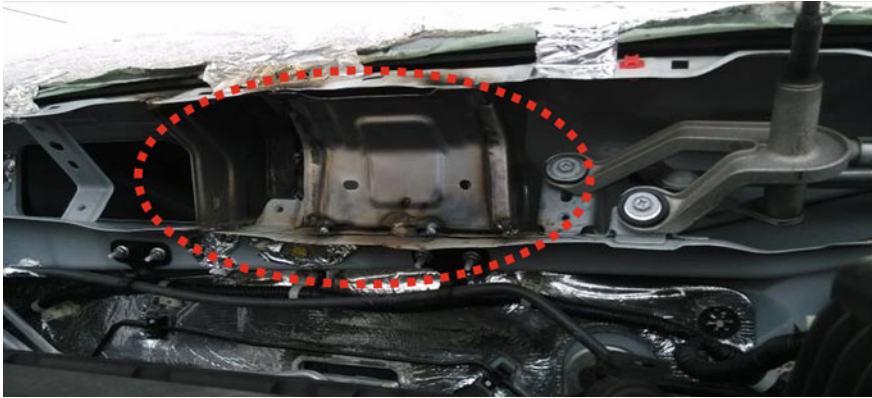


Fig. 37.14 Physical vehicle welding new bracket

Fig. 37.15 NTF contrast with new bracket

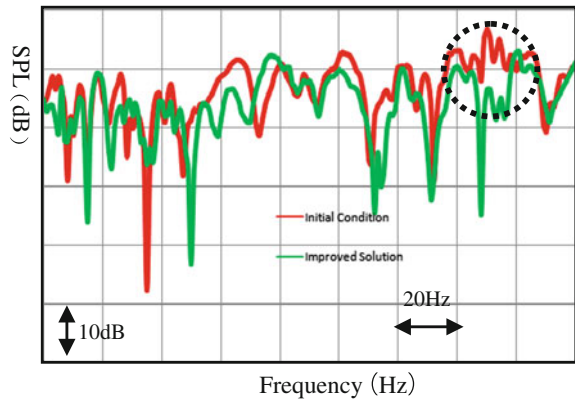
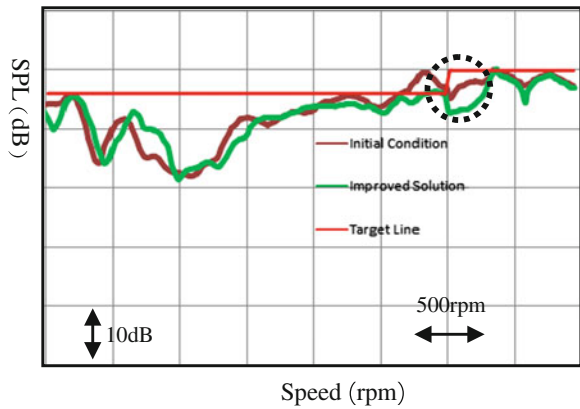


Fig. 37.16 Booming contrast with new bracket



37.6 Conclusions

To meet the need of pedestrian protection, the front windshield lower beam welding assembly was required to be designed open section. As a result, the stiffness of the front windshield and firewall was dramatically reduced, which will lead to NVH problems. In order to solve this problem, the simulation method was to optimize the booming noise in this paper, and the vibration of the front windshield and firewall was reduced by stiffing the windshield mounting structure. The improved structure was validated in real vehicle. The test also showed that enhancing windshield support structure can effectively improve the high-speed booming noise, and it may provide basis for vehicle body design.

References

1. Tonge G, Agrawal S (2013) Analysis of open plenum structure for reduction of booming noise. SAE Paper, 2013-01-0636
2. Yanan C, Zhou Q, Xu Y, Zhou Z, Liu H (2013) Vehicle interior booming noise control method based on simulation analysis. Annual Conference of Society of Automotive Engineers of China, 2013CN-NV044
3. Hwang C, Lee B, Jung P (2009) Reduction of interior booming noise for a small diesel engine vehicle without balance shaft module. SAE Paper, 2009-01-2121

Chapter 38

Optimization Design Method of 4×4 Bus Power Train Layout

Qing Chen, Ying Fu and Yongkun Hou

Abstract It takes a lot time to find the most optimized program of 4×4 bus power train layout, using original 2D or 3D design method. The mathematic modeling of a 4×4 bus power train layout's mathematic modeling can be built by using space vector method, and then, the most optimized method can be calculated by MATLAB program. This method is proved effectively by field test.

Keywords 4×4 bus · Power train layout · Space vector method · Optimization design

38.1 Introduction

A 4×4 bus is 7 m in length, with 4WD mechanism. It is used for transportation from cities and towns to mining area or oil field, which needs high trafficability. In the process of new product development, the power train layout is with front-mounted engine, front and rear rigid drive axle, transfer case which is located between front and rear axle (Fig. 38.1). This technical scheme is a low cost way to achieve 4WD, but the problem is that the angle of power train and the position of transfer case may cause great change of driveshaft angle acceleration that has a great influence on the vibration of power train. The trafficability is also affected by power train layout. The difficulty is how to find an optimization method to meet the requirements of trafficability and low vibration of power train. The original CAD draw method will take a lot time to acquire the length and angle of driveshaft and then check the design meet requirements or not. The article uses space vector

Q. Chen (✉) · Y. Fu · Y. Hou
Bus and Coach Department, R&D Center, China FAW Group Co., Ltd.,
1063 Changye Street, Changchun, Jilin, China
e-mail: chenqing1@rdc.faw.com.cn

© Springer-Verlag Berlin Heidelberg 2015
Society of Automotive Engineers of China (SAE-China) (ed.),
Proceedings of SAE-China Congress 2014: Selected Papers,
Lecture Notes in Electrical Engineering 328, DOI 10.1007/978-3-662-45043-7_38

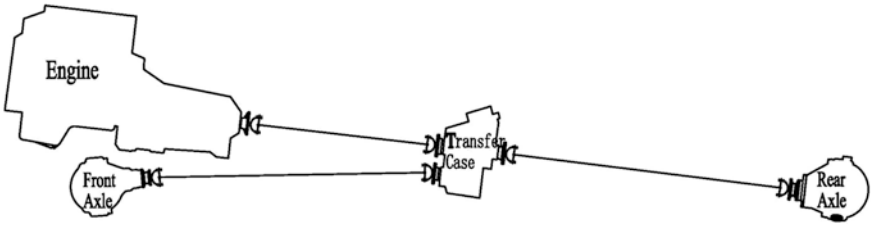


Fig. 38.1 Power train layout diagrammatic sketch

method [1] to build 4×4 bus power train layout’s mathematic modeling and program in MATLAB. And then, the most optimized method can be calculated by this MATLAB program.

38.2 Power Train Layout’s Mathematic Modeling

38.2.1 Coordinate System and Point Definition

The vehicle coordinate system definition can be found in references [2] (Fig. 38.2), and other assembly coordinates and coordinate points refer to the vehicle coordinate system. P_e , P_r , P_f , and P_{tc} are the coordinate origins of assembly coordinates. P_1 , P_2 , P_3 , P_4 , P_7 , and P_8 are the middle points of the universal joint. P_5 , P_6 , and P_9 are the middle points of flange surface.

38.2.2 Parameterization of Coordinate Points

The coordinate origin and coordinate conversion are given in Table 38.1.

The coordinate values of P_1 – P_9 can be expressed by coordinate origin value and Eulerian angles as given in Table 38.1. There are three methods to express values of these points according to the position of these points.

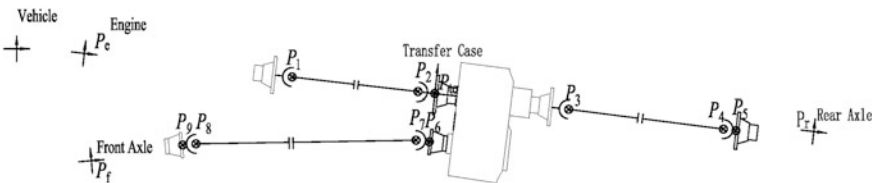


Fig. 38.2 Coordinate system and point definition

Table 38.1 The coordinate origin and coordinate conversion

No.	Coordinate	Coordinate origin value	Eulerian angle
1	Vehicle	(0, 0, 0)	(0, 0, 0)
2	Engine	$P_e (x_e, y_e, z_e)$	(0, j_e , 0)
3	Front axle	$P_f (0, 0, z_f)$	(0, j_f , 0)
4	Rear axle	$P_r (x_r, 0, z_r)$	(0, j_r , 0)
5	Transfer case	$P_{tc} (x_{tc}, y_{tc}, z_{tc})$	(i_{tc} , j_{tc} , 0)

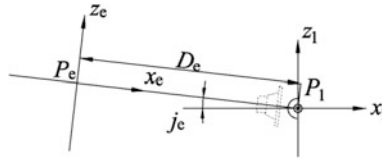


Fig. 38.3 Geometrical relationship of P_1 and P_e

38.2.2.1 Middle Points of Universal Joint Coordinate ($P_1, P_2, P_3, P_4, P_7, P_8$)

Taking P_1 as an example, P_1 can be presented by P_e , according to geometrical relationship (Fig. 38.3).

$$\begin{cases} x_1 = x_e + D_e \cos j_e \\ y_1 = y_e \\ z_1 = z_e - D_e \sin j_e \end{cases}$$

where D_e is the distance, which is from engine coordinate origin to the middle point of the universal joint coordinate in the transmission end.

P_2, P_3, P_4, P_7, P_8 can be expressed in same method by using the similar geometrical relationship.

38.2.2.2 Geometrical Relationship of Front or Rear Axle (P_5, P_9)

Taking P_9 as an example, P_9 can be presented by P_f , according to geometrical relationship (Fig. 38.4).

$$\begin{cases} x_9 = x_f + (d_{fx} \cos j_f - d_{fz} \sin j_f) \\ y_9 = y_f + d_{fy} \\ z_9 = z_f + (d_{fx} \sin j_f + d_{fz} \cos j_f) \end{cases}$$

where (d_{fx} , d_{fy} , and d_{fz}) is the relative coordinate of P_9 in front axle coordinate.

P_5 can be expressed in same method by using the similar geometrical relationship in rear axle coordinate.

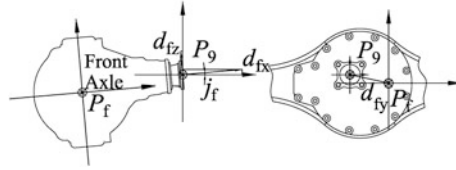


Fig. 38.4 Geometrical relationship of P_9 and P_f

38.2.2.3 Geometrical Relationship of Front or Rear Axle (P_6)

Taking P_6 as an example, P_6 can be presented by P_{tc} , according to geometrical relationship (Fig. 38.5).

$$\begin{cases} x_6 = x_{tc} - D_{tc1} \cos i_{tc} \sin j_{tc} \\ y_6 = y_{tc} - D_{tc1} \sin i_{tc} \\ z_6 = z_{tc} - D_{tc1} \cos i_{tc} \cos j_{tc} \end{cases}$$

where D_{tc1} is the distance, which is from power input flange of transfer case to power input flange of front axle.

38.2.3 Applying Space Vector Method to Operate Driveshaft Angle and Length

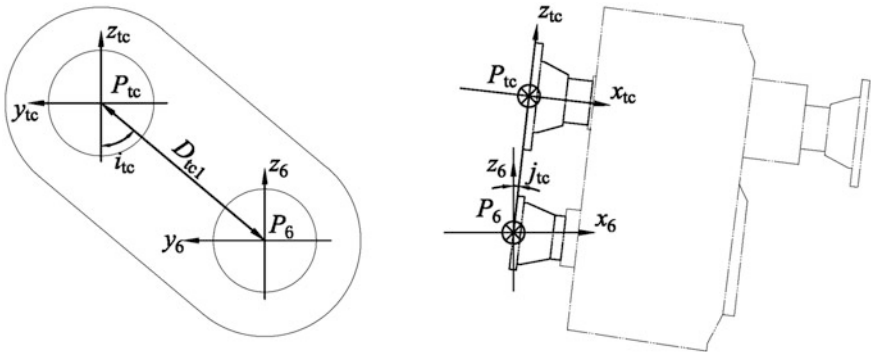


Fig. 38.5 Geometrical relationship of P_6 and P_{tc}

The length of driveshaft from transmission to transfer case is $L_3 = |\overline{P_7P_8}|$, the length of driveshaft from transfer case to rear axle is $L_2 = |\overline{P_3P_4}|$, and the length of driveshaft from transfer case to front axle is $L_3 = |\overline{P_7P_8}|$.

As shown in the Fig. 38.5, θ_1 is the angle of vector $\overline{P_8P_9}$ and vector $\overline{P_1P_2}$, θ_2 is the angle of vector $\overline{P_1P_2}$ and vector $\overline{P_2P_{tc}}$, θ_3 is the angle of vector $\overline{P_{tc}P_3}$ and vector $\overline{P_3P_4}$, θ_4 is the angle of vector $\overline{P_3P_4}$ and vector $\overline{P_4P_5}$, θ_5 is the angle of vector $\overline{P_6P_7}$ and vector $\overline{P_7P_8}$, and θ_6 is the angle of vector $\overline{P_7P_8}$ and vector $\overline{P_8P_9}$.

38.3 Constraint Condition and Objective Function Modeling

38.3.1 Constraint Condition Based on Vehicle Construction

There are several constraint conditions of assemblies' position.

- Engine angle, which is between engine crankshaft axis and vehicle Z0 plane [2], is $0-7^\circ$.
- Rear axle angle, which is between main reducer of rear axle and vehicle Z0 plane [2], is $0-7^\circ$.
- Front axle angle, which is between main reducer of front axle and vehicle Z0 plane [2], is $0-7^\circ$.
- The values of engine, front axle, and rear axle coordinate origin come from definition of vehicle.
- The variation range of transfer case coordinate origin is $x_{tc} \in [1600 \ 1900]$, $y_{tc} \in [-30 \ 30]$, and $z_{tc} \in [-240 \ -180]$.
- The variation range of transfer case angle is $i_{tc} \in [0, 90^\circ]$ and $j_{tc} \in [0, 7^\circ]$.
- Double universal joint can have constant velocity in W-type layout or Z-type layout. In Fig. 38.6, $\alpha_1 = \alpha_2$, Z-type layout is easier to achieve than W type, where $j_e = j_r = j_{tc}$.
- The ground clearance of transfer case is more than 300 mm.

38.3.2 Constraint Condition Based on Vehicle Performance

Driveshaft layout is critical factor, which affect vehicle vibration. According reference [3–5], each order vibration in driveshaft has several reasons.

- First-order vibration mainly is caused by the driveshaft residual unbalance.
- Second-order vibration is caused by there reasons.
 - The vibration is caused by variable-speed motion of unequal input and output driveshaft angle.
 - When the driveshaft has a vertical vibration, there is vertical displacement, which causes unequal input and output driveshaft angle and generates additional incentive, in intermediate support of driveshaft.

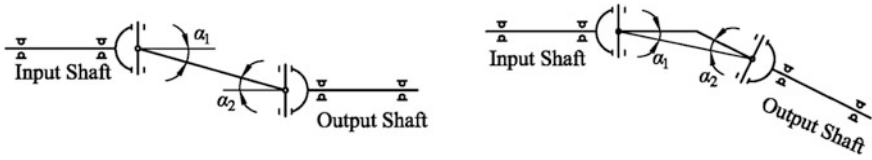


Fig. 38.6 Left figure is Z-type layout, and right figure is W-type layout

- The variable-speed motion of driveshaft causes vibration of drive axle gear.

According to the above conclusion, the first-order vibration of driveshaft is related to its own state, and the second-order vibration is related to power train layout. There are three constraint conditions that are imported to mathematics modeling so as to control second-order vibration of driveshaft.

38.3.2.1 The Design Scope Length of Driveshaft Ensured by Critical Speed

The maximum length of driveshaft ensured by critical speed:

$$L_{\max} = \sqrt{\frac{1.2 \times 10^8 \times \sqrt{D^2 + d^2}}{n_k}}$$

where D is outer diameter of driveshaft; d is inter diameter of driveshaft; $n_k = n_{\max}/S$ (n_{\max} is the top working speed; and S is the calculation of coefficient, usually is 0.7).

The driveshaft design requirement of front engine rear drive vehicle L is between 500 mm to L_{\max} .

38.3.2.2 The Design Requirement of Angular Acceleration (the Formula is in Reference [2])

In general conditions, the angular acceleration $\alpha \leq 600 \text{ rad/s}^2$, it is appropriated to relax in special conditions.

38.3.2.3 The Safety Coefficient

The driveshaft can equal to uniform hollow shaft so as to do approximate calculation of strength:

$$n_c = \frac{60\pi}{2L^2} \sqrt{\frac{E \cdot I \times 10^6}{A \cdot \rho}}$$

where n_c is dangerous speed (rpm), $L()$ is the length of driveshaft (mm), E is Young's modulus (GPa), I is the area moment of inertia, $I = \pi(D^4 - d^4)/64$ (mm⁴), and where D is driveshaft outer diameter (mm), d is driveshaft inner diameter (mm), A is cross section, $A = \pi(D^2 - d^2)/4$ (mm²); and ρ is material density (kg/mm³).

38.3.3 Objective Function Modeling

The objective function of this mathematical model is: in all independent variables that satisfied the constraint conditions, search a group of solution that the sum of angular acceleration value is minimal. It is $\sum_{i=1}^n \alpha_i$, and there are three reasons:

- The sum of angular acceleration value is the function of constraint conditions.
- The second-order vibration of driveshaft is related to angular acceleration.
- The extension ability of the model is enhanced, if the model introduces phase coefficient of driveshaft, it will suit multi-driveshaft drive system.

38.4 Computer Programs of Mathematical Model

Optimization design of power train layout belongs to constraint optimization problem.

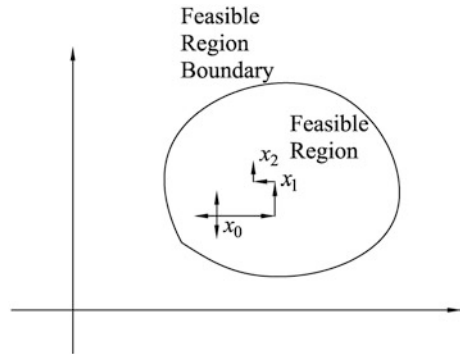
The mathematical model of constraint optimization problem is

$$\min f(x), \text{ s.t. } \begin{cases} h_i(x) = 0, & i = 1, 2, \dots, k \\ g_j(x) \geq 0, & j = 1, 2, \dots, m \end{cases}$$

where $f(x)$ is objective function, $h_i(x)$ is equality constraint conditions, and $g_j(x)$ is inequality constraints.

Coordinate rotation method can solve this function. Coordinate rotation method is based on pattern search method, which belongs to unconstrained optimization algorithm. Every search is restricted by constraint function, and the result is in feasible region. The search process is as shown in Fig. 38.7, where x_0 is initial feasible point and x_1 can be got through the pattern search. In next pattern search, the feasible point is x_2 . Every search can get a feasible point in feasible region until the loop is ended. This algorithm of computer program flow diagram is as shown in Fig. 38.8. In this computer program, independent variable, $x = [i_{tc}, j_{tc}, i_f, x_{tc}, y_{tc}, z_{tc}]$. Constraint function, $g = [\text{limit of driveshaft angle, limit of independent variable}]$.

Fig. 38.7 Coordinate rotation method [6]



bound, limit of safety factor, limit of driveshaft design length, limit of ground clearance]. Objective function $f(x)$ equals minimum value of sum of all driveshaft angular acceleration.

38.5 Program Optimization Results

There are three results calculated by program, according to use conditions and design requirements, as shown in Table 38.2. It allowed angular acceleration value exceed standard in all-wheel-drive condition because all-wheel-drive condition is less than 20 % in this vehicle and larger transfer case ground clearance is desired. The main reference value is group 3 given in Table 38.2. The group 4 is the final result of layout because of two factors:

- Equal length of front and rear axle driveshaft design for parts commonality.
- Round several angles for support parts design and processing.

38.6 Field Test

The vibration field test is executed in 4×4 bus prototype. Figures 38.9 38.10 and 38.11 show the part of results. Figures 38.9 and 38.10 show that the main vibration order of seat rail and transfer case comes from 1.35 and 2 vibration order of engine, in the condition of rapidly speeding-up in 5th speed. 1 and 2 vibration order of driveshaft come from 1.35 and 2.7 vibration order of engine, because 5th speed is overdrive. Figure 38.11 shows that the main vibration order of seat rail and transfer case is first-order engine, in the condition of rapidly speeding-up in 4th speed. The driveshaft vibration order is the same as the engine vibration order because the 4th

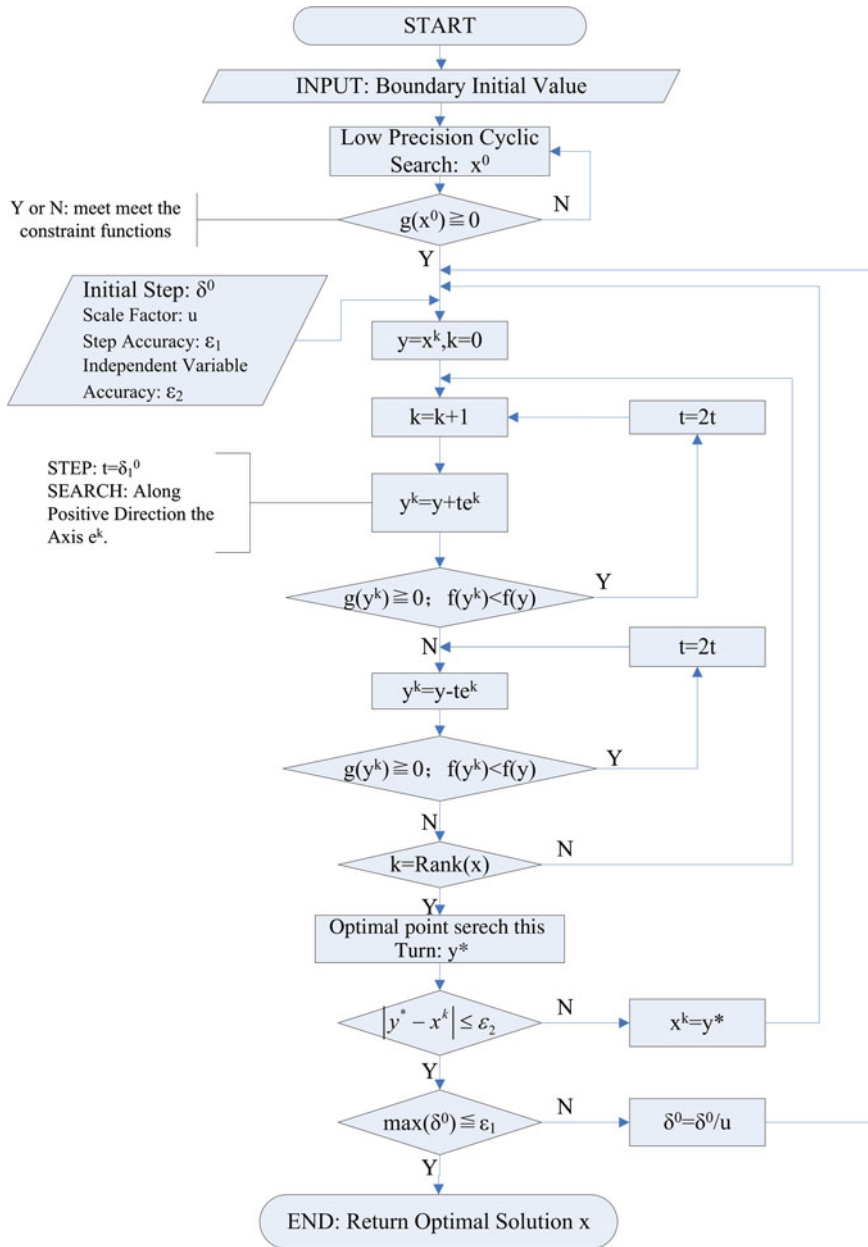


Fig. 38.8 Computer program flow diagram

Table 38.2 Program optimization result

	Group 1	Group 2	Group 3	Group 4
Target	Minimizing the sum of the angular acceleration value in 4×2	Minimizing the sum of the angular acceleration value in 4×4	Larger transfer case ground clearance	Design value
Angle of engine/TC/Rear axle	6.8	6.70	6.53	6.5
Angle of front axle	0.6	-0.29	4.5	5
X-axis rotation angle of TC	25.2	23.9	47.8	50
x_{tc}	1,999.9	2,000	1,877.1	1,883.5
y_{tc}	13.2	11.1	15.3	15
z_{tc}	-228	-232.1	-203	-206.414
TC ground clearance	257.7	251.9	340	343
Sum of the angular acceleration value in 4×2	148.7	171.6	239.4	227
Sum of the angular acceleration value in 4×4	698	663.6	1,386.5	1,458
$\theta_1/\theta_2/\theta_3/\theta_4/\theta_5/\theta_6$	0.72/0.72/ 0.91/0.91/ 5.67/2.02	0.74/0.74/ 1.00/1.00/ 5.53/1.39	0.94/0.94/1.13/ 1.13/7.70/4.06	0.92/0.92/ 1.10/1.10/ 7.75/4.6
$L_1/L_2/L_3$	1,057.7/ 1,363.2/ 1,587.7	1,058.3/ 1,362.8/ 1,587.6	932/1,488.3/ 1,475.7	940/1,482/ 1,484
Safety coefficient of driveshaft	4.1/2.47/1.38	4.1/2.47/1.38	5.28/2.07/1.60	5.2/2.1/1.58

speed is the direct gear. It is acceptable in slow speed of revolution that the large amplitude of monitoring point appears in second order of driveshaft.

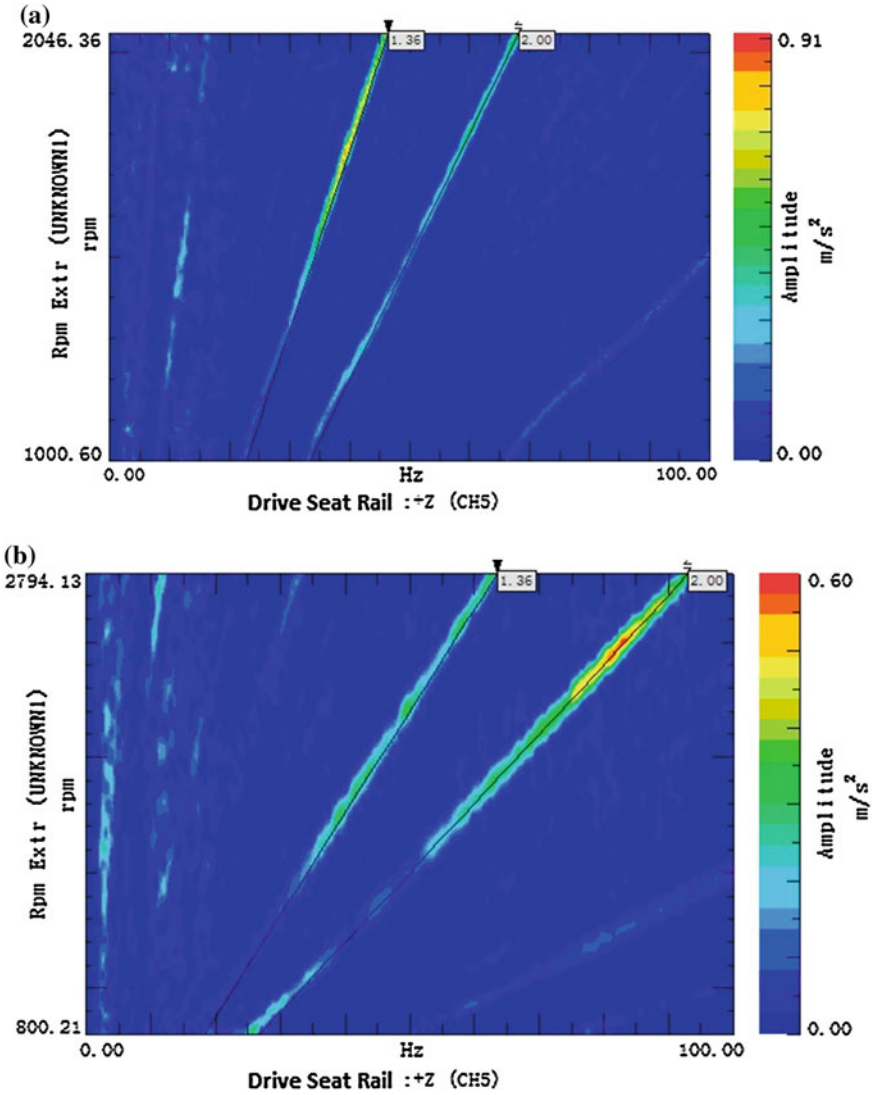


Fig. 38.9 Speed tracking map of Z vibration in seat rail (rapidly speeding-up in 5th speed).
a 4×2 mode b 4×4 mode

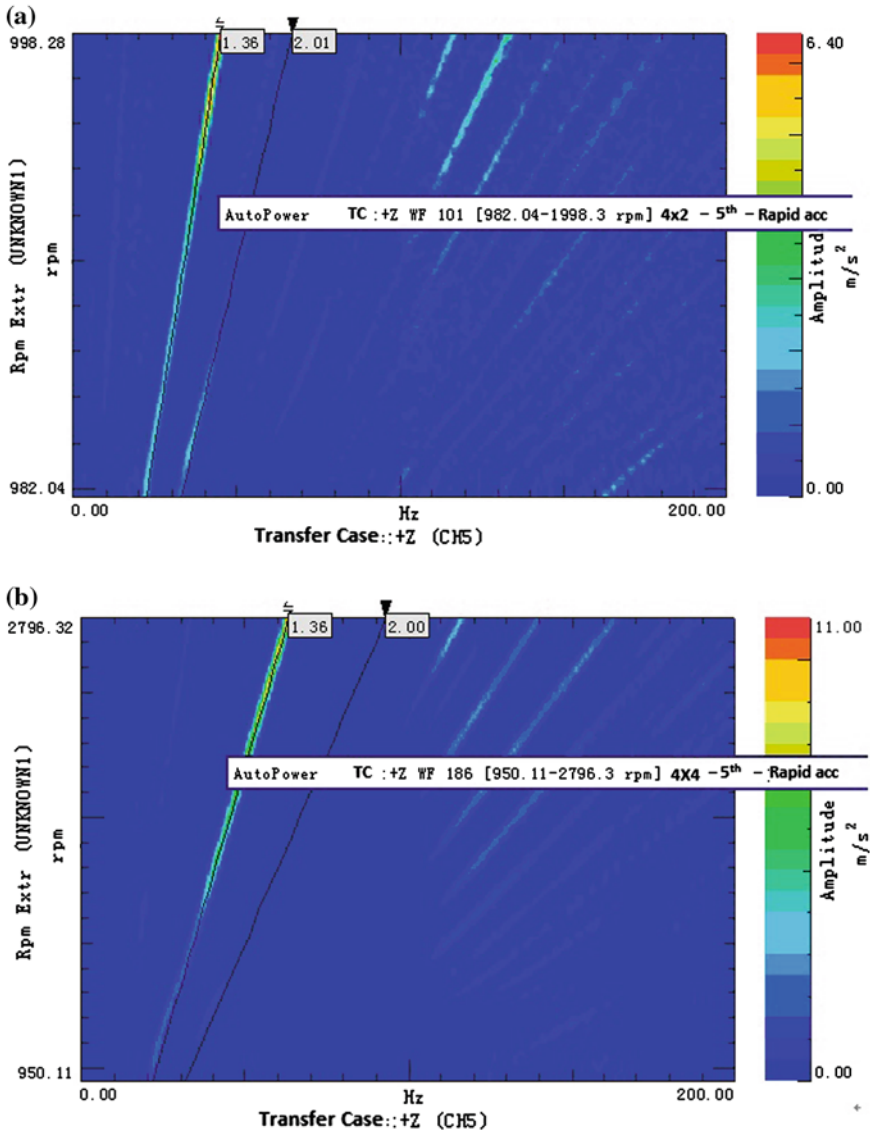


Fig. 38.10 Speed tracking map of Z vibration in transfer case (rapidly speeding-up in 5th speed). a 4 × 2 mode b 4 × 4 mode

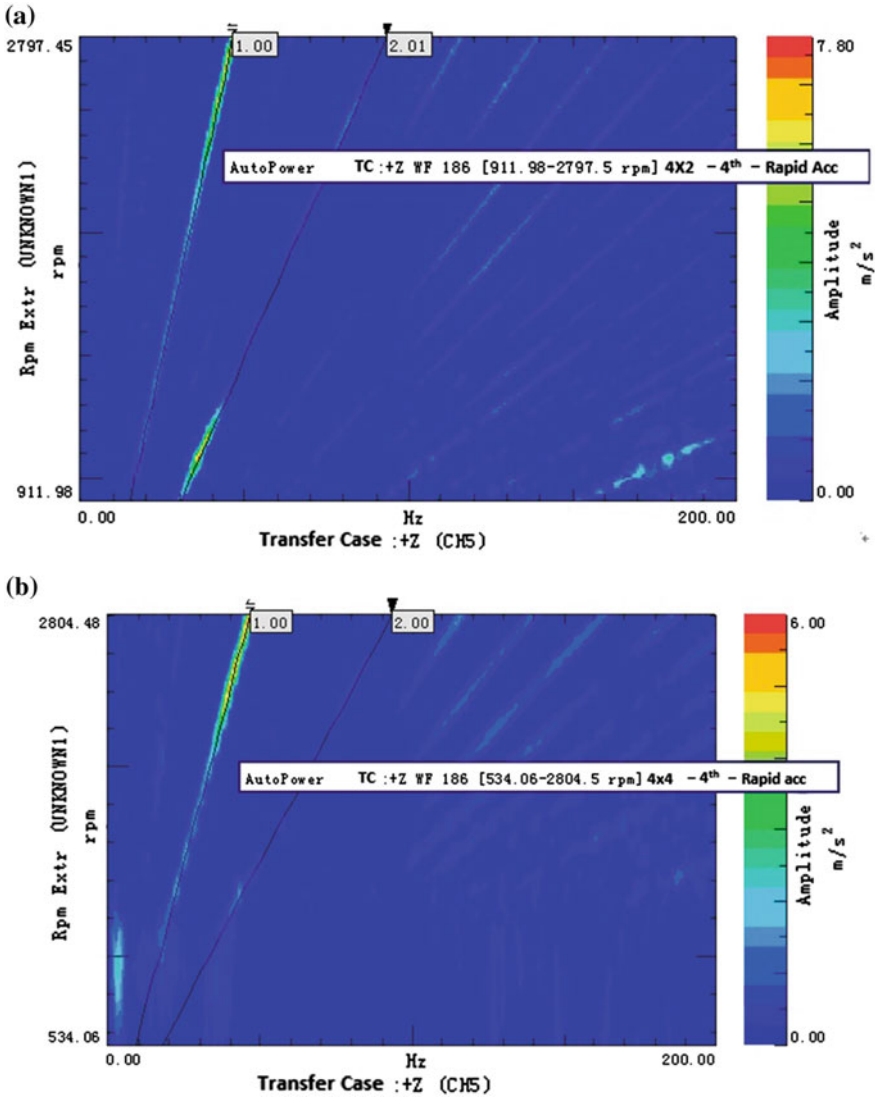


Fig. 38.11 Speed tracking map of Z vibration in transfer case (rapidly speeding-up in 4th speed). a 4×2 mode b 4×4 mode

38.7 Conclusions

This article focuses on difficulty of optimization method of 4×4 bus power train layout. The optimal solution is obtained by MATLAB program of mathematical model, which includes engine angle, front and rear axle angle, and transfer angle and position. This solution can achieve design demands, which need smaller sum of

all driveshaft angular acceleration and larger ground clearance. The field test demonstrates the effectiveness of this method. This method can improve other vehicle power train layout, and the convenience and accuracy of this method need to be tested in more vehicles in future design works.

References

1. Guo Y, Sun Z, Sun Z, Zhou Y, Zhang G (2008) The check on length and angle of propeller shaft. *Automobile Technol* 05:34–37
2. Wang W (2004) *Vehicle design*. China Machine Press, Beijing, China, pp 122–125
3. Yin J (1998) Automobile driveshaft vibration analysis. *Light Veh* 2(3):27–28
4. Zhou Y (1998) *Vehicle design manual, Vehicle and Chassis*, 268. Changchun, China
5. Xu B (2006) *Vibration analysis and optimization of commercial vehicle driveline*, master thesis. University of Qing Hua, Beijing
6. Gong C, Wang Z (2012) *MATLAB optimization calculation*, 2nd edn. Electronic Industry Press, Beijing, pp 197–200

Chapter 39

A Study on the Noise Capability of Center Air Vents System

Liqiong Mo, Liangda Li and Zhong Yang

Abstract The conventional design methods of duct structure are summarized, and the structure designing of how to reduce its working noise and of layout drawing is simply described. The main task of this study is to generally discuss the connections' structure between ducts and outlets via the CFD analysis, geometric structure analysis, and the comparison of how to find suitable locations to fix them. This essay will finally introduce a solution of how to optimize a structure of ducts and outlets, based on their results of the CFD analysis, the geometric data analysis, and the noise test.

Keywords Air ducts · Air outlets · CFD · Noise

39.1 Introduction

With the development of the automotive industry in China, GB 11555-2009 Motor vehicles-windshield demisting and defrosting systems' performance requirements and test methods has the regulations of the windshield defrosting and defogging, while modern auto manufacturers can generally achieve or even exceed these requirements, but Chinese government does not have the law of the vehicle interior noise caused by automotive air conditioning system. However, customers' demands now for cars are becoming higher and higher. Automotive companies are competitive to optimize their products in order to attract more customers to buy their cars, while NVH is one of the major points that customers focus on. This essay will present some possible strategies of how to reduce the noise of the automotive air conditioning system.

L. Mo (✉) · L. Li · Z. Yang
Vehicle Trim Development, Changan Automobile Engineering Institute,
Changan Motor Company, Chongqing 401020, China
e-mail: 656211920@qq.com

© Springer-Verlag Berlin Heidelberg 2015
Society of Automotive Engineers of China (SAE-China) (ed.),
Proceedings of SAE-China Congress 2014: Selected Papers,
Lecture Notes in Electrical Engineering 328, DOI 10.1007/978-3-662-45043-7_39

39.2 Comparisons Analysis for Cars' Central Air Ducts and Central Outlets

39.2.1 Geometric Comparison

There are two different designs of the central air ducts and central outlets with same boundary conditions, as shown in Fig. 39.1. The differences between two schemes indicated in Fig. 39.1 are that for scheme 1, it is hunched around the corner of the inlet of the central air ducts and the shape of the central outlets is not smooth, while for scheme 2, the shape of the both central air ducts and central outlets is very smooth.

39.2.2 CFD Comparison

39.2.2.1 The Total Pressure Distribution

Figure 39.2 shows the results of the total pressure distribution for the two designs through CFD analysis. It is obvious that air pressure is very low near the connecting area for scheme 2, especially in the inner corner, which is illustrated in the red rectangular boxes, but this indicated in scheme 1 shows much better. According to the result, the air pressure generally loses heavily if there is a sharp corner on the ducts. Therefore, the shape of the ducts and the outlets should be designed smoother for avoiding the loss of the air pressure.

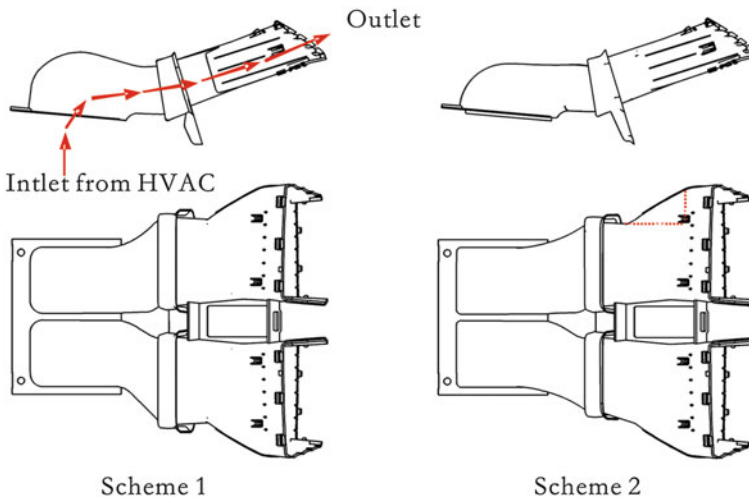


Fig. 39.1 Geometric comparison

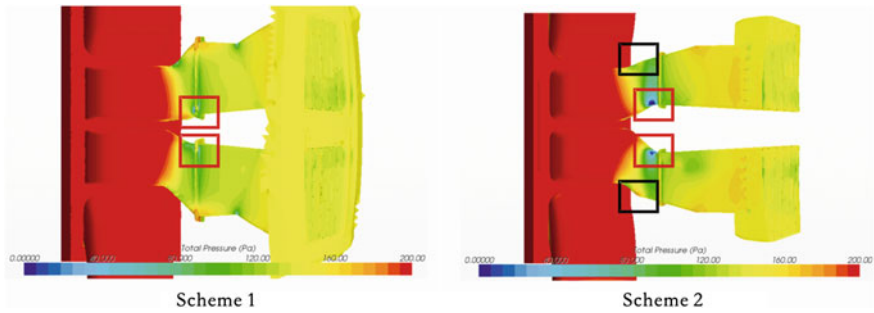


Fig. 39.2 The total pressure distribution

39.2.2.2 Section of the Vector Distribution

Figure 39.3 shows the section of the vector distribution of the CFD analysis results. The results show that the turbulence is very obvious in the sharp turn area of scheme 2, while this in scheme 1 shows much better because of its smoother shape.

According to the comparisons of section of the vector distribution on the side view in Fig. 39.4, there is more turbulence around the corner of the inlet of the central air ducts for scheme 2, compared with scheme 1, as shown in the two red circles. In addition, narrowing the dimensions of the ducts can effectively reduce the turbulence, which is illustrated in the red rectangular boxes. Furthermore, moving the connections between ducts and outlets, a suitable distance to the front can reduce the high-frequency noise which is caused by concussion from high-speed airflow.

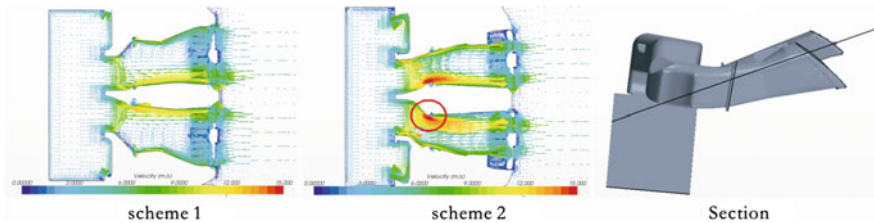


Fig. 39.3 Section of the vector distribution (vertical view)

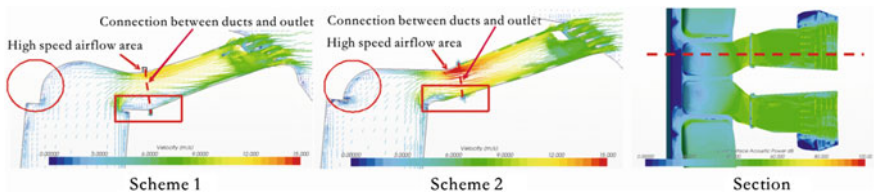


Fig. 39.4 Section of the vector distribution (side view)

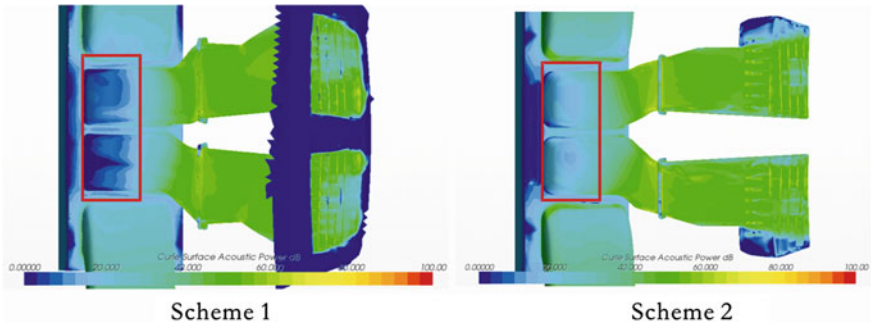


Fig. 39.5 Curl surface acoustic power distribution

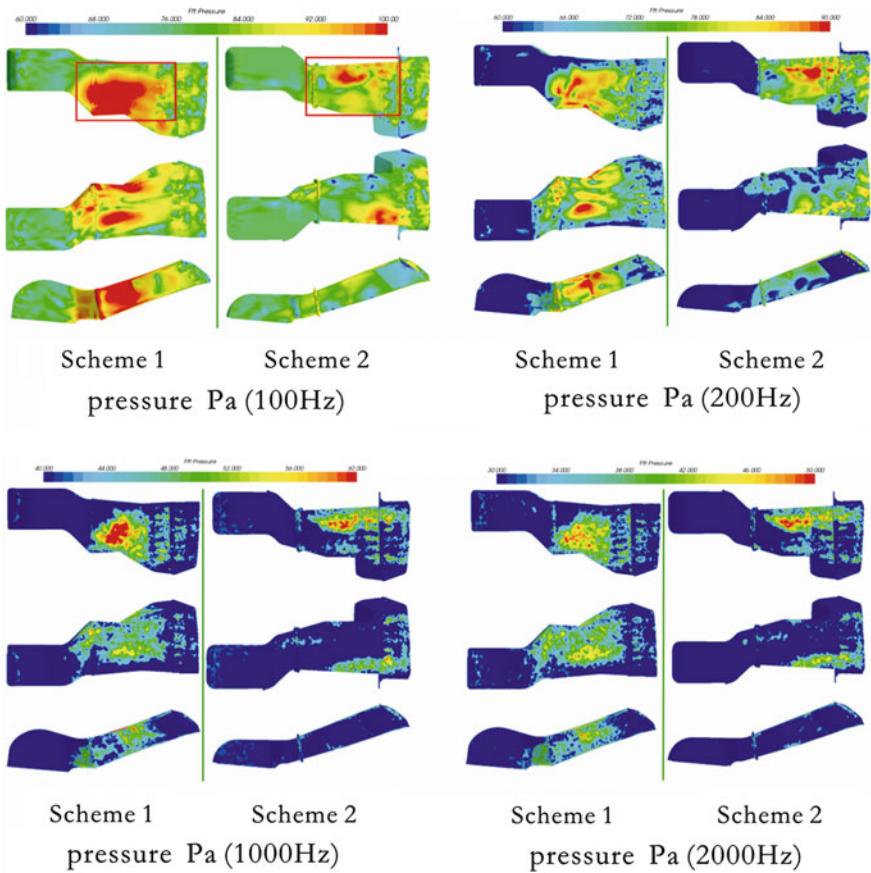


Fig. 39.6 Curl surface acoustic pressure distribution at the different frequencies

39.2.2.3 Curl Surface Acoustic Power Distribution

According to Fig. 39.5, it is clear that the curl surface acoustic power distribution in scheme 1 is very different from scheme 2 in the red rectangular boxes, because of its hunched shape design in this area that causes more turbulence.

Figure 39.6 shows the results of the curl surface acoustic pressure distribution for the different frequencies. Obviously, there is some high pressure distributed on scheme 1 where the surface shape is not smooth. With the comparison of the results at different frequencies, the results of scheme 2 show much better than the results in scheme 1.

39.2.2.4 Noise Test

For the noise test, the frequencies from 4,000 to 6,000 Hz are basically considered in this study. According to the results as shown in Fig. 39.7, the acoustic power from scheme 2 generally shows higher than it from scheme 1.

39.2.2.5 Brief Summary of Comparison of the CFD Analysis Results

See Table 39.1.

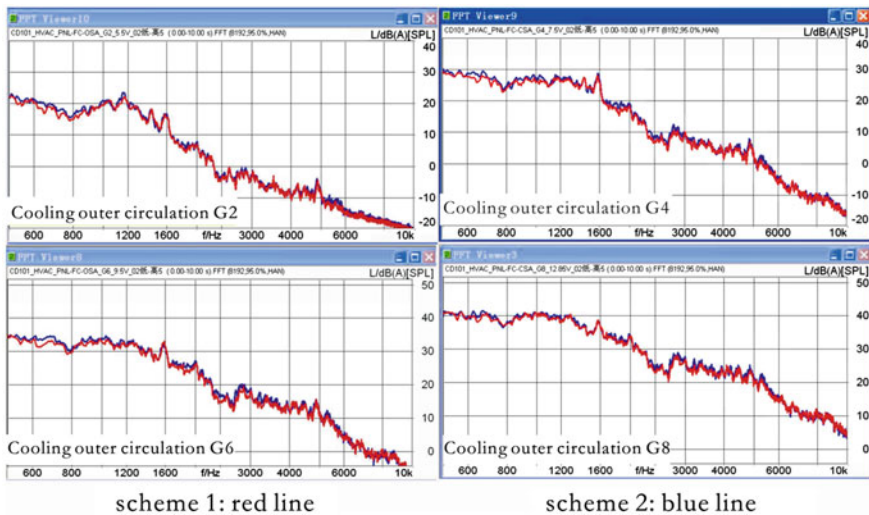
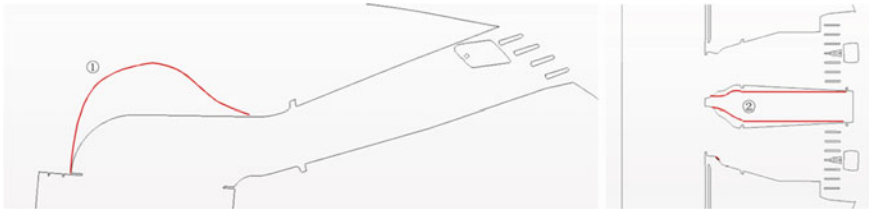


Fig. 39.7 Results of the noise test (color figure online)

Table 39.1 Brief summary of comparisons of the CFD analysis results

	Scheme 1	Scheme 2
Advantages	Less pressure loss	Well-distributed airflow
	Smooth shape in inner side	Lower noise on the high frequencies
	Less acoustic pressure	Lower acoustic power
Disadvantages	Unevenly distributed airflow	Smaller pressure loss
	Easier to have high-frequency noise	Sharp corner in inner side
	Higher acoustic power	Higher acoustic pressure

**Fig. 39.8** Diagrammatic sketch of the optimization

39.2.3 Possible Suggested Optimization

According to the results from CAE analysis, there are some possible suggestions of how to optimize the design of the ducts and the outlets, as shown in Fig. 39.8:

- Keep the hunched shape design like scheme 1 and narrow the ducts dimensions like scheme 2
- Narrowing the distance between two outlets is to extend the outlets' dimensions.

39.3 Structure Analysis of the Central Air Ducts and Central Outlets

39.3.1 Connecting Structure Analyzing Between the Central Air Ducts and Central Outlets

The both connecting structures between the central air ducts and central outlets are very similar, with 4-mm gap and there is no step of their inner face, as shown in Fig. 39.9. Moreover, the outlets will sag after a long time use, because of no fixed

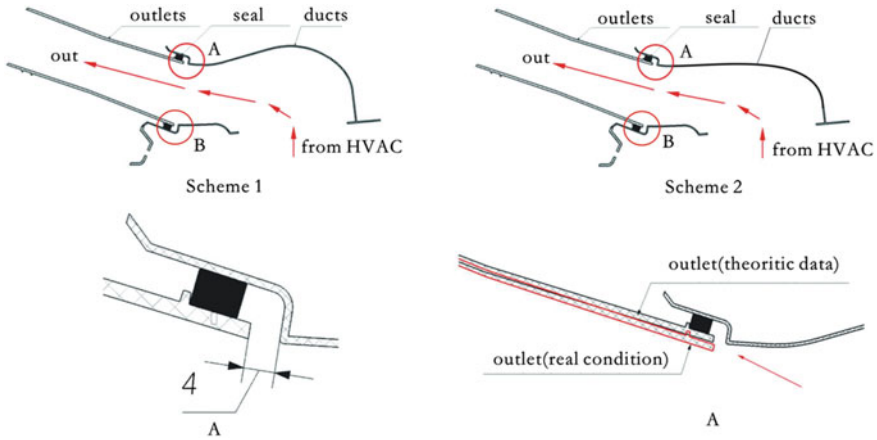


Fig. 39.9 Section of connecting structure

point between these two components and gravity, which will cause the air impact and further reduce the air pressure.

39.3.2 Possible Suggested Optimization

According to the data analysis, there are some possible suggested optimizations, as shown in Fig. 39.10:

- Set 2 mm steps and reduce the gap from 4 to 3 mm.
- Smooth the outlets edge to avoid burr and flashing.
- Design a support structure in the bottom of the outlets.

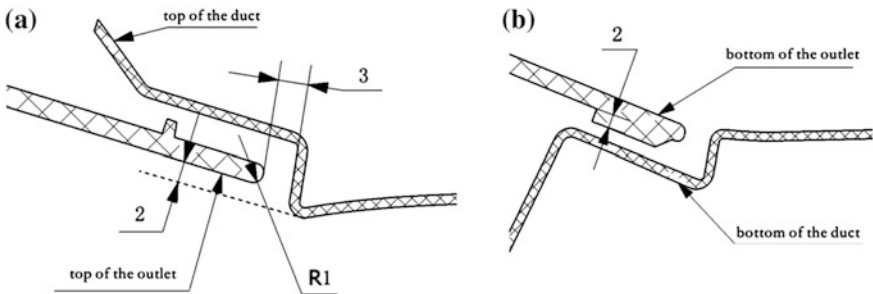


Fig. 39.10 Proposed scheme of the outlets

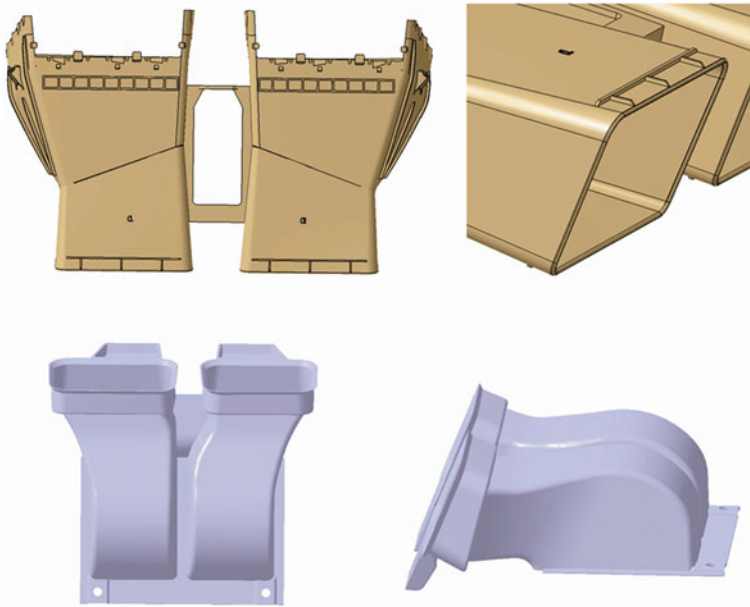


Fig. 39.11 Final data

39.4 Design Improvements

Figure 39.11 shows the 3D data of the ducts and the outlets improved via CAE analysis and geometric structure studying.

39.5 Prioritization Scheme Comparison of 2 Comparisons Analysis for Cars' Central Air Ducts and Central Outlets

39.5.1 Comparison of Curl Surface Acoustic Pressure

According to the computational analysis, it is obvious that the prioritization schemes are very well, compared with the original design, as shown in Fig. 39.12.

39.5.2 Noise Test

After a noise testing for the prioritization sample, the noise peak volume averagely reduces 8 dB within the range of 4,000–6,000 Hz, compared with the original schemes, as shown in Figs. 39.13 and 39.14.

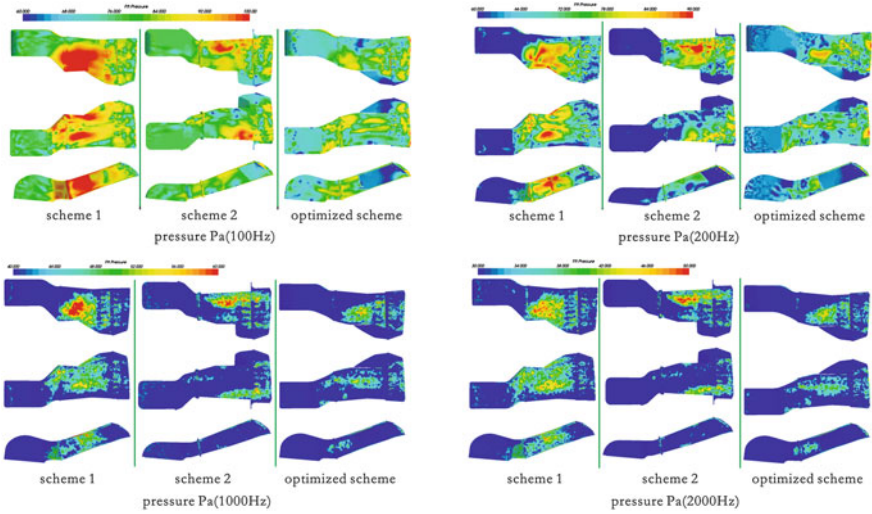


Fig. 39.12 Curl surface acoustic pressure distribution for the different frequencies

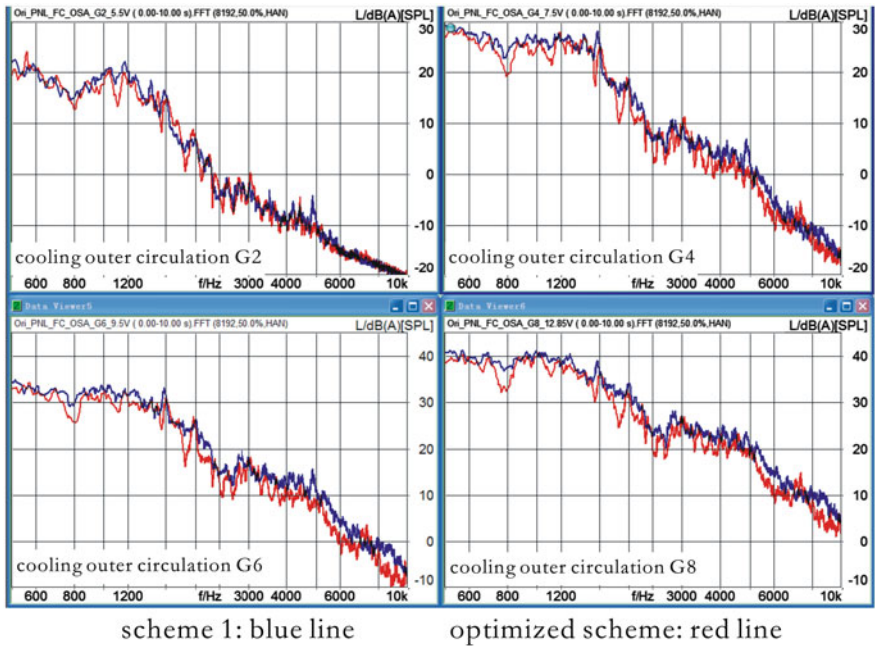


Fig. 39.13 The result of noise test (1) (color figure online)

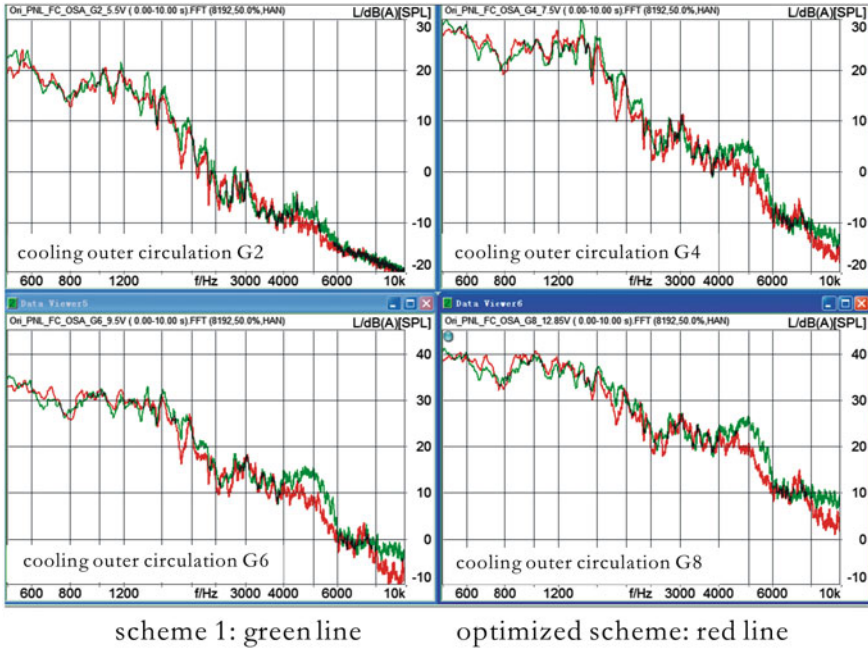


Fig. 39.14 The result of noise test (2) (color figure online)

39.6 Conclusions

In summary, there are some main points, for designing ducts and outlets, that automotive engineer should basically consider after above CAE analysis and geometric structure discussion:

1. The inner face of the ducts and the outlets should be as smoother as possible and the pipeline dimensions should not be dramatically changed.
2. High-speed airflow should be avoided around the connecting section.
3. The connecting area should not have a relative movement, and thus, finding suitable fixed points is very crucial for the ducts and the outlets.

Chapter 40

Design and Development of Pop-up Engine Hood System with Dual Elastic Buffer and Evaluation of Performance of Pedestrian Protection

Xinxian Li, Jiqing Chen and Fengchong Lan

Abstract Based on the purpose of pedestrian protection, a new Pop-up Engine Hood System (PEHS) with an effect of elastic butter is developed to reduce the injury of pedestrians in unavoidable human–car collision situation. Using the fusion of computer vision and laser scanner technology is the best way to tackle the problem of both responsiveness and robustness. Critical parameter of the device is determined. And a reusable PEHS using mechanical spring is designed by using optimization method. After setting up the 3-dimensional model and physical model, the performance of bouncing and injury protection of the system has been proved by kinematics simulation and prototype experiment.

Keywords Automobile active safety · Pedestrian protection · Pop-up engine hood system

40.1 Introduction

According to statistics in case of human–car collision, 62 % pedestrians died of head injuries. Therefore, reducing the pedestrian head injuries is an important part of pedestrian protection. Currently, the primary way to reduce head injuries is to optimize the engine hood stiffness and the interior lining panel structure. Although it is easy to use, this method may lead to the attendant change in vehicle NVH performance, while the reduction of the rigidity of the engine hood will also bring out the occurrence of secondary collisions with hard objects below, which can increase the collision damage. Pop-up Engine Hood System (PEHS) technology, because of its significant change in head protection performance and smaller change of cars original design, has become a

X. Li (✉) · J. Chen · F. Lan

School of Mechanical and Automotive Engineering, South China University of Technology, 510640 Guangzhou, China
e-mail: l.xinxian@mail.scut.edu.cn

© Springer-Verlag Berlin Heidelberg 2015

Society of Automotive Engineers of China (SAE-China) (ed.),

Proceedings of SAE-China Congress 2014: Selected Papers,

Lecture Notes in Electrical Engineering 328, DOI 10.1007/978-3-662-45043-7_40

research trend. This technology is a new way to reduce the degree of injury to pedestrian head. Before the contact between pedestrian head and engine hood, it allows the hood to rise to a certain height in order to increase the space below the hood, so the collision of the head below the hard point can be avoided.

PEHS comprises a pedestrian detection system and a pop-up device. In the current active bonnet that, in general use of passive detection of crash acceleration sensors, is less affected by weather and other outside interferences, but the requirements of system response time are extreme, and the collisions and alerts cannot be predicable. Pop-up device sorted by the lifting actuator can be divided into: gas generator device and mechanical device. The main feature of gas generator device is the speed of action. The actuator is easy to control, but its obvious disadvantages are the non-repeatability, high utilization costs and the lock mechanism while the pedestrian collided with the hood (e.g. the cases given in the literature [1]). This will increase the degree of damage, while additional supporting device with cushioning performance is required. Mechanical devices such as SMA spring served as an actuator can be crushed with the hood hinge connection. But the hinge mechanism will be destroyed and changed after each collision [2].

Based on the active pedestrian detection technology, by using a camera and laser radar joint decision-making to detect pedestrian and to avoid collision anticipation, while meeting the real-time control systems and robustness requirements, the research of reusable PEHS with dual elastic buffer can improve the unfeasibility and lack of elastic buffer in existing active. Meanwhile, the physical model of PEHS with mechanical actuator and flexible support is developed to promote an evaluation experiments. The performance of bouncing and injury protection of the system has been proved by kinematics simulation and prototype experiment.

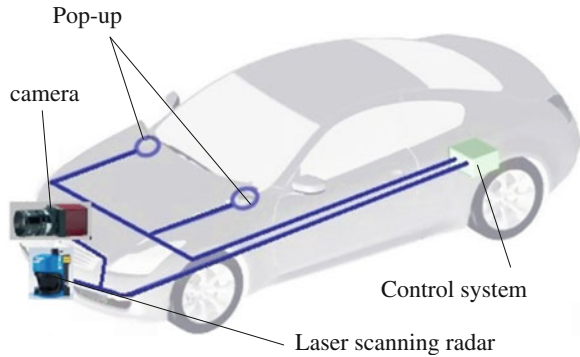
40.2 Control Technology of PEHS

40.2.1 Active Pedestrian Detection

The environment of control system, such as light, weather, varies greatly, which requires high system robustness; and in the state of motion, the real-time system is necessary, which requires the algorithm cannot be very complicated. How to simultaneously meet the requirements of both the robustness and real-time detection is a problem in the system development.

The active pedestrian detection techniques can be divided into machine vision sensors, laser radar, microwave radar and infrared sensors. Computer vision methods are the most widely used in pedestrian detection because of its long distance, large-scale, abundant information etc., but it is greatly depended on the weather and light. So the most successful systems on visual inspection at present are just for good weather conditions [3]. Laser radar has an absolute advantage on the distance, speed, processing speed, anti-jamming capability, but as its narrow detection beam, it can search only within a smaller range [4]. In 2004 Chrysler PROTECTOR project [5],

Fig. 40.1 Installation rendering of PEHS



the laser radar detection has been successfully used to distinguish the pedestrian motion estimation, track and classify pedestrian. Compared with the laser radar, the microwave radar is affected smaller by exceptional weather conditions, but it is expensive. Infrared sensor with its outstanding sensing principle behaves well in the dark with excellent detection performance [6]. Each sensor has advantages and disadvantages, but the use of sensor fusion approach in decision-making level can complement each sensor performance and achieve low false-alarm rate and high-robustness performance requirements (Fig. 40.1).

Compared with full map detection sliding window method, this paper presents a method that can greatly reduce the computation time. With the computer visual and lidar joint pedestrian detection, the front obstacle is obtained by the laser radar. After converted into a coordinate system, the pedestrian features are only extracted in the region of interest (ROI). As for the detection system, a more accurate pedestrian and classifier training methods can be used to identify pedestrians. The fusion of two sensors can also improve the accuracy of whether the pedestrian is on the hazardous area and whether bouncing device should be activated (Fig. 40.2).

40.2.2 Control Process

The control system consists of visual modules, laser radar module, sensor data converters, final processing subsystem and actuator (as shown in Fig. 40.3). When the vehicle speed exceeds its set threshold, the system is in normal working condition without causing false detection. When the speed is greater than the set threshold, the system will start to work. Firstly, the obstacles or the pedestrian is located by laser radar to get the depth information of obstacle, through which ROI is determined. Using Haar features and support vector machine (SVM) classifier training methods with high precision extract features and recognize pedestrian in a classifier. Based on the identification strategy, Haar features combined with SVM classifier are used as part of the body's posture to solve problems, with false detection rate of 90 % and the false-alarm rate of 1:10,000 (see [7]). In addition,

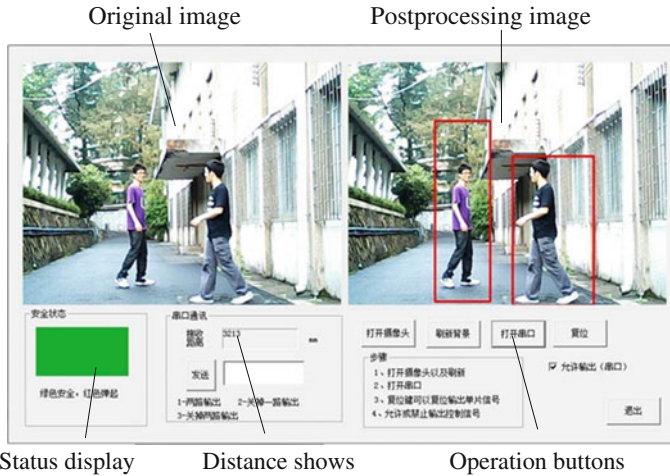


Fig. 40.2 Active pedestrian detection system interface

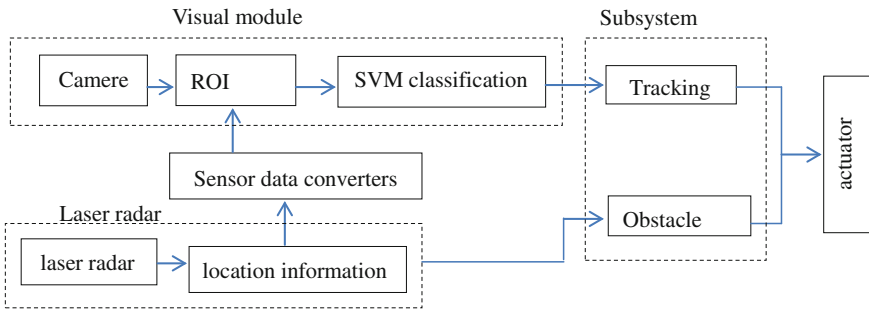


Fig. 40.3 All parts in PEHS

using a camera and laser radar joint decision-making can improve the robustness of the detection system, and reducing the number of false positives. Compared with a single visual inspection and laser radar, the number of false positives can be reduced by 74 and 80.6 % (see [8]).

40.3 Design of Key Parameters of PEHS

40.3.1 Bouncing Time

According to China adult body size standard, the height of 50 % male is 167.8 cm, and female 150.7 cm. At a speed of 40 km/h, the duration time from the contact to the head and the hood automotive collision is 97 ms (the height of pedestrian is 152 cm);

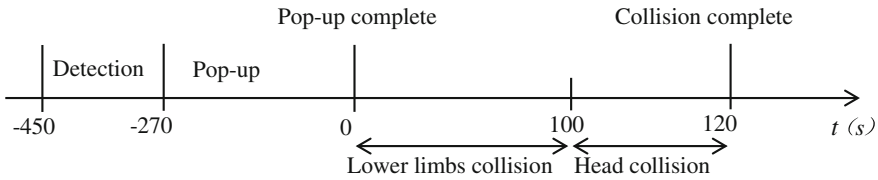


Fig. 40.4 Timeline of each part in PEHS

the time is 140 ms (177 cm) (see [9]). Set the smallest collision time 120 ms. The maximum detection range of laser scanning is 20 m, but reflectance is less than 10 % in 18–20 m. So the ROI area is only 10 m or less, 10 m for warning the driver, 5 m for judgment of dangerous situation and control of actuators. Therefore, the whole time for the sensor detection from pedestrian to pedestrian and vehicle collision lasted $T_0 = 450$ ms. Laser radar response time $T_1 = 30$ ms; trigger mechanism execution time $T_2 = 100$ ms; and the system movement time $T_s = 50$ ms. The system should finish the pop-up process before the beginning of the leg of pedestrian collides with the car. So the bouncing time is $T_p = T_0 - T_1 - T_2 - T_s = 270$ ms. With a certain safety time, set T_p as 100 ms (Fig. 40.4).

40.3.2 Bouncing Height

Bouncing height is the key parameters in PEHS design. It directly related to the pedestrian protection performance of actuator. Small bounce height cannot provide enough space for the deformation of engine hood, and the absorption of collision, while large bouncing height make it difficult to design the device. For HIC less than 1,000, requirements of the height of the head of the child and adult head models to the hood are at least 70 and 50 mm, comparatively (refer to the result given in [10]). This paper will set the rear engine design bouncing height as 100 mm, to ensure that the central and front hood also have sufficient free deformation space.

40.4 Structure Selection and Parameter Design for Pop-up Device

40.4.1 Structure Design

Several common structures in PEHS are double wishbone structure: multi-link structure and the rocker structure, as shown in Fig. 40.5. Compared with the rocker mechanism, the first two bodies are more complicated. They need large space and are hard to layout and difficult to actuate. Considering that in single power source, it

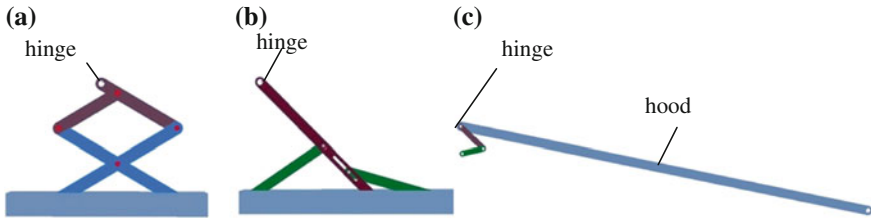


Fig. 40.5 Three common structure of actuator in PEHS. **a** Double wishbone. **b** Multi-link rods. **c** Double rocker

is difficult to drive the actuation within required response time, the spring stiffness values tend to be set large, and the buffer performance deteriorated. Therefore, the final selection is the rocker structure. Actuating force is provided by two springs on both hinge joint, which are applied to solve the problem of the spring stiffness of the one spring-driven, while the dual buffer ability during a collision is achieved.

40.4.2 Parameterized Model of Pop-up Device

After determination of the form of the structure, the parameters can be designed. For ease of calculation, the assembly of device and hood is simplified as four-bar linkage model, as shown in Fig. 40.6. At this time, method and matrix method can be used to establish the parametric model, with plural vector method used in this paper. The length of rocker 1 and a connecting rod 2 is l_1 and l_2 namely. Rocker A rotates about the hinge. Rocker covers 3 to simplify the engine length l_3 and is fixed to the latch D. And define the X axis are positive angle counterclockwise metric.

Time response active bonnet is the primary problem in meeting the bounce height and layout requirements of the premise, the shorter the time bounce hood means reaches a predetermined position in a timely manner before the pedestrian collision with hood, avoiding collisions simultaneously with the additional damage

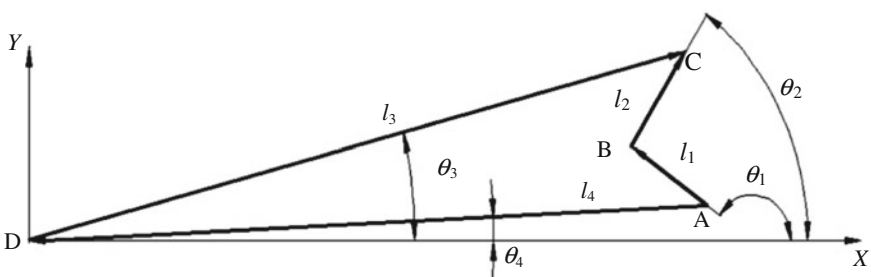


Fig. 40.6 Simplified four-bar linkage

caused by the bounce. This paper will change the speed of the engine hood bounce as the objective function.

In the simplified closed vector polygon of four-bar linkage, the closed vector equation is expressed as the plural form.

$$\vec{l}_1 + \vec{l}_2 = \vec{l}_4 + \vec{l}_3 \tag{40.1}$$

$$l_1 e^{i\theta_1} + l_2 e^{i\theta_2} = l_4 e^{i\theta_4} + l_3 e^{i\theta_3} \tag{40.2}$$

Derivation for t

$$l_1 \omega_1 e^{i\theta_1} + l_2 \omega_2 e^{i\theta_2} = l_3 \omega_3 e^{i\theta_3} \tag{40.3}$$

Using Euler’s formula

$$\begin{cases} l_1 \omega_1 \cos \theta_1 + l_2 \omega_2 \cos \theta_2 = l_3 \omega_3 \cos \theta_3 \\ l_1 \omega_1 \sin \theta_1 + l_2 \omega_2 \sin \theta_2 = l_3 \omega_3 \sin \theta_3 \end{cases} \tag{40.4}$$

The function of angular velocity ω_3 is an objective one.

$$\omega_3 = \omega_1 l_1 \sin(\theta_1 - \theta_2) / [l_3 \sin(\theta_3 - \theta_2)] \tag{40.5}$$

Set the main structure and location parameters: the length of rocker 1 is l_1 connecting rod 2 l_2 and makes abscissa x of hinge A as variable.

$$X = [l_1 \ l_2 \ x]^T \tag{40.6}$$

In this equation, the range of l_1 is [50, 80], the range of l_2 [70, 100] and the abscissa of hinge A [965, 976].

In the design of PEHS, the main limiting factors are arrangement of space. The experimental method is used to determine the length of the rockers 1 and 2. After analysing whether the size and the other parts will interference, the constraint functions can be finally determined. After several tests of the length of the lever in certain space position, the differential length of the rocker and the link is determined to be less than 45 mm.

$$|l_1 - l_2| < 45 \tag{40.7}$$

It is required that bouncing height is more than 100 mm, and the angle between the rocker and the connecting rod should be more than 85°, so that the locking does not occur to provide a buffering when it reaches the highest position. The length of stick and rod should be greater than 145 mm.

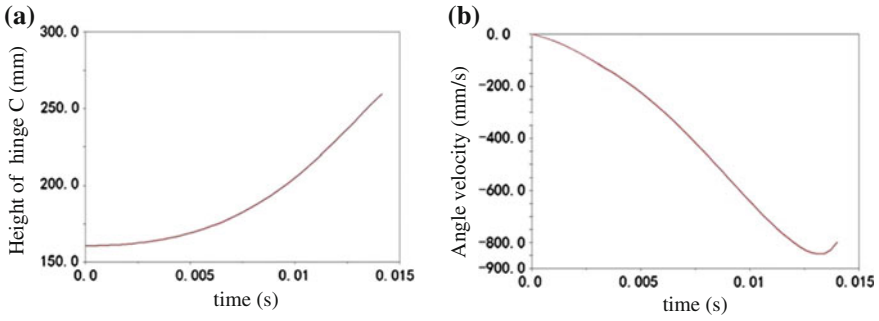


Fig. 40.7 The graph shows the height of hinge C and angle velocity of hood according to the change in time in optimized four-bar linkage model. **a** Graph of the height of hinge C. **b** Graph of angle velocity of hood

$$l_1 + l_2 > 145 \tag{40.8}$$

To sum up, the mathematical model for the four-bar linkage is

$$\begin{cases} X = [l_1 \ l_2 \ x]^T \\ \max(\omega) = \omega_3 = \omega_1 l_1 \sin(\theta_1 - \theta_2) / [l_3 \sin(\theta_3 - \theta_2)] \\ |l_1 - l_2| < 45; \quad l_1 + l_2 > 145 \end{cases} \tag{40.9}$$

The result of optimization in mathematical model shows that when $l_1 = 62$, $l_2 = 85$, $x = 962$, bouncing velocity reaches a climax with average velocity as $-181^\circ/s$. Putting this result as a basic size for designing can achieve the optimal speed in mechanism (Fig. 40.7).

40.5 Establishment of 3-dimensional Model and Dynamic Simulation

40.5.1 Establishment of 3-dimensional Model

The above optimization is used to get the basic dimensions of the 3-D model of the organization of bouncing. During establishing the model, consider the following factors:

1. The driving force of the device provided by a torsion spring and compression spring is applied on the rocker at the same time, and at the time of collision, both springs provide elastic cushion. With torsion spring directly connected to rocker and compression spring fixed inside the sleeve, the force of telescopic rod imposes on the rocker. To facilitate the installation of telescopic rod, rocker arm is designed with a triangular structure. Given in the lowest position device can

be self-locked, the torsional spring at this time should also be in the greatest extent. So under the normal state, the lower side of the triangle is designed to be parallel to the base.

2. Under normal conditions, in order to reduce vibration noise from engine or the road excitation, the noise reduction measures must be set in the actuator of PEHS. Convex is set at the back of the base to restrict connecting rod to move and to provide support for normal closed hood; and the edge of rocker has convex to make rubber and convex as interference fit, which can form the rotation torque in anticlockwise turning around the spindle in connecting rod.
3. The device is equipped with a trigger mechanism, with the function of locking and trigger. This trigger mechanism should have feature such as compact structure, timely response and action quickly. So an electromagnet with a cone pillar is chosen as the trigger mechanism. When electrified, the cone pillar pulls out the lock pin and restores it by the spring when power-off, which guarantees the deformation space of hood.

Considering all the above factors, the 3-D model of pop-up device is established as shown in Fig. 40.8. Its working process is as follows: when device is activated, 9 electric, electromagnetic switches are electrified while the lock pin 7 moves out of its locking hole. Rocker 5 in the effect of torsion spring rotates around to provide greater thrust force through storage sleeve 3. Therefore, the hood begins to pop-up. After pop-up, the device is not locked up and allows the hood the whereabouts of a certain degree, which makes it possible for double buffering effect from spring and deformation of hood (Fig. 40.9).

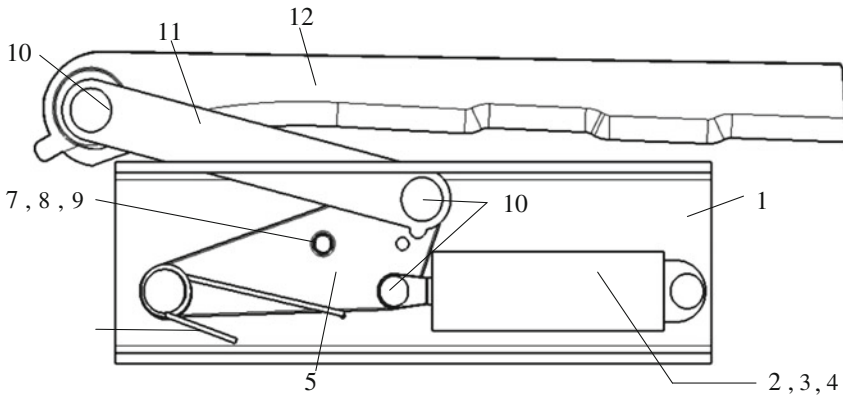


Fig. 40.8 3-D model of the device. 1 Base, 2 expansion rod, 3 telescopic tube, 4 compression spring, 5 rocker, 6 torsion spring, 7 lock pin, 8 electromagnet, 9 rebound spring, 10 melt, 11 connecting rod, 12 hinge

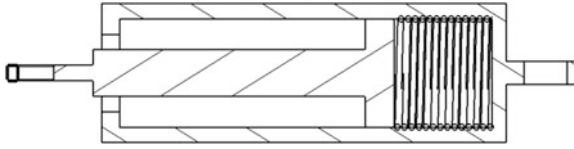


Fig. 40.9 Structural section of an expansion rod

40.5.2 Dynamic Simulation and Determination of Stiffness of Two Springs

The bouncing bodies are assembled with hood in ADAMS (the assembly model is as shown in Fig. 40.10). The model is placed in vertically downwards gravitational field. Add the rotation constraints between rocker, storage sleeve, hood latch and fixed ground, telescopic rod, rocker, connecting rod and hood hinges. The weight of simulation model is defined as 15.8 kg, and its material is steel. Taking the spring stiffness parameters into account if the stiffness is low, the driving force is not sufficient enough to pop-up the hood or the bouncing time becomes too long; if the stiffness is high, it is not conducive for assembly and makes the device be in poor performance of buffer. Therefore, the stiffness of the spring is determined in the optimized dynamic simulation. The size of the space constrains the pre-rotation angle to be 60° and the pre-compression stroke to be 30 mm. Making the compression spring stiffness to be constant, while changing the torsion spring stiffness, analyses the torsion spring stiffness variation. After determining the stiffness of the torsion spring, analyse the variation of stiffness when changing the stiffness of compression spring stiffness.

Figures 40.11 and 40.12 reflect the influence of the stiffness on two springs for pop-up performance. According to the figures, the torsion spring stiffness mainly affects hood bouncing start time. When the stiffness is 120 N/mm, the time is approaching to 100 ms; while the compression spring has a greater effect on the bouncing rate. Therefore, taking into account the time and buffer performance, the stiffness of the torsion spring is selected as 120 N/mm. According to Fig. 40.11, when the stiffness of the compression spring is 120 N/mm, the bouncing time can

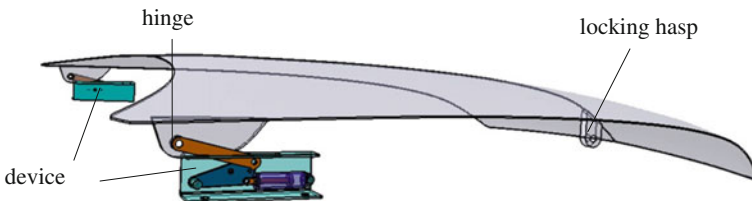


Fig. 40.10 Motion simulation model after assembled

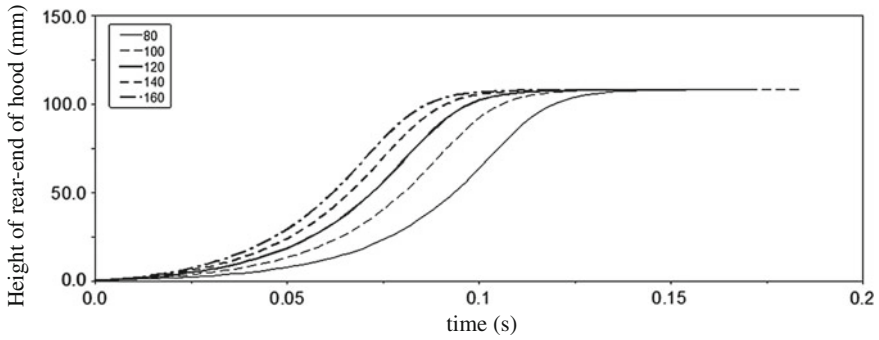


Fig. 40.11 Graph of the height of hood in the change of stiffness of torsion spring

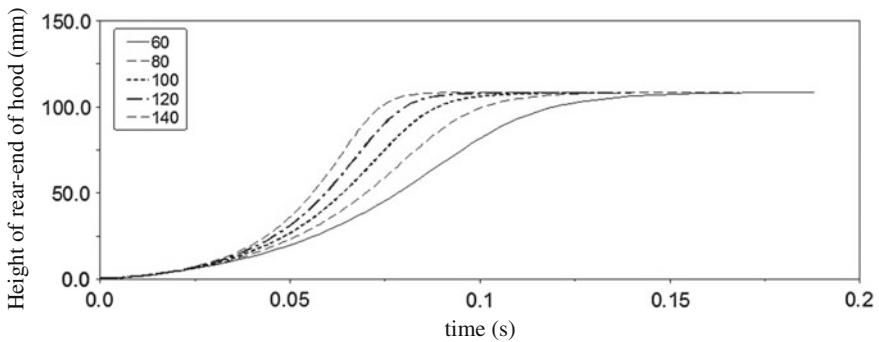


Fig. 40.12 Graph of the height of hood in the change of stiffness of compression spring

meet the requirement of 100 ms, with the time of bouncing process of 97.4 ms and bouncing height of 112.6 mm (larger than the designed height of 100 mm). Therefore, the stiffness of both the compression spring and torsion spring is determined to 120 N/mm.

40.6 Prototype Experiments and Performance Evaluation of PEHS

40.6.1 Actual Pop-up Experiment

An experimental platform is established to install engine hood and PEHS. When a pedestrian enters the default danger zone, the system quickly triggers the hood to pop-up. The whole process is shot by a video device (video screenshot as shown in Fig. 40.13). The analysis shows that the hood reaches its highest position in the 90 ms and begins to fall. The vertical height of the hood hinge from the stable



Fig. 40.13 Pop-up experiment process. a 0 ms. b 40 ms. c 90 ms

position to its initial position is 105.3 mm, which means the bouncing height and time reach the designed requirements. The experimental results show a great similarity with the simulation results in every point-in-time, which verify the effectiveness and performance of the actual performance of the bouncing body simulation model.

40.6.2 Protection Performance Evaluation of PEHS

The collision point is selected according to the following scheme. One is the comparison between two states (e.g. 1st, 7th and 2nd, 6th points), and the other is comparison between experimental study and simulation study (all the selected test point has a corresponding impact simulation for comparison). All the points must be selected equispacedly and dispersedly in the hood to reduce the deviation caused by the hood deformation between two collision points. The result of the experiment is as shown in Fig. 40.14.

In two cases, the results of head injury valued as HIC are given in Table 40.1. The hood pop, the HIC value of each point of collision head injury, has a great

Fig. 40.14 The layout of the collision point

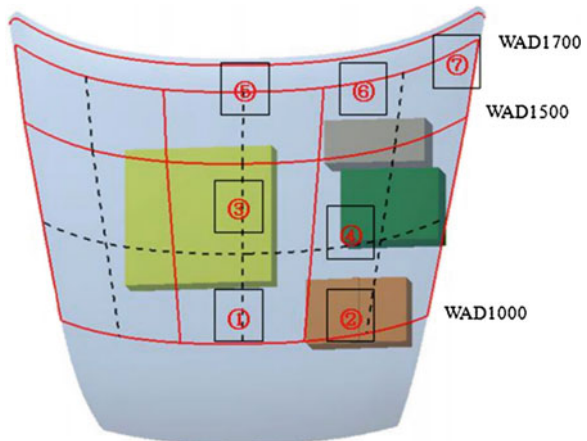
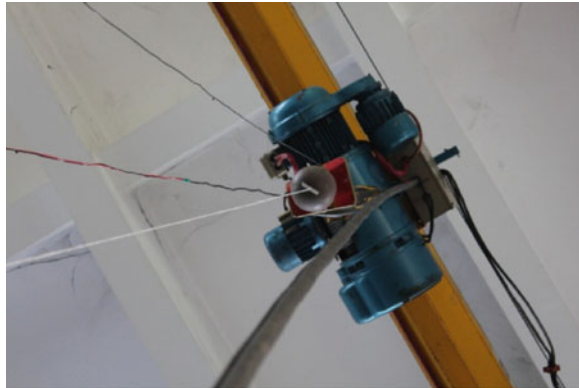


Table 40.1 Comparison of HIC value between state of pop-up and non-pop-up

	1	2	3	4	5	6	7	Average
Pop-up	434.3	442.2	308.1	349.4	304.8	357.1	380.0	368.0
Non-pop-up	1010.0	1538.0	474.2	1054.0	650.2	870.2	2065.0	1094.5
Reduction (%)	57.0	71.2	35.0	66.9	53.1	59.0	81.6	60.5
Text result	403.9	520.3	315.4	281.0	252.6	334.1	347.2	350.6
Deviation(%)	-7.0	17.7	2.4	-19.6	-17.1	-6.4	-8.6	-5.5

Fig. 40.15 Impact test for protection performance



decline with the most evident decrease of 81.6 % in engine hood hinge. Results show that PEHS significantly improves pedestrian protection performance of the hood. HIC values at all points are below the collision point 1,000. The average of all points is only 368.0, decreased by 60.5 %, compared with the non-bouncing state.

The mean value is 368.0 in simulation and 350.6 in experiment, the deviation of which is 5.5 %. Considering the influence in the transient response of acceleration and impact resistance, the deviation is still in the acceptable range. The simulation and experiment prove that PEHS has good performance in pedestrian head protection (Fig. 40.15).

40.7 Conclusions

1. The study of this paper has designed a PEHS with dual elastic buffer, including control system and pop-up actuator. In comparison with the performance of different sensors, the use of camera and laser radar as sensor proves to be effective. With the help of the distance information from the laser radar, the ROI area is determined to detect the pedestrian, through the fusion of target identification method of Haar pedestrian characteristics and the SVM classifier method. Joint decision-making by pedestrian image information and the

distance information can effectively meet the requirement of real-time performance and robustness of detection system.

2. Based on mechanism design theory, design and develop a reusable PEHS that can provide dual elastic actuation and dual elastic support. Plural vector method is used to establish the mathematical model of optimized design. Determine the basic dimension under the optimal parameters of the bouncing rate. 3-D model of PEHS is established to simulate the kinematics performance to determine the spring stiffness for goal of bouncing time requirements. Build experiment platform to carry out the actual pop-up experiment and head impact experiment, the results of which prove that the design meet the design requirements.
3. Compared with gas generator device, the device designed in this paper has better using repeatability and elastic buffer performance and can reduce the size and stiffness of the spring relatively. This device can be used as a reference for development of PHES, which is of important in practical application value to reduce pedestrian head injuries and protect the pedestrian safety.

References

1. Wang H-Y, Zhu Y-M, Wu et al (2010) Design of active hood-lifting device for pedestrian protection. *J Transp Sci Eng (Chinese)* 26(04):55–59
2. Barnes BM, Brei DE (2008) Shape memory alloy resettable spring lift for pedestrian protection. *Proc of 2008 SPIE*, 693005–693005
3. Shashua A, Gdalyahu Y, Hayun G. (2004) Pedestrian detection for driving assistance systems: single-frame classification and system level performance. In: *Proceedings of IEEE intelligent vehicles symposium*. Parma, Italy, 1–6
4. Qian HJ (2010) *Research on pedestrian detection for traffic safety*, Shanghai, Jiao Tong University (Chinese)
5. Gavrilu DM, Giebel J, Munder S (2004) Vision-based pedestrian detection: the protector system. In: *Proceedings of IEEE intelligent vehicles symposium*. Parma, Italy. 13–18
6. Chen H (2006) *Hausdorff distance-based template matching for pedestrian detection*. Tsinghua University, (Chinese)
7. Mohan A, Papageorgiou C, Poggio T (2001) Example-based object detection in images by components. *IEEE Trans Pattern Anal Mach Intell* 23(4):349–361
8. Cui et al (2007) Multi-modal tracking of people using laser scanners and video camera. *Image Vis Comput*. doi:[10.1016/j.imavis.2007.05.005](https://doi.org/10.1016/j.imavis.2007.05.005)
9. Svoboda J, Vorlicek P, Vojtisek J (2005) Pedestrian protection-influence of bonnet design. *The 10th EAEC European automotive congress*, Belgrade
10. Zellmer H, Glaeser K-P (1994) The EEVC WG10 head impact test procedure in practical use. *14th International technical conference on the enhanced safety of vehicles (ESV)*, Paper No. 94-S7-O-03

Chapter 41

Estimation of Vehicle Sideslip Angle with Adaptation to Road Bank Angle and Roll Angle

Jie Ling, Hui Chen and Fan Xu

Abstract The road bank angle and roll angle have direct influence on the vehicle's lateral motion. As a result, the accuracy of sideslip angle estimation can be improved through estimation of road bank angle and roll angle. In this paper, estimation of vehicle sideslip angle with adaptation to road bank angle and roll angle is achieved through a proposed Kalman filter at low cost based on the combination of dynamic model and kinematic model, which is developed from a three freedom model of lateral, yaw, and roll motion. Promising is the simulation results displayed in this paper.

Keywords Sideslip angle · Road bank angle · Roll angle · Kalman filter · Low-cost sensors

41.1 Introduction

Nowadays with automobile wide spreading and the higher level of vehicle use, requirements with respect to safety and comfort play increasingly significant role in auto design from the view of both customers and hence designers. As results of this fact, active safety and driving assistance systems, such as ESP, ABS, are developed. In order to ensure the operation of these systems, unignorable is the necessity of obtaining the sideslip angle accurately and instantaneously [1]. However, the sideslip angle cannot be measured directly by a common sensor, and hence, its estimation is always a prior yet difficult problem in the field of vehicle state

Research supported by National Basic Research Program of China (973 Program, No. 2011CB711200)

J. Ling · H. Chen (✉) · F. Xu
School of Automotive Studies and Clean Energy Automotive Engineering Center,
Tongji University, 201804 Shanghai, China
e-mail: hui-chen@tongji.edu.cn

© Springer-Verlag Berlin Heidelberg 2015
Society of Automotive Engineers of China (SAE-China) (ed.),
Proceedings of SAE-China Congress 2014: Selected Papers,
Lecture Notes in Electrical Engineering 328, DOI 10.1007/978-3-662-45043-7_41

estimation. Furthermore, for accurately obtaining of the sideslip angle, essential are the parameters [2] and road information, among which the road bank angle [3] and the roll angle has the direct influence on the automotive lateral motion. The lateral acceleration sensor, specifically, measures the derivative of lateral velocity and the product of longitudinal velocity, and yaw rate and the acceleration caused by the road bank angle and roll angle. Furthermore, the road bank angle and roll angle cannot be directly measured with common sensors.

Some studies on the sideslip angle estimation with adaptation to road bank angle and roll angle have been undertaken. Wenzel [4] estimates the roll angle using dynamic model for the automotive roll motion, improving the accuracy of the sideslip angle while the road bank angle has not been considered. The unknown input observer [5] is used to estimate the vehicle state and road bank angle while the roll angle is roughly estimated by a static equation [6]. Tseng [7] and Mammari et al. [8] estimate sideslip angle only with consideration to road bank angle whereas the Refs. [9–11] estimate sideslip angle with adaptation to road bank angle and roll angle. In the paper, [9–11] the Ref. [9] adds extra sensor to achieve this goal. Method of the Refs. [10, 11] gets the result without adding sensors, but the ability of noise filtering performance has not been specified.

In this paper, an algorithm based on Kalman filter is designed to improve the accuracy of estimation of sideslip angle based on instantaneous observation of road bank angle and roll angle with low-cost sensors which can be found in cars equipped with an ESP system. The value of road bank angle and the roll angle can also be used to the rollover prevention system and prevent unnecessary activation of ESP. The remainder of this paper is organized as follows: Vehicle and tyre model are built in Sect. 41.2, then the algorithm based on the Kalman filter is proposed; the performance of the algorithm is validated using simulation in Sect. 41.4; finally, the conclusion is presented.

41.2 Vehicle and Tyre Model

41.2.1 *The Relationship Among the Three Lateral Accelerations*

The value of actual lateral acceleration, the acceleration caused by the wheel force, and the acceleration measured by sensor is different; their relationship is described in Eq. (41.2.1)

$$\begin{aligned} a_y &= a_{yr} - g\psi \\ a_{yr} &= a_{ym} - g\phi \\ a_y &= a_{ym} - g\phi - g\psi \end{aligned} \tag{41.2.1}$$

where ψ is the road bank angle, ϕ is the roll angle, and g represents gravity acceleration.

41.2.2 Vehicle Lateral Model

Given the research content of the paper, a three degree of freedom double-track model is chosen to express the lateral, yaw, and roll motion. Here, the double-track means considering lateral weight transfer on the normal load of the tyres. A typical layout is shown in Fig. 41.1. In this paper, it does not involve the research on longitudinal velocity and the inclination angle is assumed to be 0°. Equation (41.2.2) describes the lateral kinematic model.

$$\dot{v}_y = -v_x\omega + a_y. \tag{41.2.2}$$

The actual acceleration a_y is given by

$$a_y = a_{ym} - g\psi - g\phi$$

where v_y is lateral velocity, v_x is longitudinal velocity, and ω is yaw rate.

Equation (41.2.3) describes the lateral dynamic model.

$$a_{ym} = a_{yr} + g\phi. \tag{41.2.3}$$

The acceleration a_{yr} caused by lateral force is given as follows:

$$a_{yr} = \frac{F_{yf} \cos \delta + F_{yr}}{m}, F_{yf} = F_{yf}^l + F_{yf}^r, F_{yr} = F_{yr}^l + F_{yr}^r$$

where F_{yf} is lateral force of front axle, F_{yr} is lateral force of rear axle, F_{yf}^l is lateral force of left front wheel, F_{yf}^r is lateral force of right front wheel, F_{yr}^l is lateral force of left rear wheel, and F_{yr}^r is lateral force of right rear wheel.

In this paper, we assume that the road bank angle varies slowly compared with the dynamics of the system to be modeled as constants in Eq. (41.2.4).

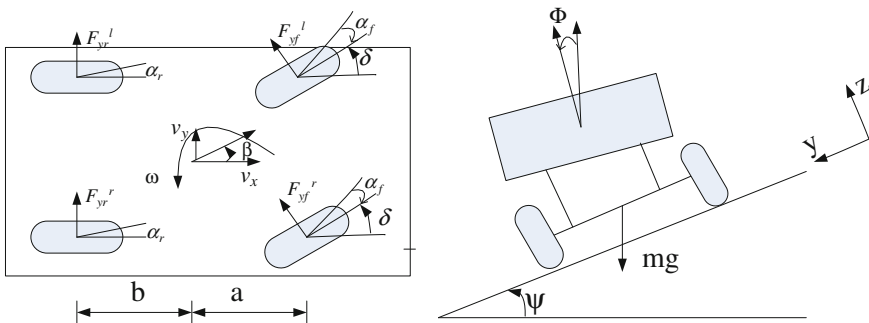


Fig. 41.1 Three degree of freedom model

$$\dot{\psi} = 0. \quad (41.2.4)$$

Roll motion [4] can be obtained from

$$\ddot{\phi} = \frac{1}{J_{sx}}(m_s h_s a_y + \phi(m_s g h_s - K) + B_\phi \dot{\phi}) \quad (41.2.5)$$

where m_s is sprung mass, h_s is height of gravity center of sprung mass, J_{sx} is the moment of inertia around the longitudinal axis, K is roll stiffness, and B_ϕ represents roll damping.

41.2.3 Tyre Model

The Magic Formula tyre model is chosen. Its basic formation is as follows:

$$F_y = D \sin(\text{Carctan}(B(1 - E)\alpha + E \arctan(B\alpha))) \quad (41.2.6)$$

where B, C, D, E is tyre model parameter, which is related to vertical load of tyres, α is tyre slip angle, and F_y is lateral force.

Taking into consideration lateral load transfer, the tyre vertical load is given by

$$F_{z,fl} = \frac{mgb}{2(a+b)} - \frac{k_{rs}}{k_{rs}+1} \cdot \frac{m a_y h_g}{B_f}, \quad F_{z,fr} = \frac{mgb}{2(a+b)} + \frac{k_{rs}}{k_{rs}+1} \cdot \frac{m a_y h_g}{B_f}$$

$$F_{z,rl} = \frac{mga}{2(a+b)} - \frac{k_{rs}}{k_{rs}+1} \cdot \frac{m a_y h_g}{B_r}, \quad F_{z,rr} = \frac{mga}{2(a+b)} + \frac{k_{rs}}{k_{rs}+1} \cdot \frac{m a_y h_g}{B_r}$$

where m is vehicle mass, K_{rs} is ratio of roll stiffness of front axle to roll stiffness of rear axle, a, b is distance from center of gravity to front/rear axle, B_f, B_r is wheelbase of front/rear axle, and h_g represents the height of center of gravity.

Sideslip angle and tyre slip angles are defined by

$$\beta = \arctan \frac{v_y}{v_x}, \quad \alpha_f = \arctan \left(\frac{v_y + a\omega}{v_x} - \delta \right), \quad \alpha_r = \arctan \left(\frac{v_y - b\omega}{v_x} \right).$$

41.3 Kalman Filter Design

A Kalman filter is designed to estimate the lateral velocity, road bank angle, and roll angle. The inputs of observer are the steering angle, yaw rate, and lateral acceleration. The Kalman filter based only on dynamic model cannot reflect the influence

of road bank angle on the lateral velocity because the road bank angle is assumed to be changing at a slow rate in this paper. As a result, a Kalman filter based on the combination of dynamic and kinematic model is designed to solve this problem. The state and measure equations are as follows. Using the Euler formula, according to the Eqs. (41.2.2), (41.2.3), (41.2.4) and (41.2.5), the Eq. (41.3.1) describes the discrete time version of state-space equation:

$$\begin{aligned} x_k &= x_{k-1} + Ts * \dot{x}_{k-1} + w_{k-1} = f(x_{k-1}) + w_{k-1} \\ y_k &= h(x_k, u_k) + v_k \end{aligned} \quad (41.3.1)$$

where,

$$x = \begin{bmatrix} v_y \\ \psi \\ \phi \\ \dot{\phi} \end{bmatrix}, \dot{x} = \begin{bmatrix} -v_x w + a_{ym} - g\psi - g\phi \\ 0 \\ \dot{\phi} \\ \frac{m_s h_s}{J_{sx}} a_y + \frac{(m_s g h_s - K)}{J_{sx}} \phi + \frac{B_\phi}{J_{sx}} \dot{\phi} \end{bmatrix}$$

$$y = [a_{ym}], h(x_k, u_k) = [a_{yr} + g\phi] = \left[\frac{F_{yf} \cos \delta + F_{yr}}{m} + g\phi \right]$$

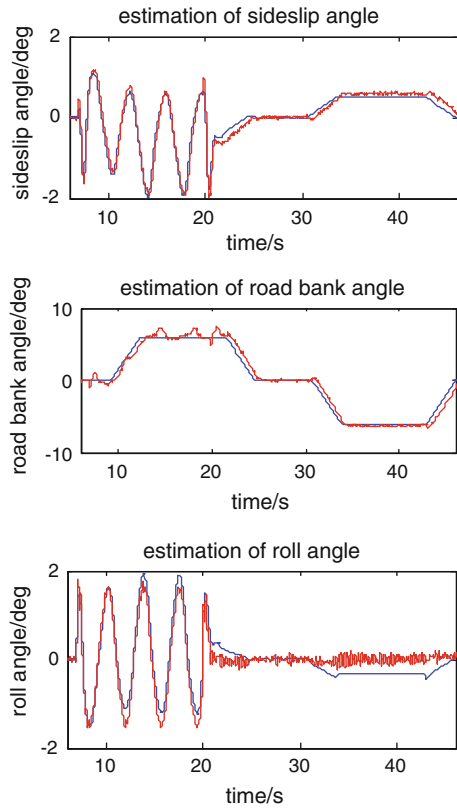
The random signals w_{k-1} , v_k represent the process noise and measurement noise, respectively. It is assumed that they are white noise independent of each other and conform to normal distribution, and their covariance matrix is Q and R, respectively.

The working process of Extended Kalman filter is given in the Ref. [12]. The covariance matrix of measurement noise means the noise of the sensor which can be obtained from off-line test. And the process noise can be considered as the difference between the estimation model and the actual model. The process noise is difficult to determine because we cannot directly obtain the process state. Therefore, this value is manually selected to be a reasonable one in this paper.

41.4 Simulations

Simulations were performed in MATLAB/Simulink environment with TESIS veDYNA to test the effectiveness of the proposed algorithm. During the test, the inclination angle is set to 0° and the peak road friction is set to 1. Since this paper focuses on lateral velocity estimation, the estimation of longitudinal velocity is not included. In this paper it is assumed that the longitudinal velocity is known.

Fig. 41.2 Slalom maneuver



In this section, slalom and double lane change maneuvers will be involved. Figures 41.2 and 41.3 show the simulation results of road bank angle and roll angle along with sideslip angle with adaptation to these two parameters. Red line represents the estimated values and blue line represents reference values in Figs. 41.2 and 41.3.

Simulation result shows that the proposed algorithm can accurately estimate the sideslip angle, road bank angle, and roll angle. The graph of roll angle estimation shows that at 33–43 s, the estimation is not very accurate which is due to the ignorance of roll angle caused by the existing of road bank angle.

The proposed algorithm was compared with the algorithm which did not take the road bank angle and road bank angle into account. The maximum absolute error of sideslip angle and its mean squared error (MSE) are given in Table 41.1. It indicates that compared with the algorithm without adaptation, the proposed algorithm not only obtained the value of road bank angle and roll angle, but also improved the accuracy of sideslip angle estimation in slalom and double lane change maneuvers.

Fig. 41.3 Double lane change maneuver

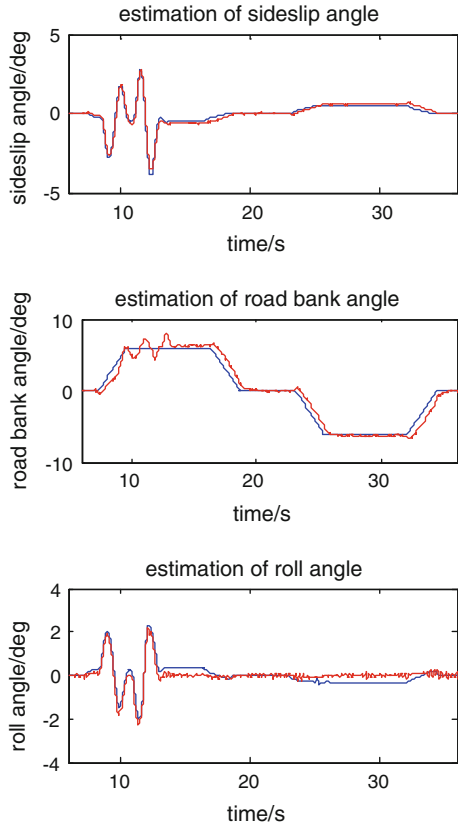


Table 41.1 Maximum absolute error and mean squared error of sideslip angle estimation

	Without adaptation		With adaptation	
	Max. absolute error	MSE (6–26 s)	Max. absolute error	MSE (6–26 s)
Slalom	0.8010	0.0821	0.3969	0.0240
Double lane change	0.9407	0.0592	0.4424	0.0218

41.5 Conclusions

Based on the combination of dynamics and kinematic models, a sideslip angle estimator with adaptation to road bank angle and roll angle at low cost is proposed. The performance is verified by the comparison between proposed algorithm and the one without adaptation. The simulation results show that the maximum absolute error of sideslip angle estimation is about two times reduced and the MSE of

sideslip angle estimation is about three times decreased. In the future, the longitudinal velocity estimation and adaptation to more parameters combined with road bank angle will be investigated.

References

1. Van Zanten AT (2000) Bosch ESP systems: 5 years of experience. Foot and Ankle
2. Xu F et al (2013) Estimation of vehicle sideslip with adaptation to tyre cornering stiffness and road friction coefficient uncertainty. SAE-China congress, Beijing
3. Ungoren AY, Peng H, Tseng HE (2002) Experimental verification of lateral speed estimation methods. *Int J Veh Auton Syst* 1(1):126–144
4. Wenzel TA, Burnham KJ, Blundell MV et al (2006) Dual extended Kalman filter for vehicle state and parameter estimation. *Veh Syst Dyn* 44(2):153–171
5. Grip HF, Imsland L, Johansen TA et al (2009) Vehicle sideslip estimation. *Control Syst IEEE* 29(5):36–52
6. Suissa A, Zomotor Z, Ttiger FB (1994) Method for determining variables characterizing vehicle handling. US
7. Tseng HE (2001) Dynamic estimation of road bank angle. *Veh Syst Dyn* 36(4–5):307–328
8. Mammari S, Glaser S, Netto M (2006) Vehicle lateral dynamics estimation using unknown input proportional-integral observers. American Control Conference
9. Ryu J, Gerdes JC (2004) Estimation of vehicle roll and road bank angle. American Control Conference 3:2110–2115
10. Kim J, Lee H, Choi S (2012) A robust road bank angle estimation based on a proportional-integral H filter. *Proc Inst Mech Eng, Part D: J Automobile Eng* 226(6):779–794
11. Sebsadji Y, Glaser S, Mammari S et al (2008) Vehicle roll and road bank angles estimation. In: *Proceedings of 17th IFAC World Congress*
12. Simon D (2006) *Optimal state estimation: Kalman, H infinity, and nonlinear approaches*. Wiley, New York

Chapter 42

Vehicle Guiding System Through Image Processing in Crash and Misuse Tests

Eloi Boix, Adrià Ferrer, Sandra Fernandez and Xavier Sellart

Abstract As newer active and passive safety systems are developed, new testing requirements have appeared along with constraints and requirements that must be overcome while at the same time maintaining higher safety and quality standards. This paper presents a modular system that makes it possible to automate hazardous tests for drivers by using path following by means of a low-cost camera or defined GPS trajectories. This project provides a solution to tests where the driver cannot be inside the vehicle due to the inherent risk and complex methodology that must be followed. The developed system, which can be installed in any vehicle, is mounted on a small pickup truck, which is used as a test vehicle. Once this control architecture has been implemented, installed and tuned, the resulting steering manoeuvring allows tests required for recently developed and future safety systems to be performed. The experimental results show that the combination of artificial vision algorithms and steering wheel controller are capable of managing the lateral guidance of a vehicle as a human driver would do.

Keywords Testing · Autonomous driving · Safety · Electronics · Rollover

E. Boix (✉) · A. Ferrer (✉) · S. Fernandez (✉) · X. Sellart (✉)
Applus+ IDIADA, Tarragona, Spain
e-mail: eboix@idiada.com

A. Ferrer
e-mail: adria.ferrer@idiada.com

S. Fernandez
e-mail: sandra.fernandez@idiada.com

X. Sellart
e-mail: xavier.sellart@idiada.com

42.1 Introduction

Safety requirements in European vehicles have increased dramatically over recent decades. The introduction of safety evaluation and awareness programmes such as Euro NCAP have contributed to the fact that safety is one of the most important criteria when acquiring a new vehicle. The success of Euro NCAP is reflected in its ability to stimulate the interest of vehicle manufacturers for safety [7]. This interest led to the development of new and innovative safety systems.

In the field of passive safety, Applus+ IDIADA perform global development projects for all types of vehicles. These projects include design, computer simulation, testing, integration of restraint systems and assessment and improvement of pedestrian and cyclist protection systems.

The main tool used to perform most of these tests is a vehicle guidance system which consists of a steel wire embedded in the floor and a truck which makes the vehicle follow a straight path. It is a very robust system in tests in which the vehicle follows a straight path resulting in a reliable system which allows testing with a high level of repeatability.

However, new and innovative systems occasionally require new test configurations and currently, these kinds of tests are carried out by specific methods which are not cost effective and can even affect the accuracy of the results. These methods solve a very limited range of test configurations, so that in some of the tests remains no solution because the trajectory that the vehicle must follow is not straight or the test configuration is extremely complex.

A new vehicle guiding system based on the movement of a pulley system which rotates the vehicle steering wheel is designed and developed to provide a solution for these tests. The system is based on the concept of autonomous driving for particular configurations, but can be implemented in any vehicle without interfering with the performance in any way. The particular requirements are the following:

- High reliability and robustness: to guarantee repeatability and durability in crashes.
- In-vehicle system: to avoid the modification of the structure and without interfering in the mass distribution.
- Electrically compatible: no electrical interference should be introduced in the vehicle.

In order to fully comply with these requirements, an in-loop processing of the images filmed by a camera enables the vehicle to follow a path marked on the floor. The steering wheel is rotated by an electric motor which receives the input of the electronic software.

The vehicle guiding system allows the tested vehicle to follow any path, which makes it a perfect tool for performing different kinds of crash test, especially car-to-car crash tests. Furthermore, the system transmission allows high-speed predefined rotation of the steering wheel, so dynamic and rollover test series can be carried out with high levels of accuracy, repeatability and safety.

The main aim of designing and developing a vehicle guidance system is to obtain a device which permits performing both complete vehicle crash and misuse tests without the vehicle being physically driven by a person. These tests are specifically as follows:

- High and very high containment tests according to EN 1317-1,2:
 - Test description: the vehicle (truck or coach) is launched against a road barrier at a certain angle
 - Impact angle: 8°, 15° or 20°
 - Speed angle: 70 or 80 km/h
 - Vehicle weight: 10,000, 13,000, 16,000, 30,000 or 38,000 kg (Fig. 42.1).
- Car-to-car tests:
 - Test description: two vehicles impact each other in order to reproduce a known accident scenario
 - Impact speed: from 30 to 90 km/h
 - Impact angle: from 0 to 90°
 - Path: any path
 - Vehicles involved: passenger vehicles, trucks or coaches (Fig. 42.2).
- Rollover tests:
 - Test description: a vehicle is launched into an embankment of 30° or 40° tilt in order to overturn the vehicle
 - Test speed: from 16 to 22 km/h
 - Vehicle embankment angle: 15°
 - Path: straight path. When the vehicle reaches the embankment, the steering wheel has to rotate at maximum speed to the highest side.
 - Vehicle involved: passenger cars (Fig. 42.3).



Fig. 42.1 Test according to EN 1317-1,2



Fig. 42.2 Car-to-car test

Fig. 42.3 Rollover test



- Misuse tests:

- Test description: the vehicle is launched against a small obstacle in order to reproduce slight accidents that do not cause damage or minor damage to either the vehicle or occupants
- Test speed: from 40 to 100 km/h
- Test angle: 0°
- Path: straight path with the possibility of performing a big radius curve at the end of the path
- Vehicle involved: passenger vehicles (Fig. 42.4).

Fig. 42.4 Misuse test

All these tests can now be performed with the automatic steering control architecture, based on a combination of artificial vision and steering wheel control that was designed and is described in this paper.

42.2 Architecture

A modular and scalable architecture [4–6] is developed in order to be able to adapt the system composition according to the test that needs to be performed. For example, in some tests, the input data needed for the artificial intelligence control and guidance system may be acquired from low-cost cameras or from GPS positions. Low-cost, off-the-shelf cameras are very appropriate for those tests that involve a crash as they provide sufficient accuracy, and since the equipment will probably be damaged or destroyed, the resulting financial loss will be lower.

Two modules are designed in order to develop the control architecture that manages the steering of the vehicle.

The detection and processing module is in charge of acquiring the image of the test track and comparing it with the reference trajectory to generate a target steering wheel turning command. It includes the artificial intelligence unit (AIU) as an embedded computer where the vision algorithm is performed.

The motor control module is in charge of the communication with the detection and processing module and performing some additional functions such as high-voltage batteries monitoring (due to safety requirements).

It includes the guidance control unit (GCU), the driver, the encoder and the DC motor. This module is responsible for mechanizing the movement of the electric motor to specific positions which guarantee the angular turn of the steering wheel to be able to change the direction of the vehicle.

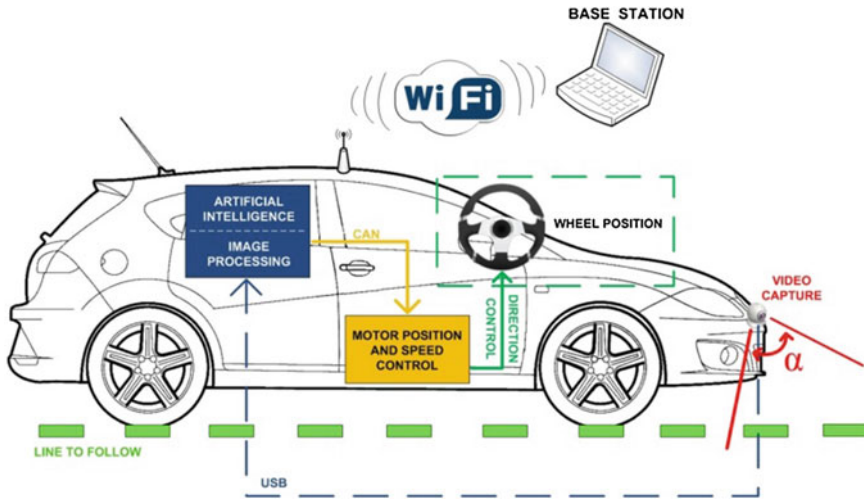


Fig. 42.5 System diagram

Figure 42.5 also shows the expansion of the WiFi module, which will be done as the next step of the project. This module allows the system to be controlled remotely by a base station where a user interface is running. The user interface will allow the engineers to define the test and configure the parameters of the system that need to be checked by an operator, such as speed of the vehicle in the probe, kind of test (misuse, fatigue, etc.), and start button.

Also, in the near future, this system will be able to control the acceleration and brake pedals of automatic vehicles, by having power over the potentiometers regulated by the pedals.

42.2.1 Artificial Intelligence Unit (AIU)

It consists of an embedded computer with CAN module which works as the thinking unit of the system as it processes the image and generates the new direction data and turning speed of the steering wheel. It is able to communicate by CAN with the GCU to send the trajectory parameters of the vehicle. The image processing is based on identifying the colour (colour tracking technique) and shapes (shapes tracking technique) to be able to determine the rectangular figure of the line on the floor by using a trapezoidal conversion (because of the perspective in the image) detecting the rectangular forms in known XY coordinates.

42.2.2 Guidance Control Unit (GCU)

Printed circuit board (PCB) is designed to facilitate the communication and data exchange between the AIU and the motor driver. It allows sending the exact position of the motor through the serial communication with the driver, which is capable of reading the encoder information attached to the motor. This electronic board also allows the connection of new signals originated by sensors making this project scalable to different applications depending on the sensors or devices which get connected: GPS, distance, speed, etc.

42.2.3 Driver

It is a specialized driver which deals directly with the encoder to fix specific positions on the electric motor. This driver uses the encoder signal as a feedback loop to verify whether the motor is in the desired position or not. The driver powers the motor until it reaches the required position and stops and puts the revolutions to 0 rpm when it reaches the position. It has its own software which allows different parameters of the motor, such as current, speed response, and turn speed, to be known.

42.2.4 Encoder

Incremental optical encoder is attached to the motor which sends the signal position to the driver. It can reach 6,000 rpm and has a resolution of 500 imp/turn.

All the electronic control units (AIU, GCU and driver) have been inserted into a shield box to perform the crash tests. Therefore, this project can be implemented to any required vehicle. In the designed box, a refrigeration system has been included by installing two fans.

From this shield box, the internal devices are accessible through the external connectors, which are designed to be flexible and can be adapted to different requirements. This provides mobility to the prototype, as it enlarges the functionalities and the implementation possibilities into multiplatform vehicles.

Figure 42.6 shows the flow data between the different devices of this project.

The AIU is an embedded computer which runs with Linux (Ubuntu) operating system and has auxiliary ports to connect external peripherals which allow its programming and offline configuration. It receives as a main feedback the captured images from the webcam in real time. Once this information is in the AIU, through the designed line detection algorithm and image processing, it is able to send the position and desired speed of the DC motor to the next system block, the GCU.

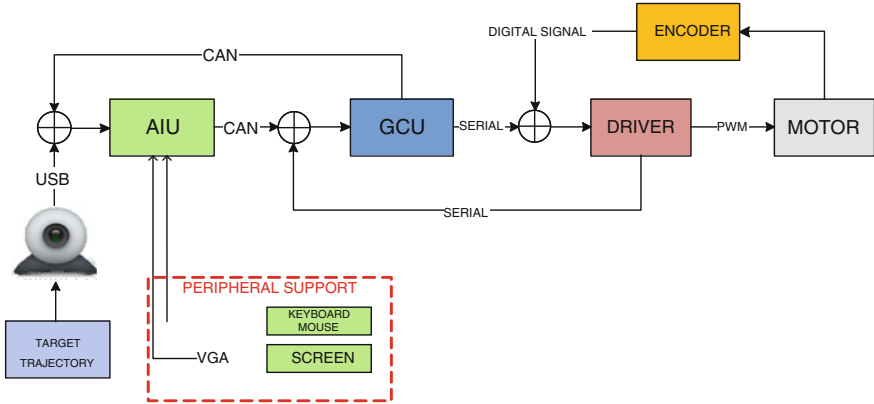


Fig. 42.6 Data flow chart

The AIU communicates with the GCU by using a CAN communication protocol. In particular, it sends a message with the 0x300 identifier with the motor desired speed and position. This information is sent in one data frame of 8 bytes size by using the first 4 bytes for the position and the next ones for the speed data.

After receiving the data frame from the AIU, the GCU answers with an acknowledge message indicating if the data retrieval was successful. Also, it provides the AIU the information about the real degrees turned by the DC motor and the coupled steering wheel, by using an internal calculation of the relation between the rotations of the motor and the rotations of the steering wheel.

Once the GCU has successfully received the position and speed data, it transmits this information to the motor driver by using RS232 protocol for converting the data. The driver answers with an acknowledgement message and provides the information about the motor current consumption and the response time of the desired position and speed.

The driver uses the digital feedback signal which is sent by the encoder to know whether the motor has arrived or not at the desired position. The driver uses an encoder as a feedback to verify if the motor has arrived to the desired position. The encoder used has a resolution of 500 impulses for each rpm. The signals A and B give the position and turn direction of the motor, while the Z signal generates 500 impulses each motor spin and allows the speed of the DC motor in revolutions per minute (rpm) to be determined.

42.2.5 Image Processing Architecture

The code implemented in the AIU is based on the image processing [4, 10], communicating by CAN with the GCU to send the trajectory information and also

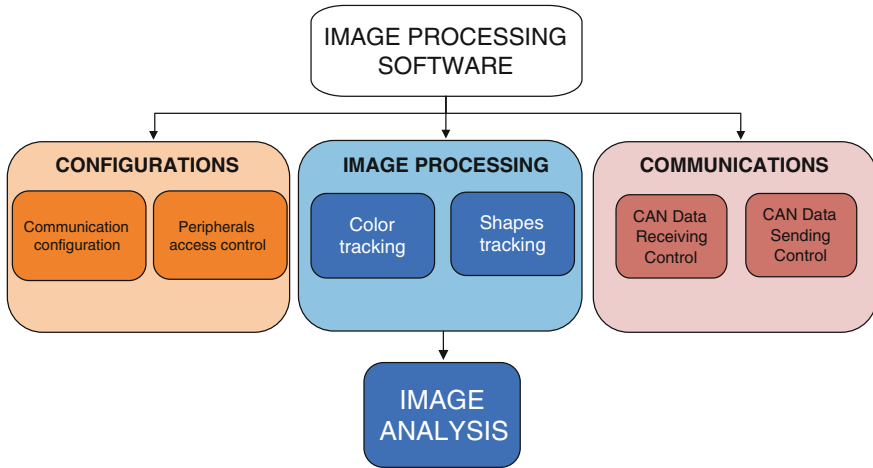


Fig. 42.7 Image processing architecture

receive parameters of the motor. This program accesses the camera and analyses each capture in real time.

Figure 42.7 shows the image processing architecture in the AIU.

The objective is to detect red and green trapezoidal rectangles and their position in the captured image [2] to determine the command to be sent to the DC motor and move the steering wheel changing the direction of the vehicle.

Depending on the position of the squares (horizontal or vertical), the command to the motor will be “to continue moving” (green vertical rectangle) or “stop the movement” (red horizontal rectangle) whether the desired configuration has been achieved or not. That means the code is not only able to detect shapes but also their position in the image to calculate the centroid (point which determines the trajectory that has to be followed) and puts it in the top middle of the rectangle.

After calculating the conversion of the centroid into a value able to define the command to be sent, the information of the motor position and speed is sent by CAN protocol to the GCU, which will adapt the data frame and convert it into serial to communicate with the driver.

The code (Forsyth, s.f.) in the AIU is always listening to the CAN channel input to detect whether new messages arrive. These messages may contain acknowledgements of the GCU and also information of the motor.

42.2.6 Steering Wheel Controller

The low-level layer is composed of an electronic control unit (ECU), a driver and a DC motor. The purpose of this module is to receive the turning command from the

high-level layer and to manage the motor attached to the steering wheel to take it to the reference position.

In Fig. 42.8, the complete steering wheel controller [1, 9, 11] is shown.

One of the main requirements of the developed system was that it had to be adjustable to any car keeping the original steering system. For this reason, a pulley system between the motor and the steering wheel was designed and developed. Before the selection of the components, the expected requirements were set. One of the goals of the project was to have a system which allows following different paths with minimum error. Furthermore, the system had to be able to move the steering wheel when the vehicle is stopped and the four wheels of the vehicle are in contact with the ground (due to some testing requirements).

Based on these premises, the time needed to turn the steering wheel from the leftmost position to the rightmost position was determined with a minimum of 5 s (see Eq. 42.1).

$$\frac{3 \text{ revolutions}}{5 \text{ s}} = 36 \text{ rpm} \tag{42.1}$$

Another important parameter with the selection of the motor was the torque, and it was set to 10 nm, which is enough to move the steering wheel of a stopped heavy-duty truck.

According to these requirements, a DCM 3F 30/06 DC motor was selected with a reduction stage of 25:2 to allow a reduction in the angular speed of the motor (from 3,000 to 240 rpm) and increase the nominal torque (from 1.5 to 18 nm). Considering the pulley system (diameter of the driving wheel = 13 cm and driven wheel = 36 cm) and the limitation of the high-voltage batteries to 48 V, the angular

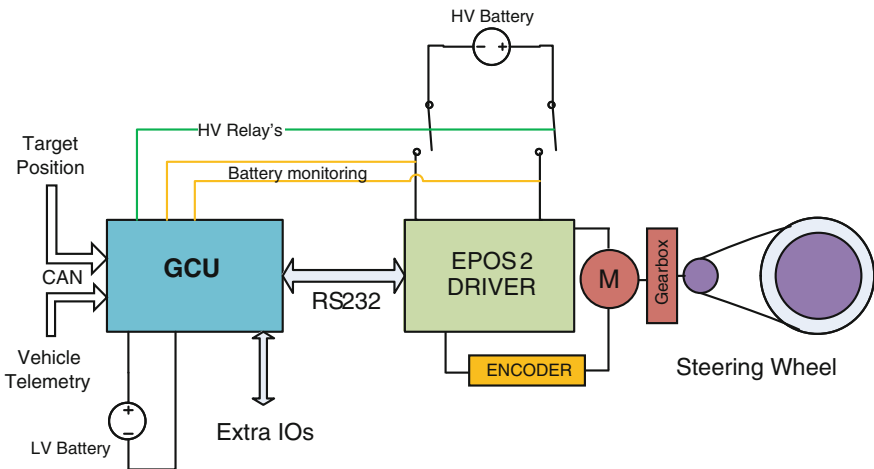


Fig. 42.8 Steering wheel controller architecture

speed and the torque were finally fixed to 55 rpm and 50 nm, respectively, fulfilling the conditions of design.

Once the motor was set, a flexible and highly efficient power stage driver was selected (EPOS2 70/10) which was able to manage the movement of the DC motor. Additionally, it was equipped with a valuable auto-tuning tool and can be controlled by various communication protocols.

The next step in the design is the development of an ECU [3] fulfilling the following requirements:

- Establishing the communication with the artificial vision unit in order to decode the target position and also send information regarding the EPOS2 driver and motor state.
- Allow the monitoring and disconnection of the high-voltage batteries which are supplying the system, avoiding the damage danger to testing engineers.
- Capability to communicate with the EPOS2 driver.
- Be ready to allow the possibility of adding new sensors to increase the flexibility of the system to future requirements.

42.3 Testing

The following three parts were tested:

- Steering wheel controller
- Image processing
- Complete system architecture.

42.3.1 *Steering Wheel Controller*

The objective of this test is to validate the GCU (ECU responsible for the control of the steering wheel). To do this, a HIL bench was developed (Fig. 42.9).

The HIL was done using National Instruments technology. A CompactRIO 9002 RT controller is used to simulate the inputs and read the outputs of the system and Test Stand software in order to automate the test cases that were defined according to the requirements' specifications. Using this technology, we were able to verify that the steering wheel controller was able to follow the control signals that were going to be sent by the AIU in the real system.

42.3.2 *Image Processing*

The testing of this module was done inside the laboratory. Different colours and shapes were tested in order to check whether the AIU was able to detect them

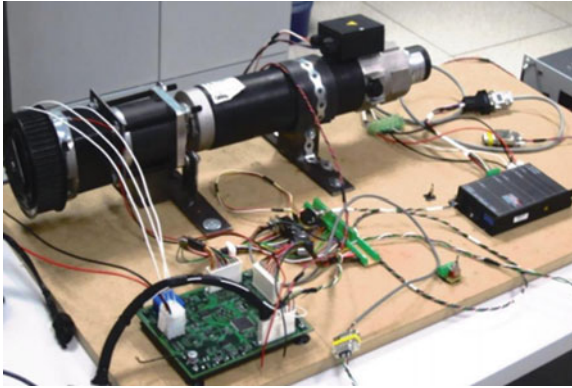


Fig. 42.9 Video frame of the trajectory tested in the validation test

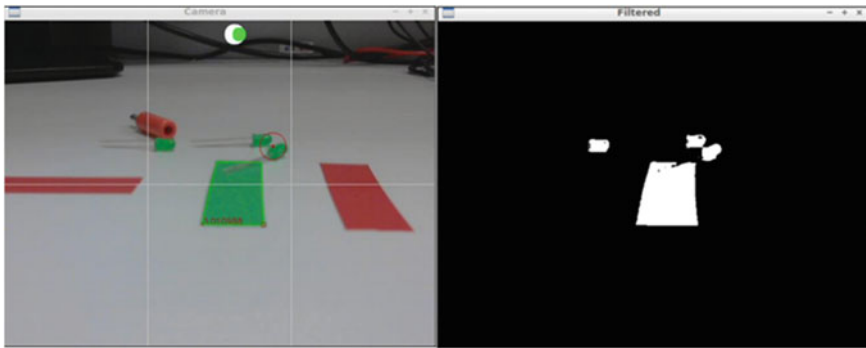


Fig. 42.10 Video frame of the trajectory tested in the validation test

correctly. The image below shows an example of the green colour detection test (Fig. 42.10).

In the image, it is shown how the system is able to detect green rectangles and then place the centroid (green point) between the upper corners of the green rectangle. The white dot indicates the average area of green in the image.

42.3.3 Complete System Architecture

Once the two modules had been individually tested, the system was integrated in a pickup truck in order to run some calibration and validation tests. Various trajectories were tested at low speed in order to calibrate the system and increase the response speed and sensitivity.

Finally, as shown in Fig. 42.11, a validation test was successfully carried out at low speed with a curve trajectory.



Fig. 42.11 Video frame of the trajectory tested in the validation test

42.4 Conclusions

The development of new and more innovative safety systems generates the need for different and new testing procedures and configurations that are not currently covered. These new configurations mainly respond to high and very high containment tests, rollover tests, misuse tests and car-to-car tests. Solutions are being developed to solve the issues these new configurations present.

This paper summarizes the development of a new system based on autonomous driving that can offer solutions for a wide variety of tests enabling new configurations and guaranteeing a high level of test repeatability and safety.

The modular system described can be implemented in any car, using artificial vision algorithms and a DC motor which drives the steering wheel.

The designed system not only enables all the tests required at present to be carried out but also allows future test configurations that are not currently being tested, but which will undoubtedly be required to be implemented in the future. The system developed is modular and scalable, allowing us to set up a technological platform to develop future automated driving tests and research projects.

The control architecture gave good results for the different paths tested on a pickup truck. A prototype system was tested at low speed, and the steering control architecture implemented had a very good performance and response to the artificial intelligence module inputs, which is particularly important to follow correctly the defined paths. The system is currently under fine-tuning developments in order to carry out high-speed tests to fully validate the system and implement its use.

In future work, other kinds of input sensors may be added to the control architecture to enlarge the variety of tests that can be carried out with the system.

References

1. Albus J (1993) A reference model architecture for intelligent systems design. In: An introduction to intelligent and autonomous control. CiteSeer
2. Baggio DL (2012) Mastering OpenCV with practical computer vision project. Packt Publishing Ltd., Birmingham
3. Barr M (1999) Programming embedded systems in C and C++. O'Reilly Media, Inc., Sebastopol
4. Batista de Oliveira (2009) Software architecture for autonomous vehicles. Dissertation, Instituto Superior Técnico, Universidade Técnica de Lisboa
5. Behere S (2013) Architecting Autonomous Automotive Systems: with an emphasis on Cooperative Driving. Thesis, KTH Royal Institute of Technology, Stockholm
6. Comité Européen Normalisation (CEN) (2010) UNE-EN 1317-1, Road restraint systems—part 1: terminology and general criteria for tests methods
7. Euro NCAP (2009) Euro NCAP moving forward—strategic roadmap 2010–2015. Euro NCAP, Brussels
8. Forsyth DA (2012) Computer vision: a modern approach. Prentice Hall, Upper Saddle River
9. Milanés V, Pérez J, Onieva E, González C, De Pedro T (2009) Electric power controller for steering wheel management in electric cars. In: Compatibility and Power Electronics, 2009, CPE'09, pp 444–449 IEEE
10. MISRA-C (2012) Guidelines for the use of the C language in critical systems. The Motor Industry Software Reliability Association (MISRA)
11. Naranjo JE, González C, García R, de Pedro T, Haber RE (2005) Power-steering control architecture for automatic driving. *Intell Transp Syst IEEE Trans* 6(4):406–415

Chapter 43

Vibration Isolation Performance Research of Commercial Truck's Cab Suspension System Based on Road Load Data

Xin Yan, Di Jiang, Zhongxiao Wang and Maolin Guo

Abstract Based on road load data of commercial truck's cab suspension system, extreme value and standard deviation of acceleration signals are statistically analyzed. And then, pseudo-damage analysis is done to get the damage attenuation level of the shock absorber. According to the theory of shock absorber vibration isolation, amplitude frequency response characteristics of the cab suspension system are acquired. Significance of the study is to find a way to evaluate the performance of commercial truck's cab suspension system. It is very useful to guide the forward design of cab suspension system from the perspective of passenger comfort and component fatigue life so that it can provide data support and improvement suggestions for the development of commercial truck cab suspension system.

Keywords Road load data · Pseudo-damage · Vibration isolation performance

43.1 Introduction

For the development of commercial truck cab, the design of suspension system is of great importance. Cab suspension design of modern commercial truck [1] mainly includes the elastic damping components selection and layout, mount bracket design, etc. The designers control the parameters of the spring and its performance requirements, including spring stiffness and maximum overall diameter, air tightness, requirement of strength, and service life. And they control its damping characteristics of shock absorber, such as the strength of lug, upper and lower limit travel requirements, etc. But they could not access to obtain vibration isolation performance of suspension in the condition of random road load, and are not able to

X. Yan (✉) · D. Jiang · Z. Wang · M. Guo
FAW R&D Center Body Laboratory, 1063 Chuangye Street, Changchun, China
e-mail: vsmal@126.com

compare different suspensions so as to get the optimal cab mount system. It is necessary to do road load spectrum measurement for the key parts of suspension system, including acceleration signal and suspension relative displacement signals. And test analysis personnel can do processing analysis for the signal data to acquire relevant information with regard to vibration isolation performance of the suspension. Therefore, the suspension system can be designed in forward direction.

43.2 Vibration Isolation Theory of Suspension Shock Absorber

Vibration isolation ability of suspension shock absorber is measured by vibration transmissibility which is defined as the ratio of response signal amplitude X_0 and input signal amplitude X_i . The standard model of shock absorber is a linear vibration system composing of a spring with rigidity coefficient K and a damper with damping coefficient C [2], as shown in Fig. 43.1.

Under steady-state sine excitation, transmissibility T of the shock absorber is expressed as follows:

$$T = X_0/X_i = \{[1 + (2\zeta\lambda)^2]/[(1 - \lambda^2)^2 + (2\zeta\lambda)^2]\}^{\frac{1}{2}} \tag{43.1}$$

where $\lambda = f/f_n$ is frequency ratio and $\zeta = C/C_c$ is damping ratio. For mass system M , natural frequency f_n and critical damping C_c are calculated as follows:

$$C_c = 2\sqrt{KM} \tag{43.2}$$

$$f_n = \frac{1}{2\pi} \sqrt{\frac{K}{M}} \tag{43.3}$$

Fig. 43.1 Single degree of freedom vibration system simplified model

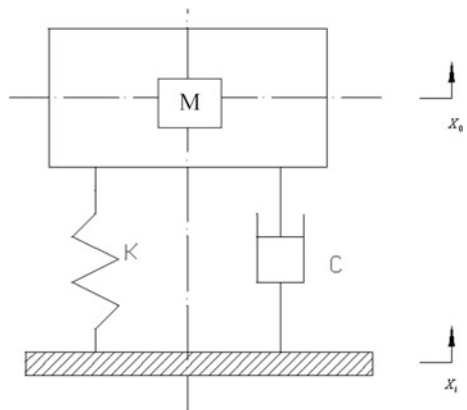
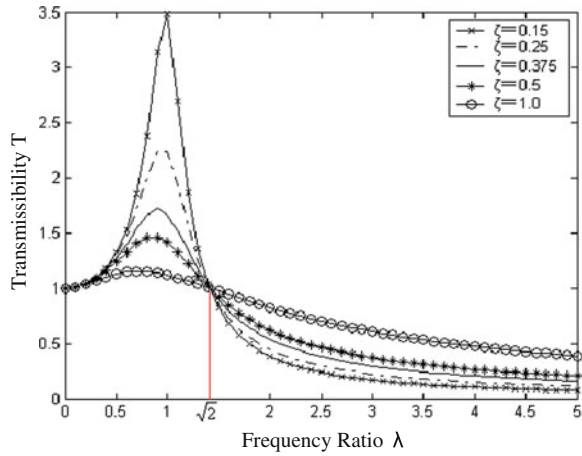


Fig. 43.2 Vibration transmissibility



The variation between transmissibility T and frequency ratio λ is shown in Fig. 43.2.

When $\lambda > \sqrt{2}$, $T < 1$, the shock absorber has played an important role in vibration attenuation which is entering the workspace as follows: When $\lambda < \sqrt{2}$, $T > 1$, the shock absorbers have played an important role in vibration amplification, namely in shock isolation; especially when $\lambda = 1$, excitation frequency is equal to the natural frequency when resonance occurs at this time. It means that the increasing damping can reduce T ; however, it can reduce the vibration isolation performance in the high frequencies ($\lambda > \sqrt{2}$).

Therefore, in order to achieve the purpose of vibration isolation, we should make the natural frequency of the system away from excitation frequency when the frequency ratio should be increased as far as possible in the permitted range [3–5]. So the suspension performance requirements can be summed up in: In the low frequency phase, it should have characteristic of large damping and stiffness; when in the high-frequency phase, the property of small damping and stiffness is necessary. In other words, the ideal vibration isolator should possess the dynamic characteristics with variable frequency.

43.3 Road Load Acquisition and Data Processing

In this paper, road spectrum load tests were for trucks A and B. The test models were both full floating heavy trucks that adopted spiral spring with shock absorber. The signal data were acquired with the regulation of speed in XX proving ground. The acceleration sensors were mounted up and down of the suspension (Fig. 43.3) which was mainly used for investigating the vibration condition close to suspension in the rough road so as to evaluate the performance of spring damper.

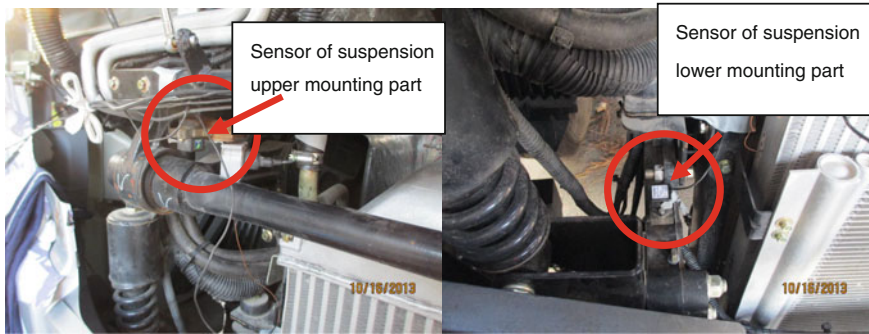


Fig. 43.3 Test sensors layout

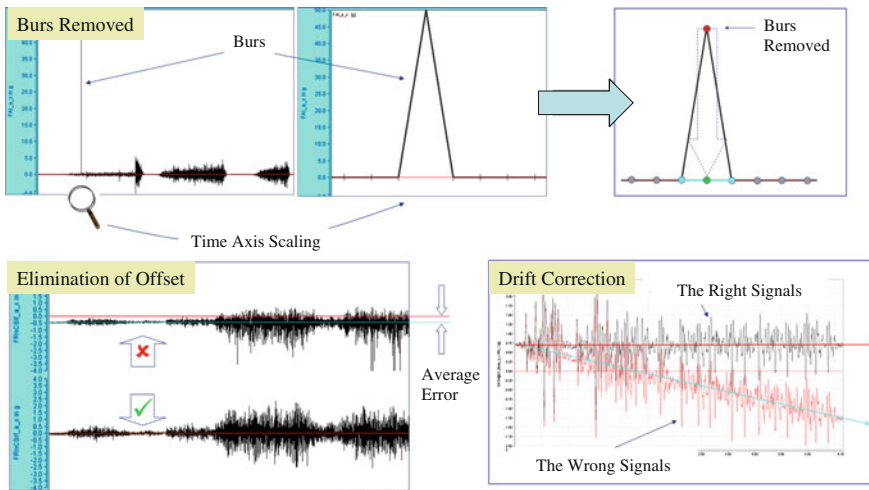


Fig. 43.4 Signal data post-processing

After measurement and preliminary check for signals by test personnel, it was necessary to do further post-processing jobs; the main work included burrs removed, elimination of offset, drift correction, cutting for typical sections, etc., as shown in Fig. 43.4.

43.4 Analysis on Road Load Data and Vibration Isolation Performance of Suspension System

43.4.1 Road Load Data Analysis

After the completion of signal processing, we analyzed the road signals firstly both for trucks A and B in motivating input end (frame) and the response output end

(cab) to compare vibration condition for signals. The main analysis items for acceleration signals included extreme value and standard deviation analysis, as well as pseudo-damage analysis. And the vibration trend could be found in transmission path from the frame to cab in the perspective of statistical investigation.

43.4.1.1 Extreme Value and Standard Deviation Analysis for Acceleration Signals

The role of extreme value analysis is to find out the largest amplitude during instantaneous impact in complex load condition. The extreme vibration situation of the measured parts could be reflected from one side, but it could not represent the typical characteristic of the road for its contingency. And acceleration standard deviation analysis can be carried out on the vibration amplitude of the signal average statistics to reflect condition of vibration for measured parts throughout the load.

As shown in Fig. 43.5, extreme acceleration amplitude value of lower mounting part (frame) for the signals which were transmitted from vehicle chassis to frame showed lager in front suspension both for trucks A and B. In the meanwhile the extreme acceleration amplitude value of upper mounting part (cabin) for the signals which were transmitted from frame to cab show different: front suspension was greater than the rear one in truck A when it was opposite for truck B. There was some phenomenon that the extreme value of response output end was greater than the one in input excitation, which meant the rear suspension of truck B went through an abnormal vibration amplification process instantaneously.

For lower mounting part, the standard deviation showed the same trend as the extreme value; the standard deviation value of truck B was 0.33, 50 % more than truck A which proved there were more severe vibration in the rear of cab, and the

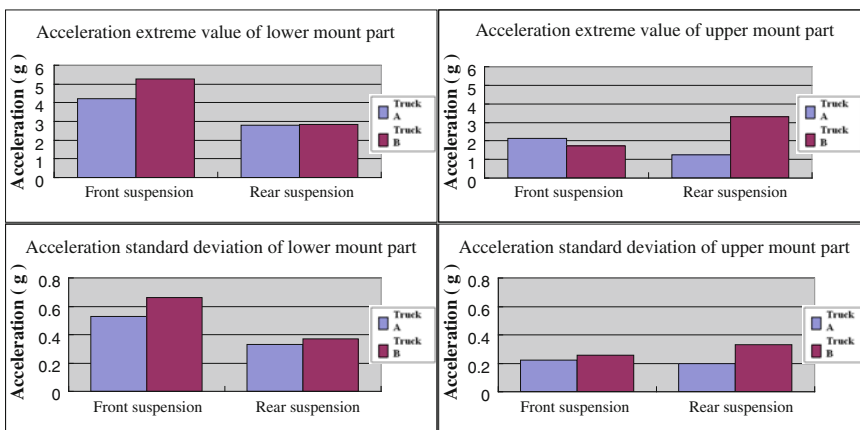


Fig. 43.5 Acceleration signal extreme value and standard deviation analysis of the typical sections

standard deviation value of lower part of the rear suspension was 0.37 with the ratio of lower part and upper part being only 1.12. It meant that the overall amplitude attenuation of vibration signal was not so well.

43.4.1.2 Pseudo-Damage Analysis

‘Pseudo-damage’ is put forward according to the linear fatigue cumulative damage theory which is used to describe the load quantity of parts damage strength, and the damage value is calculated by fatigue life estimation method in order to compare the load, but not to get the actual damage value of the parts. The rain-flow count method is used to calculate the amplitude of the signals in different frequency distribution. And then, it is possible to calculate the fatigue life for different amplitudes according to the S-N curve. At last, the pseudo-damage value could be calculated by the theory ‘Miner linear cumulative damage’ which is as shown in Fig. 43.6.

According to the theory of pseudo-damage evaluation, we analyzed the pseudo-damage of the acceleration signal for the two trucks so as to get the pseudo-damage attenuation level (multiple), as shown in Fig. 43.7; pseudo-damage attenuation level (multiple) of front suspension in truck A was slightly higher than truck B. However, there was much difference for the signals of rear suspension; the pseudo-damage attenuation level (multiple) of truck A was 80.4 when it was only 3.5 for truck B.

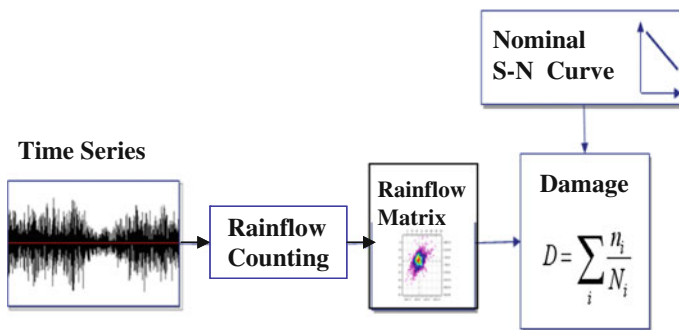
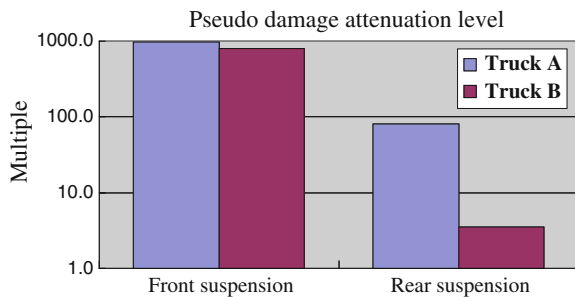


Fig. 43.6 Theory of pseudo-damage evaluation

Fig. 43.7 Pseudo-damage attenuation level



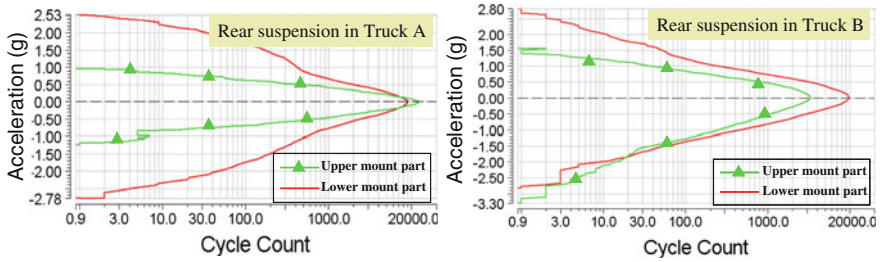


Fig. 43.8 Level-crossing count analysis

We did the level-crossing count analysis according to this situation, as shown in Fig. 43.8; the acceleration signal’s amplitude of the upper mounting part in rear suspension of truck A was greatly reduced by the effect of shock absorber when it had become small value signal with high cycle numbers. It meant that level-crossing count contour of input signals enveloped those of output signals which was in line with the typical characteristics of vibration isolation system [2]; with regard to truck B, the output signal under the condition of high amplitude did not meet the typical characteristics of vibration isolation system, while the shock absorber did not have ideal job performance in the compression stroke, and signal amplitude difference between the input and output was not obvious for the negative acceleration signal.

43.4.2 Performance of Suspension Vibration Isolation

For the vibration isolation performance of the suspension, we focus on the amplitude–frequency response characteristics of the suspension to do the comparative analysis (vibration transmissibility), as shown in Fig. 43.9. Known by the theory of suspension shock absorber vibration isolation, the starting point of the working area is the starting frequency when vibration transmissibility $T < 1$, and the frequency value is just the natural frequency of the suspension itself. The lower this value is, the sooner it can enter the work state. The exclusion zone before working frequency band is amplified on the amplitude value and energy. Starting frequency of the

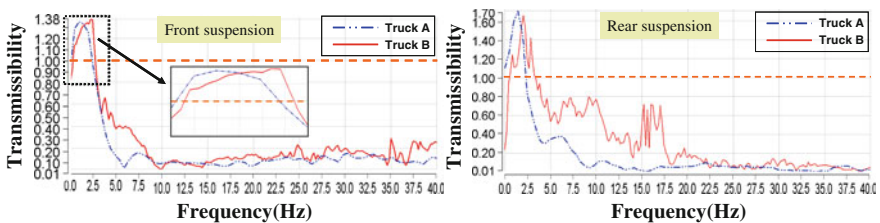


Fig. 43.9 Amplitude–frequency response characteristics analysis

working area in front suspension for truck A was slightly lower than truck B, but the value in rear suspension was much lower than truck B which meant that the energy and amplitude in low frequency band could be greatly reduced. In terms of vibration transmissibility, the vibration isolation performance of front suspension for trucks A and B was similar within the scope of 3–8 Hz; for rear suspension of truck B in the range of 5–20 Hz, not only the vibration transmissibility value was too high, but also a second resonance region appeared around 16 Hz which proved that the second-order natural frequency of suspension system was forced to appear in conventional excitation frequency of the proving ground (0–25 Hz). And this was the main reason why the vibration isolation performance of rear suspension was so weak.

43.5 Conclusions

Road load data of cab suspension system were analyzed for trucks A and B in this paper. First, we did statistical analysis on extreme value and standard deviation of the acceleration signals, and then analyzed the signal's pseudo-damage to get pseudo-damage attenuation level. At the same time, we researched data from the point of level-crossing count and studied the amplitude–frequency response characteristics in the frequency domain according to the theory of shock absorber vibration isolation. Finally, we found the problem of vibration isolation performance in the rear suspension of truck B. The main purpose is to analyze the working status and performance of suspension shock absorber from the data objectively so as to avoid mistakes by the subjective experience and the design concept 'black box.' It is very useful to guide the forward design of cab suspension system from the perspective of passenger comfort and component fatigue life so that it can provide data support and improvement suggestions for the development of commercial truck cab suspension system.

References

1. Guiyi W (1998) The design principle and the performance test of rubber shock absorber, special rubber products, (3), 45–46
2. Debao H, Xigeng S (2009) Experimental study on the constitutive relation of the rubber vibration isolator stiffness and damping. *J Vib Shock* 203 (1):156–160
3. Zhang Y (2000) Mechanical vibration mechanics, vol. 1. Jilin Science & Technology Press, China, pp 38–41
4. Weiping H, Weining B (2008) Automotive air spring vertical elastic characteristics analysis and calculation. *Machinery* 8:102–107
5. Yu F, Weining B (2005) Vehicle system dynamics, vol. 1. China Machine Press, Beijing, pp 27–29

Chapter 44

A Normalized Approach for Evaluating Driving Styles Based on Personalized Driver Modeling

Bin Shi, Wuqiang Meng, Hui Liu, Jie Hu and Li Xu

Abstract Driving style may affect fuel economy and driving ability, and therefore, its evaluation becomes an important research topic for vehicle calibration and control. In this work, we propose to evaluate the driving style by normalizing driving operations in a standard test procedure. Firstly, a personalized driver model is established for each driver by learning his/her driving operations during real-world driving. This is accomplished by using the locally designed neural network, i.e., CMAC in this work, and the real-world vehicle test data (VTD). Secondly, the established driver model is applied to speed control as required by standard test procedure, i.e., FTP-75, thus the driving operations may be normalized. Finally, the energy spectral density (ESD) is computed on normalized driving data to obtain a quantitative index for evaluating the driving style of each driver. Simulations are conducted to verify the effectiveness of the proposed scheme.

Keywords Cerebellar model articulation controller (CMAC) · Throttle position (TP) · Driver model · Fuel economy · Evaluation index · Vehicle test data (VTD) · Energy spectral density (ESD)

44.1 Introduction

Research has shown that driving style has various impacts on fuel consumption and emissions [1, 2]. Drivers who are less prone to sudden maneuvers will tend to have tight distributions of throttle position (TP) opening, and thus, the consumption of fuel

B. Shi (✉) · J. Hu · L. Xu
College of Electrical Engineering, Zhejiang University, Hangzhou 310027,
People's Republic of China
e-mail: binshi@zju.edu.cn

W. Meng · H. Liu
Ford Motor Research and Engineering (Nanjing) Co., Ltd., Nanjing,
People's Republic of China

will decrease. The differences in the driving behaviors could be due to the subconscious, as well as vehicle itself and environment [2–4]. There is a great need to develop several automatic evaluation indexes, which take account of driver characteristics by suitably modeling driver performance. It had been widely studied during the last few years. Kedar-Dongarkar and Das[5] developed a new method for driver classification for optimization of energy usage. The vehicle’s power train signals were used to classify the drivers into three categories: aggressive, moderate, and conservative. Murphey et al. [6] applied an online driver classifying system by analyzing the jerk profile of the driver. Jerk is defined as the rate of change in acceleration or deceleration. The algorithm extracts jerk features from the current vehicle speed within a short window and classifies the drivers into three classes: calm, normal, and aggressive. Canale and Malan [7] presented human-driving behavior in an urban environment. They used the stop and go signals to assess the driver’s behaviors.

Although the above researches attempted to characterize a driver in one way or another, there still exist three main issues: (a) data obtained by the simulator cannot fully represent the actual situation, (b) the raw driving data cannot be obtained under exactly the same environment and road conditions, and (c) there is no quantified evaluation index of driving style for practical use. Evaluation results may differ from person to person even if they may be classified into the same style.

In this research, firstly, a locally designed neural network, i.e., CMAC in this work, is employed to train the raw driving data. We established a personalized driver model based on the real-world driving data. Here, we take the VTD as the original training data for CMAC learning process [8]; secondly, the established driver model is normalized under the standard speed driving cycle, FTP-75 here, for example; at last, a performance index, namely, the energy spectral density (ESD) combined with the error between FTP-75 and normalized data, is suggested to evaluate the driving style. Without loss of generality, only three categories of drivers: “Aggressive,” “Moderate,” and “Mild.” The approach is verified later by K-means clustering algorithm and one-way ANOVA.

The remainder of the paper is organized as follows. The next section discusses the selection of driving data. Section 44.3 includes the modeling process of personalized driver modeling. In Sect. 44.4, we introduce a normalization process under the standard driving cycle. Section 44.5 describes the evaluation index of driver behavior. Experiment results are presented in Sect. 44.6. Finally, concluding remarks are in Sect. 44.7.

44.2 Selection of Raw Data

Driving style could be measured by accelerates and decelerates. It is reflected directly by the changes of TP and brake pressure (BP). A total of 18 classified drivers are chosen for modeling and testing, namely, No. 1 to No. 6 stand for “Aggressive” drivers, No. 7 to No. 12 for “Moderate” drivers, and No. 13 to No. 18 for “Mild” drivers.

Raw BP's distribution is shown in Fig. 44.1a. It shows that despite the larger BP's of "Aggressive" drivers, there is no significant difference between drivers of "Moderate" and "Mild." Take drivers 4 and 5, for example, they both belong to the style of "Aggressive"; however, BP's are mostly close to that of "Moderate" and "Mild," only few are larger than 400; on the other hand, "Moderate" drivers have almost the same BP operations as "Mild" drivers.

Figure 44.1b shows that TP's are evidently different for different drivers. The "Aggressive" drivers tend to have sharp TP changes, "Mild" drivers have the minimum changes, and "Moderate" drivers are in the middle. So, TP is taken as the driver's feature to evaluate the driving styles in the following research.

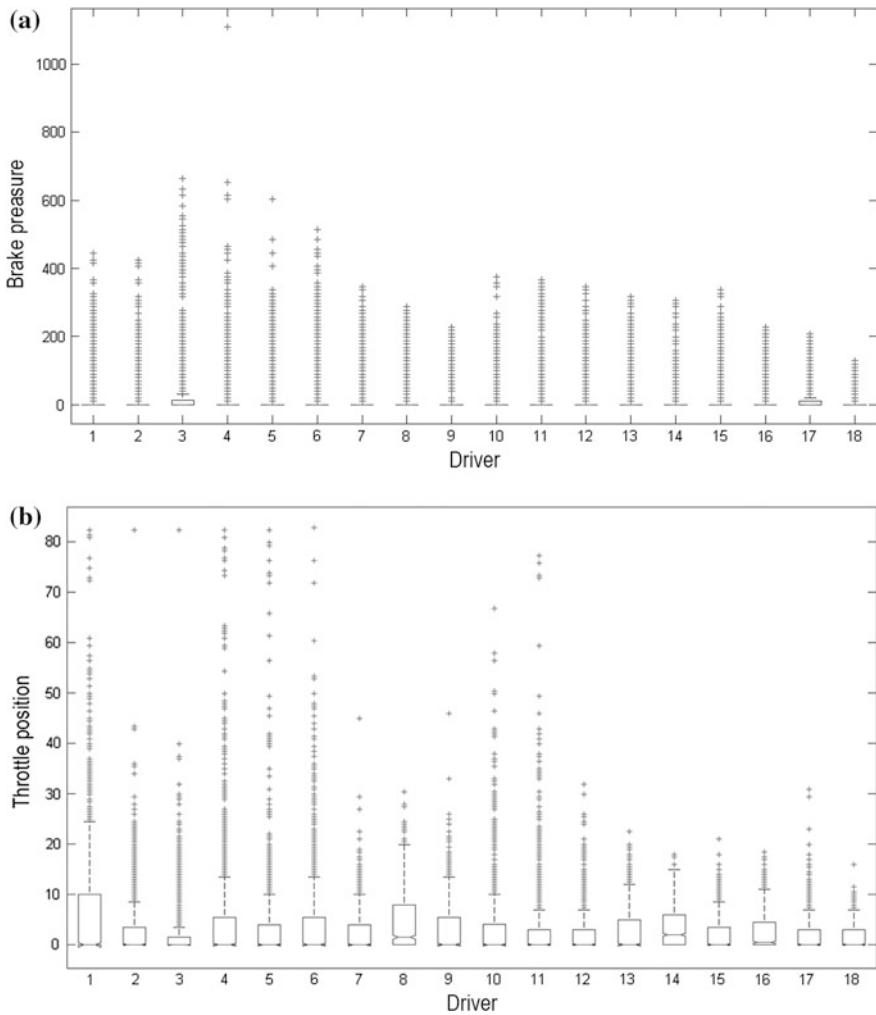


Fig. 44.1 Distribution of a BP and b TP

44.3 Personalized Driver Modeling

Neural network makes possible the personalized driver modeling. Even though the driver model is unknown and nonlinear, the driver behaviors could be presented through a supervised learning process. Therefore, we only need to know the inputs and outputs of the model.

By using the neural network, the raw TP data were converted into the personalized driver model. The cerebellar model articulation controller (CMAC) offers a practical modeling method as well as simple network architecture. It provides the advantages of fast learning and a high convergence rate [9]. CMAC learning is a competitive learning process and follows self-organizing feature map (SOFM) learning rules [10]. This makes CMAC neural network a powerful candidate tool in many traffic modeling studies. The CMAC learning rule can be represented by Eqs. (44.1)–(44.3).

$$Y_i = \sum_{j=1}^{N_L} w_j a_j(x) \quad i = 1, \dots, m \tag{44.1}$$

$$\Delta E_i = \bar{y}_s - \sum_{j=1}^{N_L} w_j a_j(x) \quad i = 1, \dots, m \tag{44.2}$$

$$w_j(t) = w_j(t - 1) + \frac{\alpha}{N_L} a_j \left(\bar{y}_s - \sum_{j=1}^{N_L} w_j a_j(x) w_j(t - 1) \right) \tag{44.3}$$

where w_j is the weight of j th memory cell. If activated, the value is 1; otherwise, it is 0. y_i is the output of CMAC, IE_i is the error between y_i and expectations, \bar{y}_s is the state of the desired output, and α is the learning constant.

As shown in Fig. 44.2, assuming $VS[t]$ is the speed output of time t , and the corresponding throttling operation is $TP[t]$. We chose the differential of $VS[t]$ and $VS[t + 1]$ as the input of the network, and $TP[t]$ as the output. After training the raw VTD, personalized driver model could be obtained. In order to implement with the established drive model, a simple car model is required. The multi-layered perceptron neural network [11] is used to train the raw TP and BP data.

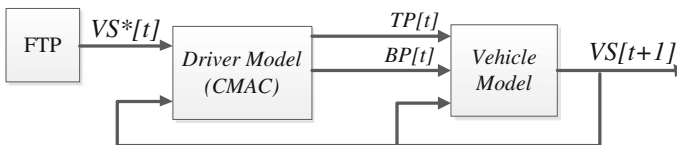


Fig. 44.2 The process of normalization

44.4 Driver Behavior Normalization

The VTD data were collected under several conditions, different driving styles (aggressive, moderate, and mild), road situations (city and highway), cities (Boston, Denver, etc.), and vehicle types (Escort, Fiesta) by Ford Motor Company. Therefore, different conditions, i.e., different cities, vehicle types, etc., may lead to different evaluation results, the research of driving personalities should proceed under the same conditions. For example, driver A drives a car on an urban road, which has speed limit of 60 km/h, and driver B on the other road has speed limit of 40 km/h. Even though A is a so-called mild driver and B is aggressive, it is difficult, due to the inconsistent speed range, to evaluate the two drivers.

Before performance analysis, driver operations shall first be normalized. US Environmental Protection Agency provides a practical FTP-75 normalized speed profile for vehicle test. FTP-75 standard driving cycle is selected as it includes various driving situations, such as straight road, right and left turn corners, etc. Then, the model's VS and TP outputs are available for driving style analyzing. Figure 44.3 shows an example for one of the drivers' performance.

In Fig. 44.3a, "Actual" means the FTP-75 speed curve, and "Model" means the personalized driver model's speed output. Figure 44.3b is the error between the two speed curves.

In summary, the normalization procedures are as follows:

1. VS and the first-order differential of VS as the input, TP as the output of network, Raw TP and VS data are trained by neural network to obtain the driver model.
2. Vehicle model is required through a simple error back propagation algorithm. We select TP, BP, and VS as the input, and the next time, VS as the output of the car model.
3. Load the established two models and execute under standard speed driving cycle. Here, we select FTP-75 as the standard speed driving cycle.

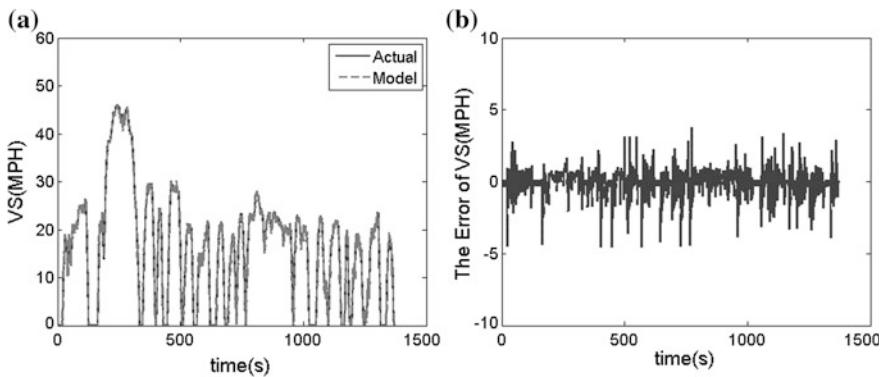


Fig. 44.3 a FTP-75 speed driving cycle and the personalized model *curve*. b Error between "Model" and "Actual"

This approach converts the VTD data into the personalized driver model and normalizes the driver operations under FTP-75 standard driving cycle.

44.5 Evaluation Index

In order to verify with the final classification results later, the raw time series require a non-time domain evaluation index because initially the driving data had not normalized yet. This part will be discussed in the data normalization chapter. ESD gives the energy carried by the time series of per unit frequency [12]. It describes how the energy of a time series is distributed with frequency. Assuming $f(t)$ is a finite energy signal, and the spectral density of $f(t)$ is the square of signal amplitude of the continuous Fourier transform [13].

$$\Phi(\omega) = \left| \frac{1}{\sqrt{2\pi}} \int_{-\infty}^{\infty} f(t)e^{-i\omega t} dt \right|^2 = \frac{F(\omega)F'(\omega)}{2\pi} \quad (44.4)$$

where ω is the angular frequency, $F(\omega)$ is the continuous Fourier transform of $f(t)$, and $F'(\omega)$ is a conjugate function of $F(\omega)$. If the signal is discrete, after finite element, still we can get the ESD:

$$\Phi(\omega) = \left| \frac{1}{\sqrt{2\pi}} \sum_{n=-\infty}^{\infty} f_n e^{-i\omega n} \right|^2 = \frac{F(\omega)F'(\omega)}{2\pi} \quad (44.5)$$

where $F(\omega)$ is the discrete time Fourier transform (DTFT) of XXX .

By this way, the raw signal is converted from a time domain signal into a frequency domain signal.

The error between FTP-75 and normalized data is an important parameter that reflects the degree of normalization. When considering the evaluation index of different drivers, this parameter is included to classify the driving style. An error-based energy spectral density (EESD) evaluation index can be developed to evaluate the driver's style. It can be described as follows:

$$Ei = \frac{\text{Ave}(\text{ESD}(\text{TP}))}{\text{Std}(\text{Err})} \quad (44.6)$$

where Ei means the evaluation index of driving style; ESD is the ESD distribution; "Ave" is the average value of ESD; and "Std" is the standard deviation of error.

44.6 Experiments

Totally, 18 drivers’ raw data, which are classified evenly into 3 groups by artificial classification in advance, were analyzed and compared first.

Due to the time series of TP are not directly comparable, an evaluation index is needed. Not only TP, raw VS could also affect the driver’s style [14]. Thus, the following typical parameters are chosen to evaluate the driving styles:

- Var. of TP σ_{TP}
- Var. of ESD σ_{ESD}
- Ave. of TP/Vehicle Speed $A_{\frac{TP}{VS}}$
- Var. of TP/Vehicle Speed $\sigma_{\frac{TP}{VS}}$

From the comparison of Table 44.1 and Fig. 44.1, it can be seen that σ_{ESD} , $\sigma_{\frac{TP}{VS}}$ and $A_{\frac{TP}{VS}}$ can distinguish among three types of driving styles. While from the extent of corresponding to the distribution of raw data, σ_{ESD} is the optimum index for its stronger capability than the others. For example, in Table 44.1, driver “Agg4” and driver “Agg1” had the largest evaluation indexes, while driver “Mode4” and “Mode5” were closer to the style of “Aggressive.” These features were very much in line with the distribution as shown in Fig. 44.1b. It should be pointed out that this raw data analysis was not aimed to evaluate any statistical results, as the data were

Table 44.1 Raw data evaluation index

Driving style	Evaluation index			
	σ_{TP}	σ_{ESD}	$A_{\frac{TP}{VS}}$	$\sigma_{\frac{TP}{VS}}$
Agg1	172.61	597,940	0.30	1.01
Agg2	163.47	68,353	0.20	0.24
Agg3	108.50	63,433	0.24	0.37
Agg4	130.58	847,400	0.46	1.48
Agg5	164.49	256,380	0.25	0.45
Agg6	124.71	174,280	0.29	0.72
Mode1	106.21	10,679	0.20	0.19
Mode2	145.74	10,133	0.23	0.23
Mode3	135.59	30,584	0.25	0.26
Mode4	208.42	74,159	0.23	0.28
Mode5	108.54	90,839	0.30	0.44
Mode6	89.12	8,739	0.25	0.26
Mild1	85.62	2,191	0.23	0.18
Mild2	86.29	1,699	0.16	0.16
Mild3	78.49	1,565	0.17	0.14
Mild4	134.27	1,415	0.16	0.09
Mild5	87.54	2,035	0.18	0.13
Mild6	79.64	445	0.18	0.09

obtained under different conditions. The aim was to show that the acquired raw data (TP and VS) had quite different values. Therefore, it is confirmed that it was a good choice, and the variables were sufficient to identify different driving styles.

For the normalized data, TP and VS can be chosen for analyzing. The following parameters are explored to evaluate the driving style (Table 44.2):

- Var. of TP σ_{STP}
- Ave. of ESD A_{SESD}
- Probability Density Distribution of TP P_{STP}
- Var. of TP based on Error σ'_{STP}
- Ave. of ESD based on Error A'_{SESD}

From the above evaluation indexes, compared with the raw data classification result, σ'_{STP} and A'_{SESD} had a better classification result. Taking the “Aggressive” drivers, for example, the maximum values of 18 drivers were “Agg4” and “Agg1.” Obviously, σ_{STP} has an unreasonable maximum value of “Agg3.” For “Moderate” drivers, both P_{STP} and σ_{SESD} performed not quite good to distinguish between “Aggressive” and “Moderate.” As it comes to σ'_{STP} and A'_{SESD} , σ'_{STP} varied between nearly 40–120 and had a good classification result for three driving styles. A'_{SESD} has a strong ability to reflect the distribution of raw data. Therefore, the two evaluation indexes would be compared by the real distribution of TP time series further.

Table 44.2 Converged data evaluation index

Driving style	Evaluation index				
	σ_{STP}	A_{SESD}	P_{STP}	σ'_{STP}	A'_{SESD}
Agg1	126.0	211.33	9.6	99.6	178.14
Agg2	86.8	117.68	6.8	83.6	137.16
Agg3	606.4	81.44	6.1	63.8	117.54
Agg4	140.4	213.84	9.0	113.3	181.91
Agg5	69.8	121.36	6.9	82.3	134.04
Agg6	141.9	141.71	7.5	89.7	149.13
Mode1	70.3	128.96	7.2	63.2	105.90
Mode2	68.5	130.97	7.8	55.6	104.11
Mode3	86.5	151.29	8.0	62.8	106.62
Mode4	93.3	140.00	7.6	64.0	108.46
Mode5	74.8	139.78	7.6	63.9	108.34
Mode6	57.3	114.84	7.0	56.8	100.04
Mild1	40.2	86.53	6.5	40.2	79.18
Mild2	41.5	89.96	6.6	45.0	86.31
Mild3	71.9	82.01	6.2	40.5	75.55
Mild4	42.2	105.53	6.3	41.2	90.26
Mild5	81.70	20,520	6.1	46.2	85.21
Mild6	80.00	22,722	6.1	44.1	83.25

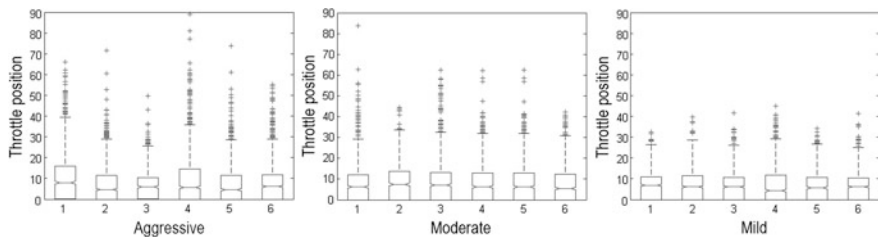


Fig. 44.4 Distributions of normalized TP for 3 different driving styles: aggressive, moderate, and mild

Figure 44.4 shows the actual distributions of 18 groups of normalized TP. From these figures, it can be clearly seen that A'_{SESD} can reflect the TP time series more accurately. For example, for drivers “Agg1” and “Agg4,” the evaluation indexes were bigger than other “Aggressive” drivers, which is more in line with the raw TP data distribution. Driver “Mode3,” “Mode4,” and “Mode5” had a relatively larger TP’s than other “Moderate” drivers. And further, through the correlation analysis between the above evaluation indexes and raw data index, the correlation coefficients of σ'_{STP} and A'_{SESD} are 0.837167 and 0.895211, respectively. Pearson’s correlation coefficient is defined as follows:

Therefore, from the result presented in Table 44.3, the correlation between the raw data and normalized data is quite correlated.

In order to verify the accuracy of evaluation indexes, take the two evaluation indexes as examples, k-means clustering algorithm was used to classify the driving styles.

Figure 44.5 shows the clustering results using the σ'_{STP} and A'_{SESD} evaluation indexes. Here, “Ei1” and “Ei2” are used to represent the evaluation indexes of σ'_{STP} and A'_{SESD} , respectively. Three dotted lines from top to bottom represent the artificial classification of “Aggressive,” “Moderate,” and “Mild” drivers’ driving styles, respectively. “X” represents the clustering center of three driving styles, and the cluster centers are 93.74, 61.47, and 42.86 for Ei1, and 156.08, 107.60, and 83.29 for Ei2. “*”, “○”, and “●” are the final clustering results of three styles. It can be noted in Fig. 44.5 that both the final clustering results are almost the same as the original artificial classification. Though driver “Agg3” was classified into “Moderate” style, from the raw data distribution, we could find that its TP distribution is more similar to the “Moderate” style.

Table 44.3 Pearson’s correlation coefficient

Pearson’s correlation coefficient	
0.8–1.0	Perfect correlation
0.6–0.8	Strong correlation
0.4–0.6	Moderate correlation
0.2–0.4	Weak correlation
0.0–0.2	No correlation

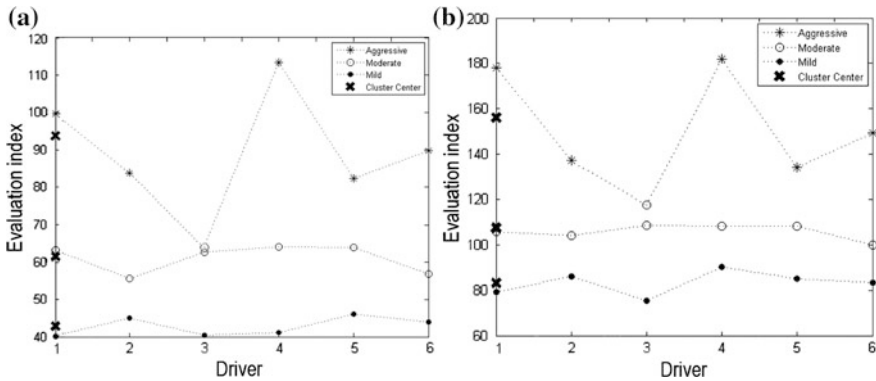


Fig. 44.5 K-means clustering results for two different evaluation indexes: **a** σ'_{STP} **b** σ'_{SED}

In short, both E_{i1} and E_{i2} have an effective classification result among three groups of different driving styles. But the discrimination is not obvious within groups, especially for “Mild” and “Moderate” driving styles of E_{i1} . And to some extent, E_{i2} can better reflect the real distribution of TP.

Finally, we use the above EESD evaluation index (E_{i2}) to classify two groups of drivers’ data, by which data were obtained from different vehicles, “Fiesta” and “Escort.”

Figure 44.6 shows that for different cars, the evaluation index will be obviously different for driving styles. For example, the cluster centers of “Fiesta” are 135.45, 96.24, and 61.23, respectively, and 218.50, 150.49, and 111.78 for “Escort.”

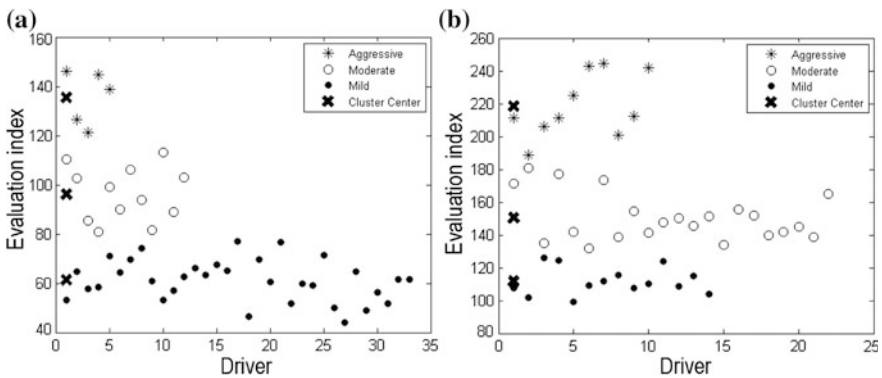


Fig. 44.6 Classifications of **a** Fiesta and **b** Escort

44.7 Conclusions

In this paper, classifying and evaluating driver performance had been studied, and it has been shown that driving styles can be identified by the operations on TP. We first presented a CMAC neural network-related algorithm to model a personalized driver model. Then, the model was normalized under FTP-75 standard speed driving cycle. The normalized data were used to build an innovative evaluation index. The evaluation index, error-based ESD, is not only able to classify the driving styles into three classes: “Aggressive,” “Moderate,” and “Mild,” but also realize a reasonable driving style evaluation for each driver. It was obtained by comparing the extracted TP feature from vehicle test data (VTD).

Results show that more “Aggressive” drivers tend to have greater evaluation index, most likely because their actions are more consistent than “Mild” and “Moderate” drivers. Moreover, the error-based ESD evaluation index has shown to be effective in evaluating the driving style. We find that “Mild” drivers have a smaller change of TP range, and this may lead to the improvement of fuel economy. In the future, driver’s operations evaluation index will be studied to achieve better fuel economy based on the evaluator that is currently under investigation.

Acknowledgement This research is supported by Ford Motor Company under grant URP 2012-6043R.

References

1. Zorrofi S, Filizadeh S, Zanetel P (2009) A simulation study of the impact of driving patterns and driver behavior on fuel economy of hybrid transit buses. In: Vehicle power and propulsion conference (VPPC’09), IEEE. IEEE, pp 572–577
2. Takei Y, Furukawa Y (2005) Estimate of driver’s fatigue through steering motion. In: IEEE international conference on systems, man and cybernetics 2005. IEEE, vol 2, pp 1765–1770
3. Goodrich MA, Boer ER (1998) Semiotics and mental models: modeling automobile driver behavior. In: Proceedings of the joint conference on science technology intelligence system ISIC/CIRA/ISAS’98, Gaithersburg, Sept 1998
4. Angkititrakul P, Miyajima C, Takeda K (2012) An improved driver-behavior model with combined individual and general driving characteristics. In: Intelligent vehicles symposium (IV), 2012 IEEE, pp 426–431
5. Kedar-Dongarkar G, Das M (2012) Driver classification for optimization of energy usage in a vehicle. *Procedia Comput Sci* 8:388–393
6. Murphey YL, Milton R, Kiliaris L (2009) Driver’s style classification using jerk analysis. In: IEEE workshop on computational intelligence in vehicles and vehicular systems (CIVVS’09). IEEE, pp 23–28
7. Canale M, Malan S (2002) Analysis and classification of human driving behaviour in an urban environment*. *Cogn Technol Work* 4(3):197–206
8. Doshi A, Trivedi MM (2010) Examining the impact of driving style on the predictability and responsiveness of the driver: real-world and symposium (IV), 2010 IEEE. IEEE, pp 232–237
9. Wahab A, Wen TG, Kamaruddin N (2007) Understanding driver behavior using multi-dimensional CMAC. In: 6th International conference on information, communications and signal processing. IEEE, pp 1–5

10. Albus JS (1975) A new approach to manipulator control: the cerebellar model articulation controller (CMAC). *J Dyn Syst Meas Contr* 97(3):220–227
11. McCall JC, Trivedi MM (2007) Driver behavior and situation aware brake assistance for intelligent vehicles. *Proc IEEE* 95(2):374–387
12. Ghaemi S, Khanmohammadi S, Tinati MA et al (2012) A hierarchical fuzzy system for modeling driver's behavior. *Int J Control Autom Syst* 10(3):517–528
13. Kuge N, Yamamura T, Shimoyama O et al (2000) A driver behavior recognition method based on a driver model framework. *SAE Trans* 109(6):469–476
14. Filev D, Lu J, Prakah-Asante K et al (2009) Real-time driving behavior identification based on driver-in-the-loop vehicle dynamics and control. In: *IEEE international conference on systems, man and cybernetics (SMC 2009)*. IEEE, pp 2020–2025

Chapter 45

Research on Performance Test Method of Lane Departure Warning System with PreScan

Qiang Zhang, Daxing Chen, Yusheng Li and Keqiang Li

Abstract A performance test method of lane departure warning system (LDWS) with PreScan software is proposed. In the process of virtual integration, the LDWS camera is located in the front of a computer monitor displaying virtual environment so as to capture pictures including lane marks and other information. Vehicle dynamic model and maneuver model run on a real-time computer, which represents a virtual vehicle and communicates with LDWS controller with CAN bus. The results show that the method will make it easier to create various test scenarios, which can save time and cost by transferring complex testing catalogues to the laboratory. The dangers presented in vehicle experiments in some critical scenarios can also be reduced. The repeatable model-based method makes it more convenient to locate the problem, which would make it easier to compare and assess the performance of LDWS produced by different companies objectively.

Keywords Lane departure warning system (LDWS) · Test scenario · Real-time simulation

Q. Zhang (✉) · D. Chen · Y. Li
Changan Automobile Global Research and Development Center, Chongqing, China
e-mail: zhangqiang3@changan.com.cn

D. Chen
e-mail: chendx@changan.com.cn

Y. Li
e-mail: liys@changan.com.cn

K. Li
State Key Laboratory of Automotive Safety and Energy, Tsinghua University, Beijing, China
e-mail: likq@tsinghua.edu.cn

45.1 Introduction

Lane departure warning system (LDWS) is a driver assistant system to reduce traffic accidents caused by lateral drifting with alert. The key performance of this system mainly consists of two parts: One is the lane marker recognition ability, and the other is the warning performance. Currently, the major evaluation methods for LDWS include field operational test and real road test. Field operational test procedures are defined in ISO 17361, even the scenarios are limited [1]. To perform the operational test, the DGPS like VBOX from RACELOGIC or RT-Range from Oxford is required to precisely measure the offset between front corner of vehicle and lane edge. The measured offsets in each scenario are used to evaluate the warning performance. After the warning performance is validated in proving ground, more than 5,000 km real road test is performed to get the statistical results of lane marker recognition ability, false alarm, and false non-alarm. In a word, the field operational test and real road test are both involved with real vehicle. A lot of resources, such as test fields, devices, and professional drivers, are required. Long test period and the sensitivity to weather also impose restrictions on it.

To solve this problem, Changan Automobile has developed a test rig based on NI software and hardware platform in 2010 [2]. The first step is to simultaneously collect the video and CAN data in typical scenarios to establish a database of LDWS scenarios. And then, these typical scenarios are used to evaluate the LDWS performance off-line. This method is time-saving; however, it would also take a lot of time to establish the database. BMW and Ford once developed camera-based active safety system test rigs based on TESIS DYNA4 [3, 4]. These test rigs are characterized by using virtual reality software to simulate the real world which will be captured by the camera. Nevertheless, due to the fact that TESIS cannot simulate the complicated weather and lighting conditions, the test scenarios are limited.

PreScan is a leading software tool which can be used for designing and evaluating ADAS and IV systems that are based on sensor technologies such as radar, laser, camera, ultrasonic, GPS, and C2C/C2I communications. Based on PreScan, one can create all kinds of traffic scenarios and cosimulate with MATLAB/Simulink easily [5]. For this reason, in this study, a virtual test system was developed to evaluate LDWS warning performance in laboratory based on PreScan. With this system, it is not required to test or collect data in real vehicle. The animation of the test scenarios is created in the virtual reality software and updated in real time. The camera of the LDWS to be evaluated is calibrated to capture the animation so as to simulate the capture actions in real vehicle test. The system communicates with LDWS controller via CAN bus, sending vehicle-related information and receiving LDWS status and warning signals. Therefore, this system can easily simulate all segments of the real vehicle test. It becomes much easier to create various scenarios and reduce workload and cost. The repeatable model-based system makes it easier to locate and reproduce problems, and it provides more objectives to compare and assess systems of different companies. The dangers presented in experiments in some critical scenarios can also be avoided.

45.2 Virtual Test System Development

Figure 45.1 illustrates the development scheme of LDWS virtual test system, including three main parts: virtual reality system, real-time simulation platform, and LDWS to be evaluated.

As shown in Fig. 45.1, the virtual reality system consists of a monitor and a graphic workstation installed with PreScan. The graphic workstation creates scenes in PreScan and displays them on the monitor. The LDWS camera aims at the monitor and then is calibrated to capture the forward scenes with lane markers. The real-time simulation platform is based on NI PXI, on which vehicle dynamic model and maneuver model run to simulate the vehicle motion in real vehicle test. The real-time simulation platform communicates with LDWS controller with CAN bus, sending signals needed for LDWS controller, such as vehicle speed, yaw rate, turning indicator, and the main switch, and receiving LDWS working status and warning signals. The positions and orientations of the host vehicle and other traffic objects are transferred through Ethernet data stream to update images on graphic workstation. A program in MATLAB can be used to process data and generate report automatically after the test completed.

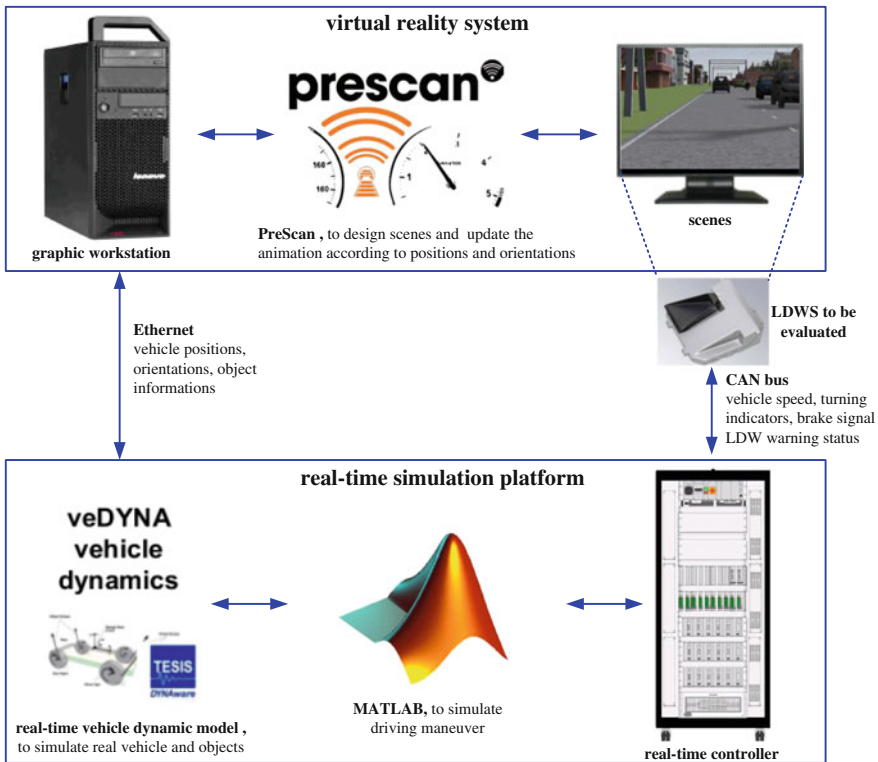


Fig. 45.1 LDWS test rig scheme

Table 45.1 The factors considered for LDWS performance evaluation

Main factors	Subfactors	Description
Road conditions	Lane marking types	Include single white continuous line, dual yellow continuous line, and one-side line
	Road types	Include curvature and slope
	Ambiguity of lane marking	Include newly paved concrete road, newly paved asphalt road, used concrete road, and used asphalt road
	Lane markers	Include arrows, words, and pedestrian crossing
	Facilities	Include guard rail, tunnel, over bridge, and building blocks
Weather conditions	Fog	Include no fog, middle fog, and heavy fog
	Rain	Include no rain, middle rain, and heavy rain
	Lighting conditions	Include against sunshine, and entering or exiting the tunnel
Traffic conditions	Vehicle types	Include motor vehicle, truck, motorcycle, and pedestrian
	Busyness	Include free driving and busy driving

45.3 Scenario Design

The scenarios of LDWS test rig are realized by virtual reality software PreScan. In order to evaluate the lane marker recognition ability more sufficiently, the designed scenarios shall cover these typical driving conditions as much as possible. Therefore, in the process of the scenario design, the factors such as road types, weather conditions, and traffic conditions shall be considered. Table 45.1 lists these specific factors important for LDWS performance evaluation.

Combining the standard scenarios in ideal environment conditions with these factors listed in Table 45.1, the sort tree method can be used to design the test cases of LDWS. This will, on the one hand, guarantee the coverage of these cases, and on the other hand, this will reduce the quantities of these cases and then improve the efficiency of the test. Figure 45.2 shows the typical scenarios created with PreScan.

45.4 Real-Time Vehicle Model

During the test, the LDWS controller will receive signals, such as vehicle speed, yaw rate, turning indicator, and system switch, and meanwhile, it will send signals such as operational status and warning status to vehicle; therefore, a real-time vehicle model like TESIS veDYNA is needed to replace a real vehicle so as to form a whole test loop.

During the process of vehicle maneuver design, the factors such as longitudinal speed, departure direction, departure speed, and depression signals (such as turning indicator) should be considered. A demonstration of lane departure maneuver is as

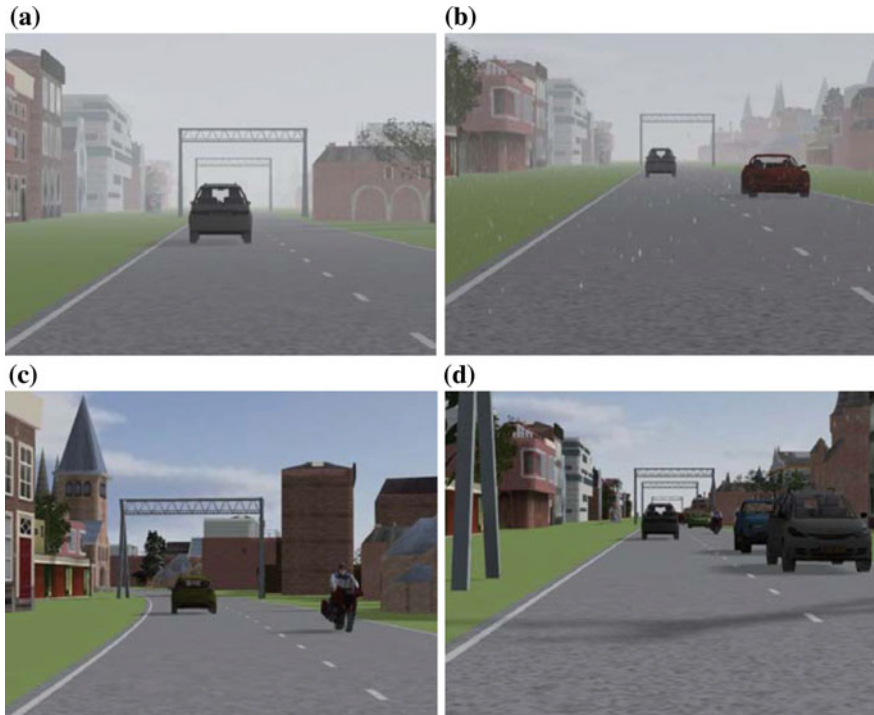


Fig. 45.2 Typical LDWS test scenes. **a** Foggy, straight (visibility = 500 m), **b** rainy, straight, **c** sunny, curve (R = 500 m), **d** busy traffic

shown in Fig. 45.3. During each test, the vehicle first drifts to one direction and then is corrected to its original lane, and after a while, it moves to the adjacent lane.

In this project, vehicle maneuver is programmed in MATLAB/Simulink and then integrated with vehicle dynamics of TESIS veDYNA. The longitudinal and lateral control interface is as shown in Fig. 45.4. The longitudinal motion is controlled by target speed, and the lateral motion is controlled by target lateral offset to the path center.

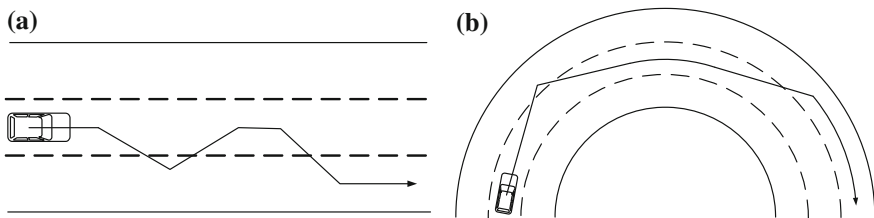


Fig. 45.3 Lane departure maneuver. **a** Departure in straight and **b** departure in curve

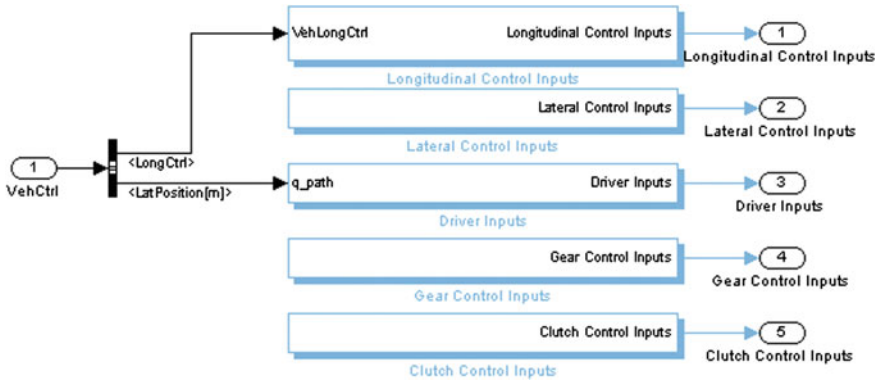


Fig. 45.4 The longitudinal and lateral control interface of TESIS

45.5 Test Application

The integrated LDWS test rig is as shown in Fig. 45.5. The monitor is covered by a dark box to prevent disturbance by the external light.

The assessment of LDWS consists of two parts: the capability to identify lane markings and the feasibility of warning mechanism. Vehicle orientation and vehicle position in relation to the lane markings should be taken into account for assessment. Figure 45.6 illustrates the classification of LDWS warning zone; the earliest warning line that varied with lateral drift velocity is located inside of lane boundary, while the latest warning line is located outside of lane boundary. If the outer edge of the corresponding front wheel locates in the warning zone when LDWS is active and there are no suppression conditions, LDWS warning is said to be reasonable. The area between two earliest warning lines is a no warning zone, and thus, the warning is not allowed. The missing warning means that no warning is triggered when the

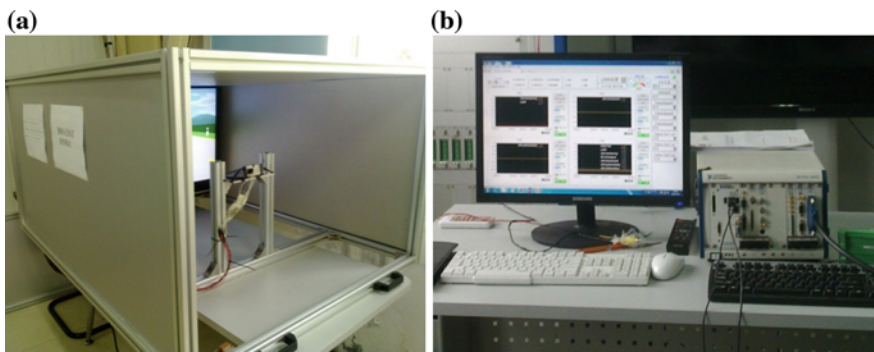
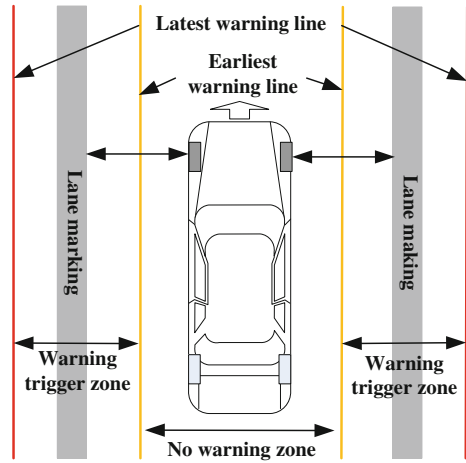


Fig. 45.5 LDWS performance test rig. a Virtual reality system and b real-time simulation platform

Fig. 45.6 LDWS warning zone demonstration



outer edge of the corresponding front wheel has already run cross the latest warning line. Warning should be suppressed when vehicle is corrected to its original lane.

The test is performed by using the scenarios defined in Sect. 45.2, and the virtual test system is developed as shown in Fig. 45.5. Figure 45.7 illustrates the test results of one supplier’s LDWS in two typical scenarios. Scenario 1 is with straight road, continuous lane markings, the weather is little rainy, vehicle maintains a constant speed at 65 km/h, and the lateral velocity is 0.2 m/s when drifting to left and changing lanes. Scenario 2 is with curve road, the curvature radius is 250 m, with discontinuous lane markings, the weather is sunny, vehicle maintains a constant speed at 65 km/h, and the lateral velocity is 0.2 m/s when drifting to left and changing lanes. For the warning status signal, 1 represents lane markings are detected and 3 indicates warning is generated. The outer edge of left front wheel relative to the central line of the road is the lateral offset, and the space between the earliest and latest warning lines is the warning trigger zone. Figure 45.7a shows that

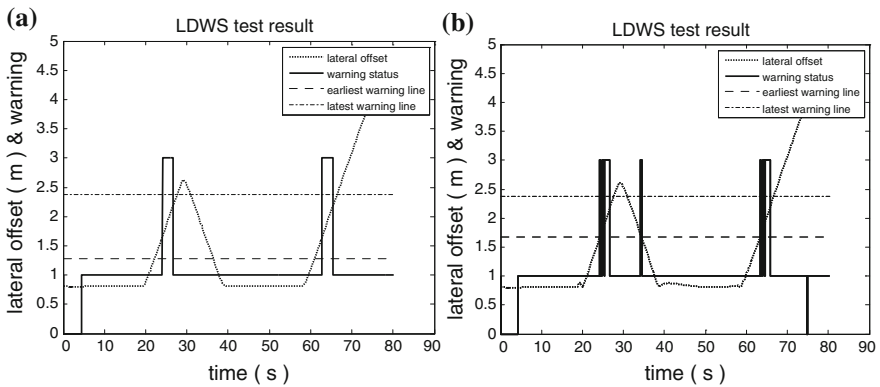


Fig. 45.7 Test results. **a** Scenario 1 and **b** scenario 2

Table 45.2 Results of LDWS performance test

LDWS	The percentage of lane marking recognition (%)	False non-alarm rate (%)	False alarm rate (%)	Suppression	One-side line
Supplier A	99.1	2	0	✓	×
Supplier B	91.3	5	2	✓	×
Supplier C	69.8	32	6	✓	×

a normal warning is triggered in scenario 1, and Fig. 45.7b indicates that the LDWS does not suppress warning when the vehicle is corrected to its original lane.

The same tests are performed for LDWS of another two suppliers, and the results are given in Table 45.2. The percentage of the lane marking recognition of supplier A is 99.1 %, the false non-alarm rate is 2 %, and the false alarm rate is 0, which will reduce the complaint from the driver. All these suppliers do not consider warning in one-side line conditions.

45.6 Conclusions

This paper developed a LDWS performance test rig based on real-time simulation and virtual reality technologies to solve the problems of the LDWS real vehicle test such as time- and cost-consuming. The key performance of LDWS is evaluated by various scenarios carefully designed for this purpose. The feasibility has been validated by testing several LDWS controllers of different companies. PreScan is a powerful tool for scene simulation, so this test rig can cover the test of any user-defined road geometry, lane marking type, lane marking color, road color, maneuver, and traffic object, it will also cover the various weather conditions such as sunny, rainy, foggy, and against the sunshine. What is more, it can also contain these complex road and traffic conditions such as shadow, tunnel, over bridge, hanging sign, and traffic flow. Besides LDWS, the test rig can be used for evaluating other camera-based active safety systems such as forward collision warning (FCW), lane-keeping assistant (LKA), pedestrian detection (PD), traffic sign recognition (TSR), parking assistant (PA), and blind spot detection (BSD).

References

1. ISO 17361 (2005) Intelligent transport systems-lane departure warning systems—performance requirements and test procedures
2. Zhang Q, Gao F (2011) A test rig and method for vehicle lane departure warning system. Patent of invention CN102313651A, (in Chinese)

3. Baderschneider M, Mertke T (2005) Test system for camera-based driver assistance systems, TESIS DYNAware GmbH/Bertrandt Ing. GmbH, Büro
4. Gunia DID, Schüling DIFHJ (2011) Model-based testing of Ford's lane keeping system. Industry measuring and testing
5. PreScan Help (2013) PreScan R6.3.0, TASS TNO

Chapter 46

Research of Distributed Vehicle Electronic and Electrical Architecture

Libo Zhang, Dongfeng Zhao and Junting He

Abstract Two development trends (integrated and distributed) of the vehicle electronic and electrical architecture as well as their advantage and disadvantage are analyzed. Based on the detail research to the distributed vehicle electronic and electrical architecture, the criteria of electronic and electrical function distribution and network design are defined. The criteria are applied to the electronic and electrical architecture development of a luxury car. The pilot car travels smoothly for approximately 5,000 km.

Keywords Electronic and electrical architecture · Distributed · Vehicle network

46.1 Introduction

46.1.1 Overview of the Vehicle Electronic and Electrical Architecture

To meet the ever-increasing demands of energy conservation, environmental protection, safety, comfort, convenience, entertainment, and luxury, more and more electronic and electrical equipment has been applied in automobiles, and as a result, the vehicle comprehensive performance has been improved greatly.

According to the analysis of the current market situation of China's automobile electronic industry from <Business information network>, the cost proportion of electronic and electrical equipment in the global vehicles cost has been increasing continuously. The data are 2 % in 1970, 5 % in 1980, 15 % in 1990, 20 % in 2000, and 25 % in 2012, and it is expected to rise to 50 % by 2015 (see the literature [1]).

L. Zhang (✉) · D. Zhao · J. He
Automotive Electronics Department, R&D Center, China FAW Co. Ltd., Changchun, China
e-mail: zhanglibo@rdc.faw.com.cn

The growing complexity of electronic and electrical system brings challenge for the design of vehicle electronic and electrical architecture. To meet the requirements of low cost and high reliability, domestic and foreign automobile manufacturers have put up their own development platform of vehicle electronic and electrical architecture.

There are two development trends of the vehicle electronic and electrical architecture. One is integrated and the other is distributed.

46.1.2 Overview of the Integrated Vehicle Electronic and Electrical Architecture

The advantage of integrated vehicle electronic and electrical architecture is that all the functions are realized only by a few ECUs (electronic control units). The total cost of electronic and electrical equipments is lower because of the simple architecture and low number of ECUs.

However, the integrated vehicle electronic and electrical architecture has some disadvantages too.

1. The layout of each ECU in the car is more difficult because of the larger ECU size.
2. There are many pins in each ECU and more wiring harness connected to ECU which make the layout and check of wiring harness difficult.
3. ECU replacement or repair cost is higher when it is damaged because the ECU cost is high.
4. The ECU functions in different cars are not the same, which make the ECU cannot be used in different cars.

46.1.3 Overview of the Distributed Vehicle Electronic and Electrical Architecture

Further decrease in ECU integration level is a distinctive feature of distributed vehicle electronic and electrical architecture. Take the electronic and electrical architecture of comfort systems as an example. It is impossible to meet the ever-increasing control requirements related to comfort systems using only one body control module (BCM). Therefore, the multiple BCM are needed. The BCMs share information through the controller area network (CAN) or local interconnect network (LIN) communication, as shown in Fig. 46.1.

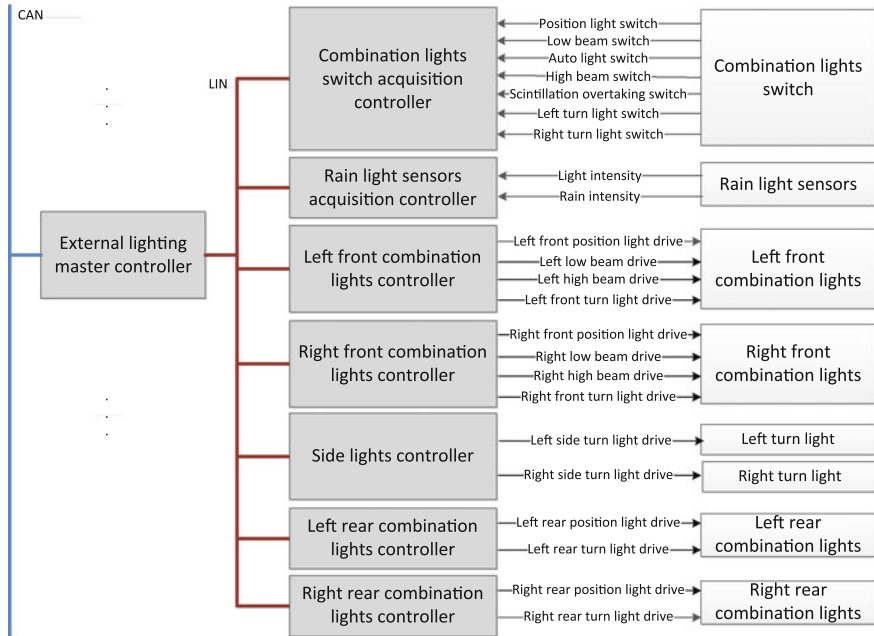


Fig. 46.1 An example of distributed vehicle electronic and electrical architecture of comfort systems

The distributed vehicle electronic and electrical architecture has many advantages. First, ECU is easy to reuse in different cars because they have the same function. Second, the layout for vehicle is easy as smaller ECU size, and some ECU can even be integrated into the actuator. Finally, the length, quantity, and weight of wiring harness are reduced greatly as the ECU is near the actuator. It not only makes car maintenance easier but also reduces the car weight. However, the distributed vehicle electronic and electrical architecture has two disadvantages too. One is the higher total ECU cost and the other is the ever-increasing difficulty of electronic and electrical architecture design.

46.2 The Criteria of Distributed Vehicle Electronic and Electrical Architecture

Most functions are performed through the coordinated control of several ECUs in the distributed vehicle electronic and electrical architecture, which increase the difficulty of electronic and electrical architecture design in two aspects. One is the function distribution of vehicle electronic and electrical system and the other is the network design of vehicle electronic and electrical function.

46.2.1 The Criteria of the Function Distribution of Distributed Vehicle Electronic and Electrical Architecture

The function distribution criteria of the distributed vehicle electronic and electrical architecture are to distribute the three major function, switch and sensor signal collecting, and control logic performing and actuator driving to different ECU as far as possible.

For example, the direction flashing function of left turn signal lamp has two input parameters and four output parameters. The input parameters are ignition switch signal and turn switch signal, while the output parameters are the four turn signal lamp driving signal, that is, the left front turn signal lamp, left-side turn signal lamp, left rear turn signal lamp, and turn signal lamp indicator. Based on the above-mentioned criteria, the function distribution of the direction flashing function is shown in Fig. 46.2. The passive entry and push start (PEPS) system is responsible for the ignition switch signal collecting; the driver front panel controller (DFPC) is responsible for the turn switch signal collecting; the left front controller (LFC) is responsible for driving the left front turn signal lamp; the driver door control unit (DDCU) is responsible for driving the left-side turn signal lamp; the rear combination light controller (RCLC) is responsible for driving the left rear turn signal lamp; the instrument cluster (IC) is responsible for driving the left turn indicating

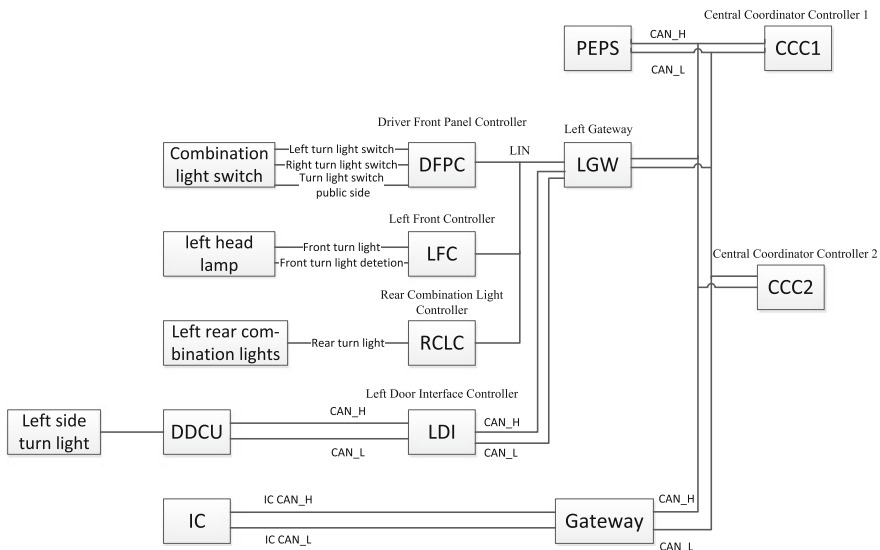


Fig. 46.2 The system wiring diagram related with the direction flashing function of left turn signal lamp

light, and the central coordinator controller (CCC) is responsible for performing the control logic of direction flashing function.

Such designed distributed vehicle electronic and electrical architecture designed has following advantages:

1. It is not needed for information communication between the signal collection ECU and actuator driving ECU, so that the ECU function is independent and simple, which results in the modular design and lower development cost.
2. Because the functions of signal collection ECU and actuator driving ECU are simplified, the ECU PCB size is getting smaller and some of them can even be integrated into sensors or actuators. It brings convenience to the ECU layout in the cars.
3. Through the modular design, the functions of signal collection ECU and actuator driving ECU are identical in different cars so that they can be used alternatively in different cars. It not only improves the reliability but also reduces the cost.
4. Because the signal collection ECU is near the sensor and the actuator driving ECU is near the actuator, the length, quantity, and weight of wiring harness are reduced greatly. It not only makes vehicle maintenance easier but also reduces the cost of wiring harness.

46.2.2 The Criteria of the Network Design of Distributed Vehicle Electronic and Electrical Architecture

The distributed vehicle electronic and electrical architecture is composed of communication network and power supply network. The architecture is hierarchical structure. The top layer is called the backbone network, and the layers below it are called local area network (LAN). Each ECU is distributed to the same segment of communication network and power supply network. For example, CCC is named the electrical equipment of backbone network that means CCC is distributed to backbone network of the communication network and backbone network of power supply network.

The criteria of the network design of distributed vehicle electronic and electrical architecture are described as below:

1. Based on the requirement of real time and importance, each ECU should be assigned to at least one segment of the network. If the ECU function is important or time critical, the ECU will be designed as an electrical equipment of backbone network; otherwise, the ECU will be designed as an electrical equipment of LAN.
2. The following factors should be taken into account when designing the architecture of local area network.

- (a) All electrical equipments controlled by the ECU in the same LAN should start working and stop working under similar conditions. For example, if all electrical equipments controlled by the ECU of LAN1 do not work when the ignition switch is in “off” position, then the intelligent power supply (IPS) controller could turn off the power supply for LAN1 when the ignition switch is turn to “off” position to save power.
- (b) The ECUs in the same LAN should be close to each other in order to reduce the wiring harness length, improve the communication effect, and reduce failure rate.
- (c) The total electrical load of all electrical equipments controlled by the ECU of each LAN should be close to each other in order to obtain the power supply balance among different LANs.
- (d) The number of LANs should be reasonably defined according to communication requirements between each ECU. If the number of LANs is too small, bus load may be too high, because the numbers of signal are too many in one LAN. Conversely, if the LANs are excessive in quantity, the gateway complexity and its development cost will be increased and the signal delay time will be extended.

46.3 The Application of Distributed Vehicle Electronic and Electrical Architecture in a FAW Luxury Car

46.3.1 The Configuration of Distributed Vehicle Electronic and Electrical System

The distributed vehicle electronic and electrical architecture has been applied to a luxury car from First Automobile Works of China (FAW). The network architecture of the car is shown in Fig. 46.3. There are total of 64 ECUs in the network. They communicate with each other through 14 CAN segments, 10 LIN segments, and 2 KWP2000 network segments to realize the electronic control of power train systems, security systems, chassis systems, information and entertainment systems, and comfort systems.

46.3.2 Improve the Reliability of Vehicle Electronic and Electrical System Using Double CCCs

The CCC is the electrical equipment of backbone network. It is the core of comfort systems to realize distributed electronic and electrical control of external lighting system, internal lighting system, and security video system.

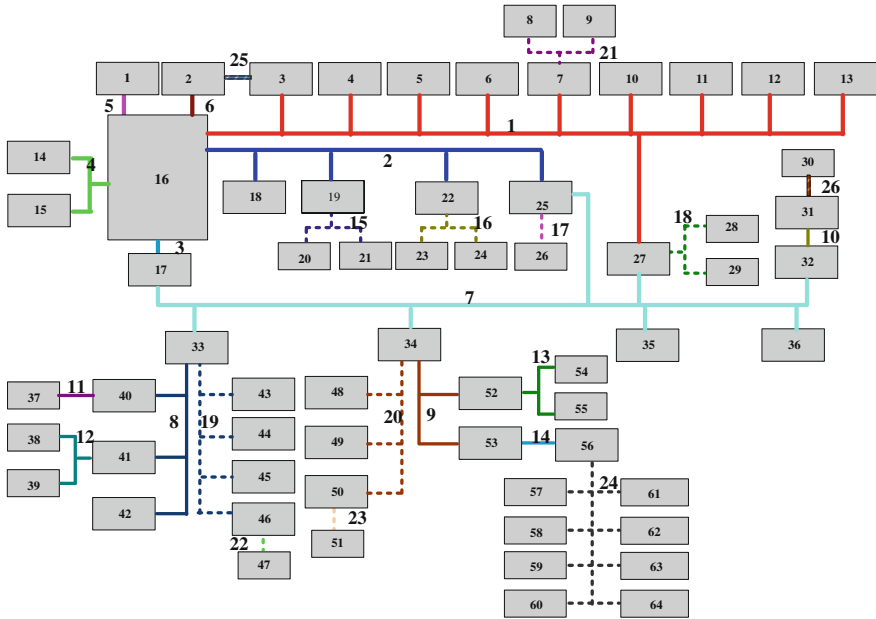


Fig. 46.3 The network architecture of distributed vehicle electronic and electrical architecture of a luxury car

The CCC collects the information related to the control logic of above functions through vehicle network and then handles the event needed to be coordinated between each ECU based on priority, and finally, the CCC sent the results in the form of command to each ECU by CAN or LIN, and the ECUs execute a command to drive actuator.

In order to improve the reliability of comfort system function, double CCC, namely CCC1 and CCC2, is used to coordinate the function of central control. The function of CCC1 and CCC2 is the same. CCC1 and CCC2 monitor each others working state so as to improve the system reliability. At the same time, the IPS monitors the working states of CCC1 and CCC2 and sends out the trouble information in time when one or two CCC failures occur.

46.4 Conclusions

To meet the requirements of low cost and high reliability of automotive electronic and electrical design, FAW has begun to study the distributed vehicle electronic and electrical architecture since 2011. The criteria of electronic and electrical function distribution and network design have been defined based on the research. At the same time, the electronic and electrical system specification, the CAN/LIN network

communication specification, and the product standard of each ECU in vehicle electronic and electrical architecture are defined. These criteria and specification have been applied to the electronic and electrical architecture development of a luxury car.

The vehicle wiring harness and related electronic and electrical devices developed based on above criteria and specification have passed the product certification tests. All tests of product, including function check, environment test, ECU performance test, connector performance test, electromagnetic compatibility test, static discharge performance test and the durability test, are subject to the relevant national standards. The pilot car has run smoothly for approximately 5,000 km.

Acknowledgments The research is support by the project “Smart car network R&D and industrialization” from the Electronic Development Fund directed by the Ministry of Industry and Information Technology of the People’s Republic of China.

Reference

1. The article “analysis of the current market situation of China automobile electronic industry” from <Business information network> (<http://www.askci.com/>). Accessed 4th Jun 2014

Chapter 47

The Gasoline Engine Starting Strategy Based on Air–Fuel Ratio Control

Zhongtian Chen, Kai Wang, Chen Shen, Feng Xu, Long Qin, Jianbo Zheng, Xue Lei and Fanwu Zhang

Abstract During the engine starting process, the speed always gets up and back to idle speed slowly, in order to solve these problems, and at the same time to control the combustion during the starting process more accurately, a gasoline engine starting strategy based on air–fuel ratio (AFR) control is developed, including intake airflow control, AFR control, and so on. By selecting the appropriate airflow and AFR, the fuel injection amount is calculated, and the test results show that the engine can start up quickly and reliably, and the starting speed will have a smooth transition to target idle speed.

Keywords Gasoline engine · Start · Intake airflow · A/F ratio

47.1 Instruction

During engine start-up period, the speed always gets up and back to idle speed slowly, and the engine could appear harmoniously shaking. In order to make the engine rotate normally as soon as possible, five or six times more than the actual fuel amount would be injected in the EFI gasoline engine. But it leads to two problems; on the one hand, although we have provided a lot of fuel, because of the cold temperature, the conditions for fuel atomization and evaporation are unfavorable. Part of fuel will be condensated on the combustion chamber and the cylinder walls. Also, the intake manifold airflow velocity is low, there is still some fuel condensation in the intake manifold wall, and all of these would bring difficulty in starting. On the other hand, global environmental concerns have led to increase stringent

Z. Chen (✉) · K. Wang · C. Shen · F. Xu · L. Qin · J. Zheng · X. Lei
Electrical and Electronic Department, Technology Center, Dongfeng Motor Corporation,
Wuhan, China
e-mail: chenzt@dfmc.com.cn

F. Zhang
General Engineer Office, Technology Center, Dongfeng Motor Corporation, Wuhan, China

vehicle emission regulations. Obviously, offering of so much fuel is not conducive to emission. In order to meet the latest and future regulations, it is particularly important to decrease cold start hydrocarbon concentrations in the exhaust gas and choose the appropriate strategy to control concentration of mixed gas [1].

In this paper, a gasoline engine starting strategy based on air–fuel ratio (AFR) control was developed. It is integrated to the independently developed ECU, by the bench test and vehicle verification with a 1.6-L engine, and the test results show that this strategy can ensure reliable starting and has a satisfactory effect.

47.2 The Factors of AFR Control

The main control objective of starting condition is engine speed, and during the process of starting, the speed should have obvious and reasonable speedup, and after the starting is completed, it could have a smooth transition to target idle speed.

For a gasoline engine, only both the amounts of airflow and fuel for combustion change over time and are strictly matched, and the engine speed could meet these requirements. AFR has direct relationship with intake manifold airflow and the amount of fuel injected which are directly affecting the speed change. The ideal AFR is 14.7, but the AFR requested must be less than 14.7 under the start condition. The changing temperature will affect the fuel evaporation and film forming; also, the changing speed has an effect on intake manifold pressure which can make the fuel evaporate in different rates. The air/fuel mixture will be back into the combustion chamber. Therefore, the engine speed and water coolant temperature are the major influencing factors from the outside.

Figure 47.1 shows the initial calibration AFR when the engine speed is 200 rpm under different water coolant temperatures. When the temperature is below zero, the fuel evaporation is very poor, and we set the initial starting AFR much leaner than 14.7. With the rising of the temperature, the fuel attached on the intake manifold wall and suspended in the manifold begins to volatilize better. More

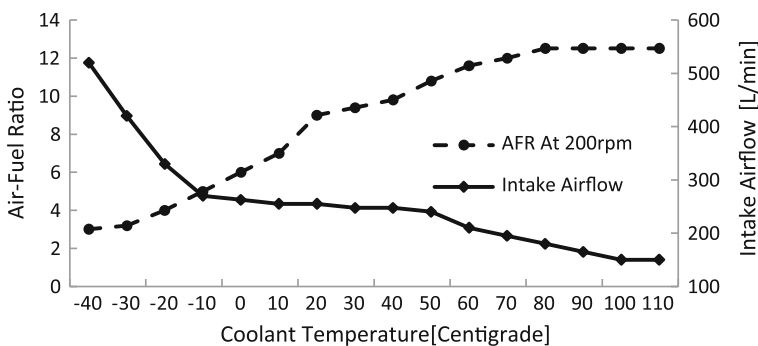


Fig. 47.1 Relation between the coolant temperature and initial AFR/intake airflow

oil-gas mixture enters into the cylinders. But the phenomenon of in completed volatilization always exists. So the initial requested AFR is always leaner than 14.7. The amount of the intake airflow is decided by temperature too. Only more fuel is unrealistic, leaner AFR requests more air, and a lager mass of air would be better for mixture entering into the cylinders quickly at a low engine speed when the engine starts.

47.3 Realization with Simulink and Verification

In this section, the main principle of the control strategy mentioned in this paper is that by reading engine sensor signal value (cooling the engine based on the speed, temperature, and crankshaft angle), the software calculates and adjusts the airflow rate and air-fuel ratio in real time. And after these are completed, we will get the basic injection pulse, and then, the pulse will pass to the other control units for further modification to achieve precise control. This paper will focus on intake airflow and start AFR control strategy. Figure 47.2 shows the block diagram model of control strategies in start-up condition.

47.3.1 Control Strategies

First, at the beginning of start-up, both the airflow and AFR control are open loop. The engine rotation is driven by the starter motor at low speed. Usually, we will set the predetermined basic starting airflow in the rich level, because of the difficulty to inhale airflow. As the speed rises, the intake airflow should be decreased gradually.

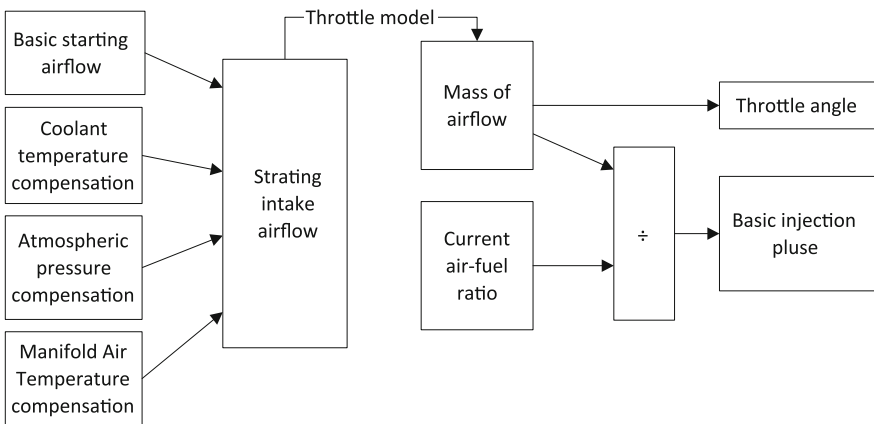


Fig. 47.2 The block diagram model of control strategies in start condition

At the same time, different air pressures and air temperatures would affect the oxygen level of the same volume of air. Therefore, the volume needs to be corrected. The calculation formula of the volume of intake airflow is given by Eq. (47.1).

$$V_{\text{AirFlow}} = V_{\text{CT}} \times \varphi \left(\frac{t_{\text{MAT}}}{t_{\text{REF}}} \right) \times A_{\text{AirPres}} + V_{\text{AirPres}} \tag{47.1}$$

where V_{AirFlow} is the current request volume of intake airflow. V_{CT} is the basic volume of airflow calibrated according to coolant temperature, $\varphi \left(\frac{t_{\text{MAT}}}{t_{\text{REF}}} \right)$ and A_{AirPres} are air temperature and atmospheric pressure coefficient, and V_{AirPres} is the pressure compensation. The control method is to reduce the intake airflow by decreasing throttle valve opening angle. The requested volume will reduce to the desired idle airflow in a predetermined period, with a decreasing factor gradually. Therefore, the engine speed reaches the target value, and the accuracy and stability of the quick warm-up system during the start-up period can be improved [2].

In order to ensure that the speed is not drastic fluctuations after entering at the idle speed, the engine have a quick warming-up process, and the air intake control method required for realizing the idle intake airflow earlier is described here. It is better to set certain conditions for the airflow control jumping into the closed loop as soon as possible. With setting values of the difference between actual and target speed and the difference between the airflow and starting idle target volume, when anyone of the two difference is reduced to a certain range, we think the engine meets the conditions, and it changes to closed-loop control. Obviously, the two differences would be influenced by external factors (e.g., coolant temperature).

As shown in Fig. 47.3, at the beginning of start-up, the program will read the initial storage AFR based on the current coolant temperature and speed in the ECU. As the starting process going on, the AFR rises gradually, to reduce the amount of fuel and emissions and optimize combustion, as time goes by, the requested AFR will close to the ideal AFR (14.7) more and more.

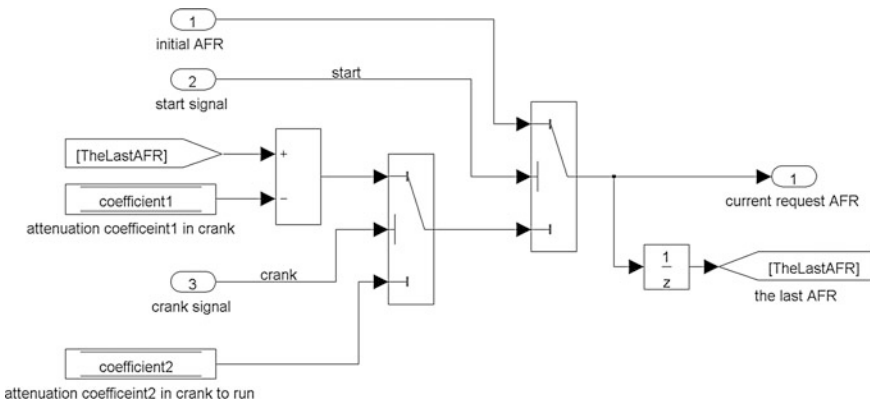


Fig. 47.3 The block diagram model of AFR control

The system has two steps: First, the speed goes up driven by the starter after turning the key (crank), because of speed drastically changing in this period, in order to avoid the speed missing control caused by the AFR changing. In this step, we add the attenuation coefficient when crankshaft turns to specific angle. The angle and coefficient for AFR decay are decided by coolant temperature. Second, when the rising speed exceeds the threshold (crank to run), the starter will stop working. The speed continues to rise and then begins to decline after a period of time. The AFR will increase to limit value of 14.7 in a relatively smaller attenuation coefficient, small steps (relative to step 1) (Fig. 47.4). The above period and coefficient factors are calibrated with the real vehicle determined by temperature.

Now, we have known the current request air intake and AFR. In throttle position system control model, we have known the corporeal quantity of air ($M = 29 \text{ g/mol}$), and we can use ideal gas equation of state to calculate the density correction coefficient (ρ_{Air}) according to the air pressure and temperature, as shown in Eq. (47.2).

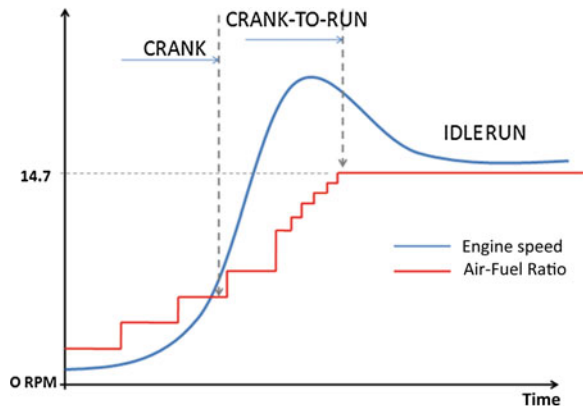
$$\rho_{\text{Air}} = \frac{M}{V} = \frac{nM}{\frac{RT}{P}} = \frac{MP_{\text{Air}}}{RT_{\text{Air}}} \tag{47.2}$$

where M is the molecular mass of air, P_{Air} is the air pressure, T_{Air} is the air temperature, and R is the ideal gas constant.

In the engine control system based on torque control, the requested volume of intake airflow (V_{AirFlow}) will affect the calculation of throttle opening angle and volumetric efficiency (VE) directly. Here, no longer say the details about this and just follow these easy instructions. VE multiplied by the engine size and density correction coefficient (ρ_{Air}) can get requested air mass under standard conditions. The requested mass and current starting air–fuel ratio (R_{AF}) can be use to calculate starting basic injection pulse width according to the Eq. (47.3).

$$T_{\text{Inj}} = \frac{\dot{m}}{R_{\text{AF}} \times N_{\text{Cyl}} \times C_{\text{Inj}}} \tag{47.3}$$

Fig. 47.4 The change of air–fuel ratio



where N_{Cyl} is the number of engine cylinder, and C_{Inj} is the characteristic constant of injector. At this point, we have got the real time changed basic injection pulse for starting. To be clear, this pulse needs to be corrected according to the battery voltage and the starting time. A lot of factors for AFR closed-loop control also need to be considered such as catalyst. And these will be described in further.

47.3.2 Vehicle Verification

To verify the starting performance of this control strategy, we integrated the control strategy in our EMS, completed code generation by MATLAB/Simulink, and downloaded to the ECU. In the vehicle test, we calibrated parameters of starting at different temperature to control engine starting, meet the requirements, and observe the starting results with INCA software and ETAS hardware equipment.

The results (Fig. 47.5) show that speed rises up to 400 rpm after the battery voltage dropped down in about 300 ms. The speed continues to rise to about 1,600 rpm and back to current target idle speed (about 900 rpm at this temperature). AFR increases to 14.7 gradually, and the volume of intake airflow decreases to the idle intake airflow control. The speed has a smooth transition to target idle speed, without speed drop-off, and the vehicle does not appear obvious jitter. The control strategy can meet the requirements of real vehicle starting.

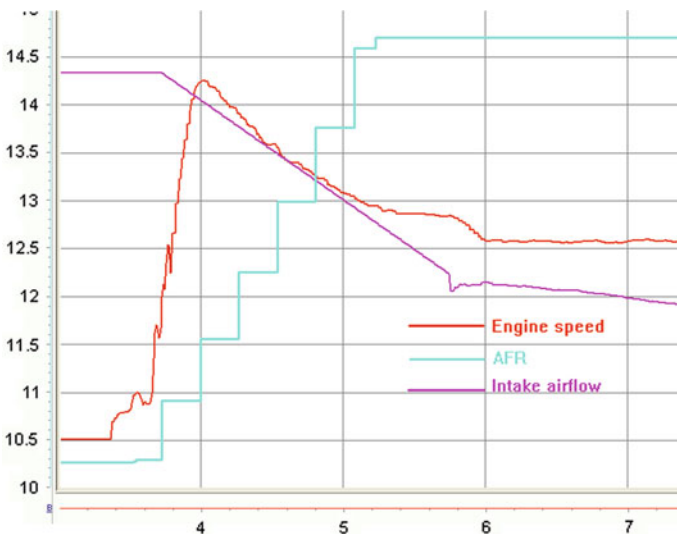


Fig. 47.5 Test results

47.4 Conclusions

A gasoline engine starting strategy based on AFR control was developed for engine start-up. The starting is a complicated nonlinear dynamic process, and by controlling the AFR precisely, we can ensure the engine start smoothly, calculate and select appropriate amount of fuel injected, and request air intake. The test results show that the engine can start up quickly and reliably. The throttle angle and injection pulse can decrease in accordance with the requirements of the control system, and the control strategy also meets the requirements of the engine start-up. In this paper, only the AFR control is studied for ensuring the start-up control to be stable and reliable. It is important to note that the ignition advance angle also played an important role in this process, some other compensations for fuel also need more study, and in the future, efforts will be done about these issues in further research, for optimizing the start-up performance and emissions.

References

1. Oguma H et al (2003) Development of third generation of gasoline P-ZEV technology. SAE Technical Paper 2003-01-0816
2. Ueno M, Akazaki S, Yasui Y, Iwaki Y (2000) A quick warm-up system during engine start-up period using adaptive control of intake air and ignition timing. SAE Technical Paper 2000-01-0551

Chapter 48

Research on Diagnostic Strategy of Planar-type Oxygen Sensor Deactivation on Gasoline Engine EMS

Long Qin, Feng Xu, Jianbo Zheng, Fanwu Zhang, Yongyi Huang, Zhongtian Chen, Xue Lei and Liuchun Yang

Abstract On-board diagnosis (OBD) system is the key part of national emission standard, and gasoline engine oxygen sensor deactivation diagnosis is one of the most important OBD functions. In this study, we, according to the principles of planar-type oxygen sensor, develop the main fault types of oxygen sensor deactivation, which consist of electrical fault and rational fault. We analyze the diagnostic strategy of the both faults, generate the strategy model by Simulink, and offer the diagnosis flowcharts. At last, we use the sensor deactivation simulators to simulate the faults. With hardware-in-the-loop (HIL) bench and chassis dynamometer tests, the results show that the diagnostic strategy of oxygen sensors is rapid and precise, and it meets the requirements of national standard.

Keywords EMS · OBD · Oxygen sensor · Emission

48.1 Introduction

The oxygen sensors are the essential components of modern engine management system (EMS), which are to detect the oxygen content in the exhaust gas and judge the real air/fuel mixture of engine. Once oxygen aging, poisoning or break, its heating element damaged, or inaccurate sensor signal value, the injection pulse width would be imprecisely controlled, and the engine will be no longer in the optimal air/fuel mixture combustion, which definitely deteriorate the emissions and reduce fuel economy [1]. GB18352.3-2005 Limits and measurement methods for

L. Qin (✉) · F. Xu · J. Zheng · Y. Huang · Z. Chen · X. Lei · L. Yang
Electrical and Electronic Department, Technology Center, Dongfeng Motor Corporation,
Wuhan, China
e-mail: qinlong@dfmc.com.cn

F. Zhang
General Engineer Room, Technology Center, Dongfeng Motor Corporation, Wuhan, China

emissions from light-duty vehicles (III,IV) defines: If emissions of engine exceed the OBD limits, the OBD system needs to light the malfunction indicator lamp (MIL), and record and store the corresponding fault codes, in order to get the fault information, diagnose and repair to repair factory [2]. In this paper, the diagnosis of oxygen sensor deactivation is focused on. Based on the platform of 1.6 L inline 4-cylinder engine, the oxygen sensor fault diagnosis strategy is developed, and the emission characteristics are analyzed with the sensor deactivation simulators.

48.2 Principles of Oxygen Sensor

Two planar oxygen sensors, types of zirconium oxide and heating, are installed in engine's exhaust pipe. Front oxygen sensor is in front of the three-way catalyst converter (TWC), and rear oxygen sensor is behind the TWC [3]. The sensor can be highly simplified like a small battery. The sensing element is placed so that one side is in contact with the ambient air and the other side is in contact with the engine exhausts. On the basis of the electrochemical theory, an electric potential difference will be generated, due to the difference in oxygen molecules on the two sides of the sensor. A high sensor voltage, above 600–700 mV, indicates that there is less oxygen in the exhausts compared to the ambient air. This means the combustion had a rich air/fuel mixture. On the contrary, a low voltage, below 200–300 mV, indicates that there was no major difference in the amount of oxygen molecules, meaning the combustion had a lean air/fuel mixture. The typical sensor voltage for planar sensor is as shown in Fig. 48.1.

The main purpose of the front oxygen sensor is to provide feedback information of the air/fuel mixture composition (rich or lean) to the EMS, for it to be able to adjust the air/fuel mixture with closed loop control [1, 4]. The sensor itself and its proper function are highly related to emission when it comes to diagnostic aspects of the EMS system. Disturbances of the sensor signal will highly affect the emissions. The main purpose of the rear oxygen sensor is to provide feedback information about the oxygen content in the exhaust emissions behind the catalytic converter. The information is used for diagnostics of the catalytic converter and for

Fig. 48.1 Typical sensor voltage for planar oxygen sensor

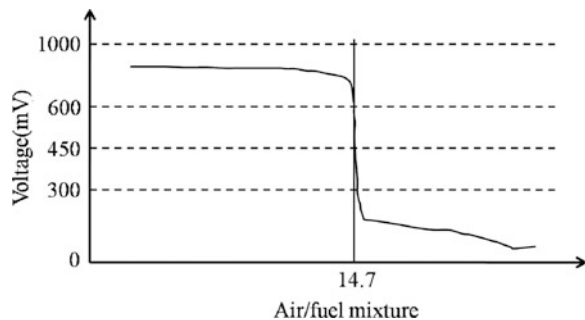
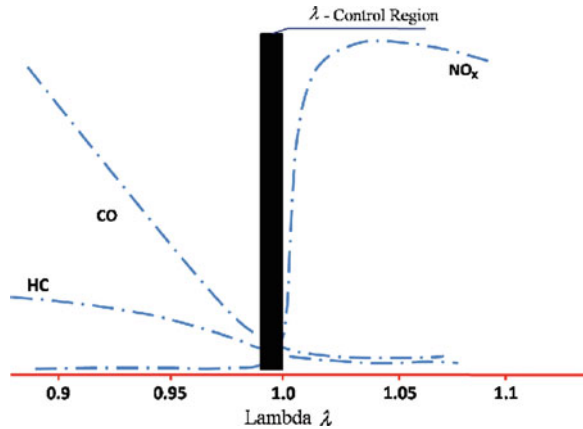


Fig. 48.2 The relationship between lambda and emissions



fine tuning of the air/fuel mixture. The lambda control strategy may differ between OEMs, but the feedback sensor normally used is oxygen sensor. As shown in Fig. 48.2, a lean air/fuel mixture (>1.01) will be heavily punished with NO_x emissions, while a rich air/fuel mixture (<0.98) will be punished with higher CO and HC emissions out from the engine.

48.3 Analysis of Diagnostic Strategy and Function Realization with Simulink

In this study, the oxygen sensor deactivation reflects on the distortion of the sensor signal. The signal distortion includes sensor electrical faults and rational fault. Specifically, electrical faults are covered with sensor short to ground (SCG), short to power (SCP), and open circuit (OC). Rational faults indicate sensor’s slow response resulting from rich-to-lean switching time or lean-to-rich switching time too long [5].

48.3.1 Oxygen Sensor Electrical Fault

When front oxygen sensor is shorted to ground, it indicates lean mixture as feedback to the fuel control. The fuel control system will respond by increasing the fuel amount to make the engine run rich. As a result, the rear sensor will react on the rich mixture and its signal voltage will increase [6]. To avoid misdetection, only if the front signal is low and the rear signal is high, the front sensor is shorted to ground.

The rear sensor, as the long-term fuel trim, has little influence on fuel injection system. When the rear sensor is shorted to ground, the rear signal is low and the front signal almost has no any abnormality.

If any of the two sensors is shorted to power or has an OC, the signal will be high. But the level the signal saturates on when experiencing a SCP or OC depends on the type of AD converter.

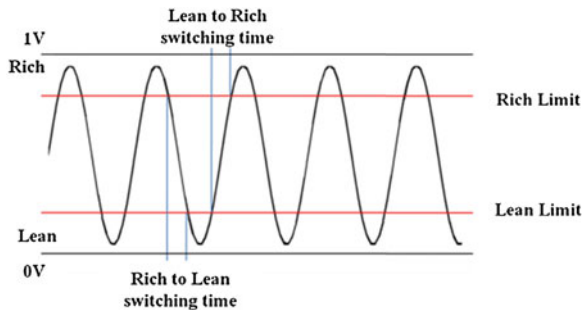
48.3.2 Oxygen Sensor's Rational Fault

The diagnostic strategy for the front oxygen sensor rationality diagnosis is to measure the time for the sensor to transition between rich and lean. Both the rich-to-lean time and the lean-to-rich time will be measured for the front sensor. The diagnostic strategy for the rear sensor is to measure the rich-to-lean switching time during a deceleration fuel cutoff. Typical oxygen sensor response is shown in Fig. 48.3.

When the switching time from lean-to-rich or rich-to-lean exceeds a certain calibration limit, it indicates that the sensor response is too slow, and thus, the engine out emissions are not controlled in a good way. The switching times from lean-to-rich and from rich-to-lean will be measured when the vehicle is driven in steady-state conditions, meaning steady engine load and engine speed. Several switching times are measured, and the average for both lean-to-rich and rich-to-lean are compared to the fail thresholds to decide pass or fail. The image below the lean-to-rich and rich-to-lean is defined, as well as the period time. The rich-to-lean and lean-to-rich times is averaged over a calibrated number of periods in order to avoid one single noise on the sensor to cause a misdetection of a failure.

When the switching time from rich-to-lean exceeds a certain calibration limit, it indicates that the sensor response is too slow, and thus, the catalytic converter diagnosis may give a better test results than what is true and also the long-term fuel trim based on the rear oxygen sensors may be wrong, which may result in uncontrolled emissions out from the engine. The switching time from rich-to-lean will be measured when the vehicle is driven in steady-state conditions and a

Fig. 48.3 Typical oxygen sensor response



deceleration fuel cutoff is induced by the driver and the rear oxygen sensor signal changes from high to low. Rich-to-lean switch time is compared to the fail threshold to decide pass or fail.

48.3.3 Function Realization with Simulink

To avoid misdetection, only with no fails of other related sensors reported, and in steady-state conditions for engine, oxygen sensor deactivation diagnosis test pass or fail reported to the diagnostic kernel [6].

According to the previous analysis, a set of oxygen sensor’s diagnostic strategy, with the period of 0.1 s, is generated with Simulink. The Simulink model about oxygen sensors electrical faults diagnosis is shown in Fig. 48.4 (taking the front oxygen sensor shorted to ground fault diagnosis as an example, and the other fault diagnosis are similar). Figures 48.5 and 48.6 show these Simulink models about the rational fault diagnosis of the front and rear sensor.

Specific diagnosis procedure about these Simulink models is shown in Figs. 48.7, 48.8, and 48.9, respectively. Specially, the Fig. 48.7 shows the diagnosis flowchart of the front oxygen sensor SCG. Figure 48.8 represents the diagnosis flowchart of the front oxygen sensor rational fault. Figure 48.9 illustrates the diagnosis flowchart of the rear oxygen sensor rational fault. As for the rational fault diagnosis, the switching time has certain stability for its non-sudden change in the time domain, so it is indispensable to filter the result of the measured switching time,

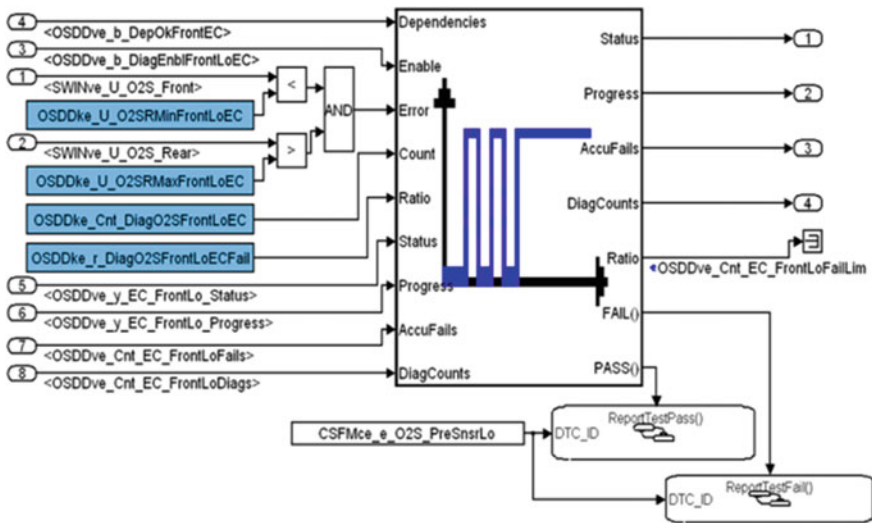


Fig. 48.4 Simulink model about the front oxygen sensor SCG

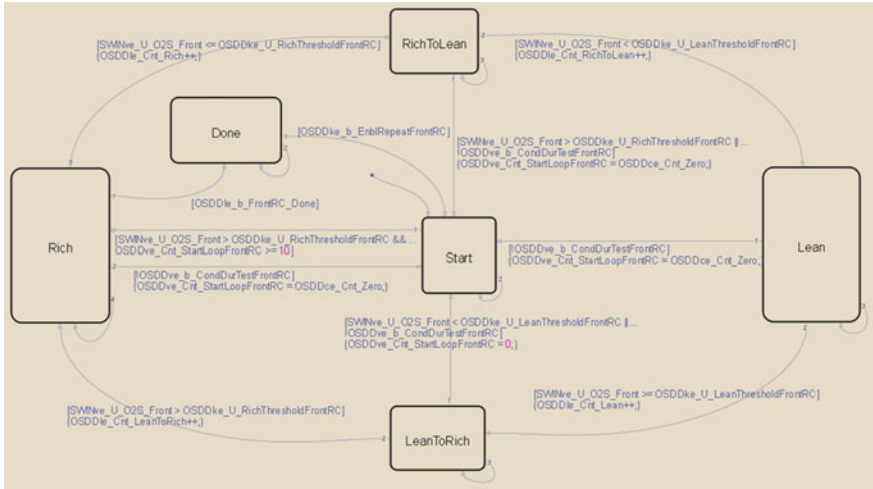


Fig. 48.5 Simulink model about the rational fault diagnosis of the front sensor

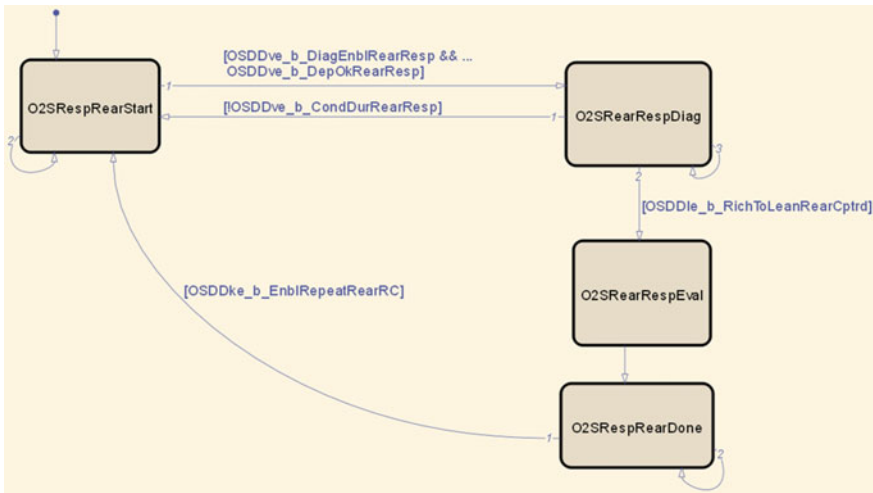


Fig. 48.6 Simulink model about the rational fault diagnosis of the rear sensor

$$t(n) = t(n - 1) + k[x(n) - t(n - 1)], \quad n = 1, 2, 3 \tag{48.1}$$

where $x(n)$ is the current unfiltered switching time; $t(n - 1)$ is the last switching time after filtering; $t(n)$ is the current switching time after filtering; the initial value $t(1)$ is set as the fail threshold; and k is the coefficient of the filter. At last, compare

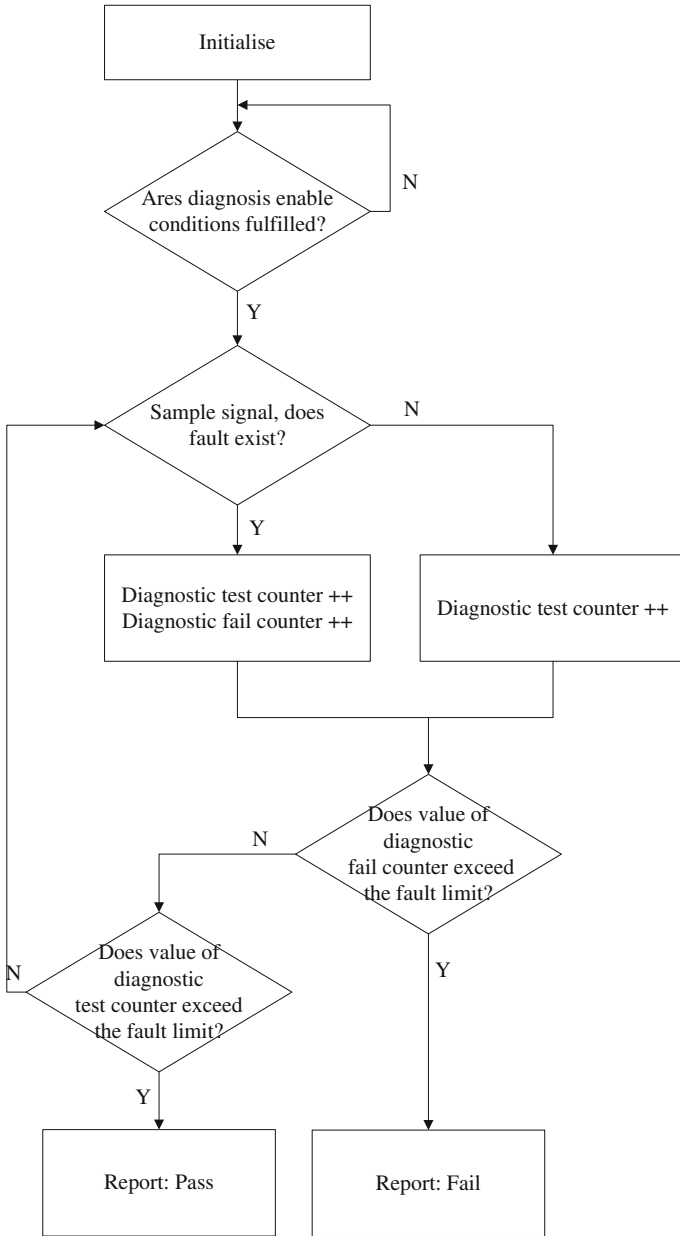


Fig. 48.7 The diagnosis flowchart of an electrical fault

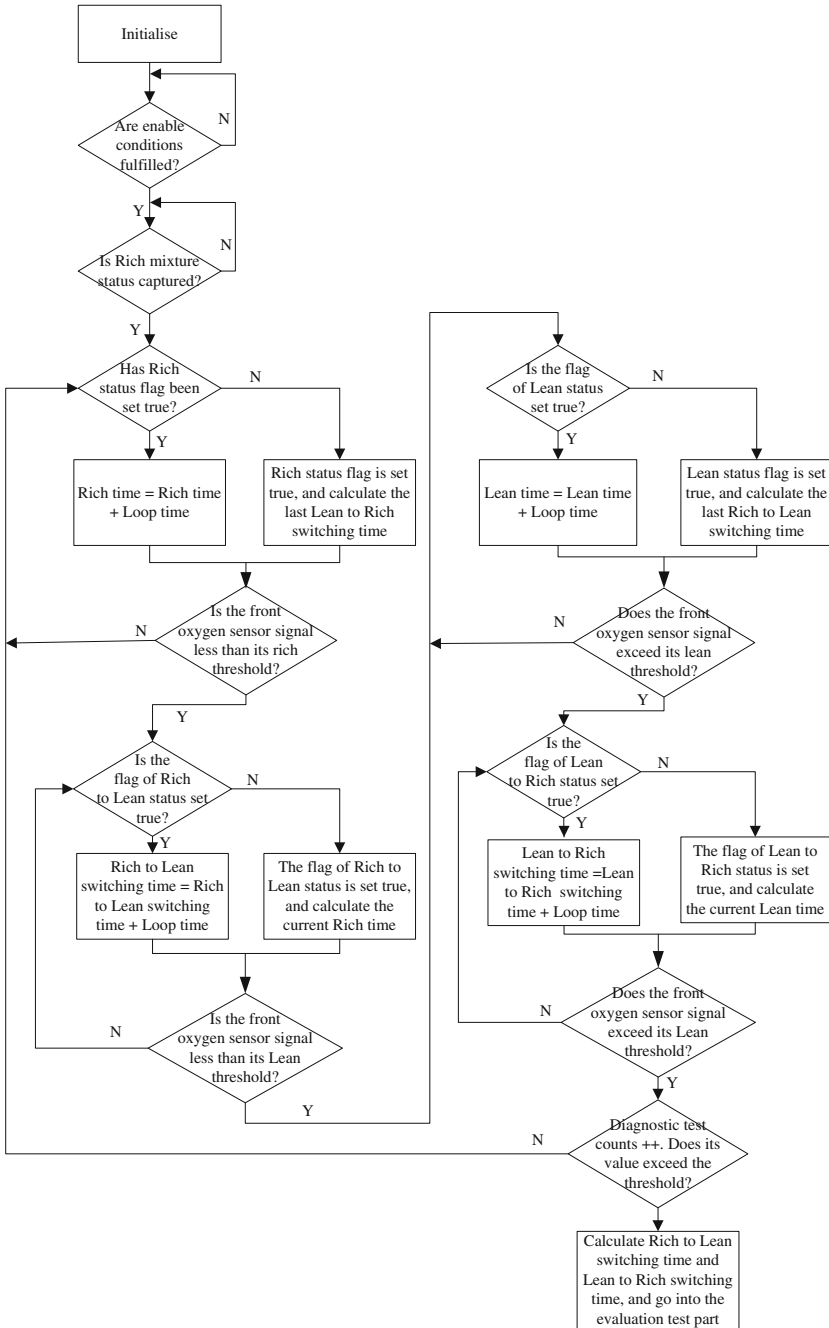


Fig. 48.8 The diagnosis flowchart of the front oxygen sensor rational fault

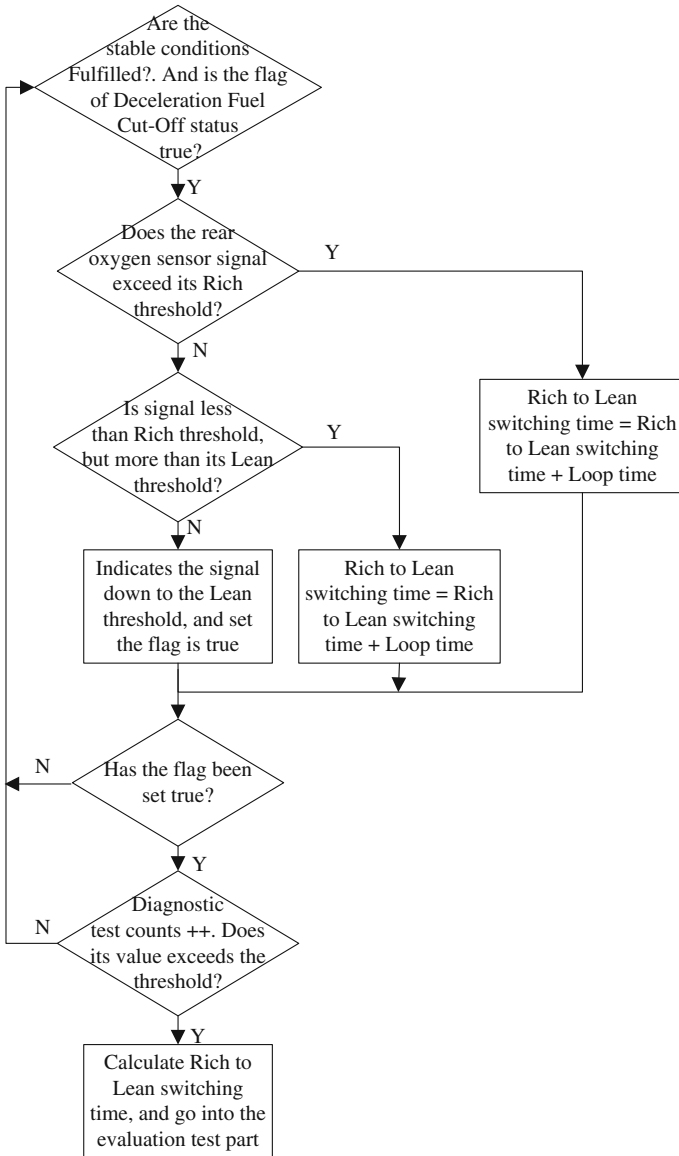


Fig. 48.9 The diagnosis flowchart of the rear oxygen sensor rational fault

the acquired $t(n)$ with the fail threshold. If $t(n)$ exceeds the fail threshold, it reports fail to the diagnostic kernel. On the contrary, pass is set if $t(n)$ is lower than the fail threshold.

48.4 Calibration Test and Results

According to the national regulation of limits and measurement methods for emissions from light-duty vehicles (CHINA III,IV), apply defective or deteriorated oxygen sensor, or use the sensor deactivation simulators to simulate the faults OBD system, which can be detected, and light the MIL in the vehicle emissions test.

As for electrical fault diagnosis, simulate the SCG, SCP, and OC in the HIL. The electrical fault threshold is the signal value acquired when the corresponding fault is set. The test result is given in Table 48.1.

As for rational fault diagnosis, simulate the emissions test in the chassis dynamometer, with the sensor deactivation simulator is connected between the oxygen sensor and EMS. If the test emission value exceeds any of OBD system emission limits, except all emissions values cannot exceed 1.2 times of the OBD limits, it indicates the sensor is deactivated, and the measured switching time is the fault threshold time. Increase the switching time gradually and calculate the emissions test result. The fault threshold time and its corresponding emissions value are given in Table 48.2.

Rational fault calibration test shows the CO content of emissions almost exactly meets the CO content limit of OBD system, and the other emissions do not reach 1.2 times of the OBD emission limits, which indicate the measured switching times are the fault threshold limits.

Table 48.1 The result of electrical fault calibration test

Fault type	The voltage of the front oxygen sensor (mV)	The voltage of the rear oxygen sensor (mV)
The front oxygen sensor (OC)	450 ± 15	/
The front oxygen sensor (SCP)	1,000 ± 20	/
The front oxygen sensor (SCG)	<40	>600
The rear oxygen sensor (OC)	/	450 ± 15
The rear oxygen sensor (SCP)	/	1,000 ± 20
The rear oxygen sensor (SCG)	/	<40

'/' indicates this value is unconsidered

Table 48.2 The result of rational fault calibration test

CO (g/km)	THC (g/km)	NOx (g/km)	The switching time (ms)
3.208	0.196	0.282	Time from rich-to-lean for the front oxygen sensor = 1,480
3.190	0.252	0.314	Time from lean-to-rich for the front oxygen sensor = 1,480
3.212	0.108	0.278	Time from rich-to-lean for the rear oxygen sensor = 2,560

48.5 Conclusions

Oxygen sensor signal, monitoring the oxygen content and its fluctuation of emissions in the exhaust pipe, is used to judge and evaluate the cylinder combustion condition for engine. In terms of the principles of oxygen sensor, the electrical fault and rational fault diagnostic strategy and its Simulink model are designed. Then, with simulators, calibration test is completely implemented. Test result indicates that the diagnostic strategy of oxygen sensor is rapid and precise, which meets the requirements of national standard.

References

1. Kakuho A, Yamaguchi K, Hashizume Y, Urushihara T et al.(2004) A study of air-fuel mixture formation in direct-injection si engines, SAE technical paper 2004-01-1946
2. GB18352.3 (2005) Limits and measurement methods for emissions from light-duty vehicles (III, IV), china environmental science press, Beijing, (in Chinese)
3. Naito S, Sugiyama T, and Nakamura Y, (2001) Development of planar oxygen sensor, SAE technical paper 2001-01-0228
4. Chen D, Jeswani P, Li J (2000) Optimization of oxygen sensor, SAE technical paper 2000-01-1364
5. Baltusis P (2004) On board vehicle diagnostics, SAE technical paper 2004-21-0009
6. Wu, Z. and Wasacz, B., Estimation of individual cylinder fuel air ratios from a switching or wide range oxygen sensor for engine control and on-board diagnosis, SAE Int. J. Engines 4 (1):813-827, 2011
7. Fantini J, Burq J.F (2003) Exhaust-intake manifold model for estimation of individual cylinder air fuel ratio and diagnostic of sensor- injector, SAE technical paper 2003-01-1059

Chapter 49

Airflow Estimation Control Strategy Based on Speed Density Method

Xue Lei, Chen Shen, Jianbo Zheng, Yao Zhou, Zhongtian Chen,
Chunjiao Zhang, Min Chen, Long Qin and Fanwu Zhang

Abstract According to the analysis of speed density method and the principle of volume estimation, the intake airflow calculation control strategy can be designed with Simulink toolbox. The Embedded Coder toolbox can be used to automatically generate the code of above control strategy and then integrate the code into the ECU. Finally, the control algorithm is verified using bench test and real vehicle test, and the result shows that this estimation algorithm can accurately estimate intake volume, which means that we achieve the desired design requirements.

Keywords Speed density method · Intake airflow calculation · Control strategy based on Simulink · Bench test

49.1 Introduction

The control of mixed air–fuel ratio is an important way to improve the power and economy and to reduce the emission of engine. Studies found that the inaccurate actual intake air amount results in fuel injection error and that is the main cause of air–fuel ratio that deviates from the stoichiometric ratio. As one of the engine operating control parameters, accurate determination of the intake air amount is the base for achieving good engine performance. If the intake air amount is imprecise, the engine will do not change the fuel injection quantity correctly with real conditions, and thus, the engine’s whole performance will deteriorate.

X. Lei (✉) · C. Shen · J. Zheng · Y. Zhou · Z. Chen · C. Zhang · M. Chen · L. Qin
Electrical and Electronic Department, Technology Center, Dongfeng Motor Corporation,
Wuhan, China
e-mail: leixue@dfmc.com.cn

F. Zhang
General Engineer Office, Technology Center, Dongfeng Motor Corporation, Wuhan, China

There are two methods to detect the intake air amount: speed density method and mass flow method, in which the former calculates the intake air amount per cycle by measuring the intake manifold pressure and temperature and the latter uses airflow meter to directly get the air amount flowing into manifold and then to calculate the intake air amount each cycle by engine speed. Relatively, mass flow method is more accurate, but due to its high cost, it is general to use the speed density method to calculate the intake air [1].

By analyzing the principle of speed density method, a strategy to estimate the intake air amount by Simulink is designed, which uses the ECU of 1.6-L inline four-cylinder engine, the results of bench test and real vehicle verification show that this strategy works well to control air–fuel ratio.

49.2 Principle of Speed Density Method

The speed density method adopts the absolute pressure signal from intake manifold pressure sensor (MAP) and then combines the intake air temperature signal (IAT), engine speed signal, the estimated charging efficiency (CE), and the amount of exhaust gas recirculation (EGR) together and uses the speed density formula to calculate the amount of air entering into the engine, in which the engine using this method is called D-type electronically controlled engine [2].

Speed density formula is the core of speed density method and simply means that the volume and density were used to get the quality of the fluid. First, we need to calculate the volume of air entering into the cylinder. We know that when the engine inhales air once, the crank runs 2 turns, and the engine runs 2 turns [3], we can take advantage of this relationship to get the intake air volume by CE at any speed. Then, the density is calculated by intake manifold pressure and temperature, using the ideal gas equation.

The formula used to calculate the intake volume of engine by CE is as follows:

$$V_{\text{air}} = \frac{\text{CE} * V_{\text{cyl}} * n}{2} \quad (49.1)$$

where CE is the charging efficiency, V_{cyl} is the cylinder volume, n is the engine speed, and V_{air} is the intake air volume in one engine circle.

The formula used to calculate the density by ideal gas equation is as follows:

$$\rho_{\text{air}} = \frac{m}{V} = \frac{nM}{\frac{nRT_{\text{air}}}{P_{\text{air}}}} = \frac{MP_{\text{air}}}{RT_{\text{air}}} \quad (49.2)$$

where M is the molar mass of the air, P_{air} is the intake manifold pressure, T_{air} is the intake manifold temperature, and R is the ideal gas constant.

In summary, we can get the intake air amount as follows:

$$m = V_{\text{air}} * \rho_{\text{air}} = \text{CE} * V_{\text{cyl}} * \frac{M}{R} * \frac{n}{2} * \frac{P_{\text{air}}}{T_{\text{air}}} \tag{49.3}$$

We can design the intake air algorithm model based on the above formulas.

49.3 Algorithm Implementation of Speed Density Method

The last chapter shows that the calculation of CE is very important for intake air amount. For engines equipped with variable valve timing (VVT), the CE is not only related to exhaust pressure/intake pressure and engine speed, but also related to the camshaft angle [4, 5] and then compensated with temperature, and CE algorithm is as shown in Fig. 49.1. When VVT angle is at different ranges, CE calculation will be different; there are 5 cases: 0–12°, 12–24°, 24–32°, 32–40°, and >40°, using Simulink blocks: Prelook up and Interpolation Using Prelook up to realize angle interpolation calculation.

CE together with IAT, intake air pressure, and engine speed is the input to Eq. (49.3) to calculate intake air amount, and its algorithm is described in Fig. 49.2.

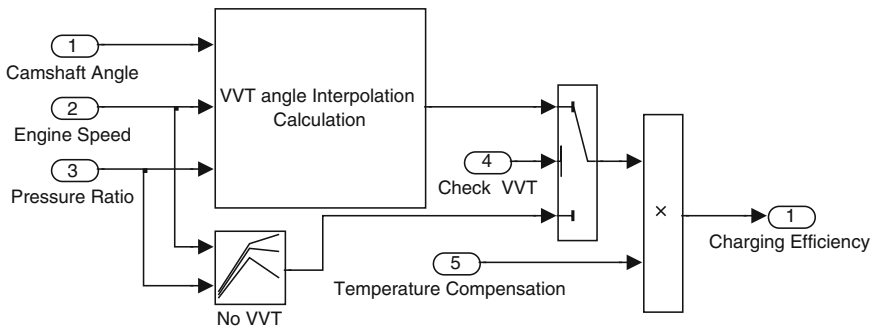


Fig. 49.1 Description of charging efficiency algorithm

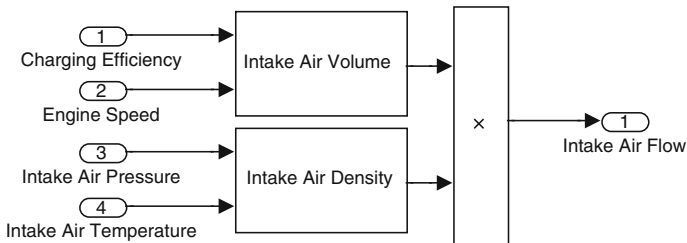


Fig. 49.2 Description of intake air amount algorithm

According to the above description of the algorithm, we can build the Simulink model in MATLAB and then use Embedded Coder toolbox to automatically generate code for the model and then integrate the code with basic software and other applied software and then finally download them to the ECU after passing compiling.

49.4 Bench Test

Since it is easier to meet the required condition of engine speed, IAT, and intake air pressure for intake air amount calculation, the initial data should be tested on the engine test bench, and then, the PC machine collects ECU variables and adjusts various parameters by INCA until the result meets the control requirements.

During the bench test, we need to adjust and modify the calibrations, tables, and MAPs of control strategy so as to achieve the desired result. Figure 49.3 shows the estimates and bench measurements of intake air amount when the engine speed ranges from 1,200 r/min up to 5,200 r/min. As can be seen from the figure, the estimated values can be kept very close to the actual intake air amount with small error remained about 0–5 %, and thus, the error can meet the required estimated error range, and the result can achieve desired effect.

49.5 Vehicle Test

To further test the performance of the control strategy, we need to verify the control effect on a real vehicle, but the verified vehicle do not install airflow measurement, so we use the air–fuel ratio and its compensation coefficient to indirectly reflect the

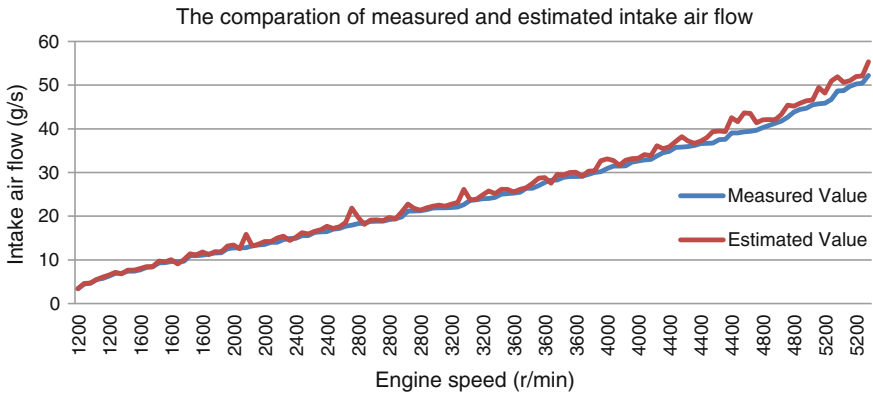


Fig. 49.3 Bench test result

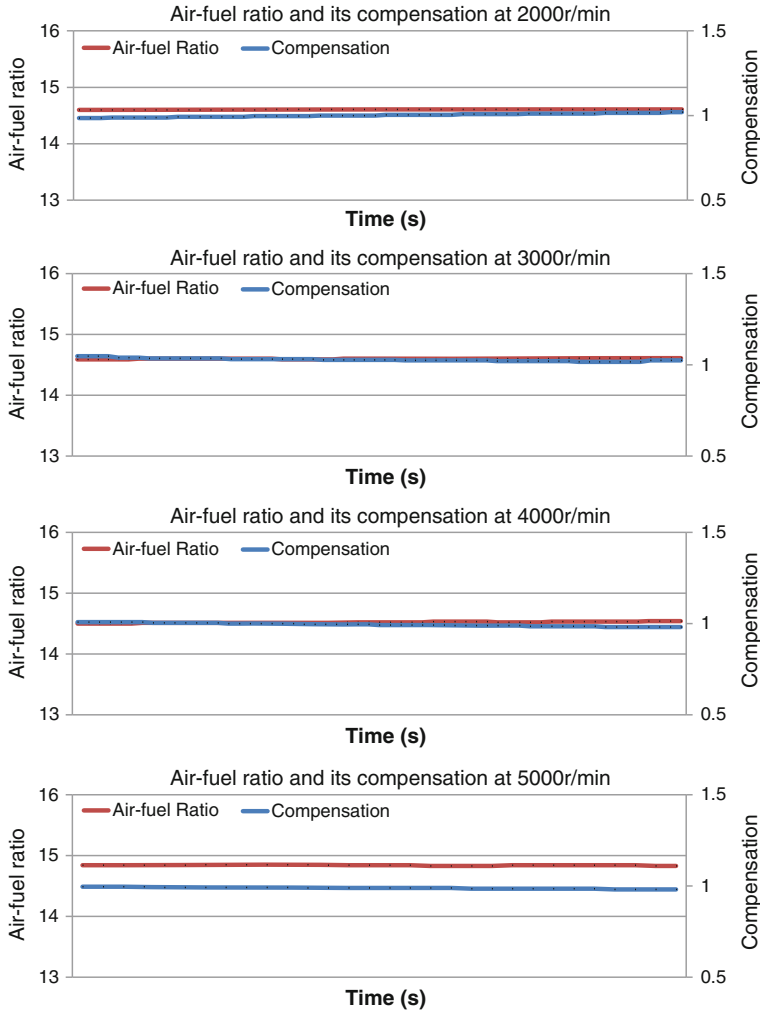


Fig. 49.4 Vehicle test result

accuracy of estimates of air; according to the air-fuel ratio control strategy, the closer the air-fuel ratio to 14.7, and the closer the compensation to 1, the more accurate the estimated air amount is. Figure 49.4 shows the result of the test. As can be seen from the figure, at different engine speeds, air-fuel ratio can stay at about 14.7, the compensation coefficient can maintain about 1, and their fluctuation is very small. Therefore, the estimate algorithm can provide accurate, real intake air amount for ECU, and thus, it enables the engine to run well.

49.6 Conclusions

In conclusion, this paper designs the intake air amount estimation model based on Simulink by speed density method, which was applied to the self-developed engine ECU, and does the bench test and vehicle test on the 1.6-L inline four-cylinder engine, and the result shows that this control strategy can meet the error requirement of estimated intake air amount and also can control the air–fuel ratio well.

It is worth to mention that the accuracy of the speed density method has a direct relationship with the accuracy of the intake manifold temperature sensor and intake air pressure sensor, and thus in the further optimization of the control strategy, what needs to be taken into consideration is to avoid the influence of sensor measurement error and delay in estimating intake air amount and then improve the reliability of estimates.

References

1. Lin X, Wang T (2012) The electronic control technology of vehicle engine. China Machine Press, Beijing
2. Wang S, Li J, Xia Q (2011) Automotive electronics. Tsinghua University Press, Beijing
3. Kolmanovsky I, Sun J, Druzhinina M (2000) Charge control for direct injection spark ignition engines with EGR. *C Am Control Conf Proc IEEE* 1(6):34–38
4. Li S, Chen H, Yu SY (2009) Nonlinear model predictive control for idle control of SI engine. In: *C Joint 48th IEEE Conference on Decision and Control and 28th Chinese Control Conference*, Shanghai, China. 6590–6595
5. Qu Z, Ma M, Zhao F (2012) Estimation and analysis of crank-angle resolved gas exchange process of spark-ignition engine. *C Geely Automobile Research Int*, 2012 SAE International, Hangzhou, China. doi:[10.4271/2012-01-0835](https://doi.org/10.4271/2012-01-0835)

Chapter 50

A Development Report of an Accurate Method of Detecting Systematic Refrigerant Leak Rate for Automotive HVAC Systems

Kelvin Zhai, Zongshan Chen and Zhiping Ning

Abstract A useful and accurate refrigerant leak rate measurement approach is presented, which will find small leak rate as low as 3 g, by utilizing liquid nitrogen as cold recourse to cool down the recovery tank, and as an alternative, the dry ice (liquidized carbon dioxide) is tested too, but it is found that the recovery accuracy can reach to 10 only.

Keywords Automotive · HVAC · Leaking rate · Refrigerant · Recovery · Liquid nitrogen

50.1 Introduction


Refrigerant is filled in the HVAC system, e.g., R134A has been used for automotive AC as the working media for years. During the life cycle, the leaking happens all the time with different rate, depending on variation of the cooling lines, sealing type, tightening force, etc. In order to find right ways to avoid excessive losing of the working media, the automakers need to know how to measure the actual leak rate for the total system so that the tightness of the seals can be improved.

Refrigerant leaks cause a lot of problems either to the automakers for heavy service expenditure or to customers for “not cold enough.” Additionally, the emission damages our fragile environment. Therefore, it is absolutely necessary to minimize the leaks.

In the world, the typical leak rate of refrigerant is 9–15 g/year [1] (Fig. 50.1), which means after 4 years of on the road, a vehicle will still have sufficient refrigerant in the system to provide comfortable cooling effects to the passengers. This explains why some imported vehicles may last 6 years or longer without demanding of refilling the medium.

K. Zhai (✉) · Z. Chen · Z. Ning
Changan Automobile Global R&D Center, 401120 Chongqing, China
e-mail: zhaiym@changan.com.cn

Fig. 50.1 The SAE publication indicates that refrigerant leak rate is 9–15 g/year for some typical vehicles



J-2727r Mini-Shed Predictions versus IMAC SHED Data

	Original J-2727 Rating	J-2727r Rating	J-2727r SHED Rating	J-2727r SHED Emissions Estimate g /yr	Actual SHED Emissions Measured g /yr
W-Car	2.3	1.8	1.23	12.3	←→ 9.5
Camry	2.6	2.0	1.62	16.2	←→ 17.8
DC-Van	2.6	2.5	1.57	15.7	←→ 15.3
Ford F-150	2.3	2.1	1.33	13.3	←→ tbd

In order to control the leaks, it is necessary to know what the current status of leaking is. Refrigerant recovery machines once were used to measure refrigerant leaking rate by comparing the differential of refrigerant charged and recovered; for instance, the known charge was 500 g and the recovered is 580 g; the difference of 20 g is found as the system leak rate in the duration of the vehicle in operation, which is usually counted as “per year” or “annual.” Unfortunately, the recovery machines seem not working so well for leak measurement, indicated by complaints of only 100 g also could be identified by many times of trials in the past years. It is apparent that the number is too large to find out what is prominent type of reasons that cause the leaks. Consequently, in minds of the operators, it has been given up for leak test purpose.

However, it is noticed that, in the world, some automakers have shown very low leak rate on their vehicles, which were ranged from 3.6 g/year as the lowest to 9.9 g/year as the highest (Fig. 50.2).

Then, how to conduct so precise leak rate test? It’s found that may be useful to use the methodology appearing in JASO Z123-2007 [3] to hit the goal after carefully review of the technical information.

50.2 Key Points of JASO Z123-2007

From the literature [3], some essential points have been drawn out to guide the experimental tests as follows: The dry ice test is resulted in 8–12 g recovery error

• Goal of leak-detecting accuracy	3 g
• Cold resource material	Liquid nitrogen
• Operation ambient temperature	15 °C+
• Vacuum pump capacity	20–30 L/m
• Vacuum time	30–60 min
• Vacuum level required	0.1 MPa
• Scale precision	±0.1 g
• Liquid nitrogen container volume	~ 1 L

Field Test Data - 1

Vehicle	# of vehicles	Single or dual	Test data (averaged)				
			Driving distance (km)	Comp. Running (hr.)	Clutch cycling (#)	Test period (yrs)	Averaged Leak (g/yr) (scattering)
Vehicle T-1 (Toyota Mark II)	3	S	17,323	138.9	50984	1.58	9.4 (Min.: 6.8, Max.: 13.0)
Vehicle T-2 (Toyota Corolla)	8	S	16,270	178.1	39645	1.58	9.1 (Min.: 6.4, Max.: 20.4)
Vehicle T-3 (Toyota Vista)	2	S	9,785	208.4	40423	1.59	7.3 (Min.: 5.5, Max.: 9.1)
Vehicle S-1 (Suzuki Lapin)	2	S	26,740	221.5	76,700	0.84	9.9 (Min.:8.5, Max.:11.3)
Vehicle N-1 (Nissan Cube)	3	S	21,473	187.3	8,619	1.42	8 (Min.: 4.2, Max.: 10.2)
Vehicle N-2 (Nissan Premera)	3	S	17,884	362.4	3,280	1.64	7.1 (Min.: 3.6, Max.: 12.0)
Vehicle N-3 (Nissan Cedric)	2	S	26,383	654.3	3,146	1.66	7.8 (Min.: 6.6, Max.: 9.0)
Vehicle N-4 (Nissan Tino)	2	S	24,031	297.4	41,024	1.66	8.1 (Min.: 7.8, Max.: 8.4)
Vehicle N-5 (Nissan Bluebird)	3	S	18,711	295.7	17,868	1.38	9.8 (Min.: 9.6, Max.: 10.2)
Vehicle N-6 (Nissan X-trail)	2	S	35,629	363.9	1,572	1.25	4.5 (Min.: 3.6, Max.: 5.4)

SAE 7th Alternate Refrigerant Systems Symposium
June 26-29, 2006

Fig. 50.2 The JAMA publication shows the fleet leak test resulted in 3.6–9.8 g/year

50.3 Dry Ice Test

Dry ice is a popular natural refrigerant, and its operational temperature is approximately $-40\text{ }^{\circ}\text{C}$, at saturation pressure of 1.0 MPa. As the first stage of the tests, it was taken as cold resource to cool down the recovery tank.

The test setup and instrumentation had been arranged as shown in Fig. 50.3, but with small non-ideal variations due to limited supply at the time, which includes:

- The recovery tank is weighted as 8,000 g with volume of 10 L, over 10 times of the targeted refrigerant of 600 g;
- The electronic scale used is 1 g rated;
- The actual links of refrigeration lines are too complex to be rational.

With 3 times of confirmation tests, the results have shown positively that a low level of recovery errors from 12 to 8 g is obtained. The tendency looks consistent

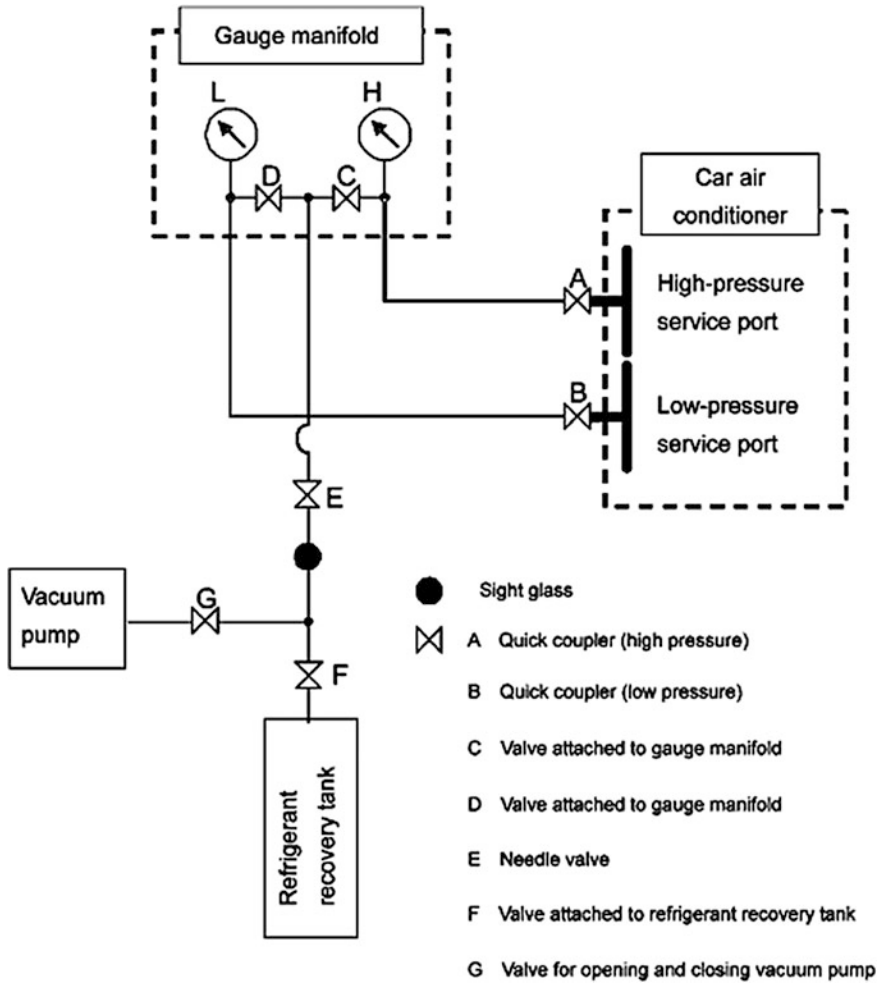


Fig. 50.3 The test setup per JASO Z123

for each test. However, the recovery duration looked very long which may take 90 min, only for the recovery procedure. In addition, the errors seem not to be further lower. See Table 50.1 for the test results.

50.4 Liquid Nitrogen Test

With the same setup as the dry ice test, the effort is to use the liquid nitrogen as the cold resource. Nitrogen is popular and environmental friendly too, but working temperature is much lower than dry ice, which normally operates at $-180\text{ }^{\circ}\text{C}$ at

Table 50.1 The dry ice test is resulted in 8–12 g recovery error

Date of the testing	Average ambient T (°C)	Refrigerant charged (g)	Initial weight of the recovery tank after vacuumed (g)	The tank weight after recovery (g)	Recovered refrigerant weight (g)	Error of the recovery (g)
2014.3.6	16	551	2,056	2,595	539	12
2014.3.20	16.5	539	4,142	4,671	529	10
2014.3.20	16.5	541	4,142	4,675	531	8

Fig. 50.4 Liquid-state nitrogen is proved as a right way to find smaller leak rate



0.46 MPa of saturation pressure (Fig. 50.4). The lower temperature makes identically differences for the recovery processing shown by much quicker recovery time as short as 20 min, in contrast to the 90 min, plus the improved recovery errors,

Table 50.2 The liquid nitrogen test is resulted in 4–6 g error of recovery

Date of the testing	Average ambient T (°C)	Refrigerant charged (g)	Initial weight of the recovery tank after vacuumed (g)	The tank weight after recovery (g)	Recovered refrigerant weight (g)	Error of the recovery(g)
2014.3.28	17.5	542	4,339	4,877	538	4
2014.3.28	17.5	541	4,339	4,874	535	6

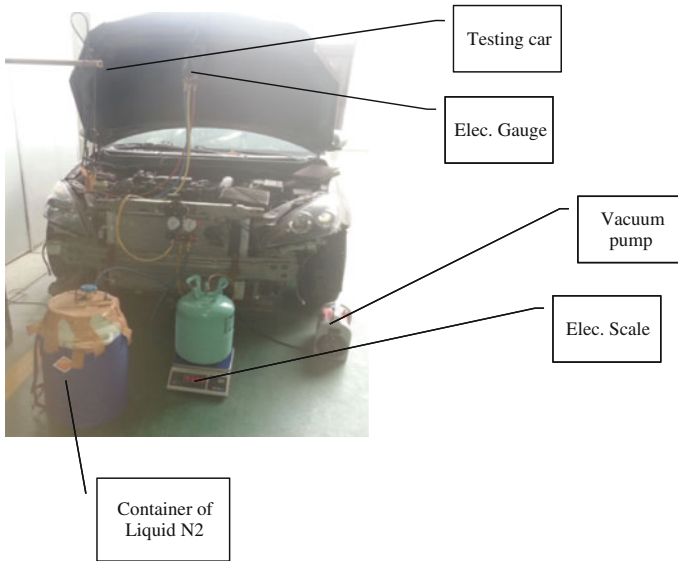


Fig. 50.5 The vehicle test setup with nitrogen liquid as the cold resource

which were in range of 4–6 g. As a result, the liquid-state nitrogen has been chosen as standard cooling source for the leak tests in Changan Automobile (Table 50.2 and Fig. 50.5).

50.5 Conclusions

- Liquid nitrogen is the optimal cooling resource for the recovery tank to detect lower leak rate as low as 3 g, which reflects 10 g/year actual vehicle leak rate with $\pm 10\%$ of error, although the experiments have reached 4–6 g level at present;
- The experimental tests conducted give the impression of being repeatable and reliable;
- The standardization of the systematic leak test for the vehicles is improving to reach the goal of 3 g, which including:
 - Reduce the gross weight of current recovery tank to 2,000 g from the original 8,000 g;
 - Improve the scale accuracy from 1 to 0.1 g;
 - Optimize the connection in the tests to simplify the refrigerant lines to reduce the errors from the longer hoses.

References

1. Baker JA (2006) SAE interior climate control standards committee, "Revising J-2727", SAE alternate refrigerants symposium, June 28
2. Ikegami T, Kikuchi K (2006) Field test results and correlation with SAE J2727, 1/22 SAE 7th alternate refrigerant systems symposium, June 26–29
3. Japanese automobile standard, JASO Z123-2007

Chapter 51

Compact Oxygen Sensor for Motorcycles: Concept of Simple Heaterless Sensors

Kinji Hodaira, Takehiro Watarai and Zhenzhou Su

Abstract The concept and evaluation results of the compact heaterless O₂ sensor (activated with exhaust gas heat) that is suitable for the fuel injection (FI) system for small motorcycles are introduced. To realize the heaterless, low-temperature operation at 280 °C is achieved using high ion conductive solid electrolytes and low interface resistance electrodes, and the element temperature could be kept at 350 °C and above during an actual vehicle EC mode driving by a small thin element and a high heat-receiving cover. As a result, early rises in temperature and early activation with the heaterless O₂ sensor are made possible at engine cold starting.

Keywords Oxygen sensor · Motorcycle · FI system

51.1 Introduction

It is expected to adopt CHINA IV emission standards for motorcycles in 2017 in China. Therefore, fuel injection (FI) systems will be required in small motorcycles that currently used conventional carburetor systems, and O₂ sensors will likely become essential as main parts in FI systems. Compared with 4-wheel vehicles, the demands on O₂ sensors for reducing mounting space, low costs, and reliability in poor environments are high when it comes to small motorcycles. Therefore, the below is a report on O₂ sensor technology with compact and simple heaterless type for meeting such demands.

K. Hodaira (✉) · T. Watarai
DENSO Corporation, 1-1 Showa-cho, Kariya-Shi, Kariya 448-8661, Japan
e-mail: kinji_hodaira@danso.co.jp

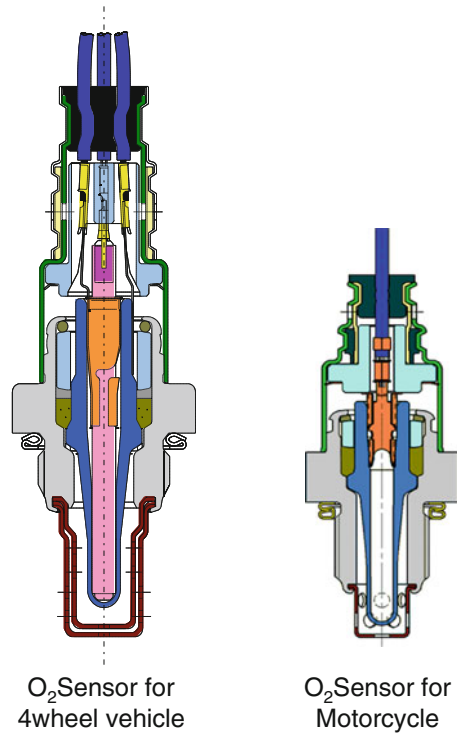
Z. Su
Shanghai Technical Center, DENSO (China) Investment Co., Ltd.,
No. 35, Yuandian Road, Minhang District, Shanghai 201108, China

© Springer-Verlag Berlin Heidelberg 2015
Society of Automotive Engineers of China (SAE-China) (ed.),
Proceedings of SAE-China Congress 2014: Selected Papers,
Lecture Notes in Electrical Engineering 328, DOI 10.1007/978-3-662-45043-7_51

51.2 Concept of Oxygen Sensor for Motorcycles

The O_2 sensor described in this paper is targeted at small motorcycles, which will become very widely spread in China. FI systems for small motorcycles require more reduced space and lower costs when compared with those for 4-wheel vehicles and large motorcycles. Therefore, the concept of O_2 sensors is compactness in design for motorcycles, heaterless with high heat receiving, and high performance in low-temperature activation as they can be operated only with exhaust gas heat due to the simplicity of their systems, power saving, and low costs of their components. Furthermore, O_2 sensors are made with a highly waterproof structure for withstanding high levels of water pressure as motorcycles require robustness for rough roads, bad weather, and high-pressure water washing due to their components being externally exposed (Fig. 51.1).

Fig. 51.1 O_2 sensor



51.3 The Designing of O₂ Sensor for Motorcycles

51.3.1 The Role of O₂ Sensor

An example for configuration of an FI system is shown in Fig. 51.2. As can be seen in Fig. 51.3, the three-way catalyst shows a high conversion efficiency with harmful HC, CO, and NO_x in exhaust gas only in a narrow area (window) close to the theoretical air–fuel ratio (AFR). This means that AFR must constantly be controlled at the center of the window in order to effectively exert the three-way catalyst. With that, the concentration of oxygen is detected with the O₂ sensor that has been attached directly below the engine, and the amount of FI is adjusted using the ECU to produce the theoretical AFR with the intake air mass.

Fig. 51.2 FI system

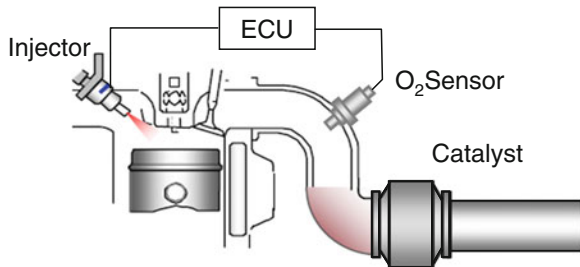
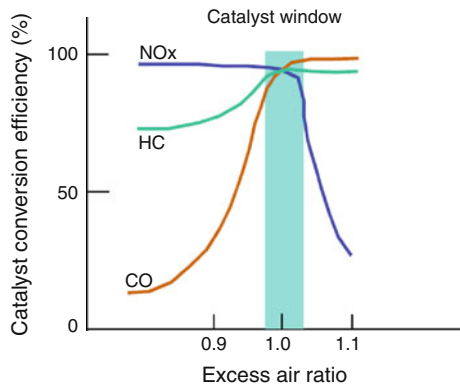


Fig. 51.3 Catalyst window



51.3.2 Heaterless O₂ Sensor Technology

51.3.2.1 The Principles of O₂ Sensors and Heaterless Design Technology

As a basic principle, O₂ sensors use zirconia solid electrolytes and oxygen concentration cells configured with platinum electrodes placed on both sides. If a reference oxygen atmosphere (normally atmospheric air) and a measured oxygen atmosphere (engine exhaust gas) are introduced to both electrodes of oxygen concentration cells, electromotive force is generated between both electrodes in accordance with the oxygen concentration (partial pressure of oxygen) ratio of both electrodes, and this becomes the sensor output. Typical oxygen concentration cells normally operate at 350 °C or more. As sensors do not have their own heating means, the exhaust heat must be effectively used along with elements that activate as low temperature as possible in order to activate O₂ sensors with heat from engine exhaust gas alone (Fig. 51.4).

51.3.2.2 Low-Temperature Activation Technology

As previously described, O₂ sensor elements are configured with zirconia solid electrolytes and platinum electrodes, and the activation performance of the elements is produced with the ion conduction resistance of solid electrolytes and gas reaction resistance of the electrodes. Therefore, they become more active as each form of resistance reduces. At solid electrolytes, resistance is controlled by the ion conductivity of the materials. At electrodes, it is controlled by the gas reactivity and the

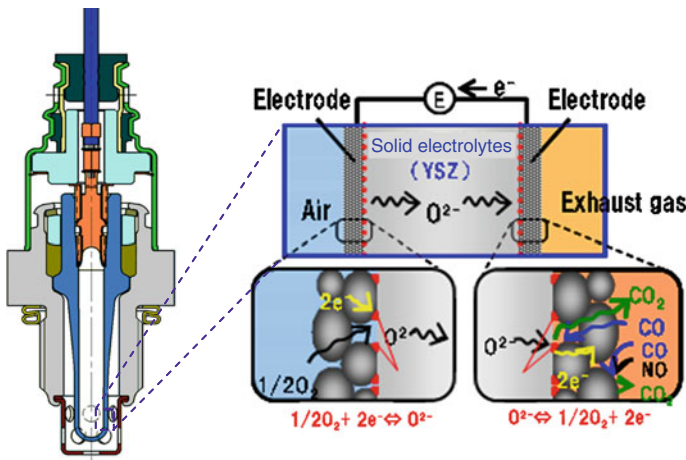


Fig. 51.4 O₂ sensor mechanism

exchange reaction resistance from the oxygen molecules to oxygen ions in the three-phase boundary of the electrodes, solid electrolyte, and gas. Each resistance characteristic is dependent on the temperatures.

Ion conduction of solid electrolytes is generated through the transferring of oxygen ion resulting from the oxygen concentration diffusion in the oxygen vacancy generated by the introduction of the yttria solid solution into zirconia, and ion conductivity is dependent on the volume of the yttria solid solution as shown in Fig. 51.5 [1]. On the other hand, mechanical strength drops with the yttria solid solution. 6 mol% has been chosen as the yttria solid solution volume for the developed product so that high ion conductivity can be maintained while securing resistance to environments with severe thermal shock.

Electrodes are made with platinum that has excellent reactivity and is formed with chemical plating that can maintain lower oxygen reaction resistance in the three-phase boundary through the forming of small pores with thin film.

Comparative results of element internal resistance which is an indicator of ion conductance are shown in Fig. 51.6. The element which low-temperature activation technology has been adopted shows a 65 % decrease in internal resistance than that of the comparative product.

51.3.2.3 Effective Utilization of Exhaust Gas Heat

In order to activate the elements with exhaust gas heat, compact and thin elements with an internal diameter of $\Phi 3.8$ mm and a thickness of 0.5 mm were realized due to high-accuracy production technology so that the elements would have low heat capacity and low heat release for high temperature rising characteristics.

The element cover with 12 pore was adopted in order to increase exhaust gas heat-receiving efficiency.

Fig. 51.5 Y_2O_3 content versus conductivity [1]

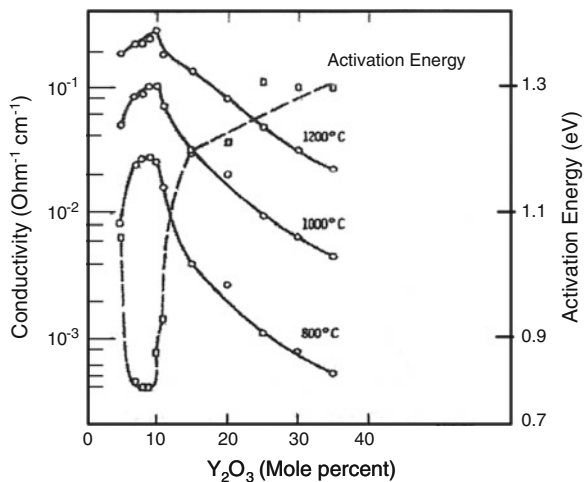
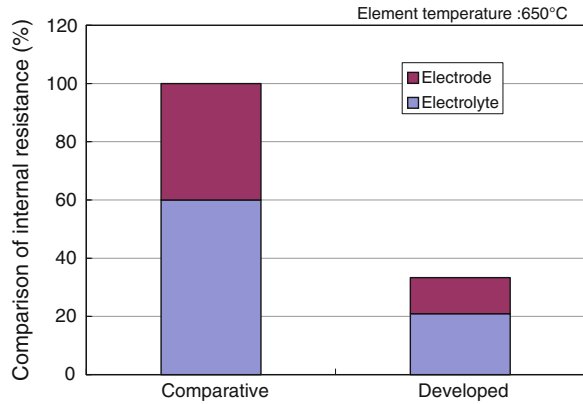


Fig. 51.6 Sensor internal resistance



Simulation results of the temperature rising characteristics for element thickness are shown in Fig. 51.7. Performance of the element with a thickness of 0.5 mm was 5 s faster than that of the comparative element with a thickness of 0.7 mm to reach 300 °C on element tip in environment temperature 450 °C, showing superiority in element activation.

Simulation Condition

- Method: Constant heat-transfer analysis
- Initial element temp.: 25 °C
- Fixed point temp.: 120 °C
- Environmental temp.: 450 °C

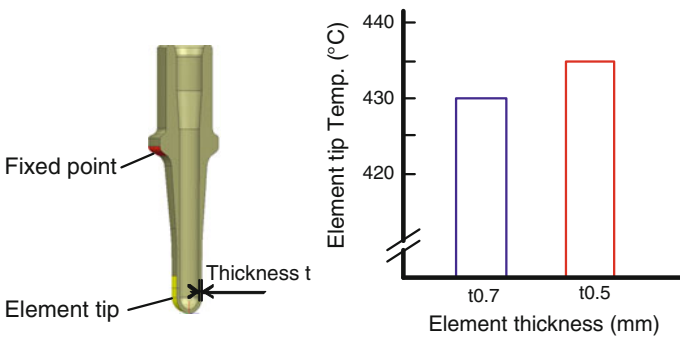


Fig. 51.7 Temperature effect of element thickness

51.4 Evaluation Results

51.4.1 Low-Temperature Activation Performance Evaluation Results

A low-temperature activation element was assembled as a sensor assembly and evaluated with the engine bench. The test conditions and results of the evaluation are shown in Fig. 51.8. The developed product maintained larger output amplitudes than the comparative product at 280 °C, which is a low element tip temperature.

51.4.2 Exhaust Gas Heat Utilization Performance Evaluation Results

Element temperature behavior was observed during operation in EC mode driving with a motorcycle in order to verify heat utilization performance with compact and

Test condition

- Engine:L4 2.4L
- Condition: Element tip temp. 280°C, 300 °C
- Test item: sensor output state with self-feedback

Test Result

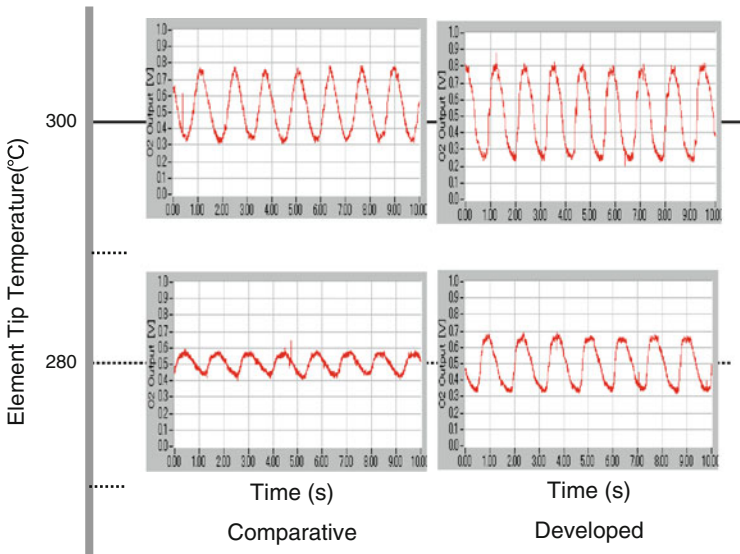
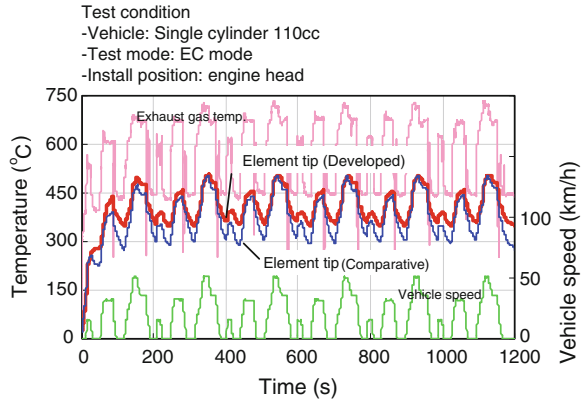


Fig. 51.8 Sensor output under low element temperature

Fig. 51.9 Sensor temperature at EC mode test



thin elements and a high temperature receiving element cover. The test conditions and the results are shown in Fig. 51.9. The evaluation results of the developed product show that the temperature of the element maintained higher temperatures than those of the comparative product and that they were 350 °C and above in all areas of the EC mode driving.

51.4.3 Observation Results of the Performance of the Developed Product

The test conditions and results of the activation performance of the developed product after the engine cold start are shown in Fig. 51.10.

In the same condition of exhaust gas temperature behavior, the element tip temperature of the developed sensor turned out 40 °C higher than that of comparative product at 20 s from engine cold start. This was the effect by the element thinning. About the sensor activation, the developed product confirmed that it was 14 s earlier than that of the comparative product at the time when the sensor output became 0.45 V which can be judged as the sensor activated.

This result shows that the lower activation temperature as well as the faster element temperature rising of developed product contributes to the faster sensor activation.

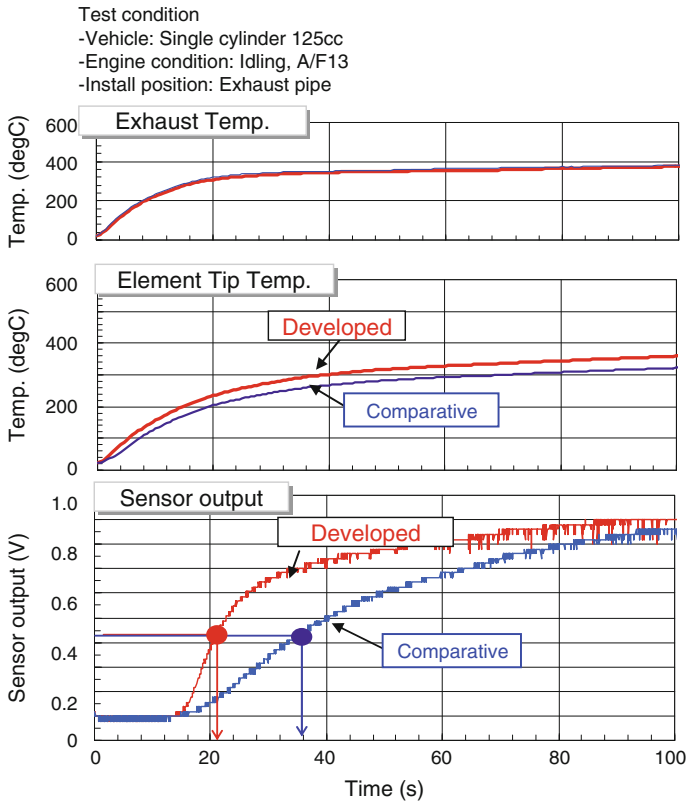


Fig. 51.10 Sensor performance at cold start

51.5 Conclusions

This has been the concept and evaluation results of the compact heaterless O₂ sensor that is suitable for the FI system for small motorcycles.

1. Lower temperature activation was achieved with high ion conductivity solid electrolytes and low interface resistance electrodes.
2. Effective utilization of exhaust gas heat was realized with compact thin sensor elements and high heat receiving element covers.
3. The developed O₂ sensor was confirmed early temperature rise and fast light off at cold start condition with an actual motorcycle.

Reference

1. Strickler DW et al. (1964) J Am Ceram Soc 47(3):122–127

Chapter 52

HMAC-SHA1 Applied in the Diagnosis Service for Security Access

Yangchun Li, Dehua Zhao, Honglei Li and Zutao Kou

Abstract As automobile comfort and security requirement are increasing, more and more ECUs have been developed. Automobile structure is becoming more complex; therefore, after-sales service is also getting more and more important. Diagnostic tester is the key equipment for after-sales service. To protect the information of the vehicle and the owner, it is not allowed that other testers are used for repairing or changing parameters except the OEM own testers. Tester communicates with ECU only after passing the security access. To ensure the confidentiality, uniqueness, and absoluteness of the security access algorithm, HMAC-SHA1 is a better choice for security access.

Keywords Tester · Diagnosis service · Security access · HMAC

As demand for cars' comfort and safety performance from customers is increasing, cars are more and more complicated. In the increasing of demand, security is critical, and improving security is necessary not only for customers, but also for OEM. For customers, using unauthorized devices for communicating with the vehicle controller and modifying the behavior of the controller parameters are very dangerous; for example, modifying the engine and car body power parts of the controller, such as stabilizing system, will affect the customer's safety. For OEM, the use of unauthorized diagnostic equipment to modify the parameters for reaching the illegal purpose also often happens, mainly because the controller is connected to the external device (diagnostic instrument) before a formal communication, and it is

Y. Li (✉) · D. Zhao (✉) · H. Li (✉)
EE Department, Brilliance R&D Center, Shenyang, China
e-mail: yangchun.li@brilliance-auto.com

D. Zhao
e-mail: dehua.zhao@brilliance-auto.com

H. Li
e-mail: honglei.li@brilliance-auto.com

Z. Kou (✉)
Shenyang Brilliance Jinbei Vehicle Company, Shenyang, China
e-mail: zutao.kou@brilliance-auto.com

lack of a mutual authentication between ECU and tester. Through diagnosis service sending a request trying to secure access authentication, the uniqueness of the required security access algorithm, not rationality and reliability, is very important, and HASH-based Message Authentication Code (HMAC) algorithm is a good choice.

52.1 The Description of Security Access Process by Diagnosis Service

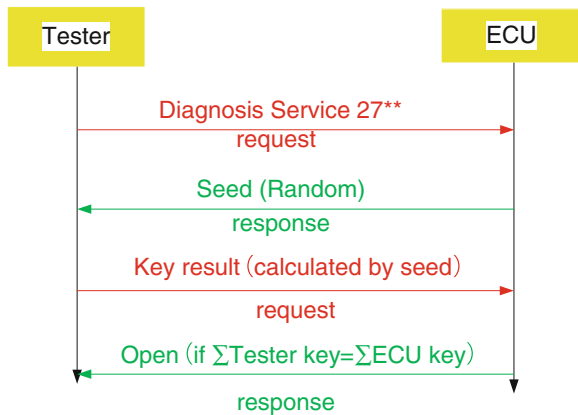
As described in Fig. 52.1, the authentication process of security access is described as below

1. Diagnosis tester wants to communicate with ECU by sending diagnosis services (27).
2. ECU responds and sends the random seed (value) to diagnosis tester.
3. ECU and tester calculate the result by the seed at the same time, and then, tester sends the result to ECU.
4. ECU matches the result with its own result. If it is the same, it will pass the authentication. If not the same, refuse to communicate with ECU.

The reason of illegal communication with ECU is the following

5. The security access algorithm is simple and can be reasoned.
6. The security access algorithm is not reasonable. The same result can be got by different seeds.
7. The seed of security access algorithm is too short, and the regulation is easy to be found.

Fig. 52.1 Security access process by diagnosis service



52.2 HMAC

52.2.1 Application of HMAC

Not each algorithm can be used for security access algorithm. The algorithm that can be used must follow the security access process and must not be simple.

HMAC uses only one seed to calculate result by HASH function. Its operation effect is authentication and authorization. The HMAC process of authentication and authorization is the same as the security access.

For the security, as illegally obtained information of a third party, it will be able to get the information only as a random number of challenge and response of HMAC as a result, and the algorithm is based on these two data calculated. Because algorithm is unknown, it cannot fake a consistent response. And a set of values can only get a set of keys; the shortcomings of not uniqueness can be overcome. So the HMAC can be used.

52.2.2 Presentation and Calculation Procedure of HMAC

52.2.2.1 Presentation of HMAC Algorithm

$$\text{HMAC}(K, M) = H(K \oplus \text{Opad} \mid H(K \oplus \text{Ipad} \mid M)) \tag{52.1}$$

Formula of meaning is shown in Table 52.1.

52.2.2.2 Calculation Procedure of HMAC Algorithm

The calculation procedure of the HMAC is described in the Fig. 52.2.

As described in the figure,

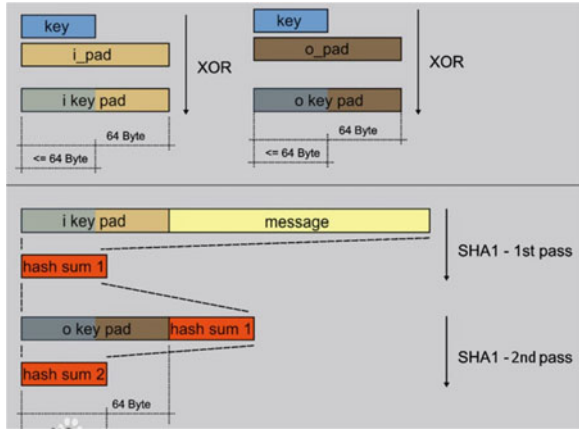
First-HASH = H (K XOR Ipad || (data to auth))

Second-HASH = H(K XOR Opad || First-HASH)

Table 52.1 Formula of meaning

Letter	Meaning
H	The category of HASH function (such as SHA-1)
K	Constant input of HMAC
M	Random value input
Opad	Repeat B times using $0 \times 5c$ (such as SHA1B = 64)
Ipad	Repeat B times using 0×36 (such as SHA1B = 64)

Fig. 52.2 Calculation procedure of HMAC algorithm



Because the process is more complicated, HMAC is enough to guarantee the reliability of the security access.

52.2.2.3 Simulation of HMAC Algorithm

The HMAC-SHA1 is exemplified and the length of seed is 16 bytes, and the software of Visual Studio can be used for simulation. The process of security access is simulated. If the results of both sides are the same, the simulation is successful (Fig. 52.3).

During the simulation, it is convenient to use the fixed seed instead of the random seed for calculation. The fixed seed is Brilliance_auto! (Fig. 52.4).

Pay attention to the result of simulation (Fig. 52.5).

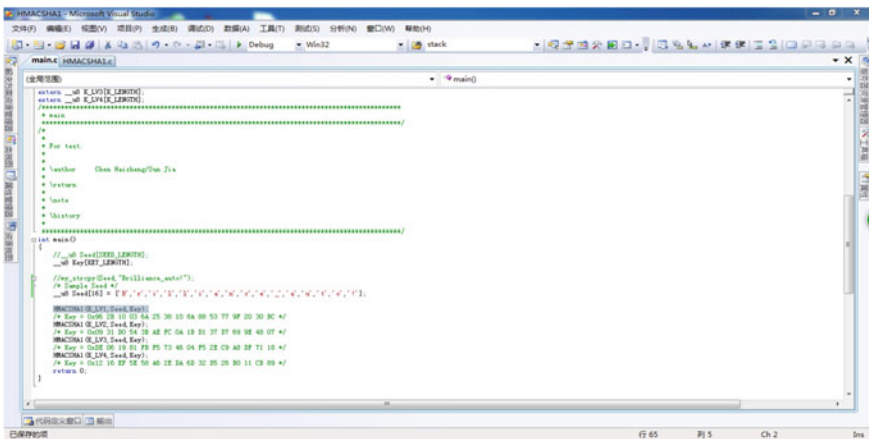


Fig. 52.3 Simulation of HMAC algorithm

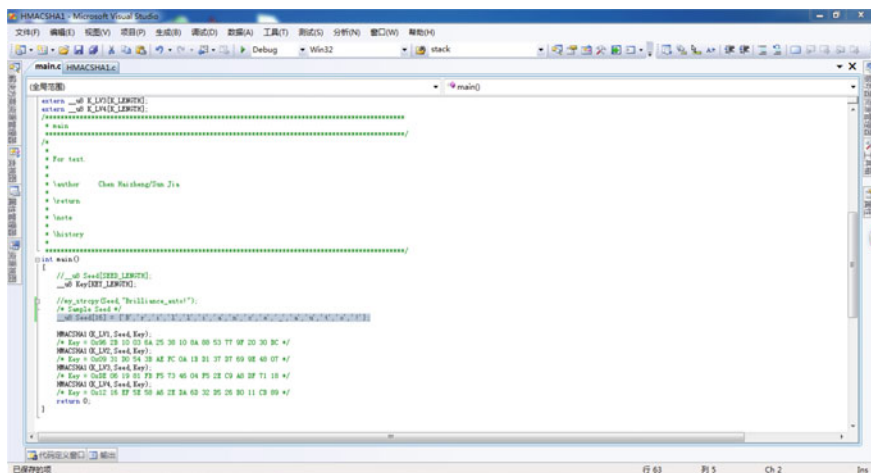


Fig. 52.4 Input of HMAC algorithm

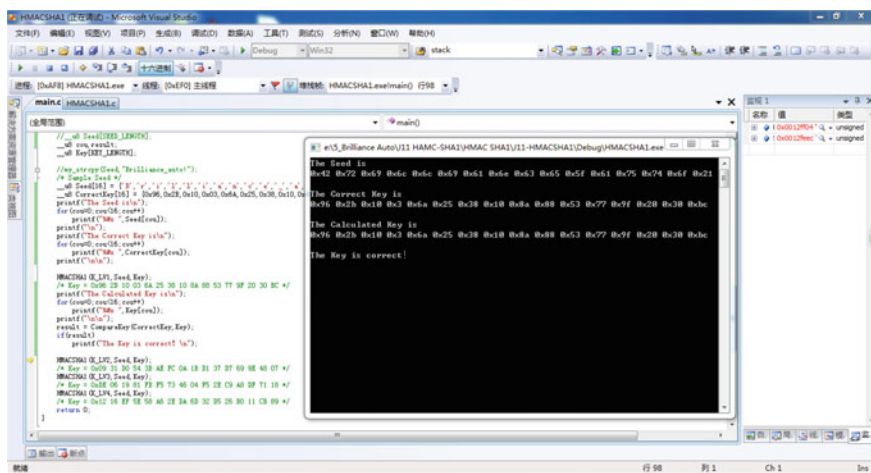


Fig. 52.5 Result of HMAC algorithm simulation

The results of both sides are the same; therefore, the simulation is successful. The security access is controlled by ECU.

52.3 Summary

The HMAC can be used as the security access algorithm by diagnostic service. The advantage of HMAC is its uniqueness and security.

HMAC-SHA1 algorithm generates 160-bit seed, it can effectively resist brute force attacks, and the algorithm has hit to reasoning through the results of the algorithm for communicating with the controller by illegal purposes.

References

1. Wang H, Lu S (2005) The journal of Shanghai Normal University. In: Message authentication mechanism based on HMAC-SHA1 algorithm, 19th edn., Shanghai
2. Bian X (2012) Vehicle diagnosis technology. Beijing Institute of Technology Press, Beijing